UNIVERSITAT POLITÈCNICA DE CATALUNYA
BARCELONATECH
Departament de Teoria del Senyal
i Comunicacions

Jorge Querol Borràs

Radio Frequency Interference Detection and Mitigation Techniques for Navigation and Earth Observation

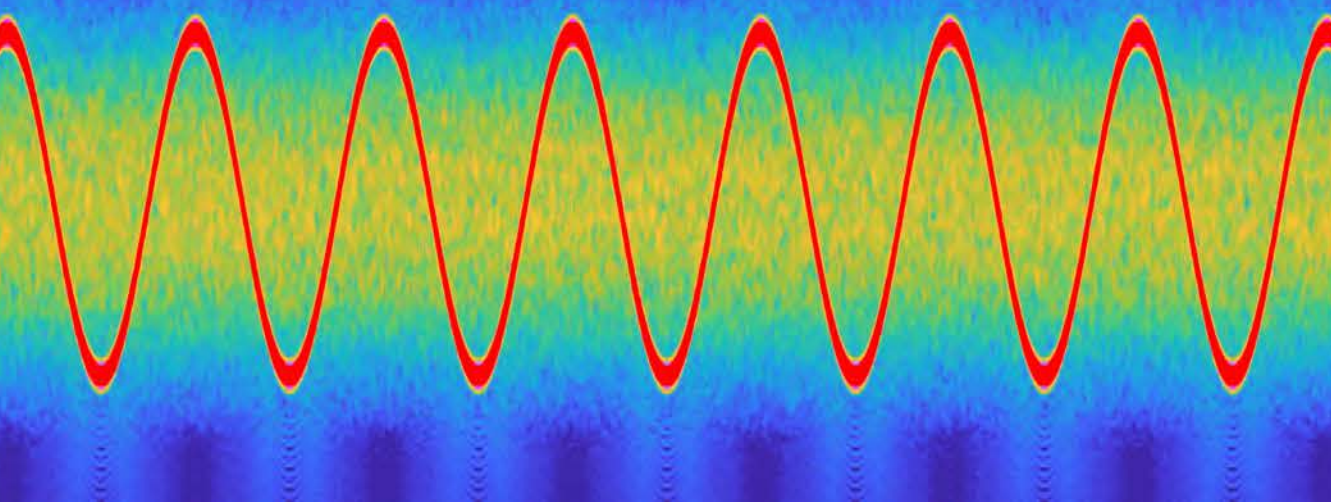

UNIVERSITAT POLITÈCNICA DE CATALUNYA BARCELONATECH

Radio frequency interference detection and mitigation techniques for navigation and Earth observation

Jorge Querol Borràs

UNIVERSITAT POLITÈCNICA DE CATALUNYA
BARCELONATECH
Departament de Teoria del Senyal
i Comunicacions

Radio Frequency Interference Detection and Mitigation Techniques for Navigation and Earth Observation

Author

Jorge Querol Borràs

Thesis Advisor

Prof. Adriano José Camps Carmona

A thesis submitted to the
Universitat Politècnica de Catalunya - BarcelonaTech (UPC)
in partial fulfillment of the requirements for the degree of
DOCTOR OF PHILOSOPHY

PhD program on Signal Theory and Communications
Remote Sensing Laboratory (RSLAB) Group
Barcelona, September 2018

Radio Frequency Interference Detection and Mitigation Techniques for Navigation and Earth Observation, *J. Querol*, PhD thesis, UPC, Barcelona, 2018.

ORCID ID: 0000-0002-8500-5534, Scopus ID: 55798789000, Researcher ID: L-4685-2014.

The author of this PhD thesis received financial support from the grant for the recruitment of early-stage research staff FI-DGR 2016 of the AGAUR / Generalitat de Catalunya.

To Alba, for her help, patience and support
To my parents, who have been always there

Acknowledgements

This PhD thesis is the result of five years of hard work. I could not achieve this goal without the contributions and support of many people. In this section, I want to say thank you to all people and entities that helped me during this journey.

First of all, I would like to express my gratitude to Prof. Adriano Camps, my PhD thesis advisor, for your support, guidance and suggestions during all these years. Thank you for the opportunity you gave me to work in your research group and to learn from your experience. You have become a mentor to me and, after all these years, I appreciate my personal and professional growth at your side. Beyond this PhD thesis, thank you for the trust you put in our business venture.

I would like to thank Dr. Giuseppe Forte for his contributions to this PhD thesis. I appreciate a lot all your advice and teachings. It was a pleasure to work with you and to follow the outstanding research you did in your PhD thesis.

Special thanks to my research colleagues and friends Raul, Alberto, Dani and Hyuk for your support during all these years. I appreciate a lot all the time we spent together discussing research topics and how much you have contributed to this PhD thesis. You have been always there in the good and bad moments. I will always remember all the coffee time moments dealing with many different topics and trying to solve the world.

Moreover, I want also to thank all people that have contributed in any way to the development of this PhD thesis. Thanks to all my former and current lab colleagues Roger, Fran, Domenico, Estefany, Jordi, Alessio, Dongliang, Joan Adrià, Juan Fran, Lara and David for the moments we have spent together. Thanks to Ricard for all the hard work you have done designing and testing the new FENIX prototype. Special thanks to Adrian for your support during the last and hard months of the PhD thesis and for your collaboration building the next FENIX prototype. Thanks to Eva, Dayal, Patrick, Adrià and José Javier, the students I have co-directed their final degree projects, for your dedication and for the trust you put on me. Thanks to Joaquim, Rubén and Albert for the technical support. Thanks Aynie, Teresa, Cristina, and Alicia for the administrative support. Thanks Josep Maria, Ferran and Jordi for the IT support. Thanks to Manel, Xavier, Eva and Jordi for the IPR and bussiness support. Thanks to Dr. Mercè Vall-llosera for your economic and administrative support. Finally, thanks to Dr. Carlos López for your advice and all the conversations we had together.

Thanks also to GMV, and in particular to Ricardo and Esteban, for your collaboration and support during the timing tests of the FENIX.

Furthermore, I would like to acknowledge all funding projects that have made possible this work. These are projects ESP2015-70014-C2-1-R “AGORA: Técnicas Avanzadas en Teledetección Aplicada Usando Señales GNSS y Otras Señales de Oportunidad”, AYA2011-29183-C02-01 “AROSA: Aplicaciones Avanzadas en Radio Ocultaciones y Dispersometría utilizando Señales GNSS y Otras Señales de Oportunidad”, AYA2010-22062-C05-05 “MIDAS-6. SMOS Productos de salinidad del oceano y humedad de la Tierra. Demostración de Mejoras y Aplicaciones. Parte UPC” from the Spanish Ministerio de Economía y Competitividad (MINECO/FEDER), project AYA2008-05906-C02-01/ESP “Sistemas GNSS-R para Futuras Misiones SMOS” from the Spanish Ministerio de Ciencia e Innovación (MICINN/FEDER), award “Passive Advanced Unit (PAU): A Hybrid L-band Radiometer, GNSS-Reflectometer and IR radiometer for Passive Remote Sensing of the Ocean” granted in 2005 by the European Science Foundation - EUropean Young Investigator (EURYI), project FP7-607126-E-GEM “European GNSS-R Environmental Monitoring” from the European Union’s Seventh Framework Programme for research, technological development and demonstration, grant Unidad de Excelencia Maria de Maeztu MDM-2016-0600 financed by the Agencia Estatal de Investigación, and projects LLAVOR (2014 LLAV 0002) and PRODUCTE (2016 PROD 00062) “FENIX - Front-End GNSS Interference eXcisor”.

Finally, I would like to thank the funding I have received to perform this PhD thesis from the grant for the recruitment of early-stage research staff FI-DGR 2016 of the AGAUR/Generalitat de Catalunya (2016FI-B00738 / 2017FI-B100072 / 2018FI-B200074).

Abstract

Radio-Frequency Interference (RFI) signals are undesired signals that degrade or disrupt the performance of a wireless receiver. RFI signals can be generated either unintentionally, mainly harmonics from lower frequency bands, inter-modulation products, and out-of-band emissions; or intentionally, commonly named jamming. RFI signals can be troublesome for any receiver, but they are especially threatening for applications that use very low power signals. This is the case of applications that rely on the Global Navigation Satellite Systems (GNSS), or passive microwave remote sensing applications such as Microwave Radiometry (MWR) and GNSS-Reflectometry (GNSS-R). Even though the existing regulations regarding the use of the spectrum, the pervasive use of wireless communications, together with the intentional hijacking of wireless receivers, makes RFI a matter of concern with a growing number of cases in the last decade.

In order to solve the problem of RFI, several RFI-countermeasures are under development. There are two main approaches: law enforcement and protection of the receivers. The former needs infrastructures able to detect and localize the source of the RFI signal in order to switch it off. The latter requires RFI detection and mitigation systems integrated into the receivers. In the literature, a number of RFI mitigation techniques have been proposed in both MWR and GNSS fields. This PhD thesis is devoted to the design, implementation and test of innovative RFI-countermeasures in both fields.

In the part devoted to RFI-countermeasures for MWR applications, first, this PhD thesis completes the development of the MERITXELL instrument. The MERITXELL is a multi-frequency total-power radiometer conceived to be an outstanding platform to perform detection, characterization, and localization of RFI signals at the most common MWR imaging bands up to 92 GHz. Moreover, a novel RFI mitigation technique is proposed for MWR: the Multiresolution Fourier Transform (MFT). An assessment of the performance of the MFT has been carried out by comparison with other time-frequency mitigation techniques. According to the obtained results, the best performance depends on the kind of RFI signal under consideration, and it occurs when the transform basis has a similar shape as compared to the RFI signal. From the results, it appears that the MFT technique is a good trade-off solution among all other techniques since it can mitigate efficiently all kinds of RFI signals under evaluation.

In the part devoted to RFI-countermeasures for GNSS and GNSS-R applications, first, a system for RFI detection and localization at GNSS bands is proposed. This system is able to detect RFI signals at the L1 band with a sensitivity of -108 dBm at full-band, and of -135 dBm for continuous wave and chirp-like signals when using the averaged spectrum

technique. This sensitivity has been achieved by using a radiometer-like architecture including a temperature stabilization system. After that, a model to evaluate the degradation of the SNR in GNSS-R measurements has been derived and validated. Besides, the Generalized Spectral Separation Coefficient (GSSC) has been proposed as a figure of merit to evaluate the Signal-to-Noise Ratio (SNR) degradation in the Delay-Doppler Maps (DDMs) due to the external RFI effect.

Given the need for RFI mitigation systems, the FENIX system has been conceived as an innovative system for RFI detection and mitigation and anti-jamming for GNSS and GNSS-R applications. FENIX uses the MFT blanking, first studied for MWR applications, as a pre-correlation excision tool to perform the mitigation. Moreover, FENIX has been designed to be cross-GNSS compatible and RFI-independent thanks to the use of the MFT, which has been proven as a good trade-off solution for RFI mitigation. First, the principles of operation of the MFT blanking algorithm are assessed and compared with other techniques for GNSS signals. Then, its performance as a mitigation tool has been proven using GNSS-R data samples from a real airborne campaign. After that, the main building blocks of the patented architecture of FENIX have been described. According to the proposed architecture, FENIX can operate in the main or auxiliary chains of a GNSS-enabled system, or it can be integrated into either the antenna or the GNSS receiver. The FENIX architecture has been implemented in three real-time prototypes. The most recent one, the FENIX-Lite, has several configurable test paths and test points that are used to validate its real-time performance. Moreover, a simulator named FENIX-Sim allows for testing its performance under different jamming scenarios.

The real-time performance of FENIX-Lite prototype has been tested using different setups. First, a customized VNA, the FENIX-Analyzer, has been built in order to measure the transfer function of FENIX-Lite in the presence of three different RFI/jamming signals, which are considered to be representative of real RFI/jamming scenarios. The results show how the power transfer function adapts itself to mitigate the RFI/jamming signal. In addition, a large but constant delay of about 1.65 ms is introduced by the inner digital signal processing blocks of FENIX. However, it can be easily calibrated and compensated. Moreover, several real-time tests with GNSS receivers have been performed using GPS L1 C/A, GPS L2C, and Galileo E1OS. The results show that FENIX-Lite provides an extra resilience against RFI and jamming signals up to 30 dB. Similar results have been obtained when direct-signal DDMs are used to assess the mitigation performance of FENIX-Lite. Furthermore, FENIX-Lite has been tested using a real GNSS timing setup. The results of these tests show that FENIX-lite provides real-time anti-jamming resilience for GNSS timing devices. Under nominal conditions, when no RFI/jamming signal is present, a small additional jitter on the order of 2-4 ns is introduced in the system. Besides, a maximum bias of 45 ns has been measured under strong jamming conditions (-30 dBm), which is still acceptable for current timing systems requiring accuracy levels of 100 ns.

Finally, the design of a backup system for GNSS in tracking applications that require high reliability against RFI and jamming attacks is proposed. Its architecture is based on one moving transmitter and multiple terrestrial stations. This minimizes the risk of being jammed. The position of the transmitter is estimated by triangulation using the Time Difference Of Arrival (TDOA) approach, while the use of Frequency-Hopping Spread-Spectrum (FHSS) modulations increases the robustness against jamming attacks.

Contents

List of Acronyms

A-D Anderson-Darling

ADC Analog-to-Digital Converter

ADP Amplitude Domain Processing

AF Ambiguity Function

AGC Automatic Gain Control

AMSR-E Advanced Microwave Scanning Radiometer for the Earth Observing System

ASIC Application Specific Integrated Circuit

BAM-KLT Bordered Auto-correlation Method - KLT

BB Base-Band

BPF Band-Pass Filter

CAF Cross-Ambiguity Function

CCC Circular Cross-Correlation

CDF Cumulative Density Function

CDMA Code Division Multiple Access

cGNSS-R conventional GNSS-R

CIR Color-Infrared

CLT Central Limit Theorem

CommSensLab Remote Sensing, Antennas, Microwaves and Superconductivity group

CPI Cross-Polarization Isolation

CSAC Chip Scale Atomic Clocks

CW Continuous Wave

CWAF Cross-WAF

CWGN Complex White Gaussian Noise

DAC Digital-to-Analog Converter

DCM Digital Clock Manager

DDM Delay-Doppler Map

DDMs Delay-Doppler Maps

DDS Direct Digital Synthesizer

DFT Discrete Fourier Transform

DME Distance Measurement Equipment

DOA Direction Of Arrival

DSP Digital Signal Processing

DSSS Direct Sequence Spread Spectrum

DUT Device-Under-Test

DWT Discrete Wavelet Transform

EAF Expected Ambiguity Function

ECEF Earth-Centered, Earth-Fixed

eLORAN enhanced LORAN

EMI Electromagnetic Interference

ESNC European Satellite Navigation Competition

ETSI European Telecommunications Standards Institute

FB Frequency Blanking

FDMA Frequency Division Multiple Access

FFT Fast Fourier Transform

FHSS Frequency-Hopping Spread-Spectrum

FIFO First-In First-Out

FIR Finite Impulse Response

FOV Field of View

FPGA Field Programmable Gate Array

GFSK Gaussian Frequency-Shift Keying

GNSS Global Navigation Satellite Systems

GNSS-R GNSS - Reflectometry

GPS Global Positioning System

GPSPDO GPS Pseudo-Disciplined Oscillator

GSA European GNSS Agency

GSSC Generalized SSC

GUI Graphical User Interface

HUTRAD Helsinki University of Technology RADiometer

I/Q In-phase and Quadrature

ID Identification

IF Intermediate Frequency

iGNSS-R interferometric GNSS-R

IIR Infinite Impulse Response

INR Interference-to-Noise Ratio

IPR Intellectual Property Rights

IQR Inter-Quartile Range

ITU International Telecommunication Union

KLT Karhunen-Loève Transform

LAURA L-band AUtomatic RAdiometer

LHCP Left-Hand Circular Polarization

LLN Law of Large Numbers

LMS Least-Mean-Squares

LNA Low Noise Amplifier

LO Local Oscillator

LORAN LOng RAnge Navigation

L-RARO L-band Radiometer-based system for RFI Observations

MAD Median Absolute Deviation

MALYGNSS Multiband Airborne L-band reflectometrY with GNSS

MBE Main Beam Efficiency

MERITXELL Multifrequency Experimental Radiometer with Interference Tracking for EXperiments over Land and Littoral

MFT Multiresolution Fourier Transform

MIR Microwave Interferometric Reflectometer

MIRAS 2D Microwave Imaging Radiometer with Aperture Synthesis

MP Mitigation Performance

MWR Microwave Radiometry

NBB Normalized Blanking Bias

NEB Noise Equivalent Bandwidth

NEU North-East-Up

NF Noise Figure

NIR Near-Infrared

NRB Normalized Resolution Bias

NTP Network Time Protocol

OFDM Orthogonal Frequency Division Multiplexing

OMT Orthomode Transducer

PB Pulse Blanking

PDF Probability Density Function

PID Proportional Integral Derivative

PLC Programmable Logic Controller

PLL Phase-Locked Loop

PNT Positioning, Navigation and Timing

PPD Personal Privacy Device

PPS Pulse Per Second

PR Pseudo-Range

PRF Pulse Repetition Frequency

PRN Pseudo-Random Noise

PSD Power Spectral Density

PSR Polarimetric Scanning Radiometer

PTP Precision Time Protocol

PVT Position, Velocity and Time

PYCARO P(Y) and C/A ReflectOmeter

q Quantile

RBW Resolution Bandwidth

RD Resolution Degradation

RED Radio Equipment Directive

RF Radio Frequency

RFI Radio-Frequency Interference

RFIs RFI signals

RGB Red-Green-Blue

RHCP Right-Hand Circular Polarization

RMS Root Mean Square

ROC Receiver Operating Characteristic

RTS Robust Tracking System

SA Spectrum Analyzer

SB Spectrogram Blanking

SDR Software Defined Radio

SES Satellite Earth Stations and Systems

SFDR Spurious-Free Dynamic Range

SIR Signal-to-Interference Ratio

SL Sample Loss

SMA Sub-Miniature version A

SMOS Soil Moisture and Ocean Salinity

SNR Signal-to-Noise Ratio

SP Signal Processing

SPDT Single-Pole Dual-Through

SSC Spectral Separation Coefficient

SSMI/S Special Sensor Microwave Imager/Sounder

STFT Short-Time Fourier Transform

TACAN TACtical Air Navigation system

TDOA Time Difference of Arrival

TF Time-Frequency

TFG Final Degree Project

TIC Time Interval Counter

TIR Thermal Infrared

TOA Time Of Arrival

TPR Total Power Radiometer

TSC Signal Theory and Communications

TXCO Temperature-Compensated Crystal-Oscillator

UART Universal Asynchronous Receiver-Transmitter

UPC-BarcelonaTech Univesitat Politècnica de Catalunya - BarcelonaTech

USRP Universal Software Radio Peripheral

UTC Coordinated Universal Time

UWB Ultra-Wide-Band communications

VBW Video Bandwidth

VIS/IR visible/infrared

VNA Vector Network Analyzer

WAF Woodward's Ambiguity Function

WD Wavelet Denoising

WGN White Gaussian Noise

WPD Wavelet Packet Decomposition

WR White Rabbit

WT Wavelet Transform

WVD Wigner-Ville Distribution

WVS Wigner-Ville Spectrum

Z-V Zavorotny-Voronovich

List of Figures

List of Tables

Part I

Introduction and state of the art

1

Chapter 1
Introduction

This Chapter presents the introduction, background, motivation, goals, and outline of this PhD thesis. Moreover, the framework in which this PhD thesis has been developed is also described. First, the problem of RFI is introduced from a general point of view, and its importance in the specific fields of GNSS and Earth Observation. After that, the background of the PhD thesis is stated. This PhD thesis integrates some elements of the previous works done by the research team which are essential to the fulfilment of its main goals. Finally, the motivation and goals of the PhD thesis are explained. The Chapter ends with a description of the structure and main contents of each Chapter of this PhD thesis.

1.1 The RFI problem

Radio-Frequency Interference (RFI) is usually defined as the phenomenon that occurs when RF energy radiated by an external source causes a malfunction of an electronic device. By extension of this definition, RFI signals (RFIs) are those RF waves that create such a malfunction. Besides that, the term Electromagnetic Interference (EMI) has a broader meaning and it is used to refer to any disturbance produced by either radiated, coupled or conducted electromagnetic energy. Thus, RFI is technically used to describe radiated EMI events, although both terms are used interchangeably in the literature. Furthermore, the term self-interference, or self-RFI, is used when the electronic device is malfunctioning due to RFIs generated by itself.

RFIs can produce a wide range of abnormal effects in the affected electronic devices, from performance degradation, data corruption, or increase in error rate, to complete disruption of its operation. They can be found anywhere since they are generated by most electronic and electrical devices like switching power sources, industrial motors, instrumentation, smartphones, personal computers, laptops, game consoles, computing servers, Wi-Fi devices, Bluetooth devices, cordless telephones, microwave ovens, light-bulbs, etc. Moreover, the consolidation of mass-market wireless communication devices together with the increasing demand for wider bandwidths of operation have fostered the problem of RFI in an overcrowded frequency spectrum. The U.S. frequency allocations chart (Figure 1.1) gives a qualitative indication of the high occupancy of the RF spectrum and, therefore, of the risk of interference between services. In addition, the European Table of Frequency Allocations [1] shows also the high number of reserved bands for different the services in the spectrum from 8.3 kHz to 3 THz.

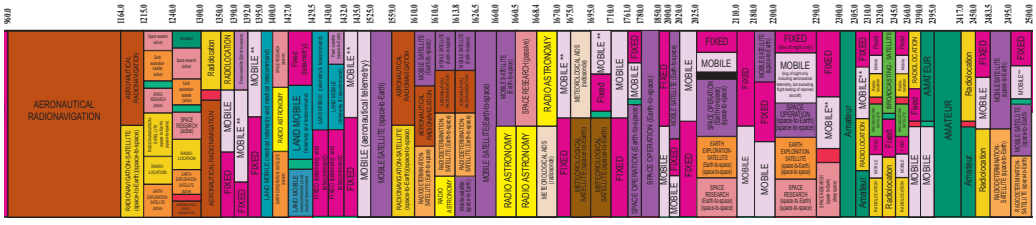

Figure 1.1: United States radio spectrum frequency allocations chart provided by the U.S Department of Commerce, National Telecommunications and Information Administration, Office of Spectrum Management. Capture of allocated services from 960 MHz to 2500 MHz as of January 2016. Extracted from `https://www.ntia.doc.gov/files/ntia/publications/january_2016_spectrum_wall_chart.pdf`

The radio spectrum regulatory authorities of each country are responsible for limiting the amount of energy that can be transmitted in the allocated frequency bands. However, signals from out-of-band emissions, harmonics or inter-modulation products of other frequency bands can easily affect the signal causing receiver desensitization. This makes the phenomenon of RFI to be one of the most important problems for regulatory authorities, but even more important for users of critical applications which reliability or security may be compromised due to RFIs.

The scarcity of spectrum has triggered the need for new standards for wireless devices.

In Europe, the Radio Equipment Directive (RED) 2014/53/EU establishes a regulatory framework for placing radio equipment on the market, with standards defining minimum coexistence and compatibility requirements for all radio devices. The European Telecommunications Standards Institute (ETSI) is currently laying down RED standards for the different categories of wireless devices. One of the standards under development is the ETSI EN 303 413, which is a European Harmonised Standard for Satellite Earth Stations and Systems (SES) and GNSS receivers.

High-quality electronic devices should include proper shielding in their enclosure which may help to control RFI emissions. However, as our lives become filled with more and more technology gadgets, the likelihood of suffering from RFI increases, either because the devices are manufactured with low-quality standards, they are not properly designed, or they have improper shielding. This last case makes the device prone to generate out-of-band emissions due to, for example, a lack of rejection filters at its output. In the case of communications, the use of highly directional antennas can also help to control the RFI problem. However, if both communications and RFI signals have the same direction of arrival, the problem still exists.

RFI can be troublesome for any kind of receiver, but especially for those systems that work with very low power signals. Two outstanding examples are Global Navigation Satellite Systems (GNSS) and Microwave Radiometry (MWR). GNSS are used in critical civilian and military applications, mainly in Positioning, Navigation and Timing (PNT) applications, and more recently in Earth observation as signals of opportunity in a sort of a bistatic radar (e.g. GNSS - Reflectometry (GNSS-R) or radio occultation). Despite almost all signals transmitted by GNSS satellites are spread-spectrum with an inherent protection to interference [2], it is not difficult to jam GNSS signals. For this reason, the International Telecommunication Union (ITU) assigned several protected frequency bands to both GNSS and MWR and set maximum interference power levels that should be controlled by the laws of each country [3].

Even though the most recent radio communication protocols include some techniques against RFIs, sometimes they are not powerful enough to deal with the increasing problem of RFI. Recently, several signal processing methods have been developed to detect and mitigate RFIs in navigation and Earth observation applications such as time and frequency domain analysis, statistical analysis or spatial adaptive filtering. Some of the techniques have already been implemented in real systems, but they do not offer a significant RFI rejection ratio or are only devoted to one particular case of RFIs. Despite most of the algorithms and mathematical models are well known in signal processing, the true step forward is to find out how to combine them together in order to maximize the RFI rejection without a priori knowledge of the interference signal.

1.2 Background

This PhD thesis has been carried out at the passive microwave remote sensing team of the Remote Sensing, Antennas, Microwaves and Superconductivity group (CommSensLab) at the department of Signal Theory and Communications (TSC) of the Univesitat Politècnica de Catalunya - BarcelonaTech (UPC-BarcelonaTech). This research team has a long experience in three main topics: synthetic aperture interferometric MWR, GNSS-R, and

RFI detection and mitigation in the field of passive microwave remote sensing. The problem of RFI is a transversal topic that affects both MWR and GNSS-R techniques, and it has been addressed in parallel to the research developed in both fields.

One of the most important contributions of the research team to the field of MWR was the development of the 2D Microwave Imaging Radiometer with Aperture Synthesis (MIRAS) [4]. MIRAS is the instrument on-board the Soil Moisture and Ocean Salinity (SMOS) mission [5] that generates brightness temperature images from which the retrieval of the geophysical variables is performed. The instrument receives the radiation emitted from Earth's surface, which can then be related to the moisture content in the first few centimetres of soil over land, and to salinity in the surface waters of the oceans.

The research team has been involved in the SMOS mission since its proposal, and in the conception of the MIRAS payload back to 1993. Many field experiments related to soil moisture and ocean salinity retrieval have been performed by the group in the framework of the SMOS activities before and after its launch in 2009.

Regarding the research performed in the field of GNSS-R, the research team has been one of the pioneers, and a world reference in the study and development of theoretical concepts, instruments and missions. Two outstanding achievements in the GNSS-R field are the ^{3}Cat2 mission and the Microwave Interferometric Reflectometer (MIR) instrument.

^{3}Cat2 is a 6-unit CubeSat mission to explore fundamental issues toward an improvement in the understanding of the bistatic scattering properties of different targets [6]. This spacecraft carries the P(Y) and C/A ReflectOmeter (PYCARO) main payload, which performs GNSS-R measurements using signals from multiple constellations (GPS, GLONASS, Galileo, and Beidou) at dual-band (L1 and L2) and dual-polarization (right- and left-hand circular polarization), over the ocean, land, and cryosphere. 3Cat-2 was launched for the August 15th, 2016 into a sun-synchronous orbit of 510-km height.

The MIR is an instrument conceived to compare advanced GNSS-R techniques, and to assess the capabilities of new signals and bands of GPS and Galileo systems. The MIR instrument is a dual-band reflectometer with two arrays, a zenith-looking RHCP for the direct signal, and a nadir-looking LHCP for the reflected one. Each array has 19 dual-band patch antennas hexagonally distributed. The antennas have 30 MHz bandwidth at L1/E1 and 25 MHz at L5/E5 and two linear polarizations [7]. The MIR validation campaign took place from April to June 2018 in Melbourne, Australia.

At CommSensLab, the problem of RFI has been particularly addressed in two previous PhD theses. The first one is titled "Radio Frequency Interference in Microwave Radiometry: Statistical Analysis and Study of Techniques for Detection and Mitigation" [8], which was defended in 2012. It deals with the development, testing and comparison of different RFI detection and mitigation algorithms based on several methods, such as time and frequency domain, wavelet and statistical analysis of the retrieved MWR signal. The second PhD thesis devoted to RFI was titled "Contributions to Radio Frequency Interference Detection and Mitigation in Earth Observation" [9], which was defended in 2014. It shows different RFI surveys in time, frequency and space; and it performs the development of different RFI detection and mitigation methods for MWR and GNSS-R.

This PhD thesis is the natural continuation of the two above mentioned PhD theses, and it also follows the future work proposed in the MSc thesis titled "Implementation of

Radio-Frequency Interference Detection and Mitigation Algorithms for Communications and Navigation" [10]. This MSc thesis deals with the implementation of an anti-jamming hardware for Global Positioning System (GPS) receivers combining time-frequency analysis and statistical filtering using normality test and robust estimation, to take profit of the best properties of each one of them.

In [10], a prototype system for RFI detection and mitigation was developed and tested with very promising results. The prototype was based on the application of the known techniques used in the field of detection and mitigation. However, its most innovative aspect was the way in which these techniques were combined in order to maximize rejection of the RFI signals. This real-time algorithm was implemented on a Field Programmable Gate Array (FPGA) device using an evaluation board for the analog to digital conversions. This algorithm can be summarized in two steps.

1. A digital bandpass filter that attenuates interference outside the corresponding band.

2. An adaptive threshold determines if the samples are contaminated with interference removing them and keeping the RFI-free signal.

The prototype was tested by connecting a commercial GPS receiver signal with a corresponding external antenna, together with an interference signal generator or jammer commercially available. In the presence of the jamming signal, the GPS receiver was not able to calculate the position from the contaminated signal. In contrast, when applying the mitigation algorithm, the GPS receiver was able to operate properly. Nevertheless, the prototype had several drawbacks such as it cannot mitigate Continuous Wave (CW) RFIs.

1.3 Motivation

I joined the research group lead by Prof. Adriano Camps in 2012 as an MSc student. The first contact I had with the field of RFI was as a firmware engineer developing the signal processing algorithm for a wavelet-based RFI mitigation system first published in [11], and included in the PhD thesis of Dr Giussepe Forte [9, Chapter 4]. This system was devoted to MWR applications, and it was implemented in an FPGA-based hardware back-end. The RFI signal was estimated by using the denoising capabilities of the wavelet transform, and then it is subtracted from the overall received signal to obtain an RFI-mitigated signal.

With this experience, I started working on my MSc thesis [10] devoted to develop an RFI mitigation system for GNSS applications. As mentioned above, the outcome of this work was a real-time anti-jamming system that combines time, frequency and statistical techniques. This work was also included in [9, Chapter 5] since Dr Giuseppe Forte co-directed my MSc thesis.

Given the strong background in the field of RFI held by the research team, I decided to start my PhD thesis following the work that was already done during my MSc thesis. Moreover, the topic of RFI was by that time a trending topic in passive remote sensing and GNSS fields, and it still is by the time of writing this PhD thesis. Since the beginning

of my MSc thesis, my interest in developing systems at the University envisioning their future deployment in the market has been there.

1.4 Goals

The main objective of this PhD thesis contributes to the development and implementation of RFI-countermeasures (detection, localization, and mitigation) for GNSS-enabled and Earth observation applications. In particular, GNSS-enabled applications include PNT, whereas Earth observation applications refer to GNSS-R and MWR. Moreover, this PhD thesis aims to describe the whole development process which includes theoretical analysis, understanding of the underlying mathematical processes used in RFI detection and mitigation techniques, algorithm simulation, real-time implementation of signal processing algorithms, RF hardware development, validation tests, and real scenario tests of such techniques.

The particular objectives of this PhD thesis are described below:

- To perform a comprehensive RFI survey at several frequency bands used in MWR to extend results presented in [9].
- To understand which are the effects of RFIs in GNSS-based instruments. Besides that, to study how RFIs affect the performance of GNSS-R instruments in terms of Signal-to-Noise Ratio (SNR) degradation.
- To assess the characteristics of the RFIs that represent the main threats for MWR and GNSS-enabled applications. This includes kinds of signal, usual sources, origin, intention, and type of effects caused to the RF receiver.
- To assess the state of the art of RFI detection and mitigation techniques, and to propose new methods, algorithms and techniques that can be used in real-time applications.
- To perform a comparison of different RFI mitigation techniques, both new and already existing, in order to determine their performance against most common kinds of RFIs.
- To design, implement and test a real-time RFI detection and localization system for GNSS bands.
- To design, implement and test a real-time RFI mitigation system for GNSS-enabled applications.
- To design, implement and test a tracking system for high-reliability applications, complementary to GNSS.

Moreover, this PhD thesis has some extra goals related to the commercial exploitation of the developed systems. Design and implementation of almost all systems are market-oriented. They have been conceived as first prototypes of potential future products. This is the main reason to develop systems that can work in real-time, but they can also be used in off-line applications.

1.5 Outline

This PhD thesis has been divided in a total of six parts which contain twelve chapters with the main contributions of the PhD thesis, a number of appendices with complementary information, and the bibliography of the list of publications. The outline of this PhD thesis is the following:

– Part I: Introduction and state of the art.

  - Chapter 1 introduces the problem of RFI and the need for developing RFI-countermeasures for GNSS-enabled applications and passive remote sensing techniques such as MWR. Then, the background of this PhD thesis is stated including previous work developed in the research group. After that, the motivation and goals of this PhD thesis are described. Finally, the outline of this PhD thesis is stated.

  - Chapter 2 describes the problem of RFI in the specific fields of MWR, GNSS and GNSS-R. RFIs are a threat for these applications due to the very low power of the signals used in each case. Some initial consideration regarding the source, type, and effects of the most common RFIs are introduced in this chapter. Furthermore, some real cases of RFI occurrences are presented as examples of the impact of the RFI on GNSS and Earth observation.

  - Chapter 3 is a revision of the state-of-the-art RFI mitigation detection and mitigation techniques. The majority of these techniques have been developed for MWR and GNSS applications, but also radio-astronomy or deep-space communications.

– Part II: RFI countermeasures for MWR applications.

  - Chapter 4 describes an RFI detection and localization system for MWR, as well as its calibration process, and the RFI survey performed at all its frequency bands. This system is based on a ground-based multisensor architecture that includes a multiband dual-polarization radiometer, a GNSS reflectometer, and several optical sensors. Moreover, the control and measurement system of the multiband microwave radiometer is described.

  - Chapter 5 describes a new technique for RFI mitigation in MWR applications. The performance of this technique is compared to other time-frequency RFI mitigation techniques. This comparison is done in terms of probability of mitigation, sample loss, and mitigation performance. Moreover, the use of the blanking approach as thresholding solution is discussed.

– Part III: RFI countermeasures for GNSS/GNSS-R applications.

  - Chapter 6 is devoted to the design and test of an instrument capable of detecting and localizing RFI signals at GNSS bands using a microwave radiometer architecture, and a combination of statistical and time-frequency digital detection techniques. The instrument has been tested using different kinds of RFI signals. Moreover, its performance has been evaluated as a function of the RFI power.

  - Chapter 7 describes how the presence of RFI signals affects GNSS-R measurements. The SSC is the standard figure of merit used to evaluate the SNR degradation due to RFI in GNSS applications. However, an in-depth assessment in the field of GNSS-R

has not been performed yet. A new figure of merit to evaluate the degradation of GNSS-R measurements in the presence of any RFI signal.

- Chapter 8 contains the introduction and description of an RFI mitigation and anti-jamming system conceived, designed and built to protect GNSS and GNSS-R systems. In particular, it introduces the need for the existence of anti-jamming systems, the requirements that are taken into account during its design, it assesses its performance as compared to other RFI mitigation techniques, and it presents an example of its application to real GNSS-R data.
- Chapter 9 describes the hardware implementation of the RFI mitigation system as well as the validation of its performance. The main building blocks of its patented architecture are described. Moreover, the three real-time prototypes of this anti-jamming system implemented during this PhD thesis are presented. Furthermore, its performance has been validated by comparing the real and theoretical performance results.
- Chapter 10 is devoted to the assessment of the real-time performance of the last prototype of the RFI mitigation system. This assessment has been done for three RFI/jamming scenarios representative of real cases. Besides, the power response and phase response of the system are measured using a custom and precise setup. After that, its real-time mitigation performance is assessed using real GNSS and jamming signals. Finally, it is tested together with a commercial GNSS-enabled timing setup.
- Chapter 11 is devoted to the design, implementation and test of a robust tracking system. The main goal of this system is to be resilient to RFI and jamming attacks and to be a backup solution for GNSS in high-critical tracking applications. To do so, the system combines hyperbolic navigation with spread-spectrum signal modulations. Thus, a comparison of the different spread-spectrum modulations is performed in order to find out the most resilient solution. Moreover, a hardware implementation of the system is proposed. Finally, preliminary results of its performance are presented and discussed.

– Part IV: Conclusions, contributions and future work.

- Chapter 12 states the main conclusions and contributions of this PhD thesis. Moreover, it presents the proposed future research lines derived from this work. Finally, there is a summary of the technology transfer actions performed during this PhD thesis.

– Part V: Appendices.

– Part VI: Bibliography and list of publications.

2

Chapter 2

RFI in GNSS and Earth observation

This Chapter describes the problem of RFI in the specific fields of MWR, GNSS and GNSS-R. RFIs are a threat for these applications due to the very low power of the signals used in each case. Some initial consideration regarding the source, type, and effects of the most common RFIs are introduced in this chapter. Furthermore, some real cases of RFI occurrences are presented as examples of the impact of the RFI on GNSS and Earth observation.

2.1 Introduction

This chapter introduces the reader to the problem of RFI in GNSS for PNT applications, and Earth observation techniques, in particular, MWR and GNSS-R. The presence of RFI signals is very critical in this particular applications mainly because of the low power level of the signals involved in these cases. There are two other cases where this also applies. They are radio-astronomy and deep-space communications. The RFI-countermeasures used in these four cases (GNSS, MWR, radio-astronomy, and deep-space communications) are very similar according to the literature. The contents of this PhD thesis are focused on GNSS and MWR applications. However, most of them also apply to radio-astronomy and deep-space communications.

This chapter includes some considerations about the origin and effects of RFI signals. Then, there is a brief description of what is MWR and some relevant RFI cases. After that, there is a brief introduction to GNSS and GNSS-R, as well as some examples of RFI signals at GNSS bands.

The contents of this chapter have been partially presented in the conference paper titled "Study of RFI signals in protected GNSS bands generated by common electronic devices: Effects on GNSS-R measurements" [12].

2.2 Considerations about RFIs

As mentioned in Chapter 1, the electromagnetic spectrum is becoming more and more used due to the ubiquitous presence of wireless electronic devices emitting and receiving electromagnetic radiation. This fact fosters the appearance of RFI which is becoming a trending topic in satellite navigation safety and Earth observation research [8–10, 12].

The origin of RFIs may be intentional or unintentional. Most common unintentional sources are spurious or harmonic signals of lower frequency bands, inter-modulation products, broadband signals overlapping reserved bands of operation, and out-of-band emissions. Furthermore, the number of candidate sources to become unintentional RFIs, is large and growing [3].

Frequently, unintentional RFI signals radiated by electronic devices have a power comparable to or even larger than the GNSS signals themselves. In [12], some examples of how RFI signals generated by common electronics used in GNSS-R devices (e.g. computers or high-speed buses) may introduce a bias in the measurements were provided. Moreover, these errors, that may be only a few decibels, may have a dramatic effect when they are translated into scientific variables (i.e. ocean altitude, soil moisture...) [13].

Moreover, RFIs can also be intentionally used for radio jamming, as in some forms of electronic warfare, threatening the integrity of applications based on RF devices. From several studies [9, 14], it emerges that most of the commercial jammers usually employ linear frequency modulated signals (i.e. chirp signals) which sweep in a range of several megahertz in a few microseconds affecting the entire band targeted by the device. A jammer can be purchased for a low price on the Internet (about 30 €) under the name of Personal Privacy Device (PPD).

Generally, two types of RFI effects can be identified in radio receivers: in-band interference

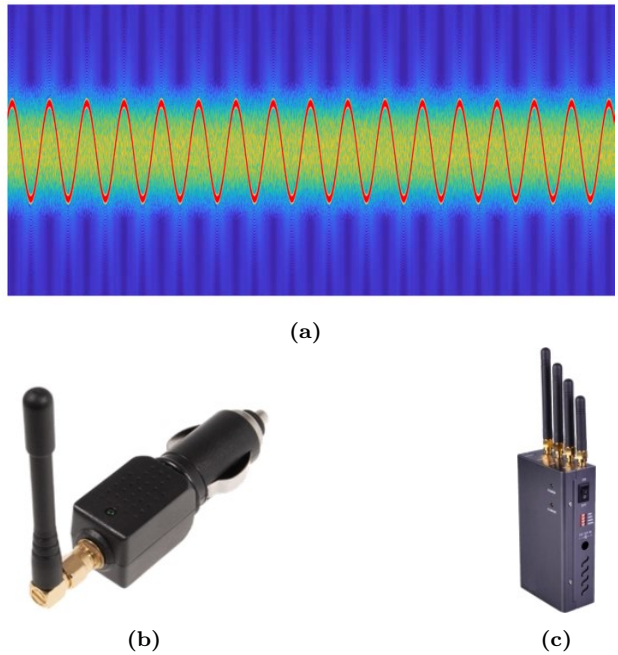

Figure 2.1: (a) A chirp signal is the typical waveform generated by commercial jammers. (b) Single-band commercial jammer with 12V car power supply. (c) Multi-band commercial jammer.

and near-band interference. The former contributes unexpectedly to the rise of noise floor and desensitizes RF receivers. The latter might interfere with proper reception through saturation of the RF detector or insufficient RF filter rejection.

In order to solve the problem of RFI, it must be addressed from both sides: law enforcement against RFI emitters, and increased robustness of GNSS receivers by using RFI mitigation techniques. On one hand, law enforcement requires more than bureaucracy. It requires systems capable of detecting RFI signal emissions in real time, with high sensitivity, and in a wide area. In addition, they must be able to locate the emitter accurately, in order to allow the authorities to find it, to disable it, and to enforce the law. On the other hand, GNSS receivers must be equipped with RFI mitigation techniques that counteract against the effect of RFI signals, and allow the receiver to keep working even under RFI conditions.

As mentioned above, remote sensing techniques used for Earth observation are very prone to suffer the RFI phenomenon due to the low power signals which they have to deal with. In particular, microwave radiometry and GNSS-R are of main concern.

On one hand, microwave radiometry is routinely used today to obtain a number of geophysical parameters. Since it measures the thermal noise power, microwave radiometers are highly sensitive, accurate, and passive instruments. RFI signals do not only concern microwave radiometers, although they are more prone to suffer from RFI since they are passive sensors. However, filtering out a frequency band implies that these frequencies

can no longer be observed by the instrument. Attempts have been made to detect and mitigate the presence of RFI in radiometers using digital signal processing [8, 11, 15].

On the other hand, GNSS Reflectometry (GNSS-R) is an innovative remote sensing approach based on the measurement and characterization of GNSS signals reflected over the Earth surface, with some advantages regarding the traditional techniques [16]. The increasing interest in GNSS-R has raised the need for developing specific algorithms to detect and mitigate RFIs in GNSS bands that, at the same time, must be able to deal with the very low power of these signals. The maximum RFI power set by the international regulations was designed to guarantee a maximum degradation of the signal to noise ratio (SNR) enough for PNT applications (i.e. navigation accuracy), but they may be critical for GNSS-R applications. For this reason, the development of the RFI detection and mitigation techniques is a matter of special interest in the GNSS-R field.

2.3 Microwave Radiometry

MWR is the science of the measurement of the noise emitted by bodies at a physical temperature higher than zero Kelvin. From these measurements, a number of geophysical parameters can be retrieved such as soil moisture, sea surface salinity, and atmospheric water vapour among others [17]. Microwave radiometers are among the most sensitive instruments, as they are designed to fulfil stringent requirements. The detailed information regarding the physical principles of microwave radiometry, the quantum theory of radiation, the Stefan-Boltzmann law for the black-body radiation, and the definition of brightness temperature can be found in [17, 18].

One of the most successful cases in the history of MWR is the SMOS mission [5]. As its name indicates, SMOS is dedicated to the observation of the surface soil moisture and the ocean salinity. The scientific payload consists of a two-dimensional passive radio-interferometer observing the Earth natural thermal noise radiating at the frequency of 1413 MHz within a narrow 17 MHz bandwidth. This frequency has been chosen both for its high sensitivity to the targeted geophysical parameters but also because it belongs to the ITU protected 1400–1427 MHz band reserved for passive applications only. This ensured that pure and clean observations of the very low-level energy radiated from the Earth thermal noise were available to retrieve the soil moisture and the ocean salinity with the expected quality.

However, MWR suffers from RFI at almost all bands, boosted by the pervasive use of wireless communications. This implies that any unexpected signal, apart from the radiometric noise, present at the same radiometric band under analysis, causes a positive bias on the final power measurements. There is a huge number of documented cases of RFI in MWR applications. Two examples of them are the case of SMOS described in [19], and the case of AMSR-E described in [20].

In [21], an RFI survey from the SMOS processing chain was presented. It illustrates the impact of RFIs on level 2 soil moisture products. Figure 2.2 shows two maps of RFI probability of occurrences obtained from SMOS observations both for ascending orbits and descending orbits. The colour-scale represents the probability from 0 (blue) to 1 (red) to detect an RFI occurrence over a 15-day window. These maps give a clear view

of which is the current impact of RFI signals on L-band microwave radiometers.

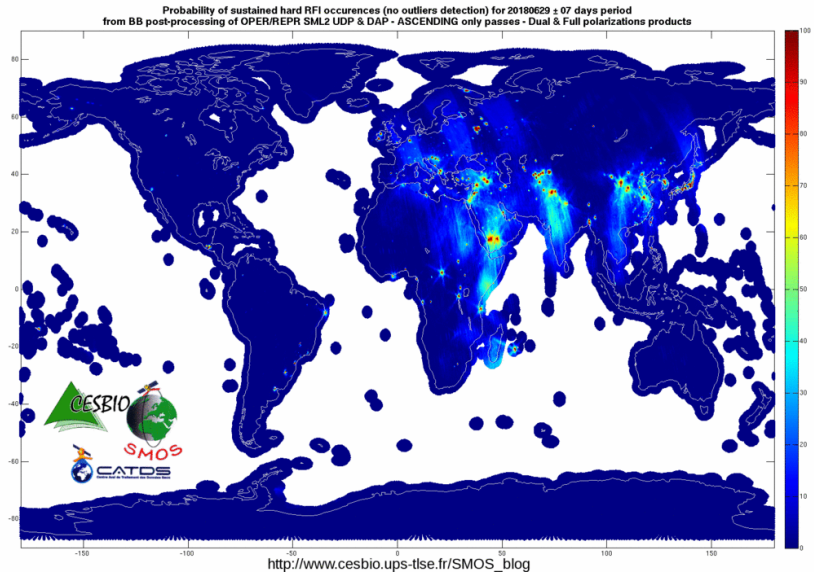

(a)

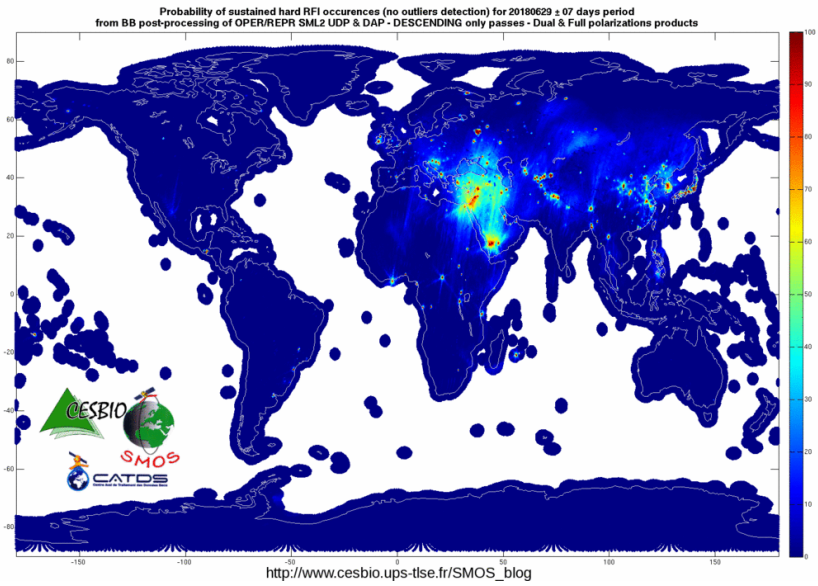

(b)

Figure 2.2: Maps of RFI probability of occurrences obtained from SMOS observations: a) for ascending orbits, and b) for descending orbits. The color-scale represents the probability from 0 (blue) to 1 (red). These maps are for the 10th of July, 2018, integrated over a 15-days window, and their updated versions can be found in `http://www.cesbio.ups-tlse.fr/SMOS-blog/`

In recent years, many studies have been done in order to solve the problem of RFI in MWR. Algorithms for RFI localization are being developed to find and switch the RFI sources off (e.g. [22]). Another approach to solve the RFI problem is the development of RFI detection and mitigation techniques, in order to deal with the RFI problem from the receiver side. There are many different approaches for RFI detection and mitigation that have been developed for microwave radiometry such as time-frequency blanking [23, 24], normality tests [25, 26] or polarimetric analysis [27, 28] among others.

The scope of this PhD thesis regarding MWR is focused on real-aperture radiometers. The application to synthetic aperture radiometers is straightforward if each element is seen as a single real-aperture radiometer, and cross-correlations are with all or a subset of the number of quantification bits (typically 8 or more) used in the mitigation process.

2.4 GNSS

Nowadays, most of the applications that require positioning and navigation services use GNSS, which have many strengths, but also some weaknesses. The power levels used in GNSS are extremely low, several dB below the background noise level, which make them very sensitive and vulnerable to the presence of any interference, either from intentional or spontaneous nature. For instance, in the GPS, the most popular and widely used among GNSS, a minimum power level, around -130 dBm, is guaranteed for GPS L1 C/A signals. Therefore, the power level at the receiver is approximately 20 dB below the thermal noise level, much weaker compared to other signals produced by the human being and of similar magnitude to the radiation coming from the outer space [3].

The use of GNSS for navigation purposes is implicit in its name. GNSS is a key technology in aviation which may be used as a complementary system in all phases of flight, in contrast to other traditional navigation solutions. Furthermore, GNSS is also used in other critical applications and emergency services for communication and temporal synchronization. Other examples include police, fire services or rescue corps.

The global time reference known as Coordinated Universal Time (UTC) is derived from hundreds of caesium clocks located at different calibration laboratories and synchronized with the time reference from GPS satellites. The stability of the reference GPS clocks is approximately about $2 \cdot 10^{-14}$ seconds, so that, it is widely used for synchronization of nodes in any network even if it requires a very high precision. The great advantage of using the GPS signal instead other traditional systems is that all nodes in the network have direct access to the primary synchronization signal. This enforces the use of GNSS for applications that require a high degree of synchronization across a wide geographic area. Such applications include electrical supply networks, telecommunication networks, astronomy tasks and banking transactions.

The operation of GNSS systems is based on synchronized Time Of Arrival (TOA) measurements. GNSS satellites have atomic clocks which achieve synchronization below ps-level. A GNSS-enabled system receives the signals coming from the different satellites, and then it demodulates the ephemeris and almanac data in order to determine their position and the time of emission of their corresponding signals. Then, it estimates the time of reception and computes the time the signal has used to travel from the satellite to

the receiver. This last time measurement is converted into a distance measurement called Pseudo-Range (PR) multiplying by the speed of light. For each satellite, the geometric figure of all points satisfying the measured PR is a sphere centred at the GNSS satellite position, and with the PR as its radius. The intersection between three spheres provides generally two points, but one is discarded, as it is far away from the Earth's surface. Consequently, the 3-D position is determined. To do so, at least a fourth satellite is necessary to compensate for clock errors.

GNSS are currently a key technology for the society due to the high number of applications that rely on them such as defence, navigation, network synchronization or banking transactions. The main GNSS constellations are GPS (USA), Galileo (EU), GLONASS (Russia) and Beidou (China). By 2020, more than 120 GNSS satellites are expected to be in orbit. GNSS signals are allocated in following frequency bands: the lower L-band (1164-1300 MHz), and the upper L-band (1559-1610 MHz). Figure 2.3 shows the spectrum occupation of each one of the services associated with the main GNSS constellations.

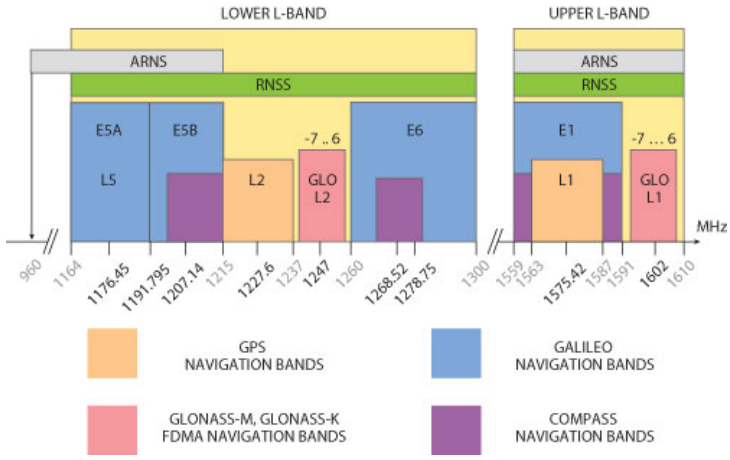

Figure 2.3: GNSS bands used by each main constellation. Extracted from `https://amsat-uk.org/2014/08/13/23-cm-band-and-wrc-2018/`

All GPS, Galileo, Beidou, and also the new GLONASS services make use of Direct Sequence Spread Spectrum (DSSS) modulations with orthonormal spreading codes that allow to achieve a multiple satellite configuration based on Code Division Multiple Access (CDMA). However, legacy GLONASS services used Frequency Division Multiple Access (FDMA) instead combined with DSSS. Figure 2.4 depicts the modulation used by each service of all GNSS constellations, its frequency band of operation, and if it is transmitted in the In-phase or the quadrature component.

GNSS transmit their signals within reserved frequency bands that are internationally protected. Despite the legal regulations, the proliferation of jammers, as well as the pervasive use of wireless communications, has increased the problem of RFI, which override the reliability of GNSS devices and may represent a security breach in critical applications.

Moreover, GPS L5 and Galileo E5 bands are shared with two wide extended aerial radio navigation systems: the Distance Measurement Equipment (DME) (civilian), and

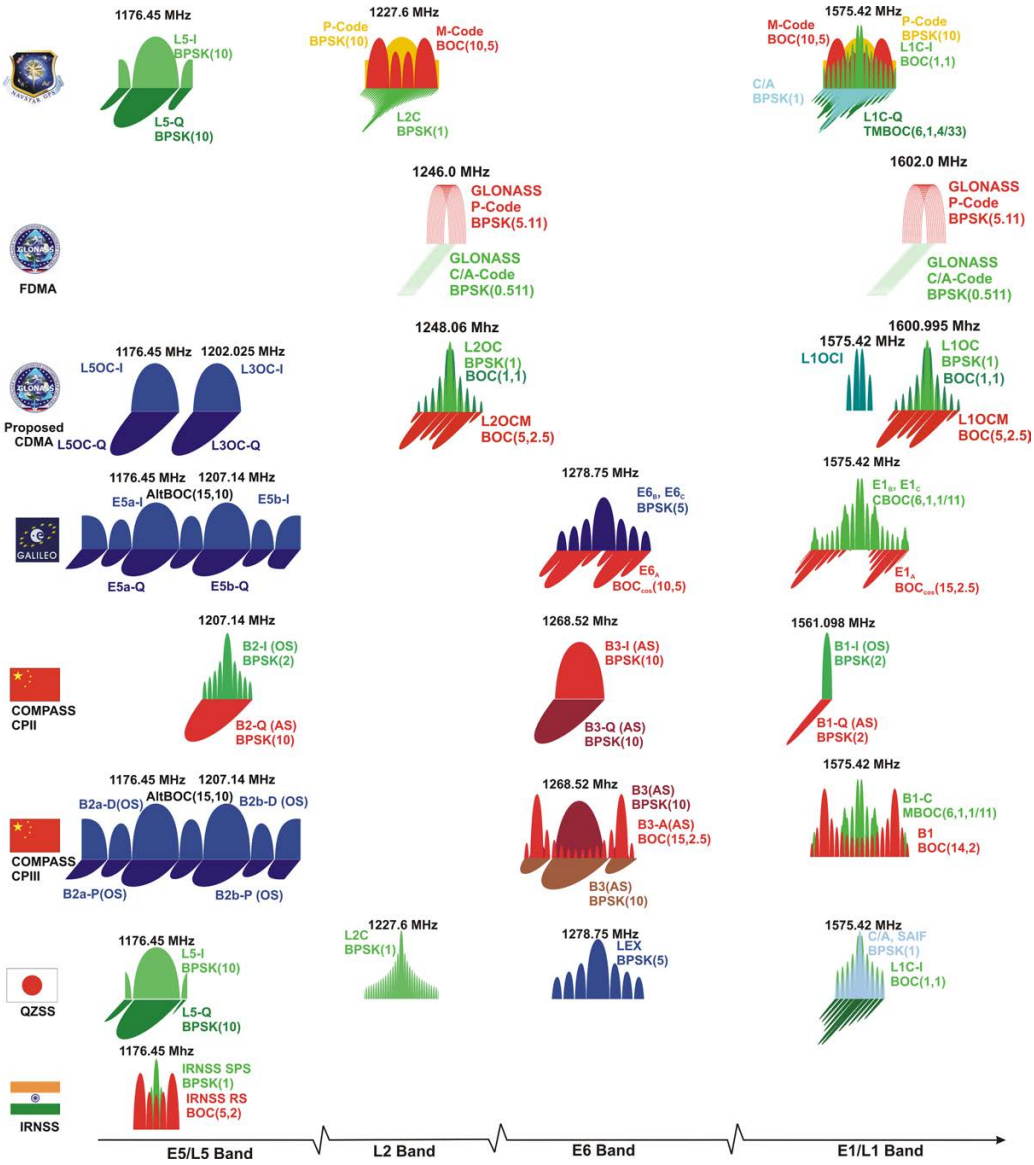

Figure 2.4: GNSS services for each band and constellation. Extracted from `https://gssc.esa.int/navipedia/index.php/GNSS_signal`

TACtical Air Navigation system (TACAN) (military), both transmitting in the band from 962 MHz to 1,213 MHz and divided into 1 MHz channels [3]. This produces the so-called cross-talk effect, which represents a degradation of the GNSS performance. This effect is well characterized for PNT applications, but it is overwhelming for GNSS-R devices [29].

Last but not least, amateur radio services in the 1240-1300 MHz band (known as the 23 cm

frequency band) have currently a secondary license and they can be a source of RFI to Galileo E6 enabled receivers. Amateur services such as radio, TV and even Moon bouncing communications operate in that band and may introduce severe harmful interference to Galileo E6 receivers (see for instance, this presentation at a recent UNOOSA ICG Meeting in Prague: `http://www.unoosa.org/pdf/icg/2014/wg/wga3.01.pdf`).

GNSS jammers are a growing threat to current GNSS-based systems, and the increasing number of interference occurrences over the last years is a proof of that. There are renowned documented cases that illustrate this fact. The incidents at Moss Landing Harbor in 2001, at San Diego in 2007, and at Newark airport in 2009 are significant examples of how a failure in the proper reception of GNSS signals can plunge a city into chaos. Further examples can be found in [30], however, these are just several known and documented cases that represent only a small fraction of current worldwide RFI events in GNSS-enabled applications (see Fig 2.5).

Moreover, a growing number of instances of unintentional interference into protected GNSS bands have been reported, some examples can be found in [3] (e.g. 2nd harmonic of TV broadcasting at 787.21 - 788.24 MHz band as a GPS L1/Galileo E1 in-band interference or air route surveillance radar at 1240 - 1370 MHz band as a GPS L2/GLONASS L2 near-band interference).

Furthermore, intentional RFI emissions generated by the so-called PPDs, or just jammers, are also powerful enough to override the current design of GNSS receivers. PPDs deliberately transmit signals at or near GNSS frequencies to make GNSS unusable within a region around the device. Although their use (but not necessarily their possession) is outlawed in most countries, these products are available on the Internet from 30 €, often not as jammers, and indeed, the number of companies selling them seems to be increasing in number.

GNSS jammers and PPD are used by criminals, but for personal privacy as well. Thieves and robbers disable GNSS tracking systems to steal high-value goods or vehicles. Truck hijacking is conducted using GNSS jammers to ensure that nobody can track the vehicle. Moreover, jammers can affect unintentionally other GNSS receivers on the area different than the original target such as Local Augmentation Area Systems (LAAS) of airports, automatic geo-located installations at ports and harbours, etc. Many official state cars use jammers for personal privacy that can override nearby systems. State buildings are also equipped with GNSS jammers to prevent for terrorist attacks, but they can interfere with other systems in an unintentionally way. The number of possible combinations is high and increasing as the number of GNSS-enabled devices is also growing.

Furthermore, there is also an additional and more recent threat posed by the so-called smart jammers. These are jammers that broadcast low power pulsed signals that are synchronized in time with the targeted GNSS system, denying the decoding of selected bits of the navigation message and thus denying the PVT as well. Again, new monitoring devices able to detect the presence of such jammers is urgently needed.

That said, it is clear that there are three main reasons that encourage the development of techniques to fight against the threat of RFI. First, the power level of the GNSS signals is inherently weak. In addition, potential sources of RFI signals can be of very different nature and, given the increasing use of the radio spectrum, the RFI is becoming

Location	Date	Cause & Impact
GPS system	March, 1993	Upload to the satellites of bad navigational data
St Charles, MO	11-21 October, 1994 May 1995	GPS/L1 interference from test equipment at nearby aerospace facility
GPS system	18 March, 1997	Anomaly that caused satellite's time to jump forward approx 2hrs and 20 minutes
New York, New Jersy	December, 1997 - January 1998	Transmitter inadvertently left on, interfering with airline flights within a 300-kilometer radius
Chesterfield, SC	15-23 April 1999	Army communications system radiating in GPS/ L1 band
GPS system	March, 2000	Upload to the satellites of bad navigational data
Moss Landing, CA	15 April – 22 May, June & Fall, 2001	TV antenna pre-amp radiating in GPS/L1 band, GPS denied throughout harbor region
GPS system	July, 2001	Clock drift out of spec on individual satellites
Mesa, AZ	13-18 December, 2001	"Unintentional jamming signal generator radiating at 1575.002 MHz, GPS denied for 180nm radius
Douglas, Isle of Man	2002	Poor CCTV camera installation blocked GPS signals
GPS system	June, 2002	Upload to the satellites of bad navigational data
GPS system	January, 2004	Upgrade to ground segment software caused problems with timing receivers
San Diego, CA	22 Jan, 2007	US Air Force, emission due to personnel error, wide-scale denial of GPS
GPS system	April, 2007	32nd satellite added causing problems with receivers not designed to handle only 31
New York, NY	2008	GPS outage and effected systems similar in character to '07 San Diego event
GPS system	January, 2010	Upgrade to ground segment software caused problems with timing receivers
GPS system	January, 2010	Clock drift out of spec on individual satellites
Leesburg, VA	July 2011 - January 2012	100mW jammers caused minor disturbance to FAA Control Center, ZDC
Newark Airport, NJ	2009 - 2011	FAA equipment going off line intermittently. Traced to a truck with a jammer driving by on frequent trips
Korea	March, 2011	U.S. military reconnaissance aircraft forced to land due to GPS jamming
Korea	March, 2011	N. Korea military jammers believed to have knocked out 146 cell sites
Iran	December, 2011	GPS meaconing used to capture U.S. drone
Las Vegas	March, 2012	DoD event, unintentional; exercised Cease Buzzer; Las Vegas airport ground stop for approximately 1 hour
Korea	May, 2012	"North Korea pumps up the GPS jamming in week-long attack"

Figure 2.5: Examples of RFI and jamming events compiled from published reports and open literature (extracted from [30]).

ubiquitous. Finally, the large number of critical applications that rely on GNSS demands research, development and implementation of products and systems whose main target is the detection, location and mitigation of RFIs.

2.5 GNSS-Reflectometry

GNSS-R is an innovative remote sensing approach based on the measurement and characterization of the GNSS signals that are reflected over the Earth surface, with some advantages regarding the traditional techniques. In the late 1980s, GNSS signals were proposed for remote sensing of the Earth's atmosphere by performing radio occultation measurements. About the same time, the idea of using GNSS signals reflected off the Earth's surface for scatterometry purposes was discussed by Hall and Cordey [31]. Martin-Neira first proposed to use them for ocean altimetry [32]. In 1998, Garrison and Katzberg demonstrated from an aircraft experiment that the GNSS signal reflections can sense ocean surface roughness and related wind [33]. The first GNSS signal reflections at steep incidence were found by chance in calibration data during the SIR-C radar experiment onboard the U.S. Space Shuttle [34].

Similar to traditional radar remote sensing, the GNSS reflectometry technique can be applied to remote sensing of various types of natural covers, such as ocean, land, ice, snow, vegetation. Since the GNSS signals are emitted at L-band, they are capable of penetrating cloud cover and are particularly sensitive to soil moisture, sea-ice salinity and snow water content.

Measuring a delay between the direct signal and the reflected one from the Earth's surface and recalculating the temporal delay into the spatial intervals turns GNSS bistatic radar into an altimeter. A GNSS altimeter can perform altitude measurements along multiple widely spaced ground tracks acquiring signals simultaneously from several satellites. On the contrary, measuring the peak power of the scattered GNSS signal and widening of its waveform make GNSS bistatic radar a multi-beam scatterometer. Then, the surface roughness and dielectric properties of the probed media may be retrieved from such measurements.

According to [35], the constraints of GNSS reflectometry are related to the relatively low power of the signal, and a fixed set of L-band frequencies and bandwidths. Since the transmitted GNSS signals of opportunity are relatively weak, the scattered signal is received only from the area around the nominal specular point on the surface called a glistening zone. The location of this point is predetermined by the relative positions of both the transmitter and the receiver with respect to the Earth's surface. Therefore, it cannot be changed at will as in the case of monostatic mapping radar where scanning beams can create a rather large and continuous swath. On the other hand, specialized monostatic radars are significantly more expensive, massive, require large antennas and high power supply which means large solar panels. So, for the price of one heavy and expensive radar satellite a constellation of small GNSS-R satellites spread over an orbit can be utilized. Such a constellation can compensate for a sparse swath of a single satellite and will increase the global coverage by decreasing the repeat time compared to a single satellite.

The basic observable properties of GNSS-R are contained in the so-called Delay-Doppler Map (DDM). The DDM is obtained by cross-correlating the reflected signal with a local replica of the pseudo-random code for the conventional case (cGNSS-R) or with the direct signal for the interferometric case (iGNSS-R) [36]. After the Doppler compensation, the DDM can be expressed as:

$$|Y(\tau, f_d)|^2_{\text{cGNSS-R}} = \int_0^T s_r(t)\, c^*(t+\tau)\, e^{j2\pi f_d t} dt, \tag{2.1}$$

$$|Y(\tau, f_d)|^2_{\text{iGNSS-R}} = \int_0^T s_r(t)\, s_d^*(t+\tau)\, e^{j2\pi f_d t} dt, \tag{2.2}$$

where $s_r(t)$ and $s_d(t)$ denote the reflected and direct signals respectively, $c(t)$ is the locally generated code of the GNSS signal, f_d is the compensated Doppler frequency, and T is the coherent integration time of the cross-correlation.

As an illustrative example of GNSS-R application, in [37], the feasibility of retrieving wind direction from the synthetic DDMs has been analyzed. Using the simulation tool P2EPS [38], the DDMs under different geometry configurations, wind speed, and wind direction have been generated. The DDMs are depicted in Figs. 2.6a, b, and c for wind directions equal to 0° 30° and 120° respectively. Then, the influence on the DDM of the direction retrieval of the wind speed regarding the elevation of the GNSS-R receiver can be studied by computing the difference between the 30° and 120° DDMs and the 0° one (Figs. 2.6d and e respectively). This work concludes that the ocean wind direction can be retrieved from the DDM shape using some specific metrics and if the SNR at the DDM is higher than 11 dB.

The effects of the RFI signals on GNSS-R devices have not been assessed in the literature. For this reason, one of the main goals of this PhD thesis is to assess so. As a first approximation, one can say that, in the case of cGNSS-R, if an interference signal $i_r(t)$ is present in addition to the noise $n_r(t)$ when the reflected signal is received ($s_r(t) = c_r(t) + n_r(t) + i_r(t)$), the DDM can be written as:

$$|Y(\tau, f_d)|^2 = |Y_{c_r}(\tau, f_d)|^2 + |Y_{n_r}(\tau, f_d)|^2 + |Y_{i_r}(\tau, f_d)|^2, \tag{2.3}$$

where the jamming power is spread over the whole GNSS signal bandwidth thanks to the spread-spectrum signal properties. However, an interference can easily corrupt a GNSS-R measurement due to the low power of the received GNSS signals.

In the case of iGNSS-R, the interference signal may be present in the reflected signal ($s_r(t) = c_r(t) + n_r(t) + i_r(t)$), in the direct signal ($s_d(t) = c_d(t) + n_d(t) + i_d(t)$) or in both. The DDM can be written in a generic way as:

$$|Y(\tau, f_d)|^2 = |Y_{s_r,s_d}(\tau, f_d)|^2_{\text{NoRFI}} + |Y_{s_r,s_d}(\tau, f_d)|^2_{\text{RFI}}, \tag{2.4}$$

where the first term represents the interferometric DDM in the absence of RFI as in [36] and the second term contains the cross-correlation of the interferences with the received signals.

This, in turn, has three kinds of sub-terms: the code-interference correlated terms with the same behavior as in the cGNSS-R case; the noise-interference correlated terms where

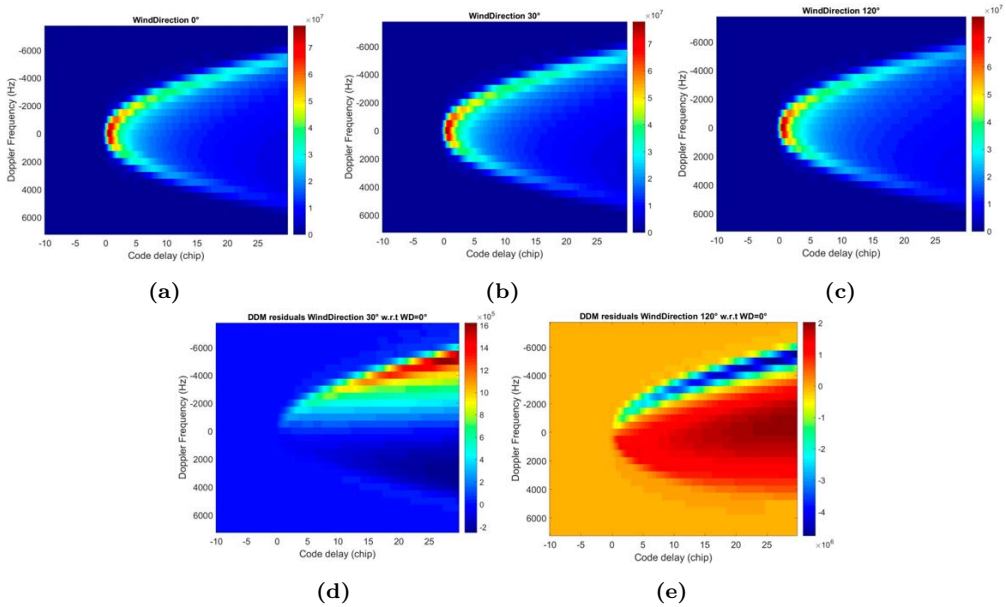

Figure 2.6: DDM simulations under different wind directions: (a) 0°; (b) 30°; (c) 120°. DDM differences with respect to the DDM of wind direction at 0°: (d) the DDM residual of wind direction of 20°; and (e) the DDM residual of wind direction of 120°. The wind speed, elevation and azimuth of the receiver are 10 m/s, 60°, and 30°, respectively.

the jamming power is not attenuated due to a presumably lack of correlation between the noise and the interference; and the interference cross-correlated term, which will have a catastrophic effect in the GNSS-R measurements if the direct and reflected received interferences are correlated. Furthermore, the latter is quite probable as both antennas are usually close to each other. Therefore, the iGNSS-R technique is much more sensitive to the presence of RFI signals than the cGNSS-R approach in most scenarios, since the Doppler and delay difference is very small.

Chapter 7 is entirely devoted to the development of the mathematical expressions to evaluate the impact of RFI and jamming signals into the DDM.

2.6 Jammers at GNSS bands

The literature related to the characterization of GNSS jammers characterization is very extensive. For example, in [39], the signals emitted by several GNSS jammers have been analyzed. From their signal characterization, it emerges that chirp signals are the most common type, which sweep large frequency ranges in short time periods. Regarding the power, it varies significantly depending on the jammer type from -10 dBm to 30 dBm. When battery jammers are considered, their transmitted power is also impacted by the charge level. Despite the large variability, the power levels measured are extremely high as compared to the power level of GNSS signals. For this reason, jammers can create serious problems for GNSS operations in large geographical areas. The conclusions from [39] are

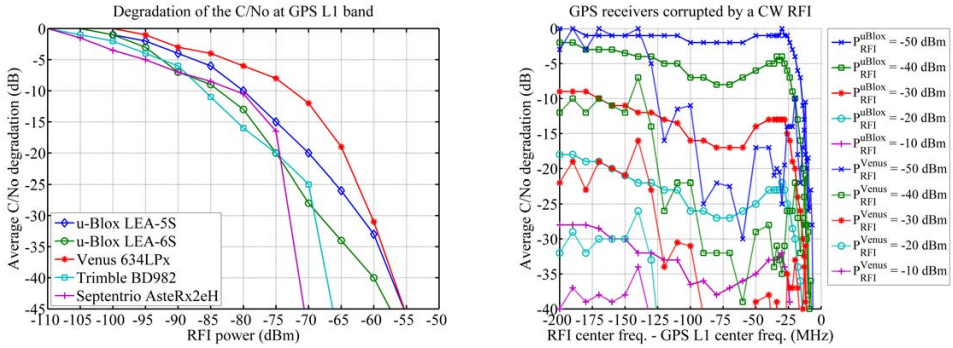

(a) **(b)**

Figure 2.7: (a) Degradation of the C/No regarding the output power of a commercial jammer in five commercial GPS receivers. (b) Degradation of the C/N_0 regarding the central frequency of a CW RFI in two commercial GPS receivers.

in perfect agreement with those drawn from the experiments at the RSLab related to characterization of GNSS jammers [9].

Moreover, the effects of the GNSS jammers have also been well studied in the literature. In [40], a figure of merit named Spectral Separation Coefficient (SSC) was defined in order to evaluate the degradation of the SNR due to the effect of an interference signal. Moreover, in [9, 14, 41, 42], the SNR degradation in GPS receivers was studied using a typical chirped jammer.

In this PhD thesis, a simple SNR degradation test was performed and presented in [12]. Four commercial GNSS receivers (in particular GPS) have been used to characterize the degradation of the SNR as a function of the RFI power. These tests were performed using a GNSS simulator running two sequential tests. One baseline with no interference and a second one with an RFI signal ramping up in power gradually. As it can be seen in Fig. 2.7a, the more powerful the jamming signal is, the higher the error in the GNSS-R measurements. This test corresponds to a chirp signal centered at the band of different GPS L1 C/A receiver.

Moreover, near-band interference can also affect the performance of the receivers. However, as it may be expected, near-band interferences must be substantially more powerful than the in-band ones in order to produce the same effects. Nevertheless, they must be taken into account when choosing the appropriate front-end of a GNSS or GNSS-R device. As an example, the performance of two GPS receivers has been tested under near-band interference with a CW RFI signal. As it is shown in Fig. 2.7b, the closer in the frequency of the CW is, the higher the measurement bias is in less or more amount depending on the RF front-end of the receiver and the power of the RFI signal.

2.7 Unintentional RFI at GNSS bands

Besides jammers, unintentional RFI signals can degrade the performance of GNSS and GNSS-R devices. As mentioned above, these unintentional sources are originated from

harmonics of lower frequency bands, inter-modulation products, out-of-band emissions or near-band interference. Therefore, the possible source of unintentional RFI should come from the adjacent bands used by GNSS. The European Table of Frequency Allocations can be found in [1].

The most prominent example of unintentional RFI is the proposal made in 2011 by Lightsquared [43] (and reborn in 2018 as Ligado [44]) to allocate a terrestrial 4G network in the US in the bands right below L1. A number of compatibility studies were completed by a Technical Working Group established on purpose by the US FCC. See `https://www.gps.gov/spectrum/lightsquared/docs/` for further information. It is very important to note that since the Lightsquared studies, a metric setting a coexistence condition, that no GNSS receiver has to see a degradation of the C/N_0 of more than 1 dB, is becoming a sort of "not-written" standard worldwide. In fact, in the European RED, the standard for GNSS receivers includes this requirement as well.

Besides this case, one of the first experiments carried out during this PhD thesis (and presented in [12]) was to measure how common electronic components can degrade the performance of GNSS-R. The two cases of RFI signals that represent a threat for GNSS-based devices presented hereinafter are a generic computer and a high-speed bus interference. The measurements were carried out with a spectrum analyzer with in-phase and quadrature demodulation features and the proper antenna for each one of the bands.

A computer has many different electronic components, each one of them working at a different frequency, with its own behaviour and emitting more or less electromagnetic radiation. The resulting signal is equivalent to an increase in the noise floor of any nearby receiver.

Sometimes, a computer is used to store and process the data coming from GNSS-R measurements. If the antenna has been close enough to the computer, these measurements may be corrupted. In Fig. 2.8, the increase of the noise floor produced by three different computers is shown, which would translate into a bias in GNSS-R measurements.

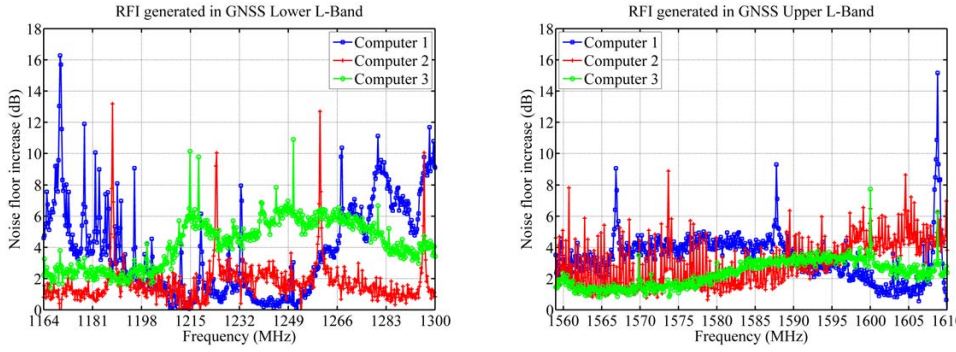

(a) **(b)**

Figure 2.8: (a) Increase of the noise floor in the GNSS lower L-band measured as the difference between the power spectrum with the computer turned on and off. (b) The same measurements in the GNSS upper L-band.

In many cases, an integrated system is more preferable than a computer in GNSS-R

field measurements due to their lightweight, reduced size and low power consumption. However, interference compatibility problems such as emissions coming from high-speed digital buses [45] may appear in these cases.

One example of RFI generated for high-speed digital buses is shown in Fig. 2.9. Despite the use of large ground plates and differential signals [45], the high number of signals in a DDR2-SDRAM device working at 533 MHz generate harmonics at GNSS frequencies that may corrupt GNSS-R measurements. The first and third harmonics have more power than the rest (see Fig. 2.9a) due to the square shape of the digital signals.

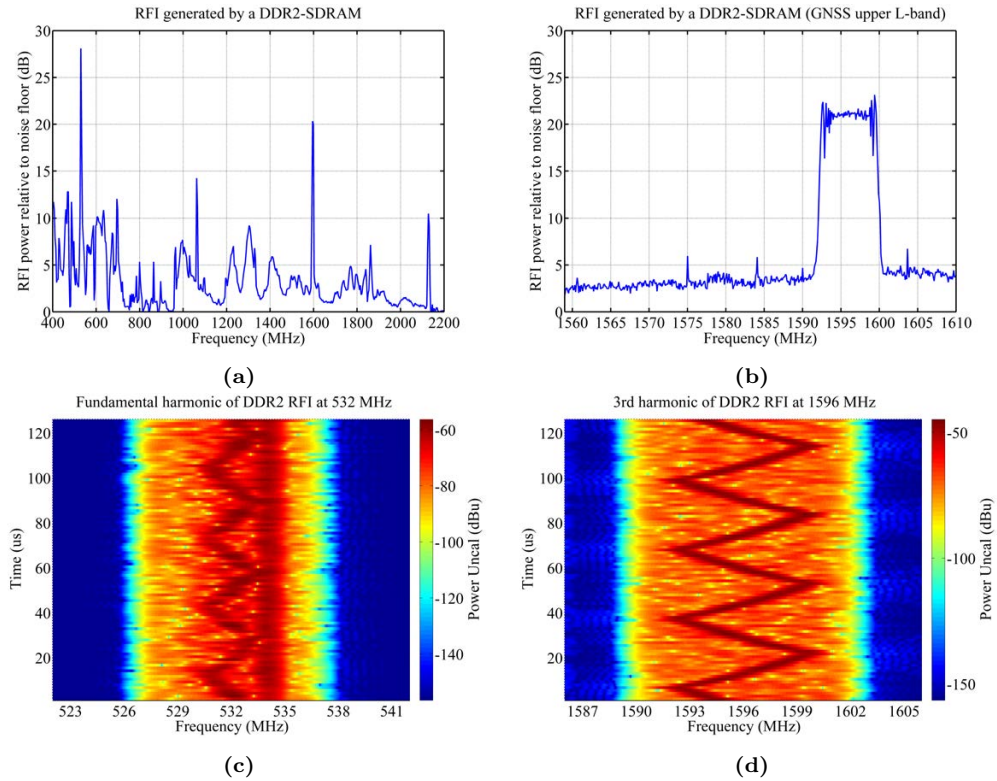

Figure 2.9: (a) Spectrum of the interference signal coming from a DDR2-SDRAM with the first four harmonics. (b) Spectrum of the DDR2 interference in the GNSS upper L-band. (c) Spectrogram of the fundamental chirp interference centered at 532 MHz. (d) Spectrogram of the 3rd harmonic interference centered at 1596 MHz overlapping partially the GLONASS L1 band.

As mentioned before, commercial jammers usually employ linear frequency modulations. Unexpectedly, the signals shown in Fig. 2.9 are also from this nature.

2.8 Conclusions

This chapter has presented a brief introduction to the problem of RFI and jamming in PNT applications using GNSS, and Earth observation using MWR and GNSS-R. More-

over, a brief introduction to the fields of MWR, GNSS and GNSS-R with some use cases and RFI examples has been stated. As a conclusion, RFI signals can be originated intentionally and unintentionally. In both cases, the performance of the receivers is degraded. In MWR, a positive bias in the measured power is introduced. In GNSS and GNSS-R, the final SNR or C/N_0 is degraded. Intentional RFI generators are usually called jammers or PPDs, and they typically are chirped waveforms. Unintentional RFI can come from many different sources, but typically they are harmonics from lower bands or out-of-band emissions. Finally, RFI and jamming signals can be any kind of signal, but they tend to be concentrated in the time-frequency domain.

3

Chapter 3

Review of RFI countermeasures

This chapter is a short revision of the state-of-the-art of RFI detection and mitigation techniques. The majority of these techniques have been developed for MWR and GNSS applications, but also radio-astronomy or deep-space communications.

3.1 Introduction

A number of RFI detection and mitigation techniques have been developed during the last years. This chapter is a brief summary of the different types of RFI-countermeasure present in the literature. The majority of these techniques have been developed for MWR and GNSS applications, but also radio-astronomy or deep-space communications. Despite the very large number of references on the literature, only a few number of them are mentioned in this chapter for the sake of simplicity. Performing an in-depth review or study of the literature in the field of RFI detection and mitigation techniques is out of the scope of this PhD thesis.

3.2 Initial considerations

The problem of RFI involves, in most cases, the detection of stochastic signals with, a priori, unknown parameters. For this reason, the RFI detection criterion should be based on the Neyman-Pearson hypothesis testing where a threshold value α is defined to discriminate between RFI-contaminated samples and RFI-clean samples [8, 10, 46, 47]. A trade-off between the probability to detect RFIs (probability of detection, P_D) and the probability to eliminate RFI-clean data falsely (probability of false alarm, P_{FA}) must be accomplished. The P_{FA} depends on the PDF of the received signal in absence of RFI. Thus, it will be always determined since the RFI-free signal will have a Gaussian (i.e. Normal) distribution in remote sensing (microwave radiometry) and almost Gaussian (SNR $\ll 0\,\mathrm{dB}$) in GNSS applications. Hence, if $s[n] = \mathbf{s}$ is the digital sampled signal at the receiver and $f(\mathbf{s}) \sim \mathcal{N}(0, \sigma^2)$,

$$P_{FA} = P(\mathbf{s} \geq \alpha) = Q\left(\frac{\alpha}{\sigma}\right) \tag{3.1}$$

where $Q(x) = 1 - \frac{1}{2}\left[1 + \mathrm{erf}\left(\frac{x}{\sqrt{2}}\right)\right]$ is the so called Q-function defined as the tail probability of the standard normal distribution [46]. However, the undetermined parameters of the RFIs will led to a lack of knowledge of the P_D.

Regarding navigation applications, post- and pre-correlation techniques [48] can be used to further improve the anti-jamming performance of the receiver. Only pre-correlation techniques will be considered within the scope of this work since they can be applied in any kind of receiver including microwave radiometry devices.

There are several methods used to combat RFIs, but the choice of technique depends on several factors such as cost, space constraints, power consumption and the environment where they are used [49]. A short summary of most known methods is presented in subsequent sections.

3.3 Time domain techniques

Time domain RFI mitigation algorithms are the simplest to implement as they only need to sample the received signal $s[n]$ and compare its power or its absolute value with a determined threshold α directly related to the power of the RFI-free signal [46]. Hence,

the most straightforward case of this technique would be when the output signal $y[n] = f(s[n], \alpha)$ is

$$y[n] = \begin{cases} s[n] & \text{if } |s[n]| \leq \alpha \\ 0 & \text{otherwise} \end{cases} \tag{3.2}$$

with $\alpha = \sigma_{\text{free}} \cdot f(P_{FA})$ being σ_{free} the standard deviation of the RFI-free signal.

This type of RFI excision is most effective when dealing with strong and short (spiked) bursts of RFI. Weak and long-lasting RFI signals are problematic because the threshold methods in the temporal domain do not work [50]. In addition, since the detected power is a smoothed (averaged) version of the instantaneous one, if the duration of the RFI peaks is shorter than the integration time they may pass undetected [8]. Several GNSS receivers implement these RFI mitigation techniques integrated within its Automatic Gain Control (AGC) stage.

3.4 Frequency domain techniques

RFI signals that belong to the group of CW narrowband signals, either with fixed or variable frequency, are very likely to be received [9] in urban environments. Two approaches can be distinguished inside the techniques devoted to detect this kind of signals.

3.4.1 Non-parametric methods

This first group of techniques includes detection algorithms based on non-parametric spectral estimation of the incoming signal, obtained by applying signal processing techniques such as the periodogram [51–53] or simply the Discrete Fourier Transform (DFT). They are typically performed comparing the spectrum of the received signal with a theoretical threshold α usually determined according to a statistical model representing the received signal. In this context, these mitigation techniques have the same effect as notch filtering removing the interference frequency components.

Nevertheless, this approach cannot be considered the best option for non-stationary interference removal. In a real interference environment characterized by the appearance of pulsed signals, dynamics of interference, as well as its spectral characteristics, change quickly in time. Therefore, the use of spectral techniques that represent the signal only in spectral domain becomes an incomplete representation unable to follow the non-stationary nature of RFIs.

3.4.2 Parametric methods

Model-based or parametric spectral estimators have been proposed as an easy to implement mitigation technique for jammers generating chirp signals, typical of the type of commercially available jammer that has become ever more present in recent years [9, 14]. The broadband nature of the chirp signal means that its impact on the RF receivers is similar to an increase in the thermal noise floor. However, the chirp signal is instantaneously narrowband: a feature that is exploited by the use of a notch filter with a highly dynamic response to variations in the frequency of RFIs [54]. For instance, in [14], an

adaptive notch filter with transfer function

$$H_n(z) = \frac{1 - z_0[n]z^{-1}}{1 - kz_0[n]z^{-1}}, \tag{3.3}$$

where k is the pole contraction factor and $z_0[n]$ is the filter zero, was simulated with successful results mitigating chirp RFIs in GNSS applications.

These adaptive notch filters are very effective for narrowband jammers and can be used in applications that require low power and small size. Their main disadvantage is that they cannot be used when the jammer does not have a predictable signal structure. [48, 49].

Frequently, this techniques can track only a CW signal. In [55], a two-pole notch filter coupled with a detection unit has been used as a basic element for the design of a multi-pole filter capable of efficiently removing more than one CW interference. The derived results provide a useful information for the design of mitigation and detection units based on the adaptive notch filters that result a computationally effective solution for CW interference mitigation.

Other parametric techniques such as ARMA models or minimum variance estimators (e.g. Capon estimator) might be also included here, but they will be considered out of the scope [51].

3.4.3 Time-Frequency space techniques

Time-frequency space techniques are the most used for detection and mitigation of real non-stationary RFI signals. This approach takes into account the coexistence of the RFI signals in both time and frequency domains, thus being able to detect CW and pulsed signals simultaneously. Nevertheless, resolution in temporal domain σ_t and in frequency domain σ_w are related and constrained by the so called Gabor limit [10,56] (the equivalent of the Heisenberg uncertainty principle in the context of signal processing) that satisfies

$$\sigma_t^2 \sigma_w^2 \geq \frac{1}{4}. \tag{3.4}$$

Furthermore, time-frequency space filtering attempts to represent the transform of the received signal in such a way that it is possible to easily distinguish the jammer from the data signal, particularly for narrowband RFI signals due to the nature of the Fourier kernel in this transform [57,58]. Moreover, since GPS signals are low power and wideband signals, the high power jammer signals can usually be distinguished very easily in time-frequency space.

Different Time-Frequency (TF) distributions such as the spectrogram and Wigner-Ville distribution can be used to represent the signal in time-frequency space. It only remains to choose an appropriate threshold to excise the jammer from the received signal to obtain the useful signal by transforming it back to the time domain. The main disadvantage of these methods lies in the fact that the jammer can be effectively separated only if it is sufficiently stronger than the GPS signal itself.

3.4.3.1 Time-Frequency implementations

Most common TF distributions are the following:

1. Short-Time Fourier Transform (STFT): STFT-based techniques are used for narrowband jamming excision and can be implemented in situations that require low power and small form factor devices. The STFT essentially moves a window $w[n]$ through the signal $s[n]$ and takes the DFT of the windowed region. So that,

$$\text{STFT}\left\{s[n]\right\} \equiv S(m,f) = \sum_{n=0}^{N-1} s[n]w[n-m]e^{-j2\pi fn}, \tag{3.5}$$

   and the so called spectrogram is defined as

$$\text{Spectrogram}\left\{s[n]\right\} \equiv |S(m,f)|^2. \tag{3.6}$$

   This approach can adapt rapidly to changing environments. The signal is filtered in the time-frequency space in order to remove the jammer components before being transformed back to the time-domain. Furthermore, the proper choice of the window function will determine the spectral leakage in the frequency-domain and the length of the temporal response. [52].

2. Filter bank: it has all advantages of STFT and it can be implemented in situations that require low power consumption, small size and poor frequency resolution. Conversely, if a high frequency resolution is desired, filter bank becomes inefficient due to the high number of needed filters whilst STFT tend to be optimum. In [59] and [60], the filter bank technique is used in navigation and Earth observation applications due to its good properties.

3. Wigner-Ville Distribution (WVD): the WVD is a TF distribution that belongs to the group of quadratic time-frequency representations and is based on the calculation of the FT of the so called Ambiguity Function (AF). The AF is a general representation of the signal auto-correlation function for non-stationary stochastic processes. So that, for

$$\text{AF}(t,\tau) = x\left(t+\frac{\tau}{2}\right)x^*\left(t-\frac{\tau}{2}\right), \tag{3.7}$$

   WVD yields to

$$\text{WVD}(t,f) = \int_{-\infty}^{\infty} x\left(t+\frac{\tau}{2}\right)x^*\left(t-\frac{\tau}{2}\right)e^{-j2\pi f\tau}d\tau. \tag{3.8}$$

   The WVD does not suffer from leakage effects as the STFT does, thus, it provides the best spectral resolution. However, if the analyzed signals have several frequency components, the WVD suffers from the so called cross-terms. These-cross terms can be partly suppressed by smoothing the WVD with low-pass 2D windows [61]. Furthermore, mitigated signals cannot be retrieved directly from WVD since it is a quadratic time-frequency representations.

3.4.3.2 Time-Frequency resolution

The selection of the window coefficients determines the amount of spectral leakage in the DFT output. To illustrate this, consider the non-windowed processing, which is equivalent to using a rectangular window. The Fourier transform of the rectangular window is a sinc function ($\text{sinc}(x) = \frac{\sin(\pi x)}{\pi x}$) with the first side-lobe 13 dB down relative to the main lobe and with subsequent side-lobes that fall off at 6 dB/octave. So that, the signal energy will be spread across the spectrum proportionally to the width of the main lobe and the height of the side-lobes of the window. Selecting a window with lower side-lobes will reduce the amount of spectral leakage. However, a lower side-lobe window results in a wider main lobe (i.e. reduced frequency resolution) [58].

According to [62], the Gaussian window is the most concentrated, simultaneously in time and frequency, and attains the uncertainty lower bound. However, it has the widest main-lobe and offers the least spectral resolution of nearby kernels. On the other hand, the rectangular window provides the best spectral resolution of nearby kernels (since it has the narrowest main-lobe), but it is unusable in restricted bandwidth applications because the high side-lobe levels and spectral leakage. Several other windows like the triangle window, trapezoidal window, Hann window and Hamming window offer a trade-off between the spectral resolution and spectral leakage, but they do not have a constant time amplitude like the rectangular window. Eventually, in [63], a new family of windows with minimum time-bandwidth product $\sigma_t \sigma_w$ for a given σ_t was derived, surpassing in performance all popular windows including the truncated Gaussian windows presented in [62].

3.5 Other space-based techniques

There are many subspace processing techniques that can perform jammer excision. In these cases, the estimation of the jammer signal can be obtained if the jammer signal is orthogonal to the useful signal in such subspace [49]. Two of the most relevant of them are the Wavelet and the Karhunen-Loève transforms.

3.5.1 Wavelet Transform

Wavelet Transform (WT) is a generalization of the linear transforms that have a kernel that is finite time, such as the STFT.

The set of orthogonal basis functions which are employed for the STFT computation can be seen as bandpass filters having equal frequency bandwidths and thus representing a set of windows in time with equal duration. This leads to a different resolution in the characterization of high frequency phenomena with respect to the resolution achieved in characterizing low frequency phenomena. Exploiting fixed windows, many cycles of a high frequency signal can be captured, while for a low frequency signal very few cycles are within the windows. Another drawback of using a transformation based on fixed windows is revealed when considering the rising part of the signal. Very narrow windows will help to localize the rising portion of the signal very well with respect to a wide window, at the expense of a loss of information in the steady part of the signal, which is better characterized by wider windows.

In order to overcome these issues, a set of functions which could better match the frequency components of the signal to be characterized is needed. From such basis functions, a filter bank where the low-pass filters response has narrower bandwidths (wider in the time domain) than the high-pass filters response can be derived. Thus, a transformation based on windows which are functions of both time and frequency such that their bandwidths get narrower as the frequency decreases is needed. These requirements are accomplished by the basis functions used to perform the WT. Eventually, the frequency term is mostly replaced by a scaling operation to have a clear boundary to the Fourier transformation [56, 64]. The concept of non-constant division of a signal in frequency domain is summarized in Fig. 3.1.

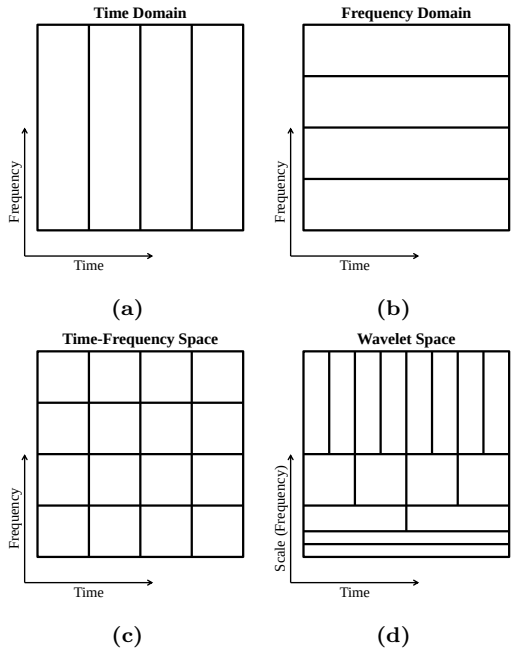

Figure 3.1: Allocation in the time-frequency space of the mentioned groups of detection and mitigation techniques: (a) time domain, (b) frequency domain, (c) time-frequency space and (d) wavelets.

The application of WT for detection and mitigation purposes in navigation and Earth observation have been studied deeply in [8,9,11,15,65,66]. However, WT with Fourier kernel (e.g. Gabor Wavelet) tested in [67] have the best detection performance for narrowband RFI signals.

3.5.2 Karhunen-Loève Transform

The Karhunen-Loève Transform (KLT) is the unique subspace transform whose kernel is calculated from its own input data [61]. References [68, 69] analyze the performance of the KLT to detect weak RF signals and how this technique can be extended to the GNSS scenario offering several advantages with respect to the other approaches.

The main advantages of the KLT compared to the DFT are the following:

- The KLT works equally well for narrowband and wideband signals, while the DFT is optimized for narrowband signals only. This feature makes the KLT more adjustable to bandwidths characteristic for GNSS signals.

- Both transforms decompose the signal using a set of base functions. When comparing these functions, one notices that the KLT is a more flexible transform, because its basis functions can be of any form. This results in a better decomposition of the signal. The DFT is very limited here because its basis kernel are strictly limited to sinusoidal functions.

- The KLT merges deterministic and stochastic analyses of the signal, which is a very powerful attribute not found in other methods. Although the set of KLT basis functions is deterministic, it does also provide information on the stochastic nature of the signal, rather characterizing an expectation of the power of the basis functions than their exact value. Consequently the KLT grades the basis functions with respect to their probable power contribution thus allowing one to efficiently distinguish the signal from the noise. This implies that, when using the KLT, the processed signal can be filtered by keeping only the most interesting, non-stochastic part and omitting the rest, which is then defined as background noise. On the other hand, when using DFT an exact power value can be determined to each sine and cosine, this being the only parameter defining the signal.

- Finally, according to [68], the KLT is able to detect much weaker signals than the DFT. Although this capability still must be confirmed by practical applications, it could have an enormous potential in the future.

The idea at the basis of the method is the decomposition of the signal in a vector space using eigenfunctions, which can have, in principle, any shape, and therefore can better adapt to the signal being processed and increase the detection performance. In particular, the decomposition starts with the estimation of the linear auto-correlation function of the signal; afterwards the Toeplitz matrix is computed and a set of eigenfunctions with their corresponding eigenvalues are extracted by solving linear equations. It can be proved that a signal containing only noise is characterized by KLT small eigenvalues. Therefore, the presence of higher eigenvalues is a proof of the presence of deterministic signals buried in the noise. Indeed, the greater benefit of the KLT transform is the capability to successfully detect not only CW RFIs, but also narrowband, wideband and chirp RFIs, which are usually arduous to handle.

Nevertheless, the biggest drawback of the KLT technique is the complexity and computational burden required to extract a very large number of eigenvalues and eigenfunctions. A possible improvement is given by the Bordered Auto-correlation Method - KLT (BAM-KLT), which in principle allows to reduce the complexity, but limiting the performance of the detection [68, 69].

An example of KLT application can be found in [70], where a rank tracking device based on the evaluation of the covariance matrix eigenvalues of the observed data record can evaluate the number of detected RFI signals.

3.6 Statistical domain techniques

Since the RFI and the desired signal are assumed to be independent stochastic processes, they have statistical properties that may be used to separate them. The statistical domain techniques, also coined Amplitude Domain Processing (ADP) in [48], are tools able to distinguish between samples that belong to different statistical distributions. Normality tests are the most used and they are dedicated to find out if a set of samples belongs to or how similar is to the Normal (Gaussian) statistical distribution. The rationale behind the use of normality tests to detect RFI in microwave radiometry, and also in navigation applications, is the fact that the useful signals follow a zero-mean Gaussian distribution, whilst, in general, man-made RFI are not Gaussian.

In [26], ten different normality tests have been analyzed in terms of their capability to detect RFI in microwave radiometry. These tests have been first validated in terms of sequence length and number of quantization bits in the absence of interference. Their capability to detect sinusoidal, chirp, pseudo-random noise and telegraphic signals has then been analyzed. From this study, it emerges that the Kurtosis is the best RFI detection algorithm for almost all kinds of interfering signals, although it is known that it has a blind spot for sinusoidal and chirp interfering signals of 50% duty cycle [25]. Moreover, the mentioned study states that the Anderson-Darling (A-D) test might be a complementary normality test that covers this blind spot, and has a very good performance for all the studied sample sizes. Other known normality tests are the Shapiro-Wilk and the Jarque-Bera among others, but they do not perform as well as Kurtosis test [26]. Examples of Kurtosis test in combination with time-frequency techniques could be found in [59] and [25].

Nevertheless, the combination of normality test techniques with other detection and mitigation techniques may be troublesome. As well as the Gabor limit is a well-known low boundary for the product of time and frequency resolution, statistical and other domains are also linked in some way. This boundary is determined by the Central Limit Theorem (CLT) [53]. For instance, in [71] or [10], a normality test is applied after a DFT and a FIR filter respectively, without taking into account that these transformations introduce a normalization effect in the original samples due to the CLT. In some way, the product between the resolution in the statistical and time domains has a low boundary.

Moreover, another approach of normality tests is shown in [48] and [71] where ADP techniques modify the amplitude of each digital sample in such a way that non-Gaussian interferences are suppressed, resulting in an overall improvement in SNR. The calculation of the optimal non-linear mapping is based on statistical decision theory and acts to deemphasise those samples in which signal detection is unlikely. To calculate the non-linear mapping, the probability density function of the signal amplitude needs to be estimated. One of the main advantages of amplitude domain processing is that it can reject very fast sweeping interferences, as it does not need to track the interference frequency.

3.7 Spatial domain techniques

Adaptive antennas use spatial domain filtering techniques to eliminate the jammer signal. Like adaptive filtering, these techniques attempt to optimize a cost function. They can

be adapted for both narrowband and wideband jammers, but have the disadvantage of not being able to handle a large number of jammers in multiple locations simultaneously.

In antenna arrays, at least two antennas are required to eliminate the effect of jammers from one location, hence such arrays cannot eliminate jammers originating from more locations than the number of antennas present. The two basic approaches to spatial filtering are null-steering and beamforming [49].

1. Null-steering uses the simple concept that navigations and remote sensing signals are much below the thermal noise level and hence any signal that has a power above the thermal noise has to be an interfering signal. The antennas in the array are weighted so that any particular signal can be cancelled. Null-steering constantly computes the weights in order to minimize the received energy level. In effect, this technique attempts to steer the antenna away from the jammer. This method has the disadvantage of potentially reducing the signal level too.

2. Beamforming tries to adjust the antenna in order to maximize the SNR. In effect, the antenna beam is steered in the direction of the desired signal. If the direction to the desired satellite is known, beamforming can effectively maximize the SNR. It is however, possible to end up in situations where the jammer is in the same direction as the signal source.

Spatial filters reject the interference in angle, rather than frequency, and can achieve large anti-jam margins against most interference waveforms, including broadband noise. Spatial filters require multielement antenna arrays, which are significantly larger and heavier than single element antennas.

Combining spatial and temporal filtering allows nulls to be steered in both angle and frequency. This leads to a system that can cancel up to the number of elements in the antenna minus one [48].

For example, in [72], a set of requirements are derived for GNSS antennas that ensure critical infrastructure timing receivers have access to sufficient satellites to derive resilient time and frequency while placing a null in all polarizations at and below the horizon. The salient feature of these antennas is a null in the gain pattern in the direction of the horizon and around all azimuth angles to suppress ground-based interference.

3.8 Polarization domain techniques

Polarization domain techniques uses the unique physical property of the electromagnetic fields, the polarization, to distinguish between RFI or useful signals. In GNSS applications, this technique can achieve impressive antijam margins against all interference waveforms that are not Right-Hand Circular Polarization (RHCP) [48]. Otherwise, in conventional radiometry, the monitoring of the third and fourth elements of the Stockes parameters of the data coming from a dual-linear polarization antenna can be a very simple solution for the detection of RFI signals. The main advantage of this technique over spatial filters is that it only requires a single antenna element (with dual polarization) and as a result is expected to be significantly lighter and cheaper [48].

3.9 Conclusions

This chapter presents a summarized version of the types of RFI detection and mitigation techniques in the related literature. They can be divided in six different domains: time, frequency, signal sub-spaces, statistical, spatial, and polarization. They can be combined in order to enhance the final performance of the mitigation algorithm.

Part II

RFI countermeasures for MWR applications

4

Chapter 4

MERITXELL: an RFI detection and localization system for MWR

This chapter describes the Multifrequency Experimental Radiometer with Interference Tracking for EXperiments over Land and Littoral (MERITXELL) instrument, and its application to the detection and localization of RFI signals for MWR. MERITXELL is a ground-based multisensor instrument that includes a multiband dual-polarization radiometer, a GNSS reflectometer, and several optical sensors. Besides that, MERITXELL is anchored to a telescopic robotic arm that allows pointing its set of antennas to any direction. The main goals of MERITXELL are twofold: to test data fusion techniques, and to develop RFI detection, localization, and mitigation techniques. The former is necessary to retrieve complementary data useful to develop geophysical models with improved accuracy, whereas the latter aims at solving one of the most important problems of microwave radiometry.

4.1 Introduction

4.1.1 MERITXELL instrument

MERITXELL is a ground-based multisensor instrument that includes a multiband dual-polarization microwave radiometer, a GNSS reflectometer, and several optical sensors. Its main goals are to test data fusion techniques and to implement different kinds of RFI detection, localization and mitigation techniques.

Microwave radiometers are one of the most sensitive instruments that exist. This sensitivity allows measuring power fluctuations on the order of Kelvin units at the antenna. Taking into account that the frequency band reserved for MWR applications at L-band has a bandwidth of 27 MHz, 1 K of resolution in power is equal to -124.3 dBm, which is of the order of the power received from GNSS satellites over the Earth's surface. Given this sensitivity, the fluctuations of the received power can be used for RFI detection, at least, they will allow detecting RFIs with a power level larger or on the order of GNSS signals, with no further processing. However, if some RFI detection techniques are applied, this sensitivity can be even higher. One of these techniques may be the spectrogram analysis. The spectrogram allows performing sub-banding, which allows increasing the detection of CW-like RFI signals [73].

Moreover, MERITXELL is mounted in a telescopic robotic arm. This arm allows to point the antenna set to any direction (taking into account some security restrictions), and therefore it enables the localization of RFI sources at MWR bands. Performing a sweep in azimuth and elevation, the Direction Of Arrival (DOA) of the RFI signal can be inferred with a resolution that depends on the antenna beam-width for each frequency band. Moreover, MERIXELL can be placed in another location since it is anchored to a mobile unit. Performing several DOA measurements, the localization of the static RFI source can be determined with high accuracy.

MERITXELL has been developed at the CommSensLab at UPC-BarcelonaTech. Three PhD theses including this one, and a number of graduate and undergraduate students, have been working in the development of this instrument since 2007. The first PhD thesis [8] was devoted to the design and development of the radio-frequency systems. The second one [9] was devoted to the system integration, and temperature stabilization. This PhD thesis, the third one, is devoted to the calibration, characterization, and control of the instrument.

This chapter describes the MERITXELL instrument, and it explains the calibration and measurement process. Part of its contents has been published in a journal paper titled "MERITXELL: the Multifrequency Experimental Radiometer with Interference Tracking for Experiments over Land and Littoral. Instrument description, calibration and performance" [74]. It also includes part of the work done in the co-directed Final Degree Project (TFG) titled "Control of the back-end and positioning systems of the MERITXELL radiometer" [75] devoted to the implementation of a software to position and obtain the desired measurements from MERITXELL instrument. Further information about the operation of the MERITXELL mobile unit, the usage of the control and positioning software, and the communication between software, positioning system, and MERTIXELL are described in Appendix B.

Application	Frequency (GHz)
Clouds water content	21, 37, 90
Ice classification	10, 18, 37
Sea oil spills tracking	6.6, 37
Rain over soil	18, 37, 55, 90, 180
Rain over the ocean	10, 18, 21, 37
Sea ice concentration	18, 37, 90
Sea surface salinity	1.4, 6.6
Sea surface temperature	6.6, 10, 18, 21, 37
Sea surface wind speed	10, 18
Snow coating	6.6, 10, 18, 37, 90
Soil moisture	1.4, 6.6
Atmospheric temperature profiles	21, 37, 55, 90, 180
Atmospheric water vapor	21, 37, 90, 180
Vegetation Water Content	1.4
Land surface temperature	7, 10
Biomass	7, 10, 19

Table 4.1: Suitable frequency bands for most prominent MWR applications. Selected frequency bands for each application have been derived from [18] and [76].

4.1.2 Multiband microwave radiometers

As introduced in Chapter 2, MWR is a passive remote sensing technique that consists of measuring the spontaneous emission of electromagnetic energy radiated by all bodies at a physical temperature higher than 0 K. Nowadays, MWR has become a common and powerful tool for Earth remote sensing because of its high accuracy and large swath, despite its low spatial resolution. MWR allows measuring remotely atmospheric and geophysical parameters with the study and analysis of the received electromagnetic spontaneous emission. Among them, prominent examples are soil moisture, sea ice concentration, snow coating, rain rate over soil and ocean, sea surface salinity and temperature, wind speed over the sea, sea oil spills tracking, atmospheric temperature profiles, water vapor profiles, or cloud liquid water content [18]. However, each of these parameters can be only measured at some particular frequency bands for several reasons such as penetration depth, resonance frequencies of the molecules or transmittance of the atmosphere, etc. The most frequently used bands for some of the already mentioned applications are listed in Table 4.1.

Almost all geophysical parameters can be measured at multiple microwave frequency bands. Therefore, multiband microwave radiometers are designed to combine data retrieved from several bands in order to achieve improved measurements. Four examples of multiband microwave radiometers, two airborne and two spaceborne, are mentioned subsequently:

- The Helsinki University of Technology RADiometer (HUTRAD) for remote sensing is an airborne radiometer which includes a non-imaging subsystem that operates at six frequencies between 6.8 and 94 GHz, with vertically and horizontally polarized channels at each frequency [77].

- The Polarimetric Scanning Radiometer (PSR) is an airborne instrument that operates at 10.7, 18.7, 37, and 89 GHz, and measures the first three modified Stokes' parameters. It has two-axes scanning capability and provides polarimetric data for microwave emission studies of both ocean and land surfaces, as well as atmospheric clouds and precipitation [78].
- The Special Sensor Microwave Imager/Sounder (SSMI/S) is a spaceborne mission which includes a 24-channel single conically scanning radiometer and represents the most complex operational satellite passive microwave imager/sounding sensor ever flown with capabilities to profile the mesosphere. The receiver subsystem accepts the energy from the six antenna feeds and provides amplification and filtering to the 24 output channel located at the 19, 22, 37, 50-60, 91, 150, and 183 GHz frequency bands [79].
- The Advanced Microwave Scanning Radiometer for the Earth Observing System (AMSR-E) is a six-frequency dual-polarized total-power passive microwave spaceborne radiometer that observes water-related geophysical parameters supporting global change science and monitoring efforts. The supported frequency bands include 6.925, 10.65, 18.7, 23.8, 36.5, and 89.0 GHz [80].

In addition to MWR, other sensors working at different bands (e.g. radar and optical sensors) can retrieve complementary data useful to develop geophysical models with improved accuracy. In the field of remote sensing, the combination of multi-sensor measurements is better known as data fusion.

One example of data fusion is the combination of GNSS-R, and L-band MWR. As already mentioned in Chapter 2, GNSS-R is an emerging technique based on the acquisition of the forwardly scattered GNSS signals over the Earth's surface [35,81]. GNSS-R performs worse than L-band MWR in terms of accuracy due to its higher sensitivity to surface roughness (i.e. speckle noise), but it has a much better spatial resolution, especially when the coherent reflection process dominates over the incoherent one [35]. Therefore, both techniques can be used together to improve the spatial resolution of the overall measurement since they are sensitive to the same geophysical parameters, for instance in the case of soil moisture [82]. The combination of MWR and GNSS-R data has also been used to improve sea surface salinity retrievals, by correcting the sea state impact on the brightness temperature using GNSS-R observables [83].

Another example of data fusion with a similar approach is the combination of MWR measurements with optical sensor data. A study performed in [84] presents a downscaling approach to improve the spatial resolution of soil moisture estimates obtained by the SMOS (Soil Moisture and Ocean Salinity) mission with the use of higher resolution visible/infrared (VIS/IR) satellite data. The results of this study show a strong correlation between VIS/IR satellite data and soil moisture status.

4.2 Instrument design

MERITXELL is a ground-based multisensor instrument which includes a multiband dual-polarization microwave radiometer with several additional features that makes it unique as compared to other instruments. Its name stands for Multifrequency Experimental

Radiometer with Interference Tracking for eXpEriments over Land and Littoral. MERITXELL has been designed to fulfill the following requirements:

- to include all passive radiometric bands up to 100 GHz used for Earth observation from a satellite (this excludes the 50-60 GHz bands [18, Chapter 1]).
- to be built using a flexible back-end system to allow custom signal processing techniques for RFI detection, localization and mitigation, and data fusion algorithms.
- to include several optical sensors such as a thermal infrared and a multispectral camera with visible and near-infrared bands. These optical sensors are able to retrieve the complementary measurements used by data fusion algorithms.
- to include a GNSS reflectometer to retrieve GNSS-R data for data fusion algorithms.
- to be mounted in a ground-based mobile platform that allows to transport it and to point it to any desired position in azimuth and elevation.

An overall diagram of all constituent blocks of MERITXELL is shown in Fig. 4.1. Preliminary versions of the instrument and its sub-systems were already introduced in [8,9,85,86]. Nevertheless, the aim of this section is to present the final version of each sub-system, as well as the final integrated instrument.

The following subsections describe each one of the different parts of the instrument, including the multiband radiometer, the temperature stabilization system, the additional sensors, and the enclosure and mobile unit.

4.2.1 Radiometer assembly

The main part of MERITXELL is the eight-band dual-polarization total-power microwave radiometer, designed with a flexible back-end structure ready to implement RFI detection, localization, and mitigation algorithms. The description of the radiometer assembly is divided in three sub-sections: antenna set, front-end, and back-end.

4.2.1.1 Antenna Set

The antenna set of MERITXELL is formed by eight dual linear polarization antennas that collect the electromagnetic radiation in different passive Earth observation bands, commonly used in microwave radiometry. These eight bands are tagged with seven standard names: L-band (1.400 GHz - 1.427 GHz), S-band (2.69 GHz - 2.70 GHz), C-band (7.14 GHz - 7.23 GHz), X-band (10.6 GHz - 10.7 GHz), K-band (18.6 GHz - 18.8 GHz, and 23.6 GHz - 24.0 GHz), Ka-band (36 GHz - 37 GHz), and W-band (86 GHz - 92 GHz). For the sake of clarity, each of the bands at K-band is coined with a different name in this work. The 18.6 GHz - 18.8 GHz band is named K', whereas the 23.6 GHz - 24.0 band is named K". Figure 4.2 shows a front view of the eight antennas of MERITXELL without their radome.

In the case of the L-, S-, and C-bands, the antennas for each band are 4x4 patch arrays with a 25° beamwidth at -3 dB, a Main Beam Efficiency (MBE) of 95%, a Cross-Polarization Isolation (CPI) better than 35 dB in the main beam (i.e. -3 dB beamwidth), and a radiation efficiency η_A of 95%. Parameters obtained for the antennas have been

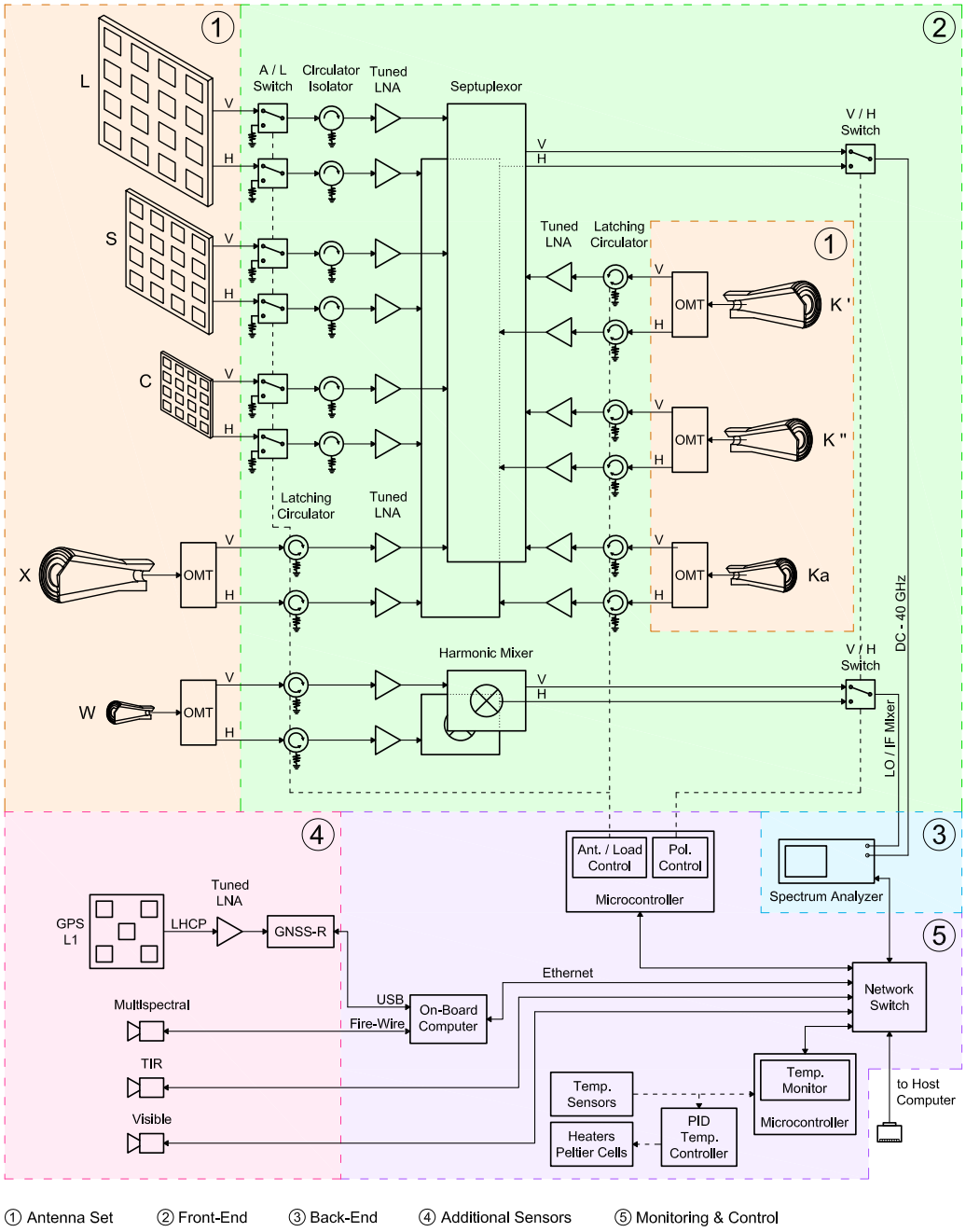

Figure 4.1: MERITXELL overall block diagram. The design has been divided in five sub-systems: (1) antenna set, (2) front-end, (3) back-end, (4) additional sensors, and (5) monitoring & control.

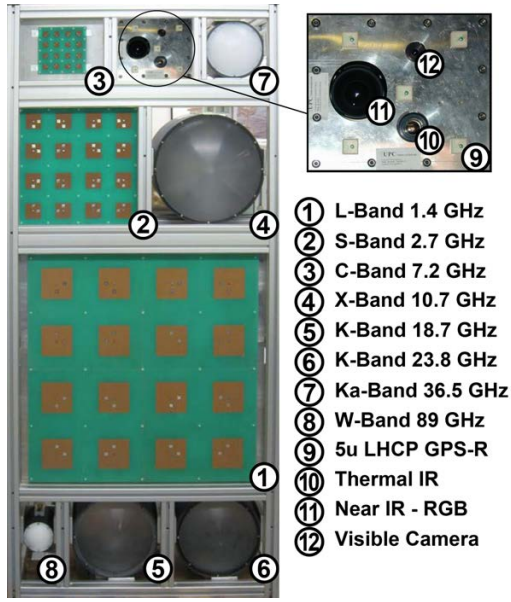

Figure 4.2: Front view of the antenna set and additional sensors of MERITXELL.

measured at UPC-BarcelonaTech anechoic chamber as mounted in the whole system. Each one of the patches that conform these array antennas is a dual-polarization coaxial-fed microstrip antenna printed in a 0.6 mm fiberglass circuit board with air as dielectric. The signals collected by the 16 patches are combined with different weights depending on the position in the array by means of a microstrip power combiner circuit for each polarization, vertical (V) and horizontal (H). Barlett (triangular) tapering is applied in both directions to reduce the side lobes and improve the main beam efficiency, a critical parameter for microwave radiometer antennas. Eventually, the signal output of each power combiner is guided through a coaxial cable to the front-end stage. These antennas have been developed following the novel architecture implemented in the L-band AUtomatic RAdiometer (LAURA) described in [87]. In fact, the one used for the L-band measurements is an improved replica of the LAURA antenna, whereas the S- and C-band antennas are scaled versions of the previous one.

For the X-, K'-, K"-, Ka-, and W-band, the chosen antenna for each one is a corrugated horn combined with a Fresnel lens that produces a Gaussian beam. The corrugated horns contribute to increase the bandwidth, as well as the MBE and CPI figures as compared to other kinds of horn antennas. The resulting antennas have a beamwidth at -3 dB with a maximum of 6° at X-band, and a minimum of 3.2° at W-band, their MBE is about 98%, their CPI is higher than 37 dB at the main beam (i.e. -3 dB beamwidth), and the radiation efficiency η_A is about 99%. The signal collected by each horn is separated into V and H polarization signals using an Orthomode Transducer (OMT). Eventually, each one of the OMT outputs feeds its corresponding waveguide to the front-end stage. Figure 4.3 shows the antenna used for the Ka-band with the corresponding output waveguides for V and H polarizations. Eventually, Table 4.2 summarizes the features of the antenna set built in MERITXELL.

Figure 4.3: Corrugated horn with its Fresnel lens used in the Ka-band with the corresponding output waveguides for V and H polarizations.

Frequency Band		Beamwidth	$\eta_{\mathbf{MBE}}$	CPI	η_A
L	1.400 GHz - 1.427 GHz	∼25°	95%	35 dB	∼95%
S	2.690 GHz - 2.700 GHz	∼25°	95%	35 dB	∼95%
C	7.140 GHz - 7.230 GHz	∼25°	95%	35 dB	∼95%
X	10.60 GHz - 10.70 GHz	6°	98%	40 dB	∼99%
K'	18.60 GHz - 18.80 GHz	5°	98%	40 dB	∼99%
K"	23.60 GHz - 24.00 GHz	4°	98%	40 dB	∼99%
Ka	36.00 GHz - 37.00 GHz	4°	98%	40 dB	∼99%
W	86.00 GHz - 92.00 GHz	3.2°	98%	37 dB	∼99%

Table 4.2: Main parameters of the eight dual-polarization microwave antennas of MERITXELL. They have been measured at UPC-BarcelonaTech anechoic chamber as mounted in the whole system.

4.2.1.2 Front-end stage

The front-end stage is composed of several sub-stages whose purpose is to condition the signals collected by the antenna set, and then, to guide them to the back-end stage. These sub-stages are depicted in the overall diagram in Fig. 4.1. The first sub-stage is used to calibrate the drifts of the amplifiers with the help of matched loads with known physical temperature. For the L-, S-, and C-band, the calibration stage is composed by a Single-Pole Dual-Through (SPDT) switch, that commutes between the signal coming from the antenna, and the matched load, followed by a circulator that acts as an isolator. For the X-, K'-, K"-, Ka-, and W-band, the scheme is similar but simplified due to the existence of the latching circulators. There is one matched load per band, and polarization and their physical temperature is measured by means of a digital temperature sensor attached to each one of them.

After that, the signal power is boosted with tuned amplifiers, one for each band and polarization. All these tuned amplifiers have a gain of at least 60 dB [9] in the band-pass frequency, with gain flatness $\leq$ 1.5 dB, noise figure $\leq$ 2.4 dB at the highest frequency band, and 1 dB compression point $\geq$ 5 dBm for the worst case.

Then, the output of each amplifier of the seven lower frequency bands (L-, S-, C-, X-, K'-, K"-, and Ka-band) are combined using two different septuplexors (7-to-1 tuned power combiners), one for the vertical and another for the horizontal polarization. After that, a SPDT switch commutes between the output of the two septuplexors, and finally, the

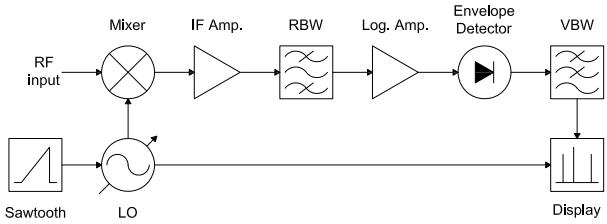

Figure 4.4: Functional diagram of a common Spectrum Analyzer.

combined signal reaches the back-end stage.

Furthermore, the W-band signal is treated in a different way as compared to the signal of the lower bands after the amplification stage. Since the bandwidth of the back-end stage can reach up to 40 GHz, the W-band signal is first down-converted to an Intermediate Frequency (IF) much lower than 40 GHz. This process is done using two specific harmonic mixers, one for the vertical, and another one for the horizontal polarization, whose features are detailed in the next section. After the down-conversion, a SPDT switch selects the polarization that is connected to the back-end stage.

Figure 4.1 summarizes the connections between the antenna set, the front-end stage and the back-end stage.

4.2.1.3 Back-end stage

The main purpose of the back-end stage is to measure the power level received at each of the eight frequency bands and each polarization. MERITXELL has been designed to perform these measurements using a common power detector, and hence, simplifying the overall design of the radiometer. Furthermore, this back-end stage allows performing real-time processing, and post-processing of the radiometric signal in order to detect RFI signals and to mitigate them.

The common power detector stage is completely performed by a Rohde & Schwarz (R&S®)FSP40 Spectrum Analyzer (SA) with a frequency range up to 40 GHz [88], that allows processing the seven lower frequency bands, from L- to Ka-band. The rationale is that the SA functional block diagram is almost identical to the back-end stage of a passive Total Power Radiometer (TPR). As can be seen in Fig. 4.4, the signal coming from the front-end stage is first down-converted to IF using a frequency mixer, and a Local Oscillator (LO). Then, the IF signal is amplified and band-pass filtered with the so-called Resolution Bandwidth (RBW). After that, the envelope is detected and low-pass filtered with the so-called Video Bandwidth (VBW). Eventually, the measurement of the power level is displayed or stored for later processing. In addition, when the LO is a variable frequency oscillator, as it is in a SA, the back-end stage becomes a spectroradiometer.

However, the real SA architecture is not identical to the functional block diagram. In fact, there are some differences even though the final performance is equivalent. The architecture of the R&S®FSP40 is based in a triple superheterodyne down-conversion followed to a digital IF stage as can be seen in Fig. 4.5 [88]. On the one hand, the triple down-conversion overcomes the difficulty of obtaining sufficient selectivity for the higher

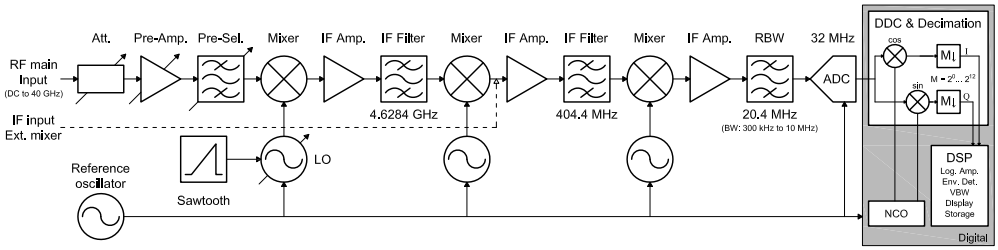

Figure 4.5: Real implemented architecture of the R&S®FSP40 Spectrum Analyzer [88].

frequencies, as compared to the former single mixer. On the other hand, the digital IF stage replaces the analog envelope detector, and the VBW, by adding versatility and functionality to the final display and storage of the data.

Furthermore, the W-band is treated in a singular way because the R&S®FSP40 main port can only reach up to 40 GHz. Therefore, the SA has been equipped with a R&S®FSP-B21 external mixer port module which enables it with the capability to receive signals centered at a frequency higher than 40 GHz. In particular, W-band signals can be processed when the SA is combined with the harmonic mixer R&S®FS-Z110. This harmonic mixer replaces the first two stages of the triple superheterodyne conversion, and therefore, it down-converts the W-band to a IF located at 404.4 MHz (see Fig. 4.5). From thereafter, the W-band signal is processed in the same way that the other seven frequency bands.

As mentioned above, the architecture of the R&S®FSP40 enables the capability of performing real-time processing of the radiometric data in order to detect RFI signals because of the inherent features of a SA. With them, the signal may be divided into several sub-bands that can be weighted to equalize or mimic arbitrary frequency responses of different instruments, time intervals, and calculate histograms and statistic moments of the received signal for each sub-band.

Moreover, the SA has the capability to store directly the In-phase and Quadrature (I/Q) components of the digital IF signal allowing a later post-processing of the radiometric data in the last stage. In this stage, the host computer performs the post-processing of the data. This includes several RFI detection and mitigation algorithms such as time-frequency blanking, normality tests, or the Multiresolution Fourier Transform (MFT) detailed in [24]. Eventually, the radiometric data can be sent out to the host computer to perform an extra off-line processing.

4.2.2 Additional sensors

MERITXELL has been equipped with other sensors at different bands, in addition to the radiometer assembly. The data collected by these additional sensors can be sent to the host computer for post-processing together with the radiometric data in order to complement and to add relevant information to the radiometric data, and at the end to perform data fusion techniques. This data is not sent either when MERITXELL is configured as a conventional radiometer, or in RFI detection applications. Besides, its

use for data fusion applications is out of the scope of this work. The additional sensors connected as in Fig. 4.1 and shown in Fig. 4.2, include a GNSS reflectometer, a Thermal Infrared (TIR) camera, a multispectral camera, and a visible camera.

4.2.2.1 GNSS reflectometer

GNSS-R can be used for the retrieval of many geophysical variables such as soil moisture [89] and ocean wind speed [90]. Moreover, GNSS-R may be used combined with L-band radiometry in order to correct errors in temperature brightness measurements induced by the characteristics of the measured surface [83]. For this reason, a GNSS-R device using GPS L1 C/A code has been installed in MERITXELL.

The antenna of the GNSS reflectometer consists of an array of 5 Left-Hand Circular Polarization (LHCP) GPS L1-band (1575.42 MHz) ceramic patches (see Fig. 4.2), with a power combiner that assigns different weights to every patch depending on its position in the array. As in L-, S-, and C-band antennas, Barlett tapering has been applied to reduce the side lobes and improve the main beam efficiency.

The output of the antenna is boosted by means of a tuned amplifier whose output is connected to a SIGE GN3S GPS sampler module [91]. The sampler module is connected by a USB cable to the onboard computer which can be accessed via Ethernet. The onboard computer acts just as a gateway between the internal devices and the host computer. GNSS-R sampled data is finally sent to the host computer for further processing.

4.2.2.2 Thermal Infrared Camera

One of the optical cameras integrated into MERITXELL is a TIR camera designed to provide thermographic imagery and repeatable temperature measurements. The data obtained with the TIR camera may be used to increase the accuracy of the radiometric measurements since it provides a real-time estimation of the physical temperature.

The TIR camera model is a FLIR A320 camera [92] with a spectral range from 7.5 μm to 13 μm, a Field of View (FOV) of 25° x 18.8°, a detector resolution of 320 x 240 pixels, and a maximum image frequency of 30 frames per second. In addition, the physical temperature can be measured with a thermal sensitivity (i.e. radiometric resolution) of 50 mK at 300 K.

4.2.2.3 Multispectral Camera

MERITXELL also includes a multispectral camera that has two configurable modes: Red-Green-Blue (RGB) or Color-Infrared (CIR). Multispectral cameras are commonly used in many remote sensing applications. In particular, the CIR configuration is chosen to study vegetation-covered areas because vegetation is highly reflective at Near-Infrared (NIR) band [93, p. 7]; whilst the RGB configuration is preferred in applications such as analyzing man-made objects, performing atmospheric and deep water imaging, or studying vegetation structures.

The multispectral camera model is a DuncanTech MS4100 [94] with a FOV of 60°, a detector resolution of 1920 x 1080 pixels, and a maximum image frequency of 10 frames

per second. The camera has 3-CCD image sensors that can work in either in RGB, or in CIR mode, and hence, it can measure electromagnetic radiation at four optical frequency bands: Blue (350 nm - 500 nm), Green (500 nm - 600 nm), Red (600 nm - 700 nm), and NIR (750 nm - 850 nm).

4.2.2.4 Video camera

The third and last camera is a Wansview NC510 IP camera [95], controlled remotely via an Ethernet connection. This camera adds real-time visible imagery to the scene from where the data is being measured.

4.2.3 Monitoring and control systems

In this sub-section, the auxiliary systems needed for thermal stabilization, temperature monitoring, instrument control, and data retrieval are introduced. All the information retrieved from these sub-systems, and the necessary commands to control them are sent to and received from an external host computer via Ethernet connection.

4.2.3.1 Enclosure

Thermal stabilization is an essential need of a microwave radiometer since variations of the physical temperature will lead to variations in the measurements. The origin of these variations is the dependence on the physical temperature of the gain and noise figure of all the elements of the radio-frequency chain. Consequently, the radiometer must be thermally insulated. This is achieved using an enclosure designed to minimize the heat exchange between inside and outside the radiometer. The walls of MERITXELL are 20 mm dual-side metalized foam boards (both for electromagnetic interference and thermal insulation), except for the front part. The antennas are covered with a 5.5 mm thick Depron® radome (a kind of white polystyrene foam), showing losses of approximately 0.25 dB at W-band. The metallic part of the walls is composed of two sheets of 1 mm thickness aluminum. Both the metallic enclosure and the white radome can be seen in Fig. 4.6, with approximate dimensions of 180x90x90 cm.

4.2.3.2 Thermal stabilization

Microwave radiometers usually work at a constant temperature higher than the outside so that the maximum antenna temperature (with no RFI signals) will be eventually lower than the internal temperature. Moreover, it is easier to perform the temperature stabilization by using heating elements. Hence, MERITXELL radiometer is designed to work at a constant temperature of around 45°C.

The temperature control is performed using a 2216L Eurotherm Proportional Integral Derivative (PID) temperature controller. The temperature inside the radiometer is measured with a PT100 temperature dependent resistance. With this temperature measurement, the PID is able to maintain the temperature inside the radiometer at a determined constant value with the control of a set of heaters and Peltier cells.

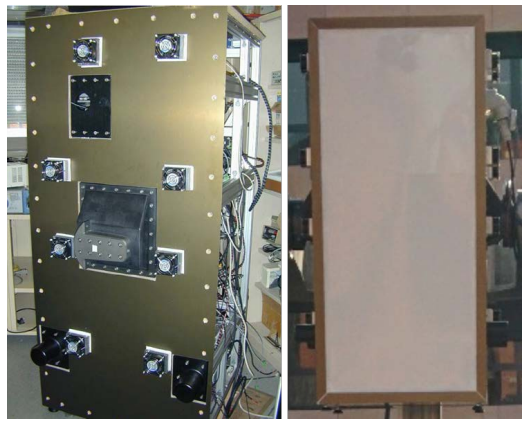

Figure 4.6: Side view of MERITXELL's enclosure (left), and front view the antenna radome (right).

4.2.3.3 Thermal monitoring

In order to measure periodically the temperatures of the matched loads and the amplifiers of each band and polarization, 32 DS18B20 digital temperature sensors (one for each of the 16 amplifiers and 16 matched loads) are used. These sensors provide temperature measurements with an accuracy of $\pm$ 0.5°C. The sensor readings are controlled by a microcontroller which makes the data available to the host computer via an Ethernet connection. Then, once the temperature values are retrieved, they can be used to calibrate and correct the radiometric measurements.

4.2.3.4 Switch control

As mentioned above, the switches and latching circulators select the polarization and the radiometric input (antenna or matched load) for the different frequency bands. A microcontroller with Ethernet connection allows controlling from the host computer the 6 switches and the 10 latching circulators that determine the radiometric input, and the 2 switches that select the polarization (see Fig. 4.1).

4.2.4 Mobile unit

As above mentioned, MERITXELL dimensions are approximately 180x90x90 cm, and the total weight is larger than 250 kilograms. These weight and dimensions make the handling of MERITXELL a very complex task. Therefore, a mobile unit was designed and manufactured by an external company in order to transport and handle the positioning of MERITXELL.

4.2.4.1 Telescopic robotic arm

This mobile unit consists of a telescopic robotic arm able to handle the radiometer and to manage its positioning, mounted on a NISSAN ATLEON truck that allows transporting

Figure 4.7: MERITXELL assembled to the telescopic robotic arm above the housing structure and the truck.

the entire system. In order to position the radiometer, the arm is capable to rise it up to 8 meters from the ground, and then to change its pointing direction using two different rotors. One controls the azimuth of MERITXELL. Azimuth can be set from 45° to 315°, where 0° is pointing to the cabin of the truck, and the angle increase in the counterclockwise direction. The other rotor controls the elevation movement, defined as the zenith angle, where it can be modified from 0° (zenith) to 155° (incidence angle of 25°). Both angle restrictions are set for safety reasons. Moreover, the telescopic arm has three states: up or measuring, down or parked, and calibration or pointing to a microwave absorber, which is used to perform the hot load calibration. All the structure is mounted inside a fiberglass housing for transportation and storage purposes. Figure 4.7 shows MERITXELL assembled to the telescopic arm above the housing structure and the truck.

Moreover, the mobile unit has four stabilization legs manually controlled covering the maximum surface allowing to work with an instrument at eight meters high withstanding winds of up to 100 km/h. Both the telescopic robotic arm and the stabilization legs work with hydraulic units.

4.2.4.2 Positioning control

The telescopic robotic arm is controlled by a Programmable Logic Controller (PLC) located in a control panel inside the truck. This PLC is connected to the host computer via

a serial connection, which sends the commands needed to move MERITXELL radiometer to the desired position. Further information can be found in Appendix B.

4.3 Instrument control

The positioning, configuration, and operation of MERITXELL are controlled by a dedicated software running on the host computer. The host computer sends and receives the desired commands to MERITXELL via Ethernet connection, whereas the communication with the PLC of the positioning system takes place via a serial port.

MERITXELL software has been designed to perform the radiometric measurements, including the selection of the frequency band and bandwidth to store the retrieved data to the host computer, and to manage the handling and positioning of the radiometer itself. Besides, the configuration and data retrieval of the additional sensors is done using their dedicated software programs. However, the positioning functionality of the presented MERITXELL software can still be used for the additional sensors (e.g. cameras).

4.3.1 Graphical user interface

MERITXELL software has a user-friendly Graphical User Interface (GUI) that allows to display the information received from MERITXELL and its positioning system, and to generate the desired configuration instructions. The operation of the software is based on the generation of a list of command instructions which are executed sequentially. The possible commands comprise the configuration of the spectrum analyzer, switch control, and positioning instructions. Figure 4.8 shows the GUI of MERITXELL software, which is divided into six blocks described below.

Block 1 allows generating the instructions related to the positioning of MERITXELL. First of all, the instrument can be set either to the store position or to the calibration position with the corresponding buttons and located inside the housing enclosure. At the calibration position, the antenna set is in front of a microwave absorber which is used as a hot load for calibration purposes. Moreover, the scan option is used to point the instrument to either a specific direction or a range of positions defined by their azimuth and elevation. In order to satisfy the security restrictions, the software does not allow to generate pointing values with an azimuth lower than 45° or larger than 315°, and an elevation greater than 155° (recall that the elevation is defined as the zenith angle). Eventually, the abort button allows the user to immediately retract the robotic arm, and to store the instrument.

Block 2 displays several parameters related to the current state of the positioning system. The arm and radiometer angles determine the current position of the two axes of the robotic arm that holds the instrument. The former is the angle between the mast and the rotation axis of MERITXELL, whereas the latter is the current elevation angle determined by the encoder of the rotation axis. In addition, the roll and pitch of the overall structure, together with the wind speed (red flag in Figure 4.8) measured with an anemometer at the top of the mast, are used to monitor if the positioning system is working under safe conditions. Furthermore, the rest of the elements of Figure 4.8 block 2 contain additional information related to the operation of the positioning system.

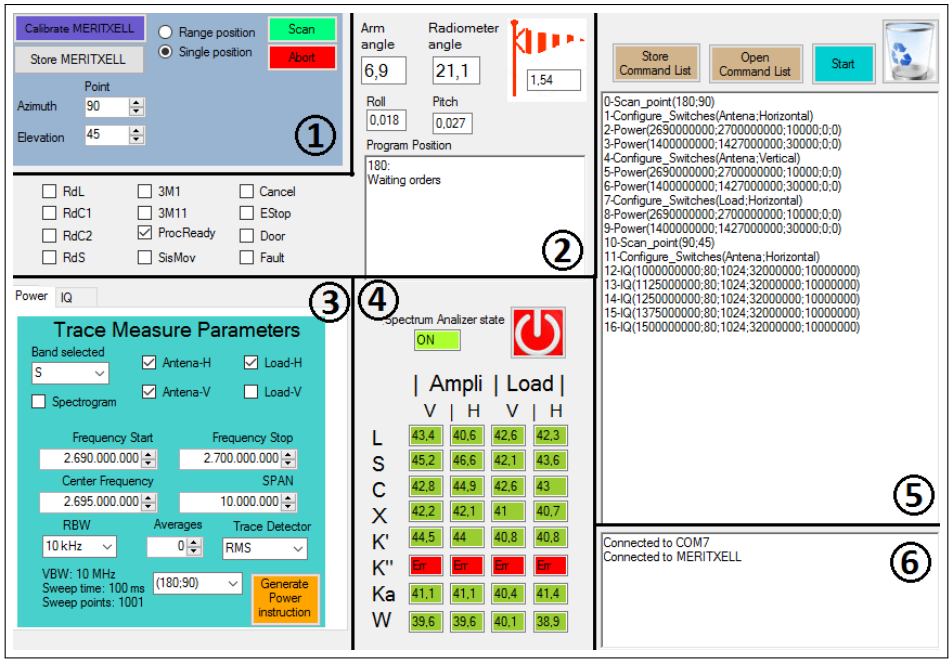

Figure 4.8: Graphical user interface of the host program used to control MERITXELL. It contains six different parts: (1) positioning control, (2) positioning monitoring, (3) measurement control, (4) temperature monitoring, (5) command list, and (6) debugger.

Block 3 generates the instructions to configure the back-end (the spectrum analyzer), and the matched load and polarization switches. The back-end can be configured to retrieve either the spectrum at the selected band, or a spectrogram (a collection of consecutive spectra), or directly sampled I/Q signals. Further details of each kind of measurement are provided in the subsequent section. Moreover, each one of these measurements can be attached to one or more scanning positions generated using Block 1. Eventually, this block also allows the user to select between measurements taken from the antenna or from the matched load, and at either horizontal or vertical polarization.

Block 4 displays the values of the temperature sensors located at the matched loads and amplifiers of each frequency band. These values are the average of the last ten temperature measurements of each sensor. This gives a resolution of 0.02 K according to the temperature sensor specifications. Moreover, the gradient of each temperature value is represented using a color code being red if the gradient is higher than 3 mK/s, yellow if it is higher than 1.5 mK/s, blue if it is lower than -1.5 mK/s, and green otherwise. These values are obtained by dividing the difference between the average of the last and the previous fifteen measurements by the mean time between the averages which is 37.5 seconds. The green color is used to indicate that the system is stable in temperature ($\pm$ 1.5 mK/s), and, if this is the case, the desired measurements can be performed. Eventually, temperature values are stored once a measurement takes place for further processing.

Block 5 shows the list of instructions to be executed. These are generated using Block 1

and Block 3, and they are executed when the“ Start” button is pressed. The instructions are executed sequentially in the order of appearance, and the program runs until all of them are done. Furthermore, the list of instructions can be saved and loaded for further executions.

Block 6 shows messages that help the user to follow the execution process and to debug possible errors.

4.3.2 Back-end configuration

As mentioned above, the back-end stage of the multiband radiometer is implemented using a spectrum analyzer R&S®FSP40. The configuration of the SA is implemented using several built-in commands sent via Ethernet connection. Block 3 of the GUI software helps the user to generate these configuration commands to get the measurements and retrieve the data. There are two modes of operation: power or I/Q measurements.

4.3.2.1 Power measurements

The power mode allows getting directly the power spectral density of the system noise measured by the SA. When several noise spectra are retrieved consecutively, their orderly aggregation conforms a spectrogram. The spectrogram allows to detect temporal changes in the spectrum, however, it requires larger communication bandwidth and acquisition time. Each point of the spectrum represents the radiometric noise power spectral density corresponding to a specific frequency in the span bandwidth, with a noise bandwidth equal to the resolution bandwidth of the SA. In order to understand clearly this last statement, the configurable SA parameters and their relationship with the radiometric performance are described subsequently.

The *center frequency* f_c determines the center point of the frequency band under analysis. According to the front-end design, there are eight usual values for this parameter, which are the center frequency of each band.

The *span* B_r is the overall receiving bandwidth to be analyzed centered at f_c. As the previous parameter, it is usually defined as the bandwidth of the eight frequency bands supported by the front-end.

The *resolution bandwidth* RBW is the bandwidth of the last and narrower bandpass filter in the IF chain (see Fig. 4.5). This value determines the noise power and resolution of each point of the spectrum. The possible values for RBW are increasing from 10 Hz to 10 MHz in steps of 1, 3 or 10 [88].

The *video bandwidth* VBW is the bandwidth of the lowpass filter set after the detector. For radiometric purposes, this value is automatically set to ten times the resolution bandwidth, VBW = 10 × RBW, in order to ensure that the peak values of the voltage after the detector are not cut off by the video filter [88].

The *sweep time* SWT is the time that the local oscillator takes to sweep the whole B_r. This parameter is automatically set to its minimum value [88]

$$\mathrm{SWT} = \mathrm{k}\frac{B_r}{\mathrm{RBW}^2}, \tag{4.1}$$

where k is a is a constant internal parameter of the R&S®FSP40.

The *number of sweep points* N_{SWP} is the number of points obtained for each spectrum measurement. Given the SA structure, samples are statistically independent if the time difference between consecutive acquisitions is at least 1/RBW. This means that the maximum number of statistically independent samples N_{IND} taken for each B_r is equal to

$$N_{\mathrm{IND}} = \frac{B_r}{\mathrm{RBW}}. \tag{4.2}$$

However, N_{SWP} can only be configured as one of the values of the set 8001, 4001, 2001, 1001, 501, 251, and 125. Therefore, this parameter is set automatically by the SA to the minimum value of the previous set that satisfies the inequality

$$N_{\mathrm{SWP}} > \frac{B_r}{\mathrm{RBW}}. \tag{4.3}$$

The *trace detector* determines the algorithm used in the detection process. There are three types of detectors: *sample* which uses a midpoint value for each sweep point, *peak* which uses the maximum or minimum detected value for each point, and *average* which uses all of the detected values within a point to calculate the final value. The default algorithm used in MERITXELL is the average of power using the Root Mean Square (RMS) of the input samples.

The power spectrum retrieved with the RMS detector contains N_{SWP} measurements of the radiometric noise in the whole bandwidth under analysis B_r. The measured power value for each point of the spectrum is

$$P_{\mathrm{RMS}}(f_p) = \frac{1}{N_{\mathrm{p}}} \sum_{m=0}^{N_{\mathrm{p}}-1} \left| s\left[m + n_{\mathrm{SWP}}\, N_{\mathrm{p}}\right] \right|^2, \tag{4.4}$$

where $n_{\mathrm{SWP}} \in [0, 1, \cdots, N_{\mathrm{SWP}} - 1]$ is the index of each sweep point, $f_p = f_c - \frac{B_r}{2} + n_{\mathrm{SWP}} \frac{B_r}{N_{\mathrm{SWP}}-1}$ is the frequency of each point of the spectrum, $s[m]$ is the linear digitized video voltage at the output of the Analog-to-Digital Converter (ADC) at the SA, and N_{p} is the number of values of the ADC per sweep point defined as

$$N_{\mathrm{p}} = F_s \frac{\mathrm{SWT}}{N_{\mathrm{SWP}}} = F_s\, T_{\mathrm{SWP}}, \tag{4.5}$$

where F_s is the sampling frequency of the ADC (32 MHz), and T_{SWP} is the sweep time per sweep point.

The *number of averages* N_{AVG} is the number of sweeps or averaged spectra per measurement. The number of averages increases proportionally the integration time. If the spectrogram option is active, N_{AVG} determines the number of consecutive spectra. Besides, if N_{AVG} is set to either 0 or 1, only one sweep is performed. The averaged spectrum can be expressed as

$$\overline{P_{\mathrm{RMS}}}(f_p) = \frac{1}{N_{\mathrm{AVG}}} \sum_{i=0}^{N_{\mathrm{AVG}}} P_{\mathrm{RMS}_i}(f_p), \tag{4.6}$$

whereas if the value of all spectrum points are averaged, the measured radiometric power over the acquisition band B_r can be defined as

$$P_m = \frac{1}{N_{\mathrm{SWP}}} \sum \overline{P_{\mathrm{RMS}}}(f_p). \tag{4.7}$$

Taking into account the parameters mentioned above and the resolution of a TPR [18, p. 359-366], the radiometric resolution of MERITXELL multiband radiometer per sweep point using the RMS detector, and several averaging points is

$$\Delta P_{\mathrm{RMS}}(f_p) = \frac{\overline{P_{\mathrm{RMS}}}(f_p)}{\sqrt{\mathrm{RBW}\, T_{\mathrm{SWP}}\, N_{\mathrm{AVG}}}} = \frac{\overline{P_{\mathrm{RMS}}}(f_p)}{\sqrt{\mathrm{RBW}\, \frac{\mathrm{SWT}}{N_{\mathrm{SWP}}} N_{\mathrm{AVG}}}}. \tag{4.8}$$

Eventually, the resolution may be increased when averaging all the points of the spectrum. However, since there may be an overlapping of the RBW from consecutive sweep points ($N_{\mathrm{SWP}} \geq N_{\mathrm{IND}}$), the overall radiometric resolution after averaging all sweep points is

$$\Delta P_m = \frac{P_m}{\sqrt{N_{\mathrm{IND}}\, N_{\mathrm{AVG}}}} = \frac{P_m}{\sqrt{\frac{B_r}{\mathrm{RBW}}\, N_{\mathrm{AVG}}}}. \tag{4.9}$$

4.3.2.2 I/Q measurements

The I/Q acquisition mode allows retrieving directly the in-phase and quadrature components of the radiometric signal. This mode is needed for advanced RFI detection and mitigation techniques in the host computer. In this mode, the radiometric signal is conditioned as in power mode until it reaches the ADC (see Fig. 4.5). Once the signal is digitized, the signal is downconverted to its baseband I/Q components, which are stored and sent to the host computer for further processing. Figure 4.9 shows a diagram of the digital downconversion structure.

Using the I/Q mode, the SA configuration parameters take a slightly different meaning as compared to the power mode:

- The *central frequency* configures the frequency of the local oscillator (external mixer in the W-band), which is fixed in this mode.
- The *reference level* determines the maximum amplitude (or power) of the dynamic range of the ADC.

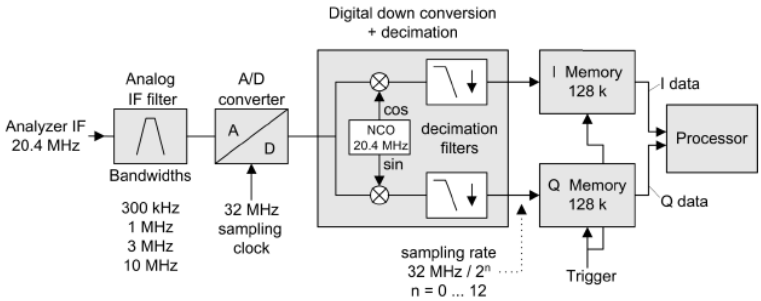

Figure 4.9: Diagram of the digital downconversion and sample retrieval of the I/Q acquisition mode.

- The *ADC filter* sets the bandwidth of the anti-aliasing filter before the ADC. It is equivalent to the RBW, but its possible values are 10 MHz, 3 MHz, 1 MHz, and 300 kHz.
- The *sample rate* sets the decimation value after the digital downconversion, and then the output sample rate. The decimation value increases in powers of 2 from 1 to 2048.
- The *number of samples* determines the size of each data acquisition. The available buffer can store is up to 128k samples.

4.4 Calibration and characterization

This section describes the measuring principle, the radiometric stability, and the calibration procedure and results of the multiband dual-polarization total power radiometer of the instrument MERITXELL.

4.4.1 Measuring principle

The goal of a radiometer is to measure the antenna temperature T_A, which is defined as the radiometric noise power collected by the antenna. However, since all the antennas have some losses, the antenna temperature measured at its output terminals T'_A is [18, p. 207-208]

$$T'_A = \eta_A \, T_A + (1 - \eta_A) \, T_{pA}, \tag{4.10}$$

where η_A is the antenna radiation efficiency, and T_{pA} is the physical temperature of the antenna. Approximate values for η_A are shown in Table 4.2. Signals received by the antennas are amplified and filtered by the front-end and back-end stages, which also introduce some additional noise. Therefore, the power level measured at the input of the detector P_R is [18, p. 350-352]

$$P_R = k_B \, G_r \, T_{sys} \, B_r = k_B \, G_r \, (T'_A + T_r) \, B_r, \tag{4.11}$$

where k_B is the Boltzmann constant, G_r is the total gain of the receiving chain, T_{sys} is the total system temperature, T_r is the equivalent input noise temperature of the receiving chain, and B_r is the system bandwidth.

In the case of MERITXELL, because of the high gain of the first stage (more than 60 dB), T_r can be approximated by the equivalent noise temperature introduced by the front-end stage, and the B_r is set by the bandwidth of the back-end stage (span parameter of the SA).

After that, the noise signal reaches the detector, and the power level measured at its output P_m can be expressed after combining previous equations as

$$P_m = G_d\, P_R + P_d = G_d\, G_r\, k_B\, (\eta_A\, T_A + (1 - \eta_A)\, T_{pA} + T_r)\, B_r + P_d, \tag{4.12}$$

where G_d is the conversion gain, and P_d accounts for a possible bias of the detector.

In order to determine the number of unknown parameters in (4.12), and hence, to know the equivalence between the antenna temperature and the measured power after the detector, a calibration procedure must be applied.

4.4.2 Calibration procedure

According to (4.12), the power measured by a radiometer is a linear function of the antenna temperature and a number of a priori unknown parameters. The calibration process is required to obtain the values of these parameters, which vary with temperature and frequency band. As detailed in Section 4.2.3.2, thermal stabilization is of crucial importance in this case, in order to keep constant the values of the unknown parameters, and in particular, the gain of the amplifiers.

Two different calibration methods are used depending on the frequency band. In the case of the three lower bands (L-, S-, and C-band), the simple hot-cold calibration [18, p. 402-404] is applied using the microwave absorber at a known temperature set in front of the antennas as hot load, and the radiometer pointing to the sky at zenith position as a cold load. On the other hand, the upper bands are calibrated combining the tipping curves method [96, 97], which is used to retrieve several cold calibration points, with the hot-cold method. Calibration using tipping curves cannot be applied at the L-, S-, and C-band because of the wide antenna pattern and its non-negligible side lobes, which start collecting radiation from the ground when the beam is not pointing to the zenith.

4.4.2.1 Hot-Cold Calibration

The hot-cold calibration is the simplest method used in calibration of microwave radiometers. It is based in a two-point linear approximation of the measured power as a function of the antenna temperature. One point corresponds to the power P_{hot} and antenna temperature T_{abs} measured at the hot calibration point (looking to the microwave absorber), and the other corresponds to the power P_{cold} and antenna temperature T_{sky} measured at the cold calibration point (looking to the sky at zenith). The hot-cold calibration can be modeled as the linear system of equations

$$\left.\begin{aligned} P_{hot} &= a\,T_{abs} + b \\ P_{cold} &= a\,T_{sky} + b \end{aligned}\right\} \tag{4.13}$$

where

$$a = G_d\,G_r\,k_B\,\eta_A\,B_r, \tag{4.14}$$

and

$$b = \frac{a}{\eta_A}\left((1-\eta_A)\,T_{pA} + T_r\right) + P_d. \tag{4.15}$$

The physical temperature of the microwave absorber can be obtained using either an external sensor or MERITXELL's TIR camera. Besides, the zenith sky temperature can be approximated by the temperature of the cosmic background plus the downwelling atmospheric temperature (T_{sky} ∼6 K, which are nearly independent of the atmospheric conditions between 1 and 10 GHz [18, p. 287]).

Therefore, measuring the values of P_{hot} and P_{cold}, a and b can be obtained from (4.13) as

$$a = \frac{P_{hot} - P_{cold}}{T_{abs} - T_{sky}}, \tag{4.16}$$

and

$$b = \frac{P_{cold}\,T_{abs} - P_{hot}\,T_{sky}}{T_{abs} - T_{sky}}. \tag{4.17}$$

Once the a and b parameters are obtained for each band, the relationship between the output and the input of the radiometer is fully characterized. In addition, the power level P_{load} measured when the switch is commuted to the matched load can be expressed using (4.14) and (4.15) as

$$P_{load} = \frac{a}{\eta_A}\left(T_{load} - (1-\eta_A)\,T_{pA}\right) + b. \tag{4.18}$$

Equation (4.18) can be also used for the hot-cold calibration, only if $T_{load} = T_{pA}$. In MERITXELL, the identity $T_{load} = T_{pA}$ is fulfilled to within ±0.5°C thanks to the thermal insulation and stabilization sub-systems.

4.4.2.2 Tipping curves

The tipping curves are a series of measurements of the sky at different zenith angles, which are adopted for convenience in the calibration of ground-based radiometers, assuming a horizontally stratified atmosphere. With the information of the sky opacity, it is possible to determine the brightness temperature of the sky at any zenith direction which can be used as a cold calibration target [96, 97].

Taking into account the radiative transfer equation under the Rayleigh-Jeans approximation and the assumption of a single layer atmosphere, the antenna temperature under a zenith angle θ is given by

$$T_A(\theta) = T_{cos}\, e^{-\tau(\theta)} + T_m(\theta)\left(1 - e^{-\tau(\theta)}\right), \tag{4.19}$$

where T_{cos} is the cosmic background radiation (~ 2.7 K), $T_m(\theta)$ is the average temperature of the troposphere, and $\tau(\theta)$ is the total slant opacity. According to [96], the slight angular dependence of $T_m(\theta)$ can be ignored for low opacity channels such as the ones selected for MERITXELL, and its value can be estimated from the ground temperature T_{gr} as $T_m(\theta) \approx T_m(0) \approx T_{gr} - 10$ K. Moreover, the total slant opacity can be defined as

$$\tau(\theta) = \tau(0)\sec(\theta), \tag{4.20}$$

where $\sec(\theta)$ is equivalent to the number of atmospheres that contribute to the antenna temperature, and then, from (4.19)

$$T_A(\theta) = T_m + (T_{cos} - T_m)\,(L_{atm})^{\sec(\theta)}, \tag{4.21}$$

where $L_{atm} = e^{-\tau(0)}$ is the total atmosphere attenuation at zenith direction.

Equation (4.21) defines the tipping curves for a ground-based microwave radiometer, which allow to determine the atmospheric opacity at zenith $\tau(0)$, and then to obtain the $T_A(\theta)$ values to be used as cold temperature points in the hot-cold calibration. Eventually, (4.21) can be combined with the hot-cold calibration procedure (4.13), in order to obtain the tipping cures in terms of measured power as

$$P_{cold}(\theta) = a\left((T_m - T_{hot}) + (T_{cos} - T_m)\,(L_{atm})^{\sec(\theta)}\right) + P_{hot}. \tag{4.22}$$

4.4.3 Calibration examples

In this subsection, the results of one example of each of the calibration procedures mentioned in the previous section are shown. Measurements have been performed in clear sky conditions, after the sunset, at a ground temperature T_{gr} of 9°C, and with the receiving chain stabilized in temperature.

The first example corresponds to the calibration of the C-band V-polarization channel. In this case, six calibration points are measured, two hot ones pointing to the microwave absorber, two cold ones pointing to the sky at the zenith, and two matched load measurements. The measurements have been taken using the following parameters: the

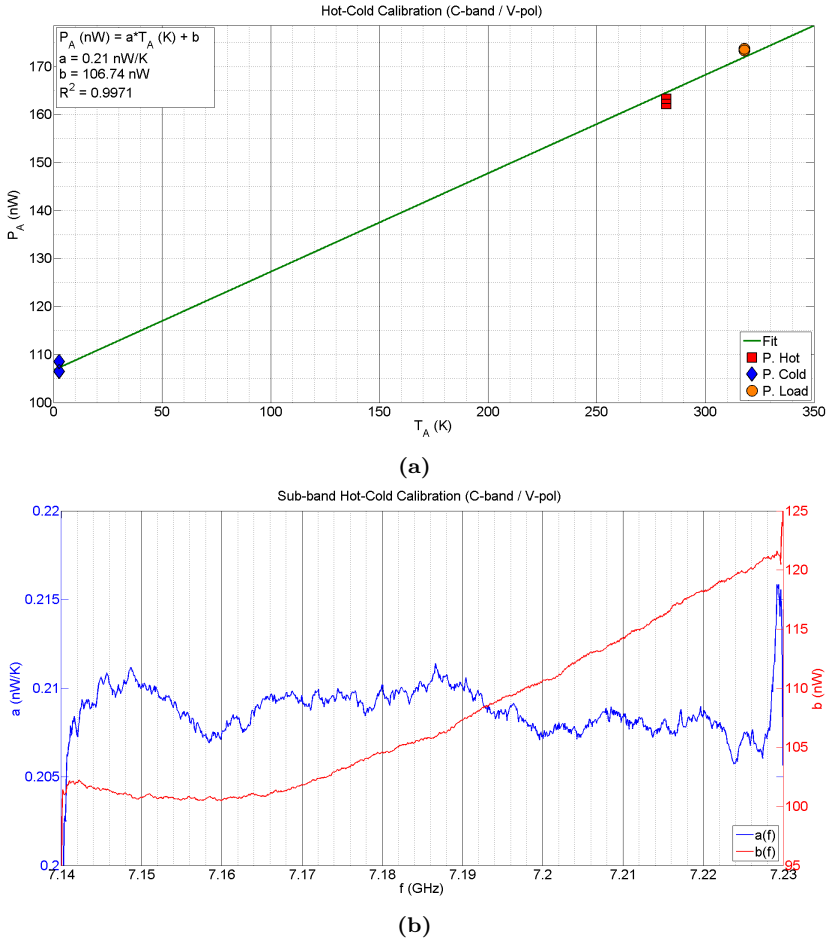

Figure 4.10: Hot-cold calibration of the C-band V-polarization channel. Sub-figure (a) shows the calibration procedure for averaged values in the whole bandwidth, whereas (b) depicts the a and b values obtained for each sub-band.

acquisition band B_r is 90 MHz, the RBW is 100 kHz, the N_{SWP} is 1001, the SWT is 9 ms, and the N_{AVG} is 1000.

Using these measurements, the a and b parameters are obtained by solving (4.14) and (4.15) using a linear regression method. Since the back-end stage provides power spectrum measurements, a and b parameters may be obtained either by averaging the whole spectrum or for particular sub-bands. If the power spectrum is averaged over the whole acquisition bandwidth, the values obtained are $a = 0.21$ nW/K, and $b = 106.74$ nW, with a R^2 parameter (i.e. coefficient of determination) equal to 0.9971. The results of the averaged hot-cold calibration for the C-band V-polarization are shown in Fig. 4.10a. On the other hand, Fig. 4.10b shows the a and b values for sub-bands equal to the RBW. In this case, it can be appreciated that the gain a fluctuates around its average value, and the bias b slightly increases with frequency. Moreover, the band-limiting effect of the

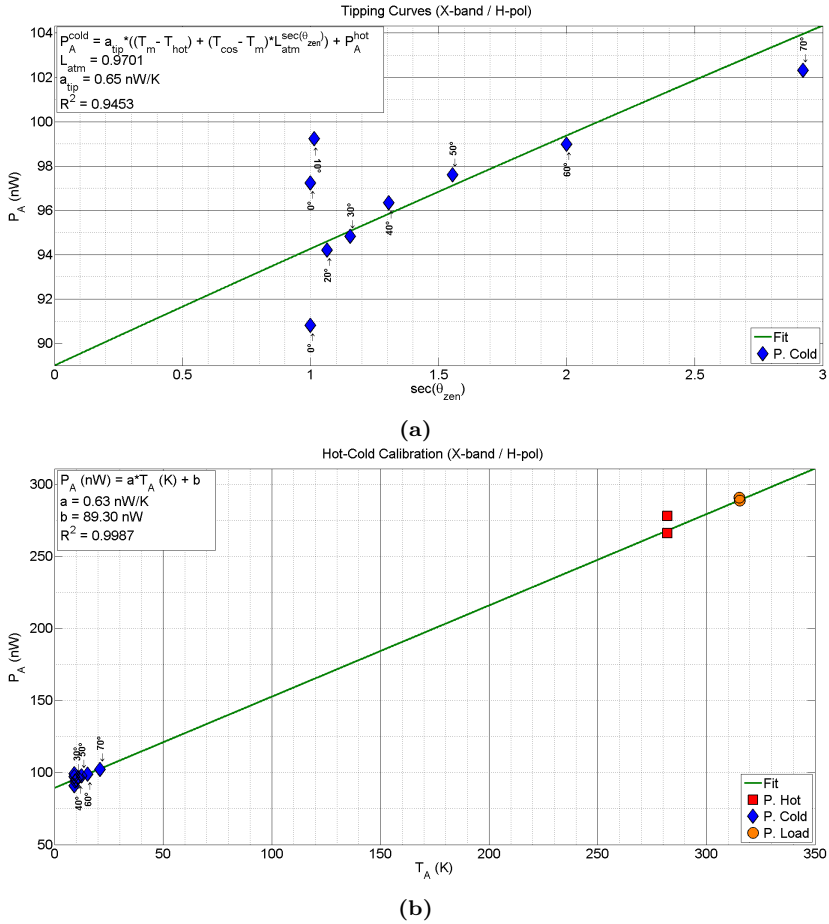

Figure 4.11: Hot-cold calibration of the X-band H-polarization channel using tipping curves. Subfigure (a) shows the power tipping curves as a function of the equivalent number of atmospheres. The elevation angle has been swept from 0° (zenith) to 70°, in steps of 10°. In subfigure (b) the hot, cold and load calibration points are depicted. The cold calibration points have been obtained using the previous tipping curves procedure.

filters generates outlier a values (minimum and maximum peaks) at the band edges.

The second example corresponds to the calibration of the X-band H-polarization channel. In this case, thirteen calibration points are measured, two hot ones pointing to the microwave absorber, nine cold ones pointing to the sky at different zenith angles, and two matched load measurements. The measurements have been taken using the following parameters: the acquisition band B_r is 100 MHz, the RBW is 100 kHz, the N_{SWP} is 1001, the SWT is 9 ms, and the N_{AVG} is 1000.

The cold calibration points have been obtained by changing the elevation angle of the radiometer from the 0° (zenith) to 70°, in steps of 10°, and one extra measurement has been acquired at the zenith position. This corresponds to values from one to approxi-

	Horizontal Polarization		Vertical Polarization	
Frequency Band	**Integration Time (s)**	**Allan Deviation ($\times 10^{-3}$)**	**Integration Time (s)**	**Allan Deviation ($\times 10^{-3}$)**
L	193	1.73	142	1.44
S	35	2.77	49	2.30
C	55	2.49	16	3.83
X	89	1.93	34	3.18
K'	29	3.62	13	4.89
K"	55	2.48	77	2.55
Ka	50	2.79	6	6.29
W	13	7.14	17	4.56

Table 4.3: Optimal integration time and Allan deviation for each the frequency band and polarization.

mately three equivalent atmospheres. Figure 4.11 shows the results of the tipping curve equation defined in (4.22) for the X-band H-polarization channel, as a function of the equivalent number of atmospheres (secant of the elevation angle). With these values and using a robust (outlier values were discarded) non-linear regression method, the total atmosphere attenuation at zenith direction L_{atm} has been estimated to be 0.9701, with an R^2 parameter equal to 0.9453. Outlier values measured at lower zenith angles are induced by the small (but enough) internal temperature differences that occur when changing the position of the radiometer, despite internal fans are installed to minimize this effect.

Once estimated the L_{atm}, the hot-cold calibration can be performed using several cold points to determine the unknown parameters. The results of the hot-cold calibration for the X-band averaged in the whole bandwidth are shown in Fig. 4.11. The a and b parameters are obtained as in the previous case. The obtained values are a equal to 0.63 nW/K, and b equal to 89.30 nW, with a R^2 parameter equal to 0.9987. Note that in the tipping curves regression the estimation of the $a = 0.65$ nW/K was also very similar.

4.4.4 Radiometric stability

Once the calibration is performed, the radiometric stability of the receiving chain has been studied. The radiometric stability is the parameter that provides information about how the calibration parameters will drift with time. The radiometric stability depends on several parameters such as temperature drifts, or instability of amplifiers gain, among others [98].

The radiometric stability is calculated as the Allan variance of the retrieved power for each band and polarization [98]. Moreover, it also determines the optimum integration time to achieve the best radiometric sensitivity.

The Allan deviation measurements (square root of the variance) for all the bands are shown in Figure 4.12. In addition, the optimum integration time, and its corresponding radiometric resolution are obtained as the minimum of the Allan deviation. These results are shown in Table 4.3.

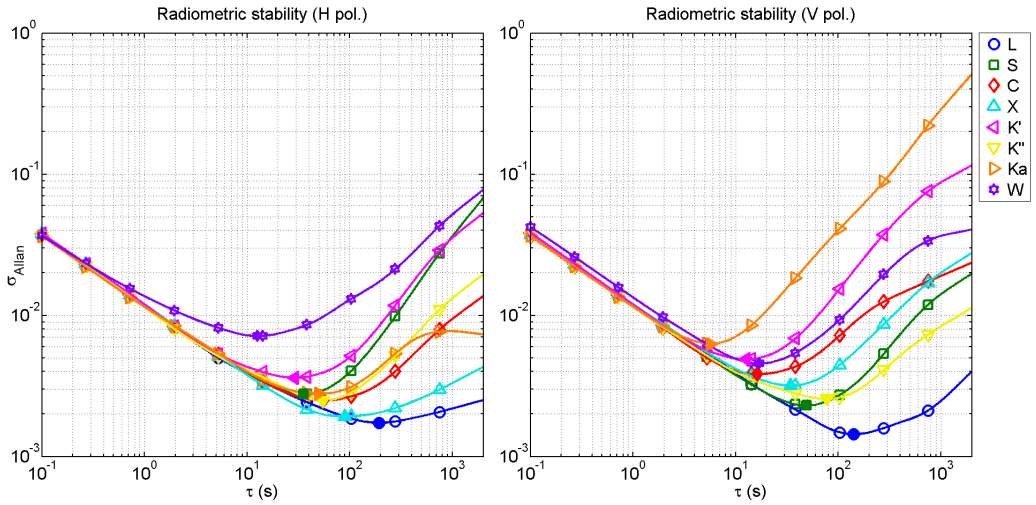

Figure 4.12: Radiometric stability obtained as the Allan variance for each frequency band and polarization (H left and V right). Filled markers represent the minimum value for each case, i.e the optimal integration time.

Results show that radiometric stability depends on the band under assessment. However, as a general trend, it can be observed that radiometric stability is higher for lower frequency bands since they have larger optimum integration times and lower Allan deviation values.

4.5 RFI measurements

4.5.1 RFI related capabilities

One of the main objectives of instrument MERITXELL is to be a flexible platform to perform experiments related to the detection, characterization, and localization of RFI signals present at the frequency bands used for passive microwave radiometry. In order to avoid self-interference, data buses have been checked to not emit any electromagnetic emission in the working bands. This was done during the assembly process of MERITXELL.

According to the back-end topology, MERITXELL can perform real-time RFI signal detection and characterization in time, frequency, and statistical domains. The power measurements allow to retrieve the spectrum of the signal under analysis, and thus, to detect RFI signal whose power is more concentrated around some frequency points of the receiving bandwidth. Moreover, thanks to the spectrogram capabilities, RFI signals can be analyzed both in time and frequency domains by identifying temporal changes in the signal spectrum.

Furthermore, the back-end of MERITXELL also allows performing a statistical analysis of the received signals. As shown in [26], several normality tests can be used to detect

the presence of RFI signals, although the combination of the Kurtosis and the Anderson-Darling tests leads to an optimum combo test without blind spots. MERITXELL allows to perform this analysis using the I/Q measurement mode and then applying such normality tests on post-processing in the host computer. In [8], a statistical analysis of RFI signals was already performed using MERITXELL.

4.5.2 Receiving chain compensation

Given the architecture of MERITXELL, the spectrum retrieved by the back-end stage is a combination of the received signal spectrum, or the spectrum under analysis, and the frequency response of the receiving chain, including the antenna and front-end stage. The non-ideal frequency response of the combination of antenna, tuned filters, and amplifiers may mask the detection of weak RFI signals. However, the frequency response corresponding to the front-end and back-end stages can still be compensated or equalized by using the spectrum of the corresponding matched load. This compensation is performed dividing point by point the power spectrum taken at the antenna by the power spectrum measured at the matched load. The result of this operation gives a measurement of the relative power of the RFI signal after the antenna over the thermal noise present at the matched noise.

4.5.3 RFI examples at MWR bands

It is known that RFI signals are a common problem in MWR bands, and MERITXELL is an outstanding platform to study and characterize them. For this reason, it is not difficult to capture some RFI signals in the majority of the bands covered by MERITXELL, especially in urban environments. The measurements presented hereinafter have been performed at the UPC-BarcelonaTech Campus Nord in Barcelona, Spain. They have been taken at both V and H polarizations, using the spectrogram feature, and the frequency response compensation has been applied. The color scale represents the power spectral density measured at the detector. These results are obtained dividing the value of the power spectrograms by the corresponding RBW used in each case (1 MHz for L-, S-, and C-band, and 10 MHz for the others).

One of the most contaminated bands is L-band. Figure 4.13 shows a capture of some RFI signals at L-band. The measurements show that at V polarization, some band-limited pulsed signals can be appreciated. Most likely, this kind of RFI signals at L-band are spurious pulses from near-band radar signals. Besides, the behavior at H polarization is even worse in this measurement. This is presumably due to the presence of second harmonics of the terrestrial broadcasting television service, which are emitted at H polarization. Moreover, the measurements at V and H polarizations have not been taken simultaneously because of the inherent structure of MERITXELL. Therefore, if the RFI signal has some temporal variations, they may not appear in both measurements.

On the contrary, K'-band has some variations in the frequency response of the receiving chain that are on the order of the variations of the received signals. This phenomenon can be appreciated in Figure 4.14. Furthermore, note that in this case the compensation of the frequency response takes more importance than in the L-band case. By applying so, it is demonstrated that the frequency response compensation is needed to check that

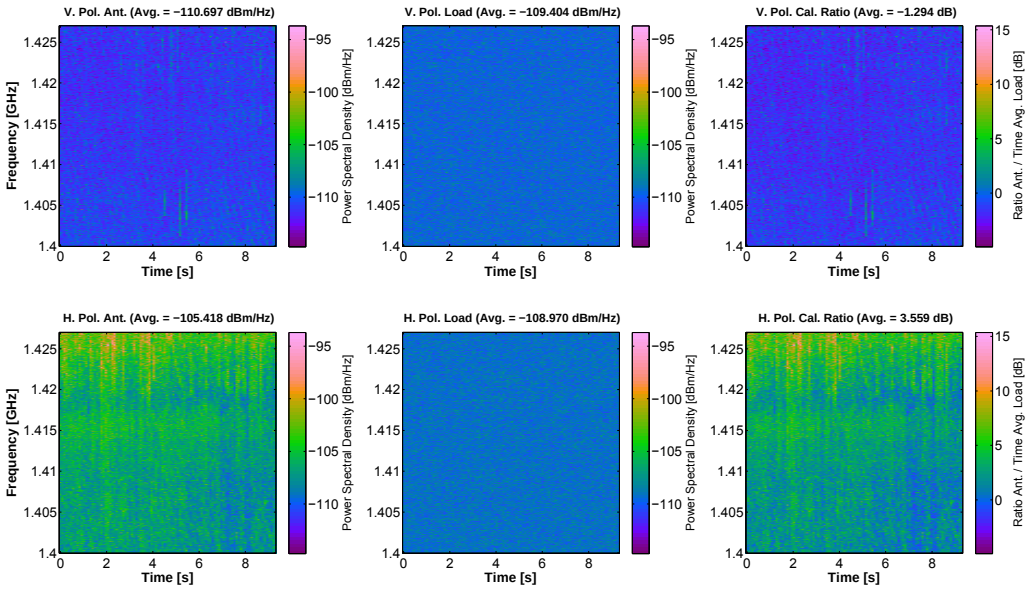

Figure 4.13: Capture of RFI signals at L-band. The upper subfigures correspond to V polarization and the lower ones to H polarization. From left to right, the subfigures correspond to spectrograms taken at the antenna, at the matched load, and after the compensation. The spectrograms corresponding to the matched load are relatively flat as compared to the RFI signals captured during the measurement process.

K'-band is free of RFI, at least in these measurements.

Figure 4.15 shows the spectrograms corresponding to the S-, C-, X-, K"-, Ka- and W-band at both V and H polarizations, with the frequency response compensation procedure already applied. Regarding the S-band, it can be appreciated that it is even more contaminated than L-band. In this case, the RFI signal is spread in time and frequency for both polarizations. Moreover, the contamination due to the adjacent services, such as WiFi hotspots, is also common at S-band.

Furthermore, the rest of bands are much cleaner of RFI signals than L- and S-band. Captures at X-band show a uniform RFI contribution in the H polarization over all the frequency band. This kind of RFI signals is commonly caused by the adjacent satellite communication services. Besides, Ka-band shows some continuous wave RFI signals at both polarizations.

In summary, the results show that the lower frequency bands are more contaminated than the higher ones due to the frequency of operation of the wide variety of electronic devices near to L- and S-band. Higher bands seem to be cleaner, not only because of the higher frequency, but also because of the much wider bandwidth, so a narrow band interference occupies a much smaller fraction of the band. However, some RFI signals have also been identified at X- and Ka-band. Eventually, in [9], a similar RFI survey was carried out with similar results.

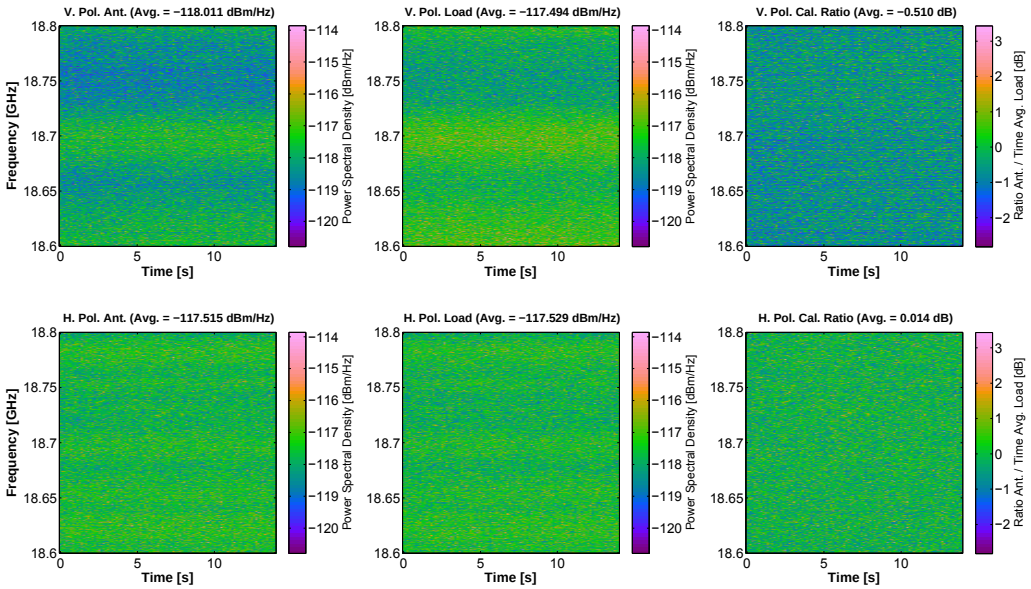

Figure 4.14: Capture of RFI signals at K'-band. The upper subfigures correspond to V polarization and the lower ones to H polarization. From left to right, the subfigures correspond to spectrograms taken at the antenna, at the matched load, and after the compensation. The spectrograms corresponding to the matched load show some variations in the frequency response of the receiving chain.

4.5.4 RFI example at GPS bands

Since a GNSS-R instrument is installed in MERITXELL, a measurement of the RFI signals present at GPS L1 band was also performed using the radiometric L-band antenna. Figure 4.16 shows that some pulsed RFI signals are also observed at the GPS L1 band. These RFI signals can still be seen despite the attenuation introduced by the antenna mismatch present when using the radiometric L-band antenna to measure at GPS L1 band. The effect of RFI signals in GPS navigation application is not as critical as the effect on MWR, due to the inherent protection of the GNSS signals. However, the presence of RFI signals is extremely critical in GNSS-R applications [99].

4.6 Summary and conclusions

The work presented in this chapter corresponds to the description of the hardware of MERITXELL, its software design, and the methods and procedures necessary to control, calibrate and perform measurements with it. The main goal of MERITXELL is twofold. On one hand, it is an outstanding platform to perform detection, characterization, and localization of RFI signals at the most common MWR bands up to 92 GHz. On the other hand, its multisensor architecture enables testing several data fusion algorithms in post-processing.

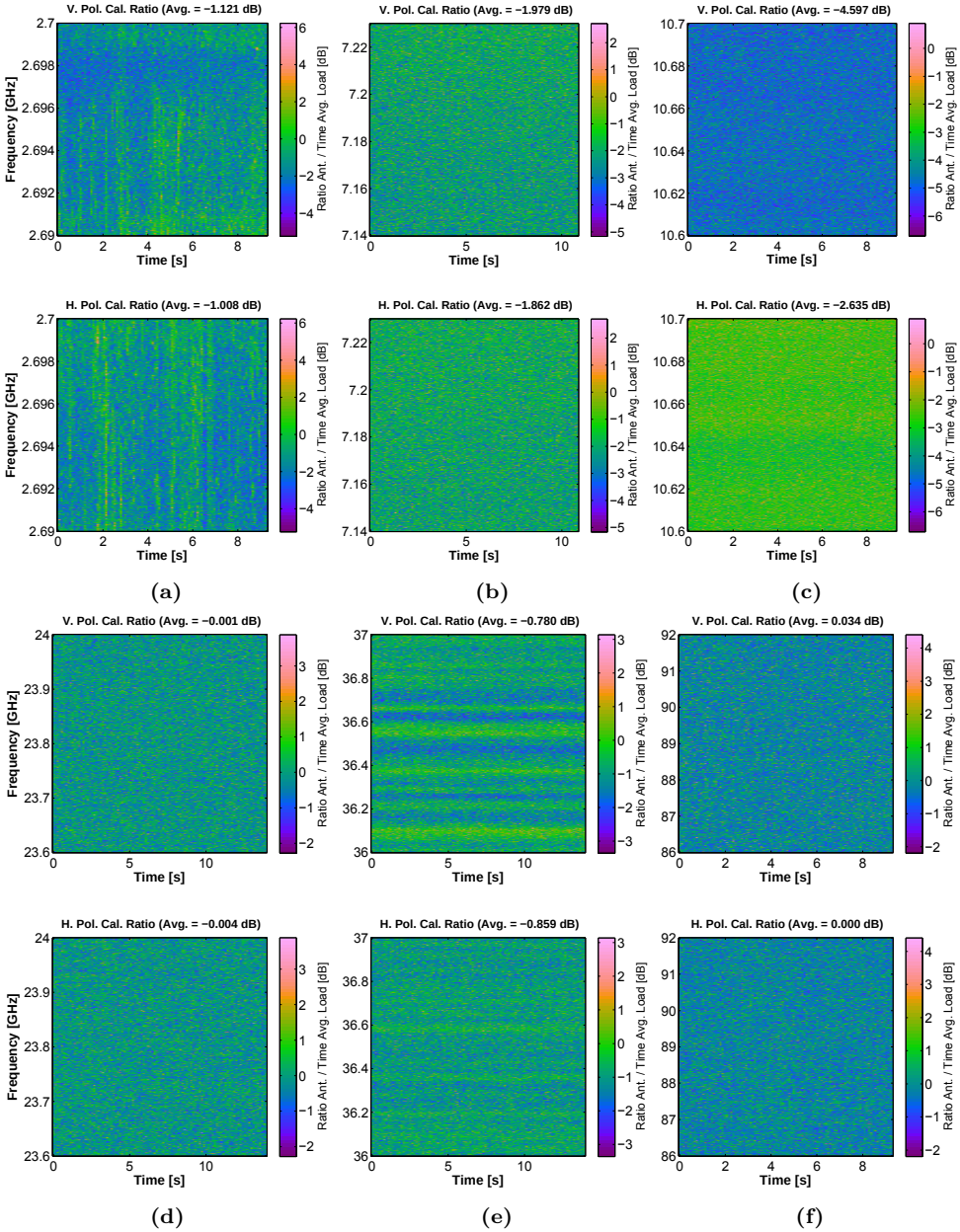

Figure 4.15: Capture of RFI signals at (a) S-, (b) C-, (c) X-, (d) K"-, (e) Ka- and (f) W-band. All captures are spectrograms with the frequency response compensation procedure already applied. The upper subfigures correspond to V polarization, and the lower ones to H polarization.

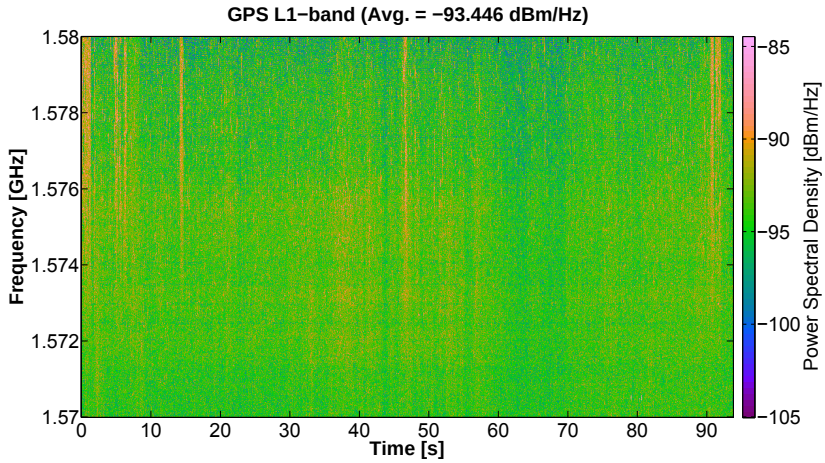

Figure 4.16: Capture of RFI signals at GPS L1 band using the L-band radiometric antenna.

5

Chapter 5

MFT: a novel RFI mitigation technique for MWR applications

This chapter describes a new technique for RFI mitigation in MWR applications. One of the main contributions of this PhD thesis is the proposal of the Multiresolution Fourier Transform (MFT) as a novel tool for RFI mitigation, both for MWR and GNSS-R. The performance of the MFT is compared to other TF RFI mitigation techniques. This comparison is done in terms of probability of mitigation, sample loss, and mitigation performance. Moreover, the use of the blanking approach as thresholding solution is discussed. According to the results presented in this chapter, the MFT technique appears as a good trade-off solution among all other techniques since it can mitigate all RFI signals under evaluation.

Table 5.1: Typical sensitivity requirements for most common microwave radiometry applications [100]. Ultimate application sensitivity requirements will change case by case.

Application	Sensitivity	Application	Sensitivity
Atmospheric temperature profile	0.3 K	Atmospheric water vapor profile	0.5 K
Cloud liquid water content	1 K	Sea surface temperature	0.3 K
Sea surface salinity	0.3 K	Sea wind speed	1 K
Sea ice concentration	2 K	Ice mapping	1 K
Rain rate	0.5 K	Oil slicks	0.3 K
Soil moisture	1 K	Snow cover	1 K

5.1 Introduction

This chapter introduces the use of the MFT for RFI mitigation in MWR applications, whereas its use in GNSS-R applications is discussed in Chapter 8. The performance of the MFT is compared to other TF RFI mitigation techniques already reviewed in Chapter 3. The results of this comparison have been presented in the conference paper "Comparison of real-time time-frequency RFI mitigation techniques in microwave radiometry" [100], and published in the journal paper "Performance Assessment of Time–Frequency RFI Mitigation Techniques in Microwave Radiometry" [24]. Moreover, this chapter also discusses the use of the blanking approach and the implications and considerations that must be taken into account for MWR applications.

5.1.1 Sensitivity requirements in MWR applications

As detailed in Chapter 2, RFI has become a dangerous threat for passive remote sensing and, in particular, for MWR. MWR is used to measure a wide number of geophysical parameters. Among them, prominent examples are soil moisture, continental ice mapping, snow cover, rain rate, sea surface salinity, wind speed over the sea, sea ice concentration, atmospheric temperature profiles, water vapor profiles, or cloud liquid water content [18]. To do so, microwave radiometers must have high sensitivity requirements of the order of a Kelvin, or even at sub-Kelvin levels (see Table 5.1). Although MWR applications operate in protected frequency bands, radiometers can be easily affected by RFI signals because the extreme sensitivity requirements. The effect of RFIs can be even harder if they are working in a secondary band allocation. As stated in [20], due to the increasing usage of the microwave spectrum by active commercial services, Earth observation using passive microwave techniques is likely to be increasingly impacted by RFI in the future.

RFI signals are either those illegally emitted at bands reserved for passive observations (in-band effect), or those that are legally emitted in adjacent bands, but a fraction of their power leaks into the bandwidth of the radiometer (near-band effect), or even a harmonic emission at a much lower frequency band. As described in Chapter 2, the presence of an RFI signal is translated into a positive bias in the Brightness Temperature (BT) measured

by the radiometer. The final outcome of RFI-contamination is that an error is introduced into the geophysical measurements (positive or negative depending on the application). For example, soil moisture maps contaminated by RFI show apparent dryer soils than actually, they are [101]. Furthermore, RFI power levels are usually much higher than the radiometric noise, and hence, MWR measurements are completely corrupted when RFI is present. According to [102], the rationale is that natural Earth emissions are not expected to produce BT measurements that exceed 330 K, but many RFI emissions could be stronger than 500 K.

5.1.2 Detection vs Mitigation

In the recent years, intense efforts have been made in order to solve the problem of RFI in MWR [19]. RFI localization techniques are being developed to find and reach RFI sources, and then to switch them off. The MERITXELL radiometer described in Chapter 4 is one of them. However, the number of worldwide RFI events is huge, and this process will take time. Therefore, RFI detection and mitigation techniques are being developed in parallel to localization solutions, in order to deal with the RFI problem from the receiver side.

As described in Chapter 3, there are many different approaches for RFI detection and mitigation that have been developed for microwave radiometry [103], but also for other fields such as radio-astronomy or navigation. Although analog techniques based on filtering may be used and useful, the most effective techniques are digital, and they are applied to a given set of samples after the receiver front-end. Statistical tests, typically normality tests [26] such as Kurtosis or Anderson-Darling, are used to determine if a set of samples belongs to a certain statistical distribution or not. Then, if it does not belong to the expected statistical distribution, the entire set of samples is discarded. Polarization tests, such 3rd and 4th Stokes parameters, are also used to detect and discard contaminated sets of samples. Multiband techniques such as the spectral difference method [20] allow to cross-check radiometric measurements among several frequency bands. Spatial filtering techniques such as beam-steering or multivariable Principal Component Analysis (PCA) use the signals received by multiple antennas [102] to determine if the radiometric signal is RFI-contaminated.

The goal of RFI mitigation is to reduce, as much as possible, the power of undesired interference signals, while keeping the maximum amount of useful signal power. In the case of MWR, the useful signal is the radiometric noise. In other words, mitigation algorithms for MWR applications are looking for minimization of the Interference-to-Noise Ratio (INR).

There are a number of approaches for RFI mitigation. Although analog techniques based on filtering may be used and are useful, the most effective techniques are digital, and they are applied to a given set of samples after the MWR front-end. There are some techniques, such as those based on statistical or polarimetric algorithms, which are able to detect whether an RFI signal is present or not in the set of samples under processing. Using this information, the set is discarded or kept for further processing (see Fig 5.1). Conversely, time-frequency techniques allow to locate and discard only a subset of those samples that are contaminated by RFI, while keeping the rest of them to retrieve radiometric measurements, which is not possible in the previous case. Nevertheless, this

mitigation procedure has a counterpart: when the number of samples is reduced, the radiometric sensitivity is also reduced, or equivalently, the resulting Noise-Equivalent Delta Temperature (NEΔT) is increased.

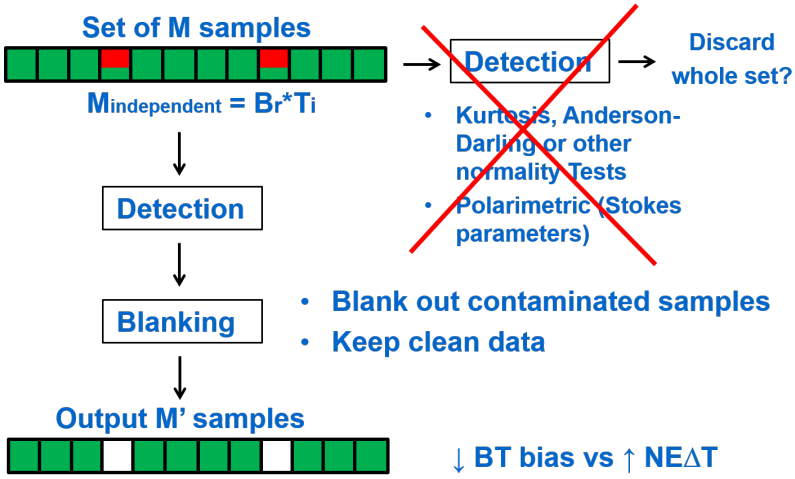

Figure 5.1: Detection techniques such statistical or polarimetric tests are applied to a whole set of samples, which should be discarded entirely if RFI-contamination is determined. However, mitigation techniques are designed to maximize the INR.

Furthermore, studies such as [9] have shown that RFI signals follow different patterns depending on the frequency band of operation, region, daytime, etc., where the system under interference conditions is operating. With this kind of information, detection and mitigation algorithms have been developed in order to optimize their performance taking into account the characteristics of the RFI signal. In addition, it has also been noticed that, since RFI signals are mostly man-made emissions, their power tends to be more concentrated in the TF space (signal or mathematical space determined by both time and frequency domains) than natural emissions, and hence their TF signature can be characterized. These facts trigger the need for a performance assessment of TF RFI mitigation signals which decompose the RFI power in the TF space to maximize their mitigation performance against different kinds of RFI signals. In addition, TF RFI mitigation techniques allow to locate and discard a subset of those samples that are contaminated by RFI, while keeping the rest of them. This allows retrieving useful radiometric measurements, which is not possible with other techniques such as polarimetric or statistical methods which discard the entire set of samples.

Figure 5.2 shows a diagram explaining the underlying qualitative performance of RFI mitigation techniques. Two different stages can be observed. At a first stage, the input signal, which is the aggregated of the radiometric thermal noise and the possible RFI signal, is linearly transformed using a given basis. Its main purpose is that the energy of the RFI signal gets concentrated in the smallest possible number of bins in the transformed domain, and hence, it is more easily detected. Meanwhile, thermal noise is as spread in the transformed domain as it was in time, because of its stochastic properties: statistically independent, white (flat spectrum), and zero mean.

At last stage, the blanking (or thresholding) process is applied sample by sample. A given function is applied to the value of each transformed sample according to a previously calculated threshold value. More details about this process are provided in the subsequent sections. After this point, the INR improves in case the transform is effective against the RFI signal. Eventually, an anti-transform could be applied only if the time-domain signal is needed. In MWR it is not the case since the BT can be calculated by integrating samples either in the time domain or in the transformed domain.

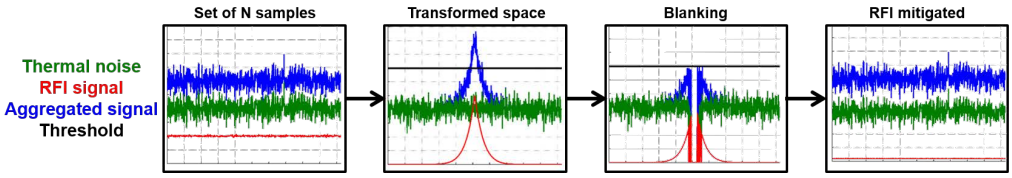

Figure 5.2: Sketch of the underlying performance of RFI mitigation techniques.

5.2 Time-Frequency RFI Mitigation techniques

In the literature of RFI mitigation techniques, there are a number of them which can be classified as TF techniques. TF techniques are those that study a signal in both time and frequency domains (i.e. TF space). Signals and their transformed representation are often tightly connected, and they can be understood better by studying them jointly, rather than separately [104]. According to how they decompose the signal in the time and frequency domains, they can be classified in four groups with increasing level of complexity: time-domain, frequency-domain, time-frequency space, and time-scale space. Figure 5.3 illustrates the approaches with diagrams about how the time-frequency space is decomposed for each case.

Several techniques may be found for each approach, and some examples of them are provided in Table 5.2. Although they are different techniques with their particular implementation, the underlying decomposition of the time and frequency domains are equivalent (e.g. a spectrogram can be implemented either using the Fourier transform or a filter bank).

In order to assess the RFI mitigation performance of each one of the approaches, the most used techniques in each case are selected for each one of the approaches. One of the most used techniques in the literature is notch filtering [14,55,105]. Notch filtering can be classified as frequency-domain technique, and it consists on applying a sharp band-stop filter adapted to the frequency of RFI signal. Notch filtering is a parametric approach. A static notch filter removes a particular frequency of the spectrum, while an adaptive one changes or tunes the center frequency of the band-stop filter according to the frequency of the RFI. Although this approach may show good results against CW or slow-rate chirp signals, their performance against other RFI signals is limited. Moreover, they introduce phase distortion when using both analog or Infinite Impulse Response (IIR) digital filters, which may affect negatively to the performance of the receivers.

For these reasons, the frequency blanking approach [59] is chosen instead of notch filtering approach. The other techniques under assessment in this chapter are Pulse Blanking (PB)

[23], Spectrogram Blanking (SB) [11], and Wavelet Denoising (WD) [65, 106]. Moreover, the wavelet transform used in the WD approach is a direct function of time and scale. However, the scale can be directly matched to frequency since wavelets expand the signal in terms of wavelet functions which are localized in both time and frequency [104], and therefore it can be considered as a TF technique.

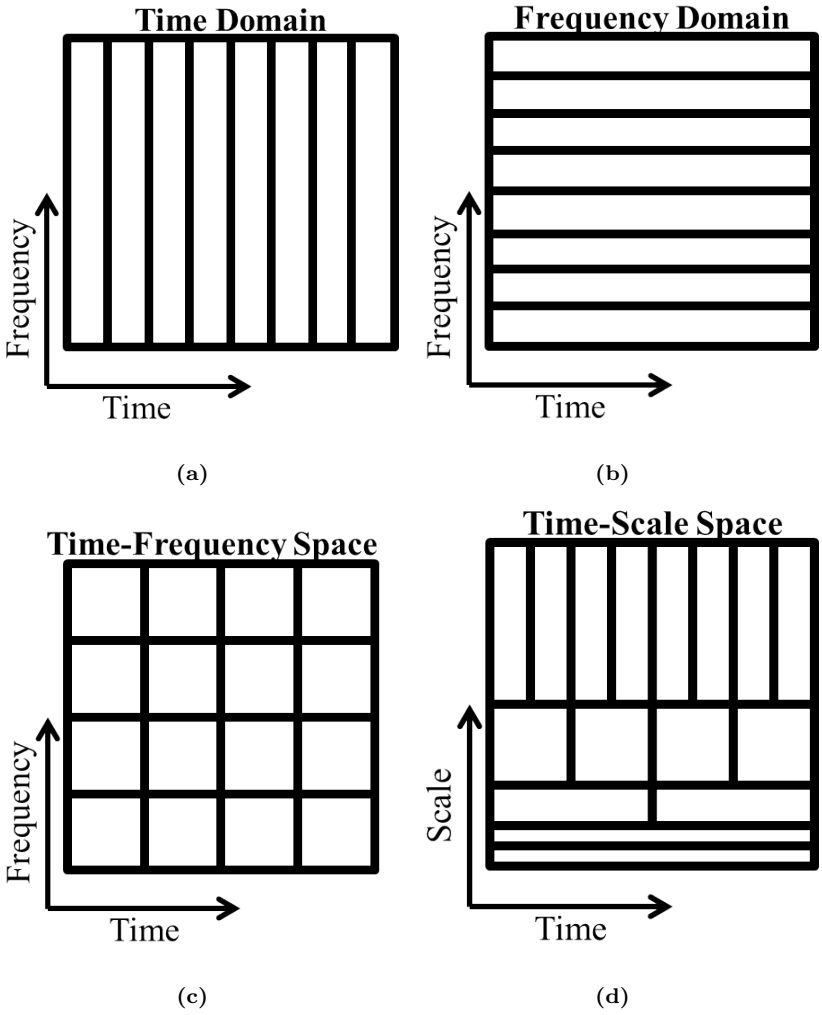

Figure 5.3: Four classical decomposition of the time and frequency domains: (a) time-domain, (b) frequency-domain, (c) time-frequency space, and (d) time-scale space.

Although different approaches decompose the TF space in different ways, they can be implemented using the same general framework which will be ultimately used to assess their mitigation performance. This general framework can be divided into three stages, which are detailed in next subsections. First, a domain transform that projects the samples into a new space determined by the approach under evaluation. Second, a detection stage which marks the RFI-contaminated samples using the Binary Hypothesis crite-

Table 5.2: List of TF RFI mitigation approaches and most used techniques [107].

Approach	*Commonly used techniques*	*Evaluated technique*
Time-domain	Pulse Blanking (PB) [23], Amplitude Domain Processing (APD) [71]	PB
Frequency-domain	notch filtering [14], Frequency Blanking (FB) [59]	FB
Time-frequency space	Spectrogram Blanking (SB) [11], filter bank	SB
Time-scale space	Wavelet Denoising (WD) [65, 106]	WD

rion [46]. And, eventually, a thresholding stage which applies a given function to the RFI-contaminated samples to increase the INR.

5.3 Domain transforms

In order to apply the digital mitigation techniques, signals must be first captured, conditioned, and digitized with the corresponding antenna and front-end. Then, input signal samples $\mathbf{x} = x[m]$ are processed considering blocks of M units, with $m \in [0, M-1]$. $\mathbf{x}$ contains interference signals $\mathbf{i}$, and thermal noise signals $\mathbf{n}$, so that, $\mathbf{x} = \mathbf{i} + \mathbf{n}$. In this work, no correlation among the M samples due to the band-limiting effect of the front-end is considered for the sake of simplicity. Therefore, if the M samples are independent, $M = \tau_p B_r$, where τ_p is the integration time or processing time and B_r is the front-end bandwidth. In case of correlated samples, the previous relationships do not apply.

Using domain transforms, the input signal samples are mapped into different signal domains depending on the technique, $\mathbf{X} = \mathcal{T}(\mathbf{x})$. Domain transforms used in RFI mitigation algorithms $\mathcal{T}(\cdot)$ must fulfill the following conditions [2]:

- to be linear, $\mathcal{T}(\mathbf{x} + \mathbf{y}) = \mathcal{T}(\mathbf{x}) + \mathcal{T}(\mathbf{y}) = \mathbf{X} + \mathbf{Y}$.
- to be invertible, $\mathbf{x} = \mathcal{T}^{-1}(\mathbf{X}) = \mathcal{T}^{-1}(\mathcal{T}(\mathbf{x}))$, so that, the signal can be recovered after the RFI mitigation process.
- to be unitary, $||\mathbf{x}||^2 = \langle \mathbf{x}, \mathbf{x} \rangle = \sum |x[m]|^2 = ||\mathbf{X}||^2$.
- to be orthogonal, $\langle \mathbf{x}, \mathbf{y} \rangle = \langle \mathcal{T}(\mathbf{x}), \mathcal{T}(\mathbf{y}) \rangle = \langle \mathbf{X}, \mathbf{Y} \rangle$.

The purpose of these transforms is to concentrate the energy of the RFI signal in the smallest possible number of bins in the transformed domain, and hence, it becomes more easily detected and mitigated a priori. At the same time, thermal noise is as spread as in the transformed domain as it was in time, because of its stochastic properties (independent, white and zero mean). The evaluated domain transforms according to their technique are described in subsequent subsections.

5.3.1 Pulse Blanking

In the PB approach, samples are taken in the time domain as they are received from the front-end, this is without applying any transformation. Therefore, $X[m] = x[m]$. This approach is optimum to detect peaks of RFI power because it has the best time resolution, $\Delta t = \tau_p/M$.

5.3.2 Frequency Blanking

In Frequency Blanking (FB), the signal is projected in the frequency-domain using the unitary DFT,

$$X[k] = \frac{1}{\sqrt{M}} \sum_{m=0}^{M-1} x[m]\, w_M[m]\, e^{-j2\pi \frac{k}{M} m}, \tag{5.1}$$

where $w_M[m]$ is the window transform, and k is the frequency bin number with $k \in [0, M-1]$. The unitary DFT fulfills Parseval's theorem, $\sum_{m=0}^{M-1} |x[m]|^2 = \sum_{k=0}^{M-1} |X[k]|^2$, and preserves noise statistics after the transformation [61]. This technique has the best frequency resolution, $\Delta f = B_r/M$. A rectangular window is considered for the sake of simplicity, since other windows may change the frequency resolution and this case is not considered for the comparison. Use of windowing functions are discussed in further sections.

5.3.3 Spectrogram Blanking (SB)

In SB, samples are projected in the TF space with a fixed time and frequency resolution using the STFT,

$$X[p, k] = \frac{1}{\sqrt{K}} \sum_{m=0}^{K-1} x[m+pK]\, w_K[m]\, e^{-j2\pi \frac{k}{K} m}, \tag{5.2}$$

where $k \in [0, K-1]$ is the frequency bin number with $K < M$, $w_K[m]$ is a rectangular window transform of length K, and $p \in [0, P-1]$ is the transformed time bin number with $M = PK$. SB represents a trade-off between time and frequency resolution (since their product is upper bounded) [63], and according to this notation, $\Delta t = \tau_p/P$, and $\Delta f = B_r/K$.

5.3.4 Wavelet Denoising (WD)

In WD, signals are decomposed into a set of wavelets with different scale using the Discrete Wavelet Transform (DWT),

$$X[p, r] = \sum_{m=0}^{r-1} x[m+pr]\, w_r[m], \tag{5.3}$$

where $r \in [2, R]$ is the scale factor, and $w_r[m]$ is the mother wavelet of scale r. In this work, the Haar wavelet [106] was chosen for simplicity, but any possible mother function may be used (Daubechies, Coiflet, Symlet, etc.) [56]. Note that if a complex Morlet wavelet is chosen instead, the resulting transform is equivalent to a DFT or a STFT with

a Gaussian window. The DWT approach has a progressive time and frequency resolution depending on the scale of the wavelet basis [65].

5.4 Multiresolution Fourier Transform

The MFT is an extension of both DWT and STFT, where the dependence between frequency and scale domain is removed. This results in a representation in three independent dimensions, which are time, frequency and scale. Then, scale stands for the temporal width of the Fourier transform window, frequency stands strictly for the frequency-shift of the window, and time stands for the time-shift of the window. Figure 5.4 illustrates how the time-frequency space is decomposed by the MFT.

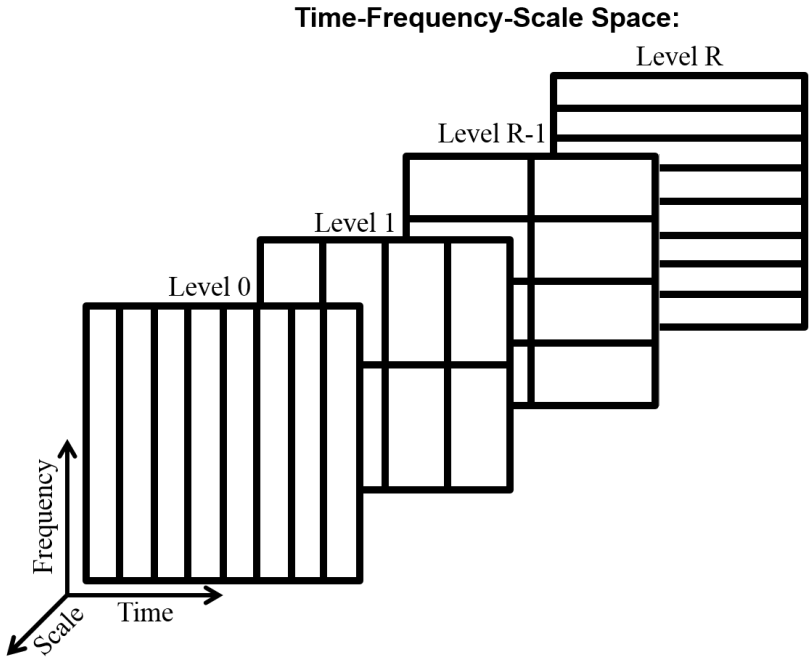

Figure 5.4: Representation of the time-frequency decomposition performed by the MFT with multiple resolution levels.

The MFT was first introduced in 1989 by A. Calway in his PhD thesis for image analysis purposes [108]. In [109], Calway described it as "a stack of windowed Fourier transforms in which the window size is varied systematically to give a multiresolution representation of the space-frequency plane. As such, it constitutes a super-set of the WT (Wavelet Transform) and WFT (Windowed Fourier Transform), providing a complete representation of the frequency domain at each scale and hence enabling regions to be analyzed over a range of frequencies, yielding a flexibility not possessed by existing WT." The MFT has been proposed for several applications. In [110], it was proposed as a tool for feature extraction and segmentation in image and audio signal analysis. In [111], it is used for

image pattern recognition.

Signal decomposition using the MFT are similar to of the so-called Wavelet Packet Decomposition (WPD) [56, 61]. WPD are also an extension of DWT, where multiple bases can also be used, but breaking the dependence between scale and frequency as in MFT. Then, an optimal sub-band tree structuring is obtained [56], which is commonly used in image feature analysis and pattern recognition. However, MFT uses a Fourier base which is optimal for real-time hardware implementations.

Although, MFT implementation may seem cumbersome given the fact that it is a technique based on the multiresolution analysis. In [112], an optimal hardware implementation is described using radix-2 Fast Fourier Transform (FFT) blocks. Further implementations of the MFT are discussed in Chapter 9.

As mentioned before, the use of MFT for GNSS and passive remote sensing applications is one of the main contributions of this PhD thesis. The work done in [107] is the first reference to the use of MFT as an RFI mitigation technique. Its results are included in Chapter 10, and they deal with RFI mitigation for GNSS and GNSS-R applications.

Following the notation of the previous section, MFT can be expressed as,

$$X[p,k,r] = \frac{1}{\sqrt{r}} \sum_{m=0}^{r-1} x[m+pr]\, w_r[m]\, e^{-j2\pi \frac{k}{r} m} \tag{5.4}$$

where $r \in [1, R]$ is the resolution or scale factor with $R \leq M$, $k \in [0, K-1]$ is the frequency bin number with $K = r$, $w_r[m]$ is a rectangular window transform of length r, and $p \in [0, P-1]$ is the transformed time bin number with $M = PK$. The previous transforms can be derived from the MFT.

5.5 Detection stage

As mentioned before, the input signal $\mathbf{x}$ can be expressed as $\mathbf{x} = \mathbf{i} + \mathbf{n}$, where $\mathbf{i}$ is the aggregate of RFI signals, and $\mathbf{n}$ is the system noise. In this work, $\mathbf{n}$ is taken as circular Complex White Gaussian Noise (CWGN) with PDF equal to $f_n(\mathbf{n}) \in \mathcal{N}(0, \sigma_n^2 \mathbf{1})$ (see Appendix A).

Since domain transforms under consideration are linear, the transformed signal can be also expressed as $\mathbf{X} = \mathcal{T}(\mathbf{x}) = \mathbf{I} + \mathbf{N}$, being $\mathbf{I} = \mathcal{T}(\mathbf{i})$, and $\mathbf{N} = \mathcal{T}(\mathbf{n})$. In addition, the orthogonality of the used transforms, together with the unitary property, comes with a fundamental statistical consequence: $\mathcal{T}(\cdot)$ transforms CWGN into CWGN [113]. Thus, $\mathbf{N}$ is also circular CWGN with PDF equal to $f_N(\mathbf{N}) \in \mathcal{N}(0, \sigma_n^2 \mathbf{1})$.

Considering the the Binary Hypothesis criterion approach [46], the detector stage must decide between two hypotheses, in this case, in the transformed domain. These are:

- $\mathcal{H}_0 : \mathbf{X} = \mathbf{N}$ if the sample is considered RFI-clean, or
- $\mathcal{H}_1 : \mathbf{X} = \mathbf{I} + \mathbf{N}$ if, conversely, the sample is marked as RFI-contaminated.

This decision is taken comparing the result of the sample energy detector test, $|\mathbf{X}|^2 = |X[\cdot]|^2$, to a determined threshold value α. According to [46], when the signal to be

detected (i.e. the RFI signal) is not known a priori, the sample energy detector may be used as a sub-optimal detector. Therefore, hypothesis $\mathcal{H}_1$ is chosen when $|\mathbf{X}|^2 > \alpha$, whereas $\mathcal{H}_0$ is chosen otherwise.

5.5.1 Detection threshold

Threshold value α is determined setting a probability of false alarm P_{FA} a priori. P_{FA} is defined as the probability to choose erroneously hypothesis $\mathcal{H}_1$ when the true hypothesis is $\mathcal{H}_0$, equivalently $P_{FA} = P(\mathcal{H}_1|\mathcal{H}_0)$. In this work, $\mathcal{H}_0$ means that no RFI is present, and then the energy of the input signal in the transformed domain is $|\mathbf{X}|^2\big|_{\mathcal{H}_0} = |\mathbf{N}|^2$ which follows a exponential distribution $f_{|\mathrm{N}|^2}(|\mathbf{N}|^2)$ (see Appendix A). Thus,

$$P_{FA} = P\left(|\mathbf{N}|^2 > \alpha\right) = \int_{\alpha}^{\infty} f_{|\mathrm{N}|^2}(|\mathbf{N}|^2)\, d\,|\mathbf{N}|^2 = e^{-\frac{\alpha}{2\sigma_n^2}}, \tag{5.5}$$

and then,

$$\alpha = 2\,\sigma_n^2\, ln\left(\frac{1}{P_{FA}}\right), \tag{5.6}$$

where $2\,\sigma_n^2$ is the variance of the circular CWGN $\mathbf{n}$.

Furthermore, the threshold value α is chosen per transformed bin, but since transformed samples have an identical distribution, α value is the same for all transformed bins. This is true thanks to the assumption of no correlation among the M samples, and white noise. However, if this is not the case, the threshold value must be chosen specifically for each bin according to P_{FA}, and its corresponding statistical distribution.

5.5.2 Probability of detection

The mitigation process requires a detection stage. The RFI signal must be first identified from the thermal noise, and this process is done statistically sample by sample using a determined threshold value of α. According to (5.6), α depends on the power or variance of the system noise, and the probability of false alarm P_{FA}, which is set a priori.

Each one of the bins of the transformed domain signal, $|\mathbf{X}|^2 = |\mathbf{I} + \mathbf{N}|^2$, follows a non-central chi-squared distribution [114–117] (see Appendix A), and its PDF can be expressed as

$$f_{|\mathbf{X}|^2}(|\mathrm{X}|^2) = \frac{1}{2\,\sigma_n^2}\, e^{-\frac{|\mathrm{X}|^2+|\mathrm{I}|^2}{2\,\sigma_n^2}}\, I_0\left(\frac{|\mathrm{X}|\,|\mathrm{I}|}{\sigma_n^2}\right), \tag{5.7}$$

where $I_0(\cdot)$ is a modified Bessel function of the first kind [118]. The probability of detection at each transformed bin $P_D(\cdot)$ is defined as the probability to choose $\mathcal{H}_1$ correctly [46], and hence

$$P_D(\cdot) = P\left(|\mathrm{X}[\cdot]|^2 > \alpha\right) = \int_{\alpha}^{\infty} f_{|\mathbf{X}|^2}(|\mathrm{X}[\cdot]|^2)\, d\,|\mathrm{X}[\cdot]|^2 = Q_1\left(\frac{|\mathrm{I}[\cdot]|}{\sigma_n}, \frac{\sqrt{\alpha}}{\sigma_n}\right), \tag{5.8}$$

where $Q_1(\cdot)$ is the Marcum Q-function of first order [2, 119, 120].

A particular RFI-contaminated sample is detected with the likelihood defined in (5.8), and then, a RFI signal can be considered as detected if any of their samples is detected.

Thus, the overall probability of detection can be defined as the likelihood of detect a RFI signal at any of the transformed bins under $\mathcal{H}_1$ condition as follows

$$P_D = 1 - \prod \left(1 - P_D(\cdot)\right). \tag{5.9}$$

P_D is usually used to assess the detection performance of each RFI mitigation algorithm regarding the RFI power, or its equivalent RFI temperature T_i. Furthermore, an alternative way of representing the detection performance of a detector is to plot P_D versus P_{FA}. This method is the so-called Receiver Operating Characteristic (ROC) [46].

5.6 Thresholding stage

The thresholding or denoising stage is the one that mitigates the RFI power from the RFI-contaminated samples in the transformed domain. The energy value of each transformed sample is compared to the previously calculated threshold value α, and then sample values are modified depending on the chosen criterion.

5.6.1 Blanking function

When a blanking approach is taken, only the RFI-clean samples in the transformed space are kept whereas RFI-contaminated samples are set to zero as follows:

$$Y[m] = \begin{cases} 0 & |X[m]|^2 > \alpha \quad \text{RFI-contaminated} \\ X[m] & \textit{otherwise} \quad \text{RFI-clean} \end{cases}, \tag{5.10}$$

where $\mathbf{Y} = Y[m]$ is the RFI-mitigated signal in the transform domain, and α is obtained from (5.6). Moreover, a blanking function $b(\cdot)$ can be defined from (5.10), so that, $\mathbf{Y}$ can be obtained as:

$$\mathbf{Y} = b\left(\mathbf{X}, |\mathbf{X}|^2 > \alpha\right), \tag{5.11}$$

where the first argument is the signal to blank, and the second one is the blanking condition.

Eventually, the RFI-mitigated signal $\mathbf{y}$ is obtained using the inverse transform of $\mathcal{T}(\cdot)$, hence:

$$\mathbf{y} = \mathcal{T}^{-1}(\mathbf{Y}). \tag{5.12}$$

In MWR this process is not mandatory since the radiometric measurements can be calculated integrating samples either in the time domain or in the transformed domain due to Parseval's theorem [2]. Furthermore, the residual RFI signal after mitigation $\mathbf{i}'$ can be calculated as:

$$\mathbf{i}' = \mathcal{T}^{-1}\left(b\left(\mathbf{I}, |\mathbf{X}|^2 > \alpha\right)\right), \tag{5.13}$$

while noise after blanking $\mathbf{n}'$ can be obtained equally as:

$$\mathbf{n}' = \mathcal{T}^{-1}\left(b\left(\mathbf{N}, |\mathbf{X}|^2 > \alpha\right)\right). \tag{5.14}$$

5.6.2 Normalized Blanking Bias (NBB)

While using the blanking thresholding method, those samples that are marked as RFI-contaminated are zeroed. However, they contain a fraction of the thermal noise power as well as RFI power at the same time. The detector stage is the one that decides statistically if that sample is likely to contain enough RFI power to be discarded according to the P_{FA}. So that, this process results in a minimization of the INR, but at the expense that a fraction of the thermal noise power is removed from the samples.

In the end, this is translated into two effects:

- a negative bias introduced in the original radiometric measurements, and
- a degradation of the radiometric resolution.

In the absence of RFI signal, the power of the radiometric signal follows an Exponential probability distribution. Since all samples with power values larger than the blanking threshold are discarded, the probability distribution of the power of the mitigated noise samples is a truncated exponential distribution as shown in Fig. 5.5. Therefore, the mean power of the mitigated noise is negatively biased as compared to the mean power noise before mitigation.

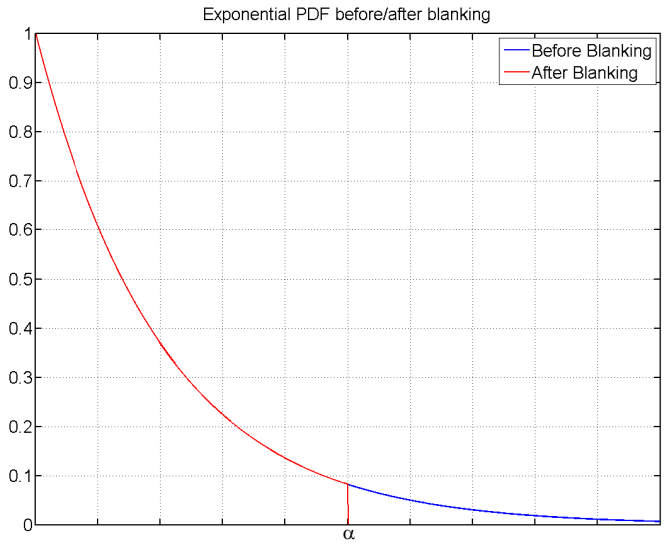

(a)

Figure 5.5: Exponential PDF before and after the blanking process.

This blanking bias introduces an error in the radiometric measurements inherent to the blanking process, even if no RFI signal is present at the antenna. However, the blanking bias can be calibrated and corrected when only thermal noise is present during the blanking process. In Appendix C, the blanking bias is derived by obtaining the expected value of the truncated Exponential distribution.

If this bias is normalized by the radiometric noise power before mitigation with no RFI

present (under $\mathcal{H}_0$ hypothesis), the Normalized Blanking Bias (NBB) can be expressed as:

$$NBB = \frac{P_n - P_{n'}}{P_n} = (1 - \ln(P_{FA}))\, P_{FA}, \tag{5.15}$$

where P_{FA} is the probability of false alarm, P_n is the average noise power before mitigation, and $P_{n'}$ is the average noise power after mitigation calculated as:

$$P_{n'} = P_n - NBB \cdot P_n. \tag{5.16}$$

Figure 5.6 shows the magnitude of NBB as a function of P_{FA}. For example, if P_{FA} is set to be 10%, the average power of thermal noise after mitigation in the absence of RFI is going to be a 33% lower than it would be without blanking.

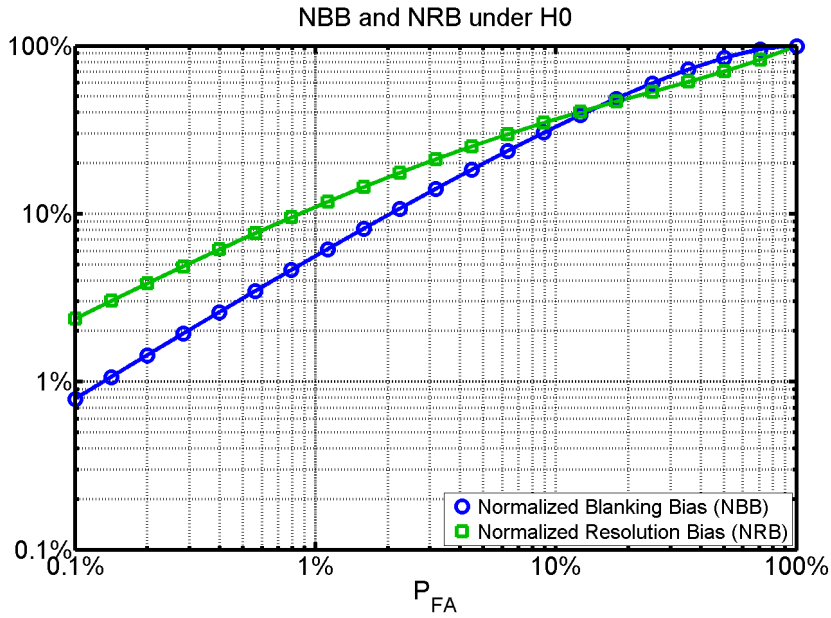

(a)

Figure 5.6: Normalized Blanking Bias (NBB) and Normalized Resolution Bias (NRB) as a function of the probability of false alarm.

Once the blanking process is performed, the actual radiometric noise power can be estimated by scaling the measured noise power by the following factor:

$$P_n^{\text{unbiased}} = P_{n'} \left(\frac{1}{1 - NBB} \right), \tag{5.17}$$

thus compensating the blanking bias.

5.6.3 Normalized Resolution Bias (NRB)

The radiometric resolution of an ideal total power radiometer, also known as radiometric sensitivity ΔT or Noise Equivalent Delta Temperature (NEΔT), is inversely proportional to the square root of the product of the noise bandwidth B_r and the integration time or processing time τ_p [18]. In Section 5.3, it has been stated that if the samples are gathered without any band-limiting correlation among them due to the front-end, then the number of processed samples M is equal to the product $B_r\tau_p$, and proportional to the number of bins in the transformed domain. That being said, the radiometric resolution can be expressed as (see Appendix C):

$$\Delta T = \frac{T_n}{\sqrt{B_r \tau_p}} = \frac{T_n}{\sqrt{M}} \tag{5.18}$$

where T_n is the system noise temperature.

Given the fact that the number of non-blanked samples is less or equal than the number of original samples, one may think a priori that the radiometric resolution could be degraded after the blanking process since it is inversely proportional to the square root of the number of samples. However, if the radiometric resolution is computed taking into account the truncated Exponential distribution, the radiometric resolution after blanking if no RFI is present is equal to (see Appendix C):

$$\Delta P_{n'} = \frac{P_n}{\sqrt{M'}} \sqrt{1 - \ln^2\left(P_{FA}\right) P_{FA} - \left(\mathrm{NBB}\right)^2}, \tag{5.19}$$

and the figure of merit Normalized Resolution Bias (NRB) can be defined as:

$$NRB = \frac{\Delta P_n - \Delta P_{n'}}{\Delta P_n} = 1 - \sqrt{\frac{1 - \ln^2\left(P_{FA}\right) P_{FA} - \left(\mathrm{NBB}\right)^2}{1 - P_{FA}}}. \tag{5.20}$$

Figure 5.6 shows the magnitude of NRB as a function of P_{FA}. Given that NRB is always positive, and that:

$$\Delta P_{n'} = \Delta P_n - NRB \cdot \Delta P_n, \tag{5.21}$$

the radiometric resolution is better (i.e. it has a lower value) if no RFI is present thanks to the blanking process. However, this result only applies for the biased radiometric noise after the blanking process.

5.6.4 Resolution Degradation (RD)

As above described, Eq. 5.17 can be used to compensate for the bias introduced in the average noise power after mitigation. If this process is used, the standard deviation of the measured noise is scaled by the same factor. Thus, the standard deviation of the unbiased radiometric noise can be expressed as:

$$\Delta P_{n'}^{\mathrm{unbiased}} = \Delta P_{n'} \left(\frac{1}{1 - NBB}\right) = \Delta P_n \left(\frac{1}{1 - NRB}\right) \left(\frac{1}{1 - NBB}\right), \tag{5.22}$$

and thus a figure of merit coined Resolution Degradation (RD) can be defined as the following ratio:

$$RD = \frac{\Delta P_{n'}^{\text{unbiased}}}{\Delta P_n} = \left(\frac{1}{1 - NRB}\right)\left(\frac{1}{1 - NBB}\right), \tag{5.23}$$

which fulfills that $RD \geq 1$. Therefore, the use of blanking introduces a loss on the radiometric resolution whose value in the absence of RFI depends on the value of the P_{FA}, and it is shown in Fig. 5.7.

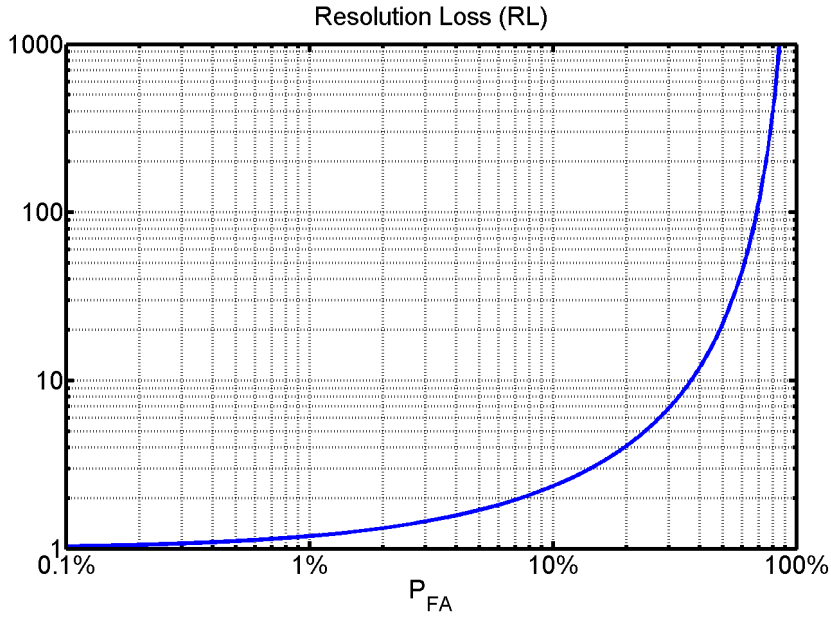

(a)

Figure 5.7: Resolution Degradation (RD) as a function of the probability of false alarm.

5.7 Evaluation criteria

In subsequent sections, the figures of merit necessary to evaluate the performance of the above-mentioned TF RFI mitigation algorithms are defined and discussed, as well as, the RFI signals considered for the assessment.

5.7.1 Mitigation performance

The main goal of RFI mitigation techniques is to maximize the Signal-to-Interference Ratio (SIR) of any receiving system. In other words, they must reduce as much as possible the power of undesired interference signals, while keeping the maximum amount of useful signal power received by the system. In MWR, the useful signal is the own thermal noise, so that, a SIR maximization problem is equivalent to minimize the INR.

The INR at the input of the mitigation algorithm can be defined as

$$\mathrm{INR}_i = \frac{P_i}{P_n} = \frac{T_i}{T_n}, \tag{5.24}$$

where $P_i = \frac{1}{M}\sum_{m=0}^{M-1} |i[m]|^2$ is the RFI power, $P_n = 2\sigma_n^2$ is the thermal noise power, k_B is the Boltzmann constant, B_r is the bandwidth of the front-end receiver, $T_i = P_i/(k_B B_r)$ is the equivalent RFI temperature, and $T_n = P_n/(k_B B_r)$ is the system noise temperature. Moreover, the INR at the output can be define equivalently as

$$\mathrm{INR}_o = \frac{P_i'}{P_n'} = \frac{T_i'}{T_n'}, \tag{5.25}$$

where $P_i' = \frac{1}{M}\sum_{m=0}^{M-1} |i'[m]|^2$ is the residual RFI power after mitigation (recall that $\mathbf{i}' = i[m]$ is the residual RFI signal from Section 5.6), and analogously T_i' is the equivalent residual RFI temperature after mitigation. Using equations (5.24) and (5.25), a figure of merit to evaluate the degree of performance of a mitigation system can be defined as

$$\mathrm{MP} = \frac{T_i'}{T_i}, \tag{5.26}$$

where MP is coined as Mitigation Performance (MP). Once defined the MP, a RFI mitigation algorithm is partially excising the RFI signal if $\mathrm{MP} < 1$, it is not working if $\mathrm{MP} = 1$, and it is introducing an extra error in the radiometric measurements if $\mathrm{MP} > 1$.

5.7.2 Probability of Mitigation

Given that mitigation process has a random behavior, the MP parameter also takes stochastic values. Then, it is possible to define a figure of merit to determine with which probability the MP parameter is going to be lower or equal than a given upper boundary. Therefore, the probability of mitigation P_M can be defined as:

$$P_M = Pr\left(\mathrm{MP} \leq \beta\right), \tag{5.27}$$

where β is the upper boundary.

5.7.3 Sample Loss (SL)

The number of non-blanked samples or bins after the blanking process (i.e. those that still contain the information regarding brightness temperature) is less or equal than the number of samples or bins at its input M. A figure of merit can be defined to study the relationship between these two quantities. The Sample Loss (SL) is defined as:

$$\mathrm{SL} = \sqrt{\frac{M}{M'}} - 1, \tag{5.28}$$

where M' is the number of non-blanked samples or bins. A similar result was also obtained in [73]. Furthermore, when no RFI is present (hypothesis $\mathcal{H}_0$), the SL is directly related to the P_{FA} as follows

$$\mathrm{SL}|_{\mathcal{H}_0} = \sqrt{\frac{1}{1 - P_{FA}}} - 1, \tag{5.29}$$

and it satisfies that $\mathrm{SL}|_{\mathcal{H}_1} \geq \mathrm{SL}|_{\mathcal{H}_0}$. Hence, the a priori chosen value for P_{FA} also determines the minimum SL introduced by the RFI mitigation algorithm.

5.8 Selected RFIs and simulation parameters

5.8.1 Selected RFI signals

In this work, six different types of RFI signals have been used in order to exhaustively test the proposed RFI mitigation algorithms. They can be classified into three groups, which are the following:

- *Pulsed signals*: their signal power is well concentrated in the time domain, so that, their peak power is usually very high. Typical sources are RADAR signals, Ultra-Wide-Band communications (UWB), and aeronautical radio-navigation signals such as the DME.

- *Chirp signals*: the carrier frequency is swept, typically linearly, across their bandwidth with a time repetition frequency. Typical sources are RADAR signals, radio harmonic from lower frequency bands (e.g. digital clock signals) and jammers.

- *Continuous signals*: they are continuous in the time domain, and they overlap partially or totally the operating bandwidth of the radiometer. Typical sources are lower harmonics, near-band carrier signals, and wide-band modulated services.

A total number of six RFI signals have been selected (two from each group) as representative RFI signals that can be found in real scenarios according to studies performed in [9]. The spectrograms corresponding to the selected RFI signals are depicted in Fig. 5.8. These six RFI signals are named as follows:

- Delta/Glitch: A single one-sample pulse simulating a glitch in the front-end signal, or a single high-power pulse captured by the antenna.

- Burst of pulses: A set of Gaussian pulses with high repetition frequency (every $\tau_p/64$) simulating DME-like signals.

- Wide-band chirp: A chirp signal sweeping across the whole radiometer bandwidth with a moderated repetition rate.

- Narrow-band chirp: A chirp signal sweeping across a fraction of the radiometer bandwidth with a slow repetition rate.

- CW/Sinusoidal/Narrow-band modulation: A tone or sinusoidal signal overlapping the radiometer bandwidth. Since narrow-band and wide-band are concepts relative to the bandwidth of the receiver, it could also simulate a narrow-band modulated signal.

- Wide-band modulation: A wide-band continuous signal overlapping the whole radiometer bandwidth simulated using a Pseudo-Random Noise (PRN) code.

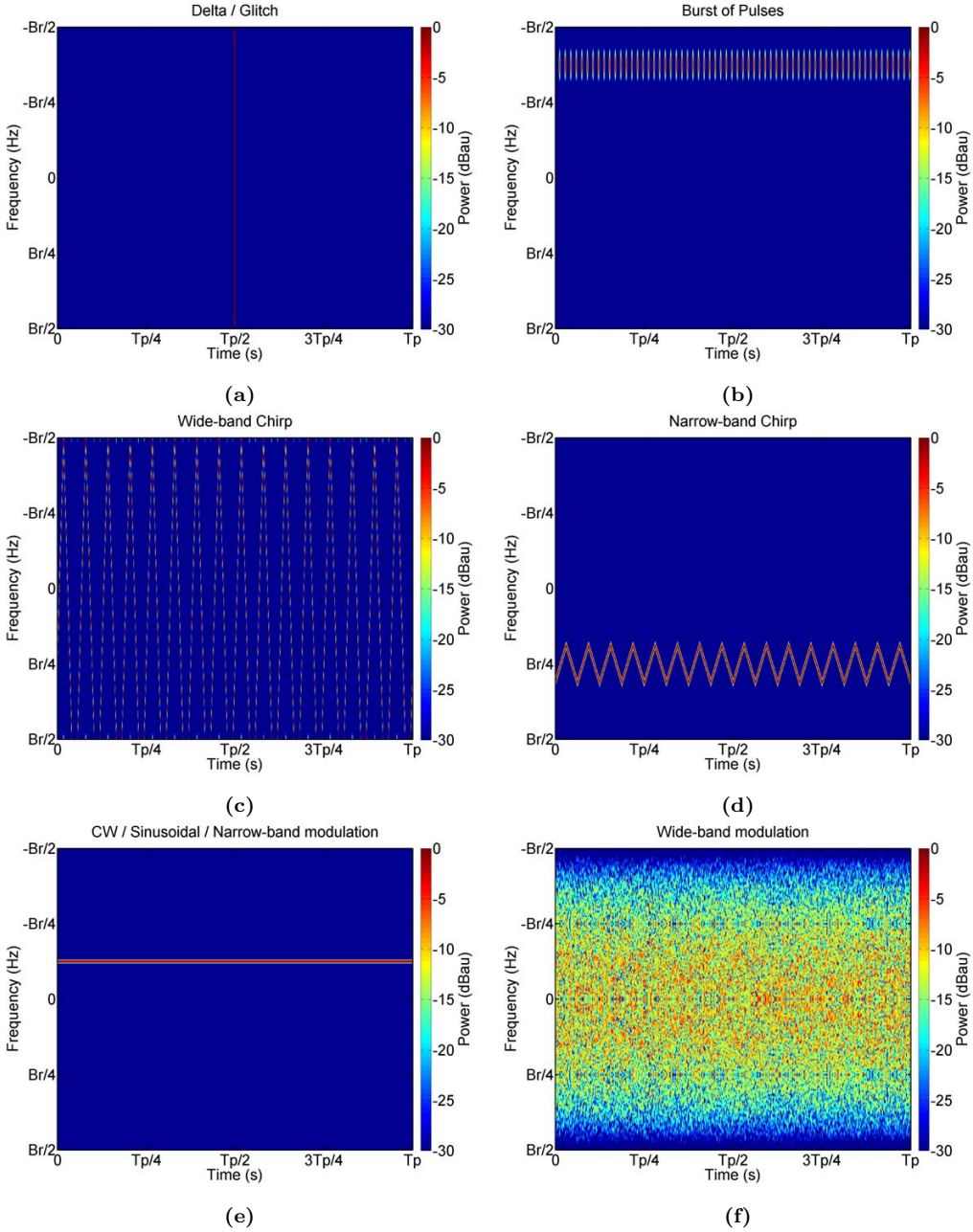

Figure 5.8: Sample RFI signals considered in the assessment: (a) delta/glitch, (b) burst of pulses, (c) wide-band chirp, (d) narrow-band chirp, (e) CW/sinusoidal/narrow-band modulation, and (f) wide-band modulation.

5.8.2 Simulation parameters

The following parameters have been taken into account during the simulation process in order to carry out the assessment of the RFI mitigation techniques. Table 5.3 summarizes

Table 5.3: Simulation parameters.

Parameter	*Description*	*Value*
M	Number of samples	2^{16}
P_{FA}	Probability of false alarm	10%
T_i	Equivalent RFI temperature	0.01 K - 1000 K
T_n	System noise temperature	250 K
NMC	Number of Monte-Carlo simulations	5000

the values for the mentioned simulation parameters.

5.8.2.1 Number of samples

As mentioned in Section 5.3, the number of samples M is equal to the time-bandwidth product of the radiometer under assumed conditions. In this work, a value of $M = 2^{16}$ has been taken for two reasons. It is a reasonable value for total power radiometers with radiometric resolution of the order of Kelvin units, $\Delta T = T_n/\sqrt{2^{16}} \simeq 1$ K. And it gives enough time and frequency resolution values, Δt and Δf respectively, to distinguish between RFI signals while simulations do not require too much processing time.

5.8.2.2 Probability of false alarm

In MWR applications, P_{FA} values in the range between 1% and 20% are common since it is not a critical value. For instance in [121], P_{FA} was set to 9.3%. In this assessment, P_{FA} has been set to 10%. Then, according to (5.29), this value yields a minimum SL of 5.4%.

5.8.2.3 Equivalent RFI temperature

In the simulations, T_i has been swept from 0.01 K to 1000 K. On one hand, T_i lower than 0.01 K does not induce a significant bias in the radiometric measurements making them very hard to detect. On the other hand, T_i higher than 1000 K are unusual, even though RFI events of this magnitude have been reported, for instance in the case of SMOS [19]. These large power RFIs are easy to detect, but they may be hard to mitigate. This is true because either they overwhelm the mitigation performance of the algorithm, or they saturate the front-end of the radiometer. However, a proper design of the front-end and mitigation stages (with a high dynamic range) can overcome this problem.

5.8.2.4 System noise temperature

It has been set to $T_n = 250$ K since the relative performance among the RFI mitigation techniques will not depend on this value.

5.8.2.5 Number of Monte-Carlo simulations

Up to 5000 Monte-Carlo simulations have been performed in this assessment.

5.9 Assessment results and discussion

5.9.1 Probability of Mitigation

The probability of mitigation P_M is the first figure of merit under evaluation in this work. Results obtained for P_M with β equal to 0.3 as a function of the equivalent RFI temperature T_i for the six selected RFI signals are depicted in Fig. 5.9. In the following points, results for each TF RFI mitigation algorithm are commented case by case.

5.9.1.1 Pulse Blanking

For PB, equivalent RFI temperature values T_i at which the RFI signals are mitigated at 99% of probability are: 0.04 K for the glitch, 17 K for the burst of pulses, 600 K for the wide-band chirp, 760 K for the narrow-band chirp, 750 K for the CW, and 770 K for the wide-band modulation. PB can detect easily RFI signals well concentrated in time.

5.9.1.2 Frequency Blanking

For FB, T_i values at which the RFI signals are mitigated at 99% of probability are: 770 K for the glitch, 2.8 K for the burst of pulses, 190 K for the wide-band chirp, 5 K for the narrow-band chirp, 0.1 K for the CW, and 64 K for the wide-band modulation. FB performs the opposite to PB, it can detect easily RFI well concentrated in frequency.

5.9.1.3 Spectrogram Blanking

For SB, T_i values at which the RFI signals are mitigated at 99% of probability are: 3.5 K for the glitch, 51 K for the burst of pulses, 15 K for the wide-band chirp, 19 K for the narrow-band chirp, 11 K for the CW, and 63 K for the wide-band modulation. SB performs better than PB and FB in their worst cases, but worse than them in their better cases.

5.9.1.4 Wavelet Denoising

For WD (with Haar base), T_i values at which the RFI signals are mitigated at 99% of probability are: 0.14 K for the glitch, 15 K for the burst of pulses, 340 K for the wide-band chirp, 600 K for the narrow-band chirp, 625 K for the CW, and 25 K for the wide-band modulation. WD performs better with RFI well localized in time, and with PRN wide-band RFI signal, since Haar mother wavelet has a rectangular shape similar to PRN chip shape.

5.9.1.5 Multiresolution Fourier Transform

Eventually, for MFT, T_i values at which the RFI signals are mitigated at 99% of probability are: 0.7 K for the glitch, 5 K for the burst of pulses, 55 K for the wide-band chirp, 20 K for the narrow-band chirp, 2.2 K for the CW, and 40 K for the wide-band modulation. MFT performs has a trade-off technique among all the others, but it does not achieve the best result of each one the other techniques.

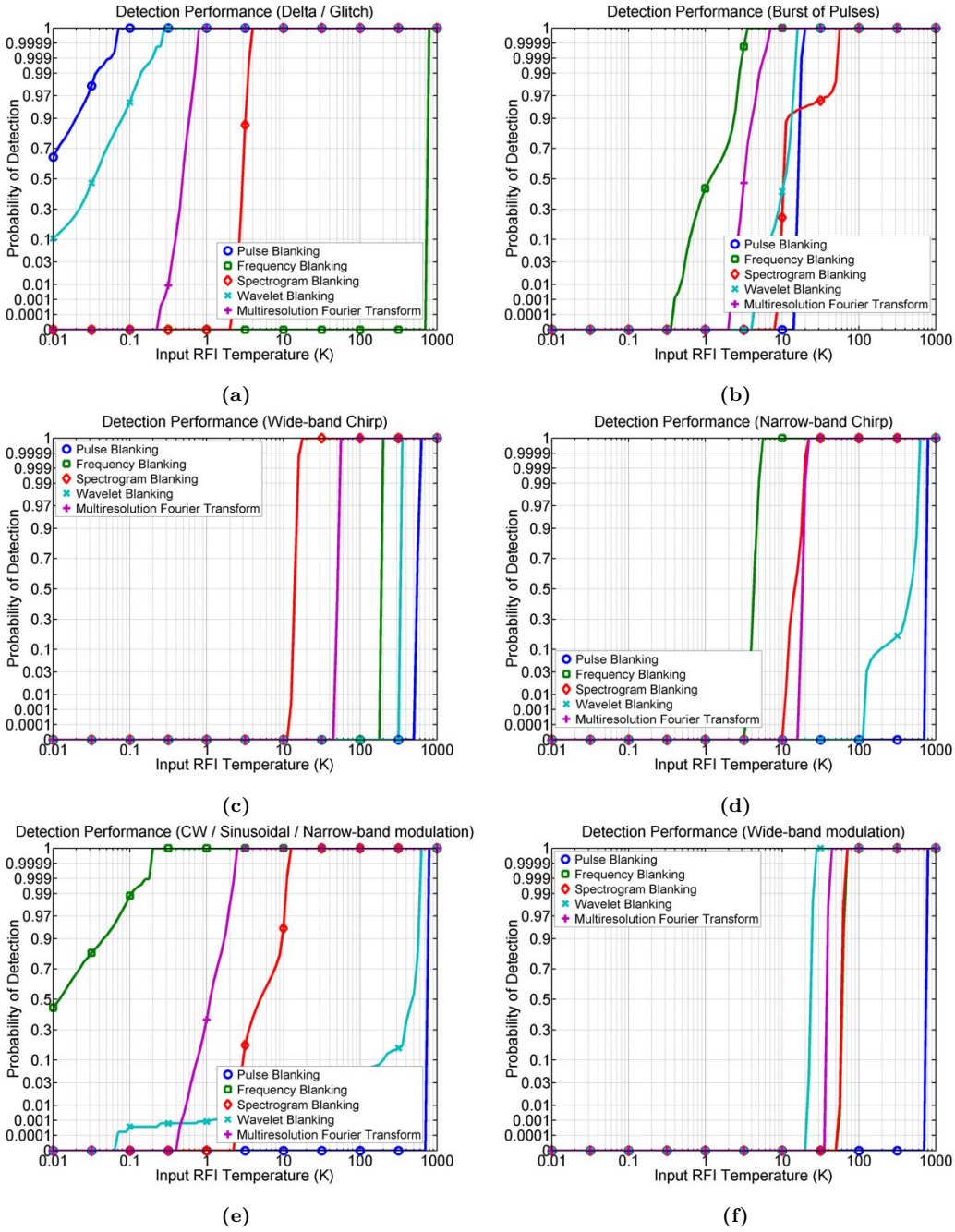

Figure 5.9: Probability of mitigation of evaluated TF RFI mitigation techniques for six different RFI signals: (a) delta/glitch, (b) burst of pulses, (c) wide-band chirp, (d) narrow-band chirp, (e) CW/sinusoidal/narrow-band modulation, and (f) wide-band modulation.

In summary, the RFI mitigation technique which performs the best in each case is the one that uses a basis in its domain transform that is similar to the RFI signal under mitigation. Mathematically, the best is achieved for that technique that maximizes the projection of the RFI power in the transformed domain. Moreover, it is remarkable that the MFT is the one that performs as the second best in all cases, and it appears as a potential trade-off technique for all RFI signals.

5.9.2 Sample loss

After P_M, the second figure of merit evaluated in this work is the SL. Results obtained for SL as a function of the input equivalent RFI temperature T_i are shown in Fig. 5.10.

The minimum SL is achieved for those TF RFI mitigation techniques that perform the best in terms of P_M for each one of the RFI signals under evaluation. In general, the larger the RFI power, the worse the SL is because there are more bins that contain significant RFI power in the transform domain, and hence they are discarded. However, this effect is minimized when the transform basis is very close to the RFI signal under mitigation. For instance, in the case of a glitch signal using PB, SL is almost equal to $\mathrm{SL}|_{\mathcal{H}_0}$ regardless the RFI power because a single bin in the transformed domain (a single sample in the time domain in this case) contains the 100% of RFI power.

The SL at $T_i = 1000$ K for the best technique in terms of P_M for each case are: 5.4% for the glitch using PB, 6.8% for the burst of pulses using FB, 8.4% for the wide-band chirp using SB, 6% for the narrow-band chirp using FB, 5.6% for the CW using FB, and 7.5% for the wide-band modulation using WD. Furthermore, using the MFT, the SL at $T_i = 1000$ K are: 12.7% for the glitch, 7.7% for the burst of pulses, 26.3% for the wide-band chirp, 18.2% for the narrow-band chirp, 16.5% for the CW, and 20.9% for the wide-band modulation.

5.9.3 Mitigation performance

Finally, the last figure of merit evaluated in this work is the MP. Results are obtained as the equivalent residual RFI temperature T_i' after mitigation as a function T_i, and they are depicted in Fig. 5.11. The blanking approach is based on a statistical detection process, so that, it is not possible to give a deterministic result when evaluating its performance. Therefore, the results for the MP are given in terms of the 99th percentile, which means that the residual interference will be equal to or less than the given value in the 99% of cases. Results for each TF RFI mitigation algorithm are commented case by case in the following points:

5.9.3.1 Pulse Blanking

For PB, maximum residual RFI temperature T_i after mitigation are: 0.03 K at $T_i = 0.03$ K for the glitch, 5.3 K at $T_i = 15.9$ K for the burst of pulses, 176 K at $T_i = 501$ K for the wide-band chirp, 236 K at $T_i = 631$ K for the narrow-band chirp, 236 K at $T_i = 563$ K for the CW, and 236 K at $T_i = 562$ K for the wide-band modulation.

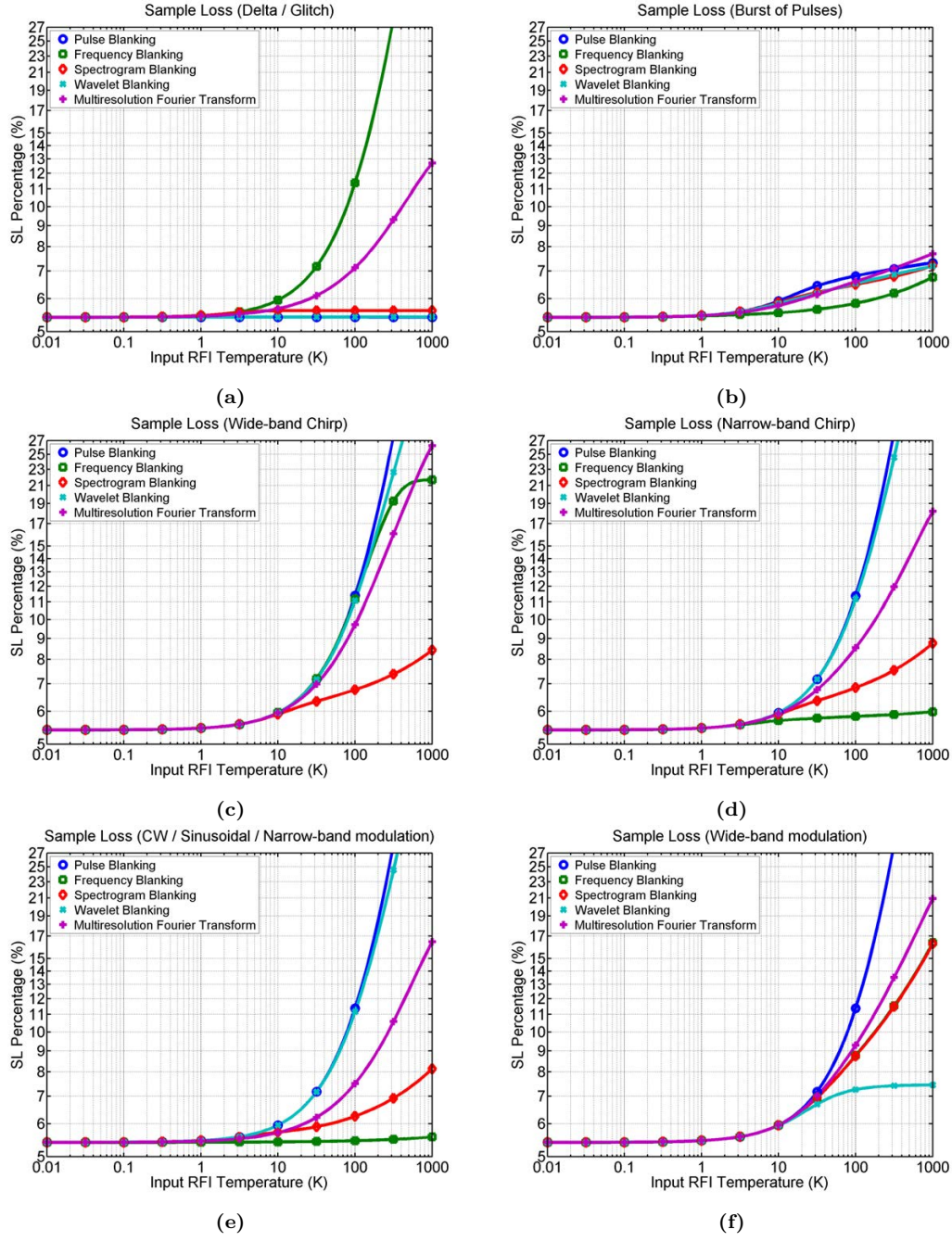

Figure 5.10: Sample loss for the evaluated TF RFI mitigation techniques for six different RFI signals: (a) delta/glitch, (b) burst of pulses, (c) wide-band chirp, (d) narrow-band chirp, (e) CW/sinusoidal/narrow-band modulation, and (f) wide-band modulation.

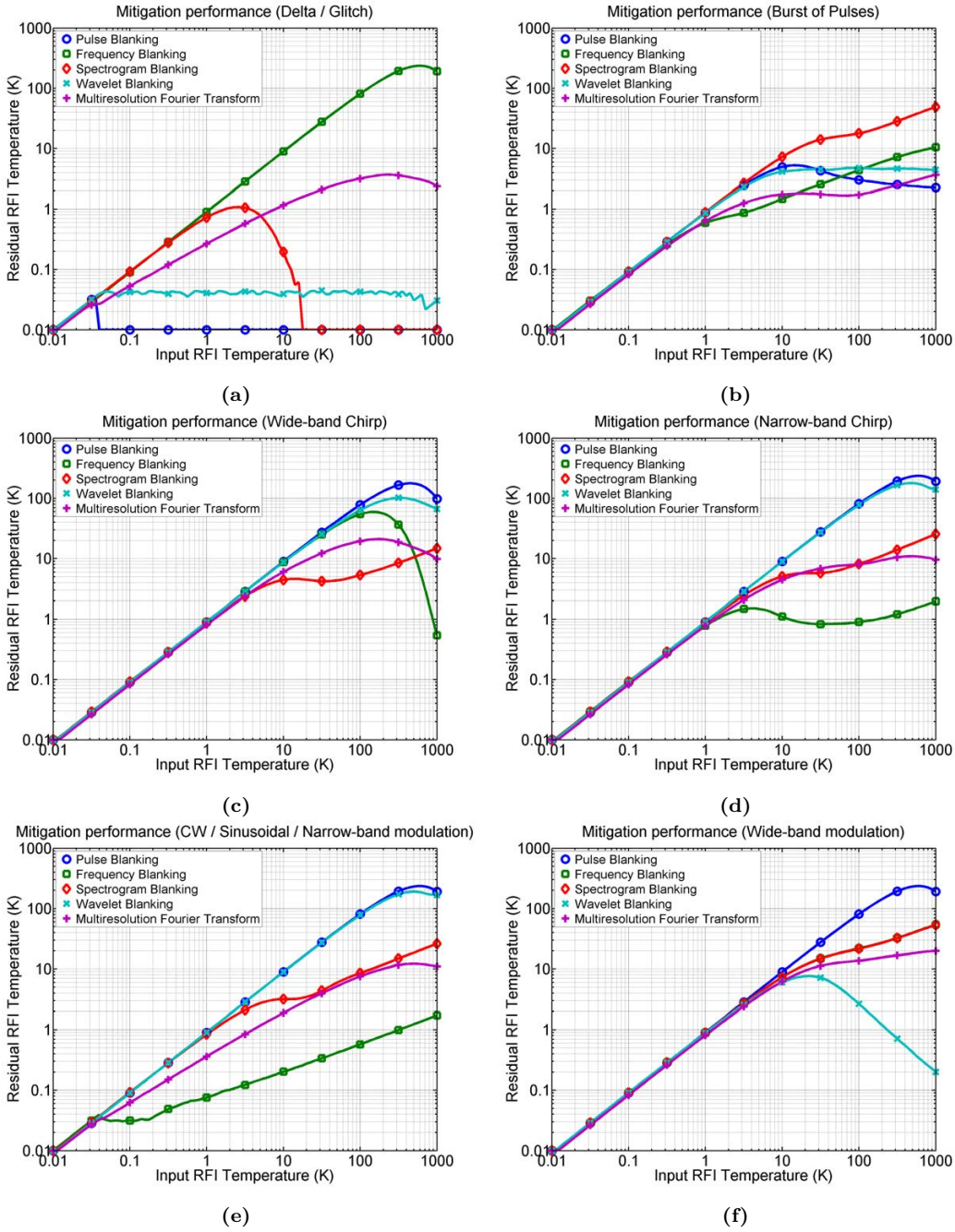

Figure 5.11: Mitigation performance of evaluated TF RFI mitigation techniques for six different RFI signals: (a) delta/glitch, (b) burst of pulses, (c) wide-band chirp, (d) narrow-band chirp, (e) CW/sinusoidal/narrow-band modulation, and (f) wide-band modulation.

5.9.3.2 Frequency Blanking

For FB, maximum residual RFI temperature T_i after mitigation are: 236 K at $T_i = 562$ K for the glitch, 10.5 K at $T_i = 1000$ K for the burst of pulses, 59 K at $T_i = 141$ K for the wide-band chirp, 2 K at $T_i = 1000$ K for the narrow-band chirp, 1.7 K at $T_i = 1000$ K for the CW, and 53.6 K at $T_i = 1000$ K for the wide-band modulation.

5.9.3.3 Spectrogram Blanking

For SB, maximum residual RFI temperature T_i after mitigation are: 2.5 K at $T_i = 1$ K for the glitch, 48.7 K at $T_i = 1000$ K for the burst of pulses, 14.8 K at $T_i = 1000$ K for the wide-band chirp, 25.4 K at $T_i = 1000$ K for the narrow-band chirp, 26.3 K at $T_i = 1000$ K for the CW, and 53.6 K at $T_i = 1000$ K for the wide-band modulation.

5.9.3.4 Wavelet Denoising

For WD, maximum residual RFI temperature T_i after mitigation are: 0.05 K at $T_i = 0.04$ K for the glitch, 4.7 K at $T_i = 100$ K for the burst of pulses, 101 K at $T_i = 316$ K for the wide-band chirp, 179 K at $T_i = 501$ K for the narrow-band chirp, 189 K at $T_i = 563$ K for the CW, and 7.6 K at $T_i = 22.3$ K for the wide-band modulation.

5.9.3.5 Multiresolution Fourier Transform

Eventually, for MFT, maximum residual RFI temperature T_i after mitigation are: 3.7 K at $T_i = 224$ K for the glitch, 3.7 K at $T_i = 1000$ K for the burst of pulses, 21 K at $T_i = 178$ K for the wide-band chirp, 10.9 K at $T_i = 501$ K for the narrow-band chirp, 12.2 K at $T_i = 501$ K for the CW, and 19.9 K at $T_i = 1000$ K for the wide-band modulation.

In summary, the best mitigation technique in terms of mitigation performance (MP) in each case is the one that has also the best performance in terms of probability of detection P_M. In general, different behaviors can be distinguished in the MP, and they are related to both SL and P_M. On one hand, if P_M is much lower than 1, the signal is hardly detected, and then, MP is close to 1, and SL tends to $\mathrm{SL}|_{\mathcal{H}_0}$ since no extra bins are discarded. On the other hand, if P_M is close to 1, and SL tends to a fixed value, RFI power is well concentrated in a set of bins in the transform domain, and the residual RFI temperature is dramatically reduced. Whereas if P_M is close to 1, but SL increases with T_i, RFI power is spread in more bins in the transformed domain, and then residual RFI temperature is still reduced but not as in the previous case.

The best mitigation technique for each one of the RFI signals are shown all together in Fig. 5.12. It can be seen that the wide-band chirp and wide-band modulation are the RFI signals that are the hardest to mitigate. Largest residual RFI temperature T_i' for the wide-band chirp is 14.8 K using SB, and for the wide-band modulation is 7.6 K using WD. Moreover, the burst of pulses, narrow-band chirp, and the CW can be mitigated below 3.7 K, 2 K, and 1.7 K using MFT, FB, and FB respectively. Finally, a glitch can be almost completely mitigated using PB.

Furthermore, mitigation performance of the MFT for each one of the RFI signals is shown in Fig. 5.13. For all RFI signals under study, the residual equivalent RFI temperature

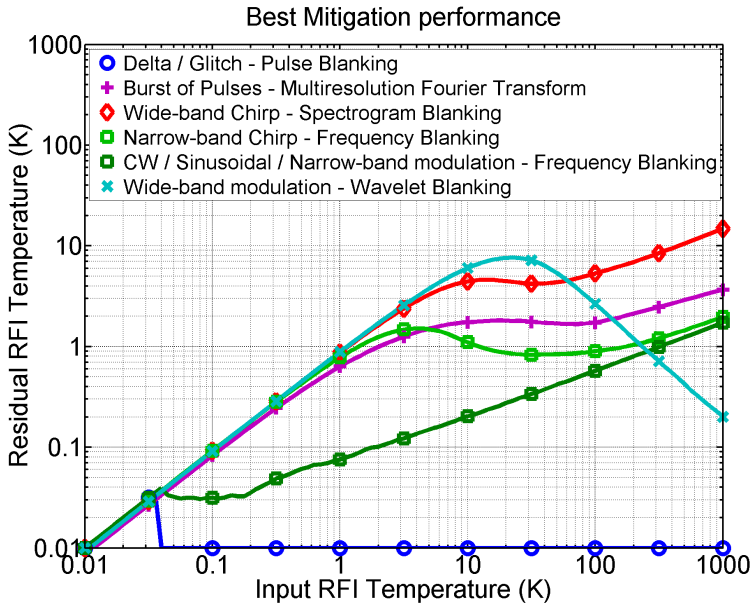

Figure 5.12: Best mitigation performance of evaluated TF RFI mitigation techniques for each one of the six RFI signals under evaluation [100].

remains below 21 K using the MFT. The combination of several resolution levels when decomposing the TF space allows the MFT to become a trade-off solution to mitigate efficiently the different kinds of RFI signals under evaluation. Even in the case of a burst of pulses, when the best detection performance is achieved by the FB, the MFT is better in terms of mitigation performance.

Table 5.4: Summary of assessment results.

	RFI signal	*Glitch*	*B. of pulses*	*WB chirp*	*NB chirp*	*CW*	*WB mod.*
Best tec.	$P_M(>99\%)$	PB 0.04 K	FB 2.8 K	SB 15 K	FB 5 K	FB 0.1 K	WD 25 K
	$\mathrm{MP}(T_i')$	PB <0.03 K	MFT <3.7 K	SB <14.8 K	FB <2 K	FB <1.7 K	WD <7.4 K
MFT	$P_M(>99\%)$	0.7 K	5 K	55 K	20 K	2.2 K	40 K
	$\mathrm{MP}(T_i')$	<3.7 K	<3.7 K	<21 K	<10.9 K	<12.2 K	<19.9 K

5.10 Conclusions

In this Chapter, three main contributions have been presented: the proposal of the MFT as a new mitigation technique, the implications of using blanking thresholding in MWR

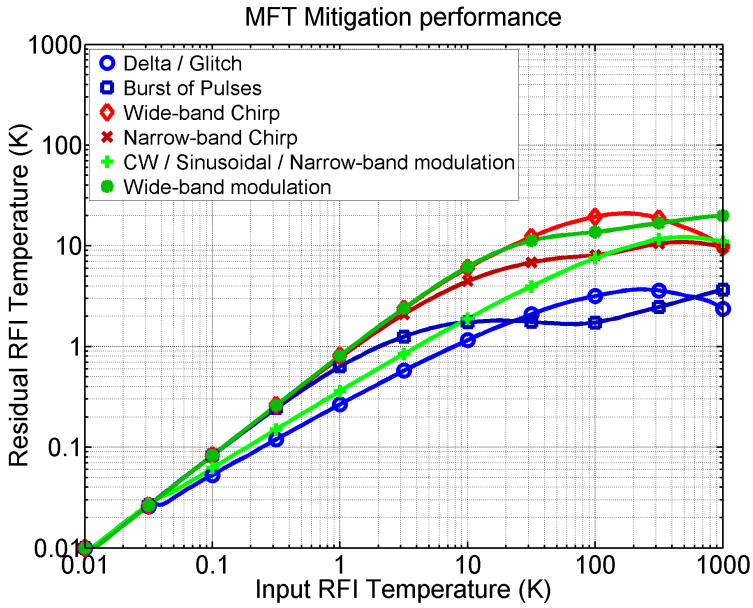

Figure 5.13: Mitigation performance of the MFT for each one of the six RFI signals under evaluation.

applications, and a performance assessment of several TF RFI mitigation techniques.

The assessment has been carried out using three figures of merit: the probability of mitigation, the sample loss, and the mitigation performance in terms of residual equivalent RFI temperature after mitigation. According to the obtained results, the best performance depends on the kind of RFI signal under consideration, and it occurs when the transform basis has a similar shape as compared to the RFI signal. For the best case performance, the maximum residual RFI signal is equal to 14.8 K. A summary of the results regarding the best probability of mitigation and best mitigation performance is shown in Table 5.4. In addition, the worst SL introduced by the blanking process is 8.4% for best case mitigation techniques, which can be considered an acceptable value (e.g. an effective radiometric resolution of 1 K will become 1.085 K with $T_i = 1000$ K in the worst case).

Moreover, the MFT technique has appeared as a good trade-off solution among all other techniques since it can mitigate all kinds of RFI signals under evaluation with a maximum residual RFI temperature of 21 K, and a worst-case SL of 26.3%. However, these results are not acceptable for MWR applications since, although RFI power is dramatically mitigated thanks to the good properties of the MFT, a residual bias after mitigation of 21 K will still corrupt the radiometric measurements. Further results of MFT performance are also shown in Table 5.4.

Part III

RFI countermeasures for GNSS/GNSS-R applications

6

Chapter 6

L-RARO: an RFI detection and localization system for GNSS/GNSS-R

This chapter is devoted to the design and test of an instrument capable of detecting and localizing RFI signals at GNSS bands using a microwave radiometer architecture, and a combination of statistical and time-frequency digital detection techniques. The instrument is named L-RARO, and it has been tested using different kinds of RFI signals. Its performance has been evaluated as a function of the RFI power. The reported sensitivities are of -108 dBm at 2 MHz bandwidth, and of -135 dBm for CW and chirp signals using averaged spectrum.

6.1 Introduction

As stated in Chapter 2, GNSS are by far the most cost-effective outdoor positioning and timing technology currently available, and this fact is enabling plenty of different applications from precision agriculture to worldwide clock synchronization. However, GNSS signals reach the Earth's surface with a very low power level, and thus, they can be easily interfered by other signals emitted (intentionally or unintentionally) at protected GNSS bands. This effect is commonly known as RFI, and it is becoming a growing problem in the last decades with the pervasive use of wireless communications.

The detection of RFI signals is one of the first steps required to help to solve this problem, together with the geolocalization of their sources. Since RFI generators (known as jammers when interference signals are intentional, and sold commercially as "Personal Privacy Devices") emit signals at GNSS bands which are protected by regulations of each country, instruments with RFI detection and localization capabilities are required by the authorities to enforce the law.

The main requirement for an RFI detector is to have an exceptional sensitivity, in order to detect very low power RFI signals, and hence to maximize the detection range of the instrument. This requirement could be met by building the detector using the architecture of one of the most sensitive instruments: the microwave radiometer. In addition, an RFI detector should be equally sensitive to different kinds of RFI signals without any a prior knowledge. For this purpose, the detector should use a combination of statistical techniques such as kurtosis or Anderson-Darling tests [8, 25], and time-frequency techniques such as the MFT [24, 107], which have been proven to perform the best against different kinds of RFI signals (see Chapter 5).

Chapter 4 described the MERITXELL multiband radiometer, which was conceived as an RFI detection and localization tool at MWR bands. Besides, MERITXELL also allows performing RFI surveys at GNSS bands in two ways. First, it has an embedded GNSS reflectometer, and second, even though its L-band antenna is tuned at 1.4 GHz, it can still receive RFI signals at L1/L2 bands.

This chapter is devoted to the development and test of a dedicated RFI detection and localization system at GNSS bands. In particular, the system is based on the microwave radiometer architecture, and it works with a combination of statistical and time-frequency digital detection techniques. The radiometer architecture has proved to be one of the most efficient solutions to improve the sensitivity of a receiver. Moreover, a portable and cost-efficient design has been taken into account during the design process, as it was done in [122, 123].

This RFI detector can be replicated to build an RFI detector network. Therefore, each node obtains the DOA of the RFI signal, and then, knowing the position of each node, it is easy to triangulate the position of the RFI source. Even though this chapter describes the design of both the detection and the localization receiving chain, only results regarding detection performance are included in the testing part. Moreover, only short-range low-power real tests have been performed in order to avoid RFI effects on nearby devices.

The instrument described in the subsequent lines has been named as L-band Radiometer-based system for RFI Observations (L-RARO), and the contents of this chapter have been

partially published in the conference paper "A Radio-Frequency Interference detector for GNSS navigation and GNSS-reflectometry applications" [124].

6.2 Design

The RFI detector described in this chapter is intended to work particularly at GNSS L1/E1 band (1.57542 GHz), with 2 MHz bandwidth B_r, but the general architecture and techniques can be easily extended to other bands. The choice has been done since it covers the most widely used GNSS service, the GPS L1 C/A, which is used in almost all applications including GNSS-R, but also the already operational Galileo E1 OS.

The need of having an increased detection performance is crucial for RFI-countermeasures. To achieve this purpose, L-RARO main features include the following:

- High sensitivity thanks to the use of a radiometer-based architecture.
- Maximization of detection range.
- Absolute power estimation (need of a calibration procedure).
- Temperature control and stabilization.
- Use of enhanced Digital Signal Processing (DSP) techniques (i.e. MFT).
- RFI characterization and localization features (detection network).

The overall architecture can be separated into three blocks: antenna, front-end, and back-end.

6.2.1 Antenna

The antenna used by the L-RARO is an array of two RHCP antenna patches tuned at the L1 band (1575.42 MHz) placed at a distance of $\lambda/2$ (≈ 9.52 cm) between them (Fig. 6.1a). Signals collected by these patches are combined using a 180° hybrid coupler (Fig. 6.1b), which sums and subtracts both signals in order to generate two different antenna patterns, one at each output connector.

The sum output corresponds to an antenna pattern with a maximum at boresight ($\theta = 0°$) with 53.5° beamwidth at -3 dB used for RFI detection purposes (Figs. 6.1c and e). Moreover, the directivity is equal to $D_s = 8.2$ dB, and the efficiency is 85% (≈ 0.7 dB loss).

On the other hand, the difference output has an antenna pattern with a minimum at boresight, used for further RFI localization purposes (see Fig. 6.1d and e). In this case, the angle where the null has an attenuation higher than 20 dB is equal to 8.2°. This determines the instrument angle resolution to localize an RFI source.

6.2.2 Front-End

The front-end architecture is based on the one commonly used in digital total-power microwave radiometers. Figure 6.2a depicts the proposed architecture. This architecture

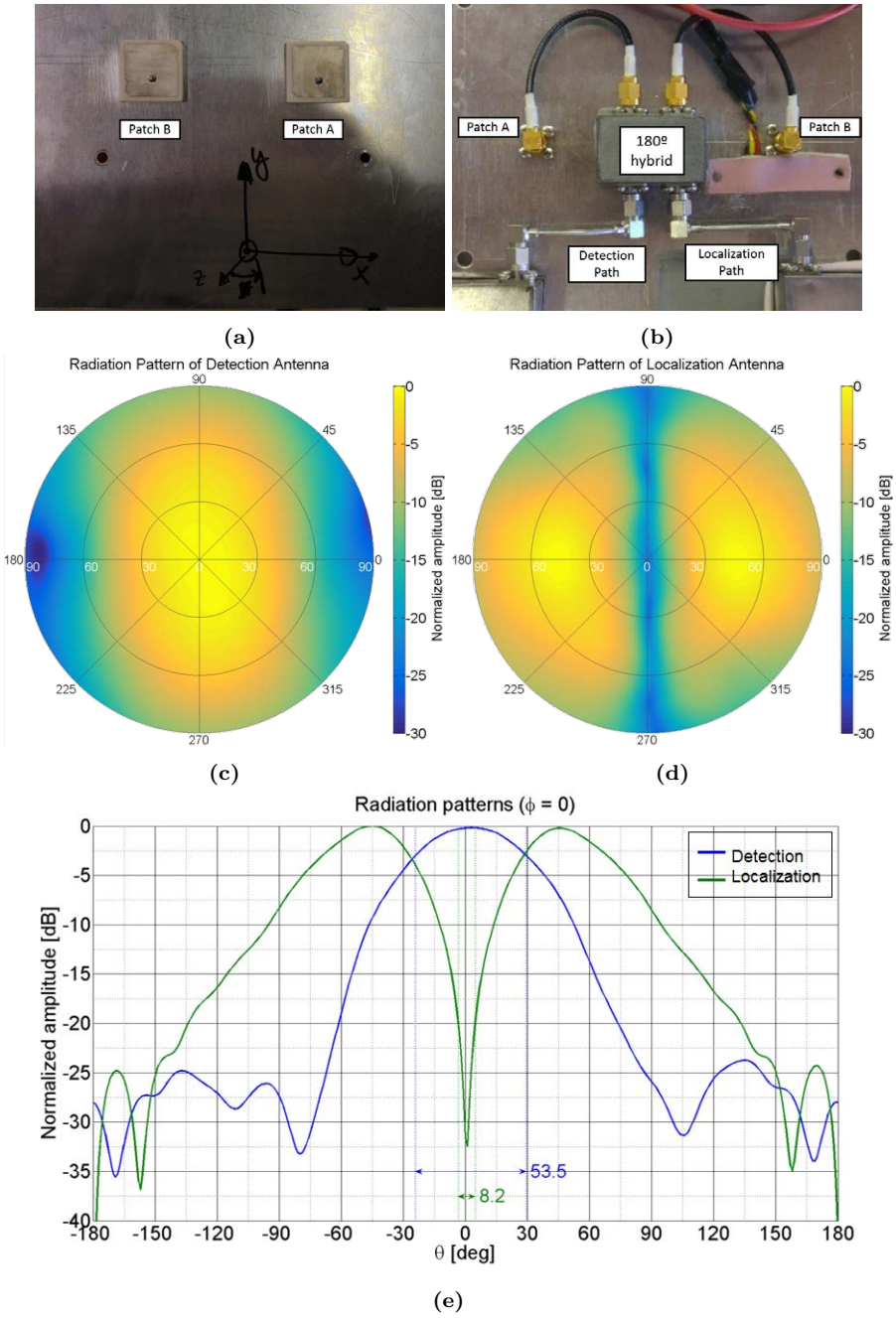

Figure 6.1: Antenna array of L-RARO: (a) two RHCP patches at a distance of $\lambda/2$, (b) 180° hybrid, (c) radiation pattern of detection path, (d) radiation pattern of localization path, and (e) cut of both radiation patterns at $\phi = 0°$.

is replicated for both antenna patterns: RFI detection and RFI localization. Moreover, in this design, a switch, a reference oscillator, and a matched load have been added for calibration purposes.

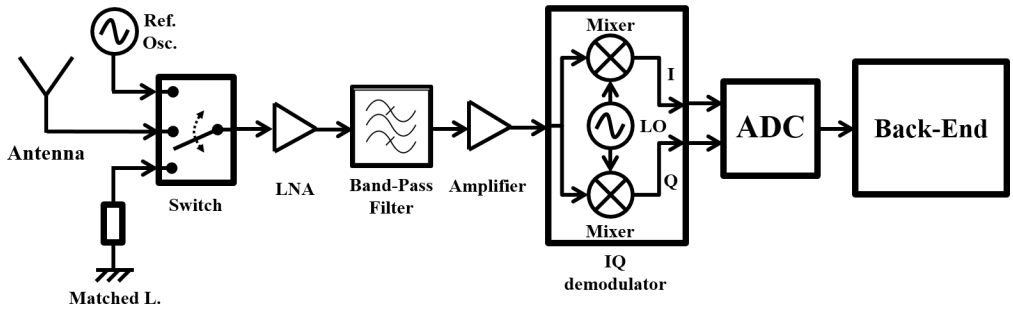

Figure 6.2: Functional front-end block diagram of the RFI detector based on the architecture of a digital total-power microwave radiometer.

A switch (model HSWA-30DR) allows commuting among the three different inputs, with insertion losses equal to 0.8 dB. The first input is connected to an external reference oscillator used for calibration purposes. The second one is connected to the corresponding antenna (detection or localization patterns). The third input is connected to a matched load with known physical temperature, also for calibration purposes.

The output of this switch is connected to a Low Noise Amplifier (LNA) (model CMA-162LN+), which has a nominal gain of 19 dB and a noise figure of 0.65 dB. The LNA amplifies the signal in order to obtain a high sensitivity, and it determines the noise figure of the whole receiver.

After the LNA, a SAW filter model TA1575IG tuned at the L1/E1 band is used to filter out near-band RFIs, and to avoid saturation of next stages. The output of the filter is amplified again using a MAR-6 wideband amplifier with a gain of 21.8 dB. These two components condition the signal for the digital stage. Taking into account the previous components, the front-end has been designed to have an equivalent noise figure of below 3 dB.

The digital stage has been implemented using a low-cost Software Defined Radio (SDR). The SDR contains a tunable I/Q demodulation stage plus a ADC. The signal coming from the last amplifier is down-converted to base-band with a maximum bandwidth of 2.048 MHz. Then, the signal is digitized with 8-bit I/Q samples. After that, digitized signals are processed in real-time at the back-end stage in order to detect possible RFI signals. Note that power is detected digitally to minimize offset drifts associated to analog systems.

The hardware is shown in Fig. 6.3 is mounted in a temperature controlled/isolated case in order to minimize temperature-induced gain fluctuations. This control allows stabilizing the temperature in a range of $\pm$ 0.5 °C. Temperature sensors are attached to the ground plane, to the RF conditioning stage (switch, amplifiers, and filter), and to the SDR. A 60 W heater injects thermal energy into the adiabatic system, and a 12 W fan allows to

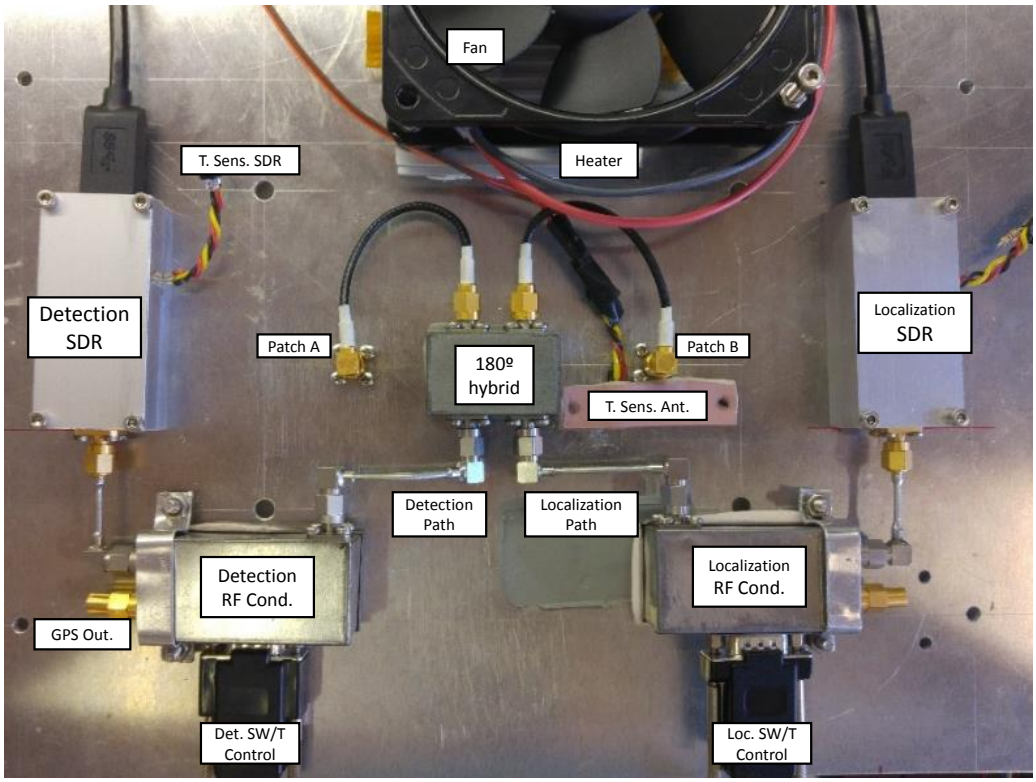

Figure 6.3: Image of the system already mounted in the back part of the antenna ground plane.

distribute the heat uniformly. More details about the temperature control system can be found in Appendix D.

Furthermore, all components have been attached to the back part of the antenna ground plane in order to minimize the size of the instrument (Fig. 6.3). The RF conditioning components have been mounted in the same case, one for each signal path (detection/localization). The control signal for the switches and temperature sensors are driven through both DB9 connectors. Moreover, a GPS output connector has been installed for further purposes (Chapter 12). Eventually, digitized samples from both SDR devices are sent to the back-end stage using USB 3 cables.

6.2.3 Back-End

The back-end stage receives the 8-bit I/Q base-band digitized samples at 2.048 Msps. The main tasks of this stage are summarized in Fig. 6.4, and listed below:

- To perform raw-sample RFI detection tests based on spectrogram and MFT.
- To calculate the power level of the set of N received samples, where N determines the power level resolution.

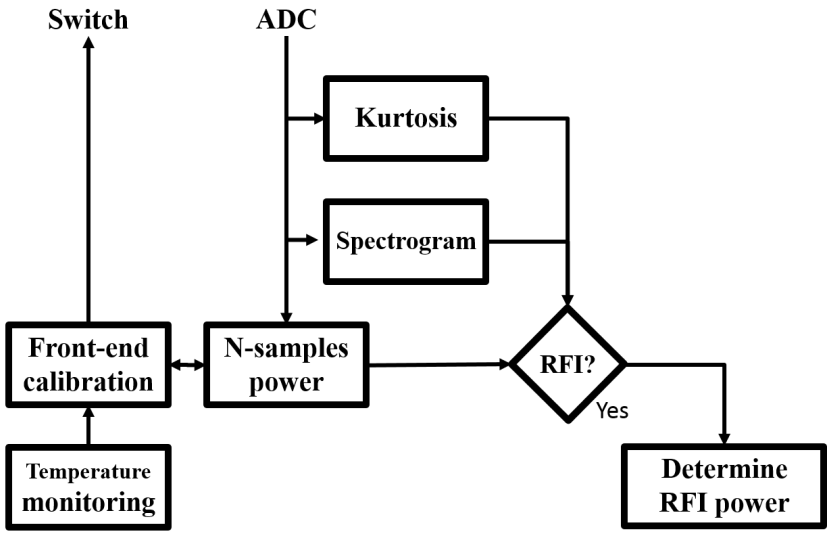

Figure 6.4: Diagram of tasks performed at the back-end stage.

- To calibrate the front-end chain by controlling a switch (set to match load or reference oscillator inputs) and by temperature monitoring/stabilization.
- To detect RFI signals by means of either the result of raw-sample tests or checking out-of-range antenna temperature measurements.
- To calculate RFI signal power using already calibrated equivalent noise and antenna temperatures.

An embedded computer is used to perform the SDR control, the N-sample power calculation, the front-end calibration, and the temperature monitoring tasks, as well as to send via Ethernet the raw samples together with the calibration information. A processing server receives the data and performs the detection and localization tasks using the information provided by the embedded computer.

6.3 Calibration

Calibration section includes the procedures to obtain the sensitivity of the instrument, to calibrate the receiving chain in order to get the absolute power measurements, which are used to compensate the transfer function of the receiving chain. These calibration procedures can be done thanks to the already mentioned logic designed to switch between the different inputs and the temperature control of the enclosure.

6.3.1 Noise Equivalent Bandwidth (NEB)

In order to determine the sensitivity of the receiver, the first step is to calculate the Noise Equivalent Bandwidth (NEB) of the whole receiving chain. This procedure is only

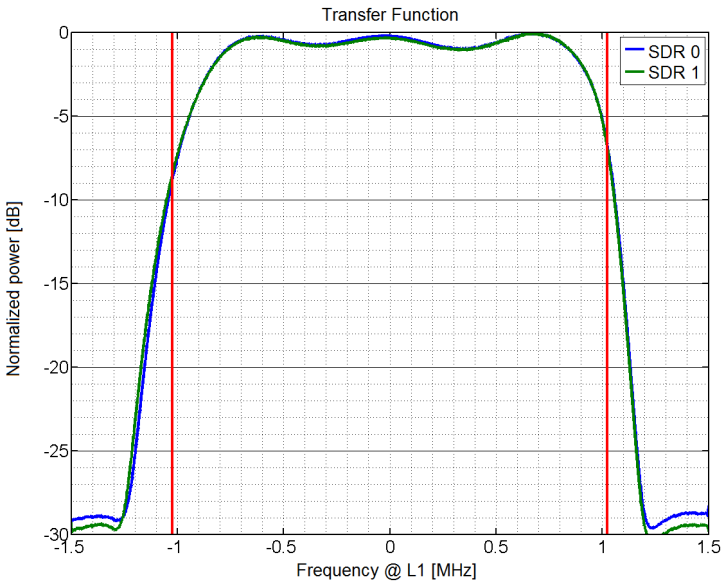

Figure 6.5: Normalized transfer function. X-axis represent frequency centered at L1 (1575.42 MHz).

required to be done once per SDR device. On the contrary, procedures described in the next subsection must be performed periodically.

To calculate the NEB, the transfer function has been estimated by injecting a chirp signal at the input of the front-end of the receiver. The chirp signal has been swept between L1 (1575.42 MHz) ± 2.048 MHz. The normalized transfer functions $\bar{H}(f)$ obtained from both receiving chains as a function of the frequency are depicted in Fig. 6.5.

Each transfer function has been obtained by superimposing three different measures: the first from 1573.372 MHz to 1575.42 MHz, the second from 1574.396 MHz to 1576.444 MHz, and the third from 1575.42 to 1577.468 MHz. Each one corresponds to a bandwidth of 2.048 MHz, and a superposition of 50% between consecutive ones. Red lines on Fig. 6.5 remark the digital bandwidth without aliasing when the SDR is tuned at L1. Moreover, only the range L1 ± 1.5 MHz has been plotted because the transfer function outside these limits was flat. Therefore, the rejection ratio for near-band RFIs is about 30 dB.

The NEB B_r (taking into account that it is a band-pass transfer function) is obtained as:

$$B_r = \frac{1}{2\pi}\left(\int_0^{\infty} \bar{H}(f)\,df + \int_0^{-\infty} \bar{H}(f)\,df\right), \tag{6.1}$$

where $\bar{H}(f)$ is the normalized transfer function. In both cases, the calculated NEB is $B_r \approx 1.8$ MHz.

Therefore; if the RFI detector is working at a stabilized temperature of $T_{sys} = 44°\text{C}$, with a noise figure equal to $F_r = 3$ dB, and the input is switched to the matched load; the

full-band sensitivity of the RFI detector is equal to:

$$P_{\text{sens}} = k_B T_{\text{sys}} B_r F_r \approx -108 \text{ dBm}. \tag{6.2}$$

Moreover, if an integration time of 1 s (2,048,000 samples) is used in the calculation of the noise power, the achieved full-band resolution is equal to:

$$\Delta P_{\text{sens}} = \frac{P_{\text{sens}}}{\sqrt{2048000}} \approx -138 \text{ dBm}. \tag{6.3}$$

6.3.2 External oscillator

The calibration of the RFI detector has been performed using a programmable reference oscillator which can be configured to generate a reference CW signal centered at the L1 band with calibrated power. This reference tone is used to calibrate periodically the gain of the whole receiving chain by sweeping its power. At the digital back-end stage, the power of the digitized samples P_{meas} can be measured to obtain such gain G as:

$$P_{\text{meas}} = G\,(P_{\text{ref}} + P_{\text{sys}}) + P_{\text{bias}}, \tag{6.4}$$

where P_{sys} is the noise system, and P_{bias} is a possible bias of the receiving detector chain. P_{sys} is a priori unknown, but the approximation $P_{\text{ref}} >> P_{\text{sys}}$ can be fulfilled if a very long FFT is applied to the received samples in order to estimate the CW power.

Since the FFT is a matched filter to the CW signal, the power measured at the peak is amplified by a factor G_{T} that depends on the number of FFT points. In this case, a 2,048,000 point FFT has been taken, which leads to a P_{meas} at the FFT peak equal to

$$P_{\text{meas}} = G\,(G_{\text{T}}\,P_{\text{ref}} + P_{\text{sys}}) + P_{\text{bias}} \approx G\,G_{\text{T}}\,P_{\text{ref}} + P'_{\text{bias}}, \tag{6.5}$$

with $G_{\text{FFT}} \sim 63$ dB, and $P'_{\text{bias}} = G\,P_{\text{sys}} + P'_{\text{bias}}$ (Fig. 6.6a).

Using this method, the reference oscillator power has been swept from -132 dBm to -82 dBm in steps of 5 dB. Figure 6.6b shows the linear power of digitized samples as a function of the reference tone power in mW. From these results, the gain value G is estimated to be $3.457 \cdot 10^7$ or 75.4 dB, and $P'_{\text{bias}} \sim 0$. With this value, the power measured at the matched load is on the order of -108 dBm, which matched with the result obtained in (6.2).

6.3.3 Transfer function compensation

Once the absolute power calibration is applied, there is one extra procedure to be done: the compensation of the transfer function. Given the switching capabilities, a periodic capture of the spectrum measured at the matched load noise can be used to compensate the transfer function of the receiving chain.

Figure 6.7a shows a first capture of the spectrum at the L1 band, plus a capture of the spectrum at the matched load. It can be appreciated that a continuous wave signal of

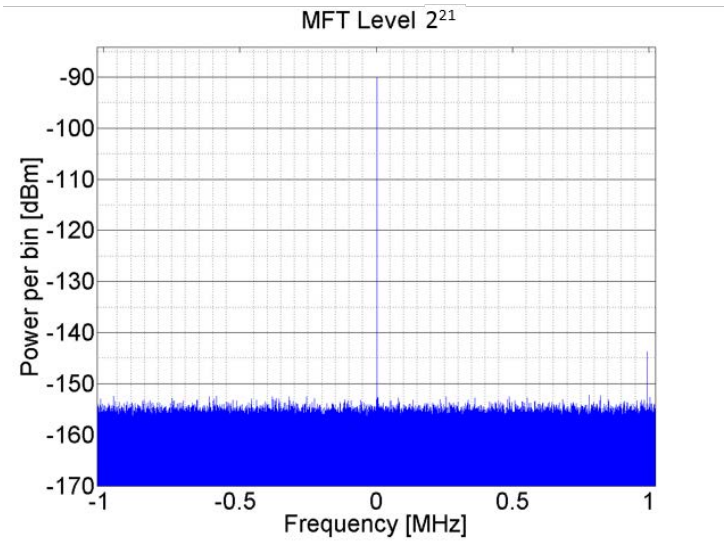

(a)

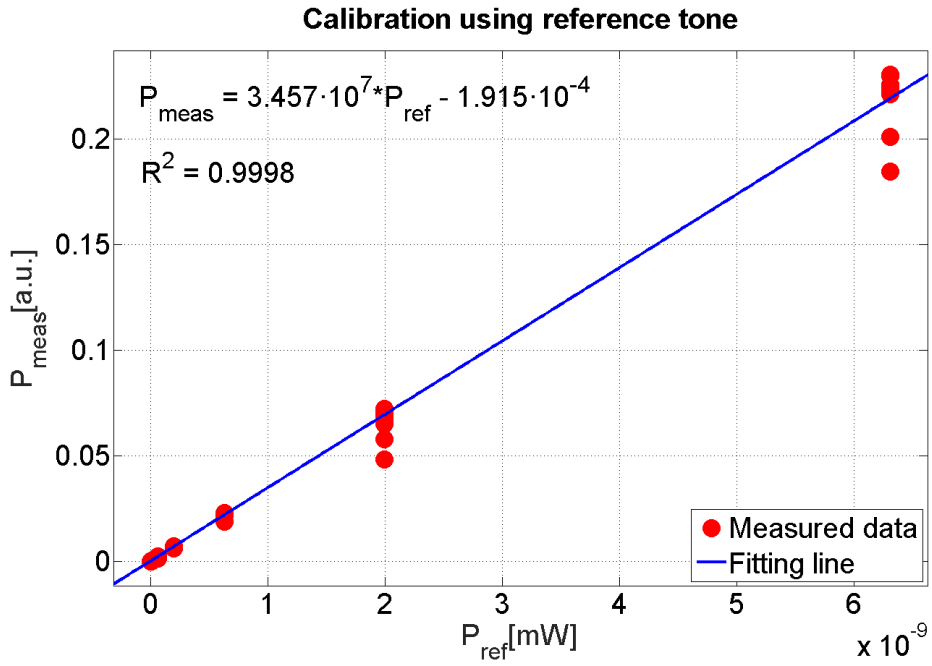

(b)

Figure 6.6: Calibration using reference tone. (a) Detection enhancement due to the use of the FFT transform. (b) Power (in arbitrary units) at the maximum of the 2,048,000 point FFT of the digitized samples as a function of the reference tone power in mW.

-129 dBm appears at 1.576 GHz. This shows an example of unintentional RFI signals present at the L1 band.

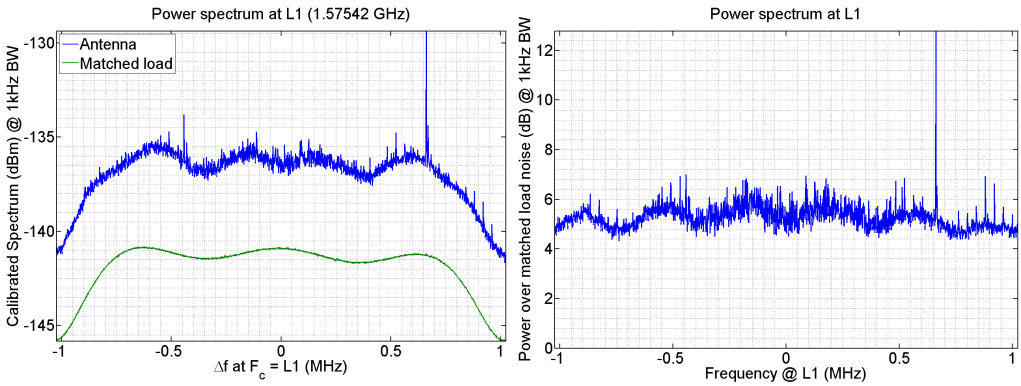

(a) **(b)**

Figure 6.7: (a) Calibrated spectrum measured at antenna and at matched load. (b) Difference between antenna and matched load spectra.

Figure 6.7b shows the difference between both spectra. The noise floor at the antenna is between 5 to 6 dB higher than at the matched load. Moreover, much more RFI spikes are revealed using this method, and it allows to compare their relative power inside the bandwidth of the RFI detector.

6.4 Tests

The following tests have been performed both inside the laboratory and using an outdoor setup. Moreover, two different kinds of tests have been performed. Calculating an averaged spectrum, and using the MFT capabilities.

Furthermore, only the RFI detection chain has been assessed. Regarding the localization capabilities of L-RARO using a network of detectors, they are discussed in the future work proposed for this PhD thesis (Chapter 12).

6.4.1 Outdoor setup

In order to validate the performance of the RFI detector in an open environment, it has been placed in a 5-meter height mast at top of the roof of Universitat Politècnica de Catalunya in Barcelona, Spain (see Figure 6.8). Moreover, an RFI generator has been placed at 40 meters in the next building with line-of-sight. Both instruments can be controlled remotely in order to perform the required tests.

Figure 6.8: RFI detector attached to the mast (top). Experiment location with 40 meters between RFI detector and generator.

6.4.2 Averaged Spectrum

6.4.2.1 In-lab unintentional

Given the design, a sensitivity of -107 dBm in the whole band is reported, as well as an RFI power estimation with a resolution of -138 dBm. Moreover, this sensitivity can be increased, for instance, when using a Fourier transform for detecting continuous wave signals.

In this subsection, an RFI detection test is performed based on calculating the spectrum at the antenna using a 2048 point FFT with 1000 averages (1-second data). Transfer function compensation has been applied in this case. Many advanced techniques such as the MFT are shown in next subsections.

Figure 6.9 shows the averaged power spectrum centered at L1 band measured at the laboratory with the presence of unintentional continuous RFI signals. A reference tone received with a power of -130 dBm has been used to measure their power level, or equivalently, the equivalent interference temperature that they introduce in a radiometer with such bandwidth. In this case, the sensitivity has been decreased to -143 dBm, and the resolution in the detection of RFI to 0.1 K.

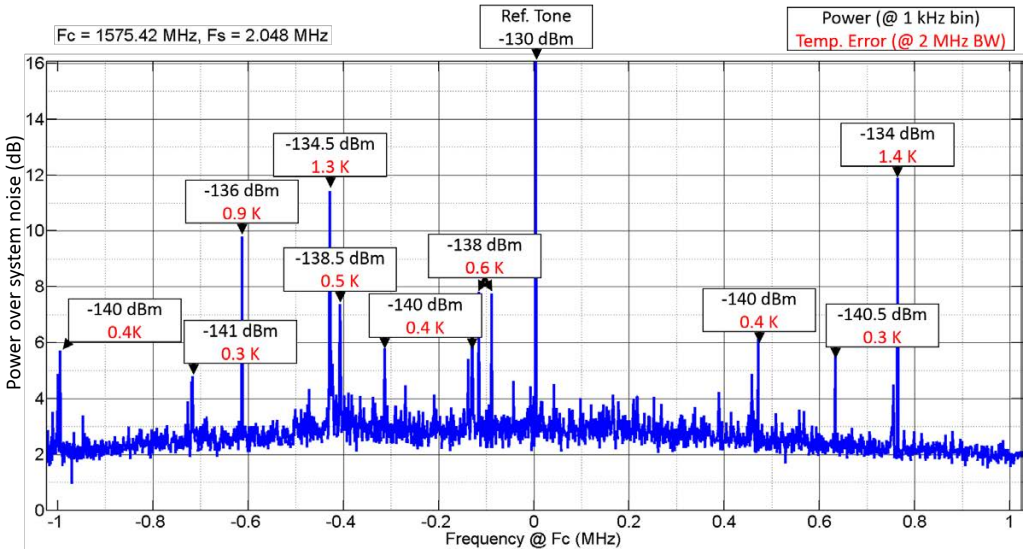

Figure 6.9: Power spectrum with a -130 dBm calibration tone centered at L1 band. The frequency resolution of the power spectrum is 1 kHz per bin, and the equivalent interference temperature has been calculated as $T_{\mathrm{eq}}\,[K] = P_{\mathrm{RFI}}\,[W]/(k_B\,B_r)$.

This test proves that electronic devices present at the laboratory such as personal computers, switched power supplies, measuring equipment, computer screens, hard drives or digital memories (e.g. DDRs at 533 MHz) are generating RFI signals that can degrade the performance of highly sensitive instruments such as microwave radiometers or GNSS reflectometers.

6.4.2.2 Jammer

As shown in the previous subsection, an averaged spectrum allows detecting very low power RFI signals. In the case of the outdoor setup, the RFI detector has been tested using different kinds of RFI signals such as pulsed, continuous wave, and chirp. Only chirp tests are considered in the following lines since all of them had equivalent results. Its performance has been evaluated as a function of the RFI power.

Figure 6.10 shows the spectrum of different RFI chirp signals emitted from the generator placed at 40-meter distance. These chirp signals have a bandwidth of 1 MHz centered at L1, a repetition period of 1 kHz, and the transmission power has been swept from -20 dBm to -50 dBm.

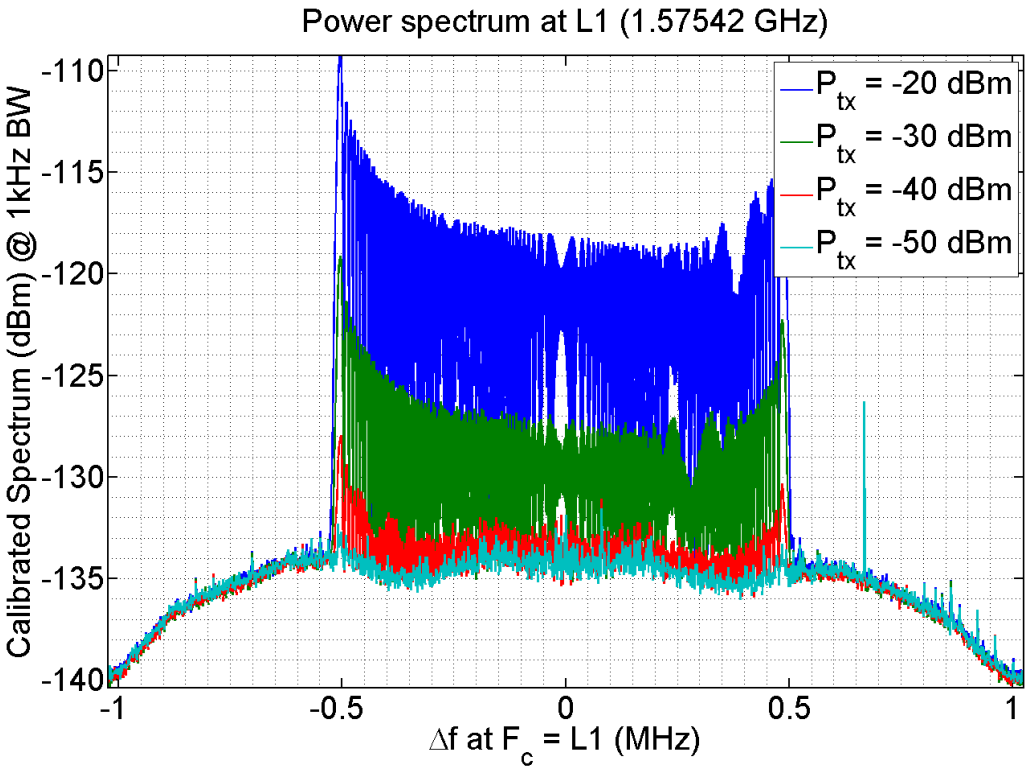

Figure 6.10: Spectrum of RFI chirp signals emitted from a 40 meter distance RFI generator with different power values from -20 dBm to -50 dBm.

No transfer compensation has been used in this test. Moreover, it can be appreciated that the unintentional CW signal shown in Fig. 6.7 is also present in this test.

6.4.3 MFT

This subsection presents some examples of RFI characterization using the MFT. In particular, four examples including unintentional in-lab, unintentional outdoors, and intentional slow and fast chirps signals are analyzed.

The MFT has been calculated taking into account resolution levels with samples equal to powers of 2. The whole set of samples is taken as $2^{21} = 2097152$, which represents 1.024 s of data. For the sake of clarity, only four of the calculated levels are represented since they are the most representative in the examples. These levels have transform windows of the following lengths: 2^0 (time), 2^6, 2^{11}, 2^{21} (whole set with the same transform window).

6.4.3.1 In-lab unintentional

Figure 6.11 shows a capture of the RFI signals present at the laboratory. Time level (2^0) shows some pulsed signals with instantaneous power up to -137 dBm, and about 30 dB

higher than the noise floor.

Intermediate levels (2^6 and 2^{11}) show the same time pulses, but also some CW RFIs. In particular, three different trends can be distinguished: four equidistant CW at -350 kHz, 50 kHz, 450 kHz, and 850 kHz; two narrow-band signals centered at -750 kHz and -400 kHz; and a single CW at 700 kHz.

Frequency level (2^{21}) shows many spikes about 12 dB about the noise floor. Some spike clusters around $\pm$ 450 kHz arise with values up to -132 dBm. If a zoom in is done, for example, around -350 kHz, it can be appreciated that lines shown at intermediate levels are also present at this level. They have a power level of about -150 dBm, and a local bandwidth of 4-6 kHz.

6.4.3.2 Outdoors unintentional

Figure 6.12 shows a capture of the unintentional RFI signals present outdoors, at top of the roof of the laboratory. Time level (2^0) shows only noise apparently. However, if a zoom in is done, some pulsed signals are revealed. They have an instantaneous power up to -154 dBm, and an apparent period equal to 125 ms.

Intermediate levels (2^6 and 2^{11}) do not show the same time pulses, but two equidistant CW can be appreciated clearly. These CW signals are placed exactly at L1 $\pm$ 500 kHz. If one tries to find the DOA of these CW signals by changing the pointing direction of the boresight of the antenna, it is easily found that they come from the sky. In [125], an anomalous behavior at GPS L1 signal was reported during May 2017. The origin of the spikes was identified to be the transmission of non-standard codes from a non-operational GPS satellite (GPS IIF-9, SVN49). This reported anomaly fits timely with the RFI signals captured during L-RARO validation experiments.

Frequency level (2^{21}) shows both peaks centered at L1 $\pm$ 500 kHz, with a power level equal to -131 dBm. Besides, many other spikes with a power level up to -138 dBm can also be appreciated. Furthermore, the RFI detector has enough sensitivity to see the spectrum of the GPS L1 C/A code, which corresponds to the central bump that is up to 10 dB over the noise floor.

6.4.3.3 Jammer

Figures 6.13 and 6.14 show a capture of jamming signals emitted by the RFI generator placed at top of the roof of the laboratory. Both RFI signals are chirps, with 2 MHZ bandwidth. One is a slow-rate chirp with a Pulse Repetition Frequency (PRF) of 10 Hz. The other is a high-rate chirp with a PRF of 1 kHz.

Both chirp signals are received at a full-band power of -108 dBm, so that, time level (2^0) shows no apparent increase of the mean power level.

In the case of the slow chirp, the RFI signal can be barely appreciated at intermediate level 2^6. However, an intermediate level 2^{11} shows clearly the shape of the sinusoidal chirp signal in the TF space. Moreover, a zoom in at this level allows to observe it even more clearly. Besides, a CW is also observed centered at -450 kHz.

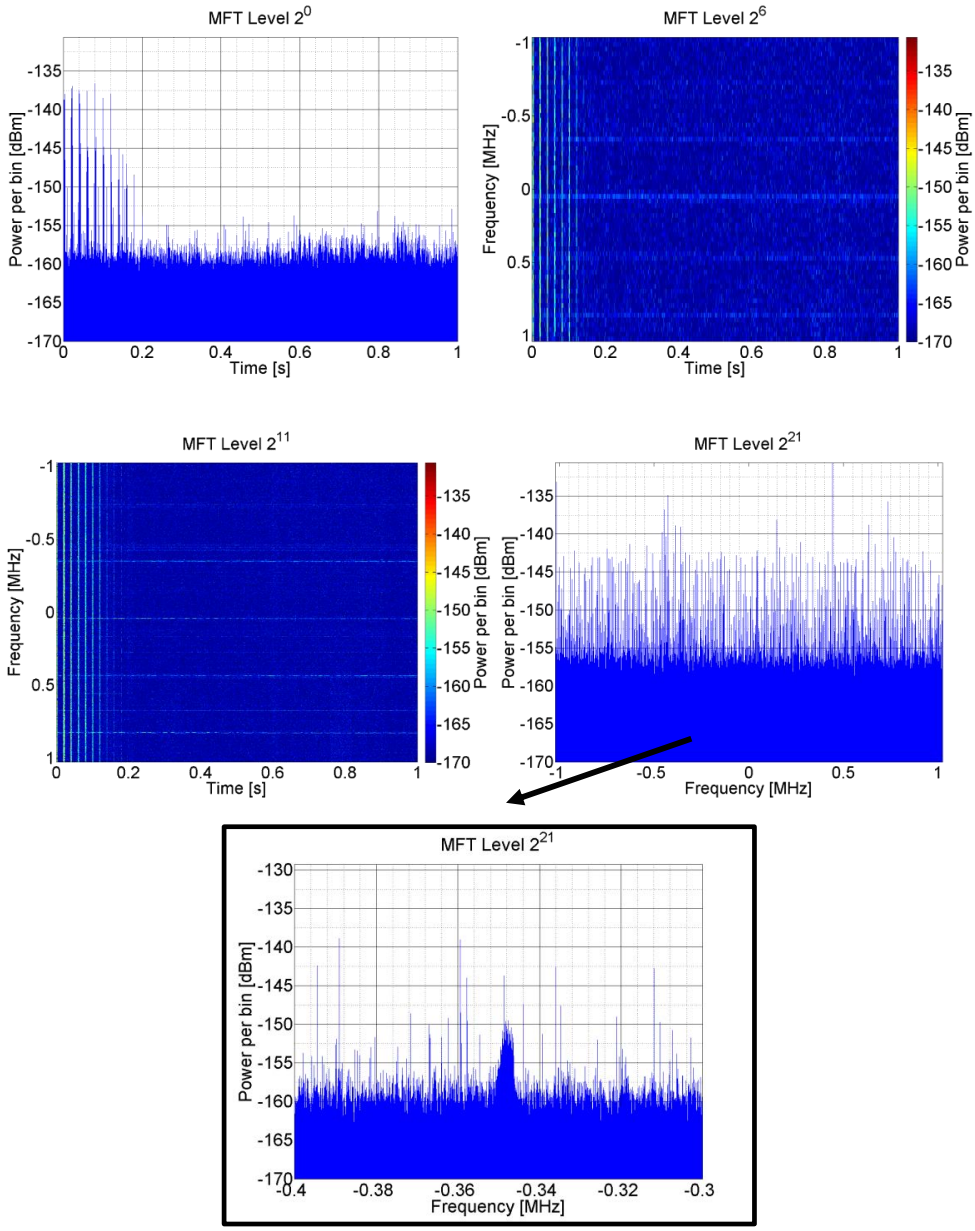

Figure 6.11: RFI detection and characterization using the MFT of unintentional RFI signals captured inside the laboratory. Several pulsed and CW RFI signals are observed. The last subfigure has been obtained by zooming in the one corresponding to the MFT 2^{21} level.

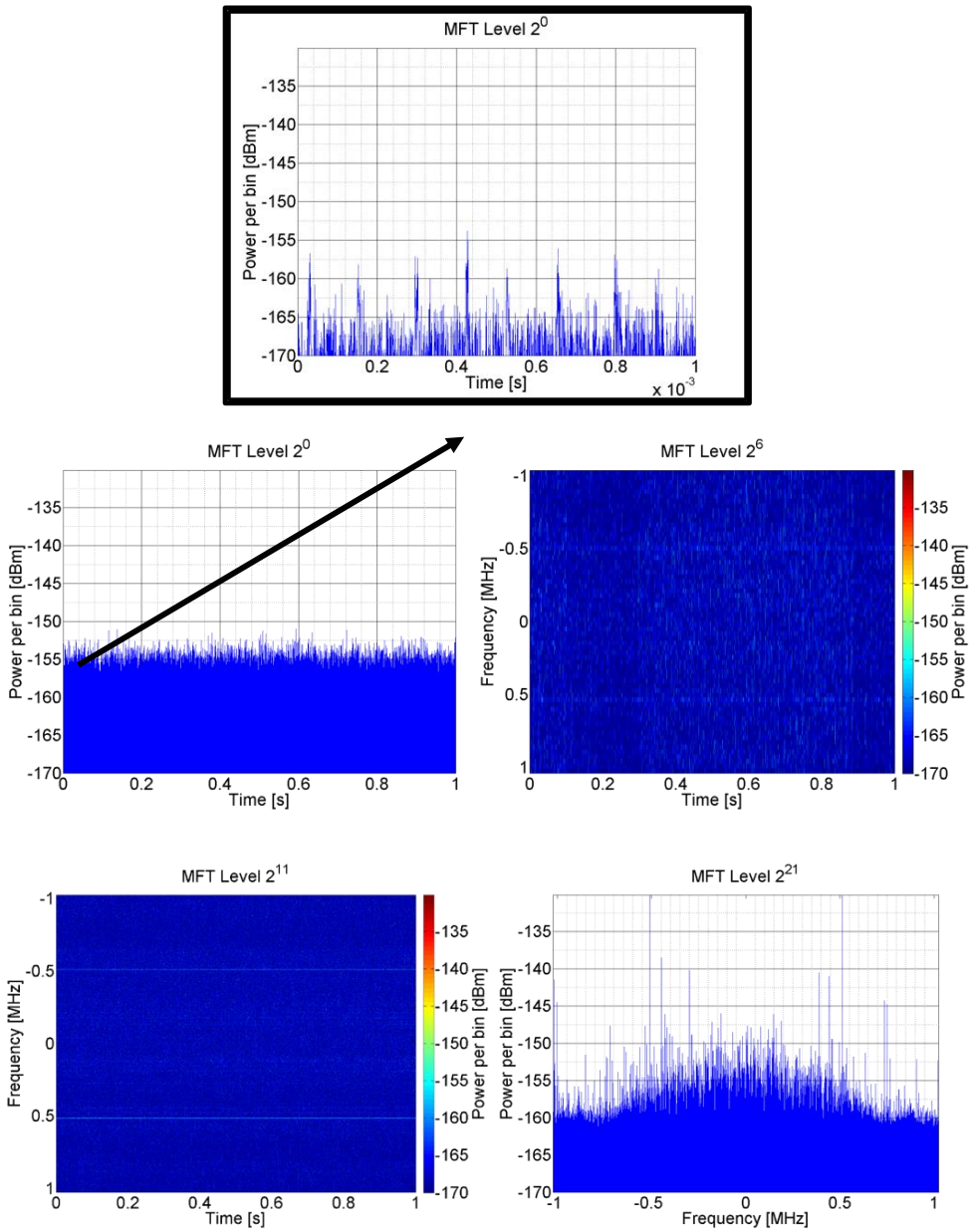

Figure 6.12: RFI detection and characterization of unintentional RFI signals captured outdoors. Pulsed signals, GPS anomalous spikes, and L1 C/A spectrum can be observed. The first subfigure has been obtained by zooming in the one corresponding to the MFT 2^0 level.

Frequency level (2^{21}) in Fig. 6.13 shows many spikes, the spectrum of C/A code, and an increase of the noise floor as compared to Fig. 6.12. This increase is due to the contribution of the power of the slow chirp inside the bandwidth of the detector.

In the case of the fast chirp, the RFI signal can be appreciated at intermediate level 2^6 as numerous vertical lines. Moreover, a zoom in at this level shows clearly the shape of the sinusoidal chirp RFI signal. However, at intermediate level 2^{11}, the RFI signal is completely spread in the T-F space. Even though, several CW or horizontal lines can still be appreciated.

Frequency level (2^{21}) in Fig. 6.14 shows an increase of the noise floor up to -134 dBm. This shows the spectrum of the chirp signal, and how it masks the rest of RFI signal spikes shown in previous plots. Even though both RFI chirp signals are received with the same full-band power, they appear to be different looking at several resolution levels of the MFT. This effect was explained in Chapter 5.

Regarding these results, MFT seems to be a good technique for RFI detection, but also for RFI characterization. The different resolution levels allow analyzing each one of the underlying mixed signals received at the antenna. These signals are usually from unknown origin, but at least they can be classified regarding their signal shape, period or nature.

6.5 Impact on GNSS signals

Once known that the RFI detector can measure the power of the undesired signals at L1, P_{rx}, the next question is how they affect GNSS measurements, and in particular, how they degrade the SNR of a DDM. GPS L1 C/A codes reach the Earth's surface with a power on the order of -127 dBm in their transmission bandwidth.

Figure 6.15 shows several DDM obtained taking 1 ms and 1 s of coherent and incoherent averaging respectively for the different RFI chirp signals used in Section 6.4.2.2.

In this case, the SNR is calculated as the ratio between the maximum value of the DDM and the standard deviation of the rest of the DDM. As expected, it can be appreciated how the SNR is degraded as the RFI power increases. The resulting SNR at the different DDMs are 21 dB (P_{rx} = -120 dBm), 20 dB (P_{rx} = -110 dBm), 16 dB (P_{rx} = -100 dBm), and no peak tracking can be observed for a P_{rx} beyond -90 dBm.

Further study on how RFI signals degrade the SNR in GNSS-R applications, how they modify the shape of DDM, and how their effects can be analytically represented have a dedicated chapter in this PhD thesis (see Chapter 7).

6.6 Conclusions

L-RARO is able to detect RFI signals at the L1 band with a sensitivity of -108 dBm at full-band, and of -135 dBm for CW and chirp-like signals when using averaged spectrum. Measurements show that a chirp RFI signal emitted from 40-meter at -30 dBm power (received at -100 dBm) degrades the SNR of GNSS-based instruments by a factor of -5 dB. With this experiment, and taking into account the reported sensitivity, the detection range of a 1 mW commercial jammer is on the order of 85 kilometers under ideal conditions

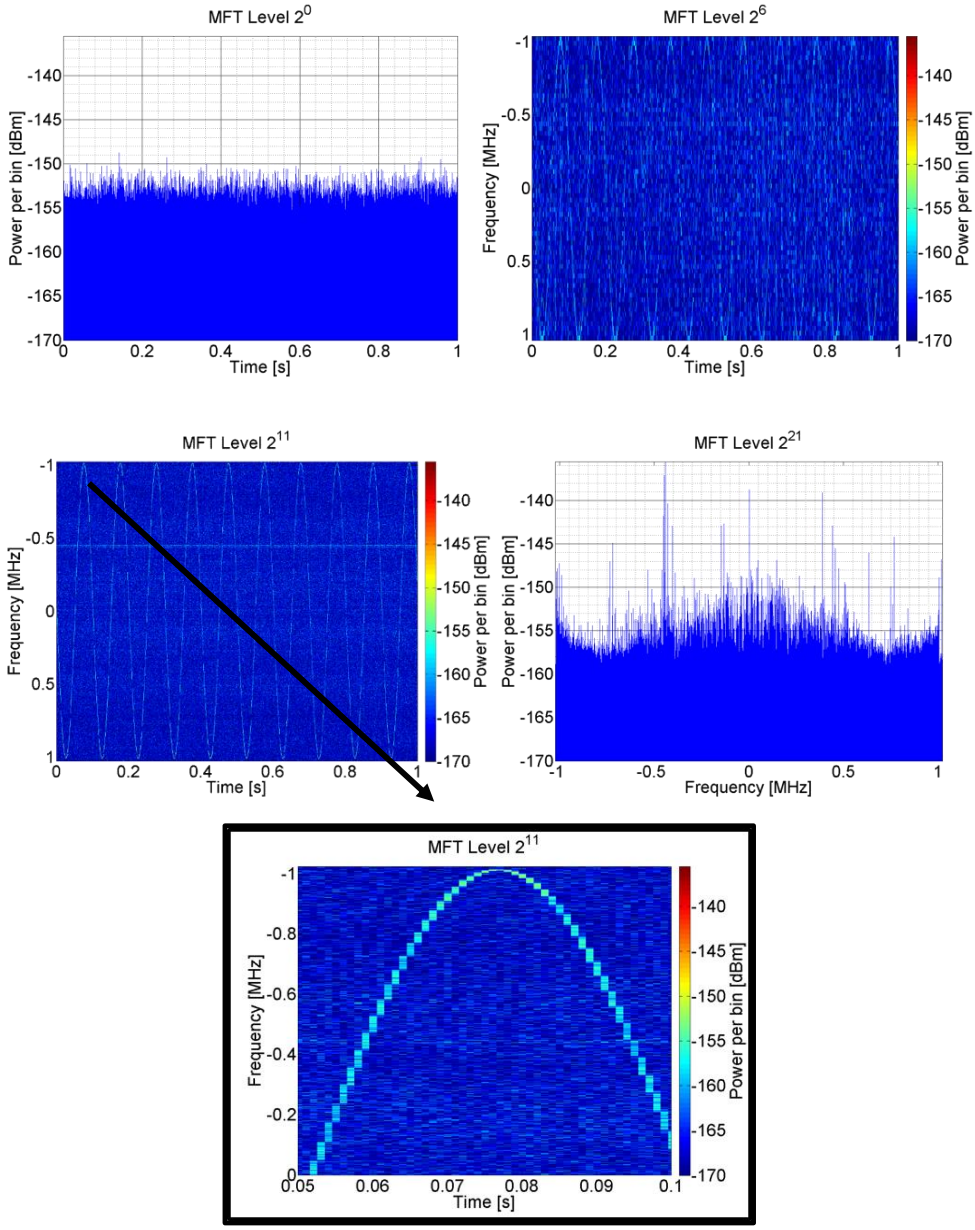

Figure 6.13: RFI detection and characterization using the MFT of an intentional low-rate chirp signal (PRF is 10 Hz and BW is 2 MHz). The last subfigure has been obtained by zooming in the one corresponding to the MFT 2^{11} level.

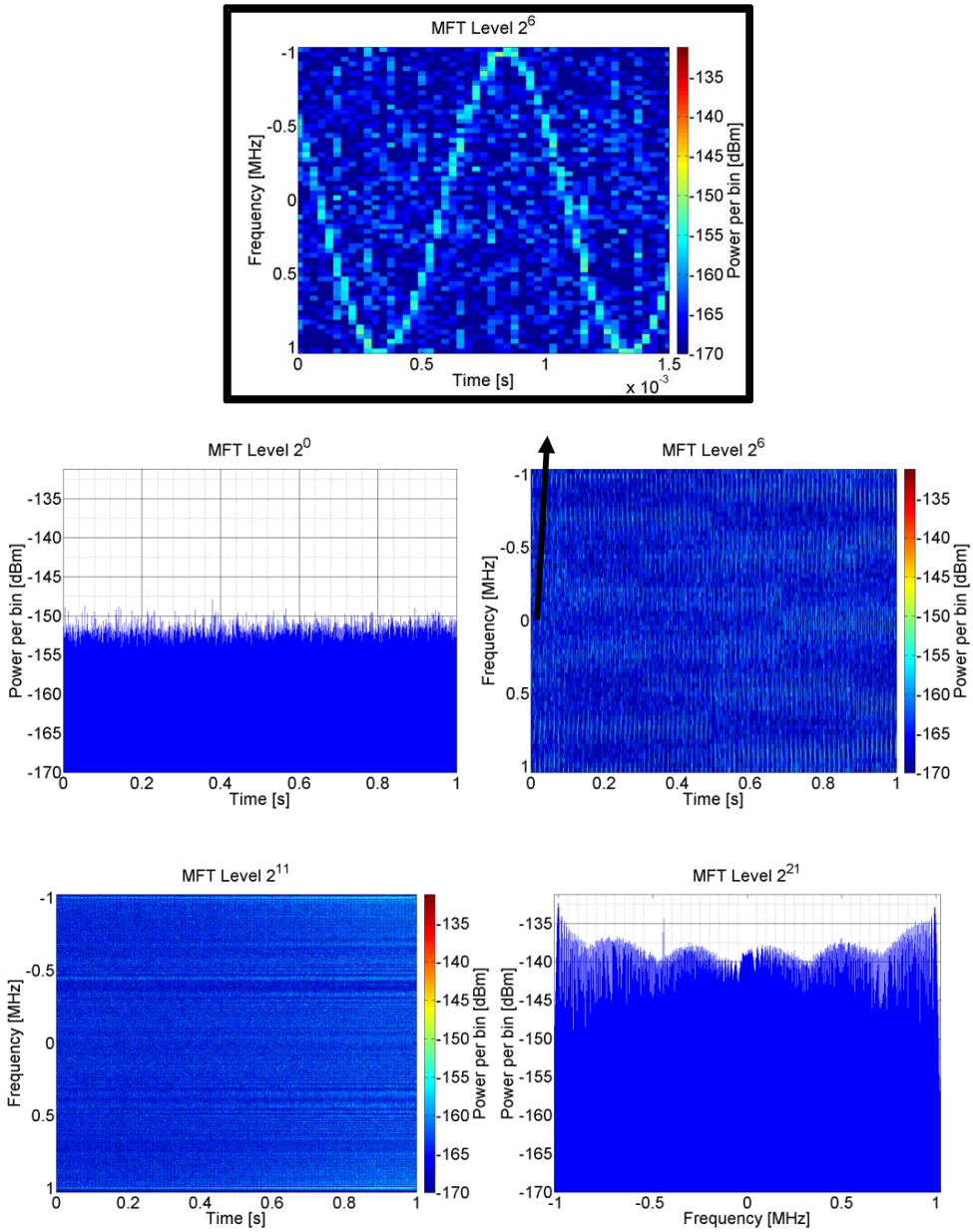

Figure 6.14: RFI detection and characterization using the MFT of an intentional high-rate chirp signal (PRF is 1 kHz and BW is 2 MHz). The first subfigure has been obtained by zooming in the one corresponding to the MFT 2^6 level.

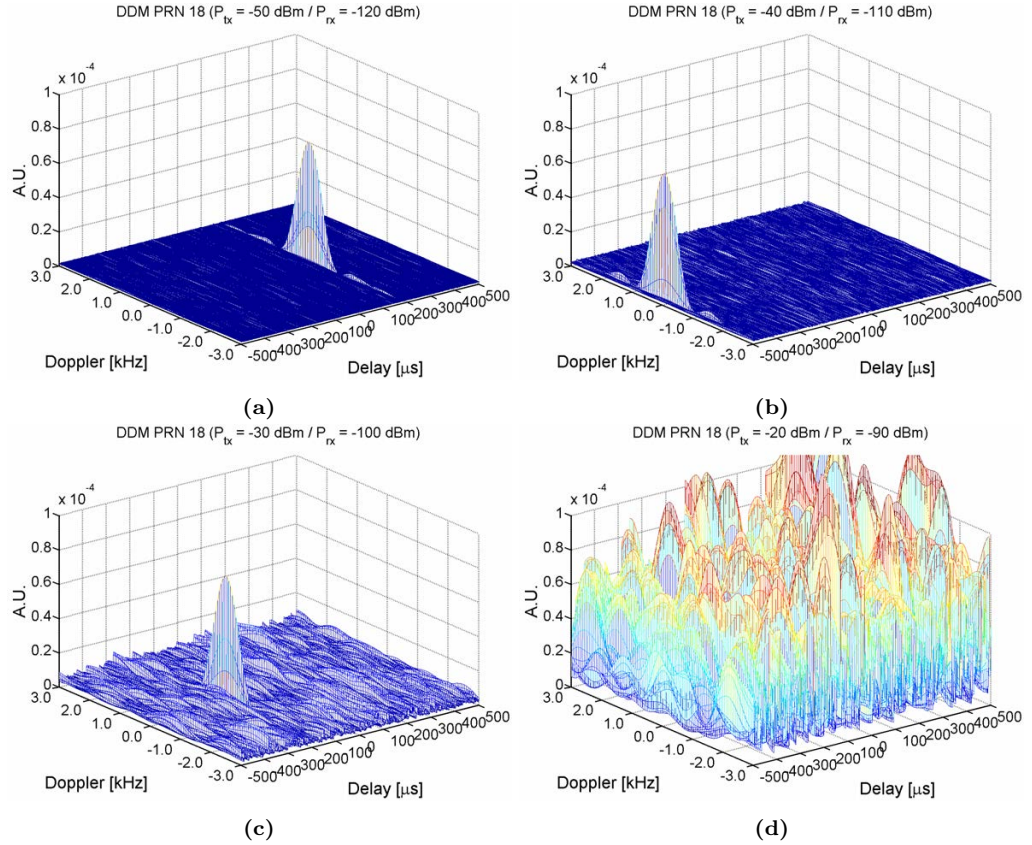

Figure 6.15: DDMs of satellite GPS L1 C/A PRN 18 with under the presence of the generated chirp RFI signals received at power level equal to (a) -120 dBm, (a) -110 dBm, (c) -100 dBm, and (d) -90 dBm.

of line-of-sight and free space propagation. Further tests regarding RFI localization and other features of L-RARO are discussed in Chapter 12.

7

Chapter 7

GSSC: a study of the effects of RFI signals in GNSS-R

This chapter describes how the presence of RFI signals affects GNSS-R measurements. The SSC is the standard figure of merit used to evaluate the SNR degradation due to RFI in GNSS applications. However, an in-depth assessment in the field of GNSS-R has not been performed yet, and particularly, on the influence of RFI on the so-called DDM. This work develops a model that evaluates the contribution of intra-/inter-GNSS and external RFI effects to the degradation of the SNR in the DDM for both conventional and interferometric GNSS-R techniques. Moreover, the Generalized SSC (GSSC) is defined as a figure of merit to account for the effects of non-stationary RFI signals. The results show that highly directive antennas are necessary to avoid interference from other GNSS satellites, whereas mitigation techniques are essential to keep GNSS-R instruments working under external RFI degradation.

7.1 Introduction

As described in Chapter 2, the consolidation of mass-market wireless communication applications together with the increasing demand of wider bandwidths of operation have fostered the problem of RFI in an overcrowded frequency spectrum. RFIs are undesirable signals that degrade or even disrupt the performance of a receiver, and they are particularly threatening for devices that use very low power signals such as GNSS receivers. Despite their inherent protection to RFI due to the spread-spectrum codes, GNSS-based instruments are prone to suffer from RFI effects.

In the last years, the number of reported RFI occurrences in GNSS has been increasing [30], even though policies are established to protect the GNSS bands. Furthermore, several studies, such as [12] and [126], have shown that, in addition to jamming signals, even unintentional RFI signals can degrade the performance of GNSS receivers. In GNSS, RFI signals include aeronavigation signals such as Distance Measurement Equipment (DME) at the GPS L5/Galileo E5 bands, spurious or harmonics of lower frequency, and even contributions of the same GNSS satellites sharing the same band of operation among others. Although anthropogenic RFI signals are the most common source, natural emissions may also be considered as RFI signals such as Sun L-band surface glints which can also affect GNSS-R measurements.

The impact of RFI signal in GNSS receivers has been studied in detail over the last decade. The SSC was defined as a figure of merit to quantify the degree of interference that a GNSS signal suffers due to other signals sharing the band of operation [127], in terms of a reduction of the SNR. Indeed, the SSC allows to characterize also GNSS intra-system and inter-system SNR degradation [128]. That is a measurement of the rejection ratio between navigation codes taken into account in their design process in order to guarantee the co-existence of multiple GNSS.

The RFI problem in GNSS is of special concern due to the high number of existing GNSS-enabled applications. One of these applications is GNSS-R, a promising technique in the field of remote sensing, that was first proposed in 1988 for scatterometry applications [31]. Later in 1993, GNSS-R was first suggested for mesoscale ocean altimetry [32], and since then, this technique has been used in the retrieval of many geophysical parameters such as sea surface state [129], sea surface salinity [130], soil moisture [131], and ocean altimetry [132] among others.

GNSS-R devices receive simultaneously the signals transmitted by multiple GNSS satellites that have been scattered by the surface of interest. This configuration is known as multistatic in radar theory [133]. There are two main GNSS-R approaches [35]. The first is the so-called conventional GNSS-R (cGNSS-R), in which the reflected signal is cross-correlated with a locally generated replica of the transmitted one. Only signals with open codes can be used in this approach (e.g. GPS L1 C/A). The second one is the so-called interferometric GNSS-R (iGNSS-R), in which the reflected signal is cross-correlated with a signal captured directly from the satellite. In this case, both open and restricted codes are used simultaneously in a specific band (e.g. C/A, C, P and M codes at GPS L1 band). Figure 7.1 illustrates the scenario corresponding to each approach. Regarding their resilience in front of RFI, cGNSS-R is not immune to RFI due to the finite rejection ratio of the spread-spectrum signal, whereas iGNSS-R is even more prone to RFI since

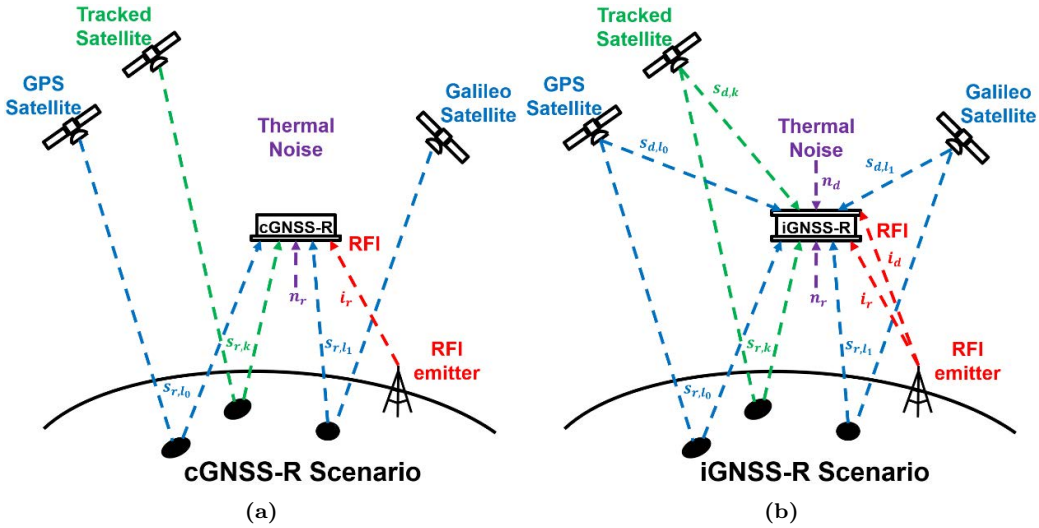

Figure 7.1: Illustrative diagram representing satellite, RFI and thermal noise signals involved in the study of the SNR degradation for a) cGNSS-R scenario, and b) iGNSS-R scenario.

an undesired signal captured by both antennas will produce a non-zero cross-correlation.

The observable that contains all the information of GNSS-R measurements is the so-called DDM, which shows how the scattering process over the surface of interest spreads the energy of the transmitted signal in the delay-Doppler space, and how this spreading changes in time. The generally accepted model for incoherent GNSS-R reflections, assuming fully diffuse scattering from rough surfaces, and originally stated for sea-surface observations, is the Zavorotny-Voronovich (Z-V) model [134]. The Z-V model can be expressed in a simplified version as a two-dimensional convolution [135], and it is equivalent to the so-called radar mapping equation [133]. The model can be expressed as in [136] as:

$$\left\langle |Y(\nu,\tau)|^2 \right\rangle = |\chi(\nu,\tau)|^2 ** \Sigma(\nu,\tau), \tag{7.1}$$

where $\langle |Y(\nu,\tau)|^2 \rangle$ is the expected DDM, ν and τ are the Doppler and delay variables respectively, the $**$ operator indicates a two-dimensional convolution in ν and τ domains, $|\chi(\nu,\tau)|^2$ is the Woodward's Ambiguity Function (WAF) of the navigation code, and $\Sigma(\nu,\tau)$ accounts for the scattering at the surface, propagation losses, antenna patterns, and the rest of terms in the bistatic radar equation. Moreover, if the reflection process is coherent because it takes place over a planar surface (e.g. calm water, ice floes, or flatlands), the measured DDM will be an attenuated version of the signal WAF. Furthermore, any combination of coherent and incoherent reflection will lead to a DDM that can be expressed as an attenuated and distorted version of the signal WAF.

The WAF is the squared modulus of the ambiguity function first proposed in [137], and it was introduced in radar theory [138] as the appropriate function to evaluate the degree of ambiguity in the measurements when the number of radar echoes is sufficiently large. This approach is translated into a non-coherent detection process after the cross-correlation,

which is used in most of the GNSS receivers [139] in order to increase the SNR. Moreover, non-coherent detection is necessary in GNSS-R applications due to the effect of speckle noise introduced in the scattering process [133], which is caused by the addition of a large number of random phased scatterers over the surface of interest.

According to the experiments carried out in [12], the effect of RFI signals in cGNSS-R is translated into an equivalent rise of the noise floor, and thus, into a desensitization of the receiver. However, these effects have not been studied in depth to the best of authors' knowledge. This chapter aims at providing a general model that accounts for the effects of RFI signals in GNSS-R instruments operating with CDMA spread-spectrum GNSS signals, including intra- and inter-GNSS interference and other external RFI signals.

The results derived in the following sections are completely general, so they can be applied to any GNSS-R scenario using the proper geometry parameters. However, for the sake of clarity, these results are illustrated using specific cases that take into account no spatial filtering (isotropic antennas), perfect specular reflection (no scattering), and equally received power for all satellites (same transmission power, propagation attenuation, and surface reflectivity).

Results presented in this chapter have been partially published in the journal paper "SNR degradation in GNSS-R measurements under the effects of Radio-Frequency Interference" [99]; and presented partially as conference papers "SNR degradation in conventional GNSS-R measurements under the effects of radio frequency interference" [140], and "Impact of Radio-Frequency Interference on Conventional GNSS-Reflectometry" [141].

7.2 General SNR model for GNSS-R

7.2.1 Signal model and detection

After the scattering process, GNSS-R signals are collected by the instrument antennas, conditioned by the front-end stage with bandwidth B_r, and finally delivered to the processing stage. The complex base-band signal at this stage can be expressed as the addition of three terms:

$$y_r(t) = s_r(t) + i_r(t) + n_r(t) = \sum_{l=0}^{L-1} s_{r_l}(t) + i_r(t) + n_r(t) \tag{7.2}$$

where the subscript r stands for "reflected" signals, L is the number of "in-view" GNSS signals, s_{r_l} corresponds to the lth signal, i_r is the aggregate of RFI signals, and n_r is band-limited thermal noise (see Fig. 7.1a).

GNSS signals are detected after the delay-Doppler correlator or "matched filter" that performs the spread-spectrum demodulation [139]. In cGNSS-R, the signal after the correlator for a particular kth tracked signal (e.g., GPS L1 C/A, Galileo E5, Beidou B2) is obtained as:

$$\chi_{y_r c_k}(\nu, \tau) = \frac{1}{T_c} \int_{T_c} y_r(t)\, c_k^*(t-\tau)\, e^{-j2\pi\nu t}\, dt, \tag{7.3}$$

where $y_r(t)$ is the received complex base-band signal defined in (7.2); $c_k \in \mathbb{C}$ is the clean replica of the kth navigation code, assumed known, deterministic and with normalized

power within the bandwidth B_r; ν and τ are the Doppler and delay variables respectively; and T_c is known as the coherent integration time.

As aforementioned, the detection process in GNSS-R must be non-coherent as in radar systems, so that the new observable after the detector becomes the expected power expressed as:

$$|\chi|^2_{y_r c_k}(\nu,\tau) = \mathrm{E}\left\{|\chi_{y_r c_k}(\nu,\tau)|^2\right\}. \tag{7.4}$$

The expected operator $\mathrm{E}\{\cdot\}$ is introduced since the signal y_r is a random process. Furthermore, it is often replaced by the average operator $\langle\cdot\rangle$ as an unbiased estimator of the expected value, and usually referred as incoherent averaging [134]. In this work, $|\chi|^2_{y_r c_k}$ is introduced as the Cross-WAF (CWAF) between y_r and c_k analogously to the definition of the (Auto-) WAF for random processes in radar theory [138]. Then, $|\chi|^2_{y_r c_k}$ turns to be equal to the measured DDM for the kth satellite signal using the cGNSS-R approach, and equivalent to the expected DDM $\langle|Y(\nu,\tau)|^2\rangle$ defined in [134]. In other words, the CWAF is the mathematical operation used to compute the measured DDM.

In iGNSS-R, the clean replica of the code c_k is replaced by the signal acquired directly from the "in-view" satellites defined as

$$y_d(t) = s_d(t) + i_d(t) + n_d(t) = \sum_{l=0}^{L-1} s_{d_l}(t) + i_d(t) + n_d(t), \tag{7.5}$$

where the subscript d stands for "direct" signals (see Fig. 7.1b), and it is analogous to (7.2). Therefore, the output of the correlator becomes $\chi_{y_r y_d}(\nu,\tau)$, and the DDM in iGNSS-R can be defined as $|\chi|^2_{y_r y_d}(\nu,\tau)$. Furthermore, signal y_d is treated as a unitless signal since it becomes the impulse response of the "matched" filter, and its power represents a non-dimensional scale factor in the iGNSS-R DDM.

7.2.2 DDM decomposition

In order to study the contribution of RFI signals to the measured DDM, the CWAF is decomposed into the terms corresponding to each signal in (7.2). Assuming that s_r, i_r, and n_r have zero mean and are statistically independent from each other, $|\chi|^2_{y_r c_k}(\nu,\tau)$ can be expressed, using the Sussman's Formula [142], as follows (see proof in Appendix E.1):

$$|\chi|^2_{y_r c_k}(\nu,\tau) = |\chi|^2_{s_{r,k} c_k}(\nu,\tau) + \sum_{\substack{l\geq 0 \\ l\neq k}}^{L-1} |\chi|^2_{s_{r,l} c_k} + |\chi|^2_{i_r c_k} + |\chi|^2_{n_r c_k}, \tag{7.6}$$

where the first term corresponds to the useful tracked signal DDM, the second one is the *cross-sat* term, the third one is the RFI term, and the last one is the thermal noise term. Figure 7.2 depicts an hypothetical example of DDM decomposition showing each one of the terms corresponding to a cGNSS-R DDM using GPS L1 C/A with $B_r = 2.046$ MHz.

The CWAF between the reflected signal of the kth tracked satellite, s_{r_k}, and its clean replica, c_{r_k}, $|\chi|^2_{s_{r,k} c_k}(\nu,\tau)$, is coined as tracked or useful signal DDM in this work. The tracked signal DDM contains all the information about the surface of interest, and hence,

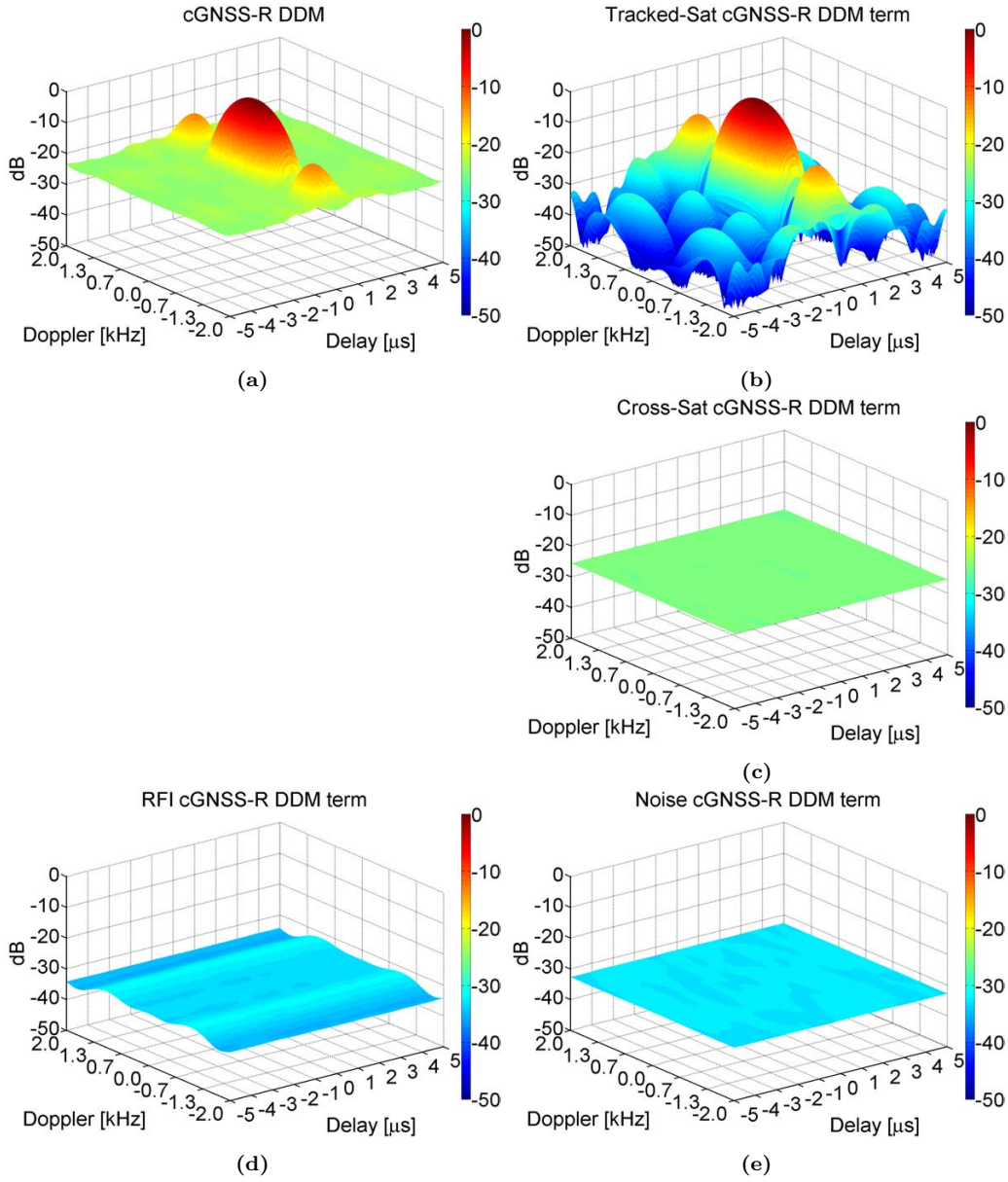

Figure 7.2: Sample decomposition of a cGNSS-R DDM. The following conditions have been assumed: GPS L1 C/A code, perfect specular reflection (no scattering), $B_r = 2.046$ MHz, $T_c = 1$ ms, and equal unitary received power for all signals. Each subplot corresponds to (a) the received DDM obtained from (7.6), (b) the tracked signal DDM, (c) the *cross-sat* term (for 10 "in-view" additional satellites: 5 GPS L1 + 5 Galileo E1), (d) the RFI term (jammer chirp RFI), and (e) the noise term. The blank space has been left for an easier comparison to sample decomposition of a iGNSS-R DDM.

the rest of the terms in (7.6) represent undesired contributions which degrade the SNR. Besides, in cGNSS-R, all of them are translated into a rise of a uniform power floor as it can be appreciated in Fig. 7.2. Among them, the *cross-sat* term include all intra- and inter-GNSS interference whereas the RFI term represents the additive contribution of external RFI signals to the received DDM. Both terms will be analyzed in detail in next sections. Eventually, assuming that the thermal noise after the front-end is a complex Gaussian stochastic process, with flat Power Spectral Density (PSD) within B_r, and equal to N_{0_r}, the noise term in cGNSS-R can be approximated as:

$$|\chi|^2_{n_r c_k} = \frac{N_{0_r}}{T_c} \int_{\nu - B_r/2}^{\nu + B_r/2} S_{c_k}(f)\, df \simeq \frac{N_{0_r}}{T_c}, \tag{7.7}$$

where $S_{c_k}(f)$ is the PSD function of c_k, and it has been considered that the range of the variations of ν is very small as compared to B_r.

On the other hand, the DDM in iGNSS-R can be obtained from $|\chi|^2_{y_r y_d}(\nu, \tau)$. Taking into account the same assumptions as in cGNSS-R, and that s_d, i_d, and n_d are statistically independent between them, the iGNSS-R DDM can be expressed as in (7.8) (see proof in Appendix E.2),

$$\begin{aligned} |\chi|^2_{y_r y_d}(\nu, \tau) = {} & |\chi|^2_{s_{r,k} s_{d,k}}(\nu, \tau) + |\chi|^2_{\textit{cross-talk}} + |\chi|^2_{\textit{cross-sat}} + |\chi|^2_{\text{RFI}}(\nu, \tau) \\ & + \left(|\chi|^2_{n_r s_{d,k}} + |\chi|^2_{s_{r,k} n_d} + |\chi|^2_{n_r n_d} \right), \end{aligned} \tag{7.8}$$

where each term represents from left to right: the useful tracked signal DDM as in (7.6) but for a GNSS composite signal, the *cross-talk* term, the *cross-sat* term, the RFI term, and the last three ones are the interferometric thermal noise terms (i.e. $|\chi|^2_{\text{noise}}$). Besides, in iGNSS-R, the subscript k is used to indicate all those codes that belong to a GNSS composite signal received from a particular satellite (e.g.; GPS L2 composed by C, P(Y), and M codes; Galileo E6 composed by CS, and PRS codes; Beidou B3 with a single code), whereas, in cGNSS-R, the subscript k refers to the particular clean code replica used in the delay-Doppler correlator (e.g GPS L1 C/A).

An example showing each one of the terms corresponding to an iGNSS-R DDM, using GPS composite L1 signal with $B_r = 30.69$ MHz, is depicted in Fig. 7.3. Note that the comparison between Figs. 7.2 and 7.3 is not direct since the assumed front-end bandwidth B_r differs in each case.

In (7.8), the *cross-talk* term appears as an exclusive effect of the iGNSS-R technique. *Cross-talk* is composed by the DDMs corresponding to the "in-view" non-tracked satellite signals, and it can have an overwhelming effect on the SNR (much higher than *cross-sat*) if it overlaps the tracked signal DDM. The overlapping between DDMs depends on the relative position and velocity between the satellites and the receiver, on the WAF of the involved signals, and on the surface of reflection. A detailed study of *cross-talk* effect is beyond the scope of this PhD thesis (see [143]).

Moreover, interferometric *cross-sat* and RFI terms are equivalent to the ones in the cGNSS-R case. Eventually, interferometric noise terms can be approximated as follows:

$$|\chi|^2_{\text{noise}} \simeq \frac{N_{0_r}}{T_c} P_{s_{d,k}} + P_{s_{r,k}} \frac{N_{0_d}}{T_c} + N_{0_r} N_{0_d} \frac{B_r}{T_c}, \tag{7.9}$$

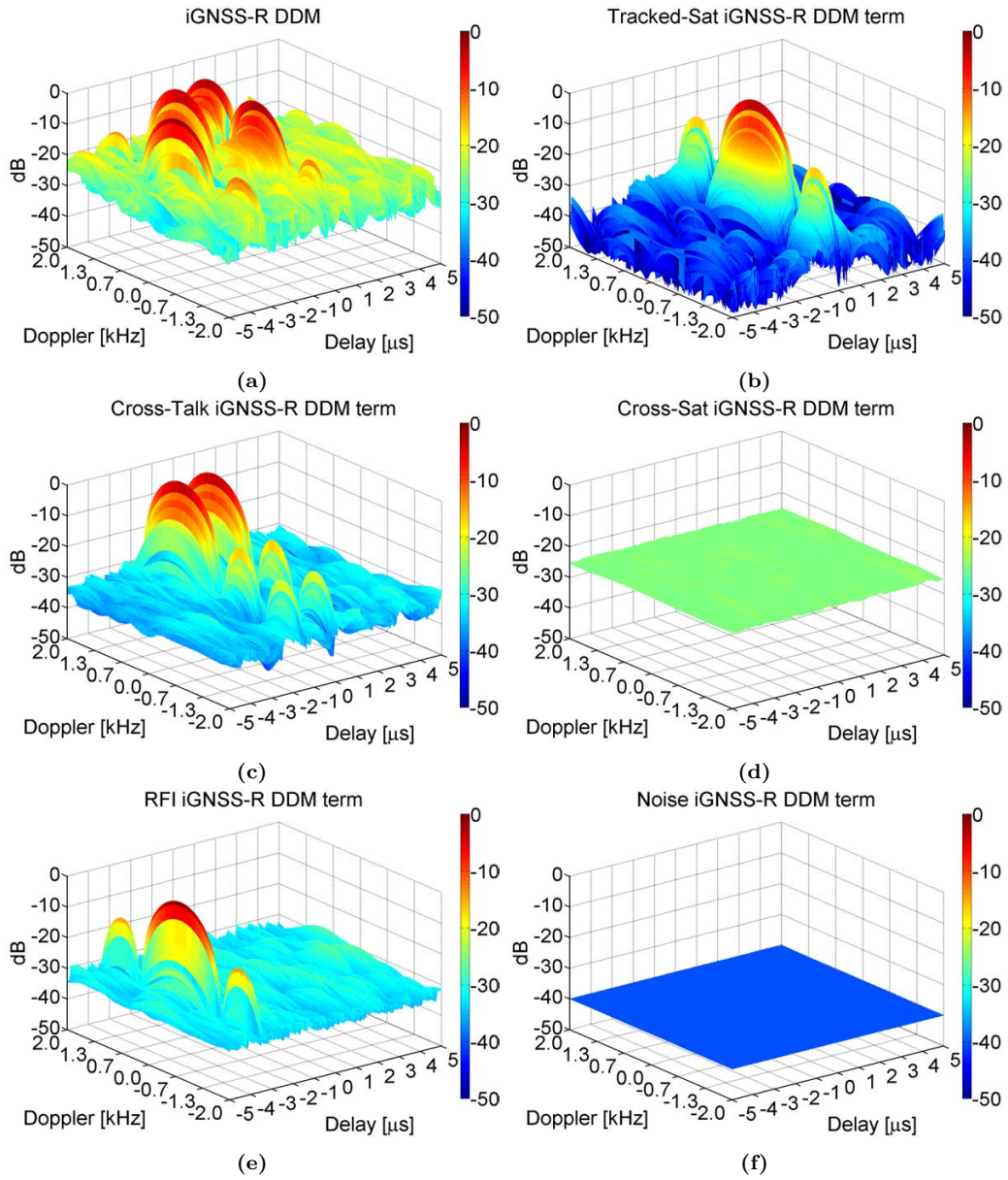

Figure 7.3: Sample decomposition of a iGNSS-R DDM. The following conditions have been assumed: GPS composite L1 (C/A, C, P(Y) and M codes), perfect specular reflection (no scattering), $B_r = 30.69$ MHz, $T_c = 1$ ms, and equal unitary received power for all signals. Each subplot corresponds to (a) the received DDM, obtained from (7.8), (b) the tracked signal DDM, (c) the *cross-talk* term (for 10 "in-view" additional satellites: 5 GPS L1 + 5 Galileo E1), (d) the *cross-sat* term, (e) the RFI term (jammer chirp RFI), and (f) the noise terms.

where T_c is the coherent integration time, N_{0_r} and N_{0_d} are the PSD of thermal noise after the respective front-end after down-looking and up-looking antennas with equal bandwidth B_r, and considering the same approximation applied in (7.7). This expression of the interferometric noise matches with the one developed in [144].

7.2.3 SNR definition and degradation

The SNR is the figure of merit that has been chosen to evaluate the impact of RFI on GNSS-R measurements, and it is typically defined at the maximum of the tracked signal DDM. In this paper, in order to maintain the whole information of the DDM, a point-to-point relation will be considered, similarly to the one used in [144]. Therefore, a general SNR definition for GNSS-R measurements considering the kth tracked satellite signal can be written as:

$$\rho_k(\nu,\tau) = \frac{|\chi|^2_{k\text{th-sat}}(\nu,\tau)}{|\chi|^2_{cross\text{-}talk}(\nu,\tau) + |\chi|^2_{cross\text{-}sat} + |\chi|^2_{\text{RFI}}(\nu,\tau) + |\chi|^2_{\text{noise}}}, \tag{7.10}$$

with every undesired term in the denominator defined according to the involved technique, and evaluated in the corresponding delay-Doppler point (ν,τ). Two examples of $\rho_k(\nu,\tau)$ are shown in Fig. 7.4 taking the values obtained from each one of the simulations performed in Fig. 7.2 and Fig. 7.3 for cGNSS-R and iGNSS-R respectively.

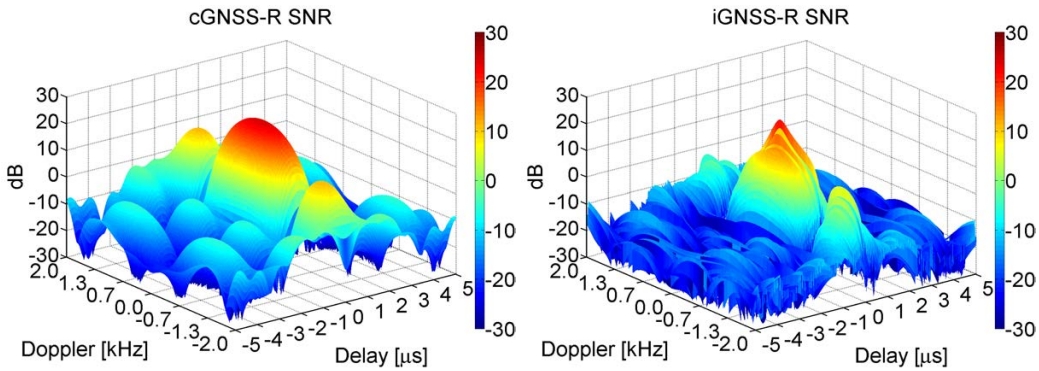

Figure 7.4: Point-to-point SNR in the delay-Doppler plane obtained from (7.10). Each subplot corresponds to: (a) cGNSS-R technique taking the terms depicted in Fig. 7.2, and (b) iGNSS-R technique according to the terms in Fig. 7.3.

Finally, the SNR degradation as a function of the undesired terms is defined with respect to the thermal SNR (i.e. $\rho_{k_{\text{thermal}}}$). The latter is the quotient between the useful signal and the corresponding thermal noise. Then, the SNR can also be expressed in the following way:

$$\rho_k(\nu,\tau) = \rho_{k_{\text{thermal}}}(\nu,\tau)\,\Delta_k(\nu,\tau), \tag{7.11}$$

where Δ_k represents SNR degradation corresponding to the combined effect of *cross-talk*, *cross-sat* and RFI terms. Furthermore, SNR degradation introduced by *cross-sat* and RFI terms are further studied in subsequent sections.

7.3 Cross-sat SNR degradation

The *cross-sat* effect appears when one or more GNSS signals, apart from the one that is used to perform the GNSS-R measurements, are captured by the instrument antennas, and they are not completely rejected by the front-end. Therefore, it represents the contribution of all the cross-correlations between these satellite signals that share the same band of operation, or at least their PSD functions are partially overlapped. Moreover, *cross-sat* determines the level of intra- and inter-GNSS interference that is fixed by design, and it is evaluated with the SSC parameter, first defined in [127]. The SSC between two signals x and y is defined as:

$$\kappa_{xy}(\nu) = \int_{B_r} \overline{S_x}(f)\,\overline{S_y}(f-\nu)\,df = \overline{S_x}(\nu) * \overline{S_y}(\nu), \tag{7.12}$$

where B_r is the bandwidth of the receiver, and $\overline{S_x}$ and $\overline{S_y}$ are the normalized PSD of x and y respectively. The SSC is measured in dB/Hz, and it reveals the rejection or attenuation per unit of bandwidth, suffered by other GNSS signals rather than the one under correlation.

As stated previously, GNSS codes have been designed for navigation purposes, and, considering that GNSS-R takes an advantage of the properties of these signals in an opportunistic way, it seems reasonable to study how much this overlapping affects to GNSS-R measurements, and, in particular, to the SNR. Furthermore, the *cross-talk* effect also takes place under the same conditions for the iGNSS-R technique, and its impact on the SNR may be even worse. Thus, the following evaluation will be considered valid if *cross-talk* effect is not present.

7.3.1 SSC values

The magnitude of the *cross-sat* degradation depends on the addition of the residual power of the undesired GNSS signals at the output of the front-end, $P_{s_{r,l}}$, weighted by the SSC between each the received code and the tracked one. According to the definition, the SSC depends on the Doppler of the receiver. Figure 7.5 shows self-SSC values (i.e. SSC between same services, but from different satellites) of GPS L1 C/A, GPS L5, Galileo E1 OS, and Galileo E5, as a function of the Doppler shift between satellites. This figure has been obtained by using (7.12).

However, the Doppler dependence can be neglected since the Doppler variations, on the order of tenths of kHz at most, are much smaller as compared to B_r. Then, SSC is taken as worst case with ν equal to 0. This is similar to the approximation applied to the noise term. SSC values (worst case) between all combinations of main GNSS codes are shown in Table 7.1 for upper L-band (1559-1610 MHz), and lower L-band (1164-1300 MHz). These values have been obtained using (7.12), and taking B_r equal to the main lobe bandwidth as in [145].

Since *cross-sat* degradation is highly dependent on the scenario: number, type, position, velocity, and emitted power of satellites; signal attenuation and scattering at the reflection surface; and antennas and front-end of the receiver; an assessment of the SNR degradation induced by the *cross-sat* phenomenon must be performed in each particular case. For the

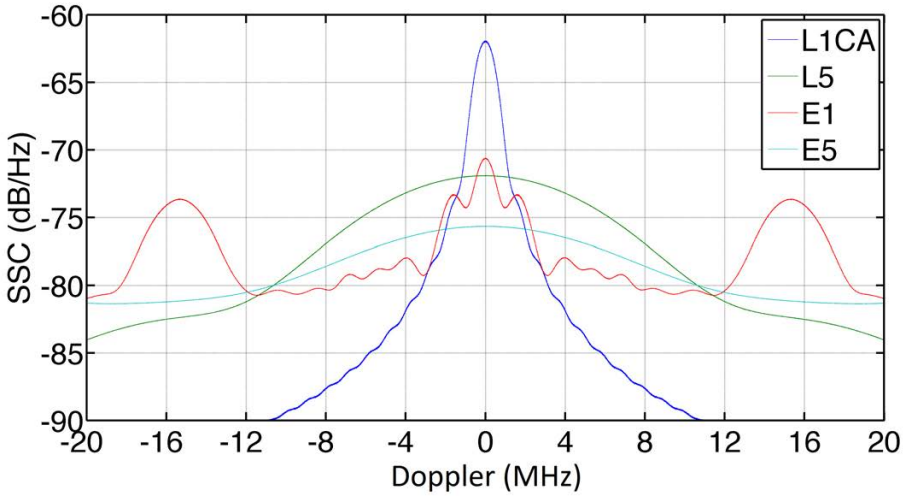

Figure 7.5: SSC value between same GNSS services (GPS L1 C/A, GPS L5, Galileo E1 OS, and Galileo E5) from different satellites as a function of the Doppler shift between them.

sake of simplicity, a general case is discussed for cGNSS-R and iGNSS-R in the following subsections.

Table 7.1: Worst case SSC values between main codes at upper (1559-1610 MHz) and lower L-band (1164-1300 MHz) GNSS bands obtained from (7.12) in dB/Hz. SSC values depend on receiver bandwidth B_r, spectrum of tracked GNSS signal used in cross-correlation, spectrum of cross-sat signals, and bandwidth where they are transmitted in B_t. Infinite negative values indicate no overlapping between GNSS signal spectra. In addition, the last row shows additional information about minimum received power for each service.

SSC [dB/Hz]		*Crossed*	**GPS**				**Galileo**		**Beidou**
Upper Band		B_t[MHz]	30.69				25.552	40.92	16.00
Tracked	B_r[MHz]	⟍	**L1CA**	**L1C**	**L1P**	**L1M**	**E1OS**	**E1PRS**	**B1**
GPS	2.046	**L1CA**	-61.81	-68.28	-70.21	-92.41	-68.26	-124.50	-∞
	14.322	**L1C**	-68.16	-65.46	-70.44	-82.94	-65.44	-103.74	-106.37
	20.46	**L1P**	-69.90	-70.43	-71.25	-79.97	-70.41	-101.47	-101.48
	30.69	**L1M**	-87.06	-81.86	-79.79	-71.55	-81.86	-86.72	-82.10
Galileo	14.322	**E1OS**	-68.13	-65.44	-70.42	-82.93	-65.42	-103.73	-106.36
	35.805	**E1PRS**	-99.08	-94.24	-86.44	-86.72	-101.15	-68.45	-69.98
Beidou	4.092	**B1**	-99.47	-95.63	-86.94	-87.49	-120.39	-73.02	-70.68
Minimum Received Power [dBW]			-161.5	-160.0	-164.5	-160.0	-157.0	-157.0	-157.0

SSC [dB/Hz]		*Crossed*	**GPS**				**Galileo**			**Beidou**			**GLONASS**
Lower Band		B_t[MHz]	30.69			24.00	51.15	40.92		36.00			20.46
Tracked	B_r[MHz]	⟍	**L2C**	**L2P**	**L2M**	**L5**	**E5**	**E6CS**	**E6PRS**	**B2OS**	**B2AS**	**B3**	**L3OC**
GPS	2.046	**L2C**	-61.81	-70.21	-92.41	-∞	-∞	-∞	-∞	-∞	-∞	-∞	-∞
	20.46	**L2P**	-69.90	-71.25	-79.97	-∞	-∞	-∞	-∞	-99.58	-90.79	-∞	-∞
	30.69	**L2M**	-87.06	-79.79	-71.55	-∞	-95.73	-∞	-∞	-93.40	-89.57	-∞	-∞
	20.46	**L5**	-∞	-∞	-∞	-71.00	-74.17	-∞	-∞	-∞	-∞	-∞	-∞
Galileo	51.15	**E5**	-110.38	-98.14	-95.73	-74.17	-74.30	-∞	-∞	-73.12	-74.35	-∞	-76.18
	10.23	**E6CS**	-∞	-∞	-∞	-∞	-∞	-68.63	-96.56	-∞	-∞	-85.82	-∞
	30.69	**E6PRS**	-∞	-∞	-∞	-∞	-∞	-85.88	-71.34	-∞	-∞	-73.48	-∞
Beidou	4.092	**B2OS**	-∞	-∞	-∞	-∞	-73.33	-∞	-∞	-64.78	-70.32	-∞	-73.93
	20.46	**B2AS**	-107.43	-95.18	-92.84	-∞	-74.36	-∞	-∞	-70.11	-71.40	-∞	-73.36
	20.46	**B3**	-∞	-∞	-∞	-∞	-∞	-83.39	-73.45	-∞	-∞	-71.40	-∞
GLONASS	20.46	**L3OC**	-∞	-∞	-∞	-∞	-76.18	-∞	-∞	-73.53	-73.35	-∞	-70.98
Minimum Received Power [dBW]			-161.5	-164.5	-160.0	-157.0	-152.0	-155.0	-155.0	-163.0	-163.0	-160.0	-

7.3.2 Cross-sat in cGNSS-R

The *cross-sat* term in cGNSS-R can be expressed as (see proof in Appendix E.3):

$$\sum_{\substack{l\geq 0\\ l\neq k}}^{L-1} |\chi|^2_{s_{r,l}c_k} \simeq \frac{1}{T_c} \sum_{\substack{l\geq 0\\ l\neq k}}^{L-1} P_{s_{r,l}}\, \kappa_{s_{r,l}c_k}, \tag{7.13}$$

and the SNR degradation when only this term is present as:

$$\Delta_{k_{cross\text{-}sat}} \simeq \left(1 + \frac{\sum_{l\neq k}^{L-1} P_{s_{r,l}}\, \kappa_{s_{r,l}c_k}}{N_{0_r}}\right)^{-1}. \tag{7.14}$$

An example of SNR degradation induced by *cross-sat* effect in cGNSS-R is depicted in Fig. 7.6. GNSS satellites from the same constellation have antenna patterns shaped to produce nearly constant power density at surface level regardless of satellite elevation. Transmitted power is also monitored and kept constant with a limited margin. However, small differences are expected due to aging. For the sake of simplicity, equal received power after the front-end for all interfering satellites has been assumed, as well as the different transmitted power for different codes. Nevertheless, the received power from each satellite is not known a priori, but a minimum received power for each service is guaranteed (see Table 7.1). Given this, the assumption of equal received power (and isotropic antennas) allows calculating approximate values of the impact of cross-sat signals on the SNR. Further results on the cross-sat effect in GNSS-R must include the particular geometry and the antenna pattern case by case.

According to results depicted in Fig. 7.6, $\Delta_{k_{cross\text{-}sat}}$ may represent a degradation of several dB in case a non-directive antenna is used. However, highly directive antennas can reduce the cross-sat effect to smaller values, although the effect produced by non-used codes from the tracked satellite will still remain.

7.3.3 Cross-sat in iGNSS-R

The *cross-sat* term in iGNSS-R can be expressed as:

$$|\chi|^2_{cross\text{-}sat} \simeq \sum_{\substack{l\geq 0\\ l\neq k}}^{L-1} \left(\frac{1}{T_c} P_{s_{r,l}} \sum_{k=0}^{L-1} P_{s_{d,k}}\, \kappa_{s_{r,l}s_{d,k}} + \frac{N_{0_r}}{T_c}\, P_{s_{d,l}} + P_{s_{r,l}}\, \frac{N_{0_d}}{T_c}\right), \tag{7.15}$$

according to Appendices E.2 and E.3. In this case, the corresponding cross-correlations between n_r and s_{d_l}, and between s_{r_l} and n_d, must be considered in addition to the combination between all non-tracked codes. The degradation $\Delta_{k_{cross\text{-}sat}}$ is defined in a similar way as in the previous case. Besides, SSC values in Table 7.1 must be recalculated using B_r equal to the composite signal bandwidth in each case.

Figure 7.7 illustrates the same example of Fig. 7.6, but considering the iGNSS-R technique. SNR degradation levels in iGNSS-R are similar to the ones seen in cGNSS-R except in GPS composite L1 which are substantially worse as compared to L1 C/A. This

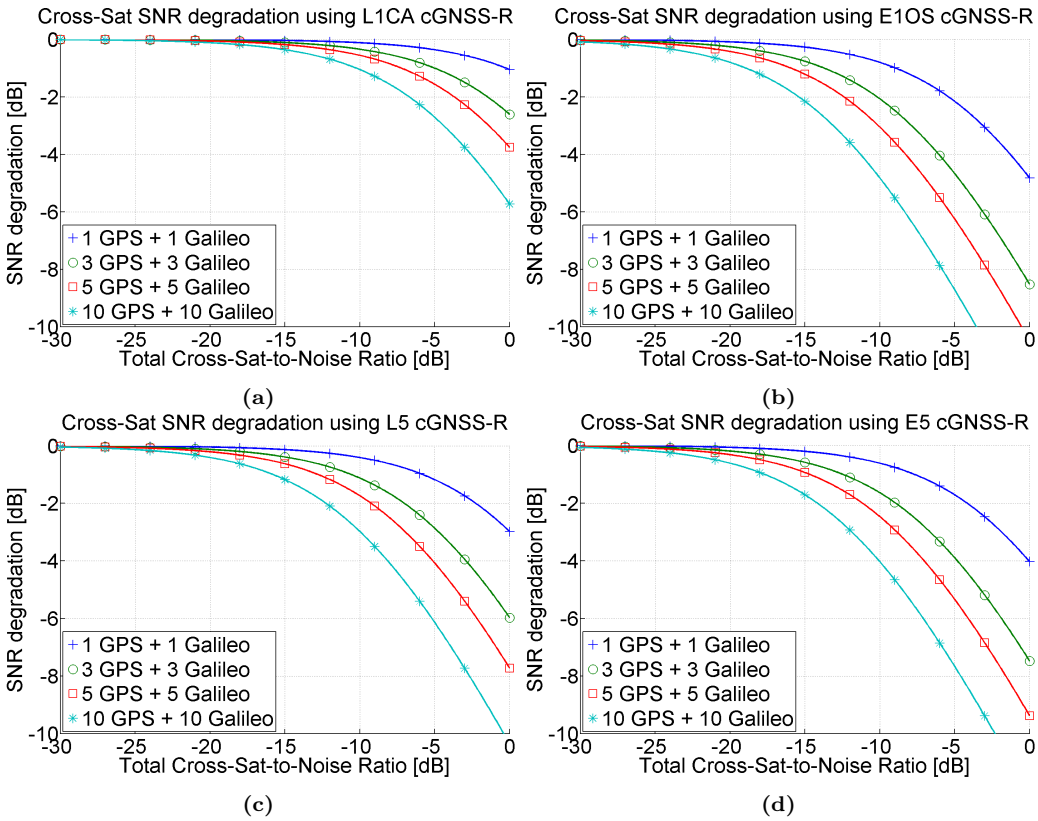

Figure 7.6: Sample SNR degradation induced by *cross-sat* effect in cGNSS-R, and obtained from (7.13) and (7.14). The following assumptions are considered: equal received power after the front-end for all satellites, isotropic antennas, and SSC values and minimum received power stated in Table 7.1. Each subplot corresponds to cGNSS-R using (a) GPS L1 C/A, (b) Galileo E1 OS, (c) GPS L5, and (d) Galileo E5. The total Cross-Sat-to-Noise ratio refers to the sum of power received from all interfering GPS and Galileo satellites, divided by the thermal noise power with N_{0_r} = -204 dBW/Hz.

is mainly given by the difference in receiver bandwidth B_r used in each case. In cGNSS-R using GPS L1 C/A, B_r = 2.046 MHz, whereas B_r = 30.69 MHz in iGNSS-R with GPS L1 band. Larger bandwidth implies more *cross-sat* received power. In addition, when comparing the iGNSS-R *cross-sat* degradation in the L1/E1 band with the L5/E5 band, the L1/E1 band is worse, because it is more "crowded" than the L5/E5 band. iGNSS-R L1 has slightly better performance than E1 because receiver bandwidth is also slightly smaller (30.69 MHz vs 35.805 MHz). The same happens when comparing L5 and E5 (20.46 MHz vs 51.315 MHz).

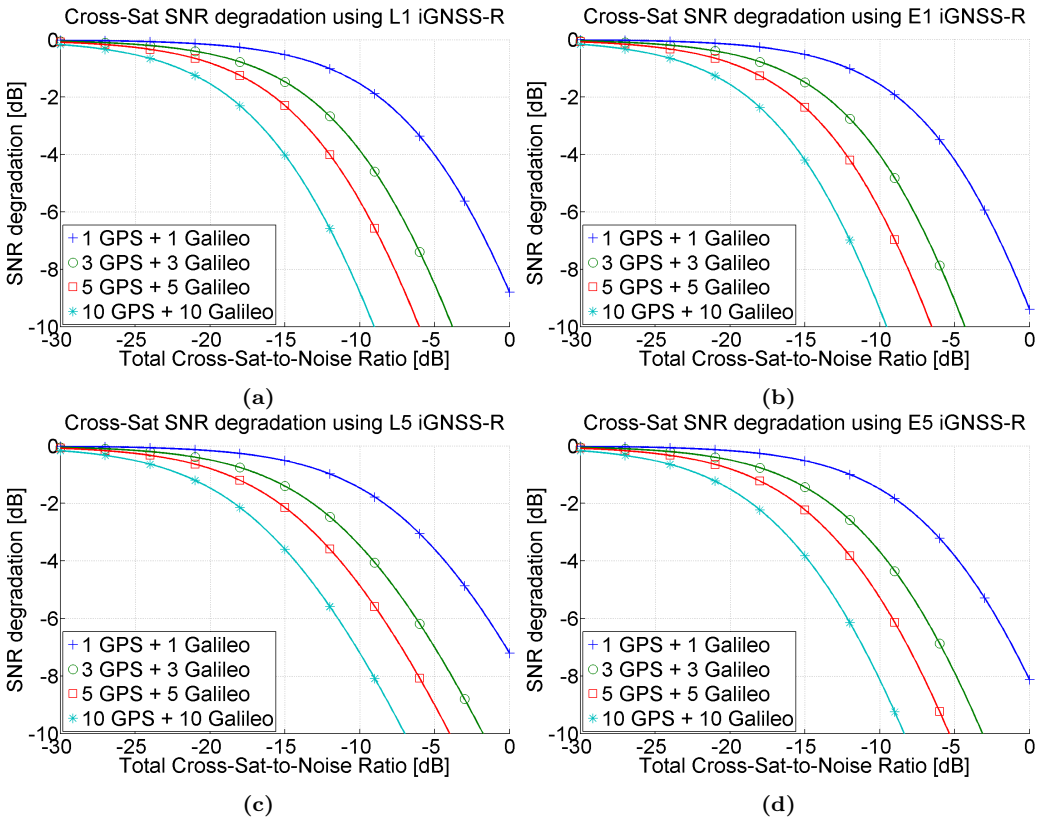

Figure 7.7: Sample SNR degradation induced by *cross-sat* effect in iGNSS-R, and obtained from (7.15) and (7.14). The following assumptions are considered: equal received power after the front-end for all satellites, isotropic antennas, and SSC values and minimum received power stated in Table 7.1. Each subplot corresponds to iGNSS-R using (a) GPS composite L1 (C/A, C, P(Y), and M codes), (b) Galileo composite E1 (OS and PRS codes), (c) GPS L5, and (d) Galileo E5. The total Cross-Sat-to-Noise ratio refers to the sum of power received from all interfering GPS and Galileo satellites, divided by the interferometric noise power with $N_{0_r} = N_{0_d}$ = -204 dBW/Hz.

7.4 RFI SNR degradation

RFI signals, besides interfering with GNSS codes, can degrade or totally disrupt the performance of GNSS-R devices. The degradation of the SNR produced by RFI signals have also been studied in GNSS using the SSC, and the level of interference is highly dependent on the kind of RFI present. However, the approach followed in the state-of-the-art is only limited to stationary RFI signals.

7.4.1 Generalized SSC

In order to evaluate the impact of any RFI (stationary or non-stationary) in GNSS-R DDMs, an extension of the SSC concept named GSSC is introduced in this work. The

GSSC between two signals x and y after the front-end is defined as:

$$\gamma_{xy}(\nu,\tau) = \frac{1}{T_c}\int_{B_r}\int_{T_c} \overline{W_x}(t,f)\,\overline{W_y}(t-\tau, f-\nu)\,dt\,df, \tag{7.16}$$

where $\overline{W_x}$ and $\overline{W_y}$ are the normalized Wigner-Ville Spectrum (WVS) [146], or non-stationary spectrum, of x and y respectively. The WVS is used instead of the PSD defined only for stationary random processes, and its use accounts for the non-stationary nature of RFI, whose spectrum may change over the time.

7.4.2 RFI in cGNSS-R

In cGNSS-R, the RFI term can be expressed using the GSSC as follows (see proof in Appendix E.3):

$$|\chi|^2_{i_r c_k} \simeq \frac{1}{T_c} P_{i_r}\,\gamma_{i_r c_k}, \tag{7.17}$$

where P_{i_r} is the RFI power at the reflected antenna, T_c is the coherent integration time, and $\gamma_{i_r c_k}$ is the GSSC, obtained from (7.16), between the RFI at the reflected antenna i_r and the clean code replica c_k. $\gamma_{i_r c_k}$ has been approximated as a constant taking into account the same assumptions as for the SSC case. Moreover, the SNR degradation when this is the dominant term is:

$$\Delta_{k_{RFI}} \simeq \left(1 + \frac{P_{i_r}\,\gamma_{i_r c_k}}{N_{0_r}}\right)^{-1}. \tag{7.18}$$

In order to validate this model, a commercial jammer that emits a 15 MHz frequency modulated chirp signal centered at L1 band has been used. The live signals in space captured by the GNSS antenna are combined with the RFI signal from the commercial jammer. Then, the aggregated signal is distributed to three commercial GPS receivers. The power of the jamming signal is controlled by using a variable attenuation. By using a power meter, a level of -120 dBm of background thermal noise has been measured. Then, the jamming power is expressed as INR in order to compare and validate the model proposed in (7.18). Figure 7.8 shows a comparison between the theoretical SNR degradation obtained using (7.18), and the one measured at the laboratory using the jammer with the three commercial GPS L1 C/A receivers.

Theoretical SNR degradation predicted by the model shows that from 25 dB of Interference-to-Noise Ratio (INR) on, SNR degradation changes -10 dB per decade. Comparing this with the curves obtained from the three GPS receivers, they show a trend similar to the theoretical degradation, but their results are between 5 and 15 dB better, mainly because they already incorporate some mitigation techniques. This result is twice valuable. On one hand, the theoretical model is validated with real measurements obtained from commercial systems. On the other hand, it demonstrates that mitigation techniques are the solution to reduce the impact of external RFI signals in GNSS-R measurements. Note that every GNSS receiver has its own behavior under jamming conditions and that it depends on its own internal architecture. This fact also triggers the use of more than one GNSS receivers when assessing the performance of RFI mitigation techniques.

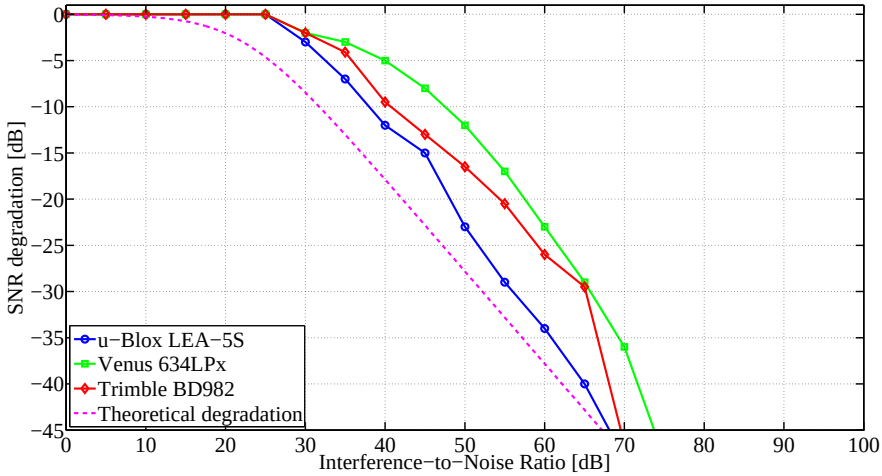

Figure 7.8: Sample SNR degradation induced by RFI effect in cGNSS-R. The used RFI signal is a 15 MHz sweep chirp jammer cross-correlated with GPS L1 C/A code. Theoretical results are compared to real measurements obtained from several commercial GPS receivers.

7.4.3 RFI in iGNSS-R

In iGNSS-R, the RFI term can be expressed as follows (see Appendices E.2 and E.3):

$$|\chi|^2_{RFI}(\nu,\tau) \simeq \frac{1}{T_c}\left(\sum_{l=0}^{L-1} P_{s_{r,l}} P_{i_d}\, \gamma_{s_{r,l} i_d} + \sum_{l=0}^{L-1} P_{i_r} P_{s_{d,l}}\, \gamma_{i_r s_{d,l}} + P_{i_r} P_{i_d}\, \gamma_{i_r i_d}(\nu,\tau) + P_{i_r} \frac{N_{0_d}}{T_c}\, \gamma_{i_r n_d} + \frac{N_{0_r}}{T_c} P_{i_d}\, \gamma_{n_r i_d}\right), \tag{7.19}$$

and the SNR degradation can be defined in an analogous way to the cGNSS-R case. In iGNSS-R, four sub-terms contribute constantly to the SNR degradation whereas there is only one that depends on ν and τ. $\gamma_{i_r i_d}(\nu,\tau)$ corresponds to the cross-correlation between RFI signals captured by both direct and reflected antennas, and it can reach magnitudes much higher than the useful signal, even if high directive antennas are used.

In order to illustrate the effects of RFI signals in iGNSS-R, GSSC values in (7.19) are depicted in Fig. 7.9 for the case of a DME RFI signal interfering GPS L5 and Galileo E5 iGNSS-R measurements. It can be appreciated that the GSSC terms $\gamma_{s_{r,l} i_d}$, $\gamma_{i_r s_{d,l}}$, $\gamma_{i_r n_d}$, and $\gamma_{n_r i_d}$ are of the order of the SSC values obtained in Section 7.3 for *cross-sat* terms, but they may depend on the DME frequency channel. However, if the received RFI power represented by P_{i_d} and P_{i_r} is much higher than the received noise and satellite signal power, the effect of RFI SNR degradation will be worse than in the *cross-sat* case. Moreover, the GSSC corresponding to a cross-correlation between direct and reflected DME signals, $\gamma_{i_r i_d}$, is concentrated in few delay lags rather than spread over the whole delay-Doppler space. This fact implies that the SNR degradation around this peak will

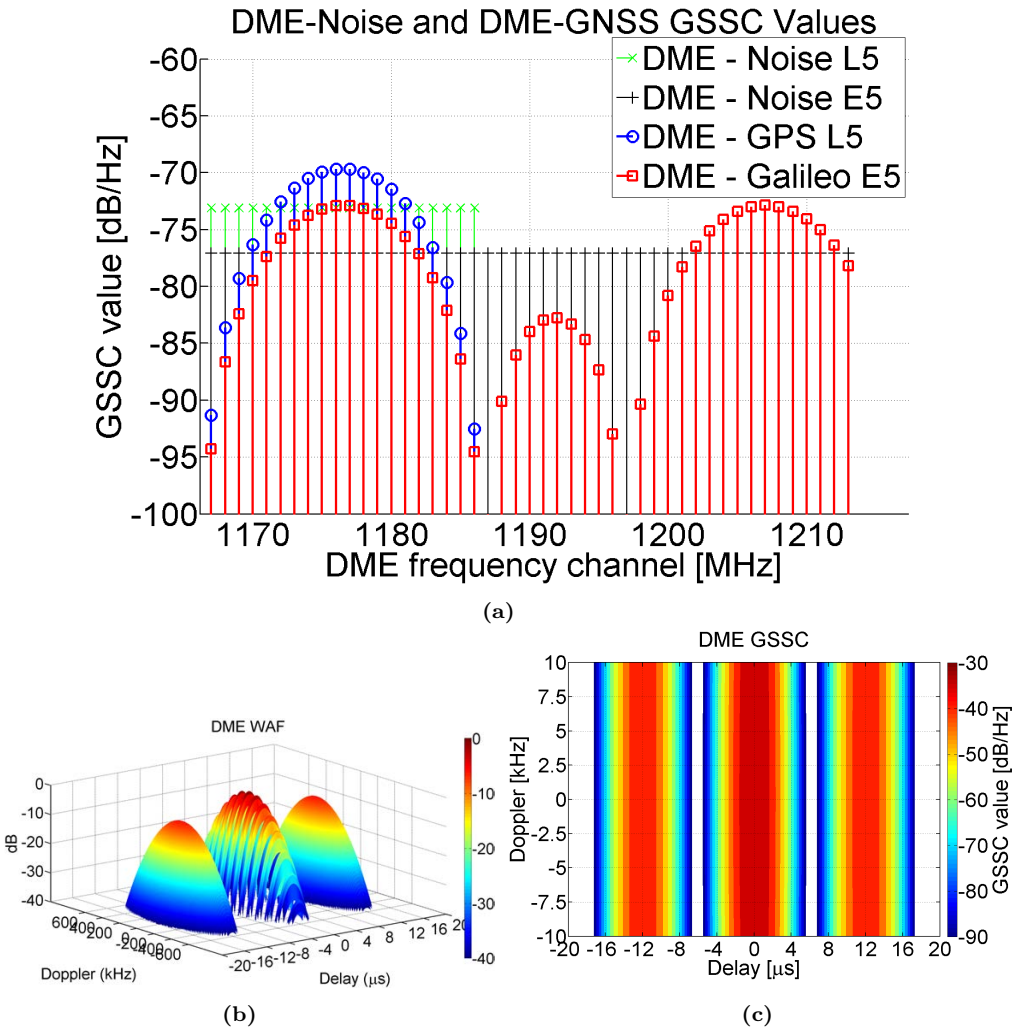

Figure 7.9: Sample GSSC values obtained using (7.16). This example considers an iGNSS-R instrument interfered with a DME RFI signal. DME spectrum is overlapped with GPS L5 and Galileo E5 spectra. Each subplot corresponds to (a) the GSSC values for crossed combinations DME to Noise, and DME to GNSS signals; and (b) normalized WAF and (c) GSSC values for DME signals present at both direct and reflected antennas.

be much higher than other terms. Further information on the impact of DME signals on iGNSS-R measurements can be found in [29].

As stated above, the GSSC between direct and reflected signals in iGNSS-R may increase the SNR degradation considerably. For the sake of completeness, the GSSC values corresponding to four typical RFI signal shapes [107] are shown in Fig. 7.10. The chosen RFI signals are a sinusoidal or CW signal, a narrow-band chirp with $B_{chirp} = 15$ MHz and 10.24 μs repetition period, a wide-band chirp with $B_{chirp} = 60$ MHz and 81.92 μs

repetition period, and a Pseudo-Random Noise (PRN) signal with 25 MHz of bandwidth. Results are shown for GPS L1 iGNSS-R with $B_r = 30.69$ MHz.

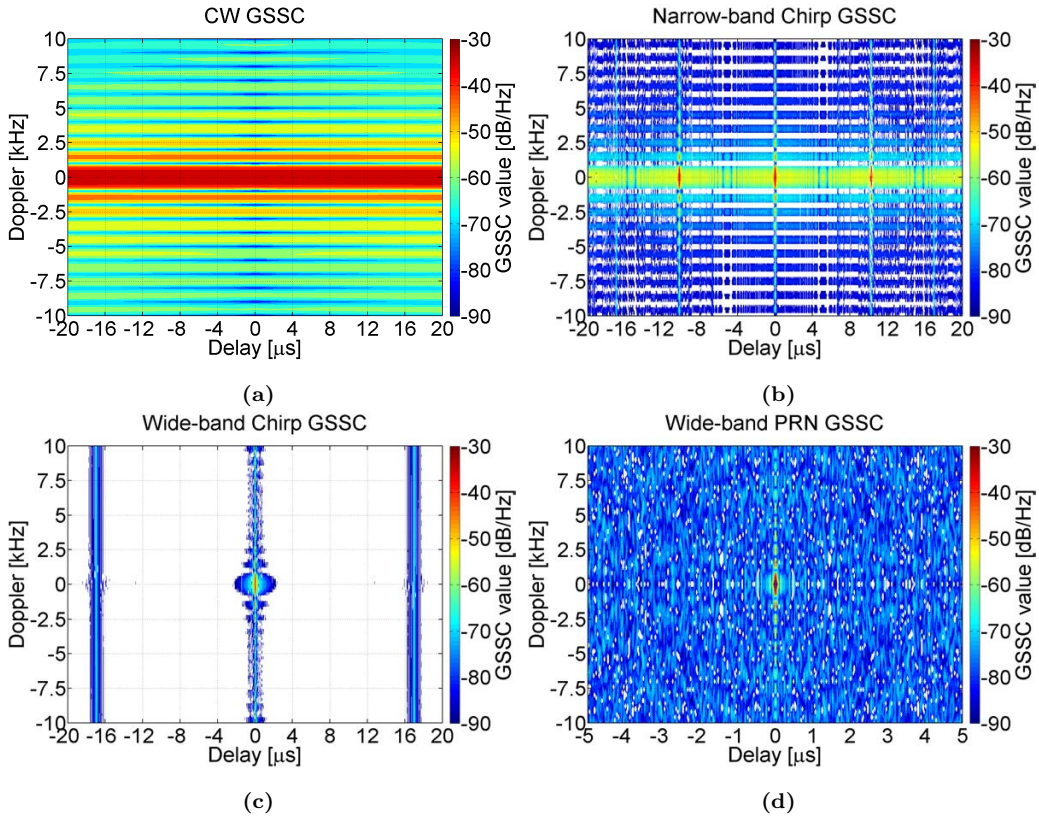

Figure 7.10: Sample GSSC values obtained using (7.16) considering GPS L1 iGNSS-R with $B_r = 30.69$ MHz under different RFI signals. Each subplot corresponds to: (a) a CW signal, (b) a narrow-band chirp with $B_{chirp} = 15$ MHz and 10.24 μs repetition period, (c) a wide-band chirp with $B_{chirp} = 60$ MHz and 81.92 μs repetition period, and (d) a Pseudo-Random Noise (PRN) signal with 25 MHz of bandwidth. Results are shown for GPS L1 iGNSS-R with $B_r = 30.69$ MHz. This analysis has been made considering jammers with high PRF and large bandwidth, which are representative of what one would observe in the field.

Figure 7.10 depicts how RFI signals whose power is more concentrated in frequency, such as CW and narrow-band chirp, are more spread in the delay domain after the correlation process. On the contrary, wide-band chirp and PRN RFI signals are more concentrated in the delay domain. This behavior is explained by the fact that delay and frequency are complementary domains [104]. Moreover, the behavior in the Doppler domain depends on the RFI signal shape itself.

CW, and in general narrow-band signals, are in principle more troublesome for GNSS-R measurements since they are more spread in the delay-Doppler space. Conversely, wide-band signals will only degrade the SNR at particular delay bins, but they can be fatal if the tracked signal DDM information is also in these bins. Therefore, the probability of SNR

degradation will be higher for narrow-band signals than for wide-band signals. However, mitigation techniques are more effective for narrow-band than for than wide-band signals.

7.5 Conclusions

In this chapter, a model to evaluate the degradation of the SNR in GNSS-R measurements has been proposed for both cGNSS-R and iGNSS-R techniques, and it has been evaluated in a general case for each technique.

Regarding cGNSS-R, the degradation of the thermal SNR can be produced by either *cross-sat* effect, or external RFI effect, or both. Moreover, they have a constant degradation over the delay-Doppler space. The *cross-sat* effect may represent the degradation of more than 10 dB considering several satellites with all existing and forthcoming GNSS signals. Nevertheless, the *cross-sat* effect can be minimized when using highly directive antennas. In particular, antenna arrays with beam-steering capabilities able to track a particular satellite, while they attenuate signals from the rest of them. On the other hand, the external RFI effect may represent a corruption of the measurements, since it is known that they can disrupt the performance of GNSS receivers. In this case, mitigation techniques must be used in order to reduce the error produced by the RFI effect [107].

The iGNSS-R technique has proven to be much more sensitive to RFI than cGNSS-R. Moreover, in this case, a new phenomenon is introduced: the *cross-talk* effect that may represent a total corruption of the measurements. *Cross-talk* together with *cross-sat* effect may also be attenuated with directive antennas. Finally, external RFI effect can have a catastrophic effect in the measurements, even worse than in cGNSS-R, and particularly when the interference is captured by both antennas: reflected and direct. In this case, the use of highly directive antennas can help to attenuate the signals captured by them. However, the RFI effect will still remain because of the multiple residual cross-correlations between RFI signals and thermal noise captured by both antennas. Therefore, mitigation techniques will be essential to improve the performance of iGNSS-R instruments under RFI conditions.

A specific mention must be given to GLONASS. Future GLONASS services will use spread-spectrum signals similar to GPS and Galileo. This will increase the number of satellites in view, thus making worse *cross-sat* and *cross-talk* effects. Regarding former GLONASS services, they combine spread-spectrum signals with a single code with Frequency Division Multiple Access (FDMA). Due to the use of different frequencies for different satellites, *cross-talk* and *cross-sat* effects will disappear in both cGNSS-R and iGNSS-R techniques, even if non-directive antennas are used. Nevertheless, external RFI signals are still troublesome. With the conventional approach, if the RFI power is well concentrated in frequency (for instance a CW RFI signal), the SNR degradation could be much higher for some GLONASS satellites (those where the RFI signal overlaps their respective spectra), as compared to GPS or Galileo satellites. The opposite would occur if the RFI signal is wide-band. Moreover, in the interferometric approach, the SNR degradation would be of similar order since the cross-correlated term between direct and reflected signal does not depend on the used GNSS.

8

Chapter 8

FENIX: an RFI mitigation system for GNSS/GNSS-R

This chapter contains the introduction and description of the FENIX, an RFI mitigation and anti-jamming system conceived, designed and built to protect GNSS and GNSS-R systems. However, FENIX can also be used in MWR applications using the theory already described Chapter 5. This is the first of the set of three chapters devoted to the FENIX. In particular, it introduces the concept of FENIX and the need for the existence of such anti-jamming system. Moreover, the requirements taken into account during its design are introduced, as well as, the use of the MFT blanking in FENIX. Regarding the MFT, this chapter introduces its use for RFI mitigation of GNSS and GNSS-R signals, it assesses its increased performance as compared to other RFI mitigation techniques, and it presents an example of its application to real GNSS-R data.

8.1 Introduction

As detailed in Chapter 2, the growing number of RFI and jamming incidents is becoming a serious threat to a wide range of radio services such as space-borne passive remote sensing, GNSS-R, spaceborne PNT services, spaceborne and terrestrial telecommunication networks. Presumably, the problem will become even worse in the future due to the proliferation of a large variety of wireless technologies around the world. RFI/jamming is seriously threatening GNSS-based systems, even though they operate in "protected" frequency bands. GNSS receivers have to deal with very low power signals located in between other frequency bands of an overcrowded spectrum, making them vulnerable to unintentional RFI. Moreover, GNSS-R instruments work with even lower power signals with a theoretical immunity to RFI that has been proved to be insufficient in real scenarios [99]. Consequently, RFI mitigation systems are necessary to solve, or at least to mitigate as much as possible, the RFI problem.

In Chapter 3, a number of RFI mitigation techniques have been mentioned. All of them have their own advantages and drawbacks in terms of performance. Besides, in Chapter 5, a comparison between time-frequency RFI mitigation techniques was performed. This study shows that the use of MFT is a good trade-off solution for RFI mitigation in MWR applications. As it will become clearer in this chapter, the use of the MFT blanking for RFI mitigation can be applied as an off-line or post-processing technique to improve the SNR. However, the true step-forward is to apply the RFI mitigation in real-time because critical applications, such as most of the ones relying on the GNSS, require it.

The FENIX design is presented in Section 8.2 as a ground-breaking solution for RFI mitigation in GNSS and GNSS applications, although it can be also used directly in MWR applications. As it will become clearer in the following sections, the mitigation approach of FENIX is similar to the one described in 5 for MWR applications. In Section 8.3, the theory of the operation of the MFT blanking is described. In Section 8.4, an example of the off-line application of the MFT blanking in real GNSS-R data is described. Finally, the last section of this chapter states the conclusions.

The results presented in this chapter have been partially presented in the conference papers "Assessment of Back-End RFI Mitigation Techniques in Passive Remote Sensing" [107], "Preliminary Results of FENIX: Front-End GNSS Interference eXcisor" [147], and "RFI Analysis and Mitigation in Airborne GNSS-R Campaign" [148]. Moreover, its design and intellectual property rights are protected by the US patent "System and method for detecting and eliminating radio frequency interferences in real time" [149].

8.2 FENIX: Front-End GNSS Interference eXcisor

FENIX stands for Front-End GNSS Interference eXcisor, and it represents the principal contribution of this PhD thesis. As its name states, FENIX has been conceived to be a front-end device. This means that FENIX is placed between the antenna system and the front-end of a GNSS receiver, and then, it performs the RFI mitigation by excising the undesired RFI signal from the useful GNSS signals.

The main goal of FENIX is the mitigation, reduction and/or cancellation, partially or completely, of RFI/jamming signals that cause desensitization, signal loss, or in general,

a malfunction of a GNSS device [149]. Thus, FENIX increases the SNR of GNSS devices connected at its output in the presence of RFI, and it allows to recover the loss of integrity while retrieving the useful signal even under jamming.

FENIX has been designed to fulfill some specific requirements that turn it into a versatile, full-compatible and plug-and-play add-on for any GNSS receiver.

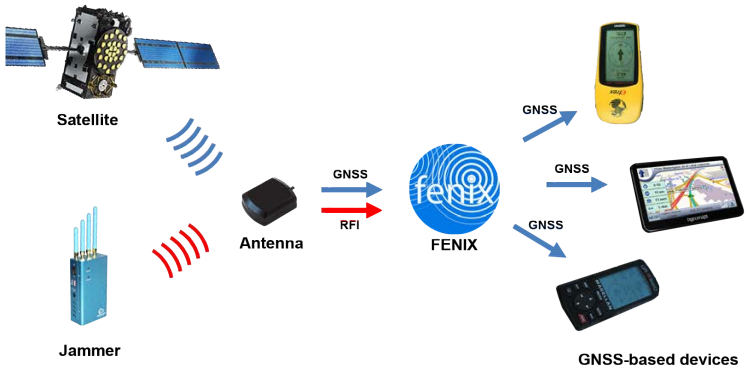

Figure 8.1: Description of the concept of FENIX.

The following subsections present the five pillars of the design of FENIX: pre-correlation excision, cross-GNSS compatibility, RFI-independent performance, real-time processing, and standalone operation.

8.2.1 Pre-correlation excision

The first requirement considered during the design of the FENIX was transparency. FENIX mitigates RFI signals in a way that it is independent and transparent to the GNSS receiver and antenna present in the system setup. This can be achieved by operating in the pre-correlation stage, just before GNSS signals reach the receiver. In this sense, FENIX collects the signal coming from the antenna, which contains the useful signal plus some undesired RFI/jamming signals, it performs its mitigation procedure by excision, and finally, it delivers the mitigated signal to the GNSS receiver. To do so, the FENIX hardware has been specifically designed for this purpose. The description of the hardware can be found in Chapter 9.

Moreover, the transparency of FENIX makes it compatible with other anti-jamming systems such as those based on antenna pattern modification or post-correlation techniques already embedded in the GNSS receiver. Hence, FENIX can operate in series with, for example, a null-steering antenna, or together with a receiver with adaptive tracking loop bandwidth. Therefore, the use of FENIX does not exclude the use of other anti-jamming devices. Besides, a receiving chain consisting of a combined set of anti-jamming devices, including FENIX, acts as a multi-layer security system against jamming attacks.

8.2.2 Cross-GNSS compatible

As detailed in Chapter 2, GNSS include several constellations of satellites (GPS, Galileo, ...) at several frequency bands (L1/E1, L2, L5/E5, ...) with different signal services (C/A, P, M, ...). Despite that, the vast majority of GNSS signals have DSSS modulations, with the only exemption of former GLONASS L1/L2 signals that combine spread-spectrum with FDMA. However, GLONASS is transitioning to DSSS-only services such as L1OC or L1CM for future inter-GNSS compatibility.

The use of DSSS modulations increases the bandwidth of the original signal, thus reducing the maximum of the spectral density of the GNSS signal. This effect, together with the low power level of GNSS signals when they reach the Earth's surface, triggers the use of RFI mitigation techniques similar to those used in passive microwave radiometers. The resulting signal from the combination of thermal noise and GNSS signals has the same spectral and statistical properties that the radiometric signal itself. Therefore, RFI mitigation signals, and in particular the use of the MFT and blanking discussed in Chapter 5, can be applied in GNSS and GNSS-R applications.

FENIX makes use of the blanking MFT procedure to perform the RFI/jamming signal excision, and hence it does not distinguish among GNSS signals or services. Conversely, it processes the combination of all GNSS signals as a whole, making FENIX a cross-GNSS compatible anti-jamming system. Nevertheless, this compatibility does not imply multi-frequency support by itself. Almost all GNSS constellations emit signals in multiple-frequencies (L1, L2, etc.). This means that there are several services of each GNSS constellation for each used frequency. FENIX processes simultaneously all GNSS services located at the same frequency. For example, the FENIX algorithm processes in parallel all services at the L1/E1/B1 band (1575.42 MHz): GPS L1C/A L1C, L1P, and L1M; Galileo E1OS and E1PRS; GLONASS L1OCM; BeiDou B1-1, B1-2, B1-C, and B1-BOC (when using a receiving chain with bandwidth larger than 30 MHz). Therefore, each frequency band must be processed in different FENIX receiving chain, tuned at the desired frequency and combined afterward (as it is done in multifrequency GNSS receivers).

Finally, the fact that FENIX operates at the pre-correlation stage implies a priori that it is cross-GNSS compatible. However, sub-banding can be used to distinguish between some services before the correlation process, since their spectral density maxima may lay at different frequencies inside the receiving bandwidth. This is not the case of FENIX, because it is designed to process the whole bandwidth at once in order to maximize the time-frequency resolution of the excision algorithm.

8.2.3 RFI-independent performance

Another requirement taken into account during the design of FENIX was the capability to mitigate any kind of RFI signal. Given the state-of-the-art of RFI mitigation algorithms, already discussed in Chapter 3, FENIX must use a non-parametric algorithm, which does not assume any a priori signal shape in the mitigation process. Parametric algorithms such as notch filtering or AGC blanking may perform better for particular RFI signals (CW and slow-rate pulsed respectively), but they are easily overridden by non-matched RFI signals. Besides, as described in Chapter 2, jammers usually generate chirped CW signals with some common patterns, but they are far from having a consistent signal

with a similar shape (linear), bandwidth and repetition period. Fading, diffraction, and multipath are other effects that can affect the RFI signal shape, thus degrading the performance of parametric techniques. Finally, the possibility of the presence of multiple RFI sources triggers the use of a non-parametric algorithm in FENIX.

FENIX uses the MFT in order to detect an mitigate simultaneously multiple RFI signals from several sources. The MFT can provide protection against man-made unintentional RFI signals and most common chirped-like jamming signals. Usually, these signals have their power concentrated in either time, frequency, or both domain, in order to maximize the instantaneous and/or spectral power density. In Chapter 5, the MFT has proven to be a good trade-off solution against different kinds of RFI signals, and FENIX takes advantage of it.

Furthermore, the presence of multiple simultaneous RFI signals with spread-spectrum modulations may be a cumbersome problem. The solution to this problem requires advanced non-parametric sub-space techniques to perform the mitigation process effectively. However, they also require huge computational burden with its additional high power requirements. Besides, the use of the MFT approach rather than other more complex processing algorithms is related to the next point: its real-time operation.

8.2.4 Real-time operation

RFI mitigation and anti-jamming must be performed in real-time in the majority of applications. GNSS signals are essentially used for positioning, navigation, and timing. In these cases, it is obvious that RFI mitigation must be performed at the same time the receiver is acquiring and tracking the satellites to deliver a Position, Velocity and Time (PVT) solution. In the presence of jamming, this PVT solution is corrupted or lost if the undesired signals are not previously mitigated.

In the case of GNSS-R, real-time mitigation is also required, especially in the case of pre-correlation algorithms. Sampling raw data from the antenna signal at several mega-samples per second generates a high volume of data, whose recording cannot be sustained for more than few hours. If the GNSS-R system has this capability, off-line RFI mitigation can be applied to the raw samples before obtaining waveforms or DDMs to retrieve the geophysical data. However, raw sampled data (often called L0 data) is usually available in small sets for testing purposes.

FENIX has been designed to work in real-time. This implies that all digital signal processing must work in pipeline mode, so that, data rate must be constant and sustainable. In this sense, the MFT has been optimized to achieve a real-time performance in an efficient way by using the FFT.

8.2.5 Standalone device

Eventually, the real-time hardware of FENIX is built in a compact, small size, light weight and low power consumption device. The main goal behind this is to provide a standalone anti-jamming system for GNSS-enabled applications, which can provide increased security to already existing receivers. FENIX offers an alternative to the state of the art, and it covers the gaps found in the same. Nevertheless, the FENIX technology is

not limited to be implemented in a standalone device. The design specifications described in previous sections make the FENIX technology compatible with its integration into a GNSS receiver, just at its front-end stage, or to be built in a Application Specific Integrated Circuit (ASIC) device alone, or in conjunction with a GNSS receiver itself.

8.3 Theory of MFT blanking in GNSS/GNSS-R

As mentioned above, FENIX makes use of the MFT to perform the mitigation of RFI and jamming signals. This section is devoted to an assessment of the performance of the MFT blanking approach in GNSS and GNSS-R systems. This assessment is performed from the theoretical point of view, and through MATLAB simulations. Therefore, this section justifies the use of the MFT from the point of view of its theoretical performance. However, the information about the related hardware and the implementation of the MFT blanking in real-time can be found in Chapter 9.

According to several studies, such as those performed on [9], RFI signals follow different patterns depending on the frequency band of operation, region, daytime, etc. Parametric mitigation algorithms have been developed in order to optimize their performance regarding the characteristics of the RFI signal. However, in some scenarios such as passive microwave remote sensing instruments and GNSS, mitigation algorithms should remove any possible RFI signal as much as possible because, otherwise, the performance of these will be completely corrupted. One of these cases is MWR, where the MFT has proven to be an efficient trade-off tool to perform RFI mitigation.

As mentioned above, the same principles can be applied in GNSS and GNSS-R. Following a similar procedure as in Chapter 5, the detection and mitigation performance of the MFT has been compared to other time-frequency RFI mitigation techniques.

Approach	*Commonly used techniques*	*Ev.*
Time-domain	Pulse Blanking (PB) [23], Amplitude Domain Processing (APD) [71]	PB
Frequency-domain	notch filtering [14], Frequency Blanking (FB) [59]	FB
Time-frequency space	Spectrogram Blanking (SB) [11], filter bank	SB
Time-scale space	Wavelet Denoising (WD) [65, 106]	WD
Time-frequency-scale space	Multiresolution Fourier Transform (MFT) [112]	MFT

Table 8.1: List of TF RFI mitigation techniques.

From the literature, five different time-frequency RFI mitigation approaches may be distinguished (see Tab. 8.1), but all of them share the same operating principle. First, the input signal is projected into the corresponding space that is, from low to high implementation complexity, time-domain, frequency-domain, time-frequency (TF) space, time-scale space, and time-frequency-scale respectively. Then, RFI-contaminated samples are detected using the Binary Hypothesis criterion [46]. Eventually, a thresholding stage excises RFI-contaminated samples from the rest, and the domain transformation is

inverted using only RFI-clean samples. The full process is summarized in Fig. 8.2 and detailed in the following subsections.

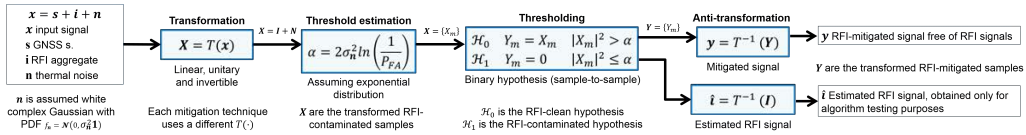

Figure 8.2: Summary of the blanking process.

8.3.1 Blanking of GNSS signals

The received signal, expressed as $\mathbf{x}$, is conditioned, and digitized with the corresponding antenna and front-end. Then, $\mathbf{x}$, can be expressed as $\mathbf{x} = \mathbf{s} + \mathbf{i} + \mathbf{n}$, where $\mathbf{s}$ represents the aggregated of all GNSS signals in view, $\mathbf{i}$ is the aggregated of possible RFI signals, and $\mathbf{n}$ is white Gaussian noise with Probability Density Function (PDF) $f_n(\mathbf{n}) \in \mathcal{N}(0, \sigma_n^2 \mathbf{1})$ with the same bandwidth than the receiver.

As mentioned above, the combination of $\mathbf{s}$ and $\mathbf{n}$ can be considered to have the same statistics as the noise itself. The main argument that supports this affirmation is that the received power of the GNSS signals is much weaker than the noise power. One can argue that the PDF of the aggregated of all GNSS signals, $\mathbf{s}$, has a Normal-like distribution, $f_{\mathbf{s}}(\mathbf{s})$. Each GNSS service signal can be seen as an independent random process, and by the CLT [53], the addition of a number of them tends toward a Normal distribution. Moreover, the PDF resulting from the sum of two independent random variables can be obtained as the convolution of their PDFs [53]. Thus, the PDF of the addition of $\mathbf{s}$ and $\mathbf{n}$ can be obtained as $f_{\mathbf{s}}(\mathbf{s}) * f_{\mathbf{n}}(\mathbf{n})$. Considering that the noise power is much larger than the GNSS signal power (i.e. $\sigma_n >> \sigma_s$), $f_{\mathbf{s}}(\mathbf{s})$ can be approximated by a Dirac function, $\delta(\mathbf{s})$. Therefore, the PDF of the aggregate of $\mathbf{s}$ and $\mathbf{n}$ also follows approximately the noise PDF $f_n(\mathbf{n})$. This result triggers the use of a similar approach to the one followed for microwave radiometry but applied to the combination of GNSS and GNSS-R signals and thermal noise. Moreover, it applies for most setups using GNSS receivers since GNSS signals are usually received below the thermal noise. However, if this is not the case, such as for example if an antenna with the sufficient directivity is used, the assumption must be discarded, and the statistics of the received signal will depend on the number of satellites in view. If it is large enough, the Gaussian still holds also because of the CLT.

8.3.2 Blanking MFT process

8.3.2.1 Domain transforms

As in Chapter 5, the performance of the MFT is compared to other time-frequency techniques. In all of them, the received signal, $\mathbf{x}$, is mapped into different signal domains, $\mathbf{X} = T(\mathbf{x})$. Domain transforms used in RFI mitigation algorithms $T(\cdot)$ must be unitary, linear and invertible, so that, the signal can be recovered after RFI-contaminated sample excision. Tab. 8.1 depicts the techniques evaluated in this work. These techniques are also described in the following lines:

- Pulse Blanking (PB) "blanks" RFI power peaks in time-domain. No transform is applied to $\mathbf{x}$ signal.
- Frequency Blanking (FB) projects $\mathbf{x}$ in the frequency-domain using the Discrete Fourier Transform (DFT).
- Spectrogram Blanking (SB) uses the Short-Time Fourier Transform (STFT) to project $\mathbf{x}$ into the TF space with fixed TF resolution.
- Wavelet Denoising (WD) decomposes $\mathbf{x}$ into a set of wavelets with different scale (Haar wavelet was chosen in this work).
- Multiresolution Fourier Transform (MFT) projects $\mathbf{x}$ into several TF spaces with different $\mathbf{x}$ resolution (scale).

8.3.2.2 Detection stage

Under Binary Hypothesis criterion, the detector stage must decide between two hypotheses in the transformed domain:

- RFI-clean sample $\mathcal{H}_0 : \mathbf{X} = \mathbf{N}$
- RFI-contaminated sample $\mathcal{H}_1 : \mathbf{X} = \mathbf{I} + \mathbf{N}$

being $\mathbf{I} = T(\mathbf{i})$, and $\mathbf{N} = T(\mathbf{n})$. The noise in transformed domain, $\mathbf{N}$, will also follow a Gaussian distribution, $f_{\mathbf{N}}(\mathbf{N}) \in \mathcal{N}(0, \sigma_n^2 \mathbf{1})$, due to the properties of $T(\cdot)$.

The decision is taken by comparing the result of a certain test applied to $\mathbf{X}$ with a determined threshold value α. The optimal test depends on the statistics of received RFI signal. In this work, the energy detector has been chosen because it is a sub-optimal solution when the RFI signal is not known a priori [46]. Therefore, hypothesis $\mathcal{H}_1$ is chosen when $|\mathbf{X}|^2 > \alpha$, whereas $\mathcal{H}_0$ is chosen otherwise.

The result of this test leads to a probability of false alarm, $P_{FA} = P(\mathcal{H}_1|\mathcal{H}_0)$, and a probability of detection, $P_D = P(\mathcal{H}_1|\mathcal{H}_1)$, that together will determine the performance of the detector. Moreover, given a certain P_{FA}, α can be obtained considering that $|\mathbf{X}|^2 \,|\, \mathcal{H}_0 = |\mathbf{N}|^2$, follows a exponential distribution $f_{|\mathbf{N}|^2}(|\mathbf{N}|^2)$. Thus,

$$P_{FA} = P\left(|\mathbf{N}|^2 > \alpha\right) = \int_{\alpha}^{\infty} e^{-\frac{|\mathbf{N}|^2}{2\sigma_n^2}} \, d|\mathbf{N}|^2, \tag{8.1}$$

and then,

$$\alpha = 2\,\sigma_n^2 \, ln\left(\frac{1}{P_{FA}}\right). \tag{8.2}$$

8.3.2.3 Thresholding stage

In the thesholding stage, only RFI-clean samples in the transformed space are kept whereas RFI-contaminated samples are discarded as follows

$$Y_m = \begin{cases} X_m & |X_m|^2 \leq \alpha \\ 0 & otherwise \end{cases}, \tag{8.3}$$

with $\mathbf{X} = \{X_0, X_1, \ldots, X_m, \ldots, X_M\}$, $\mathbf{Y} = \{Y_0, Y_1, \ldots, Y_m, \ldots, Y_M\}$, and α is obtained from (8.2). Eventually, the RFI-mitigated signal, $\mathbf{y}$, is obtained applying the inverse transform to RFI-clean samples, $\mathbf{y} = T^{-1}(\mathbf{Y})$. Moreover, estimated RFI signal can be calculated as $\hat{\mathbf{i}} = T^{-1}(\mathbf{X} - \mathbf{Y})$.

8.3.3 Assessment of MFT blanking

8.3.3.1 Simulation parameters

The performance of the MFT has been assessed versus the five mitigation techniques in Tab. 8.1 under the effects of six different RFI signals: glitch (one-sample RFI pulse), continuous wave (sinusoidal), DME pulse, narrow-band chirp (sweeping 20% bandwidth), full-band chirp, and PRN (overlapping 20% bandwidth). The Wigner-Ville distributions of each of the six RFI signals are depicted in Fig. 8.3. These signals have been chosen for the following reasons:

- *Glitch*: it is the shortest possible pulse (one sample). It may represent a slow rate pulsed signal. All its power is concentrated in a short period of time, and its PSD occupies the whole bandwidth of the receiver.

- *CW*: it is a pure tone inside the bandwidth of the receiver. It may or may not be at the center of the band. It represents the most usual kind of unintentional RFI since it may be generated by, for instance, an inter-modulation product, a near-band signal carrier or spurious signals from ADC clocks.

- *DME*: it is an aeronavigation signal allocated in a band that overlaps the L5/E5 band. It is a double-pulsed Gaussian-shaped signal with random and high repetition frequency. The two pulses are separated by 12 μs.

- *Chirps*: it is the typical signal shape generated by jammers. The *narrow-band* chirp has similar properties to jammers acquired from Internet stores. It has a 20% overlapping bandwidth. Besides, the *full band* chirp represents another jammer with a sweeping bandwidth higher than the bandwidth of the receiver.

- *PRN*: it represents a widespread signal overlapping a 20% of the bandwidth of the receiver.

The MFT performance has been assessed in terms of probability of mitigation P_M, and mitigation performance. These results have been obtained setting a $P_{FA} = 10^{-6}$, and running a Monte-Carlo simulation with 1000 realizations.

P_{FA} can be set to values much smaller than those used in microwave radiometry applications. There, the RFI miss-detection is critical, even with low power RFI signals. In that case, the eventual radiometric measure is corrupted. However, the correlation gain of GNSS signals is enough to protect the signal against low power RFI, while the RFI mitigation system can be focused on dealing with strong RFI signals. Setting P_{FA} to a low value ensures to not degrade GNSS signals when no RFI is present while allowing the mitigation to be performed when sufficient powerful RFI signals are present.

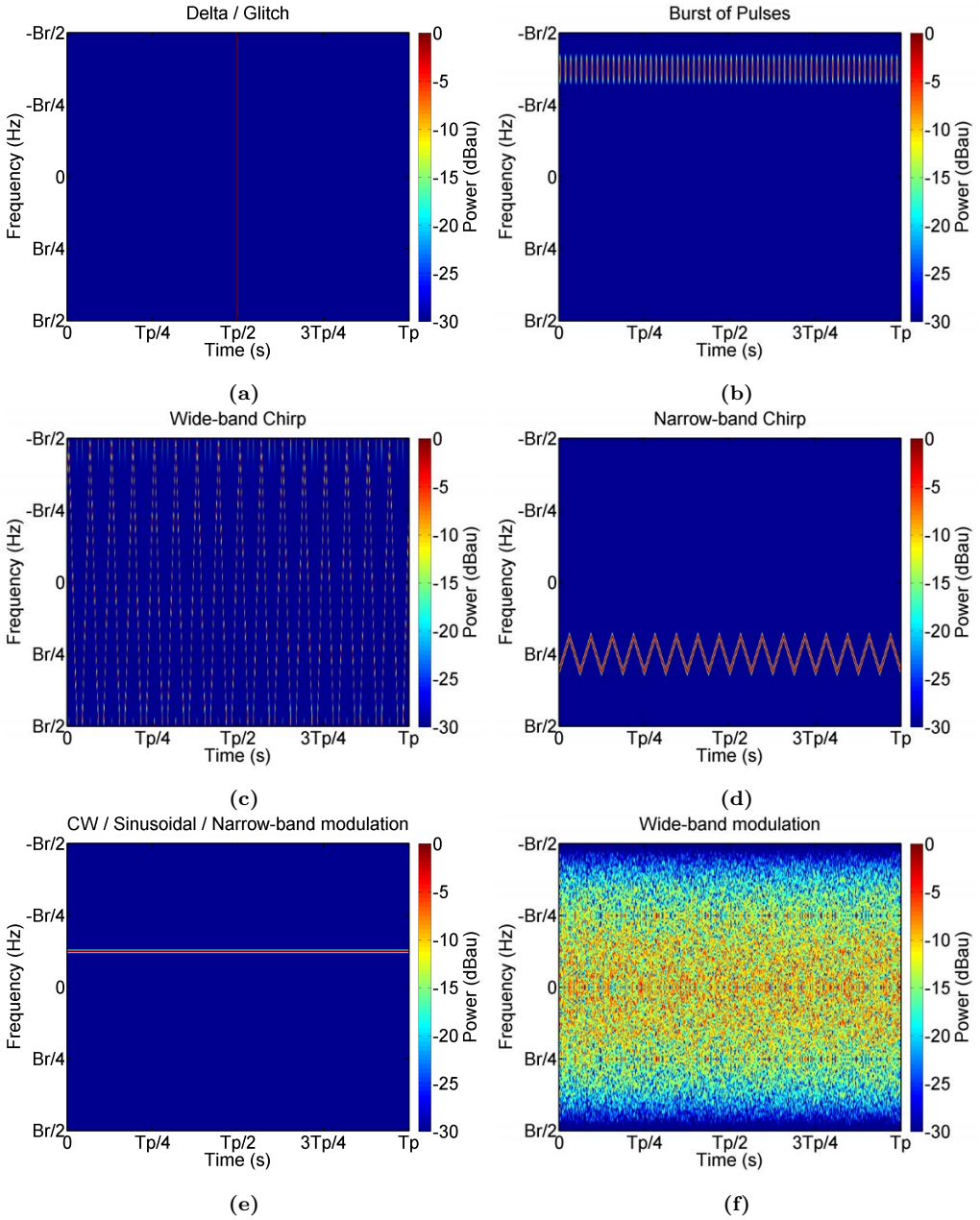

Figure 8.3: Wigner-Ville distributions of the following RFI signals: (a) glitch, (b) continuous wave, (c) DME pulse, (d) narrow-band chirp, (e) full-band chirp, and (f) PRN.

8.3.3.2 Probability of mitigation

The P_M is calculated as $P_M = P(INR_{out} < INR_{in})$, with $INR_{in} = \sum|\mathbf{i}|^2/\sum|\mathbf{n}|^2$. Figure 8.4 shows the P_M as a function of the INR. In terms of P_M at 99.9%, PB and MFT

performs the best for glitch RFI (-21 dB and -20.5 dB of INR_{in} respectively); FB and MFT are the best ones for sinusoidal RFI (both at -19 dB); MFT the best for DME pulse (-18 dB); FB, SB, and MFT is the best for narrow-band chirp (all at -6.5 dB); MFT the best for full-band chirp (-7 dB); and, WD and MFT the best for PRN RFI (-7 dB and -6.5 dB respectively).

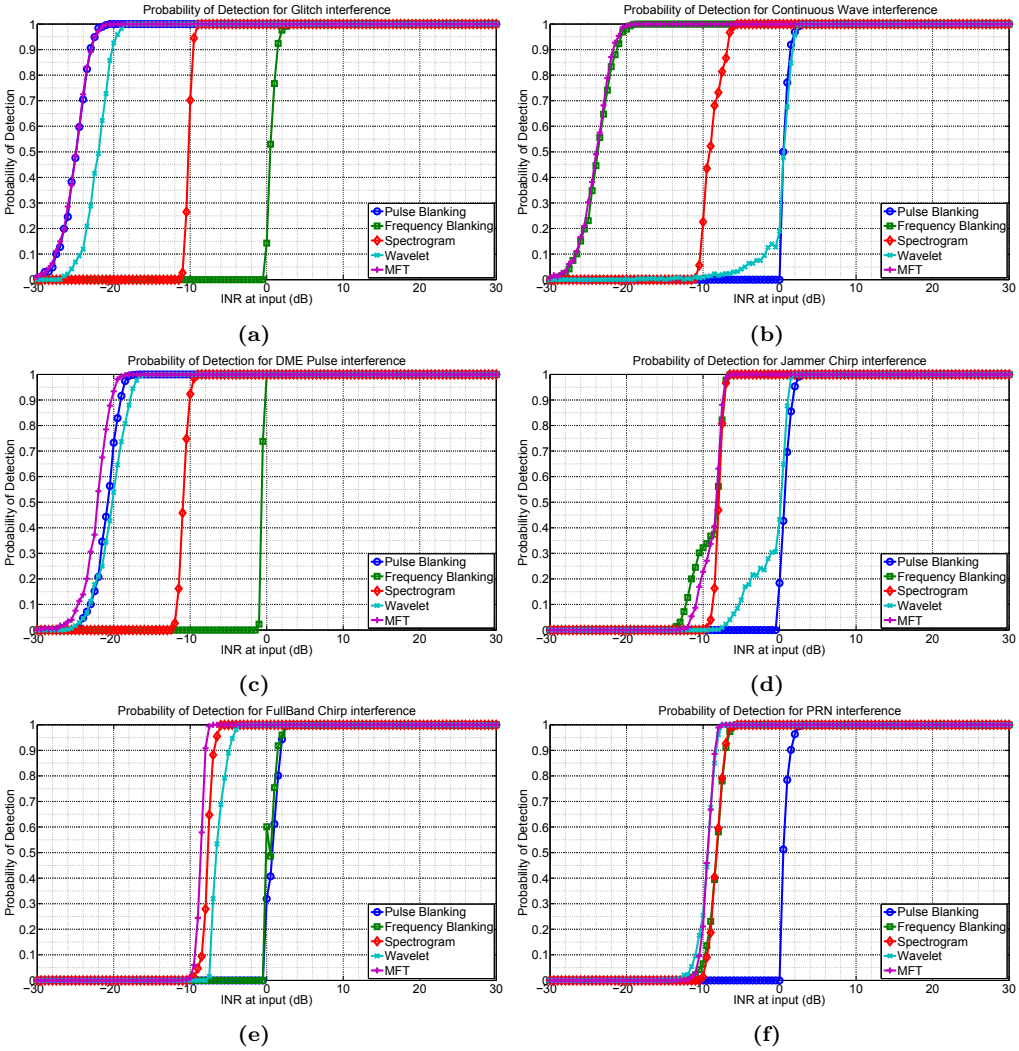

Figure 8.4: Probability of mitigation of evaluated algorithms for (a) glitch, (b) continuous wave, (c) DME pulse, (d) narrow-band chirp, (e) full-band chirp, and (f) PRN RFI signals.

8.3.3.3 Mitigation performance

The mitigation performance of each algorithm is evaluated plotting the $INR_{out} = \sum|\hat{\mathbf{i}}|^2 / \sum|\mathbf{n}|^2$ against INR_{in} (see Fig. 8.5). RFI power is reduced when P_M tends to values close to 1

as seen comparing Fig. 8.4 with Fig. 8.5. After this point, RFI power becomes hardly mitigated if INR_{in} keeps rising until the technique enters into a "saturated" region. This process takes place when the RFI power within the transformed domain has a similar energy as compared to the noise, and then the RFI-contaminated samples cannot be distinguished from RFI-clean ones.

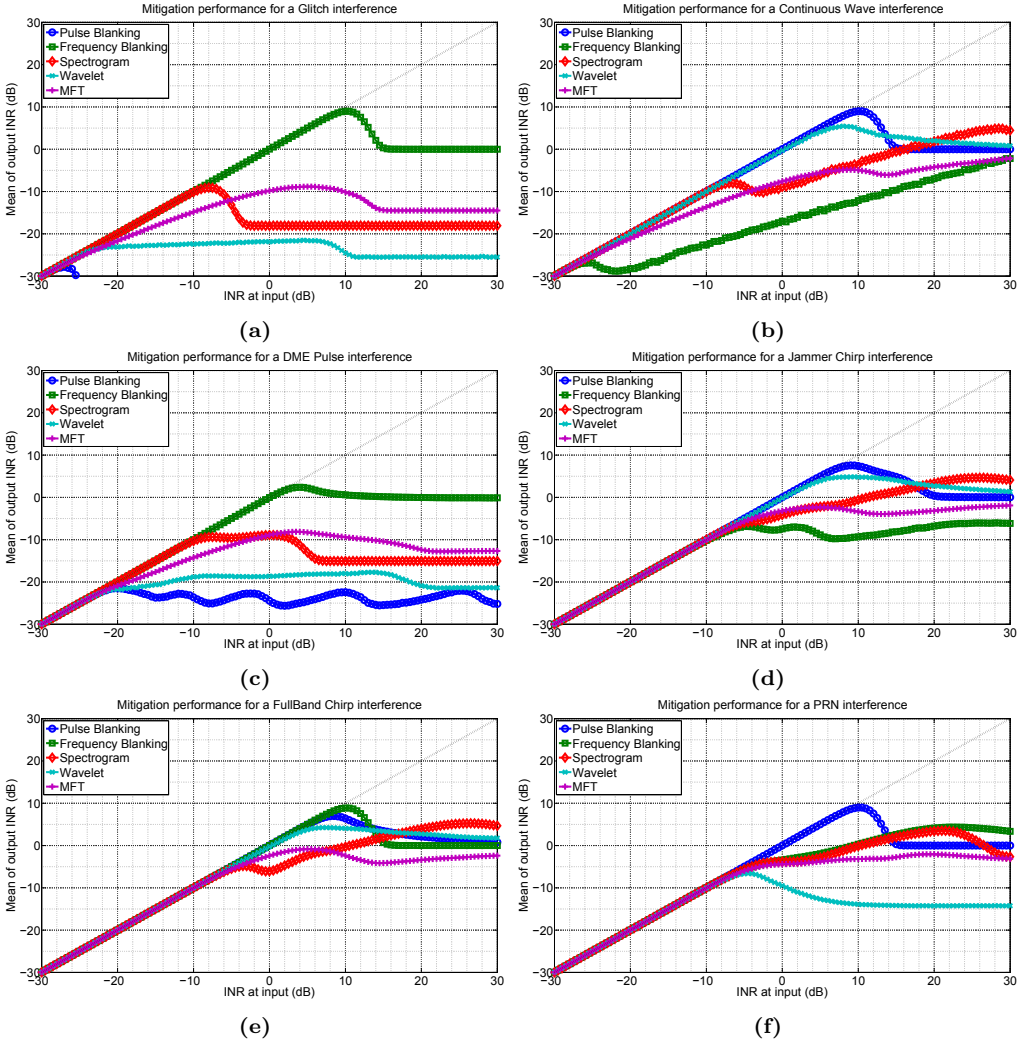

Figure 8.5: Mitigation performance of evaluated algorithms for (a) glitch, (b) continuous wave, (c) DME pulse, (d) narrow-band chirp, (e) full-band chirp, and (f) PRN RFI signals. Colorbars show normalized arbitrary units in dB or dBau.

8.3.4 Summary of MFT performance

As aforementioned, the mitigation performance of each technique depends on the RFI signal. For example, a glitch RFI can be completely mitigated using PB, a sinusoidal RFI from 5 to 25 dB with FB, and a full-band chirp is sensitive to SB.

Since the MFT method uses several multi-scale spectrograms working in parallel, the input signal is projected with several bases including the ones used in the PB, FB, and SB techniques. Figure 8.6 shows the MFT decomposition of the narrow-band chirp. In this particular case, it is clear that if the blanking is applied at level 4^2, the power of the RFI signal is mitigated efficiently.

Therefore pulsed, sinusoidal as well as chirp RFI signals can be mitigated similarly (or even better for chirps) compared to simpler techniques. Eventually, WD technique shows good performance for pulsed RFI signals, but poor for sinusoidal and chirp RFI, whereas it seems to be the best option for PRN RFI signals as suggested in [106].

From these results, MFT technique gives good RFI mitigation performance for GNSS, and GNSS-R instruments, ensuring an INR_{out} below 0 dB for the RFI/jamming signals under evaluation.

8.4 Example of MFT blanking in airborne GNSS-R data

Although FENIX has been conceived to work in real-time systems, it is of prime importance to validate the signal theory behind its performance with real data from GNSS or GNSS-R systems. This can be done with off-line data, and hence, performing post-processing, using the MFT blanking algorithm. Therefore, this section describes the results of the test of the principles of the FENIX mitigation algorithm by using real data from an airborne GNSS-R instrument flown during the HUMIT project campaign.

8.4.1 Experiment description

HUMIT is a project carried on at the Catalan Cartographic and Geologic Institute (ICGC) whose main goal is to test different passive remote sensing instruments devoted to retrieve soil moisture measurements. The first flight took place on November 30th, 2017 and it lasted approximately 4 hours. The plane took off from Barcelona airport and headed to the North-West part of Catalunya.

The plane carried 5 different instruments: a hyperspectral camera, a thermal camera, an L-band radiometer, and two GNSS reflectometers. One of the reflectometers was the Multiband Airborne L-band reflectometrY with GNSS (MALYGNSS), which is a dual-band L1/L2 GNSS reflectometer designed as a validation test for different subsystems of the MIR instrument [150]. Figures 8.7a and 8.7b show the aircraft used in the campaign and the rack where the instruments were mounted on respectively [151].

MALYGNSS is composed by a dual-channel SDR that samples synchronously the signals gathered by the up-looking and down-looking antennas. The up-looking RHCP antenna receives the direct GNSS signals, while the down-looking LHCP antenna receives the

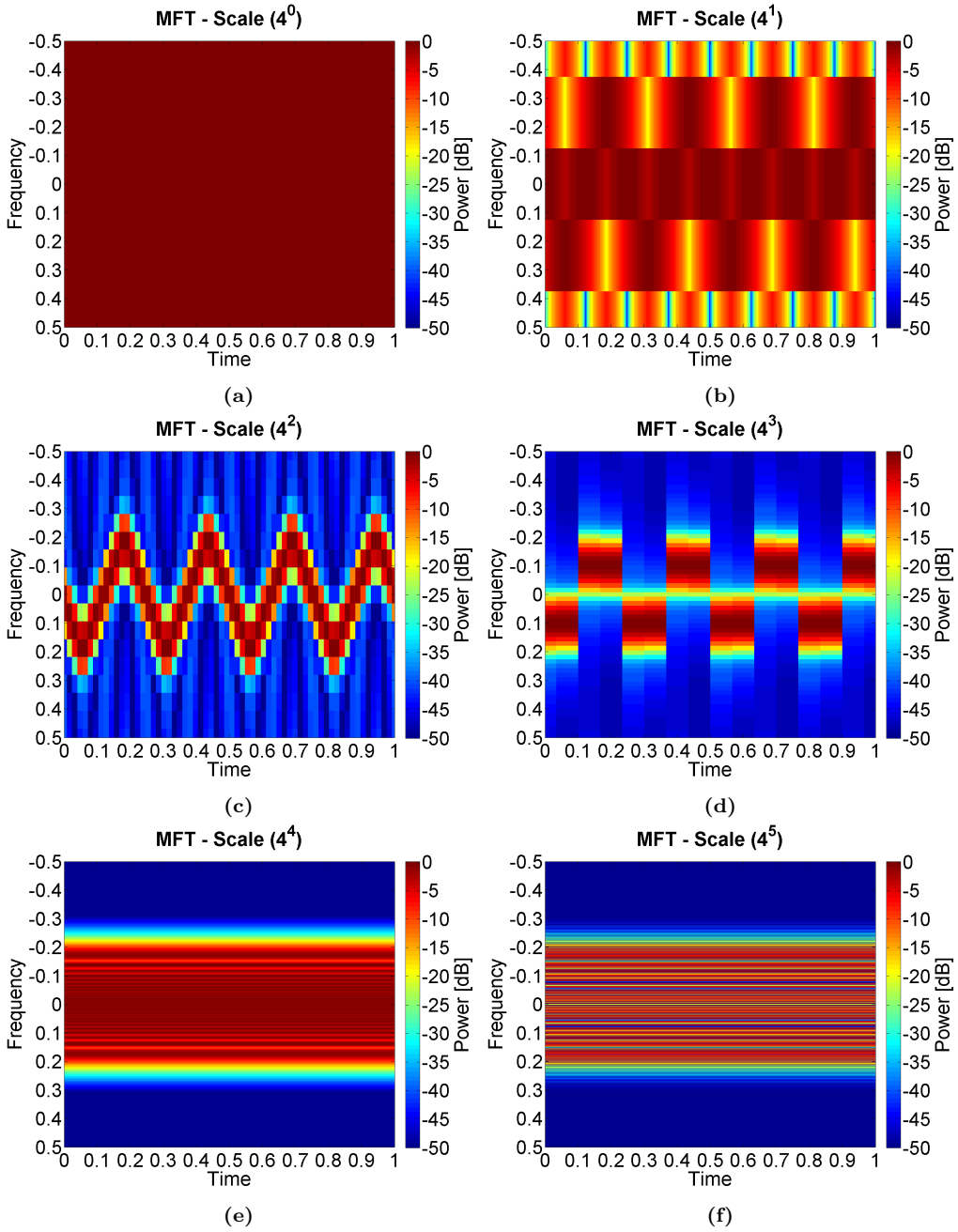

Figure 8.6: Decomposition of a chirp RFI signal each MFT level. The depicted MFT levels correspond to the following FFT length sizes: 4^0, 4^1, 4^2, 4^3, 4^4, and 4^5.

reflected GNSS signals. Both are GPS L1/L2 antennas with a gain of approximately 40 dB. The up-looking antenna signal is also used for positioning and attitude determination

of the airplane. The received signals are sampled at $F_s = 8.184$ Msps (8 x 1.023 MHz), with 16-bit I/Q samples, which are eventually stored for later post-processing. An on-demand trigger enables two 1-minute sampling periods at GPS L1 and L2 bands respectively.

The main scope of the flight was to acquire simultaneously optical and reflectometric data to perform data fusion for soil moisture retrieval. Besides, the L-band radiometer data, together with Sentinel data, are used later on as ground truth.

(a) **(b)**

Figure 8.7: (a) Aircraft used during the HUMIT campaign. (b) Rack where the set of instruments were mounted on [151].

8.4.2 RFI pre-analysis

Before applying the MFT blanking algorithm, a study to detect and identify the kind of RFI signals present in the complex-valued raw data samples x was performed. To do so, the following functions are applied and their results are discussed.

8.4.2.1 Spectrogram

In order to identify CW and other narrow-band RFI signals, the whole sample set x has been divided into subsets of 50 ms ($N_P = 409200$ samples), and then an estimation of the Power Spectral Density (PSD) for each subset x_P has been obtained using the Barlett's periodogram method. Besides, each periodogram S_P has been obtained as

$$S_P = \sum_{N_A} |\mathcal{F}\{x_F\}|^2, \tag{8.4}$$

where each x_P has been divided in N_a subsets x_F of N_F samples, and $\mathcal{F}\{\cdot\}$ represents the Discrete Fourier Transform (DFT). N_a and N_F are divisors of N_P, and their values are 1550 and 264 respectively. Furthermore, the time aggregate of all periodograms $\{S_P\}$ can be defined as the spectrogram S of sample set x.

Figure 8.8a shows a 30 s spectrogram centered at the L1 frequency (1.57542 GHz) of one of the datasets. Two CW RFI signals can be appreciated. The stronger tone is centered

at -1.5 MHz and it has intermittent behavior with a peak power 4 dB higher than GPS signals. The weaker one is centered at 2 MHz and it has a power similar to GPS signals. Moreover, some unknown time events can be appreciated at instants 3, 10, 13, and 23 s.

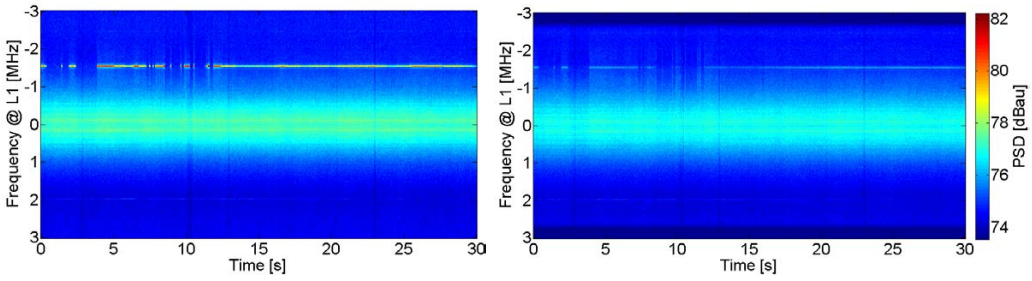

Figure 8.8: RFI analysis of 30 second data set using the Spectrogram: (a) before FENIX mitigaition, and (b) after FENIX mitigation.

8.4.2.2 Complex kurtosis

As mentioned above, the kurtosis is a statistical test frequently used in RFI detection applications. It is defined as the ratio between the fourth-order central moment and the square of the variance of a random variable. Usually, it is defined for real-valued samples, and in the case of a Normal or Gaussian distribution, the value of the kurtosis is 3. However, the kurtosis can also be defined for complex random variables as in the case of the samples at the output of an I/Q receiver. The complex kurtosis of a circular complex Normal or Gaussian random variable is equal to 2. More details about the derivation of the complex kurtosis can be found in Appendix F.

The moments of a random variable are not known a priori, and thus, they must be estimated from a set of samples. In the case of kurtosis, its estimator may be called sample kurtosis. The sample complex kurtosis of a random variable x is defined (from Appendix F) as

$$\kappa(x) = \frac{\frac{1}{N}\sum_N |x - \overline{x}|^4}{\left[\frac{1}{N}\sum_N |x - \overline{x}|^2\right]^2}, \tag{8.5}$$

where $\overline{x} = \sum_N x$ is the average value of the samples x. Since the sample complex kurtosis is a function of the samples of a random variable, it is a random variable by itself. The mean and variance of the (real) sample kurtosis, $\mathsf{k}(x)$, and complex sample kurtosis, $\kappa(x)$, of a circular complex Normal or Gaussian random variable, x, as a function of the number of samples, N, are depicted in Fig. 8.9.

The mean of the complex sample kurtosis, hereinafter just complex kurtosis, κ, as a function of the number of samples is equal to

$$E\{\kappa\} = 2\frac{N-1}{N}, \tag{8.6}$$

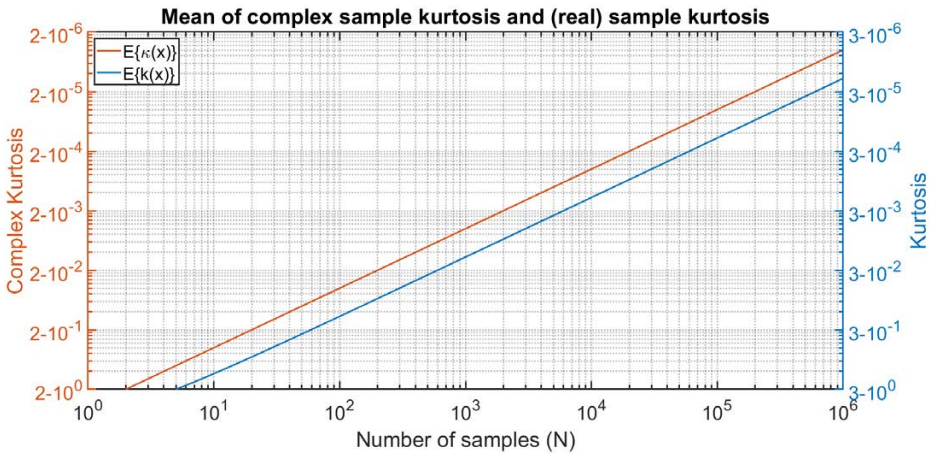

(a)

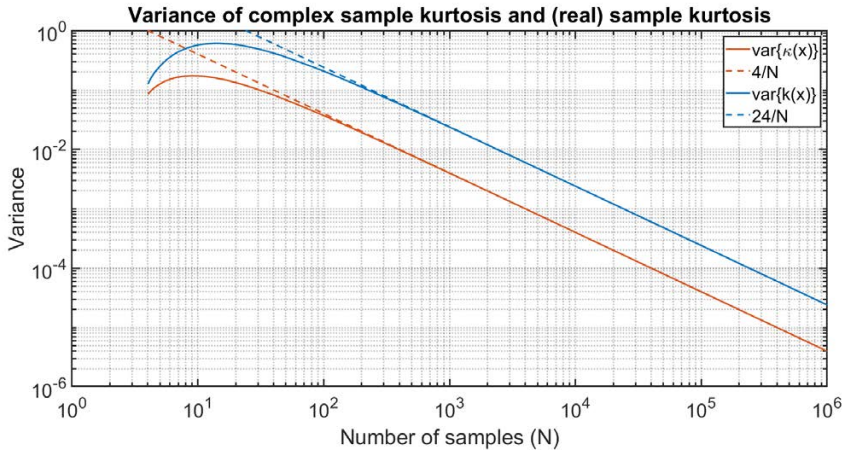

(b)

Figure 8.9: Statistics of the sample complex kurtosis of a circular complex Normal random variable: (a) mean and (b) variance.

which is biased by a factor of $(N-1)/N$, but it tends asymptotically to the theoretical value of 2. Moreover, the variance of the complex kurtosis tends asymptotically to a value of $4/N$ with increasing value of the number of samples N. Therefore, the complex kurtosis has a variance six times lower than its real counterpart, which tends asymptotically to a value of $24/N$ [114]. This gives to the complex kurtosis an improvement in terms of detection of about 2 dB as compared to the real-valued version [152].

The complex kurtosis has been applied to each 1 ms subset x_c, with a number of samples N_c equal to 8184 samples from the whole sample set x. The value of the complex kurtosis of each subset, κ_c, has been obtained using (8.5) with N_c number of samples, and an average value of each subset x_c equal to $\overline{x_c} = \sum_{N_c} x_c$.

Furthermore, the time aggregate of κ_c values is defined as the complex kurtosis time

evolution K. Its results when applied to the dataset are discussed in the subsection below, together with the definition of the spectral kurtosis.

8.4.2.3 Spectral kurtosis

Equivalently to the complex kurtosis, the spectral kurtosis for each subset x_c, κ_c^S, can be defined by applying (8.5) to the DFT of x_c, $\mathcal{F}\{x_c\}$. Besides, the spectral kurtosis time evolution K^S is defined as the time aggregate of κ_c^S.

Figure 8.10a shows the corresponding complex and spectral kurtosis. The complex kurtosis has a mean value of about 1.92 with some spikes at the above mentioned unknown events, plus other events which were not recognized in the spectrogram. The mean value indicates that samples are close to belonging to a Normal distribution, but there are some underlying effects (band-limiting, gain compression, etc.) that make it diverge from the theoretical value of 2. Moreover, its theoretical standard deviation value around the mean is equal to $\sqrt{\frac{4}{N_c}}$, or in this case ≈ 0.022. However, the observed deviation is on the order of 0.05, which is another indicator that, although samples are close to being Gaussian, there are other hidden effects.

Nevertheless, the spectral kurtosis can detect clearly the already mentioned RFI intermittent behavior.

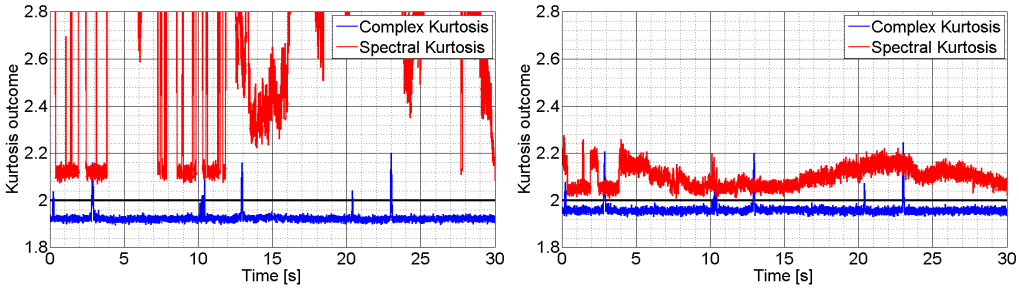

(a) (b)

Figure 8.10: RFI analysis of 30 second data set using the complex and spectral kurtosis: (a) before FENIX mitigation, and (b) after FENIX mitigation.

8.4.3 Effect of RFI in the DDMs

As detailed in Chapter 7, Delay-Doppler Maps (DDMs) are obtained cross-correlating the received signal with the corresponding clean-replica of the code. DDMs are the most general observable for GNSS-R measurements and represents the space where the delay-Doppler point corresponding to the maximum of the cross-correlation is searched both in GNSS and GNSS-R devices.

Figure 8.11 shows an example of the DDM distortion introduced by RFI and jamming signals. With no RFI, the peak of the DDM raises clearly from the lower noise floor. However, in the presence of the jammer RFI, the noise floor is raised above the maximum of the correlation peak. Therefore, the GNSS signal is completely masked by the

interference power. Under this conditions, two problems appear. First, the DDM peak cannot be located in the search space, and second, the navigation signal cannot be demodulated, even if a prior delay-Doppler point is assumed valid, because of the very low SNR present in this case. Nevertheless, this situation may change if a mitigation algorithm is applied. If this is the case, the DDM peak can still be tracked, and thus positioning and/or reflectometric measurements can still be obtained.

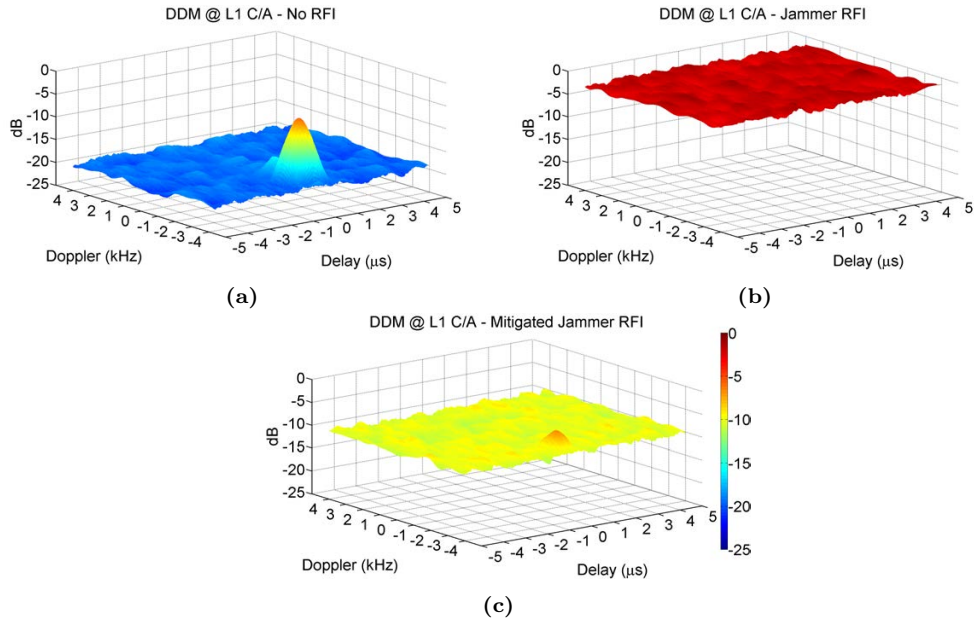

Figure 8.11: Example of the effects of RFI/jamming signal on the DDM. Three different cases are shown: (a) No RFI/jamming effect, (b) DDM under RFI/jamming effect, and (c) expected DDM after RFI/jamming mitigation

8.4.4 Mitigation using MFT blanking

In order to mitigate the effects of RFI signals on GNSS-R measurements, the FENIX algorithm is applied to the whole raw sample dataset. As detailed in previous sections, the FENIX mitigation algorithm first detects the RFI signals present on the dataset, and after that, it makes use of the MFT to project the signal in a multidimensional space. Then, the blanking (or thresholding) process is applied to the samples above an adaptive threshold. Those samples are removed from the transformed dataset because they contain the largest part of the RFI power. Eventually, mitigated samples are transformed back to the time domain.

Spectrogram and kurtosis of the FENIX output can be also calculated in order to assess how the MFT blanking algorithm mitigates the RFI signals present in the dataset. Figure 8.8b shows the mitigated spectrogram, where the main RFI peaks have been attenuated up to 5 dB, while GPS PSD has been attenuated only about 1 dB. Figure 8.10b depicts the mitigated complex and spectral kurtosis. Complex kurtosis has now a mean

value of 1.96, which represents that samples are more closer to a Gaussian distribution than before mitigation (closer to 2), but it is still showing some peaks. On the other hand, spectral kurtosis still shows some variations, but it is confined between 2 and 2.2, showing a clear improvement thanks to the mitigation process.

Moreover, RFI mitigation can also be assessed by comparing the DDMs before and after mitigation. In particular, the SNR measured at the mitigated DDMs should be higher than the one measured before mitigation. In this work, SNR at DDM is defined as the ratio between the DDM peak and the standard deviation of the rest of the DDM. Moreover, two cases are taken into account. The first one considers DDMs with a coherent integration time of 1 ms, whereas the second one uses 50 incoherent averages of the first ones.

Figure 8.12a shows the time evolution of SNR improvement for both DDM types. Furthermore, Figs. 8.12b and 8.12c show the histogram for coherent and incoherent DDMs respectively. The mean and standard deviation of the coherent SNR improvement are 0.72 dB and 0.46 dB respectively, whereas they are 1.49 dB and 0.33 dB in the case of incoherent SNR improvement.

In summary, from the analysis of one of the datasets captured by the MALYGNSS instrument, two CW RFI signals are detected and characterized. Moreover, some time events were identified, but their origin is still unknown. FENIX mitigation algorithm was applied to the contaminated dataset, and the output signal was revealed to be much cleaner than before. Moreover, the mean SNR improvement with coherent DDMs of 1 ms is 0.72 dB, whereas the SNR improvement increases to 1.49 dB when considering 50 incoherent averages. This improvement represents a reduction in the geophysical parameter estimation uncertainty, which may be needed in high accuracy application such as soil moisture retrieval.

8.5 Conclusions

This chapter has introduced the FENIX: an innovative system for RFI mitigation and anti-jamming for GNSS and GNSS-R applications. FENIX uses the MFT blanking as a pre-correlation excision tool to perform the mitigation. Moreover, FENIX is cross-GNSS compatible and RFI-independent thanks to the use of the MFT, which has been proven as a good trade-off solution for RFI mitigation. In this chapter, the principles of operation of the MFT blanking algorithm are assessed and compared with other techniques. Eventually, its performance as a mitigation tool has been proven using GNSS-R data samples from a real airborne campaign. More details on FENIX can be found in the next chapters. In particular, the description of the standalone hardware for real-time operation is done in Chapter 9, and the test and validation results using real jamming signals are presented in Chapter 10.

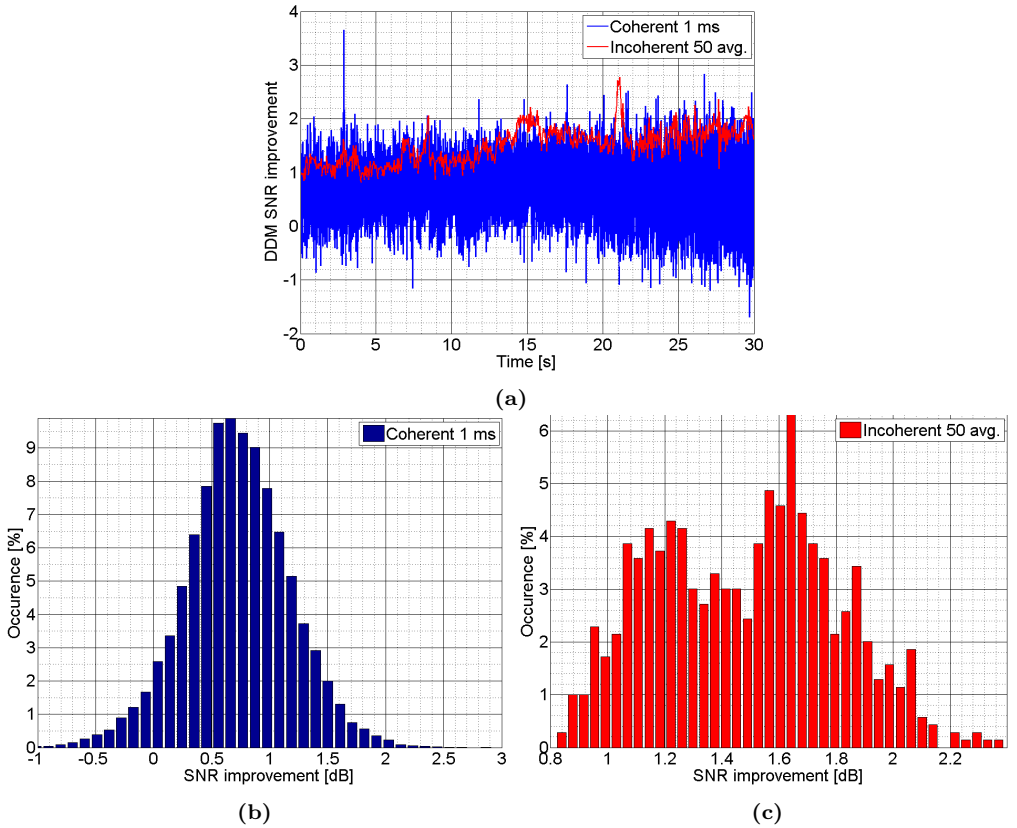

Figure 8.12: SNR improvement measured between DDMs obtained before and after applying FENIX. Subplots correspond to: (a) time evolution SNR improvement of coherent and incoherent DDMs, (b) histogram of coherent SNR improvement, and (c) histogram of incoherent SNR improvement.

9

Chapter 9

FENIX: hardware implementation and validation

This chapter describes the hardware implementation of the FENIX technology as well as its performance has been validated. This is the second chapter of the set of three devoted to the FENIX. The main building blocks of the patented architecture of FENIX are described. They are divided into two main stages, one analog and one digital. Moreover, the possible combinations to integrate FENIX technology in a GNSS-enabled system are discussed. Besides that, the three real-time prototypes implemented during this PhD thesis are presented. The most recent prototype, the FENIX-Lite, has several configurable test paths and test points that are used to validate its real-time performance. Furthermore, a simulator named FENIX-Sim allows for testing the performance of the FENIX architecture under different RFI and jamming scenarios. An example scenario has been chosen to validate the performance of the FENIX-Lite hardware using the available test points, and the results are compared to the ones obtained from the FENIX-Sim.

9.1 Introduction

FENIX has been designed to maximize the performance of the MFT blanking technique for GNSS and GNSS-R applications (Chapter 8), and for MWR applications (Chapter 5). To do so, a specific hardware has been built and tested. In particular, several prototypes have been developed during this PhD thesis. This chapter describes the main building blocks of the FENIX hardware. Besides, the different setups of FENIX in a GNSS receiving chain are stated. Moreover, a summary of each of the FENIX prototypes is presented. Furthermore, the results obtained from the validation tests and the dedicated simulator for the last FENIX prototype are stated.

The contents discussed in this chapter have been partially presented in the conference paper "Preliminary results of FENIX: Front-End GNSS Interference eXcisor" [147], and they have been defended in the BSc thesis "Real-time radio-frequency interference mitigation system for radio navigation receivers" [153]. Moreover, they follow the MSc thesis titled "Implementation of Radio-Frequency Interference Detection and Mitigation Algorithms for Communications and Navigation" [10], and its design and intellectual property rights are protected by the US patent "System and method for detecting and eliminating radio frequency interferences in real time" [149].

9.2 Block diagram

This section presents the main building blocks of FENIX divided into two different diagrams. These block diagrams describe the main operations carried out into FENIX without entering into the specific parameters of each prototype. As discussed above, the architecture of FENIX is scalable, and it may be implemented in several ways depending on the ultimate setup and application.

The functional block diagram of the system can be divided into two sub-blocks: an external analog RF stage, and an internal digital SP stage. The former one conditions the signals collected from the antenna, and it delivers them to the GNSS device; whereas the latter one filters and excises undesired RFI and jamming signals from useful GNSS signals. As it will become clearer in the next subsections, the SP stage is embedded into the RF stage.

9.2.1 RF stage

In the RF stage, the signal coming from the antenna (which may be RFI-contaminated or not) is amplified, filtered, down-converted, and digitized for subsequent processing in the FPGA. After that, the already processed signal is up-converted to the original frequency band, filtered once again, and attenuated in order to keep the GNSS receiver out of saturation. This is the main reason that makes FENIX transparent to the receiver, providing increased versatility as compared to other RFI detection and mitigation systems. Figure 9.1 illustrates a block diagram of the RF stage.

The input signal, which may be corrupted or not, enters into the FENIX board through a Sub-Miniature version A (SMA) connector. The signal is first amplified using a LNA in order to maximize the Noise Figure (NF) of the overall chain. This is especially necessary

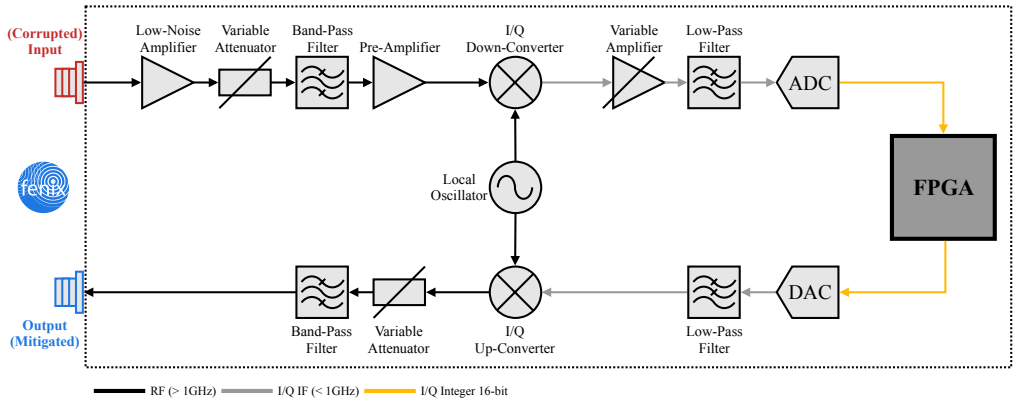

Figure 9.1: RF stage of FENIX.

if a passive antenna is used in the setup since the power losses of the first elements constrain the overall NF. Moreover, GNSS signals captured by the antenna have very low power, on the order of -125 dBm according to [139], and therefore they must be first amplified to adapt their power level to the dynamic margin of the following elements of the chain. On the contrary, if a high-gain GNSS antenna with integrated LNA is connected to the FENIX, the receiving chain may enter into saturation. In order to avoid that, a programmable and variable attenuator is placed after the LNA.

After that, a band-pass filter tuned at the desired frequency is placed. The purpose of the filter is two-fold. On one hand, it rejects near-band interferences. On the other hand, it avoids saturation and oscillations in the receiving chain. In the same way, the amplifiers are also tuned to allow only the desired frequency band to pass in order to maximize the near-band rejection effect. Finally, a pre-amplifier is placed after the band-pass filter to adapt the GNSS power level to the down-conversion stage.

The analog frequency conversion stage converts GNSS signals from the L-band down to an IF or to Base-Band (BB). This down-conversion must be reverted at the end of the mitigation process. Therefore, the up-conversion must be done using the same LO. Moreover, the down-converted analog signal at IF or BB is transformed into a digital signal using an ADC. Thus, the digital signal is a representation of the received analog signal coming from the antenna at a lower frequency, filtered and digitized, and it may be RFI-contaminated. Moreover, the signal is usually down-converted using an in-phase and quadrature (I/Q) demodulator, and thus, a dual-channel ADC is used in the digitization process.

Before the digital conversion takes place, the down-converted signal is amplified and filtered again. On one hand, a variable amplifier is used to adapt the signal power level to the dynamic margin of the ADC. On the other hand, a low-pass filter avoids aliasing effects. Aliasing may enhance the effects of near-band interference. For this reason, selective low-pass filters are required before digitizing.

The GNSS signals are then digitally processed to detect and eliminate possible RFI signals. Although there are different ways of implementing the SP stage of FENIX, the digital

signal processing algorithm is implemented in real-time with an FPGA. The output of the FENIX excision algorithm is connected to a dual-channel Digital-to-Analog Converter (DAC). Then, the RFI-mitigated GNSS signals are converted back to the analog domain at IF or BB, depending on the method used in the down-conversion.

After that, the signal is low-pass filtered again to avoid aliasing, and then up-converted to the original frequency band. Recall that the same LO is used for both up- and down-conversions. This configuration cancels out the LO frequency error introduced by the system. However, the time lapse between the instants where the signal is down- and up-converted is not zero, and it depends mainly on the delay introduced by the SP stage. However, this delay is the same for all satellites, and therefore, it does not affect to the estimation of the PVT solution. If a Temperature-Compensated Crystal-Oscillator (TXCO) is used to control the LO frequency, this frequency error can be reduced down to few Hertz, and then its effect can be neglected at the receiver.

Finally, once the RFI-mitigated GNSS signal is at the original frequency, a variable attenuator is used to avoid saturation at the GNSS receiver. Furthermore, the signal is band-pass filtered again in order to reduce the coupling of the LO at the output. Eventually, the signal is delivered to the receiver using an SMA connector.

9.2.2 SP stage

As mentioned above, the SP stage is completely digital, and it is implemented into an FPGA. An FPGA device has been chosen as the optimal solution due to the high throughput, large number of logic cells, and pipeline architecture needed to implement the FENIX mitigation algorithm. Figure 9.2 illustrates a block diagram of the SP stage.

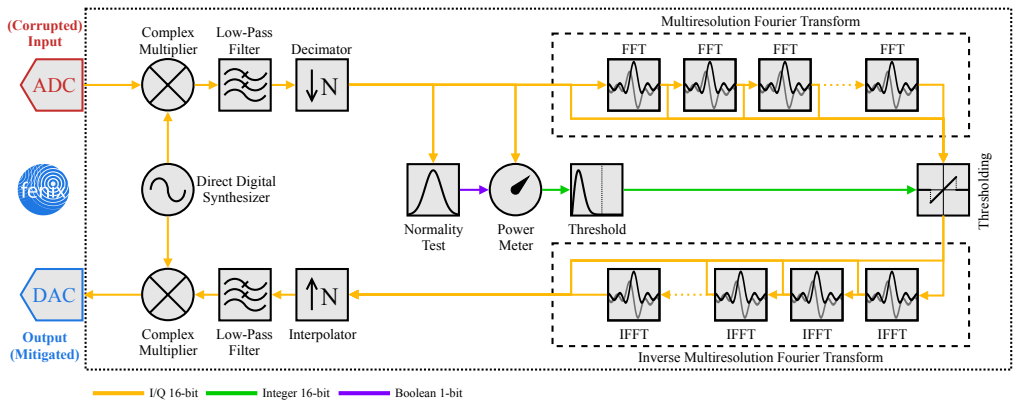

Figure 9.2: SP stage of FENIX.

The signal digitization and quantification at the ADC is performed with 12, 14, or 16 bits for each I/Q component. A value larger than 12-bit ensures a low quantification noise, and a large digital dynamic range (> 72 dB). Moreover, if the analog signal is sampled at a IF, a second and digital down-conversion is performed using 16-bit complex multipliers. The digital LO is implemented using a Direct Digital Synthesizer (DDS), which is used for both up- and down-conversion as in the RF stage. This second down-conversion is

used to remove the leakage of the analog LO. Moreover, if the signal is sampled at BB, this stage is removed.

Once the signal is at BB, it is low-pass filtered and decimated. This step is done only if the signal has been over-sampled at the ADC. This low-pass filter is performed with a Finite Impulse Response (FIR) filter with a large number of coefficients (> 128). Thus, it provides a good rejection for near-band RFI signal thanks to its high selectivity. The decimation stage is done in order to relax the clocking requirements of the following stages. As in the frequency conversion stages, the signal is interpolated to the original frequency rate, once the mitigation algorithm is applied.

Once the signal has been decimated, two tasks are performed in parallel. In the central branch, a normality test is first applied to the digital data in order to determine if the incoming samples are RFI-contaminated or not (i.e. they follow a Normal distribution or not). Thus, the properties of the signal in the statistical domain are first used to take the necessary actions in the RFI mitigation process. The result of the normality test can be obtained as a combination of independent statistical tests such as the complex kurtosis (see Appendix F) and the A-D test [26]. In this case, the complex kurtosis is used as a principal normality test, whereas the A-D test is used as an auxiliary flag to check if the kurtosis is working at its blind spot [25].

If the Normality test determines that the decimated BB samples are Normal (its output is *true*), their power (i.e. their variance σ_n^2 if zero mean) is estimated in order to obtain the threshold value (see Chapter 8). There are several procedures to estimate the power of the RFI-free samples. The simplest approach consists of using the unbiased sample variance (see Appendix F). One of the main drawbacks of this approach is the bias introduced by outliers, which may be likely to appear in RFI environments. A more trustful approach is to use robust estimators such as the Median Absolute Deviation (MAD) or the Inter-Quartile Range (IQR), which provides results less affected by outlier values [53, 154].

Once the variance of the noise has been estimated, the threshold α can be obtained as a function of the desired probability of false alarm, P_{FA}. As mentioned in Chapter 8, suitable values for P_{FA} for GNSS signals are in the range from 10^{-5} to 10^{-6}, because of their spread-spectrum correlation gain. The threshold value can be obtained both from the power of the samples (i.e exponential or chi-squared distribution), or equivalently from their root square or absolute value (i.e. Rayleigh or chi distribution). The last option is chosen in order to keep the samples working at 16-bit integer precision. Therefore,

$$\alpha = \sqrt{2}\,\sigma_n \sqrt{ln\left(\frac{1}{P_{FA}}\right)}. \tag{9.1}$$

Moreover, in the upper branch, the time-frequency decomposition of the BB samples is performed using the already mentioned MFT. A set of FFT blocks with different lengths are calculated simultaneously from the BB data. Since they have different transform length, they have different time-frequency resolution.

The MFT is an extension of both the STFT and the WT. While the Fourier transform carries out an analysis of a uni-dimensional signal in the frequency domain, the STFT is bi-dimensional in the domains of time and frequency. The WT also carries out an

analysis in two dimensions, but taking into account the time and the scale. However, the MFT directly combines the three transforms to give a representation in three dimensions, a mathematical space defined by the domains of time, frequency, and scale. In this way, the RFI signals are projected into different orthogonal spaces with different ratios of time-frequency resolution. As discussed in Chapter 5, the probability of being a version sufficiently similar to the interfering signal received in the base of the transform is maximized so as to be able to be detected in the subsequent step, once it is compared with the corresponding transformation of the useful signal. The MFT was not previously used in the state of the art for eliminating RFI, and it has been demonstrated to have better behavior than other types of transforms.

At the thresholding stage, samples with magnitude larger than the threshold α are blanked out. This procedure allows to minimize the INR, thus maximizing the SNR because of the properties of the GNSS signals buried into the thermal noise (see Chapter 8). Therefore, the thresholding excises RFI-contaminated samples from the RFI-free ones. If each resolution level performs a normalized transform, the same value of α can be applied to all of them. Once the thresholding is applied, the inverse MFT is applied to transform the RFI-mitigated signal samples back to the time domain.

9.3 Setup

As mentioned in the previous chapter, FENIX has been designed to be a standalone device, to have cross-GNSS compatibility, to work at pre-correlation stage, and to be transparent to the antenna and the GNSS receiver. However, according to the architecture described in the previous section, FENIX can be partially integrated or placed according to the four possible setups presented in Fig. 9.3. The four configurations are the following:

- *Standalone*: the default setup with all its components as detailed in the previous section, and connected between the antenna and the GNSS receiver.
- *Auxiliary*: same as standalone, but in this case, the GNSS-enabled application has two GNSS receivers: a principal one and an auxiliary one. The principal GNSS receiver is left directly connected to the antenna, whereas the auxiliary one is connected with the FENIX. The principal one provides the PVT solution in nominal condition, whereas the auxiliary one, which is protected by the FENIX, can operate in denied environments. This configuration may be necessary for safety-critical GNSS applications such as aviation or defense.
- *Antenna embedded*: this configuration aims to integrate the antenna and the FENIX in a single device. A FENIX-enabled antenna can unify the power supply, and maximize the NF of the overall system. As compared to the standalone block diagram, the only difference is that the antenna is directly connected to the LNA.
- *Receiver embedded*: this configuration integrates the GNSS receiver and the FENIX in a single device. A FENIX-powered GNSS receiver simplifies the overall system since there is no need to up-convert the IF or BB signal back to the original frequency band. Therefore, the receiving chain of the FENIX, plus the SP stage, replace the front-end of the GNSS receiver.

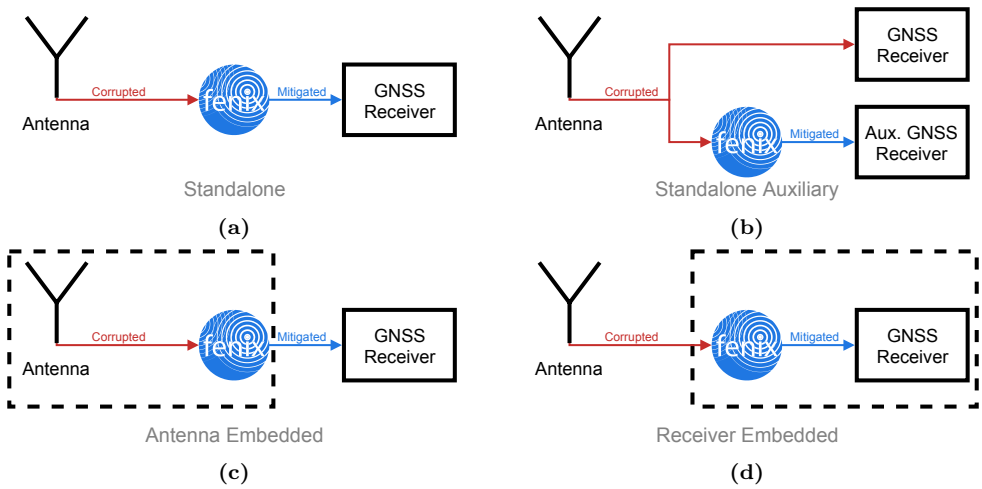

Figure 9.3: FENIX can be integrated into a GNSS-based system using different setups: (a) standalone, (b) standalone connected to an auxiliary chain, (c) integrated into the antenna, or (d) integrated into the receiver.

9.4 Prototypes

During this PhD, three different prototypes of FENIX have been implemented. This section states and summarizes the main aspects of each one of them.

9.4.1 Laboratory demonstrator

This is the first prototype, mounted using laboratory equipment, and built up with discrete components in order to maximize the customization of the receiving chain. Moreover, it is only designed to support GPS L1 C/A signal. The GPS signal is received through an active patch antenna with 30 dB of gain powered at 5 V.

Prior to the application of the RFI detection and mitigation algorithm, the received signal is amplified, filtered and down-converted from the L1 band to an IF, where it is sampled and digitized. Figure 9.4a shows the RF stage of this prototype. The selected GPS filter is the SAW filter TA1575IG that has a 2.4 MHz bandwidth, center frequency at 1575.42 MHz and 2 dB of insertion loss. The function of this filter is to reject the thermal noise and the RFI out of the GPS band. The down-conversion is performed with a Minicircuits mixer model ZFM-150-S+ connected to the signal generator R&S-SMR40 used as LO set at a frequency of 1558.78 MHz, so, it leads to an IF of 16.64 MHz.

After that, the GPS signal is digitalized with the ADC ADS4249 at a sample rate of 245.76 Msps and a maximum input voltage of 2 Vpp (10 dBm). Figure 9.4b shows the ADC/DAC board with an LPC FMC150 connector. The conversion is performed with 14 bits, which allows a minimum power signal about -84 dBm (∼6.02 dB/bit). For this reason, the microwave amplifiers placed before the ADC have such an amplification calculated to have a power of the GPS signal about -70 dBm.

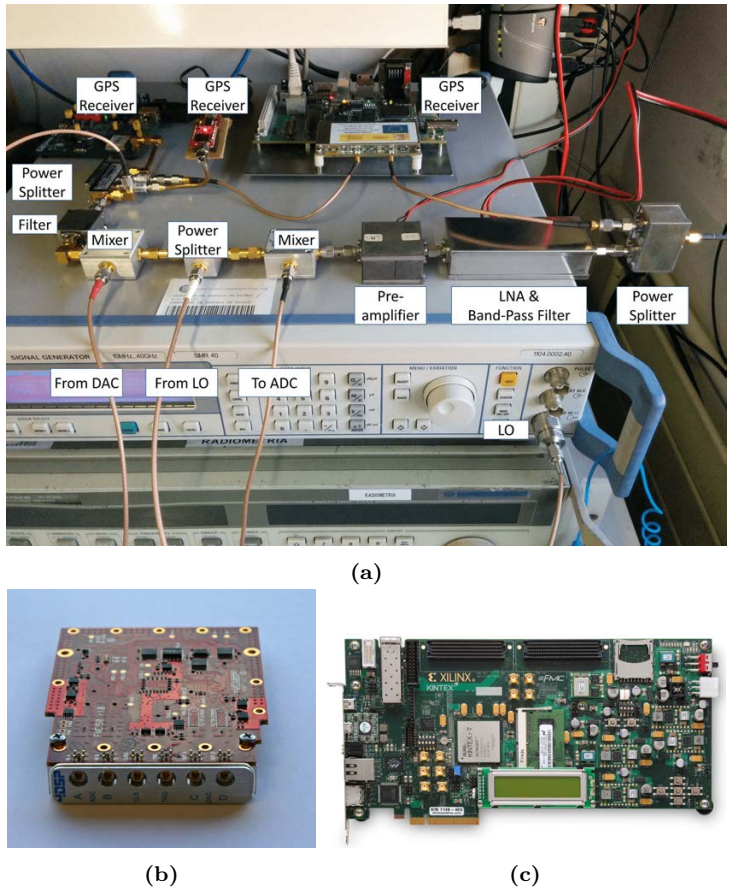

Figure 9.4: Pre-standalone or laboratory demonstrator of FENIX: (a) RF Stage, (b) high-speed ADC/DAC board, and (c) Xilinx FPGA Kintex-7 KC705 evaluation board.

The RFI detection and mitigation algorithm is implemented using a Xilinx KC705 development board with a Kintex-7 XC7K325T-2FFG900C FPGA. Figure 9.4c shows the Xilinx FPGA development board. After the GPS signal processing, the digital RFI-mitigated signal must be analog-converted and up-converted to the L1 frequency band. This up- and down-conversion of the GPS signal carrier allows to process the signal digitally at a moderate sampling rate and makes the anti-jamming hardware transparent to the GPS receiver. The DAC model is the DAC3283 with 16-bit conversion, an internal sampling clock of 491.52 MHz and a maximum output voltage of 1 Vpp. After that, the up-conversion is equivalent to the down-conversion. It is performed with a ZFM-150-S+ mixer and with the same LO signal from the R&S-SMR40 generator. Finally, the RFI-mitigated signal is attenuated and connected to the test-bed of commercial GPS receivers.

In this prototype, the MFT transform was replaced by a bank of FIR filters, since at the time of this implementation the research regarding the MFT was still in a premature stage. The bank of filters has two sub-stages. The first one consists of a digital Band-Pass

Filter (BPF) with a decimation block in the receiving chain and an interpolation block in the transmitting chain. This filter has the mission of removing near-band RFI signals, attenuate spurious signals generated in the previous stages of the analog hardware and preventing from aliasing during the decimation process.

This BPF is a FIR filter with 2048 coefficients Dolph-Chebyshev window with parameter $\alpha_{D-C} = 3$. The filter has a central frequency of $f_c = 16.64$ MHz and a bandwidth of $B = 2.38$ MHz. Thanks to the large number of coefficients and the nature of the Dolph-Chebyshev window, it is quite sharp in the frequency domain (see Figure 9.5), and since it is a FIR filter instead of an IIR filter it exhibits good phase properties [52]. Down-sampling is performed using the undersampling method [155] with a decimation (and interpolation) ratio of $M = 48$ and using the 6th alias image (the LO frequency was chosen for this purpose). Then, the new Nyquist frequency f_n, and the central frequency of the GPS band f_0 are respectively:

$$f_n = \frac{f_s}{2M} = \frac{245.76 \text{ MHz}}{2 \cdot 48} = 2.56 \text{ MHz}, \tag{9.2}$$

$$f_0 = \frac{f_c}{2N_{alias} + 1} = \frac{16.64 \text{ MHz}}{2 \cdot 6 + 1} = 1.28 \text{ MHz}. \tag{9.3}$$

Figure 9.5a shows the frequency response of the 2048-coefficient Dolph-Chebyshev window BPF. Fig. 9.5b shows a zoom of the bandpass with vertical lines indicating: the GPS signal bandwidth (green dashed), the filter bandwidth (red solid), and the 6th under-sampling alias zone (black dotted).

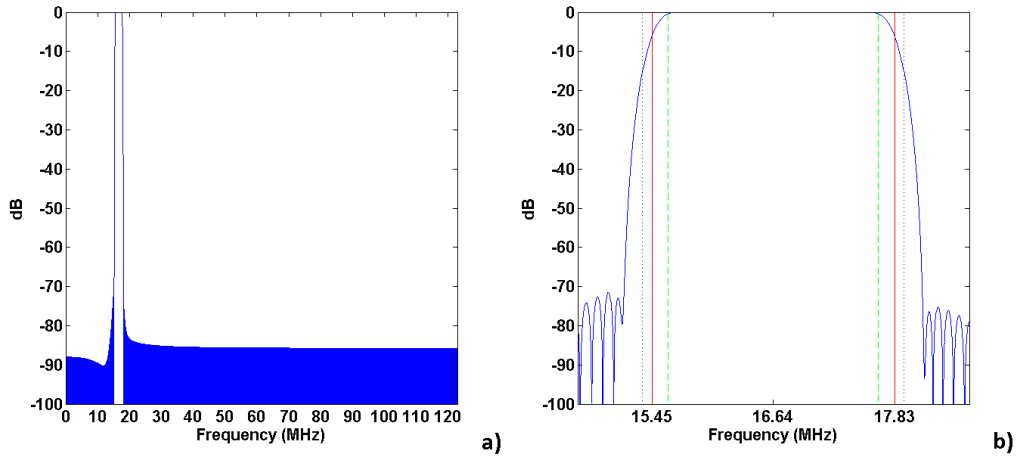

Figure 9.5: a) Frequency response of the 2048-coefficient Dolph-Chebyshev window BPF. b) Band-pass detail with vertical lines indicating: GPS signal bandwidth (green dashed), filter bandwidth (red solid) and 6th undersampling alias zone (black dotted) [10].

Moreover, the second stage is the time-frequency decomposition implemented using a bank of equal filters. The number of filters in the bank is just five because of hardware

constraints. The first of these filters is a low-pass FIR filter with a 17-tap Hann window which has very good properties to implement the inverse filter sum technique. The rest of the filters are equidistant translations in frequency (see Figure 9.6a) of the first filter (which resembles the definition of the DFT), which are grouped in such a way to obtain five real filters as follows:

$$h_k[n] = v[n] \cdot e^{-i2\pi \frac{kn}{M}}, \quad L = 2M + 1, \tag{9.4}$$

$$h_i^{FB}[n] = \left(h_i[n] + h_{M-i}[n]\right)/2, \quad i = 0, ..., 4. \tag{9.5}$$

These filters are designed in such a way that the sum of the Fourier transform of each of them is constant or almost constant. This is called the Filter Bank Sum condition. Therefore, the inverse of the filter bank analysis part is just the sum of the outputs of all the five channels. The Filter Bank Sum condition is given by $L = 2M + 1$ for a Hann window, it is the minimum value of L for which the condition is satisfied. These filters have $L = 17$ coefficients which means $M = 8$ translations in frequency and eventually $N = 5$ filters in the bank. As is shown in Figure 9.6b, the sum of the filters is almost a constant, the maximum ripple is approximate $\Delta H = 0.5$ dB which can be considered as low enough in this case.

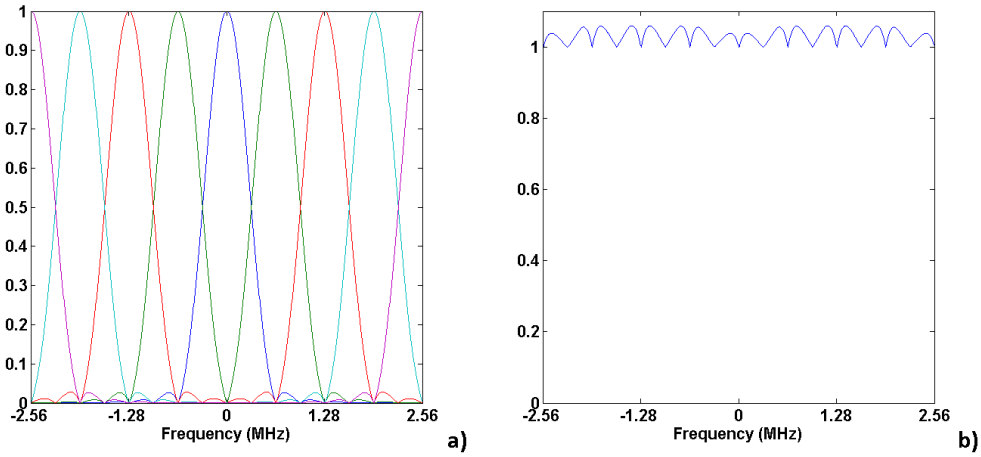

Figure 9.6: a) Frequency response of the Filter Bank composed by eight Hann window filters grouped in five real filters (in linear units). b) Filter Bank Sum condition is satisfied with a small ripple smaller than 0.5 dB (in linear units) [10].

This setup was validated using several GPS receivers, and monitoring the output signal in time and frequency with different laboratory equipment. This could be done because it was built using discrete components. Figure 9.7 shows some captures of the real-time demonstration of this FENIX prototype. Describing the steps from left to right, and top to bottom:

Figure 9.7: FENIX pre-standalone demonstration.

1. Initial setup. The commercial jammer (blue box) followed by 60 dB attenuator before its antenna is OFF. The GPS (green board) performs normally with an antenna located outdoors.
2. There is no evidence of RFI in the spectrum (frequency domain).
3. Neither in the oscilloscope (time domain). There is just thermal noise.
4. The satellites are tracked correctly (dots in the polar plot are dark blue)
5. Jamming setup. The jamming generator is turned ON.
6. The jamming spectrum is clearly seen in the analyzer.
7. The oscilloscope shows a saturated signal at the input of the GPS receiver.
8. Tracking of satellites is lost (dots in the polar plots are light blue).
9. FENIX mitigating setup. Now, the jammer is turned ON, but FENIX is activated too.
10. The spectrum analyzer shows an attenuated or mitigated RFI signal.
11. So is the signal in the time domain

12. With FENIX, GPS satellites are all tracked again, and a PVT solution is provided despite the lower C/N_0.

9.4.2 FENIX-Wide

FENIX-Wide is the second prototype of the FENIX hardware. FENIX-Wide is designed to work with wide-band GNSS signals at a single frequency band. FENIX has been implemented using an Universal Software Radio Peripheral (USRP) model x310 (see Figure 9.8c) equipped with an SBX-120 daughter-board (see Figure 9.8b), together with several external discrete RF components that will be detailed subsequently. Therefore, it is the first prototype that can be considered to be standalone, since all components can be placed in a single enclosure.

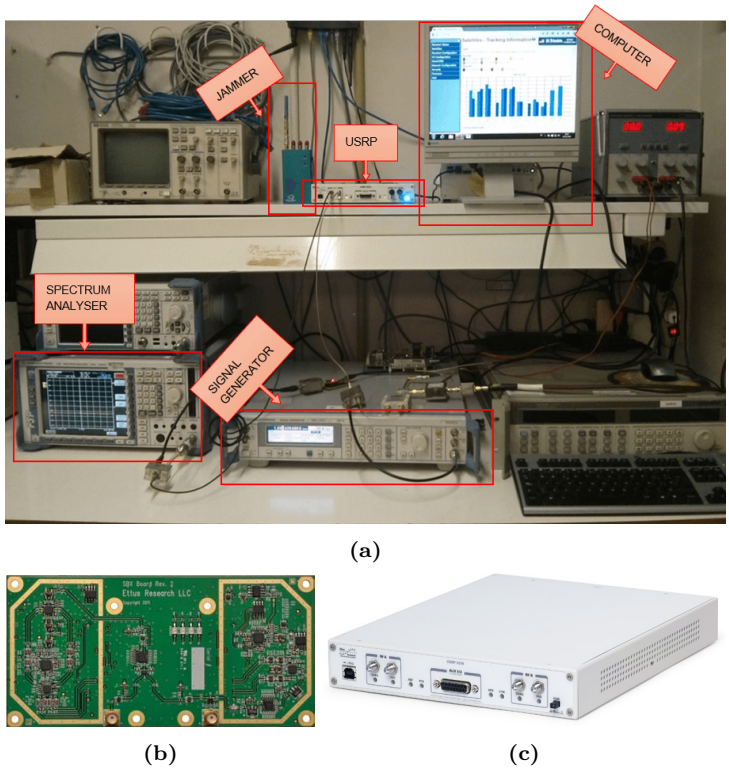

Figure 9.8: (a) Test-bed of FENIX-Wide, the second prototype of FENIX, (b) SBX-120 USRP daugtherboard, and (c) x310 USRP motherboard.

The SBX-120 board is a full-duplex wide-band transceiver that covers a frequency range from 400 MHz to 4.4 GHz by tuning its LO, and it has a bandwidth of 120 MHz. Therefore, the receiving chain can be tuned to any GNSS band such as L1 (1575.42 MHz), L2 (1227.60 MHz), or L5 (1176.45 MHz). Combined with the USRP x310 motherboard, the received signal is sampled at 200 MHz with 14-bit I/Q samples and eventually decimated to 50 MHz at BB. Moreover, an LNA, a couple of band-pass filters, and a set of attenuators are also used to condition the signal at the input and output of the SBX-120 board.

All components are tuned to the selected working band. In addition, the gain of the receiving channel is programmable with a maximum value up to 37.5 dB. Furthermore, the SP stage is implemented in a Xilinx XC7K410T FPGA that is embedded in the USRP motherboard.

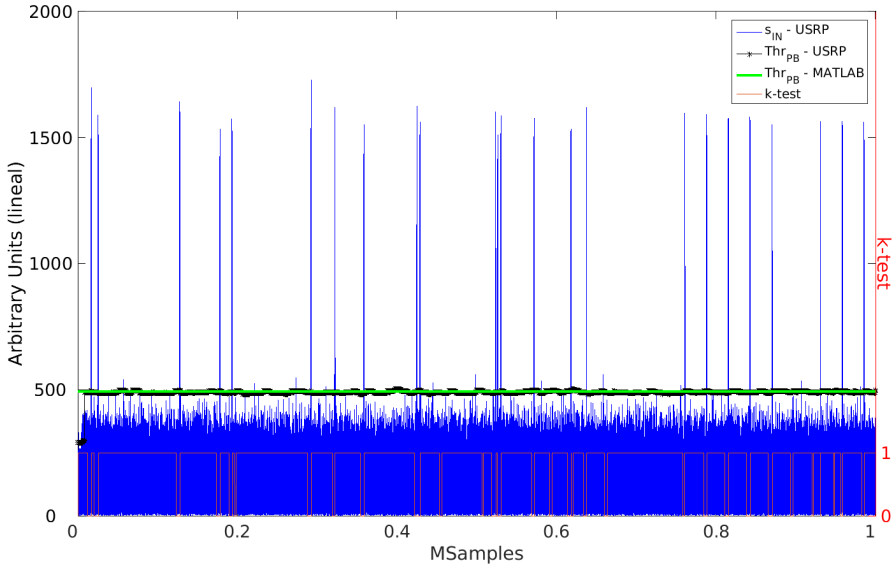

Figure 9.9: Blanking of DME pulses at L5 band using the FENIX-Wide [153].

The FENIX-Wide performance has been tested using the setup shown in Fig. 9.9a. The most relevant test with this prototype has been performed by capturing real RFI-contaminated signals at GPS L5 band. As mentioned in Chapter 2, the DME signals used for radio-navigation purposes share partially the GNSS band at L5/E5 band. Figure 9.9 shows the detection performance of the DME pulses in FENIX. The threshold is obtained from the samples at BB as explained in the previous section. Besides, its value is compared to the expected threshold value obtained through simulations. In addition, the result of the complex kurtosis test (k-test) is also shown. The results show that the kurtosis is a good detector of the DME pulses, and then, the threshold value obtained in real-time can be used to perform the blanking of DME pulses.

Even though the FENIX-Wide was conceived for wide-band GNSS signals, its design is not portable. For this reason, a smaller form version with advanced performance has been implemented in parallel: the FENIX-Lite.

9.4.3 FENIX-Lite

FENIX-Lite is the third prototype of the FENIX technology. It is implemented using an USRP model B205mini. This USRP device has a small form factor of about 9x5x2 cm, and it is USB-powered. Thus, it is completely portable and easy to integrate with already existing GNSS-based systems.

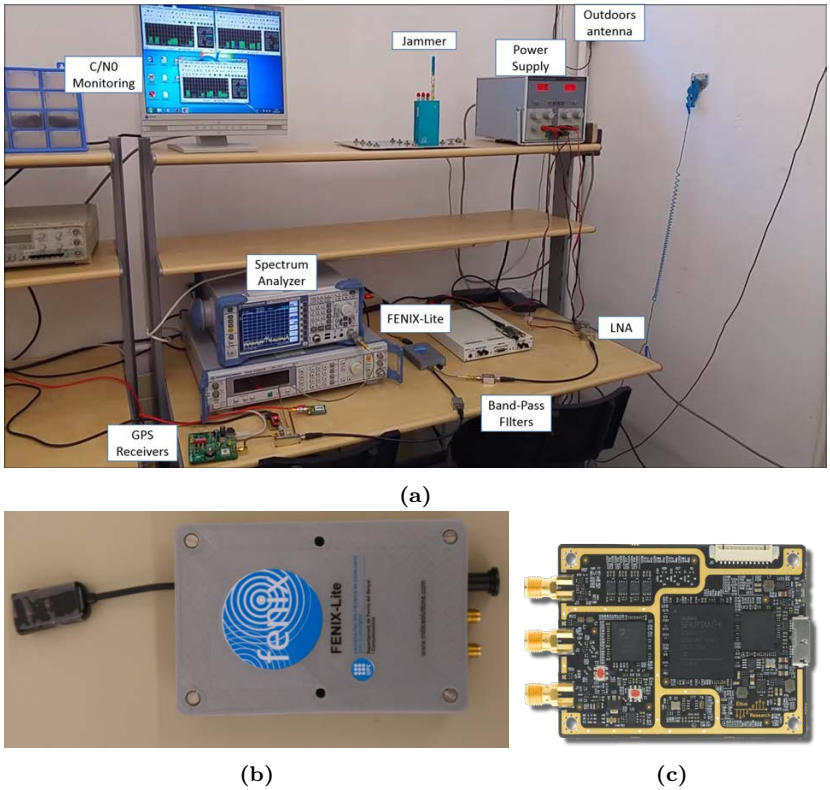

Figure 9.10: (a) Test-bed of FENIX-Lite, the third prototype of FENIX, (b) 3D-printed enclosure, and (c) B205Mini USRP device.

The USRP B205mini board, shown in Fig. 9.10c, integrates an AD9364 RF transceiver together with a Xilinx FPGA model Spartan-6 XC6SSLX75-CSG484. The AD9364 fulfills most of the requirements of the FENIX RF stage. It has an integrated 12-bit ADC and 14-bit DAC, the LO can be tuned in a wide range from 70 MHz to 6.0 GHz, its maximum bandwidth is about 56 MHz, and its NF is lower than 2.5 dB. The SP stage is implemented into the Spartan-6 FPGA.

In order to operate at L1/E1 band with narrow-band codes, the LO frequency is set to 1551.251625 MHz. Thus the L1 GNSS is down-converted to an IF frequency equal to 24.168375 MHz. Moreover, in the SP stage, a second digital down-conversion is performed to place the GNSS band to BB. GNSS signals are sampled at 55.242 Msps (54 x 1.023 MHz), and then decimated by a factor of 9 to 6.138 Msps (6 x 1.023 MHz).

Furthermore, a customized enclosure has been designed and manufactured using a 3D printer (see Fig. 9.10b). This enclosure contains the USRP board plus an RPi Zero that performs all the required actions to configure the FENIX. Besides, the FENIX-Lite has been tested using the test-bed as shown in Fig. 9.10a. GNSS signals can be obtained from either an external antenna or a R&S vector signal generator model SMU-200A. RFI and jamming signals can be generated using either a commercial jammer or a R&S signal

generator mode SMR-40. Eventually, the performance of FENIX-Lite is assessed using either a set of commercial GNSS receivers or the test paths and tests points described in the following sections.

9.5 Test paths and test points

9.5.1 Test paths

The SP stage of FENIX is designed in such a way that different signal paths can be used to tests the performance of its building blocks. In particular, its pipelined structure allows to implement loopback paths, and then to measure the response between its input and output. A total of seven different paths are implemented in the FENIX-Lite SP architecture. The configurable signal paths are the following:

1. *Raw loop*: a direct connection between the output of the ADC and the input of the DAC can be used to test the performance of the RF stage (see Fig. 9.11a).

2. *BB loop*: a connection between the output of the decimator and the input of the interpolator allows to test the performance of the digital down-conversion and the digital band-pass filtering blocks (see Fig. 9.11b).

3. *FFT loop*: a loopback connection through one of the building FFT block of the MFT, and its corresponding inverse FFT block, allows to test the performance of all FFT transform functions (see Fig. 9.11c). A selector allows to choose which FFT blocks are active and which ones are not.

4. *MFT loop*: a connection between the output of the MFT and the input of the inverse MFT allows to test the full data path without applying the thresholding function (see Fig. 9.12a).

5. *PB*: the thresholding block is directly connected to the BB signal bypassing the MFT transform (see Fig. 9.12b). It allows to test the thresholding function, and it acts as a PB mitigation algorithm.

6. *SB/FB*: only one of the FFT blocks inside the MFT is used (see Fig. 9.12c). In this configuration, the system performs as an SB or FB mitigation algorithm regarding the active selected FFT blocks.

7. *Full operation*: the last possible configuration corresponds to the full operation path of FENIX (see Fig. 9.2).

9.5.2 Test points

Besides test paths, there is another test mechanism to check the proper performance of all the building blocks of FENIX: the test points. Test points are seven points at the SP stage where a set of data samples can be retrieved, saved and processed off-line. When one of the seven points is selected, the corresponding data samples are collected in a First-In First-Out (FIFO) memory, and then they are streamed back to a host computer that stores them in a binary file. The stored data samples can be used to debug the performance

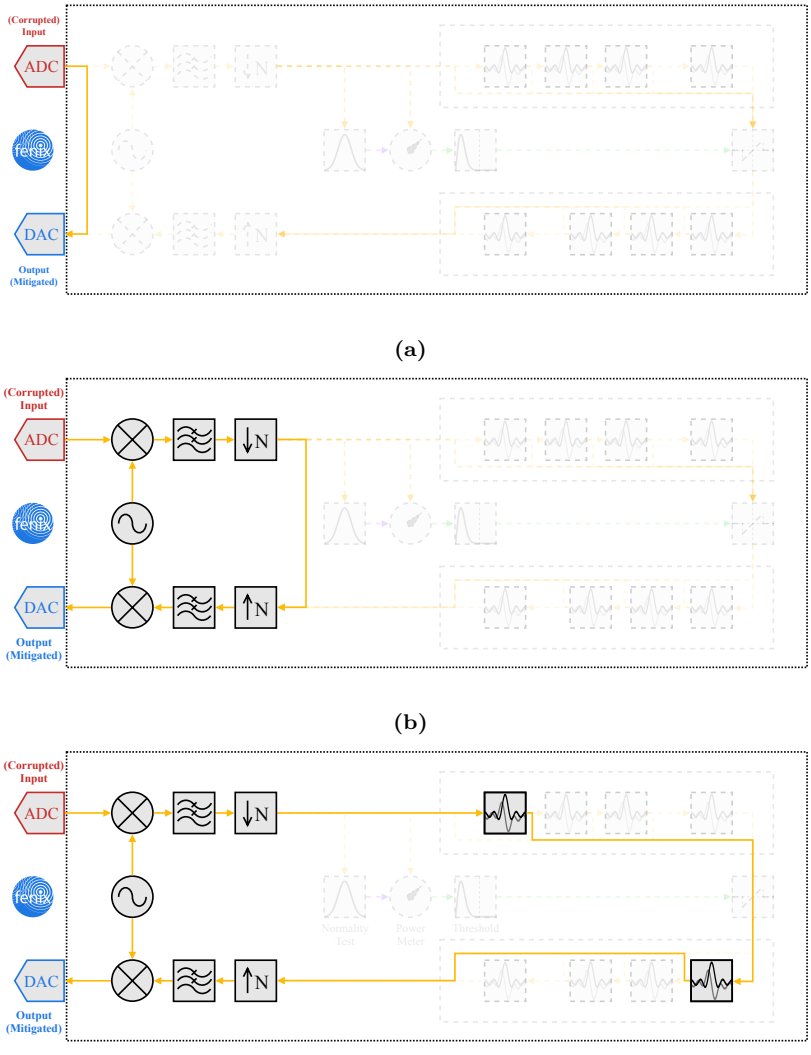

Figure 9.11: Configurable test paths 1-3 in the SP stage: (a) direct digital path from ADC to DAC, (b) BB path from decimation to interpolation, and (c) FFT path used to test direct and inverse FFT performance.

of each one of the building blocks, as it is done in the subsection corresponding to the hardware validation.

There are seven test points. The position of each of them is depicted in Fig. 9.13. The data samples captured at each test points are the following:

1. TP1: I/Q samples at the output of the ADC.

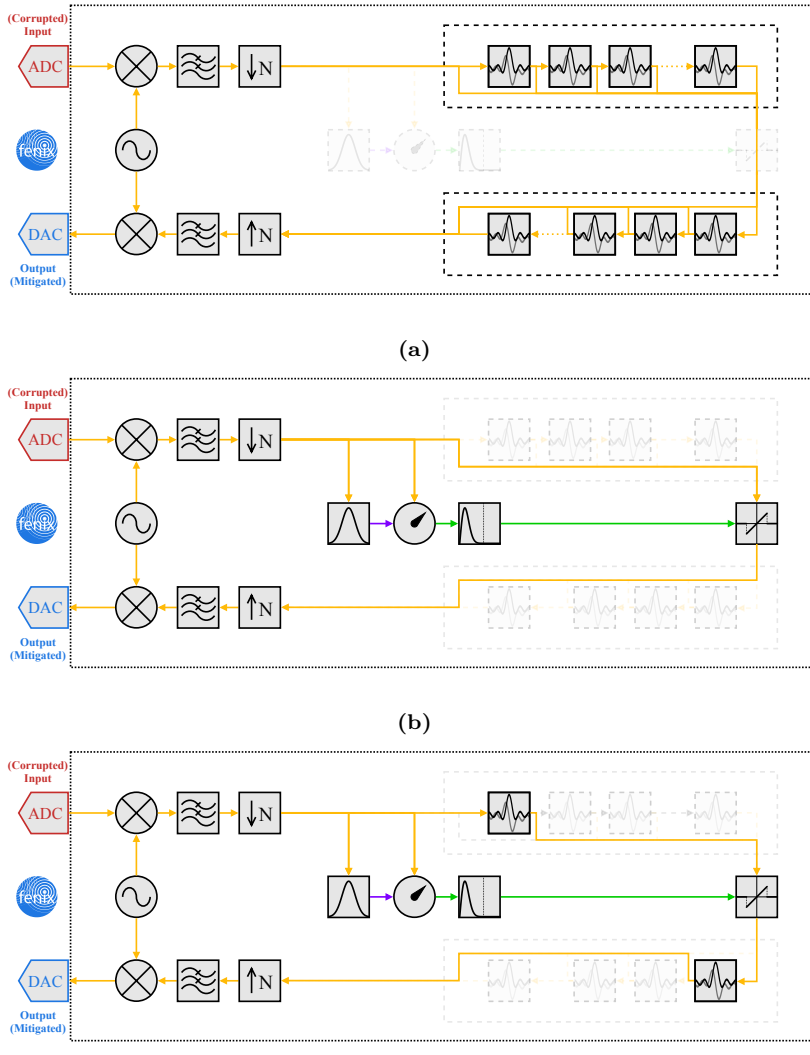

Figure 9.12: Configurable test paths 4-6 in the SP stage: (a) MFT path used to test direct and inverse MFT performance, (b) pulse blanking path used to test threshold calculation and thresholding operation, and (c) frequency blanking path used to test threshold calculation and thresholding operation together with direct and inverse FFT operation.

2. TP2: I/Q samples at the input of the DAC.
3. TP3: I/Q samples at the output of the digital down-converter.
4. TP4: I/Q samples at the input of the digital up-converter.
5. TP5: I/Q samples at the output of the MFT. The FFT selection value allows to

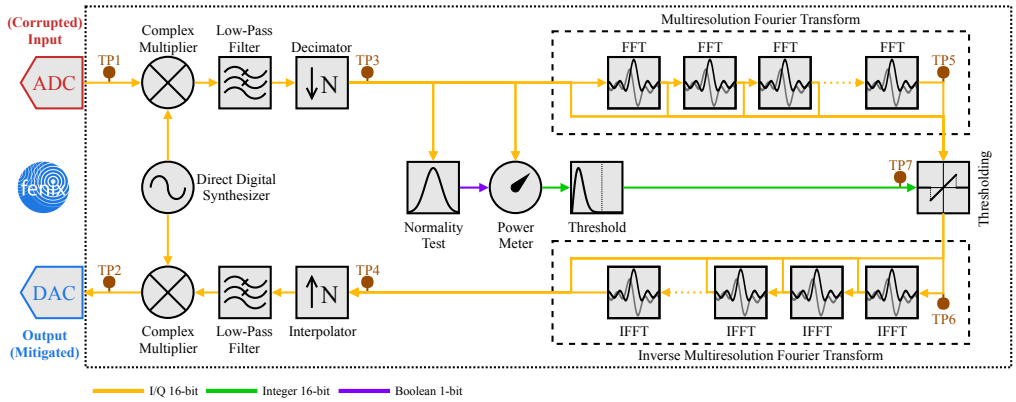

Figure 9.13: Configurable test points of the SP stage of FENIX.

choose which are the active FFT blocks in the MFT.

6. TP6: I/Q samples at the input of the inverse MFT. Since it is just after the thresholding stage, it allows to check the performance of the blanking at each MFT level.
7. TP7: estimation of the noise power, and value of the complex kurtosis.

9.6 FENIX-Sim

The development of the FENIX prototypes is an end-to-end process. The design of the hardware architecture starts with the mathematical principles and ends up with real-time tests. In the middle of this process, simulations must be done in order to check the performance of the design. Since the SP stage is completely digital, its performance can be well characterized and studied using these simulations. To do so, the FENIX simulator, or FENIX-Sim, has been developed, and an example of its results is presented in this section.

The FENIX-Sim accounts for the main differences between the mathematical model of FENIX, named *Ideal* and the one assessed in Chapters 5 and 8, and its real hardware implementation.

First, the input signal is quantified and limited by the ADC. A large number of bits ($>$ 12) has been chosen to minimize the effects of quantification. However, the level of the input signal is always limited by the maximum value of the dynamic range of the ADC. This limitation effect is likely to happen when a strong enough RFI signal is present at the input of the ADC.

Moreover, some of the blocks used in the FPGA design have been implemented by using available Xilinx IP cores. The inner design of these functions is not open, so that, their architecture cannot be implemented directly in the simulator. However, Xilinx provides C models of their IP cores which can be embedded into the simulator. The most important blocks necessary to simulate the data path processing are the decimator and interpolator BPFs and the forward and inverse FFTs.

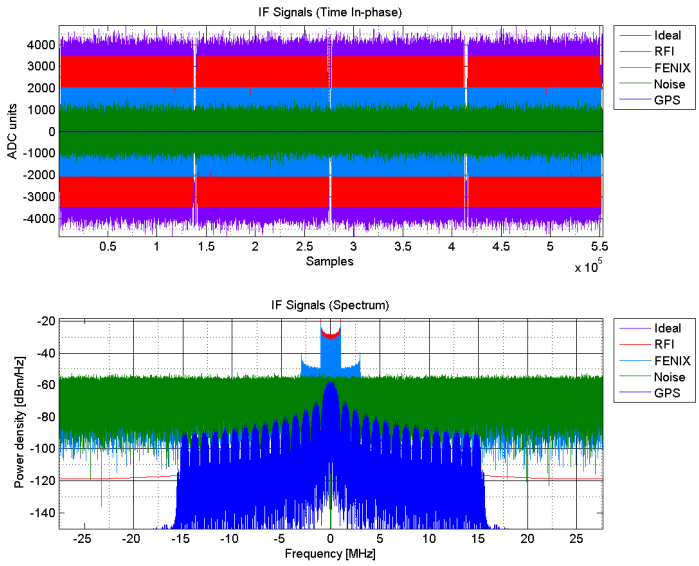

Figure 9.14: The upper sub-figure shows the time evolution of the In-phase component of the Ideal, FENIX simulated, GPS, thermal noise, and RFI signals at IF. The lower sub-figure shows the spectra of all these signals.

In order to show the performance of the FENIX-Sim, an example case with ADC saturation is studied. The FENIX-Sim first generates the GNSS, thermal noise, and RFI signals, and then, it simulates the behavior of the ADC. Both Ideal and FENIX (i.e. non-ideal) cases are simulated. As mentioned above, the Ideal case does not take into account the effect of the real implementation, but it does account for the MFT blanking.

Figure 9.14 shows the IF signals at the ADC. The three generated signals at its input are a GPS L1 C/A satellite signal ("GPS"), CWGN ("Noise"), and a chirp with 2 MHz of bandwidth and 200 Hz of repetition frequency ("RFI"). "Ideal" represents the addition of the three signals (without ADC effect), and "FENIX" is the output of the 12-bit ADC. The C/N_0 has been set to 50 dB·Hz, whereas the SIR has been set to -40 dB. Besides, all signals are taken centered at the input band for the sake of simplicity, but without losing generality.

The upper sub-figure represents the In-phase time signal. It can be appreciated that the output of the ADC is saturated since its values range between -2^{11} and $2^{11}-1$. Moreover, the lower sub-figure shows the spectra of the five signals. The GPS spectrum is below the noise despite the C/N_0 value, and the spectrum of the FENIX signal after the ADC has bee distorted due to the saturation effect. The clipping of the saturated ADC generates aliases of the original signal, which appear next to the original signal band. In the case of the Ideal signal, the aliases do not appear, as expected.

The IF signals are down-converted to BB, filtered and decimated. Figure 9.15 shows both the In-phase time and spectrum of BB signals after all these processes. In the In-phase

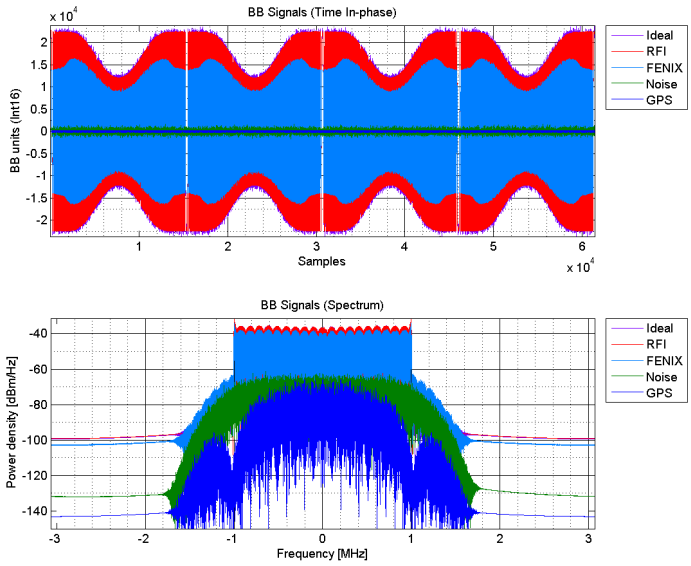

Figure 9.15: The upper sub-figure shows the time evolution of the In-phase component of the Ideal, FENIX simulated, GPS, thermal noise, and RFI signals at BB. The amplitude modulation appears because the RFI signal is sweeping across the input bandwidth of the receiver. The lower sub-figure shows the spectra of all these signals.

time sub-figure, RFI, Ideal and FENIX signals show an amplitude modulation due to the band-pass filtering. Moreover, the ordinates axis has been extended now to 16-bit values.

The BB signals are then transformed using the MFT. Hereinafter, only Ideal and FENIX signals are considered. In the FENIX-Lite, 4 resolution levels (L0 to L3) are taken into account. Besides, the FFT size of each level grows as a power of 16. Therefore, the FFT lengths of each level are 0 (no FFT) at L0, 16 at L1, 256 at L2, and 4096 at L3. Figure 9.16 shows the serialized output of the FFT corresponding to each resolution level. Moreover, the computed threshold value is also plotted or each case. It can be appreciated that for both L0 and L1 almost all samples are above the threshold level, and thus, they will be discarded at the thresholding stage. Nevertheless, at levels L2 and L3, some samples will remain after the thresholding stage.

The RFI-mitigated signal is obtained by applying the inverse MFT transform to the remaining samples after the thresholding stage. Figure 9.17 shows the comparison between the absolute time and spectrum of the both Ideal and FENIX signals before and after the mitigation process. Besides, threshold values are also plotted for comparison purposes. It can be appreciated that the overall power of the mitigated signal is much lower than it was at the input. This is due to the blanking of samples with a larger power, equivalent to the blanking bias effect studied in Chapter 5. Moreover, the mitigated spectrum is flatter than at the input because most of the RFI power has been removed. Furthermore, the blanking process introduces some spikes out of the filtered bandwidth due to its intrinsic clipping effect. These out-of-band aliases or spikes are filtered out during the digital

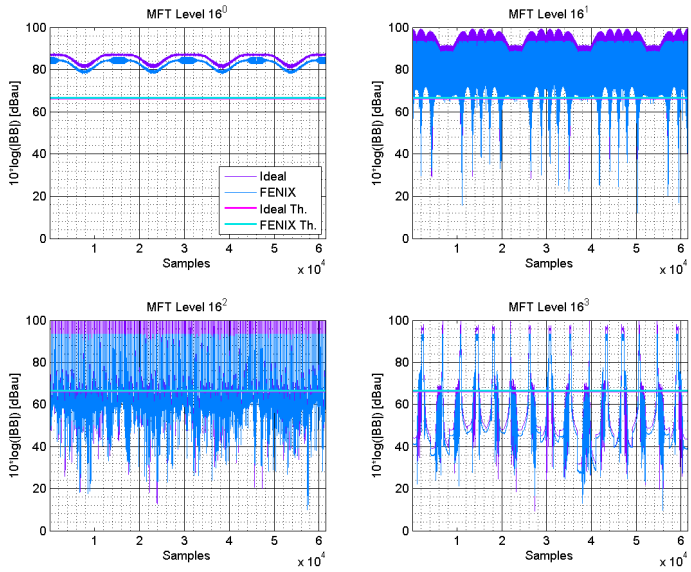

Figure 9.16: Ideal and FENIX simulated signals at different MFT levels (from 16^0 to 16^3) as they get into the thresholding stage. Both threshold levels are also overlapped.

up-conversion stage.

Eventually, the comparison between DDM computed before and after mitigation can be used to assess the final performance of the mitigation process. Figure 9.18 shows the DDMs computed using the Ideal and FENIX signals before and after mitigation. All DDMs are computed with 1 ms of coherent integration and 10 incoherent averages. Before mitigation, the correlation peak cannot be appreciated with either Ideal or FENIX signals. Even though the C/N_0 level is high (50 dB), the power of the RFI signal is too strong and then it overrides the correlation gain of spread-spectrum modulation. Recall that a DDM, the main observable in GNSS-R applications, is equivalent to the acquisition space of GNSS receiver. Therefore, a GNSS receiver cannot track the correlation peak of the satellite under the simulated conditions. However, once the FENIX mitigation algorithm is applied, the appearance of the DDM changes dramatically.

In the DDM corresponding to the Ideal signal after mitigation, two effects can be appreciated. The first is the reduction of the overall power as described above. The second, and most important, is the increase of the DDM SNR. The C/N_0 estimated from this DDM is equal to 43.2 dB·Hz. As compared to the original value, the C/N_0 has been degraded by about 6.8 dB after the mitigation process. However, this is a much better situation as compared to the results obtained before applying the FENIX mitigation algorithm.

Regarding the DDM corresponding to the FENIX signal after mitigation, the performance of the MFT blanking algorithm is good, but not as good as in the previous case. The estimated C/N_0 is equal to 39 dB, which represents a degradation of 4.2 dB as compared to the Ideal mitigated case. Besides that, the magnitude of DDM peak is lower than in

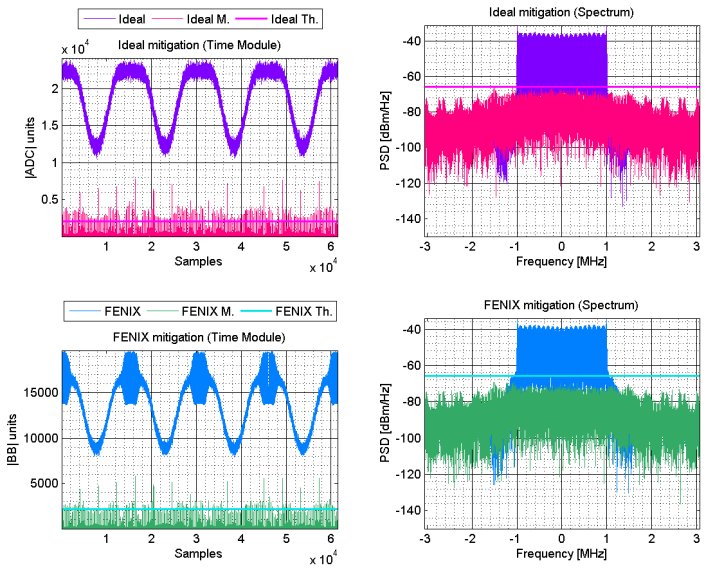

Figure 9.17: Ideal and FENIX simulated signals after mitigation by thresholding. Left sub-figures show the In-phase time evolution, and right sub-figures show the corresponding spectra. Both threshold levels are also overlapped.

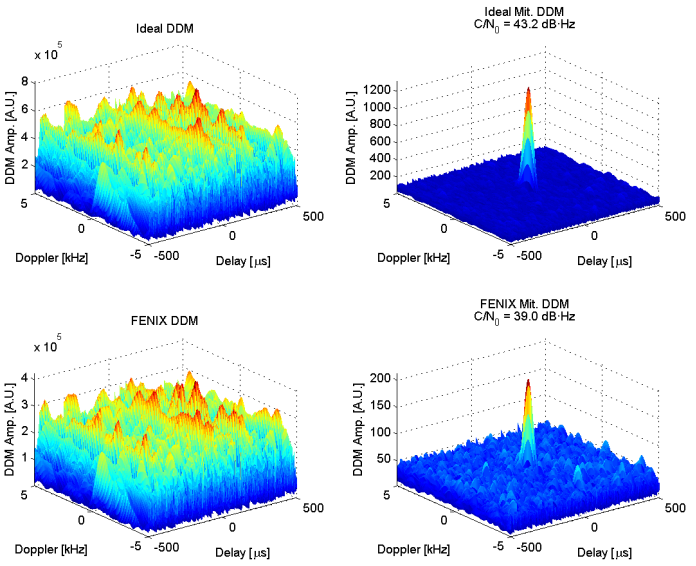

Figure 9.18: DDM comparison before and after mitigation using signals from FENIX-Sim.

the previous case.

The origin of this underperformance when comparing the FENIX and the Ideal case is the saturation of the ADC. This was one of the assumptions taken for this example in order to show how it affects to the overall performance of the FENIX mitigation algorithm. The saturation may be produced because either the RFI signal overpowers the maximum of the ADC dynamic range, or the gain of the RF stage is not optimized to maximize the dynamic range. If this is the case and the FENIX-Sim is run without saturation at the ADC, the performance of the FENIX is equivalent to the one achieved in the Ideal case. The following section shows the results of the real implemented signals under the conditions assumed in this simulation example, once the RF gain is adjusted properly.

9.7 Performance validation

This section aims to compare the data samples obtained from test points to the results from the FENIX-Sim presented in the previous section. This allows validating the proper operation of the hardware. Therefore, the same conditions as in the FENIX-Sim have been generated with real signals. GPS signals are generated by using the SMU-200A, and RFI signal with the SMR40 both from R&S. The C/N_0 is set to 50 dB·Hz, and the SIR is set to -40 dB. Moreover, the receiving gain of the RF stage has been adjusted to avoid ADC saturation as described above.

Figure 9.19 shows the In-phase time evolution and the spectrum of the IF signal captured at TP1, and the BB signal captured at TP3. The IF signal does not saturate the ADC since it ranges from ± 1600 integer steps. Its spectrum shows that GPS and RFI signals are centered at the IF frequency described before, 24.168375 MHz. Moreover, the BB signal shows equivalent amplitude modulations to the ones observed in the FENIX-Sim.

Figure 9.20 depicts the spectrograms corresponding to the four different resolutions levels of the MFT. The values of the transform have been depicted in logarithmic values just for a better visualization. At level L0, the same amplitude modulation as in the BB signal is appreciated. Levels L1 to L3 show the chirp RFI at different time-frequency resolutions. In particular, L2 contains the largest transform values, which mean that it is the best resolution level for this particular RFI signal. However, it does not mean that the rest of levels can just be discarded since they contain other features of the signal.

Figure 9.21 shows the spectrograms corresponding to each level of the MFT after the mitigation process. The transformed values are represented in linear units in this case. The maximum value is equal to 124, which corresponds to the threshold value. Values at L0 are completely wiped out, whereas only a few values at L1 remain. On the contrary, L2 and L3 show how the chirp signal has been blanked, as well as the remaining of the GPS signal at the center of the band.

Figure 9.22 shows the In-phase time evolution and the spectrum of the BB signal captured at TP4 and the IF signal captured at TP2. Both time evolution and spectrum after mitigation are very similar to its equivalent in the FENIX-Sim. BB time signal shows some spikes generated from the inverse transform of the blanked signal. However, their power is not large enough to override GNS receivers as it will become clear below. Besides, the out-of-band spikes that appear in the BB spectrum are equivalent to the ones seen

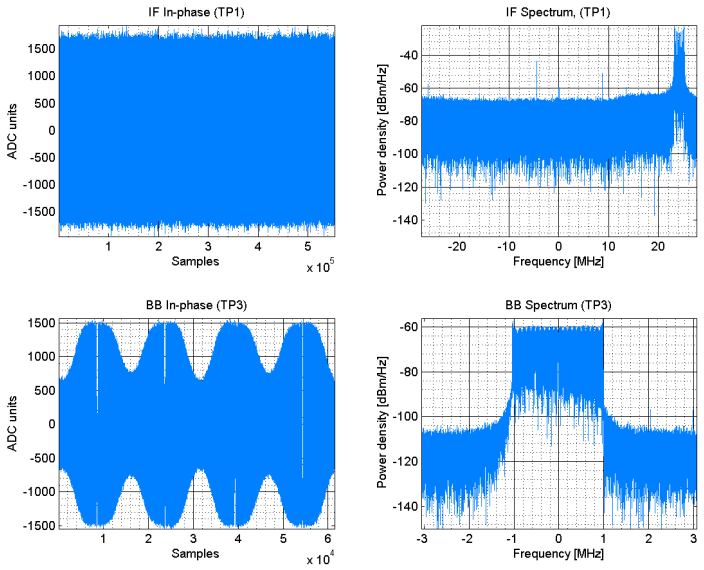

Figure 9.19: IF signal captured at TP1, and BB signal captured at TP3. In-phase time evolution and spectrum.

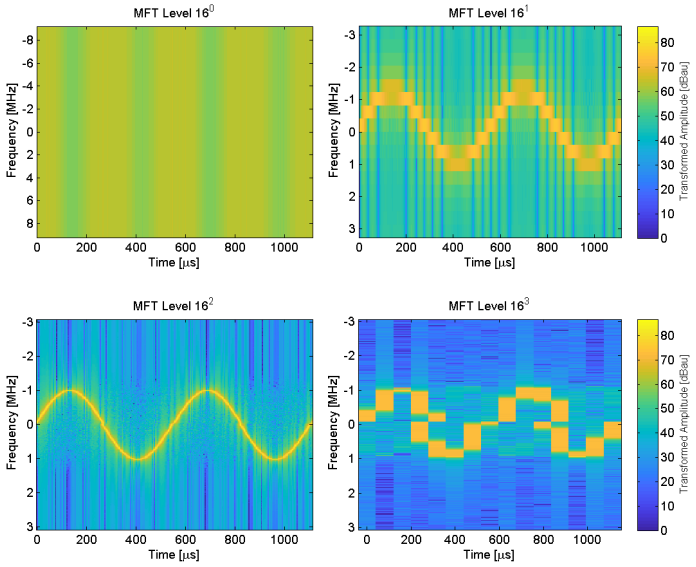

Figure 9.20: Signal at different levels of the MFT captured at TP5. The magnitude of the spectrograms is in logarithmic units for a best representation.

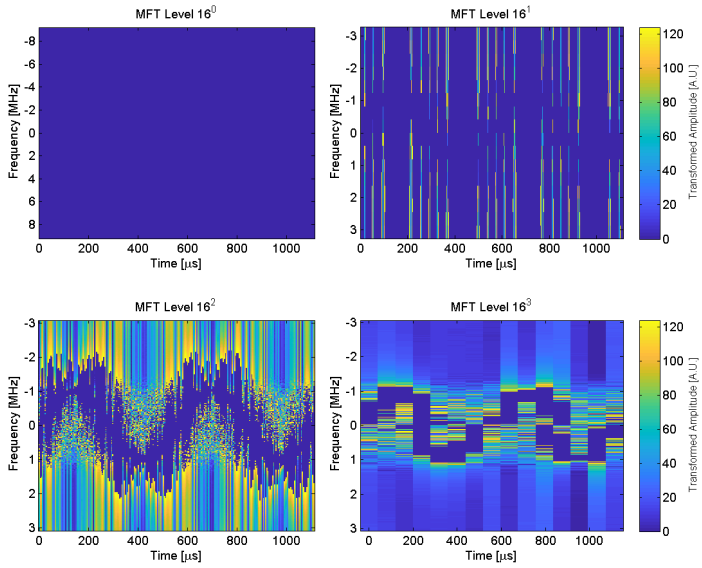

Figure 9.21: Signal at different levels of the MFT after mitigation captured at TP6. Lineal spectrograms.

in the FENIX-Sim. These out-of-band spikes are filtered by the digital up-converting stage as it is seen in the IF spectrum. Moreover, several tones appear due to the finite Spurious-Free Dynamic Range (SFDR) of the DDS. Eventually, these tones are filtered out by the RF stage.

As in the FENIX-Sim, the best way to assess the performance of the mitigation system is to compare the DDM of the signal before and after mitigation. Figure 9.23 shows both DDMs. Before mitigation, the correlation peak cannot be tracked by the GNSS receiver. However, after the mitigation, the correlation peak is clearly seen, and a value of the C/N_0 equal to 43.2 dB·Hz is estimated. This value matches the one obtained with the FENIX-Sim. This proves that the hardware has been correctly implemented according to the design requirements, and it is working in real time. Furthermore, the value estimation of the C/N_0 done by the external GPS receiver was 44 dB·Hz, yet one more proof of the performance validation.

9.8 Conclusions

This chapter describes the main building blocks of the patented architecture of FENIX divided into two main stages, the RF and the SP. According to this architecture, FENIX can operate in the main or auxiliary chains of a GNSS-enabled system, or it can be integrated into either the antenna or the GNSS receiver. The FENIX architecture has been implemented in three real-time prototypes. The most recent one, the FENIX-Lite, has several configurable test paths and test points that are used to validate its real-time

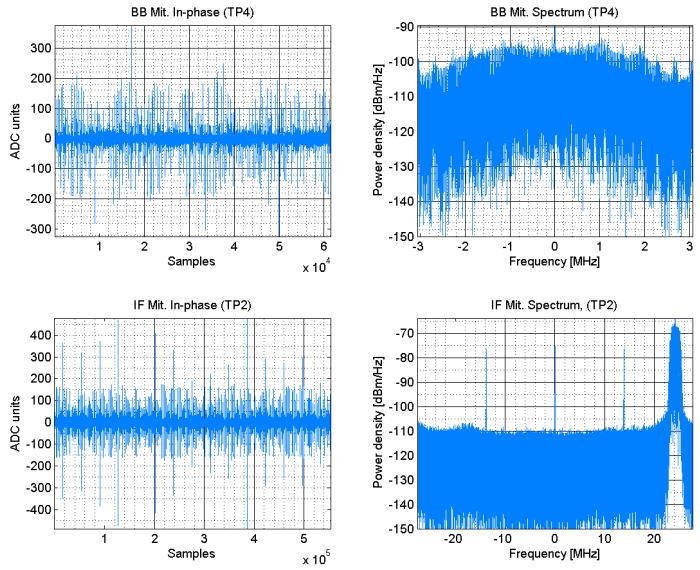

Figure 9.22: IF signal after mitigation captured at TP2, and BB signal after mitigation captured at TP4. In-phase time evolution and spectrum.

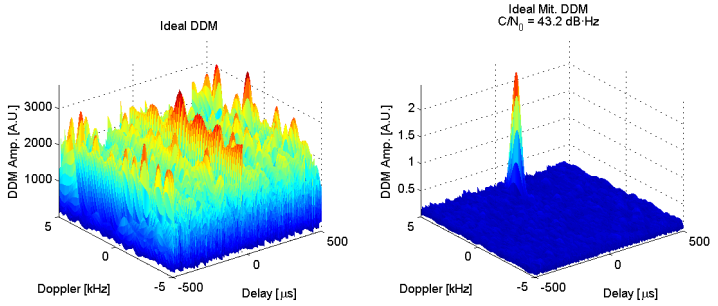

Figure 9.23: DDM comparison before and after mitigation using signals from TP3 and TP4 respectively.

performance. Moreover, a simulator named FENIX-Sim allows for testing the performance of the FENIX architecture under different RFI and jamming scenarios. An example case scenario has been chosen to validate the performance of the real-time hardware. The results show that the FENIX-Lite performs as expected in this case scenario. A discussion of which is the most representative test scenario, as well as a full assessment of the performance of FENIX is provided in Chapter 10.

10

Chapter 10

FENIX: real-time tests and timing analysis

This chapter is devoted to the assessment of the real-time performance of FENIX, and in particular, of the FENIX-Lite prototype. This is the third and last chapter of the set of three devoted to the FENIX. At the beginning of the chapter, three RFI/jamming scenarios representative of real cases, are defined. Besides, the power response and phase response of the FENIX-Lite are measured using a custom and precise setup. After that, the real-time mitigation performance of FENIX-Lite is assessed using real GNSS and jamming signals. Finally, FENIX-Lite is tested together with a commercial GNSS-enabled timing setup. All tests performed in this chapter prove that FENIX-Lite provides up to 30 dB of increased resilience against RFI and jamming signals.

10.1 Introduction

The architecture of FENIX was described in Chapter 9. It has been conceived to allow the real-time mitigation of RFI and jamming signals. Previously, in Chapter 8, the theoretical principles behind the operation were described. Besides, off-line tests with simulated and real signals were performed. This chapter presents the real-time tests performed with the FENIX-Lite prototype, which is the most advanced one by the time this PhD thesis has been written.

However, the development of an even more advanced version of FENIX is under development, which has been designed to deal with wide-band GNSS signals and multiple bandwidths simultaneously. The new design is being carried out thanks to the project PRODUCTE (2016 PROD 00062), titled "FENIX - Front-End GNSS Interference eXcisor", and funded by the AGAUR - Generalitat de Catalunya.

The contents discussed in this chapter have been partially presented in the conference papers "RFI mitigation for GNSS-R instruments: FENIX, the Front-End GNSS Interference eXcisor" [156], "Real-Time Pre-Correlation Anti-Jamming System for Civilian GNSS Receivers" [157], "FENIX, a real-time anti-jamming system for GNSS receivers" [158], "An Anti-Jamming System for GNSS Timing Applications" [159], and "Effects of Interference Mitigation in Timing Solutions of GNSS Receivers" [160]. Furthermore, the results of the FENIX assessment for GNSS-enabled timing systems has been performed in collaboration with the GMV corporation.

10.2 RFI and jamming scenarios

An RFI or jamming signal can be any undesired signal present at the bandwidth of the receiver. CW, chirp and pulsed RFI signals can be classified as signals whose energy is well-localized in the TF space. Chirp signals are usually classified as wide-band signals because their energy is spread over a frequency band. However, it can be argued that they are narrow-band signals at each time instant. The concept of TF localization is the opposite to spread or sparse in TF, which is the case of, for instance, spread-spectrum modulations. Nevertheless, they are not spread in all domains. For example, the spread-spectrum modulations of GNSS are well-localized in the delay-Doppler space. Therefore, the "spreading" of a signal is a relative term, at least in the way it has been considered in this PhD thesis.

As mentioned in Chapter 2, unintentional man-made RFI signal are well-localized in the TF space. Regarding jamming and intentional RFI signals, a spread signal requires more absolute transmitting power than, for instance, a CW signal to produce the same C/N_0 degradation at the same distance. This is the main reason why commercial jammers use TF-localized signals instead of spread-spectrum signals. Therefore, the optimization of the performance of FENIX on the mitigation of TF-localized RFI signal has two main reasons: they are the most common group of RFI signals, and the implementation of a real-time signal processing hardware is feasible thanks to the FFT.

The group of TF-localized RFI signals includes CW, chirp and pulsed signals. As mentioned in [161], a band-limited chirp signal is transformed to a pulsed signal at the output of a narrow-band enough filter. Thus, pulse-width is given by the relationship between

the bandwidths of the chirp and filter, and the pulse repetition frequency is given by the repetition frequency of the chirp. Moreover, a CW signal can be also described as a chirp with either a very low repetition frequency or a very narrow bandwidth. Figure 10.1 illustrates these relationships between CW, chirp, and pulsed signals.

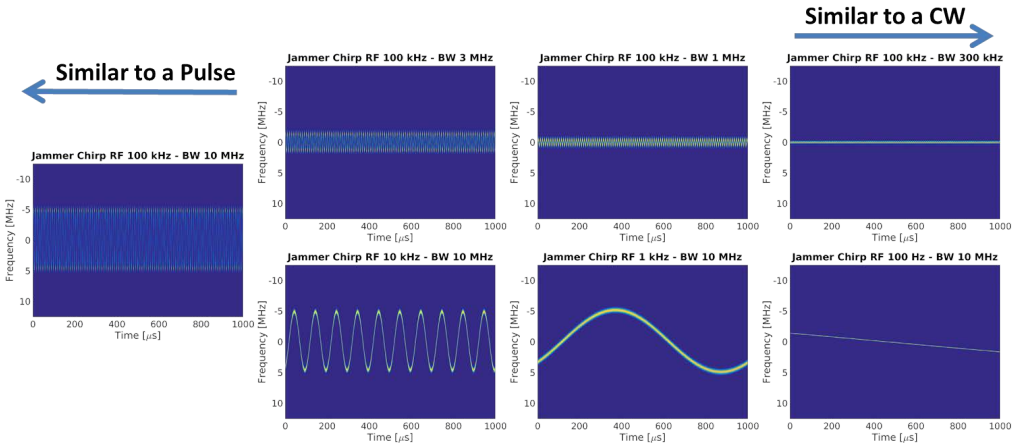

Figure 10.1: TF-localized RFI signal include CW, chirp and pulsed signals.

Even though an RFI or jamming signal can be any undesired signal present at the bandwidth of the receiver, three representative scenarios have been chosen based on the RFI surveys in the literature, and some laboratory tests. These signals are a CW and two different linear chirp signals.

CW is the most frequently observed RFI signal in the literature. It can be generated unintentionally from an inter-modulation product, a lower harmonic, or a spurious signal from a near-band service. In this work, it has been considered centered at the L1 band (1575.42 MHz) since it represents the worst case for the receiver.

Moreover, the two selected chirps signals that have been tested are also centered at the L1. The first one (*chirp #1*) has a bandwidth of 10 MHz and a repetition frequency of 100 kHz, which is the most common type of commercially available PPD. The second one (*chirp #2*) has a narrower bandwidth of 2 MHz and a repetition frequency of 200 Hz, which is one the worst type of interference according to the preliminary test performed using several GPS receivers.

In the test shown in the subsequent sections, jamming power has been swept from -90 to -20 dBm both with and without FENIX. Considering free space line-of-sight (LOS) propagation between the jammer and the receiving antenna, and a typical 2 W transmitting power jammer, this sweep corresponds to a jamming range from 30 km to 10 m (see equivalence in Table 10.1). These values have been validated in the laboratory for 10 and 30 m. Note that jamming antenna is typically a monopole with poor radiation efficiency.

Table 10.1: Equivalence between the received jamming power, and the range between the jammer and the receiver considering free space LOS propagation, and 2 W typical PPD jammer with monopole antenna.

Power [dBm]	−90	−80	−70	−60	−50	−40	−30	−20
Jamming Range [m]	30000	10000	3000	1000	300	100	30	10

10.3 FENIX-Analyzer

The first step to check the performance of the FENIX-Lite is to characterize its impulse response, or equivalently, its transfer function. Given that the FENIX detects and mitigates the RFI/jamming signal in an adaptive way, this process must be also characterized for a particular RFI scenario. In the following subsection, a methodology to perform this characterization is described.

10.3.1 Setup

The goal of the FENIX-Analyzer is to measure both magnitude and phase of the FENIX transfer function, $H(f)$. In RF systems, this measurement is usually performed by using a Vector Network Analyzer (VNA). However, this procedure does not work with FENIX. A VNA generates chirped-like signals that sweep the whole span bandwidth under measurement. When these signals are connected to the FENIX, the MFT blanking algorithm mitigates them as if they were RFI signals.

In order to overcome this issue, the FENIX-Analyzer uses pseudo-random CWGN to perform the measurements. From the statistical point, it follows a Normal distribution as well as the thermal noise, and thus, it is not mitigated by the MFT algorithm. In this case, FENIX can detect the presence of such an RFI signal because of an unrealistic increase of the thermal noise power. However, this feature is disabled under the operation of the FENIX-Analyzer.

Moreover, a VNA has multiple transmitting and receiving channels, which are synchronized by using the same internal LO. This allows to perform absolute measurements, both in magnitude and phase, as well as to measure all scattering parameters (reflection and gain parameters of multiple ports). For the sake of simplicity, the FENIX-Analyzer performs relative measurements (instead of absolute) by means of two separate channels: the measuring one and the reference one. Each channel generates its independent pseudo-random CWGN, which are transmitted synchronously, but received asynchronously. This approach simplifies the overall setup since transmitter and receiver can be independent systems, only connected to the same reference clock.

Given these requirements, the pseudo-random signals of the FENIX-Analyzer are generated by using a two-channel R&S SMU-200A vector signal generator. The SMU-200A can transmit two synchronized and phase-aligned arbitrary waveforms with a maximum sampling frequency of 100 MHz. These pre-loaded arbitrary sequences are streams of 16-bit I/Q samples with a maximum length of 2^{24} (64 MB). The measuring and reference

sample sequences are generated with a complex Gaussian random generator, and then, they are quantified at 16 bits and stored. The receiver is implemented by using an SDR model USRP X310 with an SBX-120 daughter-board. The X310 allows receiving at a maximum of 200 MSps, with a maximum bandwidth of 120 MHz. Both transmitter and receiver are connected to the same reference oscillator in order to generate the same LO frequency.

The block diagram of the FENIX-Analyzer is shown in Fig. 10.2. Channel B of the SMU-200A is used as the reference signal, which is injected directly to the X310. Channel A is used as a measuring signal, which is injected into the FENIX (or any Device-Under-Test (DUT)), and finally combined to the reference signal before entering into the X310. Besides, in the presence of an RFI, the FENIX transfer function adapts itself to the input signal in order to mitigate it as much as possible. Hence, the FENIX-Analyzer must be capable of measuring it for different RFI signals at the input of FENIX. To do so, the R&S SMR-40 signal generator is used to generate the RFI signals under evaluation. The RFI signal is combined with the measuring signal at the input of the FENIX.

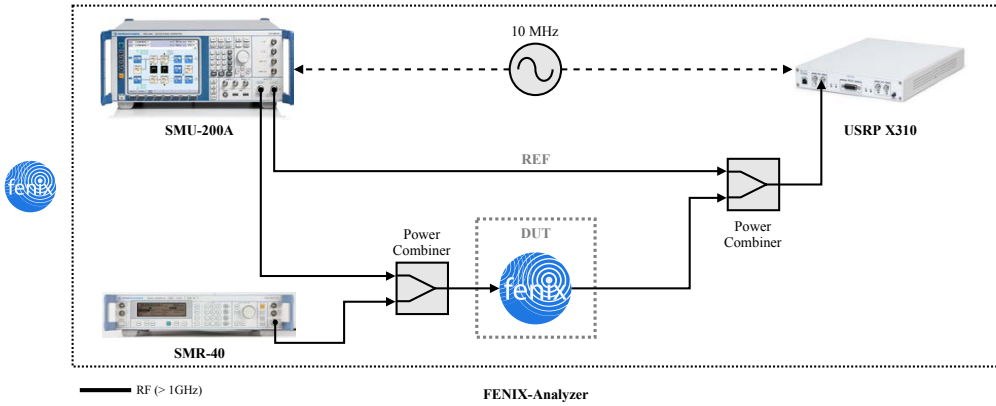

Figure 10.2: Block diagram of the FENIX Analyzer.

In order to measure the transfer function of the FENIX-Lite (which has a 2 MHz bandwidth), the transmitter sampling frequency has been set to 25 MHz, which is enough to have a measuring flat-spectrum signal. The receiver is also sampling at a frequency of 25 MHz, which is enough to measure the whole signal spectrum, and it determines a time between samples of 40 ns. Moreover, signals are transmitted at -40 dBm that ensures a good-enough SNR (∼60 dB) to neglect the effect of the thermal noise in reception.

10.3.2 Working Principle

Let us define the measuring sequence, $s[n]$, and the reference sequence, $r[n]$, as uncorrelated, zero-mean, phase-aligned, and pseudo-random CWGN sample sequences generated at $F_s = 25$ MHz and up-converted to the center of the measuring frequency band, $f_0 = 1575.42$ MHz. Both $s[n]$ and $r[n]$ have a total number of samples $N = 2^{24}$, which are generated continuously, periodically, and with no dead-time between sample set repetitions. Thus, the sample set time is equal to $T = N/F_s = \sim 671$ ms. Given that FENIX

is not an invariant system, the retrieved transfer function will be the averaged one over the measuring time T.

The receiver is also tuned at the center of the same measuring band, f_0, and it also samples at F_s. Since the LOs are physically different, their oscillation frequencies may be slightly biased. However, its effects can be neglected since this bias is on the order 1-3 Hz.

According to the FENIX-Analyzer block diagram, the received signal at BB, $y(t)$, may be expressed as

$$y(t) = h_R(t) * \left[A_r\, r(t-\tau_r)\, e^{-j\phi_r} + h(t) * A_s\, s(t-\tau_s)\, e^{-j\phi_s} + i'(t) + w(t)\right] e^{-j\Delta\phi}, \quad (10.1)$$

where $t \in [0, T)$; $h_R(t)$ is the impulse response of the receiver; $h(t)$ is the impulse response of the DUT; A_r, τ_r and ϕ_r are the amplitude, group delay and phase of the received reference signal respectively; A_s, τ_s and ϕ_s are the amplitude, group delay and phase of the received measuring signal respectively; $i'(t)$ is the mitigated RFI signal; $w(t)$ is the thermal noise at the receiver; and $\Delta\phi$ is the phase difference between the LOs. Moreover, $h_R(t)$ can be well approximated by an ideal band-limiting filter with bandwidth B_r, and thus,

$$h_R(t) \approx B_r\, \mathrm{sinc}(B_r t)\,. \quad (10.2)$$

According to the sampling theorem [2], the sampled version of the received signal, $y[n]$, is equal to $y(t = nT_s)$, with $n \in [0, N-1]$ is defined as the sample index. So is applied equivalently to $h_R[n]$, $r[n]$, $h[n]$, $s[n]$, $i'[n]$ and $w[n]$.

In order to get a coarse estimation of both group delays τ_r and τ_s, the received sample set $y[n]$ is cross-correlated with the original clean sequences $r[n]$ and $s[n]$. Since $y[n]$ is a set of N samples that include all samples of $r[n]$ and $s[n]$ circularly shifted, the Circular Cross-Correlation (CCC) is applied. For the reference signal, the CCC, $R_{yr}[m]$, is obtained as

$$R_{yr}[m] = y[m] \circledast r^*[-m] = \sum_{n=0}^{N-1} y[n] r^*[(n+m)_{\mathrm{mod}N}]. \quad (10.3)$$

Considering that the pseudo-random CWGN sample sequences are zero-mean and uncorrelated with the rest of received terms, $R_{yr}[m]$ can be approximated as

$$R_{yr}[m] \approx A_r\, B_r\, \mathrm{sinc}\left[B_r\left(m - \frac{\tau_r}{T_s}\right)\right] e^{-j(\phi_r+\Delta\phi)}, \quad (10.4)$$

and, in the same way, $R_{ys}[m]$ can be expressed as

$$R_{ys}[m] \approx h[m] \circledast A_s\, B_r\, \mathrm{sinc}\left[B_r\left(m - \frac{\tau_s}{T_s}\right)\right] e^{-j(\phi_r+\Delta\phi)}. \quad (10.5)$$

Furthermore, the cross-spectra between the received and the reference and measuring signals, $S_{yr}(f)$ and $S_{ys}(f)$ respectively, are defined as

$$S_{yr}(f) = \mathcal{F}\{R_{yr}[m]\} = Y(f)R^*(f) = A_r\,\Pi\left(\frac{f}{B_r}\right) S_r(f)\,e^{-j2\pi f\tau_r}e^{-j(\phi_r+\Delta\phi)}, \quad (10.6)$$

and

$$S_{ys}(f) = \mathcal{F}\{R_{ys}[m]\} = Y(f)S^*(f) = H(f)\,A_s\,\Pi\left(\frac{f}{B_r}\right) S_s(f)\,e^{-j2\pi f\tau_s}e^{-j(\phi_s+\Delta\phi)}, \quad (10.7)$$

where $\mathcal{F}\{\cdot\}$ is the Fourier transform; $Y(f)$, $R(f)$, $S(f)$ and $H(f)$ are the Fourier transforms of $y(t)$, $r(t)$, $s(t)$ and $h(t)$ respectively; $S_r(f) = |R(f)|^2$; and $S_s(f) = |S(f)|^2$. Hence, the transfer function of the DUT, $H(f)$, can be then expressed as

$$H(f) = \frac{S_{ys}(f)}{S_{yr}(f)}\,\frac{S_r(f)}{S_s(f)}\,\frac{1}{H_{\text{cal}}(f)}, \quad (10.8)$$

which is a relative measurement between both measuring and reference channels, and where

$$H_{\text{cal}}(f) = \frac{A_s}{A_r}\,e^{-j2\pi f(\tau_s-\tau_r)}e^{-j(\phi_s-\phi_r)}, \quad (10.9)$$

is the calibration transfer function, and B_r is larger than the bandwidth of $H(f)$ under consideration. As it happens with VNAs, the analyzer must be calibrated before starting a new set of measurement operations. $H_{\text{cal}}(f)$ can be measured by using a custom "calibration kit", which in this case is an SMA transition. This transition has been previously measured with a calibrated VNA, and their parameters have been stored for their use with the FENIX-Analyzer.

These relative measurements can be performed only if the spectra $S_r(f)$ and $S_s(f)$, and the cross-spectra $S_{yr}(f)$ and $S_{ys}(f)$ are different from zero for all values of f. Since $r[n]$ and $s[n]$ are deterministic sequences, their Fourier transforms take null values. However, if they are divided into several subsets of samples, and each of them is treated as a statistical realization of CWGN, then their spectra tend to a constant value. To do so, Bartlett's method is used [162], which is based on dividing the original set of data samples into several equal-size subsets, and then, averaging the absolute squared Fourier transform of all subsets. The resulting Bartlett's periodogram is an estimation of the PSD of the original signal. For instance, Bartlett's periodogram of the reference signal, $\hat{S}_r(f)$, is obtained as

$$\hat{S}_r(f) = \sum_{k=0}^{K-1}\left|\mathcal{F}\left\{r\left[n+k\frac{N}{K}\right]\right\}\right|^2, \quad (10.10)$$

where $n \in [0, \frac{N}{K}-1]$ and $K = 2^{12}$ is the number of averages. The same procedure is applied in order to estimate $\hat{S}_s(f)$, $\hat{S}_{yr}(f)$ and $\hat{S}_{ys}(f)$. Finally, and once the calibration is performed, the FENIX transfer function can be estimated as

$$H(f) = \frac{\hat{S}_{ys}(f)}{\hat{S}_{yr}(f)} \frac{\hat{S}_r(f)}{\hat{S}_s(f)} \frac{1}{H_{\text{cal}}(f)}. \tag{10.11}$$

10.3.3 FENIX Transfer Function

The FENIX-Analyzer has been used to measure the FENIX-Lite transfer function. This has been done for the three RFI/jamming scenarios detailed in the previous section. For each scenario, the RFI power has been swept from -10 dB to 50 dB of INR. This means that for example at 0 dB, the RFI power has the same power than the pseudo-random CWGN used for the FENIX-Analyzer measurements.

The transfer function of the FENIX-Lite, $H(f)$, can be expressed in polar form as

$$H(f) = |H(f)|\, e^{j\angle H(f)}, \tag{10.12}$$

where $|H(f)|$ is the magnitude and $\angle H(f)$ is the phase of the transfer function. The square of the magnitude is the power response, $|H(f)|^2$, which is a measure of how much each frequency component of the input signal is amplified or attenuated. Regarding the phase response, it can be decomposed in two main terms,

$$\angle H(f) = 2\pi f \tau_{\text{proc}} + \varphi(f), \tag{10.13}$$

where τ_{proc} is the constant delay introduced mainly by the digital signal processing stage of the FENIX, and $\varphi(f)$ is the remaining phase response of the transfer function.

For each RFI/jamming scenario, the power response, the phase response, and the group delay of the FENIX-Lite transfer function are calculated once the processing delay, τ_{proc}, is subtracted. This processing delay is measured to be equal to 1650258.5 ns, and it is constant since it depends mainly on the aggregated latency of all digital blocks of the SP stage. The magnitude of τ_{proc} is very large as compared to the synchronization requirements for timing applications. However, this delay can be calibrated and compensated since it is a constant.

The first RFI/jamming signal under evaluation of the CW. The results from the FENIX-Analyzer are depicted in Fig. 10.3. Without RFI, the power response shows that the band-pass of the FENIX-Lite is on the order of 2 MHz as expected. Moreover, the near-band rejection ratio is about 45 dB with a high selectivity (about 40 dB in 400 kHz). Moreover, when the CW RFI signal is present, the power response shows how the notch at the center of the band is more and more abrupt while the RFI power increases. For INR values higher than 40 dB, the whole band-pass starts being attenuated, and some notch aliases appear. This effect is produced by the saturation of the ADC, and thus, the clipping of the input signal.

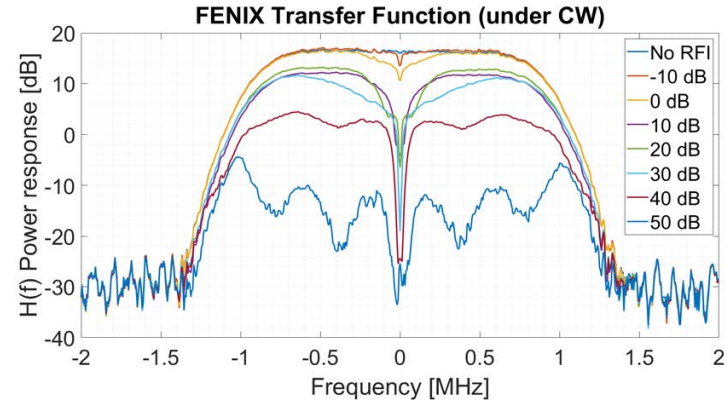

(a)

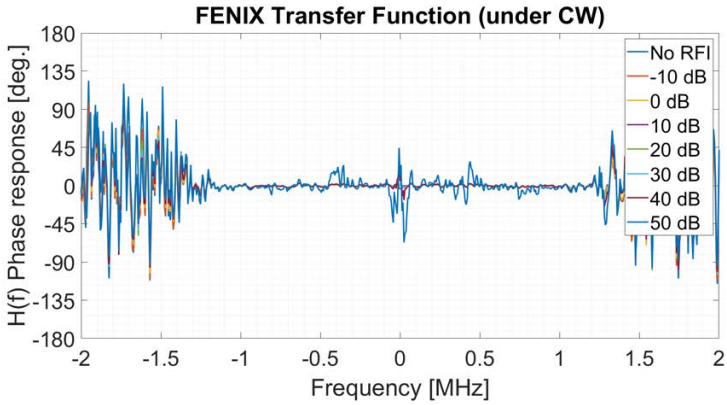

(b)

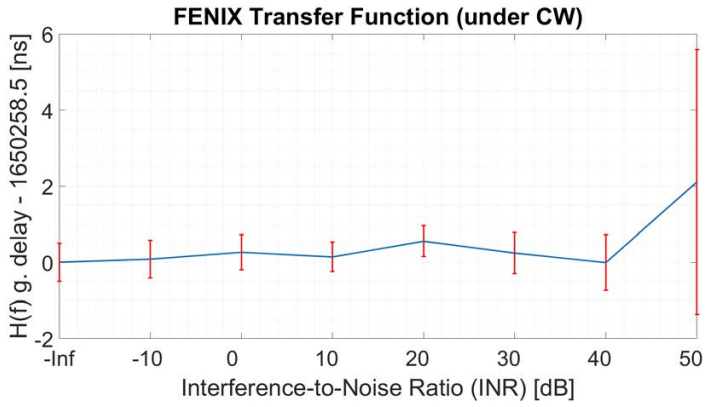

(c)

Figure 10.3: FENIX transfer function under CW RFI signal: (a) power response, (b) phase response, and (c) group delay.

Regarding the phase response under a CW RFI, it is flat within the band-pass. Besides, the phase value is not well defined in the attenuated band, as well as at the position of the notches inside the band-pass. Regarding the group delay or the derivative of the phase response at the band-pass, it is constant and equal to the processing delay, τ_{proc}. This is one of the most important results of the FENIX-Analyzer since it proves that FENIX-Lite (and FENIX in general) has a linear phase response, and thus, it does not distort the input signal. This was one of the main requirements during the design of the FENIX, and it has been achieved by using linear components and FIR filters. Furthermore, the FENIX-Analyzer is able to estimate the processing delay with a bias of about 1 ns, and a standard deviation lower than 1.5 ns, for INR lower than 40 dB. The high accuracy and precision are achieved by using averaged phase measurements.

The second RFI/jamming signal under evaluation is the chirp #1, which has a 10 MHz bandwidth and a repetition frequency of 100 kHz. The results of the FENIX-Analyzer under chirp #1 are shown in Fig. 10.4. The power response shows two different behaviors. First, the band-pass is increasingly attenuated as the RFI power increases. The blanking stage discards more samples as the RFI power increases, and then, the resulting power response becomes attenuated at its band-pass. Second, periodic notches appear due to the spectrum of the chirp #1 RFI signal. Since it has a high repetition frequency, many cycles of the time-frequency sweep fall into the processing time of the FENIX. Therefore, the original spectrum appears sampled at several points because it is multiplied by a delta train with a spacing equal to the repetition frequency of the chirp signal. When the blanking algorithm adapts itself to the RFI signal, these periodic notches appear at the power transfer function. Note that in this case the chirp signal is mapped into a pulse signal after the digital band-pass filter as it was described in the previous section. Therefore, the frequency response of FENIX for the case of chirp #1 has a similar behavior when a pulsed RFI is present.

Regarding the phase response under chirp #1, it is also flat within the band-pass of FENIX as in the previous case. Regarding the group delay as a function of the INR, the bias and standard deviation are below the ns level for INR values below 40 dB. The behavior, in this case, is even better than for CW RFI because the magnitude of the notches within the band-pass is much lower, and then, there are no discontinuities in the value of the phase.

The third RFI/jamming signal under evaluation is the chirp #2, which has a 2 MHz bandwidth and a repetition frequency of 200 Hz. The results of the FENIX-Analyzer under chirp #2 are shown in Fig. 10.5. The power response shows a similar behavior as before since it attenuates as the INR increases. In this case, there is no notch behavior because the repetition frequency is much lower. Moreover, this RFI signal is a worst case because the bandwidth of chirp #2 is equal to the bandwidth of the FENIX-Lite.

Regarding the phase response under chirp #2, it is also flat within the band-pass of FENIX as in the previous cases. Regarding the group delay as a function of the INR, the bias is below the ns level for INR values below 40 dB. However, the standard deviation is a bit larger with a maximum about 2 ns at 40 dB INR. Even though this is a worst case, the performance in terms of group delay stability remains at ns level.

These three measurement cases validate the performance of the FENIX-Lite in real-time. Moreover, they prove that FENIX-Lite can be used even with high precision and high-

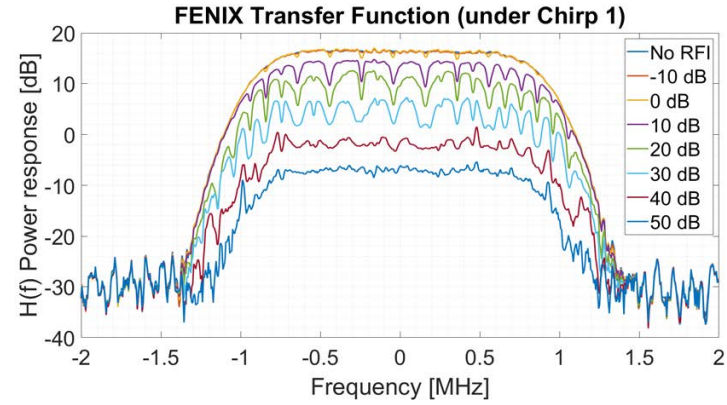

(a)

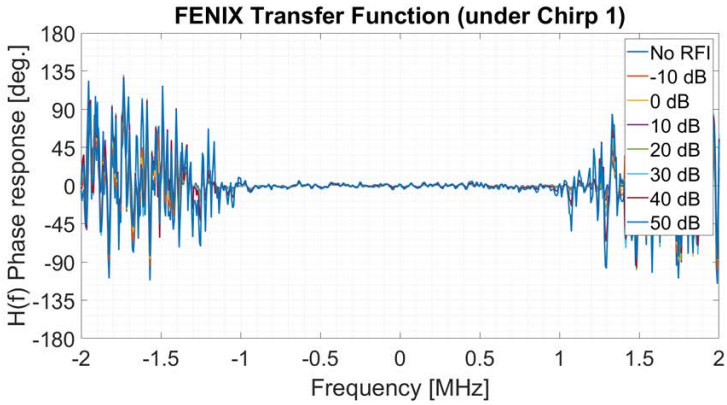

(b)

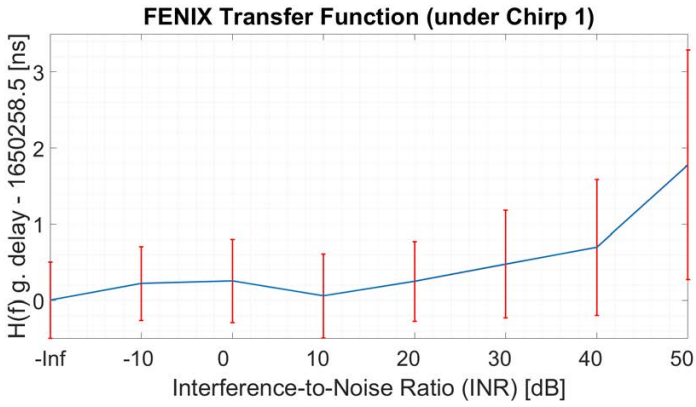

(c)

Figure 10.4: FENIX transfer function under chirp #1 RFI signal: (a) power response, (b) phase response, and (c) group delay.

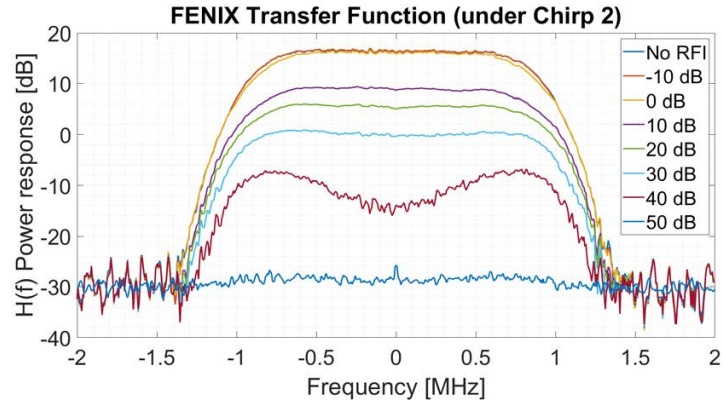

(a)

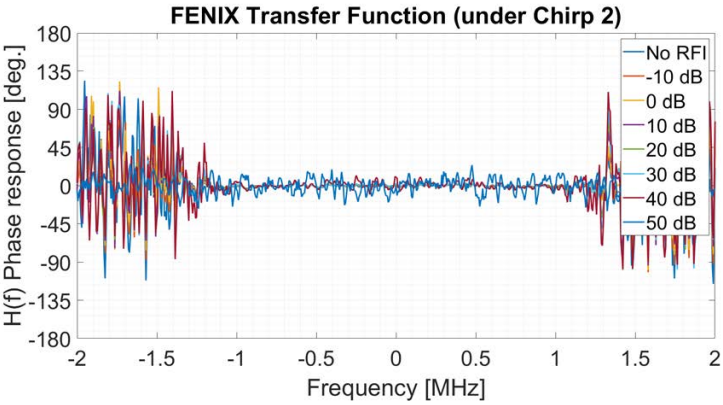

(b)

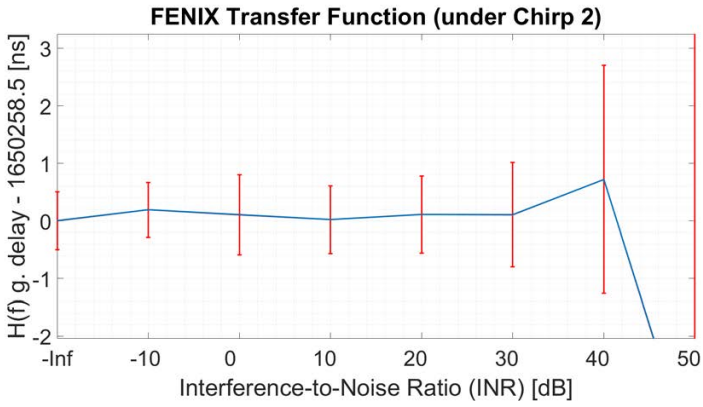

(c)

Figure 10.5: FENIX transfer function under chirp #2 RFI signal: (a) power response, (b) phase response, and (c) group delay.

performance GNSS receivers since the timing accuracy is degraded few ns in the worst case.

10.3.4 Comparison with IIR filters

As mentioned above, FENIX has been built using FIR filters rather than IIR filters. As mentioned in Chapter 3, each one of the main architectures for digital filters has its own advantages and drawbacks. IIR filters mimic analog filters and require fewer hardware resources to achieve the same selectivity as compared to FIR filters. However, this is achieved at the expense of a non-linear phase, which distorts the input signal.

In order to illustrate the effects of IIR filters, the FENIX-Sim (described in Chapter 9) has been used. Figure 10.6a shows the power and phase response of the FENIX and an IIR notch filter, both mitigating a CW at the center of the band. The FENIX Ideal (in blue color) is the theoretical behavior of the FENIX algorithm. The FENIX Simulated (in green color) corresponds to the performance of the hardware implementation taking into account quantification noise, saturation effects, etc. The IIR notch filter is defined with its Z-transform as

$$H(z) = \frac{1 - z^{-1}}{1 - 0.9z^{-1}}. \tag{10.14}$$

In this case, FENIX performs even better than the IIR in terms of power mitigation. Moreover, the phase response reveals the phase distortion introduced by the IIR filter.

Figure 10.6b shows the same comparison, but with three CW signals which are equidistant in frequency. The three pole notch filter is defined as three single pole IIR filters in cascade, and therefore its Z-transform function is

$$H_{3\mathrm{p}}(z) = \frac{\left(1 - z^{-1}\right)\left(1 - e^{j2\pi f_0}\, z^{-1}\right)\left(1 - e^{-j2\pi f_0}\, z^{-1}\right)}{\left(1 - 0.9\, z^{-1}\right)\left(1 - 0.9\, e^{j2\pi f_0}\, z^{-1}\right)\left(1 - 0.9\, e^{-j2\pi f_0}\, z^{-1}\right)}, \tag{10.15}$$

where f_0 is equal to 500 kHz divided by the sampling frequency. In this case, the IIR notches are more pronounced, but the total band-pass is much lower than with FENIX. Moreover, the distortion of the phase can be clearly appreciated. The effect of this distortion is translated into a variable group delay depending on which is and how powerful the RFI signal to be mitigated. However, the results obtained from the FENIX-Analyzer prove that this is not the case of FENIX. FENIX mitigates the RFI signal while, at the same time, the signal phase is not distorted, and the total group delay does not change.

10.4 Mitigation with GNSS receivers

This section discusses the mitigation performance of the FENIX-Lite using commercial GNSS receivers. GNSS receivers measure the quality of the signals from the satellites using the C/N_0 as a figure of merit. The C/N_0 is defined for each satellite as the ratio between the power of the GNSS signal and the power spectral density of the thermal noise [139]. This measure equivalent to the SNR, but it is independent of the bandwidth

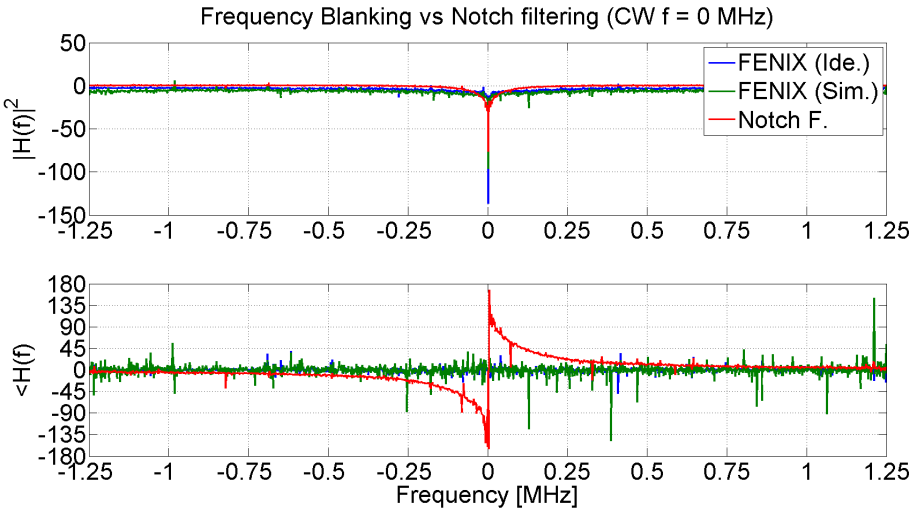

(a)

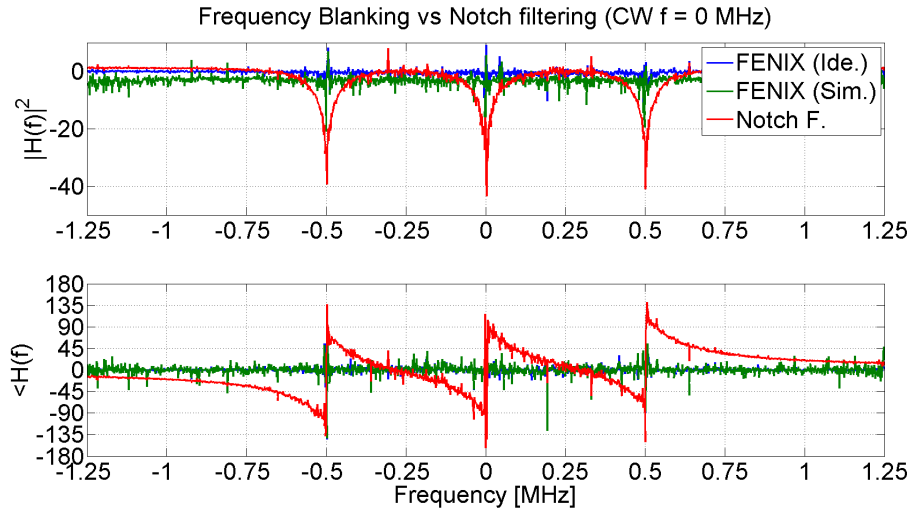

(b)

Figure 10.6: Comparison between the power and phase response of FENIX and a IIR notch filter in two scenarios: (a) a CW at zero frequency and (b) three equidistant in frequency CW signals.

of the receiver. Therefore, it can be measured at any point in the receiving chain. As discussed in Chapter 7, the effect of RFI and jamming signals is equivalent to a rise of the noise floor in the receiver, and thus, a degradation of the SNR, or the C/N_0, takes place.

The goal of FENIX is to mitigate the RFI and jamming signals present at the input of the receiver. In other words, to reduce the C/N_0 degradation due to the presence of RFI and jamming signals. Therefore, the comparison or difference between the C/N_0 degradation

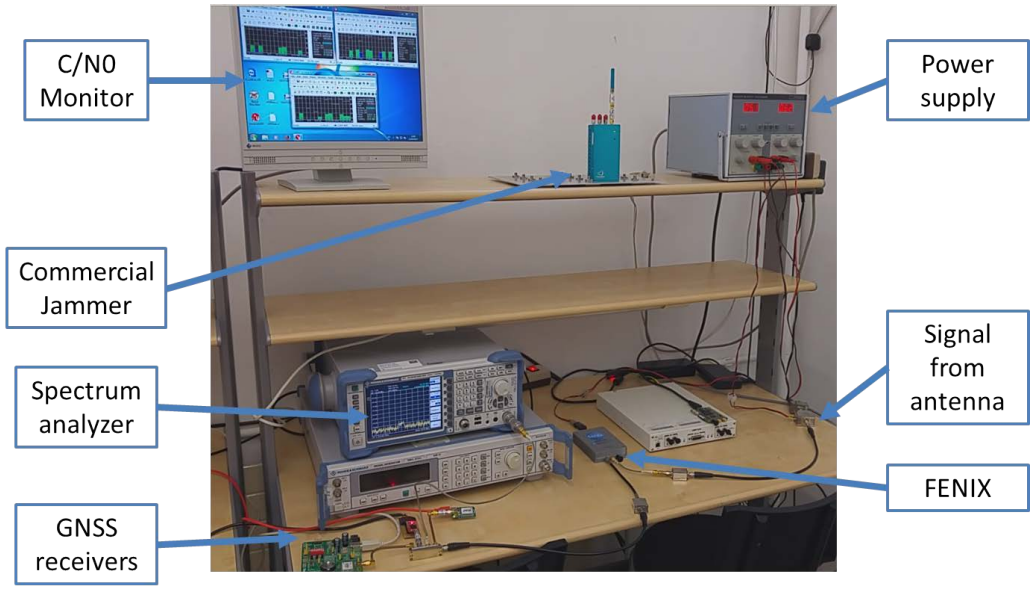

Figure 10.7: Setup used to test the real-time performance of FENIX.

with and without using FENIX seems an appropriate way to evaluate its RFI mitigation performance.

Figure 10.7 shows the setup used to test the performance of FENIX in real-time. The GNSS signals can be either received from an outdoor antenna or generated using a vector signal generator model R&S SMU-200A. Besides, the RFI and jamming signals are generated using either a commercial jammer or a signal generator model R&S SMR-40. Moreover, four commercial GNSS receivers are used to assess the C/N_0 degradation. Each GNSS receiver has its own response in denied GNSS conditions because of their internal configurations. Therefore, the use of more than one GNSS receiver is justified in order to get a complete picture of the effects of RFI signal on the C/N_0 level. These four receivers are shown in Fig. 10.8. The models of each GNSS receiver are

1. a low-cost Skytraq V634LPx that supports only GPS L1C/A [163],
2. a mid-range U-Blox LEA6S that supports only GPS L1C/A [164],
3. a high-performance Trimble BD982 that supports GPS (L1C/A, L1P, L2C, L2P and L5), Galileo (E1 and E5) and GLONASS (L1C/A, L1P and L3) [165], and
4. a high-performance Septentrio AsteRx2eH that supports GPS (L1C/A, L1P, L2C, and L2P), and GLONASS (L1C/A and L1P) [166].

These four receivers have not been chosen for any particular reason. They were just the ones available at the moment of the test were performed. Some of them have RFI detection flags which have not been taken into account during the tests.

In this section, four different tests are presented: two qualitative and other two quantitative. The qualitative test is performed using GNSS signals gathered from an outdoor

Figure 10.8: GNSS receivers used in the real-time RFI mitigation performance tests of FENIX-Lite.

antenna, and using the commercial jammer to deny the GNSS receivers. Note that two 30 dB attenuators have been placed before the antenna of the jammer in order to not affect other nearby receivers. The C/N_0 level of the GNSS receivers is monitored using the u-blox software "u-center". Figure 10.9 shows the three possible states of the setup. These three states are described subsequently, as well as the detailed views of the commercial jammer, the C/N_0 monitoring software and the spectrum analyzer are commented.

1. The GNSS signals gathered by the external antenna are delivered directly to the GNSS receivers without the presence of any RFI signal.
   (a) The commercial jammer is turned off.
   (b) The monitoring software shows high C/N_0 levels up to 55 dB-Hz.
   (c) The spectrum analyzer shows the flat spectrum corresponding to thermal noise.
2. GNSS receivers lose the tracking of the satellites under the presence of jamming.
   (a) The commercial jammer is turned on.
   (b) The monitoring software shows no being tracked GNSS satellites. Therefore, PVT solution is lost.
   (c) The spectrum analyzer shows the spectrum of the chirp RFI signal generated by the commercial jammer.
3. FENIX is connected between the antenna and the input of the GNSS receivers. FENIX mitigates the jamming signal, and GNSS receivers retrieve a PVT solution.
   (a) The commercial jammer is also turned on.
   (b) The monitoring software shows C/N_0 levels about 25 dB-Hz. GNSS receivers are working at their limit, but a PVT solution is still retrieved.
   (c) The spectrum analyzer shows the mitigated jamming signal.

This qualitative test has been performed using only GPS L1 C/A signals. A second qualitative test has been done using GPS L1C/A, GPS L2C and Galileo E1OS signals. Figure 10.10 shows the results of this second test. In this case, two FENIX-Lite have been connected in parallel, one tuned at the L1 (1575.42 MHz), and another tuned at L2 (1227.60 MHz). A comparison between the C/N_0 levels of each satellite with and without the two FENIX-Lite shows an improvement between 1 and 5 dB-Hz. Moreover, two extra satellites (one GPS and one Galileo) are tracked only when FENIX is used.

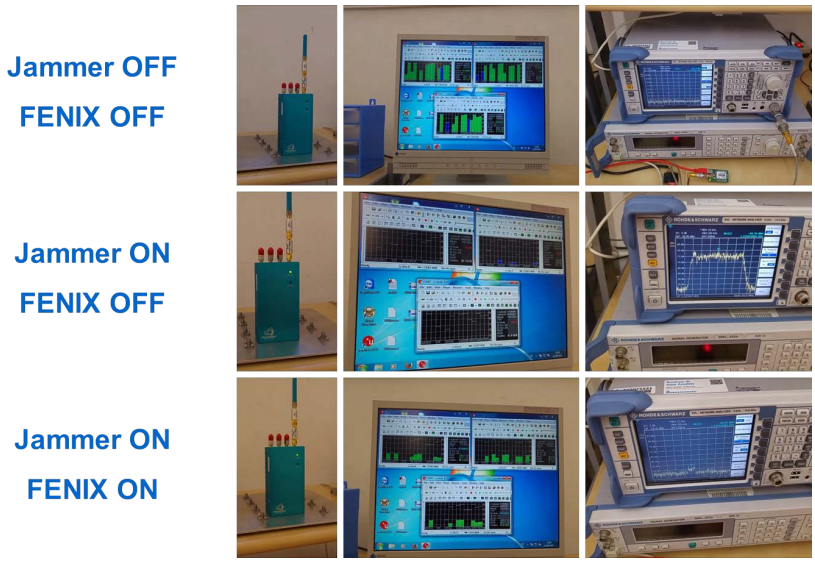

Figure 10.9: Qualitative demonstration of the real-time performance of FENIX-Lite using real GPS L1 C/A signals from an outdoors antenna, and a commercial jammer.

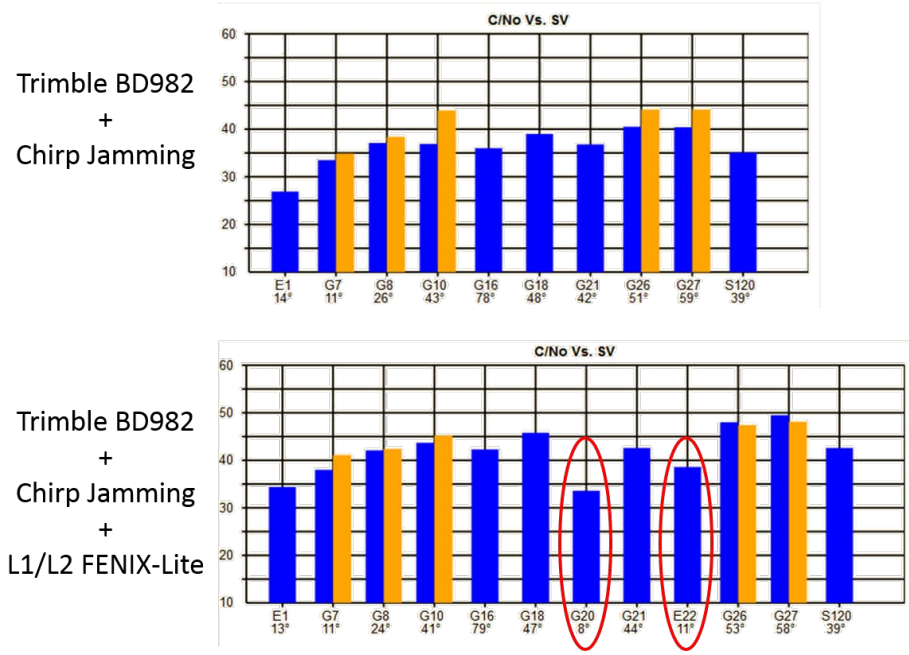

Figure 10.10: Comparison of the C/N_0 levels of GPS L1C/A, GPS L2C and Galileo E1OS signals in jamming conditions: (a) without RFI mitigation, and (b) with two FENIX-Lite, one tuned at the L1, and another tuned at L2.

The qualitative tests prove how FENIX is able to protect the GNSS receivers from jamming attacks. However, a quantitative assessment is required in order to evaluate the magnitude of the extra resilience provided by the FENIX-Lite.

The quantitative tests are performed using GPS L1 C/A and Galileo E1 OS signals. These signals are generated using the vector signal generator in order to have a control of their power, and thus, of the C/N_0 level. Besides, the RFI/jamming signals are generated using the signal generator in order to have a good control of the SIR. The C/N_0 degradation is defined as the difference between the C/N_0 level for a particular SIR value, and the C/N_0 level without interference signal. The SIR has been swept between 0 dB (same power level), and -60 dB.

As a particular case, an active GNSS antenna with an large amplifying gain (> 30 dB) delivers a power level (GNSS signals plus thermal noise) of about -70 dBm with a bandwidth of 30 MHz. If GNSS signals are received with a C/N_0 level equal to 55 dB-Hz, the power of the GNSS signals is on the order of -90 dBm. Therefore, a sweep of the SIR between 0 dB and -60 dB is equivalent to a sweep of the RFI power between -90 dBm and -30 dBm, for this particular example. These RFI power levels are the ones taken as the reference at the beginning of this chapter. However, SIR values are used for the quantitative tests for the sake of generality.

Figure 10.11 shows the C/N_0 degradation for each one of the four GNSS receivers under evaluation as a function of the SIR. The three different jamming scenarios taken into account in this chapter have been tested. Solid and dotted lines correspond to the C/N_0 degradation with and without the FENIX-Lite. As mentioned above, each GNSS receiver has its own response under jamming conditions. However, their behavior when the FENIX-Lite is considered tends to the be similar. The resilience against these jamming signals using FENIX is up to 30 dB in the best case.

Beyond a SIR of -60 dB (interference power equal to -30 dBm), the performance of the FENIX-Lite is constrained by the intrinsic limitations of the current RF hardware (amplifier saturation, ADC clipping, limited rejection between input and output, etc.). However, if the hardware limitations could be removed, the SP stage described in Chapter 9 would still perform as well as the theoretical model described in Chapter 8 foresees.

A second quantitative test has been done by using Galileo E1OS exclusively. Figure 10.12 shows the C/N_0 degradation as a function of the SIR for the three jamming scenarios mentioned above. In this case, the CW RFI signal is centered at one of the maxima of the Galileo E1OS spectrum. The tests show that Galileo is a bit more resilient than GPS to the same jamming scenarios, probably because of its increased correlation gain as compared to GPS L1 C/A signals.

10.5 Mitigation in GNSS-R

This section is devoted to a brief assessment of the performance of FENIX for GNSS-R instruments. This can be done in the with the same setup used to assess its performance with GNSS receivers (see Fig. 10.7). However, in this case, the signal is recorded before reaching the GNSS receivers, and then, direct-signal DDMs are computed and compared with and without the FENIX-Lite mitigation. This comparison gives a quantitative idea

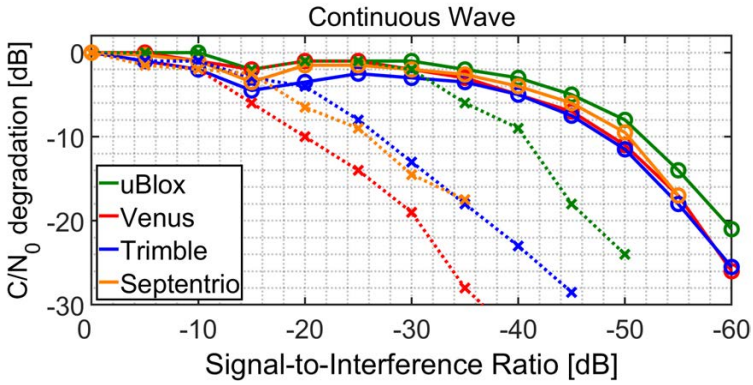

(a)

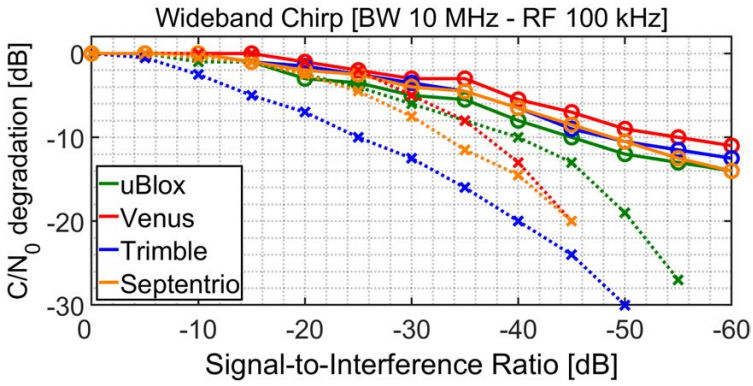

(b)

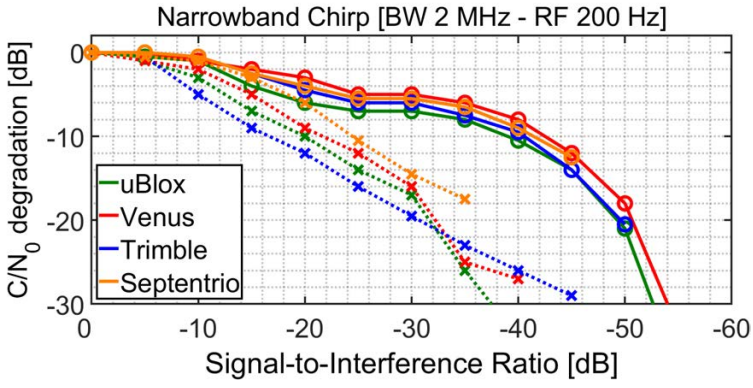

(c)

Figure 10.11: Assessment of the mitigation performance of FENIX-Lite with four GNSS receivers working with GPS L1C/A signals. All plots show the degradation of the C/N_0 as a function of the jamming power with and without FENIX-Lite. Three different jamming scenarios are considered: (a) CW, (b) chirp with 10 MHz bandwidth and 100 kHz of repetition frequency, and (c) chirp with 2 MHz bandwidth and 200 Hz of repetition frequency.

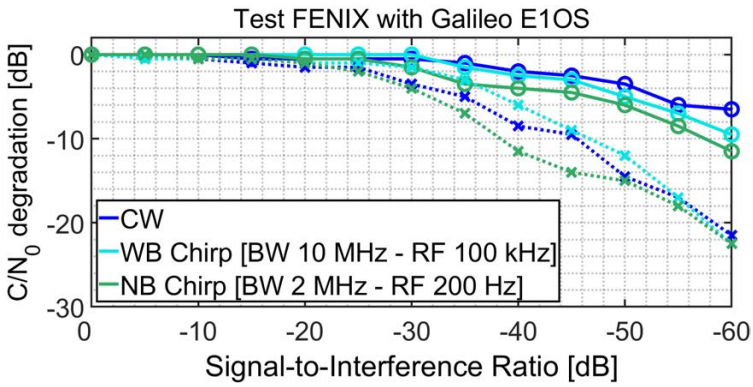

Figure 10.12: Assessment of the mitigation performance of FENIX-Lite with Galileo E1OS signals. All plots show the degradation of the C/N_0 as a function of the jamming power with and without FENIX-Lite for the three jamming scenarios under assessment.

of the effects of the RFI signal on the DDM, and how FENIX-Lite is able to mitigate them.

These tests have been performed with GNSS signals gathered from the outdoors antenna. The RFI signal has been generated using the commercial jammer, and its power has been swept by changing the number and value of the attenuators placed before its monopole antenna. Only DDMs corresponding to one satellite with GPS L1 C/A have been taken into account for the sake of simplicity. These DDMs have been computed by using 1 ms of coherent integration, plus 20 incoherent averages [35].

Figure 10.13 shows the resulting DDMs of this test. The left column shows the DDMs without FENIX, whereas the right column shows the DDMs with the FENIX-Lite mitigation. Note that both delay and Doppler values of each waveform vary because they have been taken at different time instants. The jamming power cases under assessment are no jamming, -75 dBm, -65 dBm, -55 dBm, and -45 dBm. For the cases where the peak of the DDM can be tracked, the SNR has been calculated as the ratio between the value of the DDM peak and the standard deviation of the noise floor.

The results show that without FENIX, the peak of the DDM cannot be tracked if the jamming power is above -75 dBm. Moreover, for -75 dBm, the SNR at the DDM has been degraded almost 3 dB as compared to the case without jamming. However, when the RFI mitigation of FENIX-Lite is used, the peak of the DDM can still be tracked up to a jamming power of -55 dBm. Moreover, it can be appreciated that the shape of the DDM is preserved even after the FENIX-Lite blanking algorithm is applied. The results show once again the 20-30 dB resilience against RFI/jamming signal introduced by the FENIX-Lite.

10.6 Protection of a Timing Setup

This section is devoted to an assessment of the performance of the FENIX-Lite for GNSS-enabled timing setups in terms of jamming resilience and timing performance under differ-

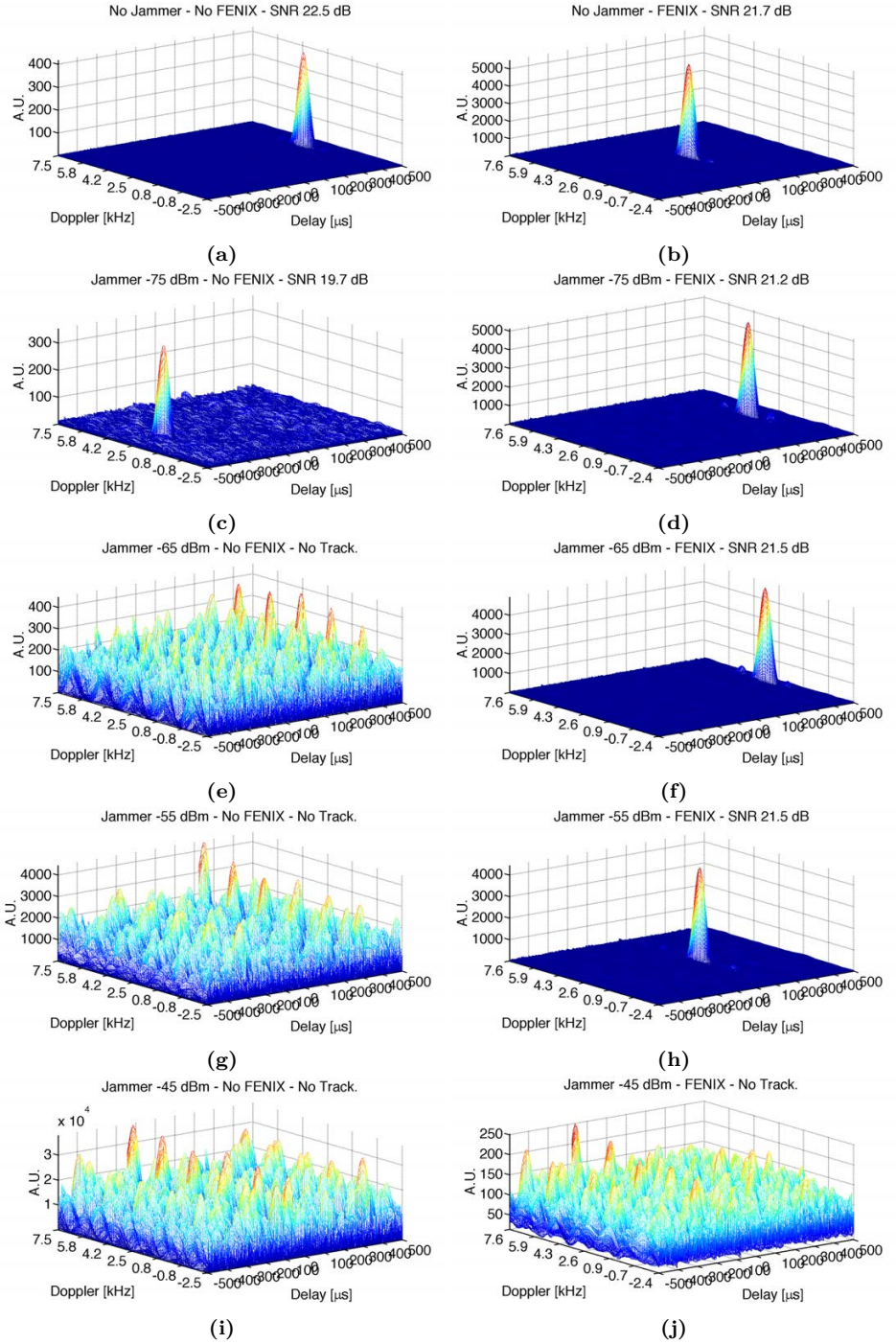

Figure 10.13: DDMs obtained with real GPS L1 C/A signals and a commercial jammer.

ent representative jamming scenarios. As already mentioned, GNSS are a key technology for timing and synchronization in critical infrastructures such as telecommunication networks, power distribution grids and finance operations, among others. GNSS guarantee 24/7 worldwide availability of their signals, which allows synchronizing multiple receivers located far away (Fig. 10.14).

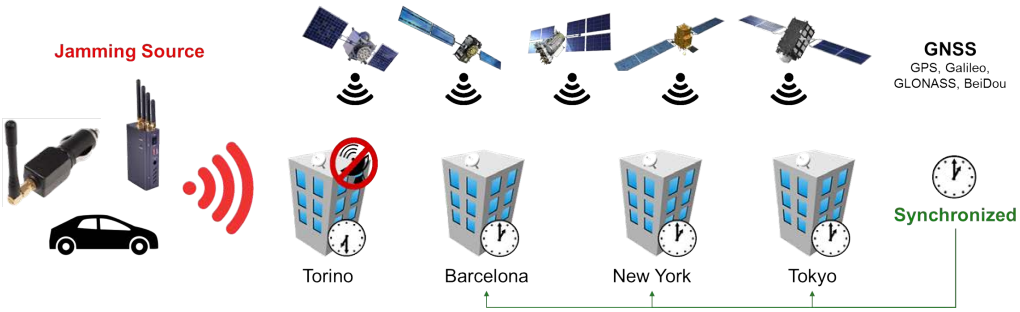

Figure 10.14: Illustration of a jamming attack on a GNSS timing system.

Recent publications have highlighted the ever-growing presence of interference sources in urban areas both from intentional and unintentional nature. On the one hand, the increasing market penetration of GNSS in critical infrastructures makes necessary the development of anti-jamming systems capable to protect them from jamming attacks. On the other hand, the overcrowding of frequency spectrum fosters the appearance of unintentional RFI events coming from GNSS near-band services. The number of these events is likely to increase with broadband technologies like 5G, which makes an intensive use of the spectrum.

10.6.1 GNSS Timing Setup

The GNSS timing setup proposed to evaluate the performance of the FENIX is based on two GNSS disciplined oscillators named DOWR, which have been developed in conjunction by Seven Solutions and GMV. DOWR stands for Disciplined Oscillator White Rabbit. The DOWR combines an u-blox LEA-M8F receiver with precise output timing protocols such as Pulse Per Second (PPS), Network Time Protocol (NTP), Precision Time Protocol (PTP), and in particular White Rabbit (WR). WR allows time distribution over optical fiber along hundreds of km with ns-level accuracy.

DOWR is currently the only product in the market combining GNSS-based time generation and WR-based time distribution. The main limitation of DOWR comes from the usage of an inexpensive, single-frequency GNSS receiver. Single-frequency makes the timing solution susceptible to ionospheric errors, which can reach tenths of ns in the worst case. Single-frequency also makes the receiver more vulnerable to jamming and interference. Although the LEA-M8F has some jamming/interference detection capabilities, it is not clear from the documentation to what extent the receiver implements also mitigation measures.

Figure 10.15 shows a diagram of the proposed GNSS timing setup. The two DOWR units are connected to a common antenna with an open-sky configuration located at the

rooftop of the building. Both LEA-M8F receivers are configured in an identical way: use only GPS and set a "fixed" antenna position. The first DOWR is used unperturbed, as PPS reference (*REF*). The second DOWR acts as the Device-Under-Test (*DUT*), in order to evaluate the combined performance of FENIX-Lite and the timing setup in terms of resilience against different common GNSS jamming and RFI scenarios.

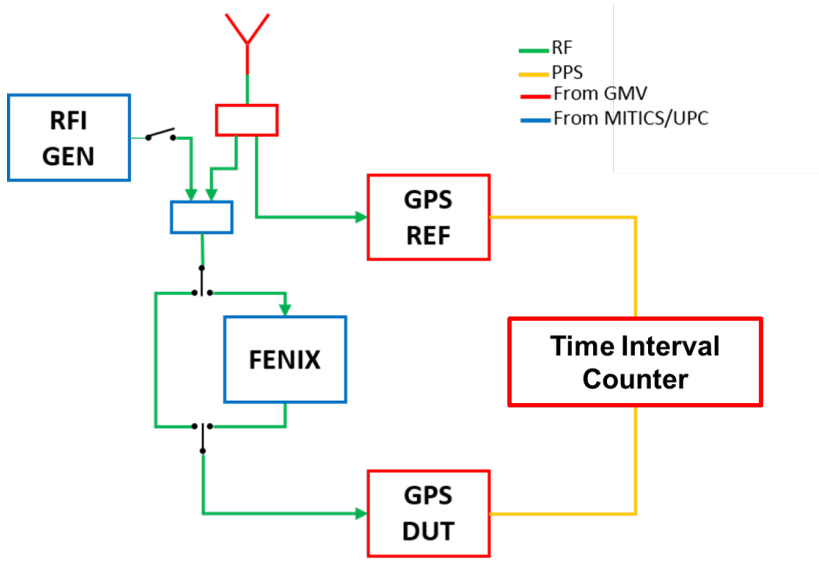

Figure 10.15: Diagram illustrating the GNSS timing setup.

Eventually, the setup is designed to measure the phase difference between PPS pulses generated by both DOWR devices, using a Time Interval Counter (TIC), and to record the GPS receiver messages while it is suffering RFI/jamming attacks. The REF DOWR is connected directly to the antenna signal, while the DUT DOWR is connected to the FENIX-lite, which receives the combined signal of the antenna and the RFI/jamming signal generator. Figure 10.16 shows a picture of the final setup tested at UPC-BarcelonaTech premises.

The results described in the following subsections have been obtained under the three different RFI/jamming scenarios taken into during this chapter. As detailed above, they are considered representative of the most common cases of real jamming scenarios.

10.6.2 Anti-jamming performance

Under no RFI/jamming conditions, the maximum C/N_0 level is around 50-52 dB-Hz, which is large enough to perform a C/N_0 degradation analysis. Once the jamming signal is injected, the C/N_0 level is degraded in concordance to the results shown in previous sections. When the C/N_0 level drops below 15-17 dB-Hz, the GPS receiver loses the signal tracking, and then no timing solution is provided. However, this happens at different jamming power level depending on whether FENIX is connected or not, and on which jamming scenario is evaluated.

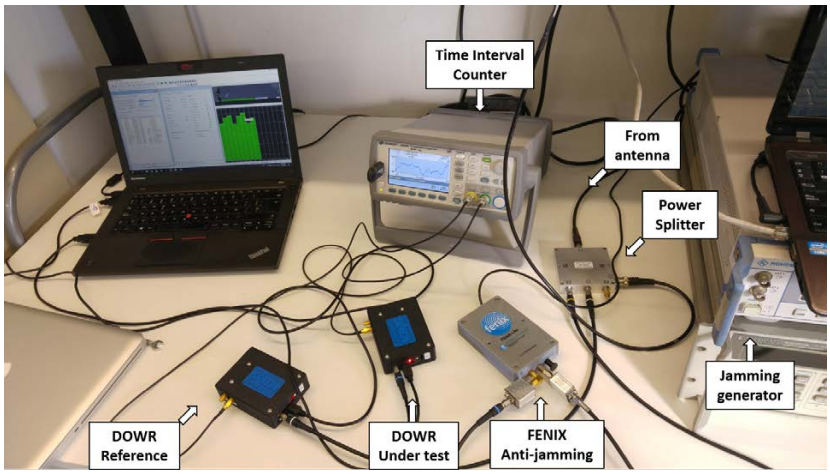

Figure 10.16: Picture of the GNSS timing setup.

In the case of a CW jamming signal, the GPS receiver works nominally with jamming power up to -60 dBm (1 km) without FENIX. Beyond that, no positioning/timing solution is provided. However, when FENIX is used, the GPS receiver can still work up to -30 dBm (30 m). The timing performance for -40 and -30 dBm CW jamming is discussed in next subsection.

Regarding chirp signal scenarios, in both cases, the GPS receiver works nominally up to -60 dBm (1 km) without FENIX. On the other hand, when FENIX is used, the GPS receiver can still work up to -50 dBm (300 m) for both chirp signals. However, timing performance is slightly different for each chirp signal scenario.

10.6.3 Timing performance

One of the observables available from the LEA-M8F receiver regarding timing performance is the uncertainty. Under no RFI/jamming conditions, the receiver reports values of 2-4 ns without FENIX, and of 4-6 ns when FENIX is connected between antenna and receiver. Figure 10.17 shows the time evolution of the phase difference for 30 minutes with and without FENIX, and its overlapped Allan's deviation.

Similar values are reported under jamming conditions for all scenarios up to -60 dBm. Beyond that, the system cannot work without FENIX as it was mentioned in the previous subsection. However, when FENIX is used, the GPS receiver is working and reporting uncertainty values of 10 ns for CW at -40 dBm (100 m), of 25 ns for CW at -30 dBm (30 m), of 7 ns for chirp #1 at -50 dBm (300 m), and of 4 ns for chirp #2 at -50 dBm (300 m).

As mentioned above, the phase difference between PPS signals coming from REF and DUT receivers is recorded using a TIC. This data allows to analyze in more detail the performance of the system under extreme jamming cases when FENIX mitigation makes the difference.

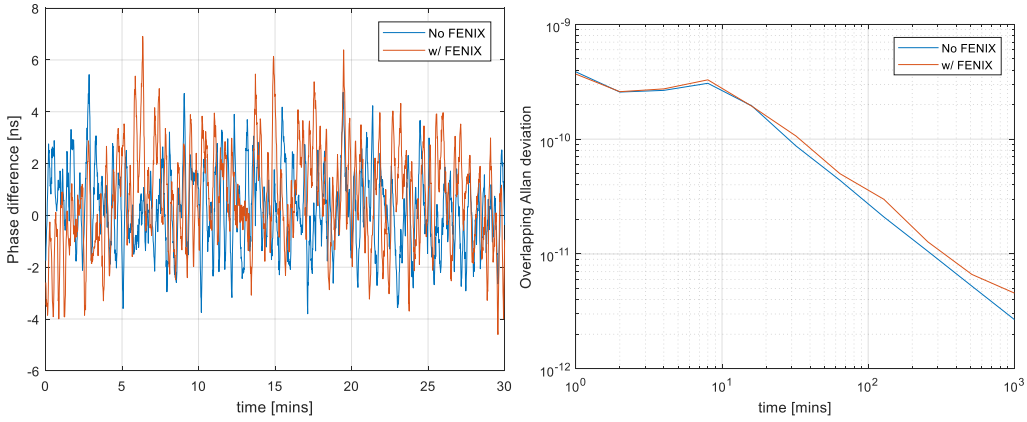

(a) (b)

Figure 10.17: (a) Time plot of phase difference between PPS signals from DUT and REF devices. FENIX constant delay of 1650225 ns has been subtracted. (b) Overlapped Allan's deviation of the phase difference.

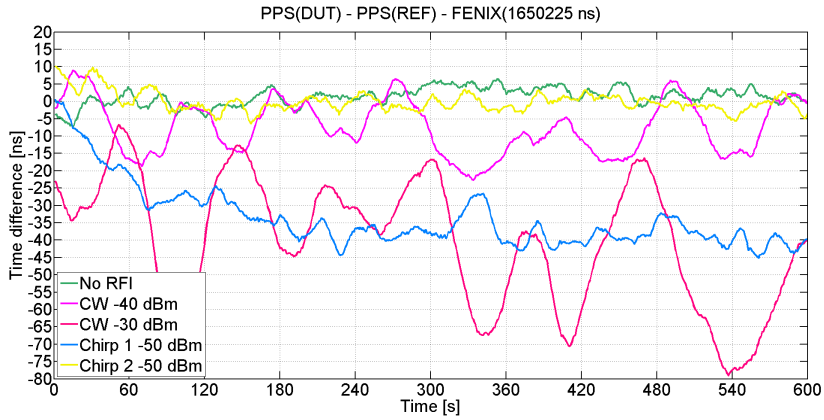

Figure 10.18: Time plot of phase difference between PPS signals from DUT and REF devices. FENIX constant delay of 1650225 ns has been subtracted in all plots.

Figure 10.18 shows the time evolution of the phase difference for 10 minutes. The mean delay measured when no RFI/jamming signal is present has been subtracted for all plots. The magnitude of this delay is about 1.65 ms, which is the contribution of all delays of FENIX internal processing blocks. This value matches with the one measured with the FENIX-Analyzer. As mentioned above, this delay is constant by construction, and thus it can be calibrated and compensated.

Moreover, the correspondence between each plot and the above-mentioned uncertainty values can be appreciated. Even though the use of FENIX allows the receiver to work under jamming conditions with an acceptable increased uncertainty, the RFI/jamming signal also introduces some bias in the phase difference. This bias is about 45 ns in the

worst case (CW -30 dBm). In the case of chirp #1 at -50 dBm, the bias is about 40 ns, but the uncertainty is much less than in the previous case. These bias values are acceptable for current telecommunication networks requiring 100 ns-level precision.

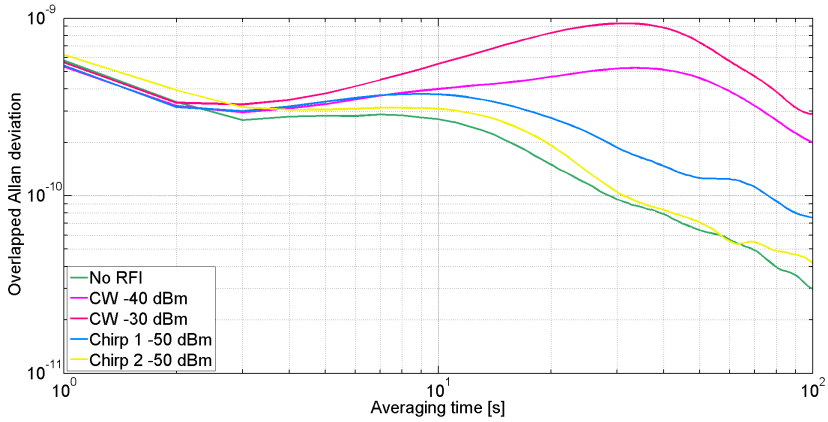

Figure 10.19: Overlapped Allan deviation of phase difference between PPS signals from DUT and REF devices for different RFI signals.

Figure 10.19 shows the overlapped Allan deviations for the above case studies. This plot shows the additional instability introduced by the RFI/jamming signal once mitigated by FENIX. Furthermore, a minimum is obtained when samples are averaged at 3 s.

One more experiment with the same setup has been conducted at GMV premises. In this case, three different records with the TIC have been taken for each jamming scenario under evaluation. These records correspond to the phase difference between PPS signals from DUT and REF devices in the following cases:

- Nominal conditions (no jamming and without FENIX).
- Jamming in harsh conditions (GPS timing but with very low C/N_0).
- Jamming with 30-40 dB (depending on the jamming signal) more power than in the previous case, but protected with FENIX.

Figure 10.20 shows the phase difference comparison between the proposed cases for a CW jamming during 10 minutes. The CW jamming is 40 dB more powerful when using FENIX. Without FENIX, the maximum error in timing is about 60 ns during the 10-minute record. However, with FENIX, the maximum timing error is about 30 ns during the same period of time, but with a jamming signal that is 40 dB more powerful.

Similarly, Figs. 10.21 and 10.22 show the phase difference comparison between the proposed cases for the chirped jamming scenarios. Chirp #1 and #2 are 30 dB and 35 dB more powerful when using FENIX. In the first case (chirp #1), the maximum error with FENIX is about 50 ns and without FENIX it is 10 ns. On the contrary, for chirp #2, the maximum error with FENIX is about 25 ns and without FENIX it is 50 ns.

These results show how FENIX mitigates the jamming signals in such a way that even with 30 to 40 dB more powerful RFI signals the maximum phase difference error between

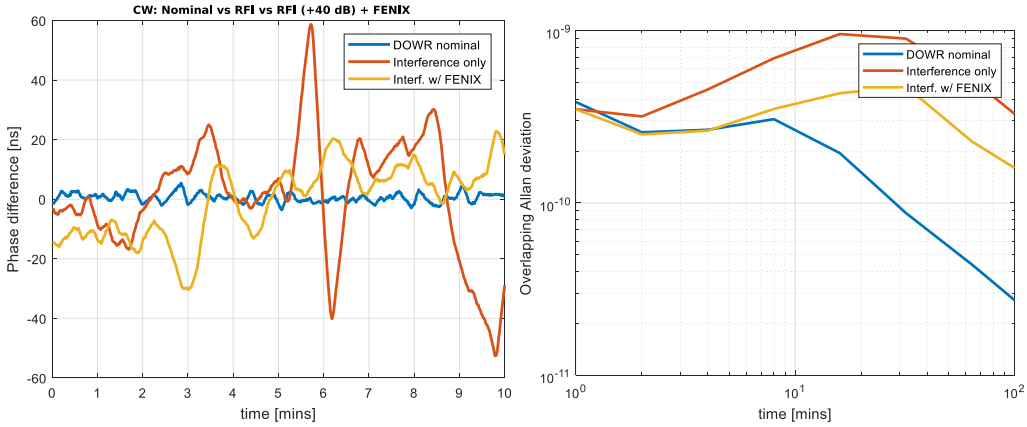

(a) **(b)**

Figure 10.20: (a) Time plot of phase difference between PPS signals from DUT and REF devices in the presence of a CW interference. FENIX constant delay of 1650225 ns has been subtracted. (b) Overlapped Allan's deviation of the phase difference.

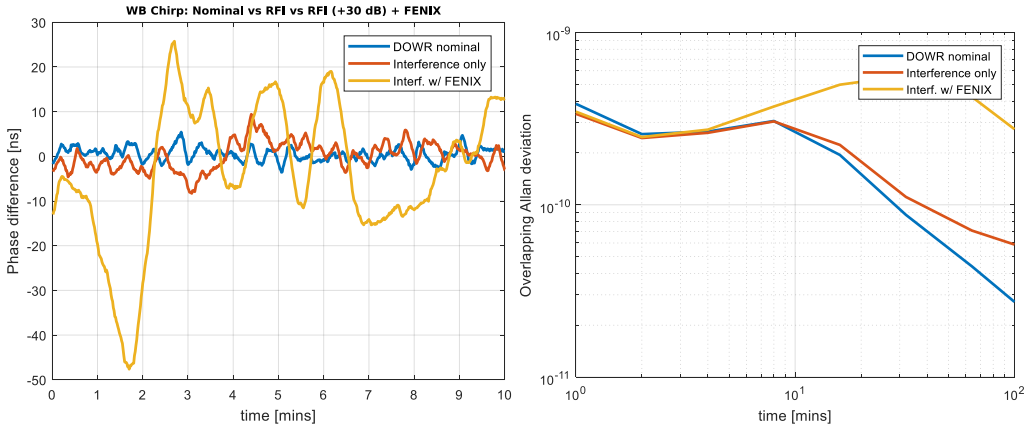

(a) **(b)**

Figure 10.21: (a) Time plot of phase difference between PPS signals from DUT and REF devices in the presence of the chirp #1 interference. FENIX constant delay of 1650225 ns has been subtracted. (b) Overlapped Allan's deviation of the phase difference.

both DOWR devices is lower than 100 ns.

10.7 Conclusions

This chapter is entirely devoted to the assessment of the real-time performance of FENIX, and in particular, of the FENIX-Lite.

A customized VNA, the FENIX-Analyzer, has been built in order to measure the transfer

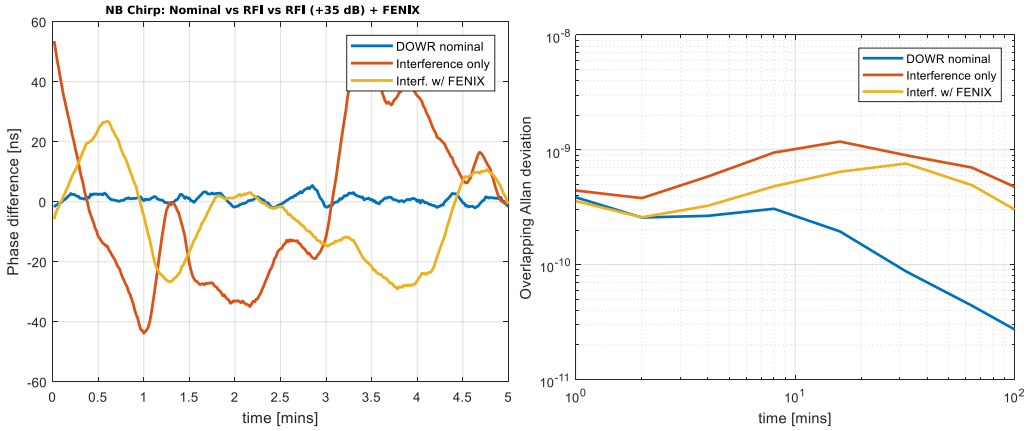

(a) **(b)**

Figure 10.22: (a) Time plot of phase difference between PPS signals from DUT and REF devices in the presence of the chirp #2 interference. FENIX constant delay of 1650225 ns has been subtracted. (b) Overlapped Allan's deviation of the phase difference.

function of FENIX-Lite in the presence of three different RFI/jamming signal, which are considered to be representative of real RFI/jamming scenarios. The results show how the power transfer function adapts itself to mitigate the RFI/jamming signal. In addition, a large but constant delay of about 1.65 ms is introduced by inner digital signal processing blocks of FENIX. However, it can be easily calibrated and compensated.

Moreover, several real-time tests with GNSS receivers have been performed using GPS L1 C/A, GPS L2C, and Galileo E1OS. The results show that FENIX-Lite provides an extra resilience against RFI and jamming signals up to 30 dB. Similar results have been obtained when direct-signal DDMs are used to asses the mitigation performance of FENIX-Lite. The resilience increase is mainly limited by the current hardware, while the SP processing stage may achieve even a better mitigation performance if hardware limitations are overcome. For example, an extra 10 dB of resilience can be added if the input signal is attenuated for an RFI power larger than -30 dBm, thus achieving a protection level up to 40 dB. This case is further discussed in Chapter 12.

Furthermore, FENIX-Lite has been tested using a real GNSS timing setup. The results of these tests show that FENIX-lite provides real-time anti-jamming resilience for GNSS timing devices. In particular, up to 40 dB for CW RFI/jamming signals, and of 30-35 dB for representative chirp signals under evaluation. Thus, FENIX allows the proposed timing system to work in the presence of jamming signals.

In addition, a trade-off between jamming resilience and time uncertainty has also been found. Under nominal conditions, when no RFI/jamming signal is present, a small additional jitter on the order of 2-4 ns is introduced in the PPS signal. Besides, a maximum bias of 45 ns has been measured under heavy jamming conditions, which is still acceptable for current timing systems requiring accuracy levels of 100 ns. Despite this trade-off, FENIX has proven to be an effective standalone solution for GNSS-based timing systems suffering from the problem of RFI and jamming.

11

Chapter 11

RTS: a robust tracking system under jamming

This chapter is devoted to the design, implementation and test of a Robust Tracking System (RTS). RTS is a terrestrial system with high robustness against RFI and jamming attacks, which aims to be a backup solution for GNSS in critical tracking applications. The RTS solves the hyperbolic navigation equations by means of the Least-Mean-Squares (LMS) algorithm in order to estimate the transmitter position. Moreover, as most GNSS, it uses a spread-spectrum signal modulation in order to achieve greater robustness against RFI signals. A comparison of the different spread-spectrum modulations is performed in order to find out the optimum solution. Moreover, a hardware implementation of the RTS is proposed. Finally, preliminary results of the performance of the RTS are presented and discussed.

11.1 Introduction

As mentioned throughout this PhD thesis, GNSS signals are very prone to suffer from jamming and RFI effects. The GNSS are used in the vast majority of tracking and positioning applications, and an increasing number of them correspond to critical applications which require a high level of security. For this reason, the research and development of new systems able to overcome the RFI problem is in progress. To this end, new interference mitigation techniques have been proposed, and also, the use of signal modulations that the increase robustness against interference are under study.

Critical applications such as the tracking of heavy vehicles, transporting dangerous goods or official state vehicles require a level of reliability that ensures that the position of the mobile is available nearly a 100% of the time. In the presence of a very high power RFI signal, GNSS-based systems, not even with RFI mitigation capabilities, can fulfill such requirements. For this reason, PNT systems complementary to GNSS are under development, which range from pure inertial systems or quantum compasses to Chip Scale Atomic Clocks (CSAC).

During the last 20 years, there have been numerous efforts to develop positioning systems independent of, and complementary to the GNSS. One example of PNT terrestrial system is an updated version of the 60's LOng RAnge Navigation (LORAN), the enhanced LORAN (eLORAN). eLORAN is independent, dissimilar, and complementary to GNSS. It works at P-band, and it provides users accurate all-weather PNT services, using hyperbolic navigation as its predecessor. Moreover, it allows the users to retain the safety, security, and economic benefits of GNSS, even when their satellite services are disrupted. eLORAN is operating in the US, but it is not fully deployed in Europe at the moment of writing this PhD thesis.

In this PhD thesis, a system named RTS is proposed as a terrestrial system complementary to the GNSS, and it has been specifically conceived and designed to track moving targets. The RTS is based on the Time Difference of Arrival (TDOA) localization technique, it uses a combination of spread-spectrum modulations in order to maximize the robustness against RFI and jamming attacks, and it requires a ground-based infrastructure with a centralized server.

The work presented in this chapter has been performed mainly by a team of undergraduate students, who have been advised by the PhD candidate. This work has been defended in three different final degree projects: "Robust tracking system in front of Radio-Frequency Interferences. Part I: Communications and hyperbolic navigation" [167], "Robust tracking system in front of Radio-Frequency Interferences. Part II: Transceivers and error estimation" [168], and "Robust Tracking System in front of Radio-Frequency Interferences. Part III: Signals, Modulations, and Reliability analysis" [169]. Moreover, an MSc student was also involved in the development of the work done under the framework of an academic collaboration grant.

11.2 System requirements

The architecture of the RTS is based on multiple receiving ground stations, and a single transmitter whose position is to be tracked (see Fig. 11.1). Moreover, the RTS uses at

least 3 receivers for 2D positioning, or 4 for 3D positioning, with known positions in order to estimate the transmitter position. The tracked mobile unit is the one that transmits a beacon signal, which is used to estimate its position in real-time. This approach is completely opposite to the one used in both GNSS and eLORAN. The nodes that suffer from the effects of RFI and jamming are the receivers, not the transmitters. Therefore, it is easier to jam just one receiver (GNSS and eLORAN cases), than multiple receivers which can be tenths of km apart.

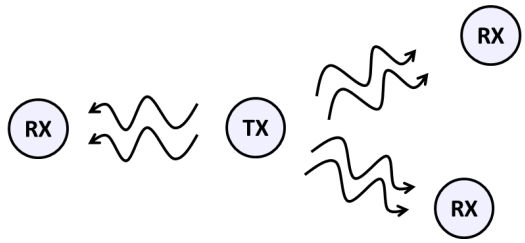

Figure 11.1: RTS TX-RXs conceptual diagram.

Moreover, the methodology proposed to determine the position of the transmitter is the TDOA method [170]. TDOA has been broadly used in many applications such as mobile phones tracking. It is a popular hyperbolic navigation methodology that uses time difference of signal arrival from target to fixed receivers. The strength of the TDOA-based localization method is that absolute time synchronization is unnecessary between receivers. Due to this characteristic, TDOA has been used extensively in real-time locating systems. In order to solve the TDOA equations, the LMS approach is used.

Hyperbolic navigation refers to a class of navigation systems based on the difference in timing between the receptions of two signals, without reference to a common clock (as in GNSS). This timing reveals the difference in distance from the receiver to the two stations. Plotting all of the potential locations of the receiver for the measured delay produces a series of hyperbolic curves. The intersection of two of such hyperbolic curves reveals the position of the receiver. Given N receivers and one transmitter, the measured TOA of the RTS signal between the transmitter and the ith receiver can be expressed as

$$\mathrm{TOA}_i = \frac{1}{c}||P_t - P_i|| + e_i = \frac{1}{c}\sqrt{(X_t - X_i)^2 + (Y_t - Y_i)^2 + (Z_t - Z_i)^2} + e_i, \tag{11.1}$$

where c is the speed of light, $||\cdot||$ is the norm operator (distance between two points), $P_t = (X_t, Y_t, Z_t)$ is the (true) position of the transmitter, $P_i = (X_i, Y_i, Z_i)$ is the position of the ith receiver, and e_i is the measurement error due to thermal noise. If the transmitter and the receivers were synchronized, this set of equations can be used to estimate the position of the transmitter (as in GNSS). However, this is not the case in order to simplify the implementation of the system. Then, the simplest approach is to define the time difference between pairs of measured TOA values. Therefore, the TDOA between the ith and the jth TOA is expressed as

$$\mathrm{TDOA}_k = \mathrm{TOA}_i - \mathrm{TOA}_j + e_k, \tag{11.2}$$

which yields a $N-1$ equation system of hyperbolic curves, and e_k is the measurement noise.

The LMS algorithm is used in adaptive filters to find the filter coefficients that allow to obtain the minimum expected value of the square of the error signal, defined as the difference between the desired signal and signal produced at the output of the filter. It belongs to the family of the stochastic gradient algorithms, i.e., the filter is adapted based on the error in the current time only. In the RTS, the LMS algorithm is used to solve the hyperbolic equations system and, thus, to retrieve the tracked transmitter position following the approach described in [170]. Thus, the estimated position of the transmitter, $\hat{P}_t$, can be obtained in a recursive form as

$$\hat{P}_t[m+1] = \hat{P}_t[m] + \mu \sum_{k=1}^{N-1} \left[\frac{\Delta'_k(P_t[m])}{||\Delta'_k(P_t[m])||^2} \left(c\,\mathrm{TDOA}_k - \Delta_k(P_t[m]) \right) \right], \tag{11.3}$$

where $\hat{P}_t[m]$ and $\hat{P}_t[m+1]$ are the last and the new estimated positions of the transmitter respectively, μ is the learning rate, and $\Delta_k(P_t[m])$ is the expected difference of distances between the transmitter and the k pair of receivers and its derivative, which can be written as

$$\Delta_k(P_t[m]) = ||P_t[m] - P_i|| - ||P_t[m] - P_j||. \tag{11.4}$$

Furthermore, the RTS uses the technology explained above combined with the use of spread-spectrum modulations in order to gain robustness against the RFI and jamming attacks. Hereby, the RTS might be used in applications that require high reliability such as transportation of dangerous goods or vehicle tracking, or in applications that need high resilience against RFI signals and thus, they cannot trust a common GNSS-enabled system.

The main specifications of the RTS are the following:

- a maximum robustness against RFI and jamming attacks,
- an accuracy on the level of tenths of meters such as in the case of eLORAN,
- under no interference conditions, GPS is used as a timing synchronization source,
- a flat-Earth model is assumed for the sake of simplicity, despite more precise coordinate system such as the WGS84 could be used,
- a transmitting frequency of 1 PPS without synchronization between nodes,
- to use the free UHF band (433 MHz) in order to reduce propagation losses as compared to S-band (2.4 GHz) for example,
- the retrieval algorithm is implemented in a central server, and
- the representation of the position is done in Google Earth using the KML format.

11.3 RTS simulator

In this section, a simulation of the LMS algorithm proposed to solve the hyperbolic navigation functions given the TDOA measurements has been implemented for two reasons. The first one is to validate the performance of the LMS algorithm. The second one is to compare the resilience of different spread-spectrum modulations in the presence of RFI and jamming signals.

11.3.1 Introduction

The main goal of this simulator is to validate the RTS design under different scenarios with different conditions. In order to simulate the whole system, the modulation simulator will be attached to the part corresponding to the hyperbolic navigation and the LMS algorithm simulation.

A GUI has been created in order to set the parameters for the simulation and to see the results in a visual and interactive way. Figure 11.2a shows the first interface where the simulator asks for the following parameters:

- Transmitter power [dBm].
- LMS algorithm parameters:
  - Number of receivers.
  - Number of iterations.
  - Error value.
  - Learning-rate.
- Environment selection:
  - Rural environment (no buildings nor constructions taken into account).
  - Urban environment (buildings and constructions taken into account).
- Modulation choice.
- RFI signal choice.
- SIR [dB].

Once the user has introduced all the parameters it can proceed to the simulation as it can be seen in Fig. 11.2b. In the left-side plot, the hyperbolic navigation curves (the hyperbolas intersecting on the transmitter spot) are depicted. These hyperbolas intersect, with more or less accuracy, at one point, which turns out to be the transmitter position. Moreover, the right-side plot shows the iterations of the LMS algorithm.

In this simulation, the selected modulation and the RFI type have been already considered. Besides, it also takes into account the SIR specified in the previous step. If a poor SIR is set, the estimation of the transmitter position by the LMS algorithm is degraded, introducing a significant error and therefore, causing an inaccurate estimation.

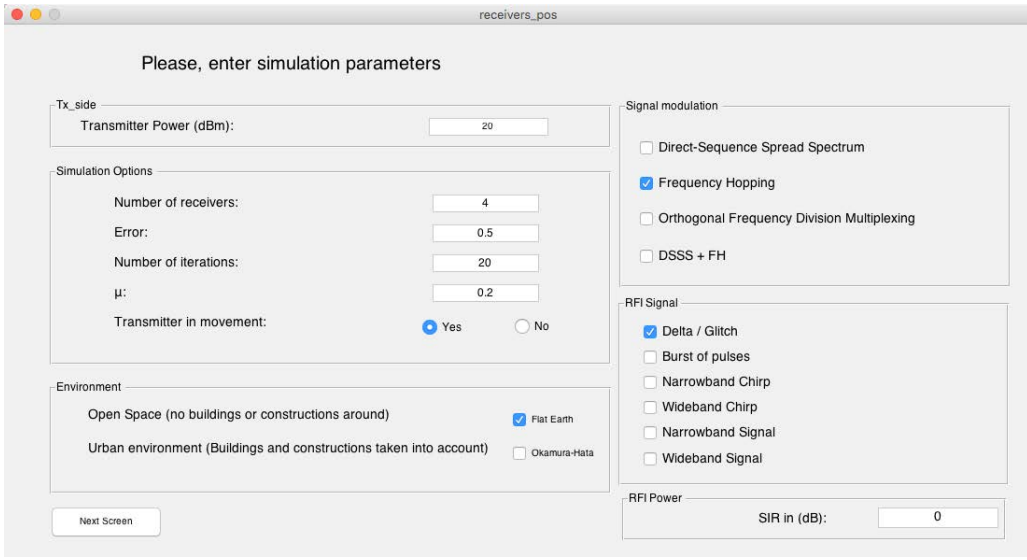

(a)

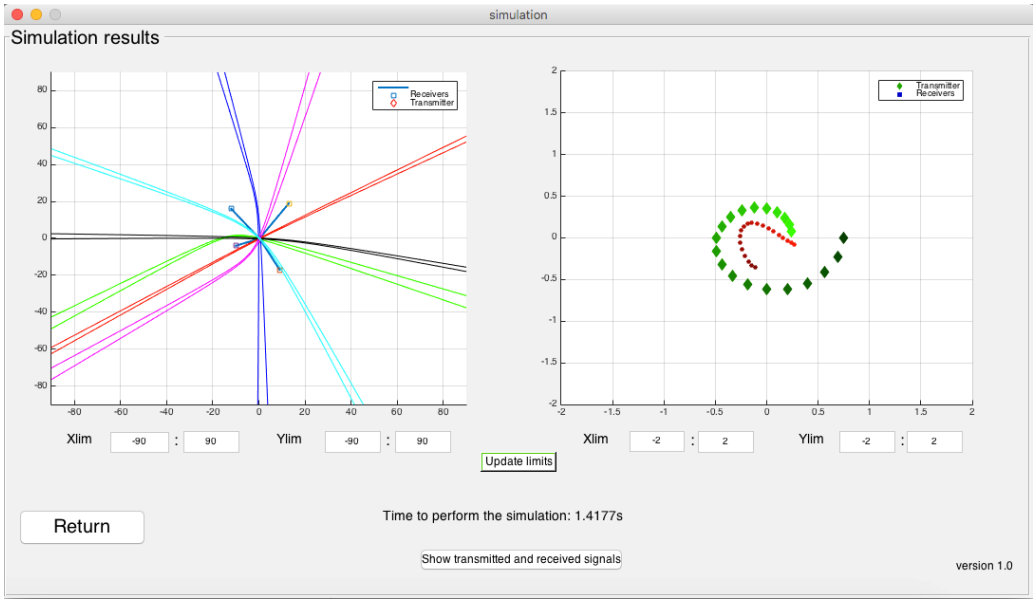

(b)

Figure 11.2: RTS simulator. (a) GUI where the simulation parameters are introduces, and (b) interface showing the results of the simulation.

Once the simulation has been performed, all signals involved in the calculations are shown. This feature is exploited in the following sub-section in order to perform an exhaustive description of every step of the simulation for each modulation under test.

11.3.2 Candidate modulations

As mentioned above, the RTS must be reliable in front of the increasing RFI problem. For this reason, a preliminary assessment of the robustness of known spread-spectrum modulations has been performed. This assessment has been divided into two parts. First, a theoretical study has determined which modulation is the most robust against the effect of RFI signals. After that, a hardware validation test has been conducted in order to prove the results of the theoretical study.

A spread-spectrum signal is one that has an extra modulation that expands the signal bandwidth beyond what is required by the underlying data modulation. Spread-spectrum communication systems are useful to suppress interference, making interception difficult, accommodating fading and multipath channels, and providing multiple-access capability. In this preliminary assessment, the most widely used spread-spectrum modulations are compared in terms of resilience against RFI and jamming signals.

In DSSS, a PRN is used to modulate the message data. This PRN code consists of pulses of a much shorter duration (much larger bandwidth) than the pulse duration of the message signal. Therefore the modulation results in a signal that has a bandwidth roughly equal to that of the PRN sequence. In this context, the duration of the PRN pulses is referred to as chip duration. The smaller this value, the larger the bandwidth of the resultant DSSS signal, and the more robust to RFI the resultant signal becomes. Moreover, the receiver must be set to the same PRN code and must listen to the incoming signal at the right time in order to properly receive and demodulate the signal.

Frequency-Hopping Spread-Spectrum (FHSS) is a technique in which the data signal is modulated with a narrowband carrier signal that "hops" in an apparently random (but predictable) sequence from frequency to frequency as a function of time over a wide frequency band. The signal energy is spread in the time domain rather than chopping each bit into small pieces in the frequency domain. This technique reduces interference because a signal from a narrowband system will only affect the spread spectrum signal if both are transmitting at the same frequency at the same time. If synchronized properly, a single logical channel is maintained. The transmission frequencies are determined by a spreading, or hopping, code. The receiver must be set to the same hopping code and must listen to the incoming signal at the right time and correct frequency in order to properly receive the signal.

Orthogonal Frequency Division Multiplexing (OFDM) is a digital multi-carrier modulation scheme that extends the concept of single sub-carrier modulation by using multiple sub-carriers within the same single channel. Rather than transmit a high-rate stream of data with a single sub-carrier, OFDM makes use of a large number of closely spaced orthogonal sub-carriers that are transmitted in parallel. Each sub-carrier is modulated with a conventional digital modulation scheme (such as QPSK, 16QAM, etc.) at a low symbol rate. However, the combination of many sub-carriers enables data rates similar to conventional single-carrier modulation schemes within equivalent bandwidths.

A comparison of the resilience against RFI and jamming has been performed in the following subsection using the RTS simulator. For this simulations, the SNR has been set to a high value (> 60 dB), so that thermal noise power does not impact to the final results. Moreover, a combination between DSSS and FHSS modulations has also been

tested. In this case, the signal is first spread using the DSSS modulation, and afterwards, the FHSS is applied in order to try to achieve even more robustness.

11.3.3 Robustness assessment

This assessment uses the relationship between input SIR and output SIR to evaluate the performance of each spread-spectrum modulation in terms of robustness against RFI and jamming attacks (see Fig. 11.3).

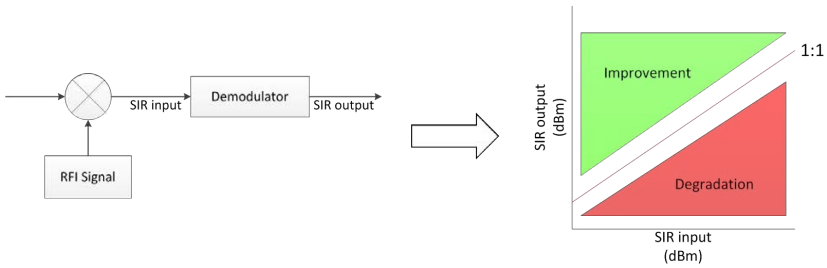

Figure 11.3: Setup used to evaluate the robustness of each spread-spectrum modulation.

In the simulations, the relative delay and phase of the different modulations is set randomly in order to represent a real-case scenario. Five hundred Monte-Carlo simulations are performed for every SIR value at the input of the demodulator. Besides, a range from -30dB to 30dB will be considered as the possible values of the SIR at its input. Once all the simulations have been performed, the percentile 95 of all simulations is calculated.

These results have been plotted in a graph in which the vertical axis represents the SIR at the output, whereas the horizontal axis represents the SIR at the input. In each plot, the 1-to-1 line has also been displayed in order to see how the modulations are performing. If the results are below the 1-to-1 line, the demodulator is introducing a further error. Conversely, if it is above the 1-to-1 line, the modulation shows an extra robustness against RFI signals. The RFI signal under evaluation are the ones used in the assessment of the MFT blanking technique. These are a delta or glitch signal, a burst of pulses, a wide-band Chirp, a narrow-band Chirp, a CW and a PRN wide-band signal. The description of these RFI signals is provided in Chapters 5 and 8. Moreover, the delay, phase and center frequency of the RFI signal in the simulations have also been generated randomly in order to account for all possible cases.

According to the results shown in Fig. 11.4, the DSSS and FHSS (without combining them) are the spread-spectrum modulations that provide the largest robustness against the RFI signals under evaluation. Despite this, the FHSS modulation can be considered as the best case because DSSS only performs significantly better (about 20 dB) than it in the CW case, and they have a very similar performance in the Delta case. Therefore, the modulation chosen for the RTS is the FHSS.

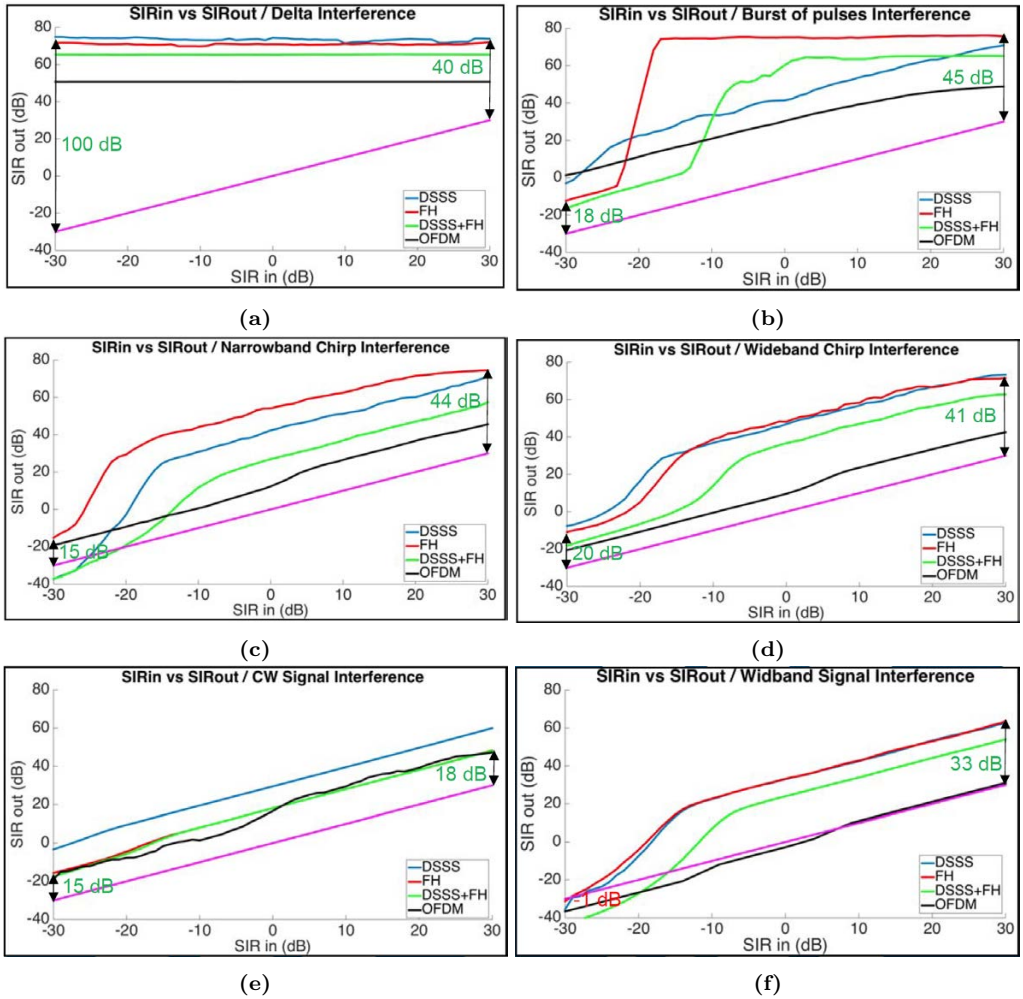

Figure 11.4: Results of the robustness assessment for every type of RFI signal under evaluation: a) Delta/Glitch signal, b) Burst of pulses, c) Wideband Chirp, d) Narrowband Chirp, e) Continuous Wave and f) Wideband signal.

11.4 Hardware implementation

This section describes the proposed hardware to implement both the RTS receivers and the transmitter. Moreover, the validation results of the resilience of the FHSS modulation are also presented.

11.4.1 RX hardware

11.4.1.1 Block diagram

The main goal of the receivers of the RTS is to measure the TOA of the signal from the transmitter and send this measure to the RTS server which ultimately estimated the position of the transmitter. To do so, the block diagram illustrated in Fig. 11.5 is proposed.

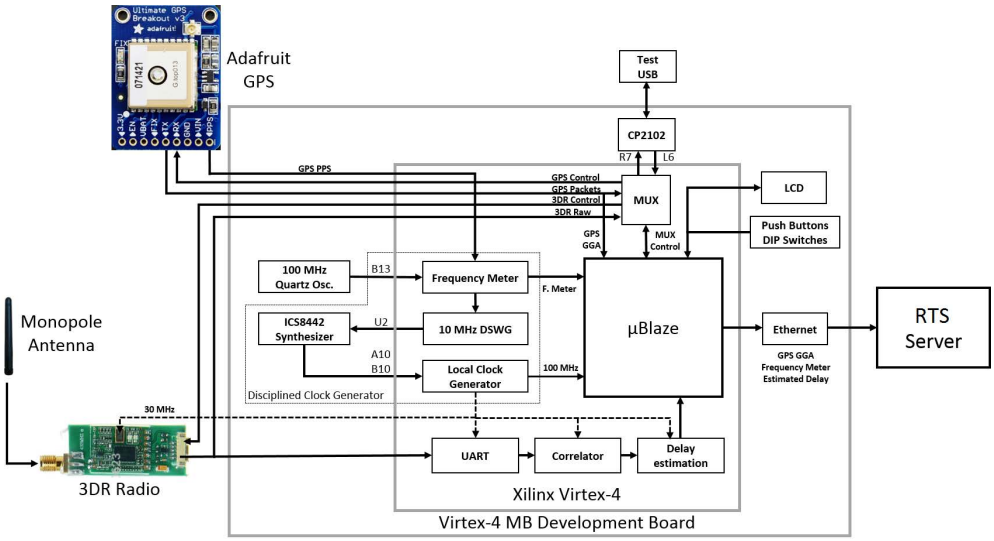

Figure 11.5: Block diagram of each RTS receiver.

The signal from the transmitter is demodulated using a 3DR 433 MHz transceiver. This transceiver implements the FHSS modulation, which has proven to be the most robust spread-spectrum modulation against RFI and jamming attacks. 3DR transceivers allow to configure the number of hopping channels, as well as the transmitting power. Despite they are usually used in full-duplex mode, they can also work unidirectional mode, which is the case of RTS. Both configuration commands and received data are sent and received through a Universal Asynchronous Receiver-Transmitter (UART).

The receiving UART is controlled with peripheral implemented in a Xilinx Virtex-4 FPGA. In particular, the development board Virtex-4 MB was used since it also provides Ethernet connectivity to the RTS receiver. When the signal from the 3DR transceiver is received, the signal delay is estimated using an internal counter.

As mentioned above, the RTS is designed so that no synchronization between transmitter and receiver is needed. However, each RTS receiver has an internal counter which must be synchronized with the others. Since the RTS server expects just relative difference measurements, the receivers provide the difference between their internal counters as a measure of the TDOA. Moreover, they also provide the true frequency at which these counters are incremented, and thus, the difference between counters can be translated into time differences.

A GPS receiver is used as a synchronization system between receivers. If no RFI signal is present, the PPS signal of an Adafruit GPS receiver is used to pseudo-discipline an internal oscillator. Moreover, the GPS can also be used to obtain the position of the receiver, which can be fixed or variable. Therefore, the GPS Pseudo-Disciplined Oscillator (GPSPDO) corrects the frequency of the clock used to increment the counter if no RFI is present. On the contrary, if the PPS signal from the GPS is not available, the local oscillator then enters into a free-running mode, and the measure of the TDOA starts degrading. This degradation depends on the stability of the local oscillator. A study of the stability is presented in the following subsection.

11.4.1.2 Clock stability

The development board has two main clock sources: a 100 MHz crystal, and a frequency synthesizer model ICS8442. The synthesizer uses a reference oscillator between at 25 MHz to generate a pure tone up to 750 MHz with an internal Phase-Locked Loop (PLL). A multiple conversion frequency strategies has been followed in order to achieve the best stability.

The 100 MHz clock is connected to the FPGA. Then, it is up-converted to 300 MHz using a Digital Clock Manager (DCM). The 300 MHz clock is used in combination to the GPS PPS signal to estimate its true frequency, and then, two digital square waves are generated, one at 30 MHz for testing purposes, and another at 10 MHz. On the other hand, the synthesizer has been configured to generate another 300 MHz clock. This last clock is also connected to the FPGA, and also down-converted to 30 MHz in order to be compared with the previous one.

Four of these clocks, the two at 300 MHz and the two at 30 MHz, are externally available at four output pins of the development board. With the help of a frequency meter model Agilent 53181A, the true frequency of each clock has been measured and recorded every second for three days. A total number of 259.200 measurements of the frequency of each clock has been obtained.

The most used tool to study the stability of an oscillator is Alan's deviation (ADEV). Figure 11.6 shows the ADEV of the four clocks. The purple and blue lines represent the 300 MHz clocks (100 MHz quartz oscillator and clock PLL). Both lines show a falling slope, arriving at a minimum, and then following a rising slope. The other two lines represent the 30 MHz generated by the GPSPDO, one derived from the crystal oscillator and the other from the PLL. As opposed to the 300 MHz clocks, they follow a falling slope up to 10^5 s. The reason is that the disciplined oscillators have better stability because their frequency is constantly corrected by the GPSPDO.

Therefore, the 30 MHz GPSPDO clock is used to determine the TDOA if the PPS is available, and the 300 MHz generated from the PLL is used if the receiver is under jamming conditions. When the 300 MHz is used, if the frequency measurement is averaged by $\tau = 10$ seconds, the best case precision of the system (calculated as the ADEV value multiplied by the speed of light) is about 18 m, which is on the order of the initial requirements.

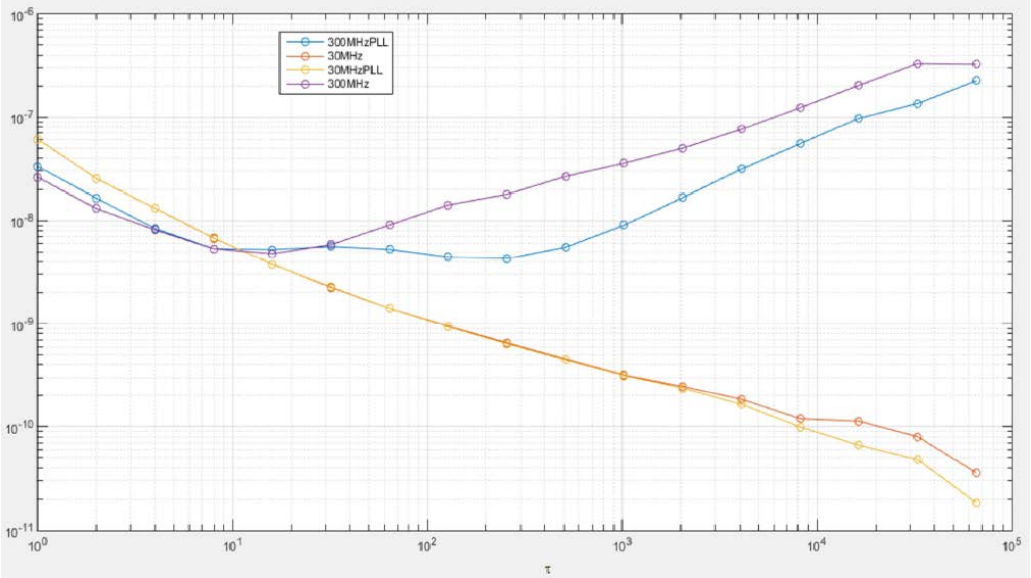

Figure 11.6: Allan's deviation of the four available clocks in the RTS receiver board: 300 MHz derived from a 100 MHz crystal (purple), 30 MHz from GPSPDO (red), 300 MHz from PLL (blue), and 30 MHz from GPSPDO + PLL (orange).

11.4.1.3 RX to server communication

The communication between the RTS receivers and the RTS server is done via TCP/IP protocol. As it can be appreciated in Fig. 11.7, the communication is done using the Ethernet connector available in the development board. Besides, a serial port connector can be used to debug the performance of the receiver locally.

A MicroBlaze micro-controller has been implemented into the Virtex-4. The main functions of the MicroBlaze are to gather all the data required by the RTS server, and then send it periodically for the calculations of the LMS algorithm. This data is composed of the value of the counter corresponding to the TOA, the estimation of the true frequency of the counter, and the position of the receiver. The first two are read on demand from two specific registers. The position of the receiver can be either read from the Adafruit GPS or set manually as a fixed position.

11.4.2 TX hardware

11.4.2.1 Block diagram

One of the best advantages of the RTS design is that the transmitter requires a very simple hardware. In this case, a 3DR transceiver is used to perform the FHSS modulation. The 3DR transceiver has a maximum transmitting power of 20 dBm, which is the maximum value allowed by the local authorities anda common value in most EU countries. Moreover, the transceiver is connected to a smartphone that generates an ID message and sends it every second to the 3DR (see Fig. 11.8). In addiion, the smartphone also supplies the

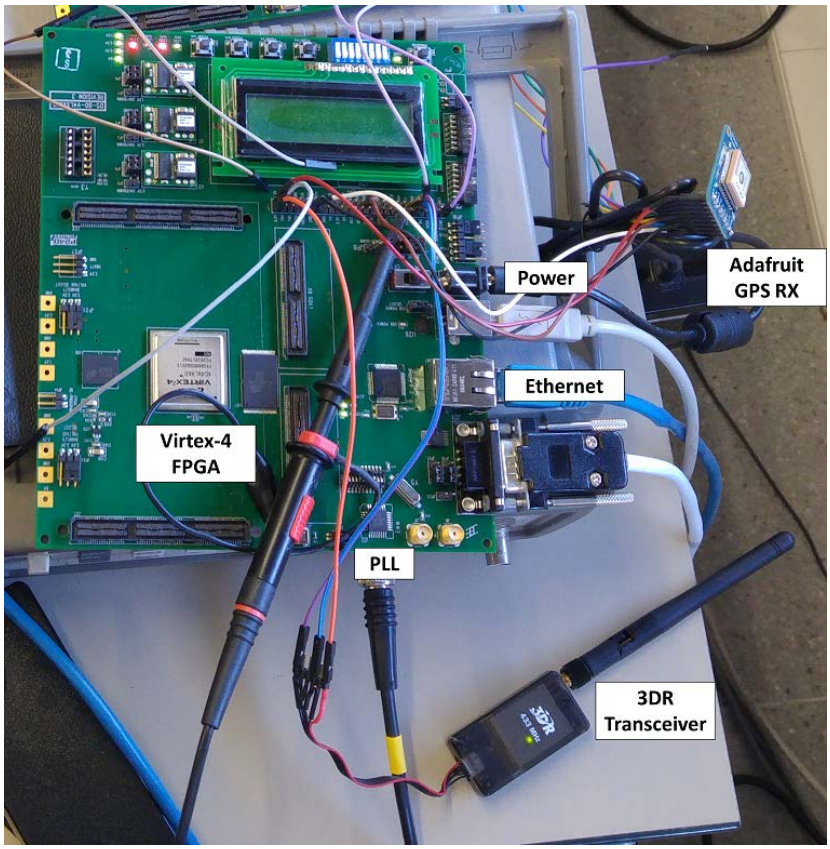

Figure 11.7: Picture of the RTS receiver implemented using a Xilinx Virtex-4 MB evaluation board.

3DR transceiver and sends its GPS position to the RTS server only for testing purposes.

11.4.2.2 FHSS resilience

Once selected as the most robust modulation for the RTS, the FHSS can be tested with real RFI signal using the 3DR transceiver. The test-bed is shown in Fig. 11.9 has been used for this purpose. The output of the 3DR receiver is combined with the RFI signal generated using a R&S SMR-40 signal generator. The combined signal is visualized in a spectrum analyzer, and it is also sampled using an RTL-SDR device. RTL-SDR is a very cheap software defined radio that uses a DVB-T TV tuner dongle based on the RTL2832U chipset. Once the combined signal is sampled and stored, the FHSS is demodulated and the output SIR is computed. Finally, the output and input SIR are compared in order to determine the robustness of the modulation.

The results of this test have been depicted in obtained in Fig. 11.10. In this case, only three types of different RFI signals have been tested (a burst of pulses, a CW and a chirp signal) since they are the most representative in during the tests using the simulator. The

Figure 11.8: Picture of the setup used to implement the RTS transmitter.

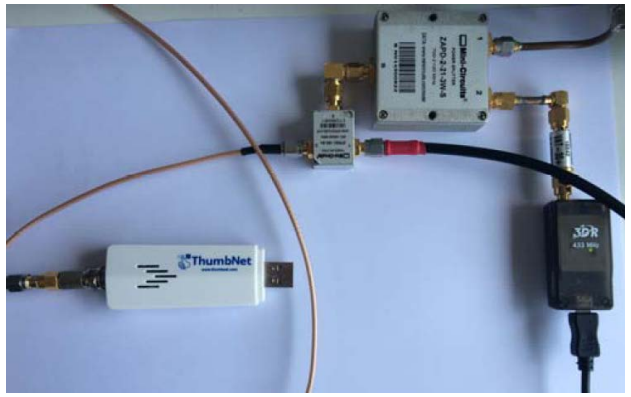

Figure 11.9: Setup used to evaluate the robustness of the FHSS modulation with real signals.

SIR at the input is obtained using the power of the 3DR transmitter and the power of the RFI generator, both known.

The test shows that the results are close to the ones obtained in the simulated case. The differences can be explained by the internal architecture of the 3DR transmitter. One of them is that the 3DR transmitter uses also a whitening transformation plus a Gaussian Frequency-Shift Keying (GFSK) modulation. Moreover, the FHSS modulation implemented in the 3DR is not exactly the same that was simulated. The reason is that the transmitter sends the data at every hop while in the simulation, the data was sent through all the sub-carriers simultaneously. Despite these differences, the results in terms of robustness for the FHSS modulation are acceptable.

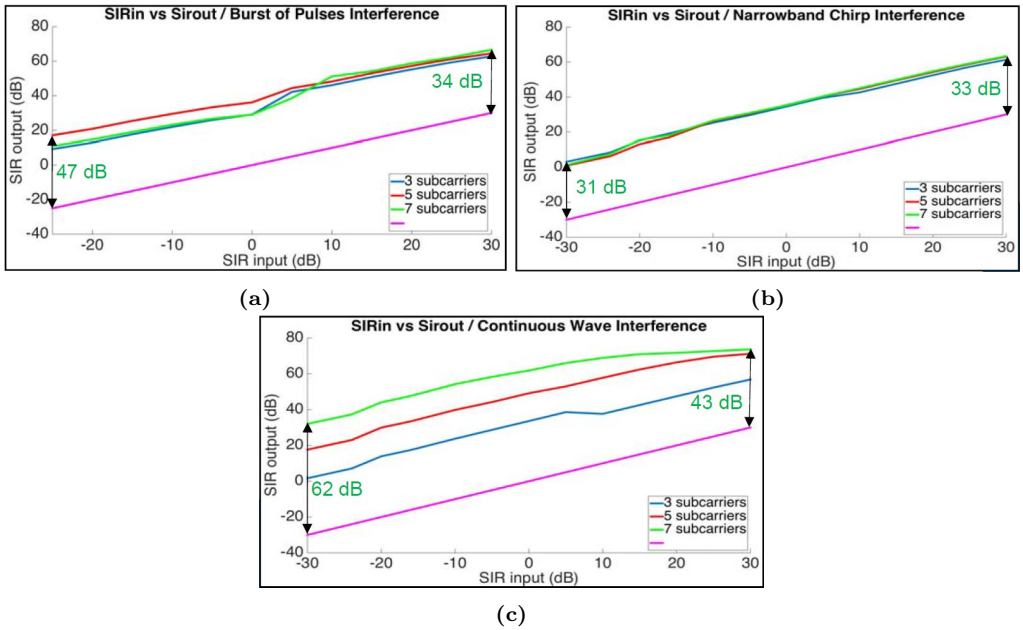

Figure 11.10: Performance of the FHSS for a changing number of sub-carriers (3: blue; 5: red; 7: green) in presence of the following RFI signals: a) a burst of pulses, b) a narrow-band chirp and c) a CW.

11.4.3 3DR transceiver problem

As mentioned above, the 3DR transceivers have been selected because they implement the FHSS modulation, which has been tested to perform well in terms of robustness against RFI and jamming attacks. However, a problem appeared during the first tests using several RTS receivers simultaneously. Even though the RTS receivers were synchronized by using the PPS signal from the GPS receiver, the data messages did not arrive at the same time to their FPGAs being all at the same distance from the RTS transmitter. This malfunctioning occurred because the 3DR transceivers send the demodulated data through an asynchronous bus. Therefore, the 3DR transceivers must be changed by custom FHSS modulators. For this reason, the results presented in the following sections contain simulated RTS receivers, but the performance of the RTS server is evaluated in real-time.

11.5 RTS server

This section deals with the implementation of the RTS server. The priority of the RTS server is to establish a connection with the clients (receivers, main priority to get their position or transmitter, which is for testing purposes), to decide if it is a receiver or transmitter (the decision depends on the received port number), to read and process the data, and finally to estimate the position. All receiving stations are connected to the Internet via Ethernet as well as the RTS server. This allows to send the data necessary

to the RTS server to retrieve the position of the tracked unit. Then, the RTS server processes the connections from the receivers, and then, it receives the necessary data that the receivers send in order to be able to execute the LMS algorithm. Moreover, once the transmitter position is retrieved, a file with all the previous estimated positions is generated in KML format. This KML file can be displayed using Google Earth and, in this way, the final user can see in a friendly way the estimated path that the transmitter has followed.

Figure 11.11 shows a flowchart of the different functions executed at the RTS server. A description of this flowchart is provided in the subsequent lines.

First of all, the RTS server initializes the data variables and creates the files where the server stores the received and retrieved data. After that, the RTS server creates a server socket which will be listening at the specified address and port. The system remains into a waiting state until any connection from the nodes is attempted. If it is established, the connection is handled and a new socket with a new thread is created in order to listen for the next connection. The RTS server creates a new socket every time a node tries to connect to the server. After a successful connection, an algorithm decides if the connection was started by the transmitter or by a receiver. The source port number determines this decision. If it is equal to 20000, it is defined that the socket connection comes from the transmitter, and otherwise, it comes from a receiver. This is necessary because the data receiving algorithm differentiates between data from the transmitter handler or from the receivers. The RTS server creates as many threads as the number of successful connections.

When a connection from a receiver is established, it is given a specific Identification (ID) number. The receiver sends the data periodically and thus, the receiving handle function remains in gathering iteratively all information necessary for the LMS algorithm. When a client socket stops sending information, the ID number is discarded, the RTS server closes the corresponding socket.

The data gathered from the receivers are the TOA counter, the estimated frequency of the local oscillator, and position of the receiver in geodetic coordinates (latitude, longitude, and height). The geodetic coordinated are transformed to ECEF coordinates in order to solve the LMS taking into account the flat-Earth approximation. Besides, the estimation of the local oscillator frequency is used to calculate the true value of the TOA from the received TOA counter. The TOA value and the ECEF coordinated are taken as input values of the LMS algorithm.

On the other hand, the thread that handles the connection from the transmitter receives only the geodetic coordinates of the transmitter (under no RFI conditions), just for comparison and final evaluation of the performance of the RTS.

After the initialization process of the RTS server, a thread devoted to the control of the execution of the LMS algorithm is launched. The LMS algorithm is executed any time at least 3 receivers have an established connection, and they are actively sending data. The correct operation of the RTS depends on the performance of the LMS algorithm.

As mentioned above, the LMS algorithm needs at least 4 receivers to retrieve a position in the 3-dimensional space (X_{ecef}, Y_{ecef} and Z_{ecef}), but it can still solve a 2-dimensional position if under several assumptions are taken. The main assumption, in this case,

relies on the hypothesis that the transmitter position yields in the plane formed by the receivers. Moreover, the LMS has two input parameters. The first is the number of iterations per retrieved point, which is limited by the processing speed of the RTS server. The more iterations, the smaller estimation error if the algorithm converges. The second parameter is the learning rate, which represents a trade-off between the stability and the convergence speed of the LMS algorithm. The effect of the learning parameter is discussed in subsequent sections.

Once the LMS algorithm has estimated the location of the transmitter, its coordinates in the ECEF reference framework are transformed back to geodetic coordinates. The geodetic coordinates are saved in a KML file that allows the user to visualize the estimated position of the transmitter over a map in Google Earth. The LMS algorithm is executed again as soon as a set of new TOA values is available.

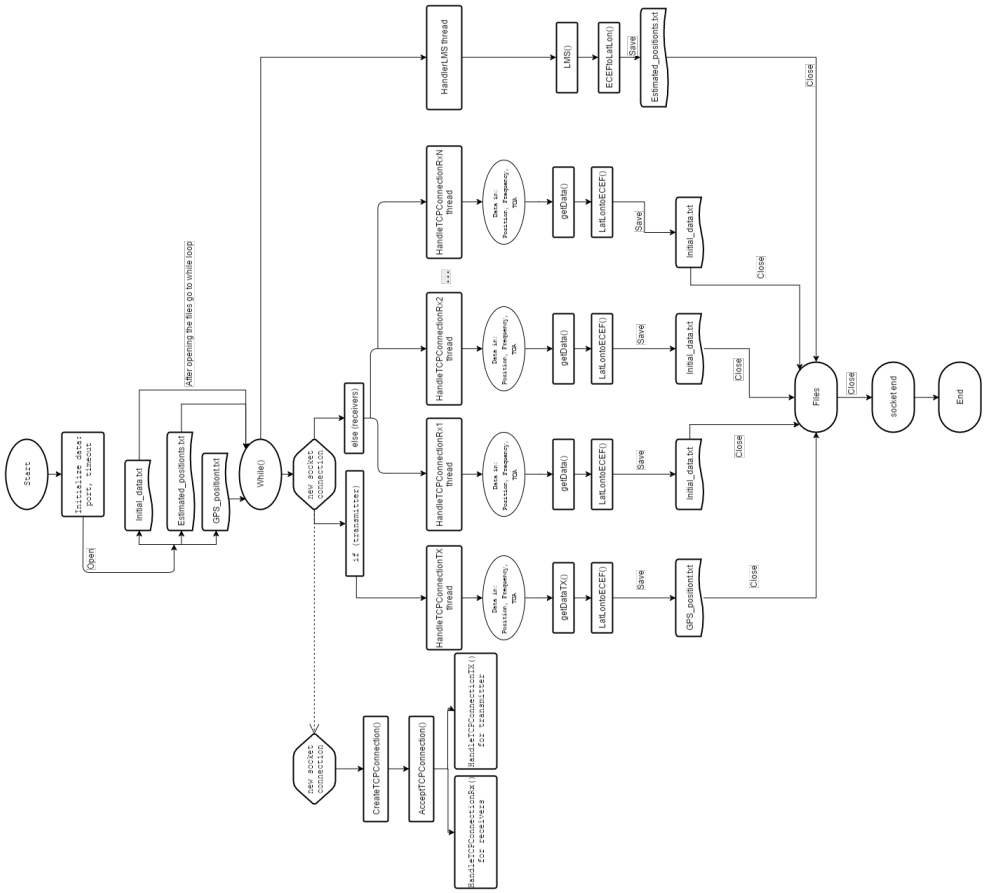

Figure 11.11: Flowchart of the different functions executed at the RTS server.

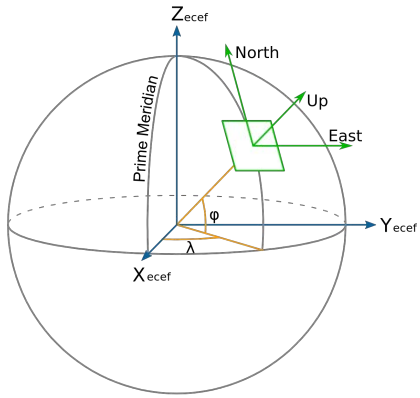

Figure 11.12: Equivalency between geodetic coordinates (latitude φ, longitude λ, and height) and ECEF coordinates (X_{ecef}, Y_{ecef} and Z_{ecef}), as well as NEU coordinates are also depicted [169].

Finally, all data (i.e. the TOA values, the frequency estimated values, the position of the receivers, and the estimated position of the transmitter) is saved in its corresponding files.

11.6 Preliminary results

An example case test has been performed in order to evaluate the real-time performance of the RTS server. The data from the transmitter and the receivers have been simulated and sent to the RTS server as if they were working in real-time. The receivers have been positioned around the Campus Nord of the UPC-BarcelonaTech in Barcelona, Spain as shown in Fig. 11.4. The distance between the receivers ranges from 250 m to 750 m. In this case, 5 receivers are taken into account. A random path inside the Campus has been simulated, and the corresponding data gathered by the receivers is sent to RTS server.

Figure 11.4a shows, in blue color, the real path followed by the transmitter, and in red color, the tracked position estimated by the RTS. It can be appreciated the height fluctuates hardly. The fluctuations are on the order of $\pm$ 30 m (height value under the ground are not shown in the map). The projection of the estimated path in the 2D plane defined by the receivers is shown in Fig. 11.4b. In latitude and longitude, the obtained error is on the order of 5 m, with some outlier values.

This example case corresponds to a velocity of the transmitter equal to 5 km/h. The speed affects the error of the final measurement. In order to characterize this, the system has also been tested at four different speeds of the transmitter. These speed values are 15, 30, 60 and 120 km/h.

Figure 11.14 depicts the absolute 2D error between the real path and the path estimated using the RTS. Sub-figures (a), (c), (e) and (g) show the evolution of the mean positioning error as a function the LMS iteration number is plotted. The speed of the transmitter increases from top to bottom. Note that the larger the speed of the transmitter, the larger is the error in the first iteration. However, they all converge to a value of about 5 km/h.

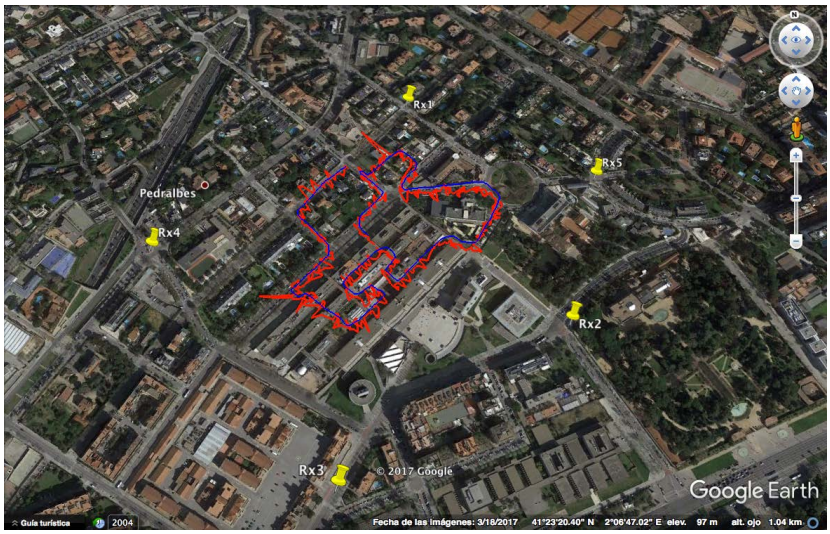

Figure 11.13: Real path followed by the transmitter in blue color, and tracked position estimated by the RTS in red color. The yellow pins correspond to the position of the receivers. The maps in the sub-figures correspond to (a) the tracked position in 3D, and (b) the projection of the estimated path in the 2D plane defined by the receivers.

Moreover, sub-figures (b), (d), (f) and (h) correspond to the PDF of the positioning error at the last LMS iteration. Note that the variance decreases with the speed. This happens because the LMS algorithm can predict better the linear increase of the position. Moreover, the learning rate, μ, has been optimized to reach the steady-state error in 30 iterations, which represents an execution time of less than 33 ms per iteration.

11.7 Conclusions

This section has presented the design of a backup system for GNSS in tracking applications that require high reliability against RFI and jamming attacks. The architecture of the RTS is based on one moving transmitter and multiple terrestrial stations. The position of the transmitter is estimated by triangulation using the TDOA approach. The FHSS modulation has been proven to be the optimal solution to increase the robustness of the system against jamming attacks. A hardware implementation for the RTS transmitter and receiver is proposed, and the FHSS modulation is tested with real RFI signal. Moreover, the RTS server receives the TDOA measurements of all RTS receiver, and then it solves the hyperbolic navigation equations by means of the LMS algorithm. The performance of the RTS server has been tested using a simulated scenario. Preliminary results show that the RTS estimates the position with a horizontal error of about 5 m up to a maximum speed of the tracked unit of 120 km/h.

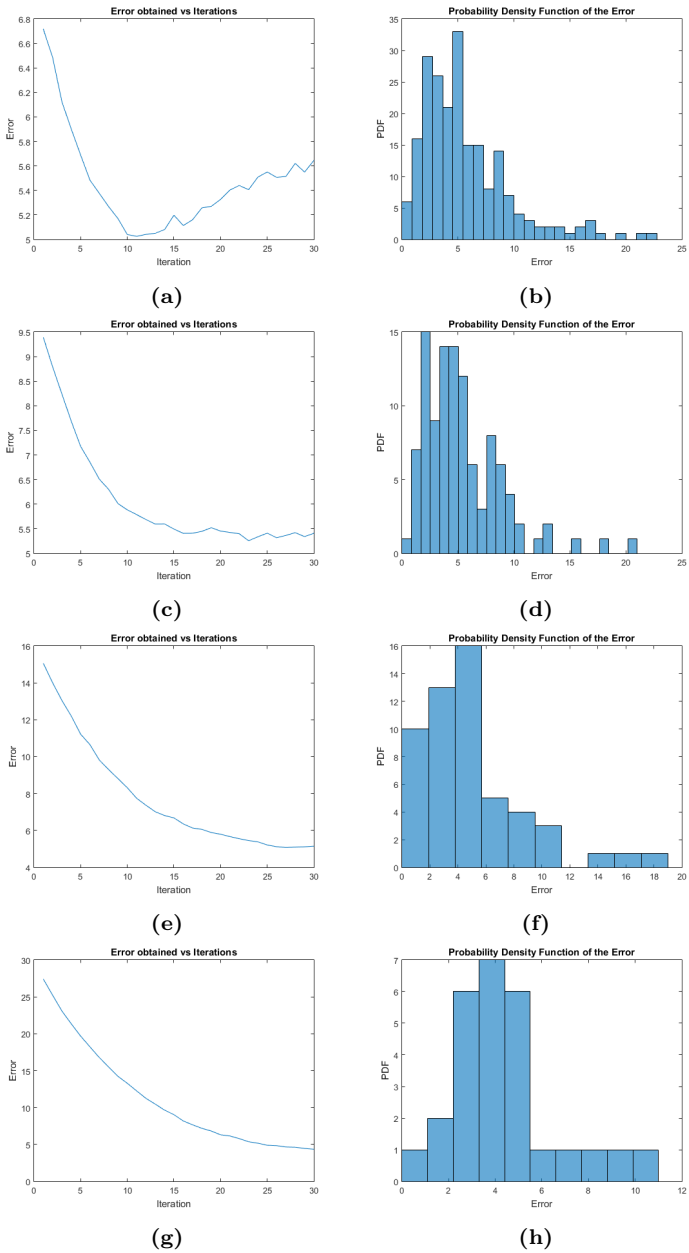

Figure 11.14: Absolute 2D error between the real path and the path estimated using the RTS. Each row of sub-figures correspond to a transmitter speed of 15, 30, 60 and 120 km/h. (a), (c), (e) and (g) sub-figures are the evolution of the mean positioning error as a function the LMS iteration number. (b), (d), (f) and (h) sub-figures correspond to the PDF of the positioning error at the last LMS iteration.

Part IV

Conclusions, contributions and future work

12 Chapter 12

Conclusions and future work

This chapter presents the conclusions and the main contributions of this PhD thesis, the future research lines derived from its contents, and the technology transfer process carried out to fund MITIC Solutions S.L., a spin-off company of the UPC-BarcelonaTech.

12.1 Conclusions

This PhD thesis is devoted to the design, implementation and test of RFI detection and mitigation techniques for navigation and Earth observation. RFIs are undesired signals that degrade or even disrupt the performance of any wireless receiver. RFI signals can be generated either unintentionally, mainly harmonics from lower frequency bands, inter-modulation products, and out-of-band emissions; or intentionally, commonly named jamming and generated from the so-called PPDs. Even though the existing regulations regarding the use of the spectrum, the pervasive use of wireless communications, together with the intentional hijacking of wireless receivers, makes RFI a matter of concern with a growing number of serious incidents in the last decade.

RFI signals can be troublesome for any receiver, but they are especially threatening for applications that use very low power signals. This is the case of PNT applications that rely on the GNSS, or passive microwave remote sensing applications such as MWR and GNSS-R. Nowadays, many liability- and safety-critical applications use the GNSS signals for their normal operation. Autonomous navigation and synchronization of telecommunication networks are two outstanding examples. Recently, GNSS are also used as signals of opportunity in a multi-static radar configuration. GNSS-R uses the GNSS signals reflected over the Earth's surface for remote sensing applications such as ocean altimetry or sea state measurements. On the other hand, MWR measures the radiation emitted by all bodies (at a temperature higher than 0 K) in order to retrieve geophysical parameters such as soil moisture, sea surface salinity, and atmospheric temperature profiles. In MWR, the presence of RFI signals introduces a positive bias in the measured power. In GNSS and GNSS-R, the final SNR or C/N_0 is degraded up to a point where the correlation peak cannot be tracked.

In order to solve, or at least mitigate, the problem of RFI, several RFI-countermeasures are under development. There are two main approaches: law enforcement and protection of the receivers. The former needs infrastructures able to detect and localize the source of the RFI signal in order to switch it off. The latter requires RFI detection and mitigation systems integrated into the receivers. In the literature, a number of RFI detection and mitigation techniques have been proposed in both MWR and GNSS fields. This thesis studies the RFI-countermeasures in each field in two separated parts.

In the part devoted to RFI-countermeasures for MWR applications, first, this PhD thesis completes the development of the MERITXELL instrument. The MERITXELL is a multi-frequency total-power radiometer (with internal frequent calibration) equipped with TIR, NIR, and VIS cameras and a GPS reflectometer. The main goal of MERITXELL is twofold. On one hand, it is an outstanding platform to perform detection, characterization, and localization of RFI signals at the most common MWR imaging bands up to 92 GHz. On the other hand, its multisensor architecture enables testing several data fusion algorithms in post-processing.

Moreover, a novel RFI mitigation technique is proposed for MWR: the MFT. An assessment of the performance of the MFT has been carried out by comparison with other TF mitigation techniques. Three figures of merit have been taken into account during the assessment: the probability of mitigation, the sample loss, and the mitigation performance in terms of residual equivalent RFI temperature after mitigation. According

to the obtained results, the best performance depends on the kind of RFI signal under consideration, and it occurs when the transform basis has a similar shape as compared to the RFI signal. From the results, it appears that the MFT technique is a good trade-off solution among all other techniques since it can mitigate efficiently all kinds of RFI signals under evaluation. However, further improvements are needed in order to fit the stringent requirements MWR applications since a residual bias after mitigation of few K for high input RFI power signal will still corrupt the radiometric measurements, although RFI power is dramatically mitigated thanks to the good properties of the MFT. Furthermore, the application of the MFT blanking to synthetic aperture radiometers is straightforward if each element is seen as a single real-aperture radiometer, and cross-correlations are with all or a subset of the number of quantification bits (typically 8 or more) used in the mitigation process.

In the part devoted to RFI-countermeasures for GNSS and GNSS-R applications, first, a system for RFI detection and localization at GNSS bands is proposed. L-RARO is able to detect RFI signals at the L1 band with a sensitivity of -108 dBm at full-band, and of -135 dBm for CW and chirp-like signals when using the averaged spectrum technique. This sensitivity has been achieved by using a radiometer-like architecture including a temperature stabilization system.

After that, a model to evaluate the degradation of the SNR in GNSS-R measurements has been proposed for both cGNSS-R and iGNSS-R techniques, and it has been evaluated in a general case for each technique. Regarding cGNSS-R, the degradation of the thermal SNR can be produced by either *cross-sat* effect, or external RFI effect, or both. It has been observed that the mean degradation is constant over the whole delay-Doppler space. The *cross-sat* effect may represent the degradation of more than 10 dB considering several satellites with all existing and forthcoming GNSS signals. Nevertheless, the *cross-sat* effect can be minimized when antenna arrays with beam-steering capabilities able to track a particular satellite, while they attenuate signals from the rest of them. On the other hand, the GSSC has been proposed as a figure of merit to evaluate the SNR degradation due to the external RFI effect. This may represent a corruption of the measurements since it is known that they can disrupt the performance of GNSS receivers. In this case, RFI mitigation techniques are necessarily used in order to reduce the error produced by the RFI effect. Regarding the iGNSS-R technique, it has proven to be much more sensitive to RFI than cGNSS-R. In this case, a new phenomenon is introduced: the *cross-talk* effect that may represent a total corruption of the measurements. *Cross-talk* together with *cross-sat* effect may also be attenuated with directive antennas. External RFI effect can have a catastrophic effect in the measurements, even worse than in cGNSS-R, if the interference is captured by both antennas, reflected and direct. In this case, the use of highly directive antennas can help to attenuate the signals captured by them. However, the RFI effect will still remain because of the multiple residual cross-correlations between RFI signals and thermal noise captured by both antennas. Therefore, mitigation techniques will be essential to improve the performance of iGNSS-R instruments under RFI conditions.

Given the need for RFI mitigation systems, the FENIX system has been conceived as an innovative system for RFI detection and mitigation and anti-jamming for GNSS and GNSS-R applications. FENIX uses the MFT blanking, first studied for MWR applications, as a pre-correlation excision tool to perform the mitigation. Moreover, FENIX has been designed to be cross-GNSS compatible and RFI-independent thanks to the use of the

MFT, which has been proven to be a good trade-off solution for RFI mitigation. First, the principles of operation of the MFT blanking algorithm are assessed and compared with other techniques for GNSS signals. Then, its performance as a mitigation tool has been proven using GNSS-R data samples from a real airborne campaign. After that, the main building blocks of the patented architecture of FENIX have been described. They are divided into two main stages, the RF and the SP. According to the proposed architecture, FENIX can operate in the main or auxiliary chains of a GNSS-enabled system, or it can be integrated into either the antenna or the GNSS receiver. The FENIX architecture has been implemented in three real-time prototypes. The most recent one, the FENIX-Lite, has several configurable test paths and test points that are used to validate its real-time performance. Moreover, a simulator named FENIX-Sim allows for testing the performance of the FENIX architecture under different RFI and jamming scenarios. An example case scenario has been chosen to validate the performance of the real-time hardware. The results show that the FENIX-Lite performs as expected in this case scenario.

The real-time performance of FENIX-Lite prototype has been tested using different setups. First, a customized VNA, the FENIX-Analyzer, has been built in order to measure the transfer function of FENIX-Lite in the presence of three different RFI/jamming signals, which are considered to be representative of real RFI/jamming scenarios. The results show how the power transfer function adapts itself to mitigate the RFI/jamming signal. In addition, a large but constant delay of about 1.65 ms is introduced by the inner digital signal processing blocks of FENIX. However, it can be easily calibrated and compensated. Moreover, several real-time tests with GNSS receivers have been performed using GPS L1 C/A, GPS L2C, and Galileo E1OS. The results show that FENIX-Lite provides an extra resilience against RFI and jamming signals up to 30 dB. Similar results have been obtained when direct-signal DDMs are used to asses the mitigation performance of FENIX-Lite. Furthermore, FENIX-Lite has been tested using a real GNSS timing setup. The results of these tests show that FENIX-lite provides real-time anti-jamming resilience for GNSS timing devices. In particular, up to 40 dB for CW RFI/jamming signals, and of 30-35 dB for representative chirp signals under evaluation. Thus, FENIX allows the proposed timing system to work in the presence of jamming signals. In addition, a trade-off between jamming resilience and time uncertainty has also been found. Under nominal conditions, when no RFI/jamming signal is present, a small additional jitter on the order of 2-4 ns is introduced in the PPS signal. Besides, a maximum bias of 45 ns has been measured under strong jamming conditions (-30 dBm), which is still acceptable for current timing systems requiring accuracy levels of 100 ns. Despite this trade-off, FENIX has proven to be an effective standalone solution for GNSS-based timing systems suffering from the problem of RFI and jamming.

Finally, the design of a backup system for GNSS in tracking applications that require high reliability against RFI and jamming attacks is proposed. The architecture of the RTS is based on one moving transmitter and multiple terrestrial stations. The position of the transmitter is estimated by triangulation using the TDOA approach. The FHSS modulation has proved to be an optimal solution to increase the robustness of the system against jamming attacks. A hardware implementation for the RTS transmitter and receiver is proposed, and the FHSS modulation is tested with real RFI signal. Moreover, the RTS server receives the TDOA measurements of all RTS receiver, and then it solves

the hyperbolic navigation equations by means of the LMS algorithm. The performance of the RTS server has been tested using a simulated scenario. The preliminary results show that the RTS estimates the position with a minimum horizontal error of about 5 m up to a maximum speed of the tracked unit of 120 km/h for a configuration with 5 receivers.

12.2 Original Contributions

This PhD thesis contributes directly to the study of the effects of RFI and jamming in the fields of MWR, GNSS and GNSS-R, and to the design and development of RFI-countermeasures for these applications. Moreover, the RFI mitigation algorithms and techniques already proposed can be also extended to other applications such as radio-astronomy, deep-space communications, satellite communications, and to commercial communications systems such as mobile communications (3G, 4G, 5G, etc.) and WiFi.

The following list contains the main original contributions of this PhD thesis.

- Unintentional RFI signals may come from unexpected sources. In particular, this is true if the receiver is using very low power signals such as a microwave radiometer or a GNSS reflectometer. A computer working very close to the antenna of the system may raise the noise floor up to 3 dB at the L-band. Moreover, other electronic components such as DDR2-SDRAM memories can generate harmonics at L-band with chirp-like waveforms that can completely overwhelm the receivers.

- The development of the MERITXELL instrument has been finished. This has taken a 10-year long process and it has involved 3 PhD theses and a number of undergraduate and master students. During this PhD thesis, the software necessary to control and calibrate the measurements has been developed. This software allows performing automatized sequential measurements at desired position and frequency band. Moreover, a brief RFI survey at different MWR has revealed RFI contamination at almost all bands.

- The MFT has been proposed as a tool for RFI mitigation in MWR. A comparative assessment among other TF RFI mitigation techniques has revealed that MFT is an optimum solution for real-time RFI mitigation systems. The MFT decomposes the RFI signal in different signal sub-spaces with different TF resolutions This allows to analyze different features of the RFI signal at each level, and hence it maximized the mitigation performance.

- RFI mitigation is often performed by using blanking thresholding in MWR. This method introduces a bias on the MWR measurements that must be taken into account in the retrieval of the brightness temperature. However, this effect has not been properly assessed in the literature. In this PhD thesis, the blanking bias has been modelled and characterized. Moreover, the degradation of the radiometric resolution has also been characterized.

- A system for RFI detection and localization at GNSS bands is proposed. It has been build using a radiometer-like architecture with temperature stabilization in order to achieve a supreme sensitivity. The system has been designed, implemented, calibrated and tested.

- A model to evaluate the degradation of the SNR in GNSS-R measurements has been proposed and evaluated for both cGNSS-R and iGNSS-R techniques. One of the found effects is the *cross-sat* effect, which is the contribution of the in-view non-tracked satellites. The *cross-sat* effect may not be relevant for PNT applications, but it must be taken into account in high-precision GNSS-R measurements.

- The GSSC has been proposed as a figure of merit to evaluate the SNR degradation due to the external RFI effect in GNSS-R measurements. GSSC accounts the non-stationary behaviour of RFI signals, and it reveals the contribution (magnitude and shape) of the RFI signals to the DDM.

- The FENIX technology has been proposed and patented for RFI mitigation in GNSS and GNSS-R. It is based on the MFT blanking approach defined for MWR applications. FENIX is a standalone real-time pre-correlation RFI-independent anti-jamming system that works between the antenna and the GNSS receiver.

- Three different prototypes of the FENIX technology have been implemented during this PhD thesis. The most advanced one, the FENIX-lite, is designed for narrow-band GNSS signals and it has been build in a portable and compact case.

- Two validation tools have been built in order to validate and test the performance of the FENIX prototypes. First, a simulator named FENIX-Sim allows to compare and validate the performance of the FENIX prototype with the expected one under different RFI and jamming scenarios. After that, a customized VNA named FENIX-Analyzer allows to measure the transfer function of the FENIX-Lite in the presence of different RFI/jamming signals.

- The performance of FENIX-Lite has been tested with commercial GNSS receivers using GPS L1 C/A, GPS L2C, and Galileo E1OS signals. The results show that FENIX-Lite provides an extra resilience against RFI and jamming signals up to 30 dB. Similar results have been obtained when direct-signal DDMs are used to asses the mitigation performance of FENIX-Lite.

- FENIX-Lite has also been tested using a real GNSS timing setup. The results of these tests show that FENIX-lite provides real-time anti-jamming resilience for GNSS timing devices. In addition, a trade-off between jamming resilience and time uncertainty has also been found. Under nominal conditions, when no RFI/jamming signal is present, a small additional jitter on the order of 2-4 ns is introduced in the PPS signal. However, it is still acceptable for current timing systems requiring accuracy levels of 100 ns.

- The design of a RTS system has been proposed as a backup system for GNSS in tracking applications that require high reliability against RFI and jamming attacks. The architecture of the RTS is based on one moving transmitter and multiple terrestrial stations using TDOA trilateration. The FHSS modulation has proved to be an optimal solution to increase the robustness of the system against jamming attacks. The performance of the RTS system has been tested using a simulated scenario with a horizontal error of about 5 m up to a maximum speed of the tracked unit of 120 km/h.

12.3 Future research lines

This PhD thesis has been an extensive work on RFI-countermeasures for MWR, GNSS and GNSS-R systems, and therefore, several future research lines can be derived from this work. The principal research lines are described in the following list.

- The MERITXELL is an outstanding platform to perform RFI characterization and localization. The MERITXELL can store I/Q samples received at all bands used by ground-based microwave radiometers. A characterization study of the RFI signals received at each frequency band can be performed by using deep-learning techniques. This will allow studying the signal shape, the repetition time, the daily or seasonal occurrence, and the possible source of the RFI signal. This information can be used to help to enforce the law and to enhance the performance of RFI mitigation systems. Moreover, if this study is done at several locations, the RFI sources can be localized by obtaining the angle of arrival, and then performing positioning by triangulation.

- The blanking bias and the resolution degradation after applying blanking in MWR measurements have been characterized under the no-RFI hypothesis. However, a method to compensate dynamically for their effect under the presence of RFI must be developed. This can be done by estimating the probability density function of the RFI signal, and then by inferring both discarded RFI and radiometric power from the original signal. This research is crucial for the future integration of RFI mitigation systems in missions with microwave radiometers.

- The mitigation performance of the MFT in MWR applications can be improved by using the correlation among the information in all resolution levels to perform the inverse transform. For low RFI power signals, an RFI signal may be detected at one level, but omitted in the others. In this case, the RFI signal is removed at the detected level, but the contribution of its power from the other levels is present at the output at the mitigation system. This is the main reason why the residual power after mitigation using the MFT is on the order of few K. However, this can be improved if, once an RFI signal is detected at one level, the equivalent bins at other levels are discarded as well. This approach may reduce dramatically the residual RFI power after mitigation, at the expense of increasing also the resolution degradation. However, MWR applications could benefit from this approach since it minimized the mean square error introduced by the RFI signals in the radiometric measurements.

- The capabilities of the RFI detector for GNSS have been tested during this PhD thesis. However, further tests can be performed. Some of the currently working monitoring techniques are based on the use of GNSS receivers and the loss of C/N_0 as the main metric that indicates the presence of an interference source. The detection range of L-RARO could be compared with that of a high sensitivity receiver (e.g., uBlox-M8). The metric that could be used for the high sensitivity receiver could be the distance such that the loss of C/N_0 reaches the value of 1 dB. Having a monitoring instrument that detects the presence of interference sources before they impact the performance of a GNSS receiver would be an key asset for some critical infrastructures such as airports or harbors. Even more so to have the possibility to

identify its direction of arrival or even the location.

- The localization capabilities of the RFI detector are still to be developed. The control algorithm must switch between detection and localization modes. The constructive antenna pattern is used for detection, whereas the notch antenna pattern is used for localization. Since the design of the system has been done to make it portable, the system must be capable to track the source of the RFI signal.
- The performance of the FENIX against large powered jamming signals is mainly limited by the saturation of the ADC. For example, an extra 10 dB of resilience can be added if the input signal is attenuated for an RFI power larger than -30 dBm, thus achieving a protection level up to 40 dB. In order to obtain the optimum working point, the C/N_0 as a function of the SIR must be well characterized. Then, the optimum gain for each working point must be obtained. Finally, the receiving gain can be controlled as a function of the input RFI signal. This research line is already being developed under the the project PRODUCTE from the AGAUR - Generalitat de Catalunya.
- The RTS can be implemented by using synchronous 433 MHz receivers, whereas the FHSS demodulation may be implemented at the FPGA.
- The MFT has shown a good performance for real-time applications. Moreover, its implementation is cost-efficient thanks to the use of the FFT. However, the research on new algorithms for superior protection of the receivers against RFI should continue. The use of transforms such as the fractional Fourier transform [171], the atomic chirplet decomposition [172], or advanced quadratic TF decompositions [173]. Another outstanding example is the use of the KLT for mitigation purposes. The KLT adapts the kernel transform to the input RFI signal thus maximizing the mitigation performance. More information on the KLT can be found in Appendix G. A fast implementation of the KLT will allow to use its benefits in real-time applications [68].

12.4 Technology Transfer

As mentioned in Chapter 1, the implementation of the algorithms, techniques and prototypes developed during this PhD thesis was market-oriented. In other words, the potential market products derived from this work were present since the starting point. It is said that there are three main pillars that sustain the University: education, research and technology transfer. All PhD theses deal with the first two, including this one. However, the connection between academia and industry plays a secondary role. In this PhD thesis, technology transfer has also taken into account.

In particular, the FENIX has been the spearhead of the technology transfer because it has been the most relevant contribution of this PhD thesis. The development of the FENIX has been funded mainly from two projects named LLAVOR 2014 and PRODUCTE 2016 from the AGAUR - Generalitat de Catalunya. The project LLAVOR is devoted to the protection of the Intellectual Property Rights (IPR), to develop pre-prototypes, and to evaluate the business potential of the technology. The project PRODUCTE is devoted to develop a business plan and to build a commercial prototype. Both projects have

contributed to protect the IPR of the FENIX technology through a U.S. patent, and to develop a commercial version of the FENIX with dual-band/wide-band support.

Moreover, the FENIX technology has been awarded with several distinctions, and it has been enrolled in different business acceleration programs. FENIX has participated in the business acceleration program at UC Berkeley Lean Launchpad 2015. FENIX has been the winner of the European Satellite Navigation Competition (ESNC) - Barcelona Challenge 2015 and it was second of the European University challenge in 2015. FENIX was one of the selected projects to participate in the EADA Market Assessment Program 2016, and it was awarded as the best project of the program sponsored by PREMO.

In order to complete the transfer technology to the market, a spin-off company of the UPC-BarcelonaTech named MITIC Solutions S.L. (MITICS) was funded in 2016. The mission of MITICS is the development of innovative state-of-the-art systems to mitigate RFI effects in GNSS-based devices. MITICS has been funded as a vehicle to capitalize the opportunities that appeared for FENIX technology that were not possible to handle from the University, as well as, to transfer further research related to interference countermeasures performed by the research team.

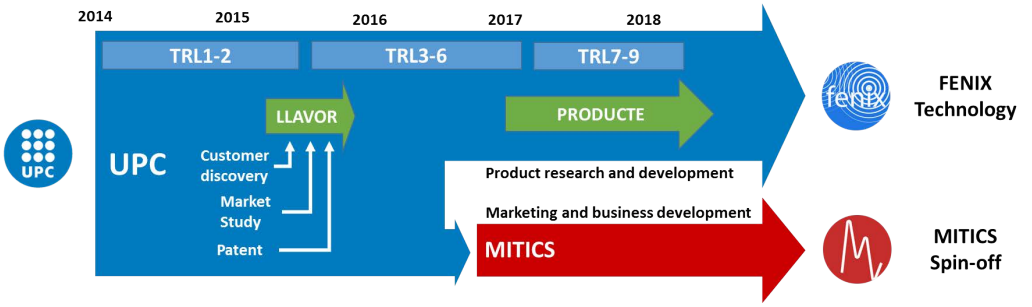

Figure 12.1: FENIX and MITICS time-line.

FENIX is the perfect partner of GNSS-based devices that need high reliability in front of RFI. Regarding the size of GNSS market, the European GNSS Agency (GSA), which is the entity evaluating the European GNSS investment return in terms of benefits to users and economic growth and competitiveness, estimated the core revenue of global GNSS market in 80 billion € in 2016 [174]. However, FENIX is not addressed to the whole market of GNSS devices. Actually, it is addressed to those GNSS applications coined as critical applications, that are those in which a malfunction of the GNSS receiver may represent economic and/or safety consequences. They represent around a 51% of the entire market or 41 billion €.

Beyond the future research lines mentioned above, MITICS will continue with the development of future products based on the FENIX technology.

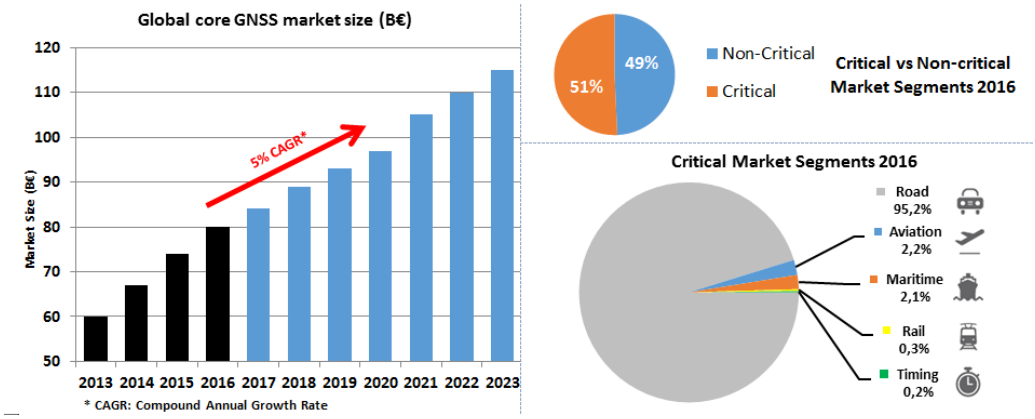

Figure 12.2: Size and expected evolution of GNSS market, and percentage size of market segments according to [174].

Part V

Appendices

A

Appendix A

Notes on probability distributions

This appendix describes some properties of the probability distributions used in this PhD thesis. These probability distributions are the Gaussian (Normal), Rayleigh, Exponential, Rice, and Non-central chi-squared distributions. Moreover, the relationship among them, as well as the main reason for their use in this PhD thesis, are also described.

A.1 Gaussian/Normal distribution

The Gaussian distribution or, as it is often called, the Normal distribution is the most important distribution in statistics and signal processing [116]. Thermal noise is generated by the movement of electrons when the matter is at a temperature above 0 K. The amplitude of the electromagnetic fields involving thermal noise has a Gaussian distributions thanks to the Law of Large Numbers (LLN). According to the LLN, the average of a large number of independent statistical process, like the movement of electrons, tends to behave as a Gaussian distribution. Moreover, thermal noise is usually called white noise since its spectrum can be approximated to be locally flat. Thus, thermal noise is usually named White Gaussian Noise (WGN) in communications systems.

The Normal distribution has a PDF given by:

$$f_{\mathbf{x}}(x) = \frac{1}{\sqrt{2\pi\sigma^2}}\, e^{-\frac{(x-\mu)^2}{2\sigma^2}} \quad x \in \mathbb{R}, \tag{A.1}$$

where μ is a location parameter, equal to the mean, and σ the standard deviation. For $\mu = 0$ and $\sigma = 1$ we refer to this distribution as the standard normal distribution [116]. For thermal noise, μ is always equal to 0, and its power P_n is equal to σ^2.

Then, the integral of the PDF, its Cumulative Density Function (CDF), can be expressed as:

$$F_{\mathbf{x}}(x) = \Pr(\mathbf{x} < x) = \frac{1}{2}\left(1 + \operatorname{erf}\left(\frac{x-\mu}{\sqrt{2\sigma^2}}\right)\right) \quad x \in \mathbb{R}, \tag{A.2}$$

where the error function erf is a tabulated function since the integral of a Gaussian function has not an analytic solution.

The Quantile (q) function is defined as the inverse of the CDF. The q function of a Normal distribution is:

$$q_{\mathbf{x}}(p) = F_{\mathbf{x}}^{-1}(p = \Pr(\mathbf{x} < x)) = \mu + \sqrt{2\sigma^2}\,\operatorname{erf}^{-1}(2p-1) \quad p \in [0,1], \tag{A.3}$$

where the erf^{-1} is the inverse of the error function.

Common used parameters:

- Mean: $\operatorname{mean}(\mathbf{x}) = \bar{\mathbf{x}} = \mu$
- Median: $\operatorname{median}(\mathbf{x}) = \tilde{\mathbf{x}} = \mu$
- Mode: $\operatorname{mode}(\mathbf{x}) = \mu$
- Variance: $\operatorname{var}(\mathbf{x}) = \sigma^2$

In I/Q signal receivers, both channels have thermal noise while receiving. Both I/Q noise signals are statistically independent and uncorrelated between them if ideal I/Q receiver is considered. As I/Q samples are represented in the complex plane (real and imaginary

components), the PDF (as well as the other statistical functions) can be repressed as a bi-dimensional function. If this is the case, I/Q thermal noise so-called CWGN. Moreover, if there is no I/Q amplitude unbalance between both channels, I/Q thermal noise is so-called circular CWGN, and then the standard deviation for both I/Q channels is equal to σ. Furthermore, μ is a complex number equal to 0, and its power P_n is equal to $2\sigma^2$, since both channels are uncorrelated.

A.2 Rayleigh distribution

If z has a circular CWGN with $\mu = 0$ and standard deviation σ for both I/Q channels, then $x = |z|$ follows a Rayleigh distribution [116]. Its PDF can be expressed as:

$$f_{\mathbf{x}}(x) = \frac{x}{\sigma^2}\, e^{-\frac{x^2}{2\sigma^2}} \quad x \in [0, \infty), \tag{A.4}$$

its CDF as:

$$F_{\mathbf{x}}(x) = \Pr(\mathbf{x} < x) = 1 - e^{-\frac{x^2}{2\sigma^2}} \quad x \in [0, \infty), \tag{A.5}$$

and its q function as:

$$q_{\mathbf{x}}(p) = F_{\mathbf{x}}^{-1}(p = \Pr(\mathbf{x} < x)) = \sigma\sqrt{-\ln\left((1-p)^2\right)} \quad p \in [0, 1]. \tag{A.6}$$

Common used parameters:

- Mean: $\text{mean}(\mathbf{x}) = \bar{\mathbf{x}} = \sigma\sqrt{\frac{\pi}{2}}$
- Median: $\text{median}(\mathbf{x}) = \tilde{\mathbf{x}} = \sigma\sqrt{\ln(4)}$
- Mode: $\text{mode}(\mathbf{x}) = \sigma$
- Variance: $\text{var}(\mathbf{x}) = \frac{4-\pi}{2}\sigma^2$

A.3 Exponential distribution

If z has a circular CWGN with $\mu = 0$ and standard deviation σ for both I/Q channels, then $x = |z|^2$ follows an Exponential distribution [116]. Its PDF can be expressed as:

$$f_{\mathbf{x}}(x) = \frac{1}{(2\sigma^2)^2}\, e^{-\frac{x}{2\sigma^2}} \quad x \in [0, \infty), \tag{A.7}$$

where $P_n = 2\sigma^2$ is the average power of the I/Q thermal noise. Then, its CDF is:

$$F_{\mathbf{x}}(x) = \Pr(\mathbf{x} < x) = 1 - e^{-\frac{x}{2\sigma^2}} \quad x \in [0, \infty), \tag{A.8}$$

and its q function is:

$$q_{\mathbf{x}}(p) = F_{\mathbf{x}}^{-1}(p = \Pr(\mathbf{x} < x)) = -2\sigma^2 \ln(1-p) \quad p \in [0,1]. \tag{A.9}$$

Common used parameters:

- Mean: $\text{mean}(\mathbf{x}) = \bar{\mathbf{x}} = 2\sigma^2$
- Median: $\text{median}(\mathbf{x}) = \tilde{\mathbf{x}} = 2\sigma^2 \ln(2)$
- Mode: $\text{mode}(\mathbf{x}) = 0$
- Variance: $\text{var}(\mathbf{x}) = \left(2\sigma^2\right)^2$

A.4 Rice distribution

If z has a circular CWGN with $\mu \neq 0$ and standard deviation σ for both I/Q channels, then $x = |z|$ follows a Rice distribution [116]. When an RFI signal is present, each one of the I/Q samples can be seen as circular CWGN with a deterministic mean equal to the absolute value of each RFI sample $|i|$.

The Rician PDF can be expressed as:

$$f_{\mathbf{x}}(x) = \frac{x}{\sigma^2} e^{-\frac{x^2+|i|^2}{2\sigma^2}} I_0\left(\frac{x\,|i|}{\sigma^2}\right) \quad x \in [0,\infty), \tag{A.10}$$

where $I_0(\cdot)$ is a modified Bessel function of the first kind [118]. Its CDF is

$$F_{\mathbf{x}}(x) = \Pr(\mathbf{x} < x) = 1 - Q_1\left(\frac{|i|}{\sigma}, \frac{x}{\sigma}\right) \quad x \in [0,\infty), \tag{A.11}$$

where $Q_1(\cdot)$ is the Marcum Q-function of first order [2, 119, 120].

A.5 Non-central chi-squared distribution

If z has a circular CWGN with $\mu \neq 0$ and standard deviation σ for both I/Q channels, then $x = |z|^2$ follows a Non-central chi-squared distribution with two degrees of freedom [116]. When an RFI signal is present, each one of the I/Q samples can be seen as circular CWGN with a deterministic mean equal to the power value of each RFI sample $|i|^2$.

Its PDF can be expressed as [175]

$$f_{\mathbf{x}}(x) = \frac{1}{2\sigma^2} e^{-\frac{x+|i|^2}{2\sigma^2}} I_0\left(\frac{\sqrt{x}\,|i|}{\sigma^2}\right) \quad x \in [0,\infty), \tag{A.12}$$

where $I_0(\cdot)$ is a modified Bessel function of the first kind [118]. Its CDF is:

$$F_{\mathbf{x}}(x) = \Pr(\mathbf{x} < x) = 1 - Q_1\left(\frac{|i|}{\sigma}, \frac{\sqrt{x}}{\sigma}\right) \quad x \in [0,\infty), \tag{A.13}$$

where $Q_1(\cdot)$ is the Marcum Q-function of first order [2, 119, 120].

B

Appendix B

MERITXELL mobile unit and software guides

This appendix contains the user guidelines necessary to operate the MERITXELL radiometer. The first section states how to stabilize the mobile unit platform, charge the radiometer and initialize the robotic arm. The second section is a quick operation guide of the dedicated MERITXELL software developed during the co-directed TFG [75]. Finally, third and fourth sections describe in detail how is the communication protocol between the PC software and the positioning and measuring units of the MERITXELL radiometer. Some of the details related to MERITXELL control and positioning program are extracted from [75], and from the operating manual of the mobile unit.

B.1 Mobile unit operation guide

This section contains several guides necessary to operate MERITXELL (Figs. B.1a-b) and PAU-SA (Figs. B.1c-d) radiometers with their mobile unit. The first subsection explains how to stabilize the platform where the mast and robotic arm are anchored. The second subsection states how to charge and discharge the radiometers to and from the robotic arm. The third subsection explains the necessary steps to initialize the mast and robotic arm so that it can start operating once the MERITXELL is already secure to it. Refer to the mobile unit manual for further details not included in this guide.

(a) **(b)** **(c)** **(d)**

Figure B.1: MERITXELL (a-b) and PAU-SA (c-d) radiometers deployed over their mobile unit.

B.1.1 Platform stabilization guide

This section contains a guide to set-up the platform in a proper position to operate with MERITXELL and PAU-SA radiometers. The platform must be set in a horizontal position within $\pm$ 1° of pitch and roll with respect to the gravity force vector. To do so, a set of digital and analog inclinometers were installed in the mobile unit. The necessary steps to set the stabilization position are described in the following list and they are illustrated in Fig. B.2:

(a) Disconnect truck lights.

(b) Release mechanical anchors.

(c) Put off plungers.

(d) Open structure legs.

(e) Put on plungers.

(f) Put on structure feet.

(g) Add wooden boards to balance the system (pay attention with the orientation of the support to allow locate metallic stair).

Figure B.2: Stabilization guide.

(h) Plug in the 3 electric connectors (named M, H, and R) outside the structure.

(i) Plug in the electric box to the power grid.

(j) Turn on the main power switch.

(k) Lock the inner door by closing it, move up to down small black switch next to pressure meter, and push "Lock door" button. This step MUST be performed in this specific order. Otherwise press "Enter request" button, open the door, and repeat this step. Besides, press "Rearm" button if blinking.

(l) Select "Manual" operation and press "Start" button.

(m) Adjust up and down legs with the outer control panel.

(n) Set pitch and roll to values close to 0° (less than ± 1° to stop the buzzer).

(o) External bubbles may help to stabilize the platform.

B.1.2 Radiometer charge/discharge

The following steps are required to charge or discharge the MERITXELL radiometer to and from the robotic arm, once the platform is stabilized (see Section B.1.1). The procedure required for PAU-SA radiometer is similar so that the same steps can be followed.

How to charge MERITXELL radiometer:

1. Pull out radiometer carriage pins/plungers (see Fig. B.3a).
2. Push radiometer carriage towards "working" position (closer to robotic arm).
3. Use long screws (2) to fix the radiometer to the robotic arm (see Fig. B.3b).
4. Put pins/plungers in the corresponding hole.
5. Use short screws (4) to secure the radiometer to the robotic arm (see Fig. B.3c).
6. Open metallic flanges (see Fig. B.3d).

How to discharge MERITXELL radiometer:

1. Close metallic flanges (see Fig. B.3d).
2. Remove and store short screws (4) (see Fig. B.3c).
3. Pull out radiometer carriage pins/plungers.
4. Remove long screws (2).
5. Use long screws to push the radiometer out of the robotic arm (use with the reversed position to as in Fig. B.3b).
6. Push radiometer carriage towards "rest" position (farther to the robotic arm one).
7. Put pins/plungers in the corresponding hole (see Fig. B.3a).
8. Remove and store long screws (2).

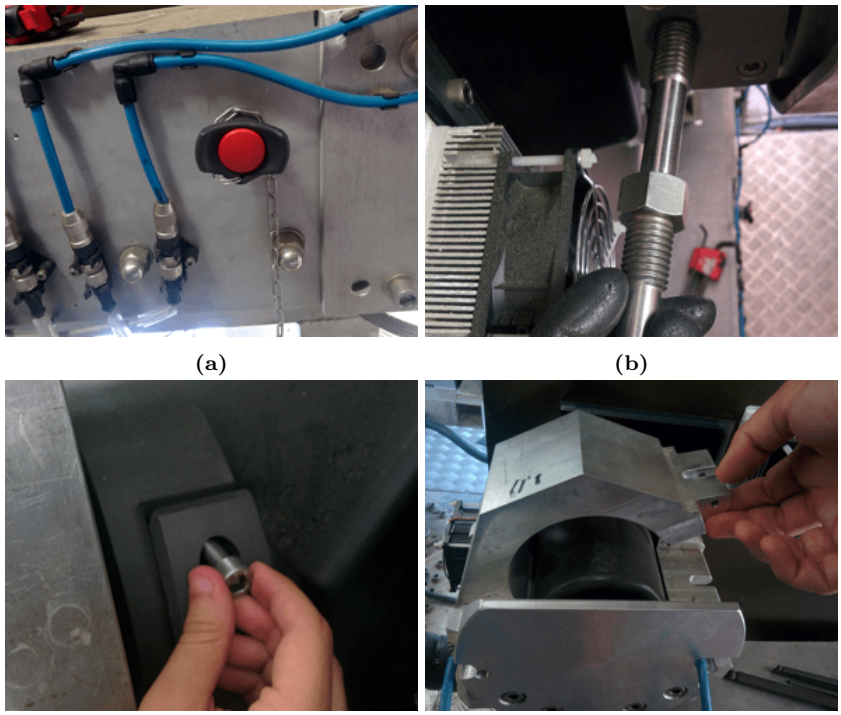

(a) **(b)**

(c) **(d)**

Figure B.3: Radiometer charge/discharge procedure.

B.1.3 Initialization guide

The following list contains the quick steps to be done before using the MERITXELL positioning and measurement software. These steps must be followed once the platform is stabilized (see Section B.1.1). If no radiometer is charged, these steps should initialize the robotic arm automatically ("HOME" operation). However, if MERITXELL radiometer is charged properly (see Section B.1.2) before the starting the initialization process, specific issue solving procedures must be taken into account. The steps to be followed are:

1. Turn on the main power switch in control panel.
2. Wait until "Conf. Bus" process is done.
3. Select "Automatic" mode in control panel.
4. Lock the inner door by closing it, move up to down small black switch next to pressure meter, and push "Lock door" button.
5. Push "Rearm" button if blinking.
6. Push "Start" button.
7. Push "Load Radiometer" button.

8. "HOME" operation is ongoing. This step may take up to 30 minutes to be completed. Some issues may appear during the process, which can be solved by the next steps:

   - If the program position is stuck at number 483, move up the robotic arm to the "working" position. Program position should change automatically to 433. Select "Manual" operation, press "Start", go to the robotic arm submenu, and press "Treball" button together with "Inhibit" button. After re-starting in automatic mode, the system should continue working.

   - Check encoder number is the system taking too much time to performs its operation. Encoder number must decrease from values larger than 1700 to values close to 1500. Otherwise, mast and robotic arm must be moved to their initial positions manually.

   - Once the MERITXELL is back to its position, change manually the program position from 156 to 110. This must be performed stopping the automatic mode, and by pressing "Shift + 1" keys twice, "0" key once, and finally "Inhibit" key once (buzzer sounds). After that, push "Load Radiometer" button, and start in automatic mode. The MERITXELL program should work nominally when finishing this process.

B.2 Software operation guide

This section describes how to use the MERITXELL software in order to position it and to obtain the desired measurements. Buttons and text boxes contained in this main window are used to generate the specific instructions hat both PLC that controls the positioning function (mast and robotic arm) and MERITXELL radiometer have to receive in order to perform the desired measurements. Further information about how the PC software communicates and operates with the positioning system (PLC) and with the MERITXELL can be found in Section B.3 and Section B.4 respectively.

The main objectives of the program GUI are to provide a user-friendly interface to display the information received from the PLC that controls the positioning system, to display MERITXELL parameters, and to generate the instructions to be sent to both positioning system and MERITXELL radiometer.

This interface is divided into 6 blocks as shown in Fig. B.4. the following subsections contain a description of each block. Blocks 1 and 2 control the interaction between the computer and the positioning system, blocks 3 and 4 configure the radiometer and display to the user the state messages, and blocks 5 and 6 have the function to save, load, launch and debug the specific instructions to be sequentially performed.

B.2.1 Block 1

This block contains the buttons to implement the operations to move the positioning systems to specific positions and to generate the positioning instructions in the command list box contained in block 5.

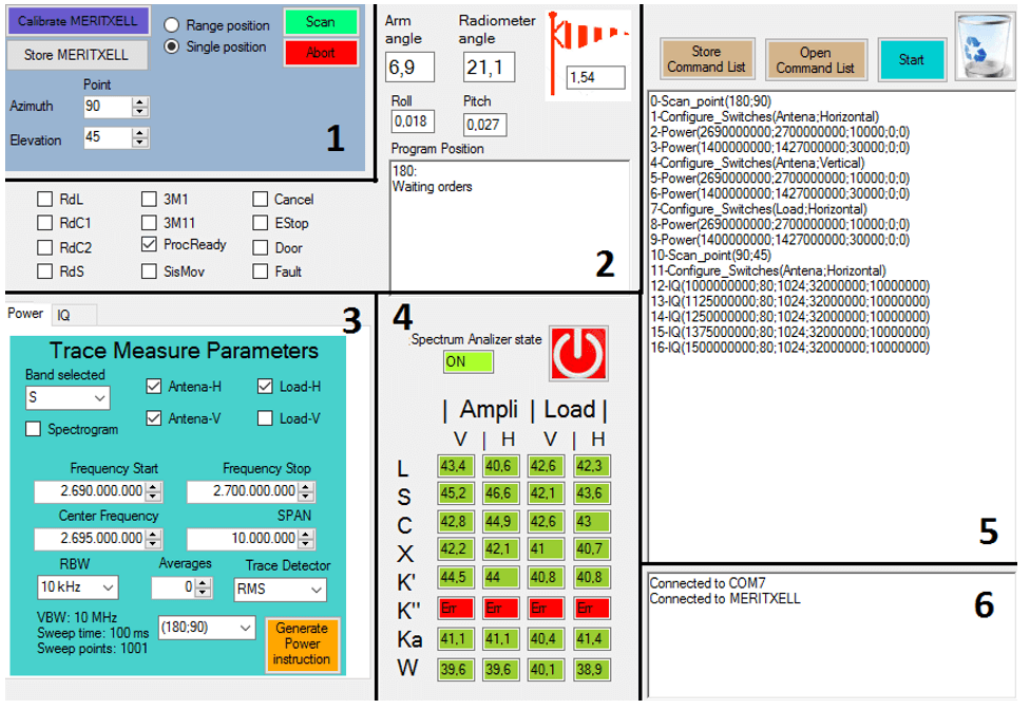

Figure B.4: Graphical user interface.

Functions of each one of the elements that appear in block 1 are detailed in the following list:

- *Upper button* is used to "Load", "Calibrate", or "Store" either MERITXELL or PAU-SA radiometers depending on current program position. See next point.
- *Lower button* is used to "Load", "Calibrate", or "Store" either MERITXELL or PAU-SA radiometers depending on current program position, with a complementary function to the "Upper button" as shown in Fig. B.5. Functions of upper and lower buttons change according to the following states:
  (a) *No radiometer loaded*: The buttons have the function of positioning the arm in the position to load MERITXELL or PAU-SA.
  (b) *MERITXELL loaded*: One of the buttons has the function to locate the radiometer in the MERITXELL calibration position, the other one locates the radiometer in the same position, but expects to discharge the radiometer, once the radiometer has been discharged, the arm will be placed in the HOME position.
  (c) *PAUSA loaded*: One of the buttons has the function to locate the radiometer in the PAU-SA calibration position, and the other to locate in the position to discharge the PAU-SA radiometer, once the radiometer has been discharged, the arm will be placed in the HOME position.

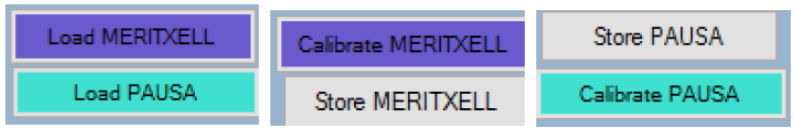

(a) **(b)** **(c)**

Figure B.5: Functions of upper and lower buttons.

- *Radio buttons*: These radio buttons have the function to switch between single point or range of points modes. These two modes are detailed subsequently:
  - *Single point*: if selected, an instruction for positioning the radiometer in a single point can be generated in the command list box by pressing the "Scan" button. Azimuth and elevation of the desired position are introduced in dedicated boxes as shown in Fig. B.6a.
  - *Range of points*: if selected, a set of positioning instructions can be generated in the command list box by pressing the "Scan" button. Azimuth and elevation of all points are introduced as starting and final values, with a determined number of values between them, and for each parameter as shown in Fig. B.6b. An algorithm to generate the instructions efficiently is applied. As shown in Fig. B.7, instructions generate the following orders: move to one azimuth value, scan all elevation values for this azimuth value, move to the next azimuth value once finished all elevation values, and repeat the operation until all azimuth values are scanned. Moreover, in order to satisfy security restrictions, the software does not allow to generate positions with azimuth value lower than 45° or greater than 315° and elevation values higher than 150°.

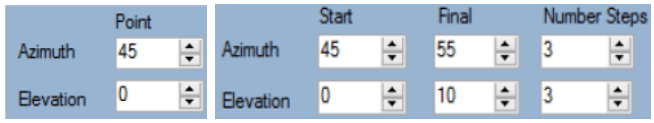

(a) **(b)**

Figure B.6: Azimuth and elevation set boxes in (a) single position mode and (b) range position mode.

- *Scan button*: This button is used to generate the instructions of the position selected depending on the mode selected as above mentioned. The communication protocol between the PC and the PLC is explained in Section B.3.3.
- *Abort button*: This button is used to store the radiometer in its position if a radiometer is loaded or locate the positioning system in Home position and, finally, close the ceiling.

B.2.2 Block 2

This part is used to display the information received by the PLC. More information about the messaging communication protocol between the PLC and the PC is detailed in

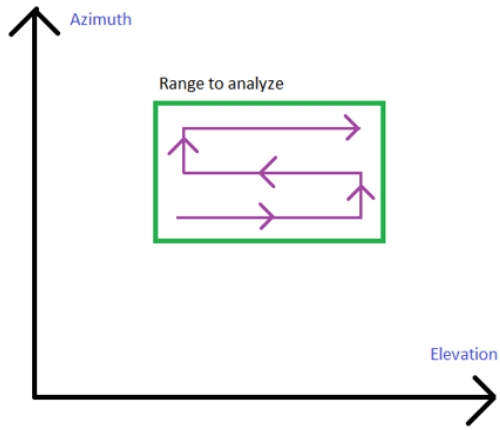

Figure B.7: Range mode.

Section B.3.1.

- *Arm angle display*: This box has the function of display the information of the arm angle, if the box is red (arm angle lower than 60°), the arm is not in "TREBALL" position, and therefore, the positioning system does not work, a message appears in the window to solve this problem.
- *Radiometer angle display*: This box has the function of showing the information of the radiometer angle received.
- *Roll display*: This box has the function of display the information of the roll received by the roll sensor.
- *Pitch display*: This box has the function of display the information of the pitch received by the pitch sensor.
- *Wind display*: This box has the function of showing the information of the wind speed received by the anemometer sensor.
- *Program Position display*: This box contains the information about the actual state of the positioning system, giving a description of the actual movement or giving orders to the user to make. See more information in Section B.3.2.
- Several flags display information generated by the PLC. See more information in Section B.3.1.

B.2.3 Block 3

This block contains allows to generate the required instructions to obtain the desired measurements. These instructions are created in the command list box (block 5), and they are executed sequentially. The instructions contain the parameters to be sent to the spectrum analyzer, which sends back the data corresponding to the required measures required to the spectrum analyzer and obtaining the measures required to the MERITXELL.

The panel contained in block 3 has two different tabs. One of them to generate the instructions to obtain the desired IQ instructions, where the input signal is sampled with an I/Q superheterodyne receiver, and samples are sent as they are to the PC. However, the other tab is used to generate POWER instructions, where the spectrograms of the input data are obtained and send back to the PC.

The panel used to generate IQ instructions is shown in Fig. B.8. Further information can be found in Section B.4.4.2. Its main functions are detailed subsequently:

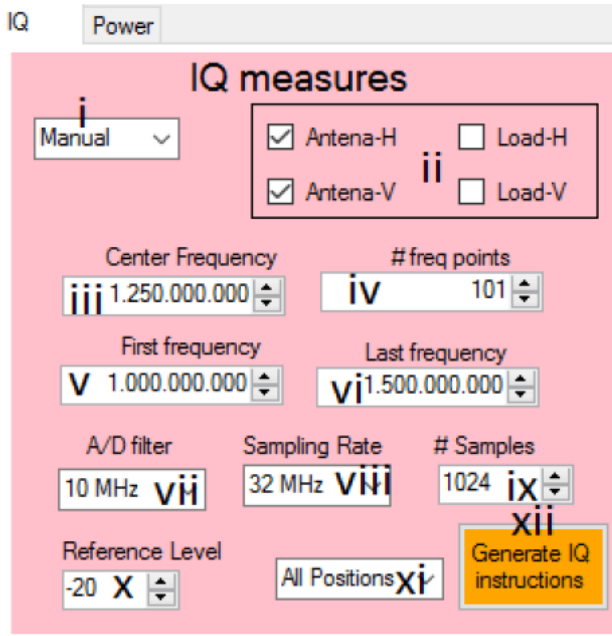

Figure B.8: IQ panel.

i *Band combobox*: It allows to set manually the parameters "iii","v" and "vi", or it sets them automatically to the corresponding values of the bands: L, S, C, X, K', K", Ka or W.

ii *Polarization and direction check-boxes*: This check-boxes has the function to generate the instructions to configure the polarization and direction switches after the button "xii" is pressed. Further information can be found in Section B.4.2.

iii *Center frequency*: This numeric box shows the value of the center of the band to analyze.

iv *Number points*: This box contains the value of the frequency values to analyze between the frequencies between "v" and "vi". After pressing the button "xii", for every switch configuration set up in "ii", N frequency equidistant between "v" and "vi" are generated. Figure B.9 shows an example explanation of the use of the parameter number of points, 3 frequencies values (1 GHz, 1.5 GHz, 2 GHz) will be generated if the number of points is 3 and the values Start and Stop are 1 GHz and 2 GHz.

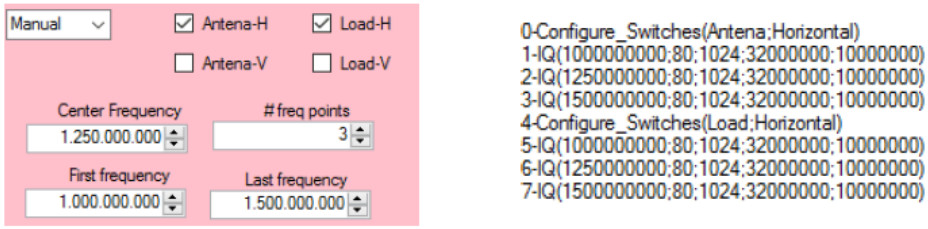

Figure B.9: Example of use of *Number of points* option.

v *First frequency*: This numeric box and the numeric box "vi" indicate the range of the frequencies values to analyze.

vi *Last frequency*: This numeric box and the numeric box "v" indicate the range of the frequencies values to analyze.

vii *AD/Filter*: This parameter is used to configure the cut-off frequency of the A/D filter.

viii *Sampling rate*: This parameter is used to configure sampling rate of the analyzer to obtain the measures.

ix *Number of samples*: This parameter is used to configure the number of measures to obtain for every frequency.

x *Reference level*: This parameter is used as the reference level of the analyzer.

xi *Positions box*: This box has the function to select in which position the instructions of configuring switches and obtain IQ measures should be placed. If the option "All positions" is selected, the instructions will be placed in all the positions existing in the command list box.

xii *Generate instructions buttons*: This button has the function of creating the instructions in the command list box, depending on the input parameters of the IQ panel.

The panel used to generate POWER instructions is shown in Fig. B.10. Further information can be found in Section B.4.4.1. Its main functions are detailed subsequently:

i *Band combobox*: same function as in IQ panel.

ii *Polarization and direction check-boxes*: same function as in IQ panel.

iii *Frequency start*: This numeric box shows the first value of the band to analyze.

iv *Frequency stop*: This numeric box shows the last value of the band to analyze.

v *Center frequency*: This numeric box shows the middle value between the values of boxes "iii" and "iv".

vi *SPAN*: This numeric box shows difference value between the values of boxes "iii" and "iv".

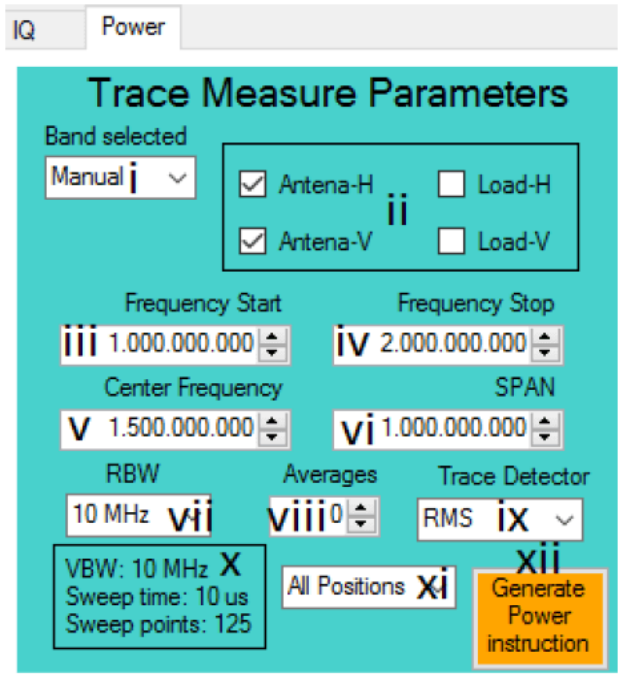

Figure B.10: Power panel.

vii *RBW*: This parameter is used to configure the cut-off frequency bandpass filter in the IF path.

viii *Average*: This parameter is used to decrease the random noise, averaging the desired measure the number of times selected in this box.

ix *Trace detector*: This parameter is used to configure the kind of trace detector: RMS, Average, Max. Peak, Min. Peak, or Sample.

x *Label VBW, Sweep time and Sweep points*: This label displays to the user the video bandwidth, sweep time and sweep points in function of the SPAN and the RBW.

xi *Positions box*: same function as in IQ panel.

xii *Generate instructions buttons*: same function as in IQ panel.

B.2.4 Block 4

This block has a turn ON/OFF button for the spectrum analyzer if necessary, a display that shows its current state, and it has a display for each temperature sensors of each amplifier and band of the MERITXELL. A detailed description of each function is done subsequently:

- *SA turn ON/OFF*: This button is used to turn on or turn off the spectral analyzer of MERITXELL manually. When the Ethernet wire is connected between the ra-

diometer and the computer, the spectrum analyzer will be turned on automatically if it is off and it does nothing if it is on. For further information go to Section B.4.1.

- *SA display*: This display is used to show the actual state of the spectrum analyzer, if it id on, the display contain the message "ON" and the color of the box is green, if it is off, the display contains the message "OFF" and the color of the box is red. The color of this box is white if no Ethernet wire is connected to the computer.
- *Amplifier/Load temperatures*: These boxes show the temperature value of the temperature sensors of the different MERITXELL amplifiers, and depending on the last measures the box change its color. For further information go to Section B.4.3.

B.2.5 Block 5

This block contains the command list box and several buttons to manage it.

The instructions of the command list box can be generated using the panels located in block 1 (positioning) and block 3 (measurement). In particular, the addition of the instructions is done either by pressing the button "Scan", or "Generate IQ instructions", or "Generate POWER instructions". These instructions can be also copy-pasted, or edited manually if it is needed. The list is automatically updated once a new instruction is added or removed. Every instruction has a number that indicates the order of execution.

The following buttons are used to manage the already generated instructions:

1. *Store command list*: This button is used to store the current command list in an external document in order to be loaded in another session.
2. *Load command list*: This button is used to load a command list generated previously.
3. *Start button*: This button has the function to start to read and do the instructions of the command list box sequentially.
4. *Rubbish button*: This button has the function to clear the command list box.

B.2.6 Block 6

This block contains the operations box. This read-only textbox is used to help the user to debug possible errors. It contains a list of the operations already performed by the program.

The messaged displayed in the operations box are of the following kinds:

- Available connections when the software is launched.
- Messages sent to the PLC.
- Information about the switches is configured correctly or not.
- Messages sent to turn on/off the spectrum analyzer.
- Step of the procedure to obtain the desired measurements.

B.3 Positioning system communication and operation

This section details the communication process between the software and the PLC that controls the positioning system in order to move the radiometer in the desired position. The positioning system is a sequential state machine with an identifier called program position. Depending on this program position value the PLC modifies the message to send and the valid expected messages to receive.

When the software is launched, to check if the computer is connected to the positioning system, the program checks if any serial port is connected to the computer. If the computer is connected to the positioning system, it is then possible to receive and send messages to the PLC.

B.3.1 Messages received

The positioning system sends periodically information about the actual state and the sensors contained in it. The information contained in ten of the bytes sent by the positioning system are the following:

- *Flags*: The first and second byte received contain information about the state of the machine and about other elements (state of the door, emergency stop button press or not, button stop active or not, etc.), each bit of these bytes contains specific information about the positioning system. The flags displayed in the software are shown in Fig. B.11.

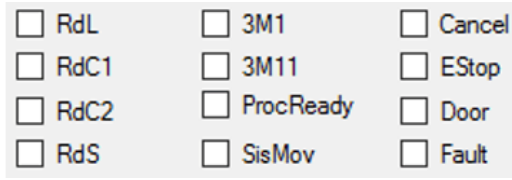

Figure B.11: Received flags.

  These flags contain the following information when enabled:

  - *RdL*: Indicates that the positioning system is in the desired position.
  - *RdC1*: Indicates that the positioning system is in the calibration position of the MERITXELL radiometer
  - *RdC2*: Indicates that the positioning system is in the calibration position of the PAU-SA radiometer.
  - *RdS*: Not implemented yet.
  - *3M1*: Elevation movement has finished
  - *3M11*: Azimuth movement has finished.
  - *ProcReady*: The system is ready to receive a new position to scan.
  - *Sismov*: The mast or the arm of the positioning system is moving.

  - *Cancel*: The system is doing the operations to store the radiometer in his HOME position and to close the ceiling.
  - *Estop*: The emergency button is pressed.
  - *Door*: The door is opened.
  - *Fault*: The stop button is pressed or the switch is not in the automatic position.

- *Arm angle*: The third and fourth byte received contains information of the actual arm angle once the positioning system is calibrated. This arm angle is calculated as:

$$Arm\ Angle = \frac{byte(3) \cdot 256 + byte(4))}{10} - 80.$$

- *Radiometer angle*: The fifth and sixth byte received contains information of the actual angular position of the radiometer once the positioning system is calibrated. This angle is calculated as:

$$Radiometer\ angle = \frac{byte(4) \cdot 256 + byte(5)}{10}.$$

- *Wind Speed*: the seventh byte has the value 0 and the eighth byte has the value 1, the ninth and tenth bytes contain information of the anemometer. This wind speed value in meters per second is calculated as:

$$Wind\ Speed = \frac{byte(9) \cdot 256 + byte(10)}{655.34}.$$

- *Roll*: When the seventh byte has the value 0 and the eighth byte has the value 2, the ninth and tenth bytes contain information of the roll sensor. This roll value in degrees is calculated as:

$$Roll = \frac{byte(9) \cdot 256 + byte(10)}{1638.35} - 10.$$

- *Pitch*: When the seventh byte has the value 0 and the eighth byte has the value 3, the ninth and tenth bytes contain information of the pitch sensor. This pitch value in degrees is calculated as:

$$Pitch = \frac{byte(9) \cdot 256 + byte(10)}{1638.35} - 10.$$

- *Program Position*: When the seventh byte has the value 0 and the eighth byte has the value 4, the ninth and tenth bytes contain information about the program position. This program position contains information about the state of the positioning system, the value of the program position is calculated as:

$$Program\ Position = byte(9) \cdot 256 + byte(10).$$

B.3.2 Program position

As commented in the previous subsection, the program position determines the state of the PLC that controls the positioning system. A list of all the known states that the PLC controller can support is presented subsequently.

Program positions when working with radiometer 2 (PAU-SA) go from 200 to 299, and they are shown in Tab. B.1. Program positions when working with radiometer 1 (MERITXELL) go from 100 to 199, and they are equivalent to those for radiometer 2. Program positions performing a folding operation go from 300 to 399, and they are shown in Tab. B.2. Program positions performing a "HOME" (or initialization) operation go from 400 to 499, and they are shown in Tab. B.3. The first column represents the initial program position, and the second one is the conditions to be fulfilled to update the program position to those in the third column.

Start	Condition	Final
201	Cilindre Braç a repòs, Gir màstil a 0º, Carros i brides Radiòmetre 2 a repòs.	202
202	Cilindre Braç a repòs, Gir màstil a 0º, Motor radiòmetre a posició radiòmetre 2 Carros i brides Radiòmetre 2 a repòs.	203
203	Tancament Obert, Cilindre Braç a repòs, Gir màstil a 0º, Motor radiòmetre a posició radiòmetre 2 Carros i brides Radiòmetre 2 a repòs.	204
204	Tancament Obert, Màstil Estès, Cilindre Braç a repòs, Gir màstil a 0º, Motor radiòmetre a posició radiòmetre 2 Carros i brides Radiòmetre 2 a repòs.	205
205	Màstil Estès, Cilindre Braç a repòs, Gir màstil a Radiòmetre 2, Motor radiòmetre a posició radiòmetre 2 Carros i brides Radiòmetre 2 a repòs.	206
206	Tancament Obert, Màstil Estès, Cilindre Braç a repòs, Gir màstil a Radiòmetre 2, Motor radiòmetre a posició radiòmetre 2 Carros i brides Radiòmetre 2 a repòs.	207
207	Tancament Obert, Màstil Recollit, Cilindre Braç a repòs, Gir màstil a Radiòmetre 2, Motor radiòmetre a posició radiòmetre 2, Carros i brides Radiòmetre 2 a repòs.	208
208	Carros i brides Radiòmetre 2 a Treball, polsador confirmació carrega.	209
209	Carros i brides Radiòmetre 2 a Treball.	220
220	Cilindre màstil a repòs, Carros i brides Radiòmetre 2 a Treball.	221
221	Màstil Recollit, Cilindre Braç a repòs, Gir màstil a Radiòmetre 2, Motor radiòmetre a posició radiòmetre 2, Carros i brides Radiòmetre 2 a Treball.	222
222	Tancament a treball, Màstil Recollit, Cilindre Braç a repòs, Gir màstil a Radiòmetre 2, Motor radiòmetre a posició radiòmetre 2, Carros i brides Radiòmetre 2 a Treball.	223
223	Màstil Estès, Cilindre Braç a repòs, Gir màstil a Radiòmetre 2, Motor radiòmetre a posició radiòmetre 2, Carros i brides Radiòmetre 2 a Treball.	224
224	Màstil Estès, Cilindre Braç a repòs, Gir màstil a Calibrat, Motor radiòmetre a posició radiòmetre 2, Carros i brides Radiòmetre 2 a Treball.	225

Start	Condition	Final
225	Tancament a Treball, Màstil Estès, Cilindre Braç a repòs, Gir màstil a Calibrat, Motor radiòmetre a posició radiòmetre 2, Carros i brides Radiòmetre 2 a Treball.	226
226	Tancament a Treball, Màstil recollit, Cilindre Braç a repòs, Gir màstil a Calibrat, Motor radiòmetre a posició radiòmetre 2, Carros i brides Radiòmetre 2 a Treball, no hi ha senyal de fi cicle calibrat.	227
227	Tancament a Treball, Màstil recollit, Cilindre Braç a repòs, Gir màstil a Calibrat, Motor radiòmetre a posició radiòmetre 2, Carros i brides Radiòmetre 2 a Treball, (Hi ha senyal de fi cicle calibrat o Fi cicle de lectures).	228
228	Tancament a Treball, Màstil recollit, Cilindre Braç a repòs, Gir màstil a Calibrat, Motor radiòmetre a posició radiòmetre 2, Carros i brides Radiòmetre 2 a Treball.	229
229	Tancament a Treball, Màstil Estès, Cilindre Braç a repòs, Gir màstil a Calibrat, Motor radiòmetre a posició radiòmetre 2, Carros i brides Radiòmetre 2 a Treball.	230
230	Màstil Estès, Cilindre Braç a Treball, Gir màstil a Calibrat, Motor radiòmetre a posició radiòmetre 2, Carros i brides Radiòmetre 2 a Treball.	279
233	Màstil Estès, Cilindre Braç a Treball, Carros i brides Radiòmetre 2 a Treball.	234
234	Màstil Estès, Cilindre Braç a Treball, Motor Radiòmetre a posició Scan, Carros i brides Radiòmetre 2 a Treball.	235
235	Màstil Estès, Cilindre Braç a Treball, Gir Màstil a Posició Scan, Motor Radiòmetre a posició Scan, Carros i brides Radiòmetre 2 a Treball, no hi ha senyal de fi cicle calibrat.	236
236	Màstil Estès, Cilindre Braç a Treball, Carros i brides Radiòmetre 2 a Treball, (Hi ha senyal de fi cicle calibrat o Fi cicle de lectures) .	279
240	Màstil Estès, Cilindre Braç a Treball, Carros i brides Radiòmetre 2 a Treball.	241
241	Màstil Estès, Cilindre Braç a Treball, Motor Radiòmetre a posició Scan, Carros i brides Radiòmetre 2 a Treball.	242
242	Màstil Estès, Cilindre Braç a Treball, Gir Màstil a Posició Scan, Motor Radiòmetre a posició Scan, Carros i brides Radiòmetre 2 a Treball, no hi ha senyal de fi cicle calibrat.	243
243	Màstil Estès, Cilindre Braç a Treball, Gir Màstil a Posició Scan, Motor Radiòmetre a posició Scan, Carros i brides Radiòmetre 2 a Treball, (Hi ha senyal de fi cicle calibrat o Fi cicle de lectures).	279
250	Màstil Estès, Cilindre Braç a Treball, Carros i brides Radiòmetre 2 a Treball.	251
251	Màstil Estès, Cilindre Braç a Treball, Motor radiòmetre a posició radiòmetre 2, Carros i brides Radiòmetre 2 a Treball.	252
252	Màstil Estès, Cilindre Braç a Repòs, Motor radiòmetre a posició radiòmetre 2, Carros i brides Radiòmetre 2 a Treball.	253

Start	Condition	Final
253	Màstil Estès, Cilindre Braç a Repòs, Gir màstil a Radiòmetre 2, Motor radiòmetre a posició radiòmetre 2, Carros i brides Radiòmetre 2 a Treball.	254
254	Tancament a treball, Màstil Estès, Cilindre Braç a Repòs, Gir màstil a Radiòmetre 2, Motor radiòmetre a posició radiòmetre 2, Carros i brides Radiòmetre 2 a Treball.	255
255	Tancament a treball, Màstil Recollit, Cilindre Braç a Repòs, Gir màstil a Radiòmetre 2, Motor radiòmetre a posició radiòmetre 2, Carros i brides Radiòmetre 2 a Treball.	256
256	Carros i brides Radiòmetre 2 a Repòs, Polsador confirmació càrrega.	260
260	Màstil Recollit, Cilindre Braç a Repòs, Gir màstil a Radiòmetre 2, Motor radiòmetre a posició radiòmetre 2, Carros i brides Radiòmetre 2 a Repòs.	261
261	Màstil Recollit, Cilindre Braç a Repòs, Gir màstil a Radiòmetre 2, Motor radiòmetre a posició radiòmetre 2, Carros i brides Radiòmetre 2 a Repòs.	262
262	Tancament a treball, Màstil Recollit, Cilindre Braç a Repòs, Gir màstil a Radiòmetre 2, Motor radiòmetre a posició radiòmetre 2, Carros i brides Radiòmetre 2 a Repòs.	263
263	Tancament a treball, Màstil Estès, Cilindre Braç a Repòs, Gir màstil a Radiòmetre 2, Motor radiòmetre a posició radiòmetre 2, Carros i brides Radiòmetre 2 a Repòs.	264
264	Màstil Estès, Cilindre Braç a Repòs, Gir màstil a Radiòmetre 2, Carros i brides Radiòmetre 2 a Repòs.	265
265	Màstil Estès, Cilindre Braç a Repòs, Gir màstil a 0^o.	266
266	Tancament a Treball, Màstil Estès, Cilindre Braç a Repòs, Gir màstil a 0^o.	267
267	Tancament a Treball, Màstil Recollit, Cilindre Braç a Repòs, Gir màstil a 0^o.	268
268	Tancament a Repòs, Màstil Recollit, Cilindre Braç a Repòs, Gir màstil a 0^o.	269
269	Tancament a Repòs, Màstil Recollit, Cilindre Braç a Repòs, Gir màstil a 0^o.	20
279	Tancament de Repòs, Màstil Estès, Cilindre Braç a Treball, Carros i brides Radiòmetre 2 a Treball.	280
280	Tancament de Repòs, Màstil Estès, Cilindre Braç a Treball, Carros i brides Radiòmetre 2 a Treball, no hi ha senyal de fi cicle calibrat.	281
281	Màstil Estès, Cilindre Braç a Treball, Carros i brides Radiòmetre 2 a Treball, Senyal de PC preparat,Senyal de Treball amb Radiòmetre 2, Senyal de començament calibració, la posició d'Scan del Màstil diferent que 0.	233
281	Màstil Estès, Cilindre Braç a Treball, Carros i brides Radiòmetre 2 a Treball, Senyal de PC preparat,Senyal de Treball amb Radiòmetre 2, Senyal de començament calibració, la posició d'Scan del Màstil igual a 0.	282
281	Màstil Estès, Cilindre Braç a Treball, Carros i brides Radiòmetre 2 a Treball, Senyal de PC preparat, Senyal de Go.	240

Start	Condition	Final
281	Màstil Estès, Cilindre Braç a Treball, Carros i brides Radiòmetre 2 a Treball, Senyal de PC preparat, senyal de fi de cicle de lectures.	250
282	Màstil Estès, Cilindre Braç a Treball, Carros i brides Radiòmetre 2 a Treball.	283
283	Màstil Estès, Cilindre Braç a Treball, Gir màstil a Calibrat, Carros i brides Radiòmetre 2 a Treball.	284
284	Màstil Estès, Cilindre Braç a Treball, Gir màstil a Calibrat, Motor radiòmetre a posició radiòmetre 2, Carros i brides Radiòmetre 2 a Treball..	285
285	Màstil Estès, Cilindre Braç a repòs, Gir màstil a Calibrat, Motor radiòmetre a posició radiòmetre 2, Carros i brides Radiòmetre 2 a Treball.	224

Table B.1: Program positions corresponding to PAU-SA operation.

Start	Condition	Final
300	Incondicional.	301
301	Els carros i les brides del Radiòmetre 1 a treball.	310
301	Els carros i les brides del Radiòmetre 2 a treball.	320
301	Els carros del radiòmetre 1 i 2 a repòs.	330
310	Els carros i les brides del Radiòmetre 1 a treball; Màstil en posició intermitja, Gir Màstil a posició Radiòmetre 1, Cilindre del Braç a repòs.	317
310	Els carros i les brides del Radiòmetre 1 a treball, (Màstil no en posició intermitja o Cilindre del Braç no a repòs.	311
311	Els carros i les brides del Radiòmetre 1 a treball.	312
312	Tancament a treball, els carros i les brides del Radiòmetre 1 a treball.	313
313	Tancament a treball, Màstil estès, els carros i les brides del Radiòmetre 1 a treball.	314
314	Tancament a treball, Màstil estès, Motor Radiòmetre en posició radiòmetre 1, els carros i les brides del Radiòmetre 1 a treball.	315
315	Tancament a treball, Màstil estès, Cilindre braç a posició Radiòmetre 1, Motor Radiòmetre en posició radiòmetre 1, els carros i les brides del Radiòmetre 1 a treball.	316
316	Tancament a treball, Màstil estès, Cilindre braç a posició Radiòmetre 1, Gir màstil posició radiòmetre 1, Motor Radiòmetre en posició radiòmetre 1, els carros i les brides del Radiòmetre 1 a treball.	317
317	Tancament a treball, Màstil replegat, Cilindre braç a posició Radiòmetre 1, Gir màstil posició radiòmetre 1, Motor Radiòmetre en posició radiòmetre 1, els carros i les brides del Radiòmetre 1 a treball.	318
318	Màstil replegat, Cilindre braç a posició Radiòmetre 1, Gir màstil posició radiòmetre 1, Motor Radiòmetre en posició radiòmetre 1, els carros i les brides del Radiòmetre 1 a repòs.	319
319	Incondicional.	331
320	Els carros i les brides del Radiòmetre 2 a treball, màstil replegat, Gir Màstil a posició Radiòmetre 2.	327

Start	Condition	Final
320	Els carros i les brides del Radiòmetre 2 a treball (Màstil no Replegat o Gir Màstil no en posició Radiòmetre 2).	321
321	Els carros i les brides del Radiòmetre 2 a treball.	322
322	Tancament a treball, Els carros i les brides del Radiòmetre 2 a treball.	323
323	Tancament a treball, Màstil Estès, Els carros i les brides del Radiòmetre 2 a treball.	324
324	Tancament a treball, Màstil Estès, Motor radiòmetre en posició radiòmetre 2, Els carros i les brides del Radiòmetre 2 a treball.	325
325	Tancament a treball, Màstil Estès, Cilindre Braç a repòs, Motor radiòmetre en posició radiòmetre 2, Els carros i les brides del Radiòmetre 2 a treball.	326
326	Tancament a treball, Màstil Estès, Cilindre Braç a repòs, Gir Màstil a posició Radiòmetre 2, Motor radiòmetre en posició radiòmetre 2, Els carros i les brides del Radiòmetre 2 a treball.	327
327	Tancament a treball, Màstil Replegat, Cilindre Braç a repòs, Gir Màstil a posició Radiòmetre 2, Motor radiòmetre en posició radiòmetre 2, Els carros i les brides del Radiòmetre 2 a treball.	328
328	Màstil Replegat, Cilindre Braç a repòs, Gir Màstil a posició Radiòmetre 2, Motor radiòmetre en posició radiòmetre 2, Els carros i les brides del Radiòmetre 2 a Repòs.	329
329	Màstil Replegat, Cilindre Braç a repòs, Gir Màstil a posició Radiòmetre 2, Motor radiòmetre en posició radiòmetre 2, Els carros i les brides del Radiòmetre 2 a Repòs, polsador de confirmació de càrrega.	330
330	Incondicional.	331
331	Tancament a treball, Els carros i les brides del Radiòmetre 2 a Repòs.	332
332	Tancament a treball, Màstil estès, Els carros i les brides del Radiòmetre 2 a Repòs.	333
333	Tancament a treball, Màstil estès, Cilindre braç a repòs.	334
334	Tancament a treball, Màstil estès, Cilindre braç a repòs, Gir màstil a 0º.	335
335	Tancament a treball, Màstil replegat, Cilindre braç a repòs, Gir màstil a 0º.	336
336	Tancament a repòs, Màstil replegat, Cilindre braç a repòs, Gir màstil a 0º.	337
337	Incondicional.	12
350	Màstil Replegat, Gir màstil a 0º.	351
351	Màstil Replegat, Gir màstil a 0º.	352
352	Tancament a treball, Màstil Replegat, Gir màstil a 0º.	353
353	Tancament a treball, Màstil estès, Gir màstil a 0º.	354
354	Tancament a treball, Màstil estès, Gir màstil a 90º.	355
355	Tancament a treball, Màstil extes, cilindre braç a repòs, Gir màstil a 90º.	356
356	Tancament a treball, Màstil replegat, cilindre braç a repòs, Gir màstil a 90º.	357
357	Tancament a repòs, Màstil replegat, cilindre braç a repòs, Gir màstil a 90º.	14

Start	Condition	Final

Table B.2: Program positions corresponding to folding operations.

Start	Condition	Final
400	(Màstil a Repòs, alguna brida dels radiòmetres a treball i el polsador de confirmació de càrrega) o el màstil a treball, o gir del màstil a calibrat R2, o el gir màstil a 0º, el màstil a posició intermitja o totes les brides a repòs.	401
401	Incondicional.	402
402	Tancament a treball.	403
403	Tancament a treball, màstil estès, cilindre braç a treball i (totes les brides del radiòmetre 1 o totes les brides del radiòmetre 2 a treball).	404
403	Tancament a treball, màstil estès, (cilindre braç a repòs o a posició intermitja) i (totes les brides del radiòmetre 1 o totes les brides del radiòmetre 2 a treball).	420
403	Tancament a treball, màstil estès, totes les brides del radiòmetre 1 a repòs, totes les brides del radiòmetre 2 a repòs.	420
404	Tancament a treball, màstil estès, cilindre braç a treball, posició gir màstil en posició de seguretat per fer un Home.	430
404	Tancament a treball, màstil estès, cilindre braç a treball, posició gir màstil deficient per fer un Home.	405
404	Tancament a treball, màstil estès, cilindre braç a treball, posició gir màstil excessiva per fer un Home.	406
405	Tancament a treball, Màstil estès, i sumem un Offset al motor del màstil per portar-lo a zona segura.	407
406	Tancament a treball, Màstil estès, i restem un Offset al motor del màstil per portar-lo a zona segura.	407
407	Tancament a treball, Màstil estès, Motor màstil aturat.	404
420	Tancament a treball, Màstil estès.	421
421	Tancament a treball, Màstil estès, i si l'encoder esta a menys de 520 punts li afegim un offset.	422
421	Tancament a treball, Màstil estès, i si l'encoder esta a mes de 520 punts.	422
422	Tancament a treball, Màstil estès, Motor màstil parat, restem 1500 punta a la posició actual.	423
423	Tancament a treball, Màstil estès, Motor parat.	424
424	Li restem el que queda per arribar a 0.	425
425	Motor parat, microruptor de 0º activat, encoder entre -1 i 1 punts de posició.	426
425	Motor parat, encoder a posició més petita que -1.	421
425	Motor parat, encoder a posició més gran que 1.	421
425	Motor parat, no hi ha senyal del microruptor de 0º.	421
426	Tancament Obert, màstil estès, motor parat.	450
430	Tancament a treball, Màstil estès, Cilindre braç a treball.	431

Start	Condition	Final
431	Tancament a treball, Màstil estès, Cilindre braç a treball, senyal posició Home Motor Radiòmetre, incrementem 10000 punts la posició del motor del radiòmetre.	432
431	Tancament a treball, Màstil estès, Cilindre braç a treball, no senyal posició Home Motor Radiòmetre.	433
432	Tancament a treball, Màstil estès, Cilindre braç a treball, Motor radiòmetre parat, senyal posició Home Motor Radiòmetre.	431
432	Tancament a treball, Màstil estès, Cilindre braç a treball, Motor radiòmetre parat, no senyal posició Home Motor Radiòmetre.	433
433	Tancament a treball, Màstil estès, Cilindre braç a treball, decrementarem 2000 punts la posició del motor del radiòmetre.	434
434	Tancament a treball, Màstil estès, Cilindre braç a treball, Motor radiòmetre parat.	433
434	Tancament a treball, Màstil estès, Cilindre braç a treball, senyal posició Home Motor Radiòmetre, Movem el valor actual del motor al punt de destí.	435
435	Tancament a treball, Màstil estès, Cilindre braç a treball, Motor radiòmetre parat.	460
450	En aquests passos es genera el Home del motor del màstil.	480
460	En aquests passos es genera el Home del motor del radiòmetre.	469
469	Tancament a treball, Màstil estès, cilindre braç a treball, brides radiòmetre 1 a treball.	470
469	Tancament a treball, Màstil estès, cilindre braç a treball, (brides radiòmetre 2 a treball o totes les brides a repòs).	475
470	Tancament a treball, Màstil estès, cilindre braç a treball.	471
471	Tancament a treball, Màstil estès, cilindre braç a treball, Motor radiòmetre a posició per radiòmetre 1.	472
472	Tancament a treball, Màstil estès, cilindre braç posició intermitja , Motor radiòmetre a posició per radiòmetre 1.	480
475	Tancament a treball, Màstil estès, cilindre braç a treball.	476
476	Tancament a treball, Màstil estès, cilindre braç a treball, (motor radiòmetre a posició radiòmetre 2 o totes les brides a repòs).	477
477	Tancament a treball, Màstil estès, cilindre braç a repòs, (motor radiòmetre a posició radiòmetre 2 o totes les brides a repòs).	480
480	Tancament a treball, màstil estès, cap motor amb Home.	400
480	Tancament a treball, màstil estès, Motor Radiòmetre amb Home, motor màstil sense Home.	400
480	Tancament a treball, màstil estès, Motor Radiòmetre sense Home, motor màstil amb Home.	481
480	Tancament a treball, màstil estès, Motor Radiòmetre amb Home, motor Màstil amb Home.	490
481	Tancament a treball, Màstil estès.	482
482	Tancament a treball, Màstil estès, Gir màstil a 180º.	483
483	Tancament a treball, Màstil estès, Cilindre braç a treball, Gir màstil a 180º.	430

Start	Condition	Final
490	Tancament a treball, Màstil estès, Cilindre braç a repòs, Brides Radiòmetre 2 a treball.	493
490	Tancament a treball, Màstil estès, Cilindre braç a repòs, Brides Radiòmetre 1 i Radiòmetre 2 a repòs.	491
490	Tancament a treball, Màstil estès, Cilindre braç a posició intermitja , Brides Radiòmetre 1 a treball.	495
491	Tancament a treball, Màstil estès, Cilindre braç a repòs.	492
492	Tancament a treball, Màstil estès, Cilindre braç a repòs, Gir màstil a 0º.	497
493	Tancament a treball, Màstil estès, Cilindre braç a repòs.	494
494	Tancament a treball, Màstil estès, Cilindre braç a repòs, Gir màstil a posició Radiòmetre 2.	497
495	Tancament a treball, Màstil estès, Cilindre braç a posició intermitja.	496
496	Tancament a treball, Màstil estès, Cilindre braç a posició intermitja, Gir màstil a 180º.	497
497	Tancament a treball, Màstil replegat.	498
498	Tancament a treball, Màstil replegat.	499
499	Tancament a treball, Màstil replegat, Gir màstil a 0º.	10
499	Tancament a treball, Màstil replegat, Gir màstil a posició radiòmetre 2.	256
499	Tancament a treball, Màstil replegat, Gir màstil a 180º.	156

Table B.3: Program positions corresponding to "HOME" operations.

B.3.3 Send messages

Some of the states of the positioning systems require to receive a message to change the state of the machine. In this application, the last messages sent by the computer to the positioning system are resent periodically.

The PLC will interpret the messages received by the computer, the information of the message should have ten bytes with the following structure:

- First & second byte: Contain information of some flags to send.
- Third & Fourth byte: Contain information of the azimuth desired to move, only valid for messages related to move the positioning system to a position to scan.
- Fifth & Sixth byte: Contain information of the elevation desired to move, only valid for messages related to move the positioning system to a position to scan.
- Seventh, eighth, ninth & tenth byte: These fourth bytes should have always the values [13,10,13,10].

It is possible to divide the necessary messages used to change the state of the positioning systems in two blocks explained in the following pages.

B.3.3.1 Move to selected azimuth and elevation

In this kind of message, the values of the third, fourth, fifth and sixth bytes contain information of the desired position to go and the value of the second byte should have

the value 128.

Figure B.12 shows the information necessary to program the desired azimuth.

The fourth byte has the value:

- Azimuth If azimuth < 256
- Azimuth-256 If azimuth > 256

The third byte has the value:

- 0 If azimuth < 256
- 1 If azimuth > 256

The sixth byte has the value:

- 0 always

The fifth byte has the value:

- Elevation

Figure B.12: How to program desired azimuth parameter.

To perform scan movements it is necessary to send three kinds of messages in the correct order, with the required information (azimuth and elevation), the information of the kind of message is contained in the first byte. As a result, the positioning messages have the format shown in Fig. B.13.

Byte1	128	Azimuth or Azimuth-256	0 or 1	Elevation	0	13	10	13	10

Figure B.13: Azimuth & elevation position messages.

To move the system is mandatory send the previous message, the value that should have the Byte1 should follow values in Fig. B.14.

Byte1	Description of the functionality of this message
17	When the program position is 127, 180 or 181 the system deploy the mast (if is not up) and positioning the system in the required azimuth and elevation. When the system is in the required position, the program state changes to the state 142
1	When the program position is 142, the system requires a confirmation message that the system arrived to the required position. After the confirmation message is read, the program state changes to 143.
3	When the program position is 143, the system sends to the computer the flag RdL, the system requires read a confirmation that the flag is read correctly. After this message is sent, the program state changes to 180.

Figure B.14: Byte 1 values for azimuth & elevation position messages.

B.3.3.2 Move to particular positions

In this kind of message, the values of the third, fourth, fifth and sixth bytes are ignored and only are considered to interpret the first and second byte. The messages necessary to program a particular position should have the format shown in Fig. B.15.

Byte1	Byte2	X	Y	W	Z	13	10	13	10

Figure B.15: Particular position messages.

To move the system is mandatory to send the previous message, values of Byte1 and Byte2 should be in concordance with those shown in Fig. B.16.

Byte1	Byte2	Description of the functionality of this message
65	130	When no radiometer is charged, it moves the positioning system to the position to load the MERITXELL radiometer. When radiometer MERITXELL is charged, it moves the positioning system to the position of MERITXELL calibration.
129	130	When no radiometer is charged, it moves the positioning system to the position to load the PAUSA radiometer. When radiometer PAUSA is charged, it moves the positioning system to the position of PAUSA calibration.
33	128	When no radiometer is charged, it moves the positioning system to the home position and close the sealing. When a radiometer is charged, it moves the positioning system to the position to discharge the radiometer and closes the celling.
3	128	When the radiometer is in the calibration position, it moves the radiometer to "treball" (operative) position.

Figure B.16: Byte 1 & byte 2 for particular position messages.

B.4 MERITXELL communication and operation

This block of the software has the function to interact with the spectrum analyzer and the PICs of the MERITXELL system, the MERITXELL system has two PIC microcontroller, one of them to configure the switches and the other to get the temperature values of the sensors and to activate the system to turn on/off the spectrum analyzer.

Once the program is started, and in order to check if the computer is connected to the MERITXELL system, the program sends a ping to the direction of one of the PICs, located at the IP direction 147.83.38.250. If the computer is connected to the spectrum analyzer, it is possible to do the following functions.

B.4.1 Turn ON/OFF the spectrum analyzer

Once the software is launched and connected to the MERITXELL, the program is configured to turn on the spectrum analyzer automatically if a connection to the PIC exists.

When the software is launched, the computer sends a ping to the spectrum analyzer, it can be in four possible states. Regarding the current state of the analyzer, it performs the operation detailed in Fig. B.17.

State	What software do?
On	Create a new instrument driver session and open a session to the specified device.
Off	A message to turn ON the analyser is sent, then, after waiting 70 seconds (time to turn ON the analyser), it creates a new instrument driver session and opens a session to the specified device.
Turning On	The software assumes that the spectrum analyser is off because it doesn't reply the ping message, and therefore, the spectrum analyser is shut down automatically.
Turning Off	The software assumes that the spectrum analyser is on because it reply the ping message, and therefore, the spectrum analyser won't be turned on automatically.

Figure B.17: Spectrum analyzer states.

To show the actual state of the spectrum analyzer a box is created, this box contains the text "On" and green color if the spectrum analyzer replies the pings (see Figure B.18), else contains the text "Off" and should be in red color. To turn on and off the analyzer automatically and create the instrument driver session when changing the state off to on, a button is created.

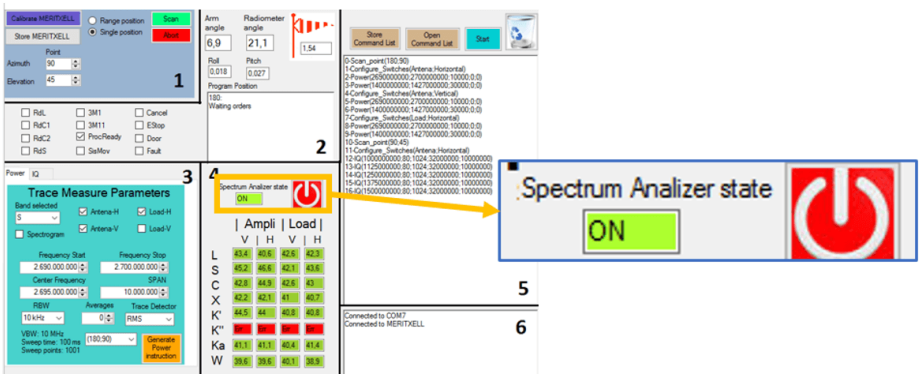

Figure B.18: Spectrum analyzer state display & manual button.

Internally, to change the state of the analyzer, two messages of 4 bytes will be send to the PIC located in the IP direction 147.83.38.222, the first one with the value in decimal [170,0,0,113] and the other message, will be sent after 1500 ms of the first message with the value [170,0,0,112].

With these messages, the PIC realize the functions to activate the mechanical part to push the button of the analyzer.

B.4.2 Configure Switches

Once the software reads an instruction that contains the words the following message is sent to the PIC located at the IP direction 147.83.38.250.

Depending on the value of the less significant bit of the last two bytes, the switches will be configured in one position or in the other position.

The message to configure the switches should have the format shown in Fig. B.19.

A	A	0	0	0	0	4	2	0	Dir	0	Pol
1010	1010	0000	0000	0000	0000	0100	0010	0000	000X	0000	000Y

Figure B.19: Configure switches message.

Once the message is correctly sent, if the value of the less significant bit it is zero (Y = 0), the polarization switch selects the horizontal position, it is one selects the vertical position (Y = 1). However, if the value of the less significant bit of the byte preceding the final byte is zero (X = 0), the polarization switch selects the horizontal position, it is one it selects the vertical position (Y = 1).

If the switches are configured correctly, the PIC sends to the computer 4 bytes with the message [170,0,0,119], if this message is received, the following instruction can be read.

B.4.3 Get temperature of the sensors

If the connection between MERITXELL and the computer exists, the computer requests periodically to the PIC located at the IP 147.83.38.222 the temperature of the MERITXELL temperature sensors.

To request to the PIC the temperature, a message of 12 bytes is sent with the following structure:

- 4 most significant bytes: Contains the information of the message is a temperature request, the value of this messages are: [170,0,0,1] or [170,0,0,2] depending on the sensor to evaluate.
- 8 less significant: Contains the information on the serial number of each sensor. Serial numbers are shown in Fig. B.20. Once the message is correctly received, the PIC sends to the computer two bytes with information of the temperature of the sensor requested.

The value of the temperature in Celsius degrees is the result of the following operation:

$$T(^{\circ}C) = HighByte \cdot 16 + LowByte/16$$

Sensor information										
Band	Amplfier/load	Polarization	Serial Number							
L	Amplifier	H	19	65	217	2	0	0	229	29
L	Amplifier	V	28	71	60	2	0	0	149	30
L	Load	H	188	81	60	2	0	0	41	31
L	Load	V	204	36	217	2	0	0	198	28
S	Amplifier	H	130	17	217	2	0	0	246	15
S	Amplifier	V	157	13	217	2	0	0	212	14
S	Load	H	141	18	217	2	0	0	156	13
S	Load	V	135	36	217	2	0	0	75	12
C	Amplifier	H	22	4	217	2	0	0	53	3
C	Amplifier	V	83	18	217	2	0	0	75	1
C	Load	H	253	74	217	2	0	0	175	0
C	Load	V	8	74	217	2	0	0	54	2
X	Amplifier	H	30	62	217	2	0	0	173	16
X	Amplifier	V	120	28	217	2	0	0	167	17
X	Load	H	159	5	217	2	0	0	132	18
X	Load	V	43	254	216	2	0	0	6	19
K'	Amplifier	H	143	38	217	2	0	0	105	21
K'	Amplifier	V	43	22	217	2	0	0	109	20
K'	Load	H	103	2	217	2	0	0	6	22
K'	Load	V	64	41	217	2	0	0	189	23
K''	Amplifier	H	37	46	217	2	0	0	196	8
K''	Amplifier	V	135	46	217	2	0	0	210	11
K''	Load	H	235	65	217	2	0	0	54	10
K''	Load	V	75	77	217	2	0	0	75	9
Ka	Amplifier	H	49	58	217	2	0	0	32	5
Ka	Amplifier	V	50	219	207	1	0	0	187	4
Ka	Load	H	165	44	217	2	0	0	173	6
Ka	Load	V	9	2	217	2	0	0	214	7
W	Amplifier	H	110	46	217	2	0	0	73	26
W	Amplifier	V	73	57	217	2	0	0	87	24
W	Load	H	98	21	217	2	0	0	192	27
W	Load	V	183	47	217	2	0	0	214	25

Figure B.20: Serial numbers of each temperature sensor.

If the most significant bit is 1, the temperature is negative, and it is calculated as:

$$T(^{\circ}C) = HighByte \cdot 16 + LowByte/16 - 65536$$

The average of the current temperature (the average is calculated as the average of the last 10 temperature measures) of every sensor show be displayed in the form as we can

see in Fig. B.21.

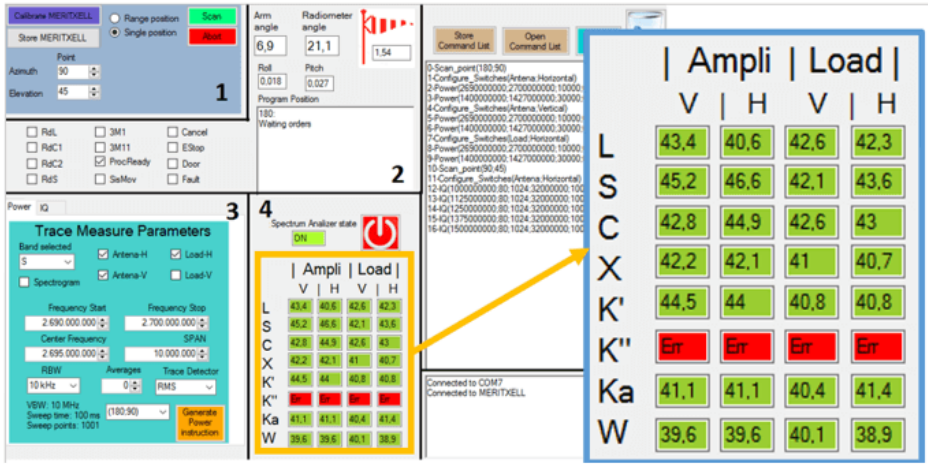

Figure B.21: Temperature sensor display.

The time required to get and process the information on the 32 temperature sensors is between 2 and 2.5 seconds, the value displayed not will be refreshed until the temperature values of all sensors are received.

If the temperatures received by the PIC are not valid values, the display shows the message "Err" and the color of the box changes to red.

Depending on the temperature gradient the box changes the color. The temperature gradient is calculated as the average of last 10 temperatures values minus the average of the eleventh to thirtieth last temperature values.

The temperature gradient is represented using different colors (see Fig. B.22). The colors used are the following:

- Red: Temperature gradient greater than 0.1 °C.
- Yellow: Temperature gradient between 0.05 °C and 0.1 °C.
- Green: Temperature gradient between -0.05 °C and +0.05 °C.
- Blue: Temperature gradient lower than -0.05 °C.

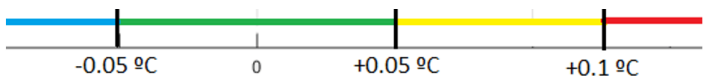

Figure B.22: Temperature gradient vs colour box.

B.4.4 Acquisition of the measurements

This part of the software consists of the configuration of the spectrum analyzer contained in the radiometer (model FSP40 by Rohde & Schwarz) to get the measurements and

generate the files with the measures obtained.

Once the software reads an instruction that contains the words "Power" or "IQ" the software sends messages to the spectrum analyzer to obtain the desired measurements.

To configure the FSP40, the manufacturer provides the drivers, the DLL, and the class to invoke the DLL functions. To invoke the DLL functions it is necessary to generate in the software an object of the class given by the manufacturer in order to call the methods to configure the spectrum analyzer.

The software is implemented to obtain two kinds of measurements.

B.4.4.1 Power measurements

In this kind of measurements, the software configures the spectrum analyzer with the desired inputs to get the desired POWER measurements.

To obtain power measurements, some of the parameters are configured by the user and the other settings are configured automatically. The parameters to be configured are the following:

- *Center frequency*: this parameter is used to configure the frequency of the local oscillator or the frequency of the external mixer (to measures frequency values up to 40 GHz). This parameter is configured together with the Span using the function given by the manufacturer called "ConfigureFrequencyStartStop".
- *Span*: this parameter configures the difference between the frequency start and stop to be analyzed, this parameter is configured together with the center frequency using the function given by the manufacturer called "ConfigureFrequencyStartStop".
- *Resolution Bandwidth*: this parameter is used to set the bandpass filter in the IF path, this parameter is configured using the method "ConfigureSweepCoupling" (this function configures the RBW, the VBW or the sweep time depending if one of the inputs is 0, 1 or 2 respectively). The available values to be configured are 10 MHz, 3 MHz, 1 MHz, 300 kHz, 100 kHz, 30 kHz, 10 kHz, 3 kHz, 1 kHz, 300 Hz, 100 Hz, 30 Hz, and 10 Hz.
- *Video Bandwidth*: this parameter is configured automatically and sets the bandwidth of the low-pass filter directly after the envelope detector, it is configured using the method "ConfigureSweepCouplingAuto" (this function configures automatically the RBW, the VBW or the sweep time depending if one of his inputs is 0, 1 or 2 respectively). The value configured automatically is the immediate value larger than the Resolution Bandwidth. The available values to be configured are 10 MHz, 3 MHz, 1 MHz, 300 kHz, 100 kHz, 30 kHz, 10 kHz, 3 kHz, 1 kHz, 300 Hz, 100 Hz, and 30 Hz.
- *Sweep time*: this parameter is set automatically and set the time to cover the span required, it is configured using the method "ConfigureSweepCouplingAuto" (this function configure automatically the RBW, the VBW or the sweep time depending if one of his inputs is 0, 1 or 2 respectively). The value configured automatically is approximately close than the result of the relation between the span and the square

of the resolution bandwidth.

$$ST = \frac{Span}{RBW^2}$$

- *Number of averages*: to obtain measures with a given number of averages to, for example, reduce the effects of white Gaussian noise. To configure the number of averages two methods are called "ConfigureAveraging" to switch on the average calculation for the selected trace and "ConfigureAveragingCount" to configure the averaging count. The number of averages increases proportionally to the integration time.

$$\tau_i = \frac{ST}{Number\ sweep\ points} \cdot Number\ of\ averages$$

- *Number of sweep points*: this parameter is configured automatically and it configures the number of measurement points per sweep, the function to configure it is called "ConfigureSweepPoints". The value configured automatically is the lower available value that satisfies the following inequation:

$$Number\ sweep\ points > \frac{Span}{RBW},$$

  within the subset of values 8001, 4001, 2001, 1001, 501, 251, and 125.

- The *radiometric resolution* is proportionally with $\frac{1}{\sqrt{\tau_i}}$, therefore, the radiometric resolution increases proportionally with the square root of the number of sweep points.

- *Trace detector*: it selects the algorithm to capture the value of the samples. The method to configure it is called "ConfigureTraceDetector". The available trace detector that can be configured in this software are:

  - RMS: Square root of the mean square value of samples taken within the bin for a dedicated point of the display
  - Average: Average value of the samples taken within the bin for a dedicated point on the display.
  - Max. Peak: Obtains the maximum video signal between the last display point and the present display point.
  - Min. Peak: Obtains the minimum video signal between the last display point and the present display point.
  - Sample: Pick one point within a bin.

B.4.4.2 I/Q measurements

The procedure to obtain the I/Q measurements is divided into three blocks (the mixer, the low-pass filter, and the A/D converter).

To get the desired I/Q measure some of the parameters are configured by the user and the otherness are configured automatically, before configuring the parameters to obtain

the I/Q measures is mandatory call the method "ConfigureTraceIQDataAcquisition" to switch the I/Q data acquisition on.

Finally, to obtain the measurements, the function to get them is called "ReadTraceIQ-Data".

The parameters to be configured are the following:

- *Central frequency*: This parameter configures the frequency of the local oscillator or the frequency of the external mixer used in the mixer. To configure this frequency the method used is called "ConfigureFrequencyCenter".
- *Reference Level*: This parameter configures the vertical position of the captured data used as a reference for amplitude measurements. The reference level is established by the function "ConfigureReferenceLevel".
- *Sampling Rate*: This parameter has the function to configure the number of measures acquired per second in the A/D, this parameter can be configured with one of the inputs of the method "TraceIQSet". The available values to be configured are 32 MHz, 16 MHz, 8 MHz, 4 MHz, 2 MHz, 1 MHz, 500 kHz, 250 kHz, 125 kHz, 62.5 kHz, 31.25 kHz, and 15.625 kHz.
- *A/D Filter*: This parameter configures the cut-off frequency of the A/D filter, this parameter can be set with one of the inputs of the method "TraceIQSet". The available values to be configured are 10 MHz, 3 MHz, 1 MHz, and 300 kHz.
- *Number of samples*: This parameter configures the number of samples to obtain, and can be configured with one of the inputs of the "TraceIQSet" method. The maximum number of measures to be obtained should be lower than 130,550.

C

Appendix C

Derivation of NBB and NRB

This appendix shows the derivation of the Normalized Blanking Bias (NBB) and Normalized Resolution Bias (NRB) parameters. Moreover, demonstration of mean and standard deviation of radiometric noise are also presented.

C.1 Statistics under $\mathcal{H}_0$ before mitigation

Noise power probability density function before mitigation (from Appendix A):

$$f_{|\mathbf{N}|^2}(|\mathrm{N}|^2) = \frac{1}{2\,\sigma_n^2}\, e^{-\frac{|\mathrm{N}|^2}{2\,\sigma_n^2}} = \frac{1}{P_n}\, e^{-\frac{|\mathrm{N}|^2}{P_n}} \quad x \in [0, \infty), \tag{C.1}$$

Noise power cumulative density function before mitigation (from Appendix A):

$$F_{|\mathbf{N}|^2}(|\mathrm{N}|^2) = 1 - e^{-\frac{|\mathrm{N}|^2}{P_n}} \quad x \in [0, \infty), \tag{C.2}$$

Threshold as a function of probability of false alarm (from Appendix A):

$$\alpha = -P_n \ln\Big(1 - F_{|\mathbf{N}|^2}(\alpha)\Big) = P_n \ln\left(\frac{1}{P_{FA}}\right), \tag{C.3}$$

Mean of noise power before mitigation:

$$\begin{aligned}
\mathrm{E}\left\{|\mathrm{N}|^2\right\} &= \int_0^\infty |\mathrm{N}|^2 \; f_{|\mathbf{N}|^2}(|\mathrm{N}|^2)\, d\,|\mathrm{N}|^2 \\
&= \int_0^\infty |\mathrm{N}|^2 \, \frac{1}{P_n}\, e^{-\frac{|\mathrm{N}|^2}{P_n}} d\,|\mathrm{N}|^2 \\
&= -\,|\mathrm{N}|^2\, e^{-\frac{|\mathrm{N}|^2}{P_n}}\Big|_0^\infty + \int_0^\infty e^{-\frac{|\mathrm{N}|^2}{P_n}} d\,|\mathrm{N}|^2 \\
&= -P_n\; e^{-\frac{|\mathrm{N}|^2}{P_n}}\Big|_0^\infty \\
&= P_n
\end{aligned} \tag{C.4}$$

Mean of averaged noise power before mitigation:

$$\begin{aligned}
\mathrm{E}\left\{\left\langle |\mathrm{N}|^2 \right\rangle\right\} &= \left\langle \mathrm{E}\left\{|\mathrm{N}|^2\right\}\right\rangle \\
&= \frac{1}{M} \sum_{m=0}^{M-1} \mathrm{E}\left\{|\mathrm{N_m}|^2\right\} \\
&= \mathrm{E}\left\{|\mathrm{N}|^2\right\}
\end{aligned} \tag{C.5}$$

Variance of noise power before mitigation:

$$\begin{aligned}
\operatorname{Var}\left\{|\mathrm{N}|^2\right\} &= \mathrm{E}\left\{\left(|\mathrm{N}|^2 - P_n\right)^2\right\} \\
&= \mathrm{E}\left\{\left(|\mathrm{N}|^2\right)^2\right\} - (P_n)^2 \\
&= \int_0^\infty \left(|\mathrm{N}|^2\right)^2 f_{|\mathbf{N}|^2}(|\mathrm{N}|^2)\, d\,|\mathrm{N}|^2 - (P_n)^2 \\
&= \int_0^\infty \left(|\mathrm{N}|^2\right)^2 \frac{1}{P_n}\, e^{-\frac{|\mathrm{N}|^2}{P_n}}\, d\,|\mathrm{N}|^2 - (P_n)^2 \\
&= -\left(|\mathrm{N}|^2\right)^2 e^{-\frac{|\mathrm{N}|^2}{P_n}}\Big|_0^\infty + 2\int_0^\infty |\mathrm{N}|^2\, e^{-\frac{|\mathrm{N}|^2}{P_n}}\, d\,|\mathrm{N}|^2 - (P_n)^2 \\
&= 2\,(P_n)^2 - (P_n)^2 \\
&= (P_n)^2
\end{aligned} \tag{C.6}$$

Variance of averaged noise power before mitigation:

$$\begin{aligned}
\operatorname{Var}\left\{\left\langle|\mathrm{N}|^2\right\rangle\right\} &= \mathrm{E}\left\{\left(\left\langle|\mathrm{N}|^2\right\rangle - \mathrm{E}\left\{\left\langle|\mathrm{N}|^2\right\rangle\right\}\right)^2\right\} \\
&= \mathrm{E}\left\{\left(\left\langle|\mathrm{N}|^2\right\rangle - P_n\right)^2\right\} \\
&= \mathrm{E}\left\{\left(\left\langle|\mathrm{N}|^2\right\rangle\right)^2\right\} - (P_n)^2 \\
&= \mathrm{E}\left\{\frac{1}{M^2}\sum_{m_1=0}^{M-1}|\mathrm{N}_{\mathrm{m}_1}|^2 \sum_{m_2=0}^{M-1}|\mathrm{N}_{\mathrm{m}_2}|^2\right\} - (P_n)^2 \\
&= \frac{1}{M^2}\sum_{m=0}^{M-1}\mathrm{E}\left\{\left(|\mathrm{N}_{\mathrm{m}}|^2\right)^2\right\} + \frac{1}{M^2}\sum_{m_1=0}^{M-1}\sum_{\substack{m_2\geq 0 \\ m_2\neq m_1}}^{M-1}\mathrm{E}\left\{|\mathrm{N}_{\mathrm{m}_1}|^2\,|\mathrm{N}_{\mathrm{m}_2}|^2\right\} - (P_n)^2 \\
&= \frac{M}{M^2}\,\mathrm{E}\left\{\left(|\mathrm{N}|^2\right)^2\right\} + \frac{M^2-M}{M^2}\left(\mathrm{E}\left\{|\mathrm{N}|^2\right\}\right)^2 - (P_n)^2 \\
&= \frac{1}{M}\,\mathrm{E}\left\{\left(|\mathrm{N}|^2\right)^2\right\} + \left(1-\frac{1}{M}\right)(P_n)^2 - (P_n)^2 \\
&= \frac{1}{M}\left(\mathrm{E}\left\{\left(|\mathrm{N}|^2\right)^2\right\} - (P_n)^2\right) \\
&= \frac{1}{M}\operatorname{Var}\left\{|\mathrm{N}|^2\right\}
\end{aligned} \tag{C.7}$$

Standard deviation of averaged noise power (radiometric resolution) before mitigation:

$$\begin{aligned}\Delta P_n &= \sqrt{\frac{1}{M}\operatorname{Var}\left\{|\mathrm{N}|^2\right\}} \\ &= \frac{P_n}{\sqrt{M}}\end{aligned} \tag{C.8}$$

C.2 Radiometric power under $\mathcal{H}_0$ after mitigation

Noise power probability density function after mitigation (truncated Exponential distribution):

$$f_{|\mathbf{N}'|^2}(|\mathrm{N}'|^2) = \frac{1}{P_n}\, e^{-\frac{|\mathrm{N}'|^2}{P_n}}\, \Pi\left(\frac{|\mathrm{N}'|^2 - \alpha/2}{\alpha}\right) + P_{FA}\, \delta\left(|\mathrm{N}'|^2\right) \quad x \in [0, \infty), \tag{C.9}$$

where the rectangular function $\Pi(\cdot)$ represents the truncation of the original Exponential function from 0 to α, and the Dirac delta function $\delta(\cdot)$ accounts for the blanked values originally larger than α necessary to fulfill the new PDF to have an area equal to 1. Nevertheless, the Dirac delta function $\delta(\cdot)$ has no impact on the subsequent results.

Mean of noise power after mitigation:

$$\begin{aligned}\mathrm{E}\left\{|\mathrm{N}'|^2\right\} &= \int_0^\infty |\mathrm{N}'|^2\; f_{|\mathbf{N}'|^2}(|\mathrm{N}'|^2)\, d\,|\mathrm{N}'|^2 \\ &= \int_0^\alpha |\mathrm{N}'|^2\, \frac{1}{P_n}\, e^{-\frac{|\mathrm{N}'|^2}{P_n}}\, d\,|\mathrm{N}'|^2 + \int_0^\infty |\mathrm{N}'|^2\; P_{FA}\, \delta\left(|\mathrm{N}'|^2\right)\, d\,|\mathrm{N}'|^2 \\ &= -|\mathrm{N}'|^2\, e^{-\frac{|\mathrm{N}'|^2}{P_n}}\Big|_0^\alpha + \int_0^\alpha e^{-\frac{|\mathrm{N}'|^2}{P_n}}\, d\,|\mathrm{N}'|^2 \\ &= -|\mathrm{N}'|^2\, e^{-\frac{|\mathrm{N}'|^2}{P_n}}\Big|_0^\alpha - P_n\, e^{-\frac{|\mathrm{N}'|^2}{P_n}}\Big|_0^\alpha \\ &= -\alpha\, e^{\frac{-\alpha}{P_n}} - P_n\, e^{-\frac{\alpha}{P_n}} + P_n \\ &= P_n\left(1 - \left(1 + \frac{\alpha}{P_n}\right) e^{-\frac{\alpha}{P_n}}\right) \\ &= P_n\left(1 - \left(1 - \ln\left(P_{FA}\right)\right) P_{FA}\right) \\ &= P_{n'}.\end{aligned} \tag{C.10}$$

Mean of averaged noise power after mitigation:

$$\begin{aligned}
\mathrm{E}\left\{\left\langle \left|\mathrm{N}'\right|^2 \right\rangle\right\} &= \int_0^{\alpha} \left\langle \left|\mathrm{N}'\right|^2 \right\rangle \, f_{|\mathbf{N}'|^2}(\left|\mathrm{N}'\right|^2)\, d\left|\mathrm{N}\right|^2 \\
&= \left\langle \int_0^{\alpha} \left|\mathrm{N}'\right|^2 \, f_{|\mathbf{N}'|^2}(\left|\mathrm{N}'\right|^2)\, d\left|\mathrm{N}'\right|^2 \right\rangle \\
&= \frac{1}{M} \sum_{m=0}^{M-1} \left(\int_0^{\alpha} \left|\mathrm{N}'_{\mathrm{m}}\right|^2 \, f_{|\mathbf{N}'|^2}(\left|\mathrm{N}'_{\mathrm{m}}\right|^2)\, d\left|\mathrm{N}'_{\mathrm{m}}\right|^2 \right) \\
&= \int_0^{\alpha} \left|\mathrm{N}'\right|^2 \, f_{|\mathbf{N}'|^2}(\left|\mathrm{N}'\right|^2)\, d\left|\mathrm{N}'\right|^2 \\
&= \mathrm{E}\left\{\left|\mathrm{N}'\right|^2\right\}.
\end{aligned} \tag{C.11}$$

Thus, the Normalized Blanking Bias (BB) can be defined as:

$$\begin{aligned}
\mathrm{NBB} &= \frac{P_n - P_{n'}}{P_n} \\
&= \frac{P_n - P_n \left(1 - \left(1 - \ln\left(P_{FA}\right)\right) P_{FA}\right)}{P_n} \\
&= \left(1 - \ln\left(P_{FA}\right)\right) P_{FA}.
\end{aligned} \tag{C.12}$$

Therefore, the mean noise power after mitigation can be calculated as:

$$P_{n'} = P_n - \mathrm{NBB} \cdot P_n. \tag{C.13}$$

C.3 Radiometric resolution under $\mathcal{H}_0$ after mitigation

Variance of noise power after mitigation:

$$
\begin{aligned}
\mathrm{Var}\left\{|\mathrm{N}'|^2\right\} &= \mathrm{E}\left\{\left(|\mathrm{N}'|^2 - P_{n'}\right)^2\right\} \\
&= \mathrm{E}\left\{\left(|\mathrm{N}'|^2\right)^2\right\} - (P_{n'})^2 \\
&= \int_0^\infty \left(|\mathrm{N}'|^2\right)^2 f_{|\mathbf{N}|^2}(|\mathrm{N}'|^2)\, d\,|\mathrm{N}'|^2 - (P_{n'})^2 \\
&= \int_0^\alpha \left(|\mathrm{N}'|^2\right)^2 \frac{1}{P_n}\, e^{-\frac{|\mathrm{N}'|^2}{P_n}} d\,|\mathrm{N}'|^2 - (P_{n'})^2 \\
&= -\left(|\mathrm{N}'|^2\right)^2 e^{-\frac{|\mathrm{N}'|^2}{P_n}}\Big|_0^\alpha + 2\int_0^\alpha |\mathrm{N}'|^2\, e^{-\frac{|\mathrm{N}'|^2}{P_n}} d\,|\mathrm{N}'|^2 - (P_{n'})^2 \\
&= -\alpha^2\, e^{-\frac{\alpha}{P_n}} + 2\,P_n P_{n'} - (P_{n'})^2 \\
&= -(P_n)^2\, \frac{\alpha^2}{(P_n)^2} e^{-\frac{\alpha}{P_n}} + (P_n)^2 - (P_n)^2 + 2\,P_n P_{n'} - (P_{n'})^2 \\
&= (P_n)^2 \left(1 - \left(\frac{\alpha}{P_n}\right)^2 e^{-\frac{\alpha}{P_n}}\right) - (P_n - P_{n'})^2 \\
&= (P_n)^2 \left(1 - \left(\frac{\alpha}{P_n}\right)^2 e^{-\frac{\alpha}{P_n}} - \left(\frac{P_n - P_{n'}}{P_n}\right)^2\right) \\
&= (P_n)^2 \left(1 - \ln^2(P_{FA})\, P_{FA} - (\mathrm{NBB})^2\right)
\end{aligned}
\tag{C.14}
$$

Variance of averaged noise power after mitigation (over M' which is the number of non-

mitigated samples):

$$
\begin{aligned}
\operatorname{Var}\left\{\left\langle\left|\mathrm{N}'\right|^2\right\rangle\right\} &= \mathrm{E}\left\{\left(\left\langle\left|\mathrm{N}'\right|^2\right\rangle - P_{n'}\right)^2\right\} \\
&= \mathrm{E}\left\{\left(\left\langle\left|\mathrm{N}'\right|^2\right\rangle\right)^2\right\} - \left(P_{n'}\right)^2 \\
&= \mathrm{E}\left\{\frac{1}{\left(M'\right)^2}\sum_{m_1=0}^{M'-1}\left|\mathrm{N}'_{\mathrm{m}_1}\right|^2\sum_{m_2=0}^{M'-1}\left|\mathrm{N}'_{\mathrm{m}_2}\right|^2\right\} - \left(P_{n'}\right)^2 \\
&= \frac{1}{\left(M'\right)^2}\sum_{m=0}^{M'-1}\mathrm{E}\left\{\left(\left|\mathrm{N}'_{\mathrm{m}}\right|^2\right)^2\right\} \\
&\quad + \frac{1}{\left(M'\right)^2}\sum_{m_1=0}^{M'-1}\sum_{\substack{m_2\geq 0\\ m_2\neq m_1}}^{M'-1}\mathrm{E}\left\{\left|\mathrm{N}'_{\mathrm{m}_1}\right|^2\left|\mathrm{N}'_{\mathrm{m}_2}\right|^2\right\} - \left(P_{n'}\right)^2 \\
&= \frac{M'}{\left(M'\right)^2}\mathrm{E}\left\{\left(\left|\mathrm{N}'\right|^2\right)^2\right\} + \frac{\left(M'\right)^2 - M'}{\left(M'\right)^2}\left(\mathrm{E}\left\{\left|\mathrm{N}'\right|^2\right\}\right)^2 - \left(P_{n'}\right)^2 \\
&= \frac{1}{M'}\mathrm{E}\left\{\left(\left|\mathrm{N}'\right|^2\right)^2\right\} + \left(1 - \frac{1}{M'}\right)\left(P_{n'}\right)^2 - \left(P_{n'}\right)^2 \\
&= \frac{1}{M'}\left(\mathrm{E}\left\{\left(\left|\mathrm{N}'\right|^2\right)^2\right\} - \left(P_{n'}\right)^2\right) \\
&= \frac{1}{M'}\operatorname{Var}\left\{\left|\mathrm{N}'\right|^2\right\}
\end{aligned}
\tag{C.15}
$$

Standard deviation of noise power after mitigation:

$$
\begin{aligned}
\Delta P_{n'} &= \sqrt{\frac{1}{M'}\operatorname{Var}\left\{\left|\mathrm{N}'\right|^2\right\}} \\
&= \frac{P_n}{\sqrt{M'}}\sqrt{1 - \left(\frac{\alpha}{P_n}\right)^2 e^{-\frac{\alpha}{P_n}} - \left(\mathrm{NBB}\right)^2} \\
&= \frac{P_n}{\sqrt{M'}}\sqrt{1 - \ln^2\left(P_{FA}\right)P_{FA} - \left(\mathrm{NBB}\right)^2}
\end{aligned}
\tag{C.16}
$$

Normalized Resolution Bias (NRB)

$$\begin{aligned}
\mathrm{NRB} &= \frac{\Delta P_n - \Delta P_{n'}}{\Delta P_n} \\
&= \frac{\frac{P_n}{\sqrt{M}} - \frac{P_n}{\sqrt{M'}} \sqrt{1 - \ln^2\left(P_{FA}\right) P_{FA} - \left(\mathrm{NBB}\right)^2}}{\frac{P_n}{\sqrt{M}}} \\
&= 1 - \sqrt{\frac{M}{M'}} \sqrt{1 - \ln^2\left(P_{FA}\right) P_{FA} - \left(\mathrm{NBB}\right)^2} \\
&= 1 - \sqrt{\frac{1 - \ln^2\left(P_{FA}\right) P_{FA} - \left(\mathrm{NBB}\right)^2}{1 - P_{FA}}}
\end{aligned} \tag{C.17}$$

D

Appendix D

Temperature control

This appendix describes the temperature controller used in L-RARO instrument. The introduction states the need of using temperature stabilization in high sensitive RF instruments. After that, the design of the subsystem is detailed. Finally, some results regarding the performance of the temperature controller are commented.

D.1 Introduction

Temperature stabilization in RF systems is essential to achieve high sensitivity and resolution in the measurements. In particular, microwave radiometers, which require radiometric resolution on the order of 1 K (or better), must include temperature stabilization subsystems that keep the operating temperature with fluctuations below the Kelvin unit.

This also applies to an RFI detector with high sensitivity requirements as L-RARO. In order to make clearer the need of having temperature stabilization, some measurements were performed with L-RARO hardware without its external enclosure. Figure D.1a shows the time evolution of matched load physical temperature during 48 hours, as well as, the power measured in linear arbitrary units with the RFI detector input switched to the matched load.

This temperature was measured with a temperature sensor located inside the RF conditioner box (see Fig. 6.3), and very close to the matched load. Besides, they have been taken inside the laboratory and close to a window. So that, during evening and night, the temperature went down to 23 °C, whereas, at noon, the temperature rised up to 38 °C because Sun radiation impacted directly on the instrument.

A priori, one may expect the measured power to be linear and proportional to the variation of the physical temperature of the matched load. However, as depicted in Fig. D.1b, this is not true. One reason that explains this behavior is the dependence of the amplifier gain with temperature variations, which is indeed inversely proportional. In Fig. D.1b, it can be appreciated that below 301.5 K (28.5 °C), the cluster of power measurements has a negative derivative variation as a function of temperature. Therefore, amplifier gain dependence was higher than the temperature dependence in this range. However, above 301.5 K, the behavior is the opposite. Moreover, the deviation of temperature estimation using these measurements can be as high as 8 K.

This example makes clear that temperature stabilization is necessary for the RFI detector. So that, power variations due to temperature dependencies of the electronic components are eliminated.

D.2 Temperature controller

In order to control the working temperature of L-RARO, the hardware has been placed in a temperature isolated enclosure, and a temperature controller has been designed to stabilize the temperature within previously established limits.

Figure D.2 shows a block diagram describing the connections among the different parts of the temperature controller. The controller has four main parts: several temperature sensors, a PID controller, a heater, and communication system. These four parts are controlled using an Arduino Mega, which has enough computational capacity to perform the required operations. The different parts are described in subsections below.

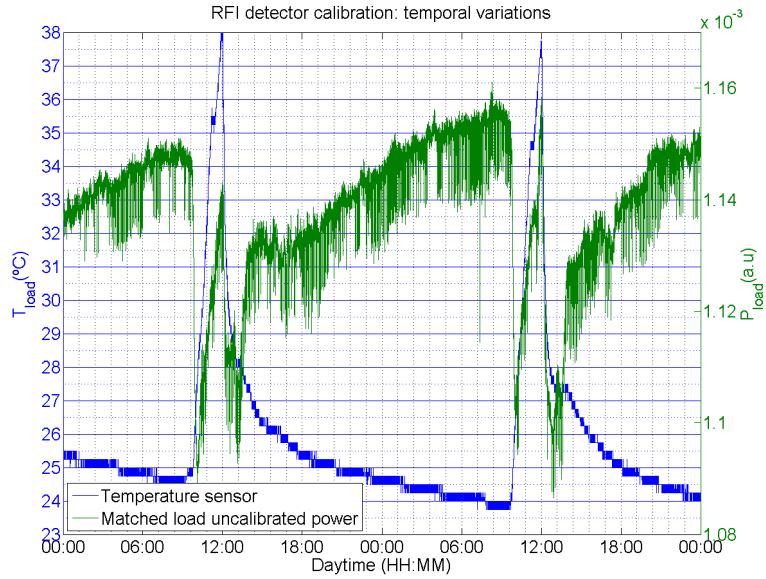

(a)

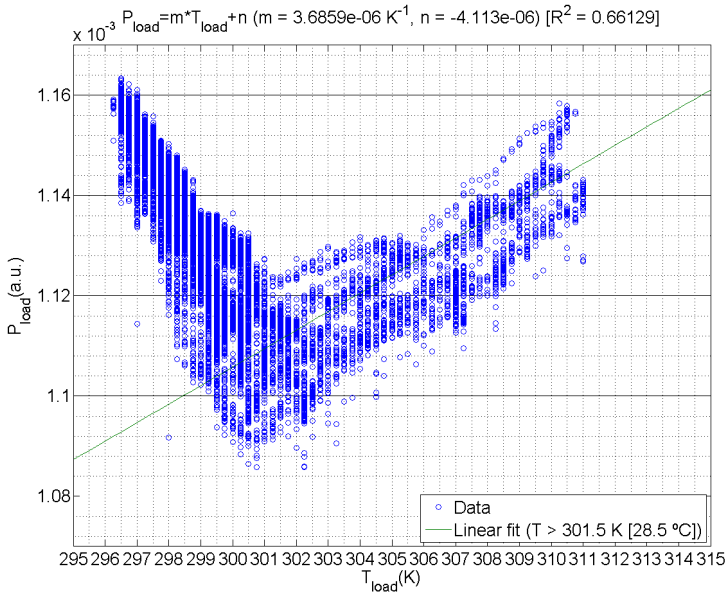

(b)

Figure D.1: (a) Time evolution of matched load physical temperature and power measured by the RFI detector in linear arbitrary units. (b) Measured power as a function of matched load temperature.

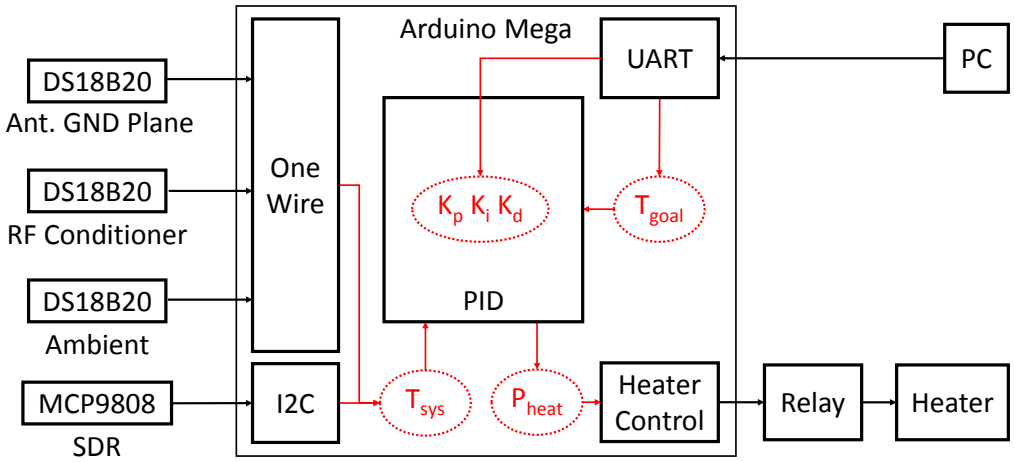

Figure D.2: Diagram of the subsystems conforming the temperature controller.

D.2.1 Temperature sensors

There are four temperature sensors located in different places of L-RARO hardware:

- Antenna ground plane (DS18B20).
- RF conditioner next to calibration matched load (MCP9808).
- RTL heat sink (DS18B20).
- Outside the enclosure to monitor ambient temperature (DS18B20).

As indicated above, three of these sensors are model DS18B20, and the fourth one is model MCP9808. The temperature sensor located at the RF conditioner is the model MCP9808 because of its tiny integrated package, which allows to place it very close to calibration matched load.

The DS18B20 is a programmable resolution 1-Wire digital thermometer [176]. 1-Wire bus requires only one line (plus ground) both for communication with the Arduino Mega and for power supplying. DS18B20 measurement range is defined from -10 °C to 85 °C for a whole range accuracy of ±0.5 °C. Besides, Fig. D.3a shows the actual accuracy as a function of temperature. An accuracy error of -0.2 °C and a precision of ±0.25 °C defined as ±3 standard deviation can be appreciated for instance. Nevertheless, the main goal of this controller is to stabilize the temperature rather than get accurate measurements. For this reason, measurement resolution has been set to 0.125 °C (11 bits), so that finer grained temperature measurements allow better adjustment of heating power, even though eventual temperature resolution is determined by sensor specifications (±0.25 °C).

The MCP9808 is a ±0.5 °C maximum accuracy digital temperature sensor [177]. However, its typical accuracy within from -20 °C and 100 °C is ±0.25 °C. Besides, Fig. D.3b

shows the actual accuracy as a function of temperature. An accuracy error of -0.05 °C and a precision of ±0.25 °C defined as ±3 standard deviation can be appreciated for instance. This sensor is controlled using an industry standard 400 kHz, 2-wire, SMBus/I2C compatible serial interface. The resolution has been set to 0.25 °C.

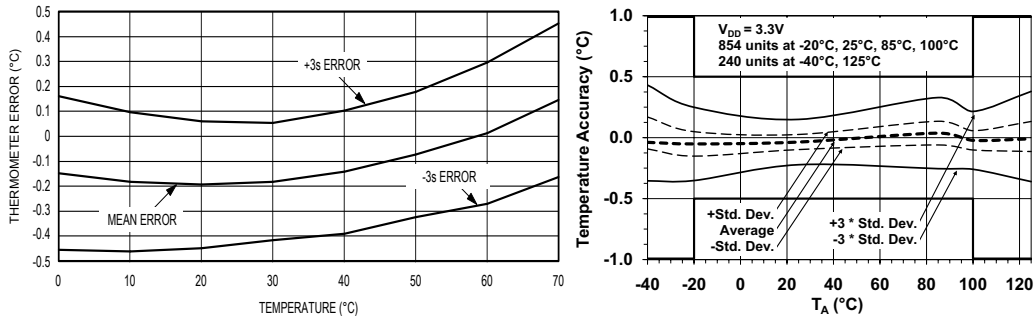

Figure D.3: Typical error performance curve: (a) DS18B20 [176] and (b) MCP9808 [177].

The 1-Wire and I2C controllers are running in the Arduino Mega board. The 1-Wire protocol has been implemented using a software driver, whereas the I2C protocol is controlled using the embedded CPU peripheral. Temperature measurements are retrieved every second from all four sensors.

D.2.2 PID controller

The PID controller acts as a control loop feedback mechanism that calculates an error value ($e(t)$) as the difference between a desired set point (T_{goal}) and the measured temperature (T_{sys}). Then, it applies a correction in the heating actuator (A_{heat}) based on the proportional, integral, and derivative terms (denoted P, I, and D respectively) which give the controller its name.

The measured temperature (T_{sys}) used in the PID controller is the one corresponding to the antenna ground plane, since it acts as a heat sink for all electronic components.

The heating actuator is defined as a normalized value between 0 and 255, and it can be expressed as:

$$A_{heat} = K_p\, e(t) + K_i \int_0^t e(t')\, \mathrm{d}t' + K_d \frac{\mathrm{d}e(t)}{\mathrm{d}t}, \tag{D.1}$$

where K_p, K_i, and K_d denote the coefficients for the proportional, integral, and derivative terms respectively.

Moreover, PID coefficients K_p, K_i, and K_d have been set to values 10, 0.5 and 2 respectively. These values have been retrieved using the manual tuning method described in [178].

This tuning method is to first set K_i and K_d values to zero. Then, increase the K_p until the output of the loop oscillates, then the K_p should be set to approximately half of that value for a "quarter amplitude decay" type response. After that, increase K_i until any

offset is corrected in sufficient time for the process. However, a too large K_i will cause instability. Finally, increase K_d, if required, until the loop is acceptably quick to reach its reference after a load disturbance. However, a too large K_d will cause excessive response and overshoot.

A fast PID loop tuning usually overshoots slightly to reach T_{goal} more quickly [178]. However, some systems cannot accept overshoot, in which case an overdamped closed-loop system is required, which will require a K_p setting significantly less than half that of the K_p setting that was causing oscillation.

D.2.3 Heater

The heater is a 60 W resistance that works at 220 V. It is turned on and off using a mechanic relay working at 5 V, and driven by the heat controller implemented in the Arduino Mega.

The heat controller transforms the value of the heating actuator (P_{heat}) into train of impulses that turn on and off the relay, ans thus it modulates the power delivered by the heater. Therefore, the actual heating power is obtained as:

$$P_{heat}[W] = \frac{60}{255} A_{heat}. \tag{D.2}$$

Furthermore, a fan placed just over the heater allows to recirculate the heat flow and to minimize heat gradients inside the enclosure.

D.2.4 Communications

A serial communication between the PC and the temperature controller allows setting the goal temperature (T_{goal}), as well as, all PID constants. Moreover, it allows logging of all parameters in order to study the current performance of the temperature controller.

D.3 Performance

As mentioned before, the PID controller uses the sensor placed on the antenna ground plane as T_{sys}, and then, the PID constants and T_{goal} are programmed using serial communication. In the temperature controller described in this appendix, T_{goal} has been set to 44 °C, since it is a temperature high enough to be controlled by using an electric heater to heat the system up, and the ambient temperature to cool it down.

Figure D.4 shows a 2-hour plot of all parameters of the temperature controller. In this case, the ambient temperature was forced to change in a range between 17 °C and 21 °C.

It can be appreciated that T_{sys} or the ground plane temperature T_{GND} is stabilized in a range of ± 0.375 °C (worst case) around 44 °C. In the case of the temperature of the RTL T_{RTL}, it is stabilized in a range of ± 0.5 °C (worst case), and it shows a bias of -0.25 °C. T_{RTL} stability is worse because the sensor is not placed as close as T_{GND} is to the heater, but it is still in the desired range. Besides, the bias is not relevant because it is not affecting the calibration since it is constant. The same can be said about the

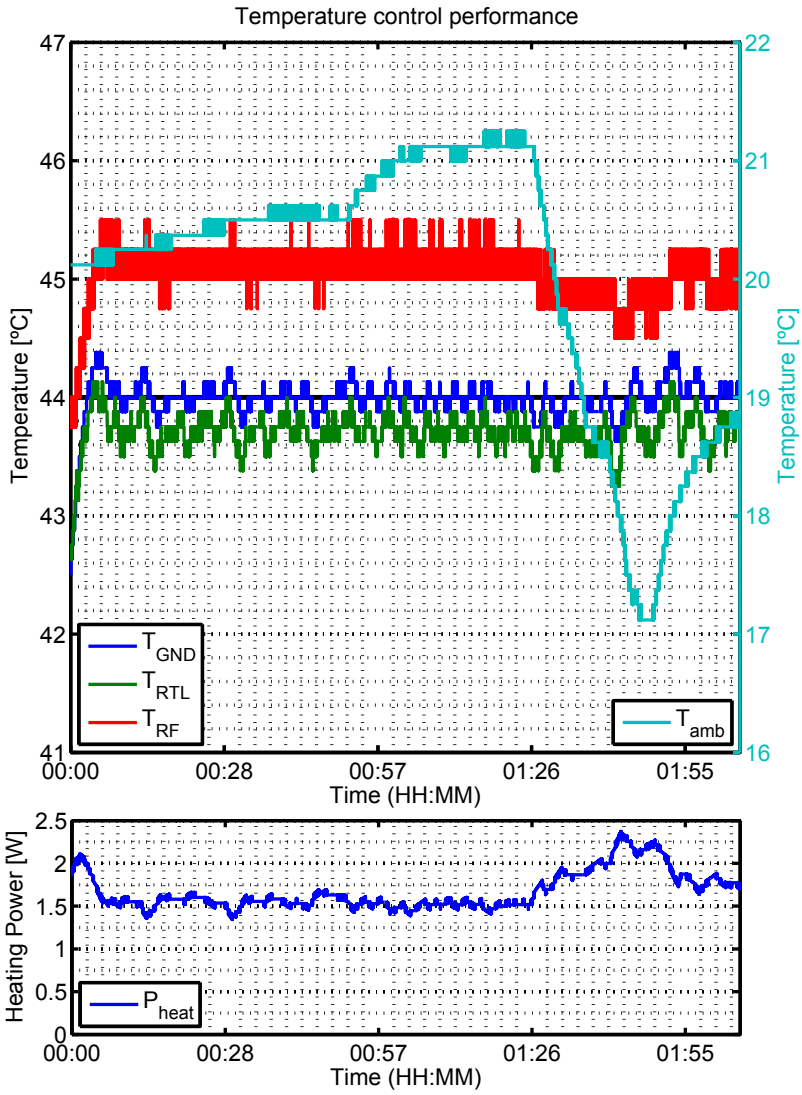

Figure D.4: Performance of the temperature controller.

temperature of the RF conditioner T_{RF}. Its stability is within ± 0.5 °C (worst case), and its bias is about +1 °C. Recall that this last temperature sensor has a programmed resolution of 0.25 °C, whereas the rest have 0.125 °C.

Regarding the PID controller, it shows a slightly overshoot behavior, not higher than 0.375 °C. However, it is able to stabilize the error $e(t) = T_{goal}(T) - T_{sys}(t)$ within the desired range.

Eventually, the heating power is in a range between 1.4 W and 2.4 W. It can be appreciated that it is higher at the beginning, when heating the system up, and when the ambient temperature falls down to 17 °C. Moreover, it is about 1.5 W when the ambient temperature change slowly between 20 °C and 21 °C.

Summarizing, the implemented temperature controller is able to stabilize the system temperature at 44 °C and within a stability range of ± 0.5 °C.

E

Appendix E

Derivation of CWAF and GSSC

This appendix shows the mathematical derivation of the fundamental terms decomposition of DDM in conventional and interferometric GNSS-R. Moreover, it also states the definition of a new figure of merit named GSSC, and its relationship with the classical SSC.

E.1 Derivation of DDM decomposition in cGNSS-R

The CWAF has been defined as the operation needed to calculate the measured DDM in GNSS-R, and, for two generic signals x and y, it is computed as:

$$|\chi|^2_{xy}(\nu,\tau) = \mathrm{E}\left\{|\chi_{xy}(\nu,\tau)|^2\right\}. \tag{E.1}$$

In the state of the art, the Sussman's formula was introduced in [142] as a general proof of several properties of ambiguity functions such as the Siebert's theorem [179] and the Stutt's invariant relation [180], and states that if a Cross-Ambiguity Function (CAF) is defined as:

$$\chi_{xy}(\nu,\tau) = \int x(t)\, y^*(t-\tau)\, e^{-j2\pi\nu t} dt, \tag{E.2}$$

the following identity is fulfilled:

$$\chi_{xy}(\nu,\tau)\, \chi^*_{wz}(\nu,\tau) = \iint \chi_{xw}(\nu',\tau')\, \chi^*_{yz}(\nu',\tau')\, e^{j2\pi(\nu'\tau-\nu\tau')} d\nu'\, d\tau', \tag{E.3}$$

so that, the modulus squared of any CAF can be expressed as:

$$|\chi_{xy}(\nu,\tau)|^2 = \chi_{xy}(\nu,\tau)\, \chi^*_{xy}(\nu,\tau) = \iint \chi_{xx}(\nu',\tau')\, \chi^*_{yy}(\nu',\tau')\, e^{j2\pi(\nu'\tau-\nu\tau')} d\nu'\, d\tau'. \tag{E.4}$$

This expression was derived for infinite coherent integration time, however, this is always finite. In order to obtain an expression equivalent to (E.4) for finite T_c, the equation defined for the delay-Doppler correlator in (7.3) is modulus squared as follows:

$$\begin{aligned} |\chi_{xy}(\nu,\tau)|^2 = &\left[\frac{1}{T_c}\int_{T_c} x(t_1)\, y^*(t_1-\tau)\, e^{-j2\pi\nu t_1} dt_1\right] \\ &\left[\frac{1}{T_c}\int_{T_c} x(t_2)\, y^*(t_2-\tau)\, e^{-j2\pi\nu t_2} dt_2\right]^* \\ &= \iint \frac{1}{T_c}\,\Pi\left(\frac{t_1}{T_c}\right)\frac{1}{T_c}\,\Pi\left(\frac{t_2}{T_c}\right) x(t_1)\, y^*(t_1-\tau) \\ &x^*(t_2)\, y(t_2-\tau)\, e^{-j2\pi\nu(t_1-t_2)} dt_1\, dt_2. \end{aligned} \tag{E.5}$$

Applying the change of variables $t_1 = t$ and $t_2 = t-\tau'$ with $dt_1\, dt_2 = |J(t,\tau')|\, dt\, d\tau' = dt\, d\tau'$ being J the Jacobian matrix of the transformation, (E.5) yields:

$$\begin{aligned} |\chi_{xy}(\nu,\tau)|^2 = &\iint \frac{1}{T_c}\,\Pi\left(\frac{t}{T_c}\right) x(t)\, x^*(t-\tau') \\ &\frac{1}{T_c}\,\Pi\left(\frac{t-\tau'}{T_c}\right) y^*(t-\tau)\, y(t-\tau-\tau')\, e^{-j2\pi\nu\tau'} dt\, d\tau', \end{aligned} \tag{E.6}$$

Then, using the inverse of the identities:

$$\widetilde{\chi}_{xx}(\nu',\tau') = \int \frac{1}{T_c}\,\Pi\left(\frac{t}{T_c}\right) x(t)\,x^*(t-\tau')\,e^{-j2\pi\nu' t}\,dt = sinc(T_c\,\nu') \underset{\nu'}{*} \chi_{xx}(\nu',\tau'), \quad \text{(E.7a)}$$

and

$$\begin{aligned}\widetilde{\chi}_{yy}(\nu'',\tau') = \int \frac{1}{T_c}\,\Pi\left(\frac{t-\tau'}{T_c}\right) y^*(t-\tau)\,y(t-\tau-\tau') \\ e^{-j2\pi\nu''(t-\tau)}\,dt = \left[sinc(T_c\,\nu'')\,e^{-j2\pi\nu''(\tau'-\tau)}\right] \underset{\nu''}{*} \chi_{yy}(\nu'',\tau'),\end{aligned} \quad \text{(E.7b)}$$

eq. (E.6) can be expressed as:

$$\begin{aligned}|\chi_{xy}(\nu,\tau)|^2 &= \iint \left[\int \widetilde{\chi}_{xx}(\nu',\tau')\,e^{j2\pi\nu' t} d\nu'\right] \\ &\quad \left[\int \widetilde{\chi}_{yy}(\nu'',\tau')\,e^{j2\pi\nu''(t-\tau)} d\nu''\right]^* e^{-j2\pi\nu\tau'}\,dt\,d\tau' \\ &= \iint \widetilde{\chi}_{xx}(\nu',\tau') \int \widetilde{\chi}^*_{yy}(\nu'',\tau')\left[\int e^{-j2\pi(\nu''-\nu')t} dt\right] \\ &\quad e^{j2\pi\nu'' \tau} e^{-j2\pi\nu\tau'}\,d\nu''\,d\nu'\,d\tau' = \iint \widetilde{\chi}_{xx}(\nu',\tau') \int \widetilde{\chi}^*_{yy}(\nu'',\tau')\,\delta(\nu''-\nu') \\ &\quad e^{j2\pi(\nu''\tau-\nu\tau')} d\nu''\,d\nu'\,d\tau' = \iint \widetilde{\chi}_{xx}(\nu',\tau')\,\widetilde{\chi}^*_{yy}(\nu',\tau')\,e^{j2\pi(\nu'\tau-\nu\tau')} d\nu'\,d\tau',\end{aligned} \quad \text{(E.8)}$$

where $\widetilde{\chi}_{xx}$ and $\widetilde{\chi}_{yy}$ are windowed and delayed versions of χ_{xx} and χ_{yy} respectively. Indeed, the last ones correspond to the auto-correlation functions of the input signals using correlator defined in (7.3) as done in [138]. Therefore, if x and y are already taken windowed by T_c and delayed by τ, $\widetilde{\chi}_{xx} = \chi_{xx}$, $\widetilde{\chi}_{yy} = \chi_{yy}$, and (E.8) is equivalent to (E.4). Henceforth, this last statement will be assumed.

Eventually, substituting (E.8) (or equivalent (E.4)) in (E.1), and considering statistical independence between x and y, the CWAF yields:

$$\begin{aligned}|\chi|^2_{xy}(\nu,\tau) &= \mathrm{E}\left\{|\chi_{xy}(\nu,\tau)|^2\right\} = \mathrm{E}\left\{\iint \chi_{xx}(\nu',\tau')\,\chi^*_{yy}(\nu',\tau')\,e^{j2\pi(\nu'\tau-\nu\tau')} d\nu'\,d\tau'\right\} \\ &= \iint \mathrm{E}\left\{\chi_{xx}(\nu',\tau')\right\}\mathrm{E}\left\{\chi^*_{yy}(\nu',\tau')\right\} e^{j2\pi(\nu'\tau-\nu\tau')} d\nu' d\tau' \\ &= \iint A_x(\nu',\tau')\,A^*_y(\nu',\tau')\,e^{j2\pi(\nu'\tau-\nu\tau')} d\nu'\,d\tau',\end{aligned} \quad \text{(E.9)}$$

where A_x and A_y are the Expected Ambiguity Function (EAF) of signals x and y respectively. This expression will be used to prove the DDM decomposition for cGNSS-R stated in (7.6).

Therefore, using (E.9), the CWAF in (7.4) can be expressed as a function of A_{y_r} and A_{c_k}. A_{c_k} is the EAF of the tracked code, whereas A_{y_r} is the EAF of the received signal after the front-end obtained from:

$$A_{y_r}(\nu,\tau) = \frac{1}{T_c}\int_{T_c} \mathrm{E}\left\{y_r(t)\, y_r^*(t-\tau)\right\} e^{-j2\pi\nu t}\, dt. \tag{E.10}$$

$\mathrm{E}\left\{y_r(t)\, y_r^*(t-\tau)\right\}$ can be expanded using the terms of y_r in (7.2) as follows:

$$\begin{aligned}
\mathrm{E}\left\{y_r(t)\, y_r^*(t-\tau)\right\} &= \mathrm{E}\left\{\left[\sum_{l=0}^{L-1} s_{r_l}(t) + i_r(t) + n_r(t)\right]\right. \\
&\quad \left.\left[\sum_{l'=0}^{L-1} s_{r_{l'}}^*(t-\tau) + i_r^*(t-\tau) + n_r^*(t-\tau)\right]\right\} \\
&= \sum_{l=0}^{L-1} \mathrm{E}\left\{s_{r_l}(t) s_{r_l}^*(t-\tau)\right\} + \sum_{\substack{l\geq 0 \\ l\neq l'}}^{L-1}\sum_{l'=0}^{L-1} \mathrm{E}\left\{s_{r_l}(t) s_{r_{l'}}^*(t-\tau)\right\} \\
&\quad + \sum_{l=0}^{L-1} \mathrm{E}\left\{s_{r_l}(t)\, i_r^*(t-\tau)\right\} + \sum_{l=0}^{L-1} \mathrm{E}\left\{s_{r_l}(t)\, n_r^*(t-\tau)\right\} \\
&\quad + \sum_{l'=0}^{L-1} \mathrm{E}\left\{i_r(t) s_{r_{l'}}^*(t-\tau)\right\} + \mathrm{E}\left\{i_r(t)\, i_r^*(t-\tau)\right\} + \mathrm{E}\left\{i_r(t)\, n_r^*(t-\tau)\right\} \\
&\quad + \sum_{l'=0}^{L-1} \mathrm{E}\left\{n_r(t)\, s_{r_{l'}}^*(t-\tau)\right\} + \mathrm{E}\left\{n_r(t)\, i_r^*(t-\tau)\right\} + \mathrm{E}\left\{n_r(t)\, n_r^*(t-\tau)\right\} \\
&= \sum_{l=0}^{L-1} \mathrm{E}\left\{s_{r_l}(t) s_{r_l}^*(t-\tau)\right\} + \mathrm{E}\left\{i_r(t)\, i_r^*(t-\tau)\right\} + \mathrm{E}\left\{n_r(t)\, n_r^*(t-\tau)\right\},
\end{aligned} \tag{E.11}$$

assuming that s_r, i_r and n_r are statistically independent between them, that $\mathrm{E}\left\{s_{r_l}(t) s_{r_{l'}}^*(t-\tau)\right\} = 0$ because of code orthogonality, and that $\mathrm{E}\left\{i_r(t)\right\} = \mathrm{E}\left\{n_r(t)\right\} = 0$, without loss of generality. Then, (E.10) can be expressed as:

$$A_{y_r}(\nu,\tau) = \sum_{l=0}^{L-1} A_{s_{r,l}}(\nu,\tau) + A_{i_r}(\nu,\tau) + A_{n_r}(\nu,\tau), \tag{E.12}$$

and, eventually, the DDM decomposition stated in (7.6) is obtained by substituting (E.12) in (E.9) yielding:

$$\begin{aligned}
|\chi|^2_{y_r c_k}(\nu,\tau) &= \sum_{l=0}^{L-1} |\chi|^2_{s_{r,l} c_k}(\nu,\tau) + |\chi|^2_{i_r c_k}(\nu,\tau) + |\chi|^2_{n_r c_k}(\nu,\tau) \\
&= |\chi|^2_{s_{r,k} c_k}(\nu,\tau) + \sum_{\substack{l\geq 0 \\ l\neq k}}^{L-1} |\chi|^2_{s_{r,l} c_k} + |\chi|^2_{i_r c_k} + |\chi|^2_{n_r c_k},
\end{aligned} \tag{E.13}$$

where the dependence with ν and τ in the last terms has been omitted since it does not apply. This result may be derived intuitively taking into account the statistical independence between the additive terms of the input signal.

E.2 Derivation of DDM decomposition in iGNSS-R

The derivation of the DDM in the case of iGNSS-R can be obtained from expressions in Appendix E.1. First, using (E.9), the CWAF can be expressed as:

(E.14)

$$|\chi|^2_{y_r y_d}(\nu,\tau) = \mathrm{E}\left\{|\chi_{y_r y_d}(\nu,\tau)|^2\right\}$$

$$= \iint A_{y_r}(\nu',\tau')\, A^*_{y_d}(\nu',\tau')\, e^{j2\pi(\nu'\tau-\nu\tau')} d\nu'\, d\tau',$$

since y_r and y_d are assumed statistically independent. Besides, the EAF of y_d can be written as:

$$A_{y_d}(\nu,\tau) = \sum_{l'=0}^{L-1} A_{s_{d,l'}}(\nu,\tau) + A_{i_d}(\nu,\tau) + A_{n_d}(\nu,\tau), \tag{E.15}$$

considering the same assumptions and derivations taken in (E.10), (E.11), and (E.12), but for the direct received signals in (7.5). Eventually, substituting (E.12) and (E.15) in

(E.14), the interferometric CWAF yields:

$$
\begin{aligned}
|\chi|^2_{y_r y_d}(\nu,\tau) = \iint & \left[\sum_{l=0}^{L-1} A_{s_{r,l}}(\nu',\tau') + A_{i_r}(\nu',\tau') + A_{n_r}(\nu',\tau')\right] \\
& \left[\sum_{l'=0}^{L-1} A^*_{s_{d,l'}}(\nu',\tau') + A^*_{i_d}(\nu',\tau') + A^*_{n_d}(\nu',\tau')\right] e^{j2\pi(\nu'\tau-\nu\tau')} d\nu' d\tau' \\
= \iint & \left[\sum_{l=0}^{L-1}\sum_{l'=0}^{L-1} A_{s_{r,l}}(\nu',\tau')\, A^*_{s_{d,l'}}(\nu',\tau') + \sum_{l=0}^{L-1} A_{s_{r,l}}(\nu',\tau')\, A^*_{i_d}(\nu',\tau')\right. \\
& + \sum_{l=0}^{L-1} A_{s_{r,l}}(\nu',\tau')\, A^*_{n_d}(\nu',\tau') + A_{i_r}(\nu',\tau') \sum_{l'=0}^{L-1} A^*_{s_{d,l'}}(\nu',\tau') \\
& + A_{i_r}(\nu',\tau')\, A^*_{i_d}(\nu',\tau') + A_{i_r}(\nu',\tau')\, A^*_{n_d}(\nu',\tau') + A_{n_r}(\nu',\tau') \sum_{l'=0}^{L-1} A^*_{s_{d,l'}}(\nu',\tau') \\
& \left. + A_{n_r}(\nu',\tau')\, A^*_{i_d}(\nu',\tau') + A_{n_r}(\nu',\tau')\, A^*_{n_d}(\nu',\tau')\right] e^{j2\pi(\nu'\tau-\nu\tau')} d\nu'\, d\tau' \\
= & \sum_{l=0}^{L-1}\sum_{l'=0}^{L-1} |\chi|^2_{s_{r,l}s_{d,l'}}(\nu,\tau) + \sum_{l=0}^{L-1} |\chi|^2_{s_{r,l}i_d}(\nu,\tau) + \sum_{l=0}^{L-1} |\chi|^2_{s_{r,l}n_d}(\nu,\tau) \\
& + \sum_{l=0}^{L-1} |\chi|^2_{i_r s_{d,l}}(\nu,\tau) + |\chi|^2_{i_r i_d}(\nu,\tau) + |\chi|^2_{i_r n_d}(\nu,\tau) \\
& + \sum_{l=0}^{L-1} |\chi|^2_{n_r s_{d,l}}(\nu,\tau) + |\chi|^2_{n_r i_d}(\nu,\tau) + |\chi|^2_{n_r n_d}(\nu,\tau).
\end{aligned}
\tag{E.16}
$$

The last formula can be simplified in order to obtain the following expression for DDM decomposition for the kth composite satellite signal using iGNSS-R:

$$
\begin{aligned}
|\chi|^2_{y_r y_d}(\nu,\tau) = |\chi|^2_{s_{r,k}s_{d,k}}(\nu,\tau) + |\chi|^2_{\textit{cross-talk}}(\nu,\tau) \\
+ |\chi|^2_{\textit{cross-sat}}(\nu,\tau) + |\chi|^2_{\mathrm{RFI}}(\nu,\tau) + |\chi|^2_{\mathrm{noise}}(\nu,\tau),
\end{aligned}
\tag{E.17a}
$$

where the last four terms are defined as follows:

$$
|\chi|^2_{\textit{cross-talk}}(\nu,\tau) = \sum_{\substack{l\geq 0 \\ l\neq k}}^{L-1} |\chi|^2_{s_{r,l}s_{d,l}}(\nu,\tau),
\tag{E.17b}
$$

$$
|\chi|^2_{\textit{cross-sat}}(\nu,\tau) = \sum_{\substack{l\geq 0 \\ l\neq l'}}^{L-1}\sum_{l'=0}^{L-1} |\chi|^2_{s_{r,l}s_{d,l'}}(\nu,\tau) + \sum_{\substack{l\geq 0 \\ l\neq k}}^{L-1} |\chi|^2_{s_{r,l}n_d}(\nu,\tau) + \sum_{\substack{l\geq 0 \\ l\neq k}}^{L-1} |\chi|^2_{n_r s_{d,l}}(\nu,\tau),
\tag{E.17c}
$$

$$|\chi|^2_{\text{RFI}}(\nu,\tau) = \sum_{l=0}^{L-1} |\chi|^2_{s_{r,l}i_d}(\nu,\tau) + \sum_{l=0}^{L-1} |\chi|^2_{i_r s_{d,l}}(\nu,\tau) + |\chi|^2_{i_r i_d}(\nu,\tau) + |\chi|^2_{i_r n_d}(\nu,\tau) + |\chi|^2_{n_r i_d}(\nu,\tau), \tag{E.17d}$$

and

$$|\chi|^2_{\text{noise}}(\nu,\tau) = |\chi|^2_{s_{r,k}n_d}(\nu,\tau) + |\chi|^2_{n_r s_{d,k}}(\nu,\tau) + |\chi|^2_{n_r n_d}(\nu,\tau). \tag{E.17e}$$

Eventually, (7.8) has been obtained from the combination of (E.17a) and (E.17e), and omitting the dependence with ν and τ in the terms where it does not apply.

E.3 Derivation of the GSSC and reduction to SSC

A CWAF, and particularly the result obtained in (E.8), can be expressed in an alternative way as a function of the WVS of each one of the involved signals, which are the Fourier transform of the their respective EAF, which are related as follows [104]:

$$A_x(\nu,\tau) = \frac{1}{T_c} \iint_{T_c} W_x(t,f)\, e^{-j2\pi(\nu t - f\tau)}\, dt\, df, \tag{E.18}$$

with the WVS defined as:

$$W_x(t,f) = \int \mathrm{E}\left\{x(t)\, x^*(t-\tau)\right\} e^{-j2\pi f\tau}\, d\tau, \tag{E.19}$$

taking into account the time window T_c as in Appendix E.1. Then, substituting (E.18) into (E.9), $|\chi|^2_{xy}$ can also be written as:

$$\begin{aligned}
|\chi|^2_{xy}(\nu,\tau) &= \iint \left[\frac{1}{T_c}\iint_{T_c} W_x(t,f)\, e^{-j2\pi(\nu' t - f\tau')} dt\, df\right] \\
&\quad \left[\frac{1}{T_c}\iint_{T_c} W_y(t',f')\, e^{-j2\pi(\nu' t' - f'\tau')} dt'\, df'\right]^* e^{j2\pi(\nu'\tau - \nu\tau')} d\nu'\, d\tau' \\
&= \frac{1}{T_c^2}\iint_{T_c} W_x(t,f) \iint_{T_c} W_y(t',f') \left[\int e^{j2\pi\nu'(t'-t+\tau)} d\nu'\right] \\
&\quad \left[\int e^{-j2\pi(f'-f+\nu)\tau'} d\tau'\right] dt'\, df'\, dt\, df \\
&= \frac{1}{T_c^2}\iint_{T_c} W_x(t,f) \iint_{T_c} W_y(t',f')\, \delta(t'-t+\tau) \\
&\quad \delta(f'-f+\nu)\, dt'\, df'\, dt\, df = \frac{1}{T_c^2}\iint_{T_c} W_x(t,f)\, W_y(t-\tau, f-\nu)\, dt\, df \\
&= \frac{1}{T_c^2}\, W_x(\tau,\nu) ** W_y(\tau,\nu),
\end{aligned} \tag{E.20}$$

where the reality and commutative properties of the WVS have been applied [104]. This result resembles the definition of the SSC in [181], but in this case, it involves the convolution of non-stationary spectrum functions. For this reason, a more general figure of

merit is defined in this PhD thesis, which is the GSSC. The GSSC between two generic signals x and y is defined as:

$$\gamma_{xy}(\nu,\tau) = \frac{1}{T_c}\,\overline{W_x}(\tau,\nu) * * \overline{W_y}(\tau,\nu), \tag{E.21}$$

where W_x and W_y have been normalized dividing by their respective power P_x and P_y, in analogy to the classical SSC. Therefore, using (E.21), (E.20) yields:

$$|\chi|^2_{xy}(\nu,\tau) = \frac{1}{T_c}\,P_x\,P_y\,\gamma_{xy}(\nu,\tau). \tag{E.22}$$

The use of the WVS accounts for non-stationary random processes, whose spectra may change over time. However, if the random process x is stationary (i.e. its statistical moments are constant over time), or at least quasi-stationary (i.e. its statistical moments are constant over a fraction of time T_c), the WVS becomes the stationary PSD [146]:

$$W_x(t,f) = S_x(f), \tag{E.23}$$

and, in this case, the GSSC yields:

$$\begin{aligned}\gamma_{xy}(\nu,\tau) &= \frac{1}{T_c}\,\overline{W_x}(\tau,\nu) * * \overline{W_y}(\tau,\nu) = \frac{1}{T_c}\iint_{T_c}\overline{W_x}(t,f)\,\overline{W_y}(t-\tau,f-\nu)\,dt\,df \\ &= \frac{1}{T_c}\iint_{T_c}\overline{S_x}(f)\,\overline{S_y}(f-\nu)\,dt\,df = \int\overline{S_x}(f)\,\overline{S_y}(f-\nu)\,df.\end{aligned} \tag{E.24}$$

Therefore, in this case, the GSSC is equivalent to the classical definition of SSC in [181]:

$$\gamma_{xy}(\nu,\tau) = \kappa_{xy}(\nu) = \overline{S_x}(\nu) * \overline{S_y}(\nu), \tag{E.25}$$

and a CWAF can be expressed as:

$$|\chi|^2_{xy}(\nu,\tau) = \frac{1}{T_c}\,P_x\,P_y\,\kappa_{xy}(\nu). \tag{E.26}$$

Furthermore, considering an ideal transfer function for the front-end with bandwidth B_r, the GSSC can be written as in (7.16), and the classical SSC turns to be equal to the one in (7.12).

F

Appendix F

Complex Kurtosis

This appendix shows the derivation and statistics of the complex kurtosis used as a RFI detector in this PhD thesis. First, the definition of the moments of real- and complex-valued random variables is done. Then, the moments are evaluated for the particular cases of Normal and circular complex Normal distributions. After that, the definition of complex kurtosis used in this PhD thesis as a normality test is stated. Eventually, the expressions and statistics of the sample kurtosis and the sample complex kurtosis are discussed.

F.1 Moments of a random variable

According to [53], the nth-order *moment* of a (real-valued) random variable x is defined as

$$\mu_n(x) = E\{x^m\} = \int_{-\infty}^{\infty} x^m f_x(x)\, dx, \tag{F.1}$$

where $f_x(x)$ is the PDF of x, $x \in \mathbb{R}$, and $m \in \mathbb{N}$. In particular, the first-order moment, $\mu_1(x) = E\{x\} = \mu(x)$, is the *mean* value of x. The second-order moment, $\mu_2(x) = E\{x^2\}$, is the *mean-squared value* or *instantaneous power*.

Corresponding to the moments, the nth-order *central moment* of x is defined as

$$\lambda_n(x) = E\{(x - \mu(x))^m\} = \int_{-\infty}^{\infty} (x - \mu(x))^m f_x(x)\, dx. \tag{F.2}$$

In particular, $\lambda_1(x) = E\{(x^m - \mu(x))\} = 0$, and, if the mean value is zero, $\mu(x) = 0$, the (non-central) moments and central moments coincide, $\lambda_n(x) = \mu_n(x)$. Besides, the second-order central moment is the *variance* of x, denoted as $\sigma^2(x)$, and defined as $\mu_2(x) =$.

$$Var\{x\} = \lambda_2(x) = E\{(x - \mu(x))^m\} = \sigma^2(x). \tag{F.3}$$

The quantity $\sigma(x) = \sqrt{\lambda_2(x)}$ is the *standard deviation* of x, and it is a measure of the spread (or dispersion) of the observed values of x around its mean $\mu(x)$. Note that, the instantaneous power can then be expressed as $\mu_2(x) = \sigma^2(x) + \mu^2(x)$.

Furthermore, and corresponding to the non-central and central moments, the nth-order *normalized moment* of x is defined as the nth-order central moment of x divided by the nth power of the standard deviation of x. Therefore,

$$\gamma_n(x) = \frac{\lambda_n(x)}{\sigma^m(x)} = E\left\{\left(\frac{x - \mu(x)}{\sigma(x)}\right)^m\right\} = E\{z^m\} \tag{F.4}$$

is the nth-order normalized moment of x, while $z = (x - \mu(x))/\sigma(x)$ is the normalized version of the random variable x. Note that, $\gamma_n(x)$ is a dimensionless quantity (conversely to $\mu_n(x)$ and $\lambda_n(x)$), and the following relationships yield $\gamma_n(x) = \mu_n(z)$, $\gamma_1(x) = \mu(z) = 0$, and $\gamma_2(x) = \sigma^2(z) = 1$.

The quantity *skewness* is defined as the third-order normalized moment of x, and expressed as

$$\gamma_3(x) = \frac{\lambda_3(x)}{\sigma^3(x)} = E\{z^3\}. \tag{F.5}$$

The skewness characterizes the degree of asymmetry of a distribution around its mean. It is zero if the density function is symmetric about its mean value, it is positive if the shape leans towards the right, or it is negative if it leans towards the left.

Eventually, the quantity *kurtosis* is defined as the fourth-order normalized moment of x, denoted as $\mathsf{k}(x)$, and expressed as

$$\mathsf{k}(x) = \gamma_4(x) = \frac{\lambda_4(x)}{\sigma^4(x)} = E\left\{z^4\right\}. \tag{F.6}$$

The kurtosis measures the relative flatness or peakedness of a distribution about its mean. Besides, the *excess kurtosis* of x is defined as the kurtosis of x minus 3, which is the kurtosis value of a Normal random variable. Thus, the excess kurtosis compares the flatness or peakedness of a distribution to a Normal distribution. Distributions with zero excess kurtosis are called mesokurtic, distributions with positive excess kurtosis are called leptokurtic (slenderized-shaped), and distributions with negative excess kurtosis are called platykurtic (broaden-shaped). In some cases, the kurtosis is defined as the excess kurtosis, especially if it is derived from the cumulants of x instead of from the moments of x (see [53]).

Figure F.1 summarizes the properties of the four principal quantities derived from moments of random variables.

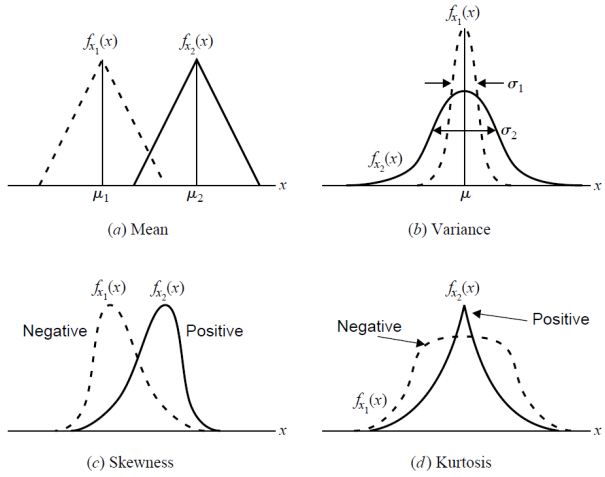

Figure F.1: Illustration of mean, variance, skewness and kurtosis [53].

F.2 Moments of Normal random variable

From Appendix A, the PDF of a Normal distribution is given by

$$f_{\mathbf{x}}(x) = \frac{1}{\sqrt{2\pi\sigma^2}}\, e^{-\frac{(x-\mu)^2}{2\sigma^2}} \quad x \in \mathbb{R}, \tag{F.7}$$

where μ is the mean and σ the standard deviation of x. Therefore, the first moment of x, $\mu_1(x)$, is equal to $\mu(x) = \mu$, and the second central moment, $\lambda_2(x)$ is equal to $\sigma^2(x) = \sigma^2$.

The Normal distribution follows the following property [182],

$$\lambda_n(x) = \begin{cases} 0 & \text{if } m \text{ is odd,} \\ (m-1)\ \sigma^m & \text{if } m \text{ is even,} \end{cases} \tag{F.8}$$

where $\chi!!$ denotes the double factorial of χ, that is, the product of all numbers from χ to 1 that have the same parity as χ. Therefore, the skewness of a Normal variable x is zero, $\gamma_3(x) = 0$, and its kurtosis, $\mathsf{k}(x)$, is given by

$$\mathsf{k}(x) = \gamma_4(x) = \frac{\lambda_4(x)}{\sigma^4(x)} = \frac{3\sigma^4(x)}{\sigma^4(x)} = 3. \tag{F.9}$$

As mentioned above, the result $\mathsf{k}(x) = 3$ is used as a reference value to compare the flatness of other distributions to the Normal distribution. Eventually, Table F.1 summarizes all first fourth-order moments of a Normal random variable x.

Order $[n]$	Non-central $[\mu_n(x)]$	Central $[\lambda_n(x)]$	Normalized $[\gamma_n(x)]$
1	μ [Mean]	0	0
2	$\mu^2 + \sigma^2$	σ^2 [Variance]	1
3	$\mu^3 + 3\,\mu\,\sigma^2$	0	0 [Skewness]
4	$\mu^4 + 6\,\mu^2\,\sigma^2 + 3\,\sigma^4$	$3\,\sigma^4$	3 [Kurtosis]

Table F.1: Summary of the moments of a Normal random variable x.

F.3 Moments of a complex-valued random variable

A complex-valued random variable can be defined as an joint bi-variate random variable (real x_i and imaginary x_q), where their values are combined as a complex number, $x = x_i + jx_q$, and thus $x \in \mathbb{C}$. According to [183], the nth-order moment of a complex random variable x is defined as

$$\mu_{p,q}(x) = E\left\{x^p\, x^{*q}\right\}, \tag{F.10}$$

where $x \in \mathbb{C}$; $p, q \in \mathbb{Z}^+$; $m = p + q$; and $m \in \mathbb{N}$. Besides, symmetric moments are complex conjugates, $\mu_{q,p}(x) = (\mu_{p,q}(x))^*$, and if $x \in \mathbb{R}$, all nth-order moments are equal. The complex moment definition is a extended version of real moments. The mean of x can be expressed as $\mu(x) = \mu_{1,0}(x) = (\mu_{0,1}(x))^*$, and the instantaneous power of x as $\mu_{1,1}(x) = E\left\{|x|^2\right\}$.

In the same way, the nth-order central moment of a complex random variable x is defined as

$$\lambda_{p,q}(x) = E\left\{(x - \mu(x))^p\, (x - \mu(x))^{*q}\right\}. \tag{F.11}$$

The variance of x is then expressed as $\sigma^2(x) = \lambda_{1,1}(x)$, while $\varsigma(x) = \lambda_{2,0}(x)$ is defined as the *pseudo-variance* of x [183, 184]. Note that, $\lambda_{1,0}(x) = 0$. The ratio between the pseudo-variance and the variance of x is used to measure the circularity of x [183, 184]. The circularity quotient of x, $\varrho(x)$, is then defined as

$$\varrho(x) = \frac{\lambda_{2,0}(x)}{\lambda_{1,1}(x)} = \frac{\varsigma(x)}{\sigma^2(x)}. \tag{F.12}$$

A random variable x with $\varrho(x)$ equal to zero is said to be *second-order circular* [184].

Furthermore, the nth-order normalized moment of a complex random variable x is defined as

$$\rho_{p,q}(x) = \frac{\lambda_{p,q}(x)}{\sigma^m(x)} = E\left\{\left(\frac{x-\mu(x)}{\sigma(x)}\right)^p \left(\frac{x-\mu(x)}{\sigma(x)}\right)^{*q}\right\} = E\left\{z^p\, z^{*q}\right\}, \tag{F.13}$$

where $\sigma(x) = \sqrt{\lambda_{1,1}(x)}$ is the standard deviation of x, and z is the normalized version of the random variable x (as in the real moment definition). Note that, $\rho_{p,q}(x)$ is a dimensionless quantity (conversely to $\mu_{p,q}(x)$ and $\lambda_{p,q}(x)$), and the following relationships yield $\rho_{p,q}(x) = \mu_{p,q}(z)$, $\rho_{1,0}(x) = \mu_{1,0}(z) = 0$, and $\rho_{1,1}(x) = \sigma^2(z) = 1$.

Given this definition of normalized the nth-order normalized moment of a complex random variable x, the quantities of real random distributions for skewness and kurtosis can be expressed, respectively, as $\rho_{3,0}(x)$ and $\rho_{4,0}(x)$. However, these quantities do not have unique extensions for complex random variables, since there are two non-symmetric (i.e. non-redundant) third-order moments, and three non-redundant fourth-order moments. Thus, for a complex random variable x; the two measures of skewness are $\rho_{3,0}(x)$ and $\rho_{2,1}(x)$; and the three measures of kurtosis are $\rho_{4,0}(x)$, $\rho_{3,1}(x)$, and $\rho_{2,2}(x)$ [183,184]. Note that, if x is degenerate (i.e. $x_i = 0$ or $x_q = 0$), all skewness and kurtosis quantities are equal to their real respective counterparts. Hence, in this sense, all the complex kurtosis coefficients above are valid generalizations of the real kurtosis [184].

F.4 Moments of a complex Normal random variable

As mentioned in Appendix A, the probability distribution at the output of an I/Q demodulator when receiving thermal noise can be modeled as a complex Normal distribution. The output signal, $x \in \mathbb{C}$, can be expressed as $x = x_i + jx_q$, where x_i and x_q are the in-phase and quadrature components respectively, both following a Normal distribution. In particular, $x_i \sim \mathcal{N}(\mu_i, \sigma_i^2)$, and $x_q \sim \mathcal{N}(\mu_q, \sigma_q^2)$. As a general case, σ_i and σ_q might be different because of an unbalance between I and Q components at the receiver. Moreover, they might be cross-correlated due to a leakage between channels. Given that, x follows a (generalized) complex Normal distribution with PDF equal to

$$f_x(x) = \frac{1}{2\pi\sqrt{|\Sigma|}} \exp\left(-\frac{1}{2}\left(\mathbf{x}-\boldsymbol{\mu}\right)^T \Sigma^{-1} \left(\mathbf{x}-\boldsymbol{\mu}\right)\right), \tag{F.14}$$

where $\mathbf{x}^T = (x_i\ x_q)$, $\boldsymbol{\mu}^T = (\mu_i\ \mu_q)$, Σ is the covariance matrix defined as

$$\Sigma = \begin{pmatrix} \sigma_i^2 & \sigma_{iq} \\ \sigma_{iq} & \sigma_q^2 \end{pmatrix}, \tag{F.15}$$

where $\sigma_{iq} = E\left\{(x_i - \mu_i)\,(x_q - \mu_q)\right\}$ is the covariance between x_i and x_q, and $|\Sigma|$ is the determinant of Σ.

According to [185], the complex Normal PDF of x, $f_x(x)$, can also be expressed in terms of the moments of a complex-valued random variable as follows

$$f_x(x) = \frac{1}{\pi\sqrt{\sigma^4(x) - |\varsigma(x)|^2}} \exp\left(\frac{\sigma^2(x)\,|x - \mu(x)|^2 - \langle (x - \mu(x))\,, \varsigma(x)\rangle}{\sigma^4(x) - |\varsigma(x)|^2}\right), \tag{F.16}$$

where $\mu(x) = \mu_{1,0} = \mu_i + \mu_q$ is the mean of x, $\sigma^2(x) = \lambda_{1,1}(x) = \sigma_i^2 + \sigma_q^2$ is the variance of x, and $\varsigma(x) = \lambda_{2,0}(x) = \sigma_i^2 - \sigma_q^2 + 2j\,\sigma_{iq}$ is the pseudo-variance of x. Recall that the circularity quotient ϱ is defined as $\varsigma(x)/\sigma^2(x)$.

Regarding the higher-order normalized moments of x, the complex Normal distributions fulfill the following condition

$$\lambda_{p,q}(x) = E\left\{(x - \mu(x))^p\,(x - \mu(x))^{*q}\right\} = 0, \tag{F.17}$$

if $m = p + q$ is an odd number [184, 185]. This property is the equivalent to the odd-vanishing moments of a (real) Normal distribution. Then, the two skewness quantities, $\rho_{3,0}(x)$ and $\rho_{2,1}(x)$, are equal to zero. Moreover, the three kurtosis quantities can be expressed as a function of the real kurtosis as

$$\rho_{4,0}(x) = \varrho^2\,\mathsf{k}(x_0), \quad \rho_{3,1}(x) = \varrho\,\mathsf{k}(x_0), \quad \rho_{2,2}(x) = \tfrac{2}{3}\left(1 + \tfrac{1}{2}|\varrho|^2\right)\mathsf{k}(x_0), \tag{F.18}$$

where $\mathsf{k}(x_0) = \mathsf{k}(x_i) = \mathsf{k}(x_q) = 3$ is the real kurtosis of either the real or imaginary part of x. Note that, both x_i and x_q follow a (real) Normal distribution. Hence, all kurtosis quantities are simply a scaled version of the real kurtosis of their real and imaginary parts [184].

Furthermore, a complex Normal distribution x is *circular* if its pseudo-variance $\varsigma(x)$ is equal to zero [184, 186], and thus, its circularity quotient ϱ is also equal to zero. The condition,

$$\varsigma(x) = \sigma_i^2 - \sigma_q^2 + 2j\sigma_{iq} = 0, \tag{F.19}$$

is only fulfilled if, and only if, the real and imaginary parts of x have equal variance $\sigma_i^2 = \sigma_q^2$, and they are uncorrelated, $\sigma_{iq} = 0$. Note that, since $\mu_i = \mu_q = 0$, then, $E\left\{x_i\,x_q\right\} = 0$.

The signal x at the output of an I/Q demodulator, with no I/Q unbalance and no leakage between channels, receiving thermal noise follows a circular complex Normal distribution,

and it is known as CWGN (see Appendix A). According to [184, 185], the circularity condition implies that all the non-absolute moments vanish, that is

$$\mu_{p,q} = \lambda_{p,q} = E\left\{x^p\, x^{*q}\right\} = 0, \quad \text{if } p \neq q, \tag{F.20}$$

and hence all normalized moments $\rho_{p,q}(x)$ with $p \neq q$ are equal to zero. Therefore, the kurtosis quantities $\rho_{4,0}(x)$ and $\rho_{3,1}(x)$ are equal to zero. The only non-vanishing kurtosis coefficient is $\rho_{2,2}(x)$, which can be related to the real kurtosis as

$$\rho_{2,2}(x) = \frac{2}{3}\mathsf{k}(x_i) = \frac{2}{3}\,\mathsf{k}(x_q) = 2. \tag{F.21}$$

F.5 Definition of complex kurtosis as a Normality test

As detailed in Chapter 3, the (real) kurtosis has been extensively used for RFI detection in microwave radiometers, since it can be used to as a normality test. Moreover, in [184], a function of the kurtosis coefficient $\rho_{2,2}(x)$ is proposed as a normality test for complex random variables. This test statistic is defined as

$$\frac{\rho_{2,2}(x)}{1+\frac{1}{2}|\varrho(x)|^2} - 2, \tag{F.22}$$

where both the kurtosis quantity $\rho_{2,2}(x)$ and the circularity test ϱ must be estimated from the data. Besides, an estimator of $\varrho(x)$ is proposed and defined as the ratio between $\rho_{4,0}(x)$ and $\rho_{3,1}(x)$. In [187], this test statistic was proven to perform better than the real kurtosis test.

However, in this PhD thesis, the test statistic defined as *complex kurtosis*, $\kappa(x)$, and used to evaluate the normality of a complex Normal distribution is an estimator of the kurtosis quantity $\rho_{2,2}(x)$ itself, and thus

$$\kappa(x) = \rho_{2,2}(x) = \frac{E\left\{|x-\mu(x)|^4\right\}}{\left[E\left\{|x-\mu(x)|^2\right\}\right]^2} = 2 + |\varrho(x)|^2. \tag{F.23}$$

The complex kurtosis, $\kappa(x)$, is equal to 2 if x is a circular complex Normal random variable. If the circularity condition is not fulfilled, the constant 2 must be corrected by adding the factor $|\varrho(x)|^2$, which is taken as a known (or previously calibrated) parameter rather than a variable to be estimated. Recall that, given the definition of circularity quotient, $\varrho(x)$, the correction factor is equal to

$$|\varrho(x)|^2 = \left|\frac{\varsigma(x)}{\sigma^2(x)}\right|^2 = \left|\frac{E\left\{(x-\mu(x))^2\right\}}{E\left\{|x-\mu(x)|^2\right\}}\right|^2 = \frac{\left[\sigma_i^2-\sigma_q^2\right]^2 + 4\,\sigma_{iq}^2}{\left[\sigma_i^2+\sigma_q^2\right]^2}, \tag{F.24}$$

where $x = x_i + jx_q$, σ_i^2 is the variance of x_i, σ_q^2 is the variance of x_q, and σ_{iq} is the covariance between x_i and x_q.

The same result is obtained if the fourth-order central moment of x is developed into the moments of the real x_i and imaginary x_q components as

$$\begin{aligned}\kappa(x) &= \frac{E\left\{|x-\mu(x)|^4\right\}}{\left[E\left\{|x-\mu(x)|^2\right\}\right]^2} = \frac{1}{\sigma^4(x)} E\left\{\left[(x_i-\mu_i)^2+(x_q-\mu_q)^2\right]^2\right\} \\ &= \frac{1}{\sigma^4(x)}\left[E\left\{(x_i-\mu_i)^4\right\}+E\left\{(x_q-\mu_q)^4\right\}+2E\left\{(x_i-\mu_i)^2(x_q-\mu_q)^2\right\}\right],\end{aligned} \tag{F.25}$$

and hence, by using the Isserlis' theorem [188, 189], the complex kurtosis yields

$$\begin{aligned}\kappa(x) &= \frac{3\sigma_i^4+3\sigma_q^4+2\sigma_i^2\sigma_q^2+4\sigma_{iq}^2}{\left[\sigma_i^2+\sigma_q^2\right]^2} = \frac{2\left[\sigma_i^2+\sigma_q^2\right]^2+\left[\sigma_i^2-\sigma_q^2\right]^2+4\sigma_{iq}^2}{\left[\sigma_i^2+\sigma_q^2\right]^2} \\ &= 2+\frac{\left[\sigma_i^2-\sigma_q^2\right]^2+4\sigma_{iq}^2}{\left[\sigma_i^2+\sigma_q^2\right]^2} = 2+|\varrho|^2.\end{aligned} \tag{F.26}$$

F.6 Sample kurtosis of a Normal random variable

In practical situations, the true statistics of a random process is not known a priori, and thus it must be estimated somehow. When dealing with measured signals, only a fraction of time or a set of samples is available to derive its statistics. In this cases, it is said that the moments of the random process are obtained as sample moments since their estimation is obtained from a sample version of the whole [190]. Therefore, the *sample moments* of a random variable x can be defined corresponding to its (statistical) moments.

This section only deals with some of them, in particular, those that are more relevant in previous sections. These are: mean, variance, and kurtosis; and they are only obtained for the particular case of samples belonging to a Normal random variable x. Moreover, being a function of random variables, sample moments are themselves a random variable, so their PDFs (if known) and moments are stated in this section, most of them reported from [114].

The *sample mean*, $\mathbf{m}$, of N samples of a Normal random variable x is defined as

$$\mathbf{m}(x) = \frac{1}{N}\sum_{n=1}^{N} x_n, \tag{F.27}$$

where x_n are each sample of x. The mean of $\mathbf{m}(x)$ is equal to

$$E\left\{\mathbf{m}(x)\right\} = E\left\{\frac{1}{N}\sum_{n=1}^{N} x_n\right\} = \frac{1}{N}\sum_{n=1}^{N} E\left\{x_n\right\} = \mu(x), \tag{F.28}$$

and hence, the sample mean is an unbiased estimator of the mean. Besides, it follows a Normal distribution, $\mathbf{m}(x) \sim \mathcal{N}\big(\mu(x), \sigma^2(x)/N\big)$ [114].

The *sample variance*, $\mathbf{s}$, of N samples of a Normal random variable x is defined as

$$\mathbf{s}(x) = \frac{1}{N}\sum_{n=1}^{N}\left[x_n - \mathbf{m}(x)\right]^2, \tag{F.29}$$

where $\mathbf{m}(x)$ is the sample mean of x. The mean of $\mathbf{s}(x)$ is equal to

$$\begin{aligned}
E\left\{\mathbf{s}(x)\right\} &= E\left\{\frac{1}{N}\sum_{n=1}^{N}\left[x_n - \mathbf{m}(x)\right]^2\right\} = E\left\{\frac{1}{N}\sum_{n=1}^{N}\left[x_n - \frac{1}{N}\sum_{n=1}^{N} x_n\right]^2\right\} \\
&= \frac{1}{N}\sum_{n=1}^{N}\left[E\left\{x_n^2 - \frac{2}{N}x_n\sum_{l=1}^{N} x_l + \frac{1}{N^2}\sum_{l=1}^{N} x_l \sum_{r=1}^{N} x_r\right\}\right] = \frac{1}{N}\sum_{n=1}^{N}\left[\frac{N-2}{N}E\left\{x_n^2\right\}\right. \\
&\qquad \left. - \frac{2}{N}\sum_{l\neq n}^{N} E\left\{x_n\, x_l\right\} + \frac{1}{N^2}\sum_{l=1}^{N} E\left\{x_l^2\right\} + \frac{1}{N^2}\sum_{l=1}^{N}\sum_{r\neq l}^{N} E\left\{x_l\, x_r\right\}\right] \\
&= \frac{1}{N}\sum_{n=1}^{N}\left[\frac{N-2}{N}\mu_2(x) - 2\frac{N-1}{N}\mu^2(x) + \frac{1}{N}\mu_2(x) + \frac{N-1}{N}\mu^2(x)\right] \\
&= \frac{N-1}{N}\left(\sigma^2(x) + \mu^2(x)\right) - \frac{N-1}{N}\mu^2(x) = \frac{N-1}{N}\sigma^2(x).
\end{aligned} \tag{F.30}$$

Hence, $\mathbf{s}(x)$ is a biased estimator of the variance by a factor of $(N-1)/N$, which follows a chi-squared distribution,

$$\mathbf{s}(x) \sim \frac{\sigma^2(x)}{N}\chi^2_{N-1}, \tag{F.31}$$

with variance equal to $2(N-1)\sigma^4(x)/N^2$ [114].

Given the sample mean and the sample variance, the *sample kurtosis* can be defined in the same way as the fourth central sample moment normalized by the square of the sample variance, or

$$\mathbf{k}(x) = \frac{\mathbf{l}_4(x)}{\left[\mathbf{s}(x)\right]^2} = \frac{\frac{1}{N}\sum_{n=1}^{N}\left[x_n - \mathbf{m}(x)\right]^4}{\left[\mathbf{s}(x)\right]^2} = \frac{\frac{1}{N}\sum_{n=1}^{N}\left[x_n - \frac{1}{N}\sum_{n=1}^{N} x_n\right]^4}{\left[\frac{1}{N}\sum_{n=1}^{N}\left[x_n - \frac{1}{N}\sum_{n=1}^{N} x_n\right]^2\right]^2}. \tag{F.32}$$

In order to calculate the mean of the sample kurtosis, first, the mean of the fourth-order central sample moment is obtained as

$$\begin{aligned} E\left\{\mathbf{l}_4(x)\right\} &= E\left\{\frac{1}{N}\sum_{n=1}^{N}\left[x_n-\mathbf{m}(x)\right]^4\right\} \\ &= E\left\{x_n^4-4x_n^3\mathbf{m}(x)+6x_n^2\mathbf{m}^2(x)-4x_n\mathbf{m}^3(x)+\mathbf{m}^4(x)\right\}, \end{aligned} \tag{F.33}$$

where each one of the expected value terms is equal to,

$$E\left\{x_n^4\right\} = \mu_4(x) = \mu^4(x)+6\mu^2(x)\sigma^2(x)+3\sigma^4(x), \tag{F.34}$$

$$\begin{aligned} E\left\{x_n^3\mathbf{m}(x)\right\} &= E\left\{x_n^3\frac{1}{N}\sum_{l=1}^{N}x_l\right\} = \frac{1}{N}\left[E\left\{x_n^4\right\}+\sum_{l\neq n}^{N}E\left\{x_n^3x_l\right\}\right] \\ &= \frac{1}{N}\left[\mu_4(x)+(N-1)\mu_3(x)\mu(x)\right] \\ &= \frac{1}{N}\left[\mu^4(x)+6\mu^2(x)\sigma^2(x)+3\sigma^4(x)+(N-1)\left(\mu^4(x)+3\mu^2(x)\sigma^2(x)\right)\right] \\ &= \mu^4(x)+\frac{3(N+1)}{N}\mu^2(x)\sigma^2(x)+\frac{3}{N}\sigma^4(x), \end{aligned} \tag{F.35}$$

$$\begin{aligned} E\left\{x_n^2\mathbf{m}^2(x)\right\} &= E\left\{x_n^2\frac{1}{N^2}\sum_{l=1}^{N}x_l\sum_{p=1}^{N}x_p\right\} \\ &= \frac{1}{N^2}\left[E\left\{x_n^4\right\}+2\sum_{l\neq n}^{N}E\left\{x_n^3x_l\right\}+\sum_{l\neq n}^{N}E\left\{x_n^2x_l^2\right\}+\sum_{l\neq n}^{N}\sum_{p\neq n,l}^{N}E\left\{x_n^2x_lx_p\right\}\right] \\ &= \frac{1}{N^2}\left[\mu_4(x)+2(N-1)\mu_3(x)\mu(x)+(N-1)\mu_2^2(x)\right. \\ &\qquad \left.+(N-1)(N-2)\mu_2(x)\mu^2(x)\right] \\ &= \frac{1}{N^2}\left[\mu^4(x)+6\mu^2(x)\sigma^2(x)+3\sigma^4(x)+2(N-1)\left(\mu^4(x)+3\mu^2(x)\sigma^2(x)\right)\right. \\ &\qquad +(N-1)\left(\mu^4(x)+2\mu^2(x)\sigma^2(x)+\sigma^4(x)\right) \\ &\qquad \left.+(N-1)(N-2)\left(\mu^4(x)+\mu^2(x)\sigma^2(x)\right)\right] \\ &= \mu^4(x)+\frac{N+5}{N}\mu^2(x)\sigma^2(x)+\frac{N+2}{N^2}\sigma^4(x), \end{aligned} \tag{F.36}$$

$$
\begin{aligned}
E\left\{x_n \mathbf{m}^3(x)\right\} &= E\left\{x_n \frac{1}{N^3}\sum_{l=1}^{N} x_l \sum_{p=1}^{N} x_p \sum_{r=1}^{N} x_r\right\} \\
&= \frac{1}{N^3}\left[E\left\{x_n^4\right\} + 4\sum_{l\neq n}^{N} E\left\{x_n^3 x_l\right\} + 3\sum_{l\neq n}^{N} E\left\{x_n^2 x_l^2\right\}\right. \\
&\qquad \left. + 6\sum_{l\neq n}^{N}\sum_{p\neq n,l}^{N} E\left\{x_n^2 x_l x_p\right\} + \sum_{l\neq n}^{N}\sum_{p\neq n,l}^{N}\sum_{r\neq n,l,p}^{N} E\left\{x_n x_l x_p x_r\right\}\right] \\
&= \frac{1}{N^3}\left[\mu_4(x) + 4(N-1)\mu_3(x)\mu(x) + 3(N-1)\mu_2^2(x)\right. \\
&\qquad \left. + 6(N-1)(N-2)\mu_2(x)\mu^2(x) + (N-1)(N-2)(N-3)\mu^4(x)\right] \\
&= \frac{1}{N^3}\left[\mu^4(x) + 6\mu^2(x)\sigma^2(x) + 3\sigma^4(x) + 4(N-1)\left(\mu^4(x) + 3\mu^2(x)\sigma^2(x)\right)\right. \\
&\qquad + 3(N-1)\left(\mu^4(x) + 2\mu^2(x)\sigma^2(x) + \sigma^4(x)\right) \\
&\qquad \left. + 6(N-1)(N-2)\left(\mu^4(x) + \mu^2(x)\sigma^2(x)\right) + (N-1)(N-2)(N-3)\mu^4(x)\right] \\
&= \mu^4(x) + \frac{6}{N}\mu^2(x)\sigma^2(x) + \frac{3}{N^2}\sigma^4(x),
\end{aligned}
\tag{F.37}
$$

$$
\begin{aligned}
E\left\{\mathbf{m}^4(x)\right\} &= E\left\{\frac{1}{N^4}\sum_{l=1}^{N} x_l \sum_{p=1}^{N} x_p \sum_{r=1}^{N} x_r \sum_{t=1}^{N} x_t\right\} \\
&= \frac{1}{N^3} E\left\{x_l \sum_{p=1}^{N} x_p \sum_{r=1}^{N} x_r \sum_{t=1}^{N} x_t\right\} = \mu^4(x) + \frac{6}{N}\mu^2(x)\sigma^2(x) + \frac{3}{N^2}\sigma^4(x),
\end{aligned}
\tag{F.38}
$$

and, hence, the expected value of the fourth-order central sample moment is equal to

$$
E\left\{\mathbf{l}_4(x)\right\} = 3\frac{(N-1)^2}{N^2}\sigma^4(x). \tag{F.39}
$$

Furthermore, from [191], the unbiased excess sample kurtosis for a Normal random variable is equal to

$$
\frac{N^2\left((N-1)E\left\{\mathbf{l}_4(x)\right\} - 3(N-1)\left[E\left\{\mathbf{s}(x)\right\}\right]^2\right)}{(N-1)(N-2)(N-3)} = 0, \tag{F.40}
$$

and hence, the expected value of the kurtosis can be expressed as

$$
E\left\{\mathbf{k}(x)\right\} = \frac{E\left\{\mathbf{l}_4(x)\right\}}{\left[E\left\{\mathbf{s}(x)\right\}\right]^2}\frac{N-1}{N+1} = \frac{3(N-1)^2\sigma^4(x)/N^2}{(N-1)^2\sigma^4(x)/N^2}\frac{N-1}{N+1} = 3\frac{N-1}{N+1}, \tag{F.41}
$$

Therefore, the sample kurtosis is a biased estimator of the kurtosis by a factor of $(N+1)/(N-1)$. The probability distribution of the sample kurtosis has not a closed form, or at least, it is not any of the current known distributions. For values of N between 30 to 300, the probability distribution of the sample kurtosis is close to a Gumbel distribution, and for N between 3000 and 30000, it resembles a Birnbaum–Saunders distribution, but none of those describes its behavior for all values of N simultaneously. However, for N greater than 50000 [187], the distribution of the sample kurtosis fits a Normal distribution, $\mathbf{k}(x) \sim \mathcal{N}(3, 24/N)$, thanks to the CLT [114, 192, 193].

F.7 Sample kurtosis of a complex Normal random variable

The sample moments of a complex Normal random variable can be defined equivalently to the real case. The sample mean of a complex Normal random variable $x = x_i + jx_q$ coincides with the real case, but with $\mathbf{m}(x) \in \mathbb{C}$ and $\mathbf{m}(x) \sim \mathcal{CN}\left(\mu(x), \sigma^2/N\right)$. Moreover, the sample variance of x is defined as

$$\mathbf{s}(x) = \frac{1}{N}\sum_{n=1}^{N} |x_n - \mathbf{m}(x)|^2, \tag{F.42}$$

where $\mathbf{m}(x)$ is the sample mean of x. The sample variance is a biased estimator of the variance by a factor of $(N-1)/N$ as in the real case, and in the case of a complex Normal distribution it follows the chi-squared distribution

$$\mathbf{s}(x) \sim \frac{\sigma^2(x)}{N}\chi^2_{(2N-2)}, \tag{F.43}$$

with variance equal to $8(N-1)\sigma^4(x)/N^2$.

As for the real case, the sample complex kurtosis is defined as the ratio between the fourth-order central sample moment and the square of the variance as

$$\boldsymbol{\kappa}(x) = \frac{\frac{1}{N}\sum_{n=1}^{N}\left|x_n - \frac{1}{N}\sum_{n=1}^{N} x_n\right|^4}{\left[\frac{1}{N}\sum_{n=1}^{N}\left|x_n - \frac{1}{N}\sum_{n=1}^{N} x_n\right|^2\right]^2}. \tag{F.44}$$

In this case, its mean and variance have been assessed numerically rather than analytically. From the results presented in Chapter 8, it yields that the mean complex sample kurtosis $\boldsymbol{\kappa}(x)$ is

$$E\{\boldsymbol{\kappa}(x)\} = 2\frac{N-1}{N}, \tag{F.45}$$

and thus, the sample estimator is biased by a factor of $(N-1)/N$. Moreover, as for the real case, if the number of samples N is large enough (greater than 50000), the distribution

of the complex sample kurtosis fits a Normal distribution thanks to the CLT. However, the variance of complex sample kurtosis for a circular complex Normal random variable is $4/N$, six times smaller than for the real case, and hence $\boldsymbol{\kappa}(x) \sim \mathcal{N}(2, 4/N)$. This is one of the reasons that contribute to its enhanced detection performance. Eventually, the study of the statistics of the complex sample kurtosis without the assumption of circularity is out of the scope of this appendix.

Appendix G

Karhunen-Loève Transform

This appendix shows the calculation of the basis of the KLT, and its application to obtain the direct and inverse transforms.

The KLT is able to find the best basis that minimizes the total mean squared error in the Hilbert space spanned by the eigenfunctions of the covariance matrix of the input signal $\mathbf{x}$.

Considering that $\mathbf{x}$ is a sample function of a stochastic process $\{x(t)\}$ with zero mean, then

$$\mathbf{x} = [x_0, x_1, \ldots, x_{L-1}]^T \tag{G.1}$$

is a set of random variables with length equal to L whose expected values are

$$\boldsymbol{\mu_x} = E\{\mathbf{x}\} = \mathbf{0}, \tag{G.2}$$

their covariance matrix is

$$C_{\mathbf{x}} = E\left\{(\mathbf{x} - \boldsymbol{\mu_x})\,(\mathbf{x} - \boldsymbol{\mu_x})^H\right\} = E\left\{\mathbf{x}\mathbf{x}^H\right\}, \tag{G.3}$$

or equally

$$C_{\mathbf{x}}(k,l) = E\left\{x_k\, x_l^*\right\} \quad k,l \in [0, L-1] \tag{G.4}$$

for each entry of $C_{\mathbf{x}}$.

The Karhunen-Loève theorem states that a set of samples $\mathbf{x}$ of a stochastic process $\{x(t)\}$ can be expanded according to the formula

$$\mathbf{x} = \Phi\,\mathbf{z} \tag{G.5}$$

where the columns of the matrix

$$\Phi = [\boldsymbol{\phi}_0, \boldsymbol{\phi}_1, \ldots, \boldsymbol{\phi}_{L-1}] \tag{G.6}$$

are deterministic orthonormal functions $\boldsymbol{\phi}_k$ that represent the behavior of $\mathbf{x}$ in the time domain and must fulfill the condition

$$\boldsymbol{\phi}_k^H\,\boldsymbol{\phi}_l = \delta(k-l), \tag{G.7}$$

whereas $\mathbf{z}$ is a vector of statistically independent random variables with zero mean that contain the probabilistic behavior of the process $\{x(t)\}$ and whose covariance matrix is

$$C_{\mathbf{z}} = E\left\{\mathbf{z}\mathbf{z}^H\right\} = \mathrm{diag}\{\boldsymbol{\lambda}\} = \Lambda \tag{G.8}$$

with

$$\lambda_k = E\left\{z_k\, z_k^*\right\} > 0. \tag{G.9}$$

Combining the Karhunen-Loève expansion with the definition of covariance matrix of $\mathbf{x}$ in the following way

$$C_{\mathbf{x}} = E\left\{\mathbf{x}\mathbf{x}^H\right\} = E\left\{\Phi\,\mathbf{z}\mathbf{z}^H\Phi^H\right\} = \Phi\,E\left\{\mathbf{z}\mathbf{z}^H\right\}\Phi^H = \Phi\,\Lambda\Phi^H, \tag{G.10}$$

we yield to the equation system

$$C_{\mathbf{x}}\,\boldsymbol{\phi}_k = \lambda_k\,\boldsymbol{\phi}_k \tag{G.11}$$

which reveals that λ_k and $\boldsymbol{\phi}_k$ are the eigenvalues and eigenfunctions of $C_{\mathbf{x}}$.

That said, the direct KLT is the linear transformation

$$\mathbf{X} = \mathcal{K}\{\mathbf{x}\} = \Phi^H \mathbf{x} \tag{G.12}$$

which adapts itself to the shape of the input signal $\mathbf{x}$ by adopting as a new reference frame in the Hilbert space the basis spanned by the eigenfunctions, $\boldsymbol{\phi}_k$, of the covariance matrix of the input signal, $C_{\mathbf{x}}$. Besides, the inverse KLT is the linear transformation

$$\mathbf{x} = \mathcal{K}^{-1}\{\mathbf{X}\} = \Phi\, \mathbf{X} \tag{G.13}$$

that fulfills

$$\mathcal{K}^{-1}\{\mathcal{K}\{\mathbf{x}\}\} = \Phi\Phi^H \mathbf{x} = \mathbf{x}. \tag{G.14}$$

Part VI

Bibliography and list of publications

Bibliography

[1] Electronic Communications Committee (ECC) within the European Conference of Postal and Telecommunications Administrations (CEPT), "The European Table of Frequency Allocations and Applications in the Frequency Range 8.3 kHz to 3000 GHz (ECA Table)." [Online]. Available: https://www.ecodocdb.dk/download/2ca5fcbd-4090/ERCREP025.pdf (Cited on pages 4 and 25.)

[2] J. G. Proakis, *Digital Communications*, 4th ed., ser. McGraw-Hill series in electrical and computer engineering, S. W. Director, Ed. McGraw-Hill Higher Education, 2001, vol. 11, no. 2. (Cited on pages 5, 81, 85, 86, 200, and 262.)

[3] M. Powe and J. I. R. Owen, "GNSS Frequency Protection Requirements," EUROCONTROL Experimental Center, EEC Report No. 337 (Project NAV-4-E1), Tech. Rep., 1999. [Online]. Available: http://www.eurocontrol.int/sites/default/files/content/documents/communications/061999-gnss-frequency-protection-requirements-eec-report-337.pdf (Cited on pages 5, 12, 16, 18, and 19.)

[4] J. Font, A. Camps, A. Borges, M. Martín-Neira, J. Boutin, N. Reul, Y. H. Kerr, A. Hahne, and S. Mecklenburg, "SMOS: The Challenging Sea Surface Salinity Measurement From Space," *Proceedings of the IEEE*, vol. 98, no. 5, pp. 649–665, may 2010. (Cited on page 6.)

[5] Y. H. Kerr, P. Waldteufel, J.-P. Wigneron, S. Delwart, F. Cabot, J. Boutin, M.-J. Escorihuela, J. Font, N. Reul, C. Gruhier, S. E. Juglea, M. R. Drinkwater, A. Hahne, M. Martín-Neira, and S. Mecklenburg, "The SMOS Mission: New Tool for Monitoring Key Elements ofthe Global Water Cycle," *Proceedings of the IEEE*, vol. 98, no. 5, pp. 666–687, may 2010. (Cited on pages 6 and 14.)

[6] H. Carreno-Luengo, A. Camps, P. Via, J. F. Munoz, A. Cortiella, D. Vidal, J. Jane, N. Catarino, M. Hagenfeldt, P. Palomo, and S. Cornara, "3Cat-2—An Experimental Nanosatellite for GNSS-R Earth Observation: Mission Concept and Analysis," *IEEE Journal of Selected Topics in Applied Earth Observations and Remote Sensing*, vol. 9, no. 10, pp. 4540–4551, oct 2016. (Cited on page 6.)

[7] R. Onrubia, D. Pascual, J. Querol, H. Park, and A. Camps, "Beamformer characterization of the MIR instrument: The microwave interferometric reflectometer," in *2017 IEEE International Geoscience and Remote Sensing Symposium (IGARSS)*, vol. 2017-July. IEEE, jul 2017, pp. 5026–5029. (Cited on page 6.)

[8] J. M. Tarongí, "Radio Frequency Interference in Microwave Radiometry: Statistical Analysis and Study of Techniques for Detection and Mitigation," Ph.D. dissertation, UPC-BarcelonaTech, mar 2012. [Online]. Available: http://www.tdx.cat/handle/10803/117023 (Cited on pages 6, 12, 14, 30, 31, 35, 44, 47, 70, and 106.)

[9] G. F. Forte Véliz, "Contributions to radio frequency interference detection and mitigation in Earth observation," Ph.D. dissertation, Universitat Politècnica de Catalunya, jun 2013. [Online]. Available: http://www.tdx.cat/handle/10803/285320 (Cited on pages 6, 7, 8, 12, 24, 31, 35, 44, 47, 50, 71, 78, 92, and 152.)

[10] J. Querol Borràs, "Implementation of Radio-Frequency Interference Detection and Mitigation Algorithms for Communications and Navigation," M.Sc. Thesis, UPC-BarcelonaTech, nov 2013. [Online]. Available: http://upcommons.upc.edu/pfc/handle/2099.1/19575 (Cited on pages 7, 12, 30, 32, 37, 170, 177, and 178.)

[11] G. Forte, J. Querol, H. Park, and A. Camps, "Digital back-end for RFI detection and mitigation in earth observation," in *2013 IEEE International Geoscience and Remote Sensing Symposium - IGARSS*. Melbourne, VIC, Australia: IEEE, jul 2013, pp. 1908–1911. (Cited on pages 7, 14, 35, 80, 81, and 152.)

[12] J. Querol, G. F. Forte, and A. Camps, "Study of RFI signals in protected GNSS bands generated by common electronic devices: Effects on GNSS-R measurements," in *2014 IEEE Geoscience and Remote Sensing Symposium*, Quebec, Canada, 2014, pp. 4050–4053. (Cited on pages 12, 24, 25, 128, and 130.)

[13] A. Alonso-Arroyo, G. F. Forte, A. Camps, H. Park, D. Pascual, R. Onrubia, and R. Jove-Casulleras, "Soil Moisture mapping using forward scattered GPS L1 signals," in *2013 IEEE International Geoscience and Remote Sensing Symposium (IGARSS)*, Melbourne, VIC, Australia, jul 2013, pp. 354–357. (Cited on page 12.)

[14] D. Borio, C. O'driscoll, and J. Fortuny, "Tracking and Mitigating a Jamming Signal with an Adaptive Notch Filter," *InsideGNSS*, pp. 67–73, apr 2014. (Cited on pages 12, 24, 31, 79, 81, and 152.)

[15] G. F. Forte, J. M. Tarongi, V. DePau, M. Vall-llossera, and A. Camps, "Experimental Study on the Performance of RFI Detection Algorithms in Microwave Radiometry: Towards an Optimum Combined Test," *IEEE Transactions on Geoscience and Remote Sensing*, vol. 51, no. 10, pp. 4936–4944, oct 2013. (Cited on pages 14 and 35.)

[16] S. Jin, G. P. Feng, and S. Gleason, "Remote sensing using GNSS signals: Current status and future directions," *Advances in Space Research*, vol. 47, no. 10, pp. 1645–1653, may 2011. (Cited on page 14.)

[17] W. Emery and A. Camps, *Introduction to Satellite Remote Sensing*. Elsevier, 2017. (Cited on page 14.)

[18] F. T. Ulaby, R. K. Moore, and A. K. Fung, *Microwave remote sensing: Active and passive. Volume 1 - Microwave remote sensing fundamentals and radiometry*. London: Artech House Publishers, 1981, vol. 1. (Cited on pages 14, 45, 47, 61, 62, 63, 64, 76, and 89.)

[19] R. Oliva, E. Daganzo, Y. H. Kerr, S. Mecklenburg, S. Nieto, P. Richaume, and C. Gruhier, "SMOS Radio Frequency Interference Scenario: Status and Actions Taken to Improve the RFI Environment in the 1400–1427-MHz Passive Band," *IEEE Transactions on Geoscience and Remote Sensing*, vol. 50, no. 5, pp. 1427–1439, may 2012. (Cited on pages 14, 77, and 94.)

[20] E. Njoku, P. Ashcroft, T. Chan, and Li Li, "Global survey and statistics of radio-frequency interference in AMSR-E land observations," *IEEE Transactions on Geoscience and Remote Sensing*, vol. 43, no. 5, pp. 938–947, may 2005. (Cited on pages 14, 76, and 77.)

[21] P. Richaume, Y. Soldo, E. Anterrieu, A. Khazaal, S. Bircher, A. Mialon, A. Al Bitar, N. Rodriguez-Fernandez, F. Cabot, Y. Kerr, and A. Mahmoodi, "RFI in SMOS measurements: Update on detection, localization, mitigation techniques and preliminary quantified impacts on soil moisture products," in *2014 IEEE Geoscience and Remote Sensing Symposium*. IEEE, jul 2014, pp. 223–226. (Cited on page 14.)

[22] H. Park, V. Gonzalez-Gambau, A. Camps, and M. Vall-llossera, "Improved MUSIC-Based SMOS RFI Source Detection and Geolocation Algorithm," *IEEE Transactions on Geoscience and Remote Sensing*, vol. 54, no. 3, pp. 1311–1322, mar 2016. (Cited on page 16.)

[23] B. Guner, J. T. Johnson, and N. Niamsuwan, "Time and frequency blanking for radio-frequency interference mitigation in microwave radiometry," *IEEE Transactions on Geoscience and Remote Sensing*, vol. 45, no. 11, pp. 3672–3679, 2007. (Cited on pages 16, 80, 81, and 152.)

[24] J. Querol, R. Onrubia, A. Alonso-Arroyo, D. Pascual, H. Park, and A. Camps, "Performance Assessment of Time–Frequency RFI Mitigation Techniques in Microwave Radiometry," *IEEE Journal of Selected Topics in Applied Earth Observations and Remote Sensing*, vol. 10, no. 7, pp. 1–11, 2017. (Cited on pages 16, 52, 76, and 106.)

[25] R. D. De Roo, S. Misra, and C. S. Ruf, "Sensitivity of the Kurtosis Statistic as a Detector of Pulsed Sinusoidal RFI," *IEEE Transactions on Geoscience and Remote Sensing*, vol. 45, no. 7, pp. 1938–1946, jul 2007. (Cited on pages 16, 37, 106, and 173.)

[26] J. M. Tarongi and A. Camps, "Normality Analysis for RFI Detection in Microwave Radiometry," *Remote Sensing*, vol. 2, no. 1, pp. 191–210, dec 2009. (Cited on pages 16, 37, 69, 77, and 173.)

[27] A. Gasiewski, M. Klein, A. Yevgrafov, and V. Leuskiy, "Interference mitigation in passive microwave radiometry," in *IEEE International Geoscience and Remote Sensing Symposium*, vol. 3. Toronto, ON, Canada: IEEE, 2002, pp. 1682–1684. (Cited on page 16.)

[28] N. Skou, S. S. Kristensen, T. Ruokokoski, and J. Lahtinen, "On-board digital RFI and polarimetry processor for future spaceborne radiometer systems," in *2012 IEEE International Geoscience and Remote Sensing Symposium*. Munich, Germany: IEEE, jul 2012, pp. 3423–3426. (Cited on page 16.)

[29] R. Onrubia, J. Querol, D. Pascual, A. Alonso-Arroyo, H. Park, and A. Camps, "DME/TACAN Impact Analysis on GNSS Reflectometry," *IEEE Journal of Selected Topics in Applied Earth Observations and Remote Sensing*, pp. 1–10, 2016. (Cited on pages 18 and 144.)

[30] "Power Utilities. Mitigating GPS Vulnerabilities and Protecting Power Utility Network Timing," Symmetricom Inc., San Jose, California, Tech. Rep., 2013. [Online]. Available: https://www.aventasinc.com/whitepapers/WP{_}Power{_}Utilities.pdf.[Lastaccessed]2016-07-26. (Cited on pages 19, 20, and 128.)

[31] C. Hall and R. Cordey, "Multistatic Scatterometry," in *International Geoscience and Remote Sensing Symposium, 'Remote Sensing: Moving Toward the 21st Century'.*, 1988, pp. 561–562. (Cited on pages 21 and 128.)

[32] M. Martin-Neira, "A Passive Reflectometry and Interferometry System (PARIS) - Application to ocean altimetry," *ESA journal*, vol. 17, no. 4, pp. 331–355, 1993. (Cited on pages 21 and 128.)

[33] J. L. Garrison, S. J. Katzberg, and M. I. Hill, "Effect of sea roughness on bistatically scattered range coded signals from the Global Positioning System," p. 2257, 1998. (Cited on page 21.)

[34] S. T. Lowe, J. L. LaBrecque, C. Zuffada, L. J. Romans, L. E. Young, and G. A. Hajj, "First spaceborne observation of an Earth-reflected GPS signal," *Radio Science*, vol. 37, no. 1, pp. 7–1–7–28, jan 2002. (Cited on page 21.)

[35] V. Zavorotny, S. Gleason, E. Cardellach, and A. Camps, "Tutorial on Remote Sensing Using GNSS Bistatic Radar of Opportunity," *IEEE Geoscience and Remote Sensing Magazine*, vol. 2, no. 4, pp. 8–45, dec 2014. (Cited on pages 21, 46, 128, and 214.)

[36] F. Martin, A. Camps, H. Park, S. D'addio, M. Martin-Neira, and D. Pascual, "Cross-Correlation Waveform Analysis for Conventional and Interferometric GNSS-R Approaches," *IEEE Journal of Selected Topics in Applied Earth Observations and Remote Sensing*, vol. 7, no. 5, pp. 1560–1572, may 2014. (Cited on page 22.)

[37] D. Guan, H. Park, A. Camps, Y. Wang, R. Onrubia, J. Querol, and D. Pascual, "Wind direction signatures in GNSS-R observables from space," *Remote Sensing*, vol. 10, no. 2, 2018. (Cited on page 22.)

[38] H. Park, A. Camps, D. Pascual, R. Onrubia, A. Alonso-Arroyo, and F. Martin, "Evolution of PAU/PARIS End-to-end Performance Simulator (P2EPS) towards GNSS reflectometry, radio occulation and Scatterometry simulator (GEROS-SIM)," in *2015 IEEE International Geoscience and Remote Sensing Symposium (IGARSS)*. IEEE, jul 2015, pp. 4757–4760. (Cited on page 22.)

[39] D. Borio, J. Fortuny-Guasch, and C. O'Driscoll, "Spectral and Spatial Characterization of GNSS Jammers," in *7th GNSS Vulnerabilities Solutions Conference*, Baska, Croatia, apr 2013, pp. 1–17. (Cited on page 23.)

[40] J. W. Betz, "Effect of Narrowband Interference on GPS Code Tracking Accuracy," *Proceedings of the ION National Technical Meeting*, pp. 716–723, 2000. (Cited on page 24.)

[41] D. Borio, "A Statistical Theory for GNSS Signal Acquisition," Ph.D. dissertation, Torino, Politecnico di, 2008. (Cited on page 24.)

[42] D. Borio, C. O'Driscoll, and J. Fortuny, "GNSS Jammers: Effects and countermeasures," in *2012 6th ESA Workshop on Satellite Navigation Technologies (Navitec 2012) & European Workshop on GNSS Signals and Signal Processing*. IEEE, dec 2012, pp. 1–7. (Cited on page 24.)

[43] D. A. Divis, "The Fallout from GPS vs. LightSquared," *InsideGNSS*, 2012. (Cited on page 25.)

[44] B. Parkinson, "A grave threat to GPS and GNSS," *GPS World*, 2018. (Cited on page 25.)

[45] J. Chen, W. Shi, A. J. Norman, and P. Ilavarasan, "Electrical impact of high-speed bus crossing plane split," *2002 IEEE International Symposium on Electromagnetic Compatibility*, vol. 2, 2002. (Cited on page 26.)

[46] S. M. Kay, *Fundamentals of Statistical Signal Processing: Detection theory*. Englewood Cliffs, New Jersey: Prentice-Hall PTR, 1993. (Cited on pages 30, 81, 84, 85, 86, 152, and 154.)

[47] H. L. Van Trees, *Detection, Estimation, and Modulation Theory*. John Wiley and Sons, Inc., 2001, vol. 1. (Cited on page 30.)

[48] M. Trinkle and D. Gray, "GPS interference mitigation; overview and experimental results," in *2001 5th International Symposium on Satellite Navigation Technology and Applications (SatNav)*. Canberra, Australia: Menay / GPS Society, 2001, pp. 1–14. (Cited on pages 30, 32, 37, and 38.)

[49] A. Kandangath, "Jamming Mitigation Techniques for Spread Spectrum Communication Systems," *Signal Processing for Wireless Communications*, pp. 1–13, dec 2003. (Cited on pages 30, 32, 34, and 38.)

[50] W. A. Baan, "RFI mitigation in radio astronomy," in *2011 30th URSI General Assembly and Scientific Symposium (URSIGASS)*, Istanbul, Turkey, aug 2011. (Cited on page 31.)

[51] F. Castanié, *Spectral Analysis: Parametric and Non-Parametric Digital Methods*. John Wiley and Sons, Inc., 2003. (Cited on pages 31 and 32.)

[52] A. V. Oppenheim, R. W. Schafer, and J. R. Buck, *Discrete Time Signal Processing*, 3rd ed. Pearson Education, Limited, 1999. (Cited on pages 31, 33, and 177.)

[53] D. G. Manolakis, V. K. Ingle, and S. M. Kogon, *Statistical and adaptive signal processing: spectral estimation, signal modeling, adaptive filtering, and array processing*. Artech House: signal processing library, 2000. (Cited on pages 31, 37, 153, 173, 320, and 321.)

[54] D. Borio, C. O'Driscoll, and J. Fortuny, "GNSS jammers: Effects and countermeasures," in *6th ESA Workshop on Satellite Navigation Technologies: Multi-GNSS Navigation Technologies Galileo's Here, NAVITEC 2012 and European Workshop on GNSS Signals and Signal Processing*, Noordwijk, Nederlands, dec 2012, pp. 1–7. (Cited on page 31.)

[55] D. Borio, L. Camoriano, and L. Lo Presti, "Two-Pole and Multi-Pole Notch Filters: A Computationally Effective Solution for GNSS Interference Detection and Mitigation," *IEEE Systems Journal*, vol. 2, no. 1, pp. 38–47, mar 2008. (Cited on pages 32 and 79.)

[56] S. Mallat, *A Wavelet Tour of Signal Processing: The Sparse Way*, 3rd ed., Academic Press, Ed. Elsevier Science, 1999. (Cited on pages 32, 35, 82, and 84.)

[57] R. Rifkin and J. J. Vaccaro, "Comparison of narrowband adaptive filter technologies for GPS," in *2000 IEEE Position Location and Navigation Symposium*, San Diego, SA, United States, mar 2000, pp. 125–131. (Cited on page 32.)

[58] P. Capozza, B. Holland, T. Hopkinson, and R. Landrau, "A single-chip narrow-band frequency-domain excisor for a Global Positioning System (GPS) receiver," *IEEE Journal of Solid-State Circuits*, vol. 35, no. 3, pp. 401–411, mar 2000. (Cited on pages 32 and 34.)

[59] C. S. Ruf, S. M. Gross, and S. Misra, "RFI detection and mitigation for microwave radiometry with an agile digital detector," *IEEE Transactions on Geoscience and Remote Sensing*, vol. 44, no. 3, pp. 694–706, mar 2006. (Cited on pages 33, 37, 79, 81, and 152.)

[60] A. Thiel and M. Ammann, "Anti-Jamming techniques in u-Blox GPS receivers," 2009. (Cited on page 33.)

[61] A. N. Akansu and R. A. Haddad, *Multiresolution Signal Decomposition: Transforms, Subbands, and Wavelets*. Academic Press, 2001. (Cited on pages 33, 35, 82, and 84.)

[62] D. Chakraborty and N. Kovvali, "Generalized normal window for digital signal processing," in *2013 IEEE International Conference on Acoustics, Speech and Signal Processing (ICASSP)*, Vancouver, BC, Canada, may 2013, pp. 6083–6087. (Cited on page 34.)

[63] S. Starosielec and D. Hägele, "Discrete-time windows with minimal RMS bandwidth for given RMS temporal width," *Signal Processing*, vol. 102, pp. 240–246, sep 2014. (Cited on pages 34 and 82.)

[64] L. Musumeci and F. Dovis, "A comparison of transformed-domain techniques for pulsed interference removal on GNSS signals," in *2012 International Conference on Localization and GNSS (ICL-GNSS)*, Starnberg, Germany, jun 2012, pp. 1–6. (Cited on page 35.)

[65] A. Camps and J. M. Tarongi, "RFI Mitigation in Microwave Radiometry Using Wavelets," *Algorithms*, vol. 2, no. 3, pp. 1248–1262, sep 2009. (Cited on pages 35, 80, 81, 83, and 152.)

[66] M. Bahoura and H. Ezzaidi, "FPGA-implementation of wavelet-based denoising technique to remove power-line interference from ECG signal," in *2010 10th IEEE International Conference on Information Technology and Applications in Biomedicine (ITAB)*, Corfu, Greece, nov 2010, pp. 1–4. (Cited on page 35.)

[67] L. Musumeci and F. Dovis, "Use of the Wavelet Transform for Interference Detection and Mitigation in Global Navigation Satellite Systems," *International Journal of Navigation and Observation*, vol. 2014, pp. 1–14, feb 2014. (Cited on page 35.)

[68] C. Maccone, *Mathematical SETI: Statistics, Signal Processing, Space Missions*. Berlin, Heidelberg: Springer Berlin Heidelberg, 2010. (Cited on pages 35, 36, and 254.)

[69] A. Szumski and G. W. Hein, "Finding the Interference: Karhunen-Loève Transform as an instrument to Detect Weak RF signals," *InsideGNSS*, pp. 57–64, jun 2011. (Cited on pages 35 and 36.)

[70] W. Yu, Y. Deng, X. Wang, X. Qi, and Y. Liu, "Radiofrequency interference suppression in synthetic aperture radar based on singular spectrum analysis with extended – FAPI subspace tracking," *IET Radar, Sonar and Navigation*, vol. 6, no. 9, pp. 881–890, dec 2012. (Cited on page 36.)

[71] R. J. Landry, P. Boutin, and A. Constantinescu, "New anti-jamming technique for GPS and GALILEO receivers using adaptive FADP filter," *Digital Signal Processing: A Review Journal*, vol. 16, no. 3, pp. 255–274, may 2006. (Cited on pages 37, 81, and 152.)

[72] E. Lundberg and I. McMichael, "Novel Timing Antennas for Improved GNSS Resilience," 2018. [Online]. Available: https://www.mitre.org/sites/default/files/publications/pr18-0336-novel-timing-antennas-for-improved-gnss-resilience.pdf (Cited on page 38.)

[73] J. M. Tarongi and A. Camps, "Radio frequency interference detection and mitigation algorithms based on spectrogram analysis," *Algorithms*, vol. 4, no. 4, pp. 239–261, 2011. (Cited on pages 44 and 91.)

[74] J. Querol, J. M. Tarongí, G. Forte, J. J. Gómez, and A. Camps, "MERITXELL: The Multifrequency Experimental Radiometer with Interference Tracking for Experiments over Land and Littoral—Instrument Description, Calibration and Performance," *Sensors*, vol. 17, no. 5, p. 1081, may 2017. (Cited on page 44.)

[75] J. J. Gómez López, "Control of the back-end and positioning systems of the MERITXELL radiometer," M.Sc. Thesis, Universitat Politècnica de Catalunya, 2017. [Online]. Available: http://upcommons.upc.edu/handle/2117/100261{#}.WoLH71JbJ60.mendeley (Cited on pages 44 and 263.)

[76] World Meteorological Organization, "Observing Systems Capability Analysis and Review Tool (OSCAR)." [Online]. Available: https://www.wmo-sat.info/oscar/ (Cited on page 45.)

[77] M. Hallikainen, M. Kemppinen, K. Rautiainen, J. Pihlflyckt, J. Lahtinen, T. Tirri, I. Mononen, and T. Auer, "Airborne 14-channel microwave radiometer HUTRAD," in *IGARSS '96. 1996 International Geoscience and Remote Sensing Symposium*, vol. 4. Lincoln, NE, USA: IEEE, may 1996, pp. 2285–2287. (Cited on page 45.)

[78] J. Piepmeier and A. Gasiewski, "Polarimetric scanning radiometer for airborne microwave imaging studies," in *IGARSS '96. 1996 International Geoscience and Remote Sensing Symposium*, vol. 2. IEEE, 1996, pp. 1120–1122. (Cited on page 46.)

[79] D. B. Kunkee, G. A. Poe, D. J. Boucher, S. D. Swadley, Y. Hong, J. E. Wessel, and E. A. Uliana, "Design and Evaluation of the First Special Sensor Microwave Imager/Sounder," *IEEE Transactions on Geoscience and Remote Sensing*, vol. 46, no. 4, pp. 863–883, apr 2008. (Cited on page 46.)

[80] T. Kawanishi, T. Sezai, Y. Ito, K. Imaoka, T. Takeshima, Y. Ishido, A. Shibata, M. Miura, H. Inahata, and R. Spencer, "The advanced microwave scanning radiometer for the earth observing system (AMSR-E), NASDA's contribution to the EOS for global energy and water cycle studies," *IEEE Transactions on Geoscience and Remote Sensing*, vol. 41, no. 2, pp. 184–194, feb 2003. (Cited on page 46.)

[81] E. Cardellach, F. Fabra, O. Nogués-Correig, S. Oliveras, S. Ribó, and A. Rius, "GNSS-R ground-based and airborne campaigns for ocean, land, ice, and snow techniques: Application to the GOLD-RTR data sets," *Radio Science*, vol. 46, no. 6, dec 2011. (Cited on page 46.)

[82] A. Alonso-Arroyo, A. Camps, A. Monerris, C. Rudiger, J. P. Walker, R. Onrubia, J. Querol, H. Park, and D. Pascual, "On the Correlation Between GNSS-R Reflectivity and L-Band Microwave Radiometry," *IEEE Journal of Selected Topics in Applied Earth Observations and Remote Sensing*, vol. 9, no. 12, pp. 5862–5879, dec 2016. (Cited on page 46.)

[83] E. Valencia, A. Camps, J. F. Marchan-Hernandez, H. Park, X. Bosch-Lluis, N. Rodriguez-Alvarez, and I. Ramos-Perez, "Ocean Surface's Scattering Coefficient Retrieval by Delay–Doppler Map Inversion," *IEEE Geoscience and Remote Sensing Letters*, vol. 8, no. 4, pp. 750–754, jul 2011. (Cited on pages 46 and 53.)

[84] M. Piles, N. Sanchez, M. Vall-llossera, A. Camps, J. Martinez-Fernandez, J. Martinez, and V. Gonzalez-Gambau, "A Downscaling Approach for SMOS Land Observations: Evaluation of High-Resolution Soil Moisture Maps Over the Iberian Peninsula," *IEEE Journal of Selected Topics in Applied Earth Observations and Remote Sensing*, vol. 7, no. 9, pp. 3845–3857, sep 2014. (Cited on page 46.)

[85] J. M. Tarongi and A. Camps, "Multifrequency experimental radiometer with interference tracking for experiments over land and littoral: Meritxell," in *2009 IEEE International Geoscience and Remote Sensing Symposium*. Cape Town, South Africa: IEEE, jul 2009, pp. IV–653–IV–656. (Cited on page 47.)

[86] V. Depau, J. Tarongi, G. Forte, and A. Camps, "Preliminary performance study of different radio-frequency interference detection and mitigation algorithms in microwave radiometry," in *2012 12th Specialist Meeting on Microwave Radiometry and Remote Sensing of the Environment (MicroRad)*. Rome, Italy: IEEE, mar 2012, pp. 1–4. (Cited on page 47.)

[87] R. M. Villarino Villarino, "Empirical Determination of the Sea Surface Emissivity at L-band: A contribution to ESA's SMOS Earth Explorer Mission," Ph.D. dissertation, UPC-BarcelonaTech, oct 2004. [Online]. Available: http://www.tdx.cat/handle/10803/6884 (Cited on page 49.)

[88] Rohde and Schwarz, "FSP Spectrum Analyzer." [Online]. Available: https://www.rohde-schwarz.com/us/manual/r-s-fsp-operating-manual-manuals-gb1{_}78701-39944.html (Cited on pages 51, 52, and 59.)

[89] N. Rodriguez-Alvarez, A. Camps, M. Vall-llossera, X. Bosch-Lluis, A. Monerris, I. Ramos-Perez, E. Valencia, J. F. Marchan-Hernandez, J. Martinez-Fernandez, G. Baroncini-Turricchia, C. Perez-Gutierrez, and N. Sanchez, "Land Geophysical Parameters Retrieval Using the Interference Pattern GNSS-R Technique," *IEEE Transactions on Geoscience and Remote Sensing*, vol. 49, no. 1, pp. 71–84, jan 2011. (Cited on page 53.)

[90] E. Valencia, V. U. Zavorotny, D. M. Akos, and A. Camps, "Using DDM asymmetry metrics for wind direction retrieval from GPS ocean-scattered signals in airborne experiments," *IEEE Transactions on Geoscience and Remote Sensing*, vol. 52, no. 7, pp. 3924–3936, 2014. (Cited on page 53.)

[91] "SiGe GN3S Sampler v.2." [Online]. Available: http://www.sparkfun.com/products/8238 (Cited on page 53.)

[92] FLIR, "Industrial Automation IR Camera." [Online]. Available: http://flir-a320.ru/files/upload/general/610/1548/090722{_}A320{_}datasheet{_}eng.pdf (Cited on page 53.)

[93] N. Pettorelli, *The Normalized Difference Vegetation Index*. Oxford: Oxford University Press, oct 2013. (Cited on page 53.)

[94] DuncanTech, "High Resolution 3-CCD Digital Multispectral Camera." [Online]. Available: http://prom-sys.com/pdf/MS4100.pdf (Cited on page 53.)

[95] Wansview, "Network IP box Camera." [Online]. Available: https://www.wansview.us/NC510-p/nc510.htm (Cited on page 54.)

[96] Yong Han and E. Westwater, "Analysis and improvement of tipping calibration for ground-based microwave radiometers," *IEEE Transactions on Geoscience and Remote Sensing*, vol. 38, no. 3, pp. 1260–1276, may 2000. (Cited on pages 63 and 65.)

[97] Li Wu, ShuSheng Peng, ZeLong Xiao, TaiYang Hu, and JianZhong Xu, "Calibration of a W band radiometer using tipping curve," in *2010 International Symposium on Signals, Systems and Electronics*. IEEE, sep 2010, pp. 1–3. (Cited on pages 63 and 65.)

[98] D. V. Land, A. P. Levick, and J. W. Hand, "The use of the Allan deviation for the measurement of the noise and drift performance of microwave radiometers," *Measurement Science and Technology*, vol. 18, no. 7, pp. 1917–1928, jul 2007. (Cited on page 68.)

[99] J. Querol, A. Alonso-Arroyo, R. Onrubia, D. Pascual, H. Park, and A. Camps, "SNR Degradation in GNSS-R Measurements Under the Effects of Radio-Frequency Interference," *IEEE Journal of Selected Topics in Applied Earth Observations and Remote Sensing*, vol. 9, no. 10, pp. 4865–4878, oct 2016. (Cited on pages 72, 130, and 148.)

[100] J. Querol, R. Onrubia, D. Pascual, A. Alonso-Arroyo, H. Park, and A. Camps, "Comparison of real-time time-frequency RFI mitigation techniques in microwave radiometry," in *2016 14th Specialist Meeting on Microwave Radiometry and Remote Sensing of the Environment (MicroRad)*. Espoo, Helsinki, Finland: IEEE, apr 2016, pp. 68–70. (Cited on pages 76 and 101.)

[101] L. Dente, Z. Su, and J. Wen, "Validation of SMOS Soil Moisture Products over the Maqu and Twente Regions," *Sensors*, vol. 12, no. 12, pp. 9965–9986, jul 2012. (Cited on page 77.)

[102] L. Li, E. Njoku, E. Im, P. Chang, and K. St.Germain, "A Preliminary Survey of Radio-Frequency Interference Over the U.S. in Aqua AMSR-E Data," *IEEE Transactions on Geoscience and Remote Sensing*, vol. 42, no. 2, pp. 380–390, feb 2004. (Cited on page 77.)

[103] S. Misra, P. N. Mohammed, B. Guner, C. S. Ruf, J. R. Piepmeier, and J. T. Johnson, "Microwave Radiometer Radio-Frequency Interference Detection Algorithms: A Comparative Study," *IEEE Transactions on Geoscience and Remote Sensing*, vol. 47, no. 11, pp. 3742–3754, 2009. (Cited on page 77.)

[104] L. Cohen, *Time-frequency Analysis*, ser. Electrical engineering signal processing. Prentice Hall PTR, 1995. (Cited on pages 79, 80, 145, and 317.)

[105] J. Samson, "Wavelets and Notch Filtering: Innovative techniques for mitigating RF Interferences," *InsideGNSS*, pp. 54–62, 2011. (Cited on page 79.)

[106] G. F. Forte, J. Querol, A. Camps, and M. Vall-llossera, "Real-Time RFI Detection and Mitigation System for Microwave Radiometers," *IEEE Transactions on Geoscience and Remote Sensing*, vol. 51, no. 10, pp. 4928–4935, oct 2013. (Cited on pages 80, 81, 82, 152, and 159.)

[107] J. Querol, A. Alonso-Arroyo, R. Onrubia, D. Pascual, and A. Camps, "Assessment of back-end RFI mitigation techniques in passive remote sensing," in *2015 IEEE International Geoscience and Remote Sensing Symposium (IGARSS)*. Milan, Italy: IEEE, jul 2015, pp. 4746–4749. (Cited on pages 81, 84, 106, 144, 146, and 148.)

[108] A. D. Calway, "The multiresolution Fourier transform : a general purpose tool for image analysis," PhD thesis, University of Warwick, 1989. [Online]. Available: http://wrap.warwick.ac.uk/id/eprint/49949 (Cited on page 83.)

[109] A. Calway, "Image analysis using a generalised wavelet transform," in *IEE Colloquium on Applications of Wavelet Transforms in Image Processing*, 1993. (Cited on page 83.)

[110] R. Wilson, A. Calway, and E. Pearson, "A generalized wavelet transform for Fourier analysis: the multiresolution Fourier transform and its application to image and audio signal analysis," *IEEE Transactions on Information Theory*, vol. 38, no. 2, pp. 674–690, mar 1992. (Cited on page 83.)

[111] A. Calway and R. Wilson, "Curve Extraction in Images Using a Multiresolution Framework," *CVGIP: Image Understanding*, vol. 59, no. 3, pp. 359–366, may 1994. (Cited on page 83.)

[112] X. Wen and M. Sandler, "Calculation of radix-2 discrete multiresolution Fourier transform," *Signal Processing*, vol. 87, no. 10, pp. 2455–2460, 2007. (Cited on pages 84 and 152.)

[113] D. L. Donoho and I. M. Johnstone, "Adapting to unknown smoothness via wavelet shrinkage," *Journal of the American Statistical Association*, vol. 90, no. 432, pp. 1200–1224, 1995. (Cited on page 84.)

[114] M. G. Kendall, A. Stuart, R. F. Sletto, and M. G. Kendall, "The Advanced Theory of Statistics," *American Sociological Review*, vol. 10, no. 3, p. 443, 1945. (Cited on pages 85, 163, 326, 327, and 330.)

[115] M. Evans, N. Hastings, and B. Peacock, *Statistical Distributions*, 2000, vol. 2, no. 4. (Cited on page 85.)

[116] C. Walck, "Handbook on statistical distributions for experimentalists," 2007. (Cited on pages 85, 260, 261, and 262.)

[117] R. T. Short, "Computation of rice and noncentral chi-squared probabilities," 2012. (Cited on page 85.)

[118] M. Abramowitz and I. A. Stegun, *Handbook of Mathematical Functions with Formulas, Graphs, and Mathematical Tables*, 1964. (Cited on pages 85 and 262.)

[119] J. I. Marcum, "A Statistical Theory of Target Detection By Pulsed Radar," *IRE Transactions on Information Theory*, vol. 6, no. 2, pp. 59–267, 1960. (Cited on pages 85 and 262.)

[120] A. Nuttall, "Some integrals involving the Q-function," *Naval underwater Systems Center*, vol. 21, no. 1, pp. 95–96, 1972. (Cited on pages 85 and 262.)

[121] J. R. Piepmeier, J. T. Johnson, P. N. Mohammed, D. Bradley, C. Ruf, M. Aksoy, R. Garcia, D. Hudson, L. Miles, and M. Wong, "Radio-Frequency Interference Mitigation for the Soil Moisture Active Passive Microwave Radiometer," *IEEE Transactions on Geoscience and Remote Sensing*, vol. 52, no. 1, pp. 761–775, jan 2014. (Cited on page 94.)

[122] K. Tapping and M. Leech, "RTLSDR-based, Software Defined Radio Alternative to Switched Radiometers for Continuum Radio Astronomy." (Cited on page 106.)

[123] M. Celep, e. Yaran, Y. Gülmez, and A. Dolma, "Characterization of a total power radiometer," *Turkish Journal of Electrical Engineering and Computer Sciences*, vol. 20, no. 6, pp. 870–880, 2012. (Cited on page 106.)

[124] J. Querol, R. Onrubia, D. Pascual, H. Park, and A. Camps, "A Radio-Frequency Interference detector for GNSS navigation and GNSS-reflectometry applications," in *International Geoscience and Remote Sensing Symposium (IGARSS)*, vol. 2017-July, 2017. (Cited on page 107.)

[125] F. Dovis, "Anomalous GPS signals reported from SVN49," *GPS World*, vol. June, 2017. (Cited on page 119.)

[126] M. Wildemeersch, A. Rabbachin, E. Cano, and J. Fortuny, "Interference assessment of DVB-T within the GPS L1 and Galileo E1 band," in *Programme and Abstract Book*

- *5th ESA Workshop on Satellite Navigation Technologies and European Workshop on GNSS Signals and Signal Processing, NAVITEC 2010*, 2010. (Cited on page 128.)

[127] J. W. Betz, "Effect of Partial-Band Interference on Receiver Estimation of C/N0: Theory," *Technical Report, The MITRE Corporation*, pp. 716–723, 2001. (Cited on pages 128 and 136.)

[128] J. Betz and B. Titus, "Intersystem and intrasystem interference with signal imperfections," in *PLANS 2004. Position Location and Navigation Symposium (IEEE Cat. No.04CH37556)*, 2004, pp. 558–565. (Cited on page 128.)

[129] A. Alonso-Arroyo, A. Camps, H. Park, D. Pascual, R. Onrubia, and F. Martin, "Retrieval of Significant Wave Height and Mean Sea Surface Level Using the GNSS-R Interference Pattern Technique: Results From a Three-Month Field Campaign," *IEEE Transactions on Geoscience and Remote Sensing*, vol. 53, no. 6, pp. 3198–3209, jun 2015. (Cited on page 128.)

[130] R. Sabia, M. Caparrini, and G. Ruffini, "Potential Synergetic Use of GNSS-R Signals to Improve the Sea-State Correction in the Sea Surface Salinity Estimation: Application to the SMOS Mission," *IEEE Transactions on Geoscience and Remote Sensing*, vol. 45, no. 7, pp. 2088–2097, jul 2007. (Cited on page 128.)

[131] N. Rodriguez-Alvarez, X. Bosch-Lluis, A. Camps, M. Vall-llossera, E. Valencia, J. Marchan-Hernandez, and I. Ramos-Perez, "Soil Moisture Retrieval Using GNSS-R Techniques: Experimental Results Over a Bare Soil Field," *IEEE Transactions on Geoscience and Remote Sensing*, vol. 47, no. 11, pp. 3616–3624, nov 2009. (Cited on page 128.)

[132] E. Cardellach, A. Rius, M. Martin-Neira, F. Fabra, O. Nogues-Correig, S. Ribo, J. Kainulainen, A. Camps, and S. D'Addio, "Consolidating the Precision of Interferometric GNSS-R Ocean Altimetry Using Airborne Experimental Data," *IEEE Transactions on Geoscience and Remote Sensing*, vol. 52, no. 8, pp. 4992–5004, aug 2014. (Cited on page 128.)

[133] A. W. Rihaczek, *Principles of high-resolution radar*. McGraw-Hill, 1969. (Cited on pages 128, 129, and 130.)

[134] V. U. Zavorotny and A. G. Voronovich, "Scattering of GPS signals from the ocean with wind remote sensing application," *IEEE Transactions on Geoscience and Remote Sensing*, vol. 38, no. 2, pp. 951–964, 2000. (Cited on pages 129 and 131.)

[135] T. Elfouhaily, D. R. Thompson, and L. Linstrom, "Delay-Doppler analysis of bistatically reflected signals from the ocean surface: Theory and application," *IEEE Transactions on Geoscience and Remote Sensing*, vol. 40, no. 3, pp. 560–573, 2002. (Cited on page 129.)

[136] J. F. Marchan-Hernandez, A. Camps, N. Rodriguez-Alvarez, E. Valencia, X. Bosch-Lluis, and I. Ramos-Perez, "An efficient algorithm to the simulation of delay-Doppler maps of reflected global navigation satellite system signals," *IEEE Transactions on Geoscience and Remote Sensing*, vol. 47, no. 8, pp. 2733–2740, 2009. (Cited on page 129.)

[137] J. Ville, "Theorie et applications de la notion de signal analytique," *Cables et Transmissions*, vol. 2A, no. 1, pp. 61–74, 1948. (Cited on page 129.)

[138] P. Woodward, "Radar Ambiguity Analysis," *R.R.E. Technical Note No 731*, vol. February, 1967. (Cited on pages 129, 131, and 313.)

[139] E. Kaplan and C. Hegarty, *Understanding GPS: Principles and Applications, Second Edition*. Artech House, 2005. (Cited on pages 130, 171, and 207.)

[140] J. Querol, A. Alonso-Arroyo, R. Onrubia, D. Pascual, and A. Camps, "SNR degradation in conventional GNSS-R measurements under the effects of radio frequency interference," in *8th Workshop on GNSS Reflectrometry*, GFZ, Potsdam, Germany, may 2015, p. 1. (Cited on page 130.)

[141] J. Querol, R. Onrubia, D. Pascual, A. Alonso-Arroyo, H. Park, and A. Camps, "Impact of Radio-Frequency Interference on Conventional GNSS-Reflectometry," in *2015 IEEE Young Professionals Conference on Remote Sensing*. Barcelona: IEEE, dec 2015. (Cited on page 130.)

[142] S. Sussman, "Least-square synthesis of radar ambiguity functions," *IRE Transactions on Information Theory*, vol. 8, no. 3, pp. 246–254, 1962. (Cited on pages 131 and 312.)

[143] D. Pascual, H. Park, R. Onrubia, A. A. Arroyo, J. Querol, and A. Camps, "Crosstalk Statistics and Impact in Interferometric GNSS-R," *IEEE Journal of Selected Topics in Applied Earth Observations and Remote Sensing*, pp. 1–10, 2016. (Cited on page 133.)

[144] M. Martín-Neira, S. D'Addio, C. Buck, N. Floury, and R. Prieto-Cerdeira, "The PARIS ocean altimeter in-Orbit demonstrator," *IEEE Transactions on Geoscience and Remote Sensing*, vol. 49, no. 6 PART 2, pp. 2209–2237, 2011. (Cited on page 135.)

[145] D. Pascual, A. Camps, F. Martin, H. Park, A. A. Arroyo, and R. Onrubia, "Precision bounds in GNSS-R ocean altimetry," *IEEE Journal of Selected Topics in Applied Earth Observations and Remote Sensing*, vol. 7, no. 5, pp. 1416–1423, 2014. (Cited on page 136.)

[146] W. Martin and P. Flandrin, "Wigner-Ville spectral analysis of nonstationary processes," *IEEE Transactions on Acoustics, Speech, and Signal Processing*, vol. 33, no. 6, 1985. (Cited on pages 142 and 318.)

[147] J. Querol, E. M. Julian, R. Onrubia, A. Alonso-Arroyo, D. Pascual, and A. Camps, "Preliminary Results of FENIX: Front-End GNSS Interference eXcisor," in *2016 IEEE International Geoscience and Remote Sensing Symposium (IGARSS)*. Beijing, China: IEEE, jul 2016. (Cited on pages 148 and 170.)

[148] J. Querol, R. Onrubia, D. Pascual, J. Castellvi-Esturi, H. Park, and A. Camps, "RFI Analysis and Mitigation in Airborne GNSS-R Campaign," in *2018 IEEE International Geoscience and Remote Sensing Symposium (IGARSS)*. Valencia, Spain: IEEE, jul 2018. (Cited on page 148.)

[149] J. Querol Borràs and A. J. Camps Carmona, "System and method for detecting and eliminating radio frequency interferences in real time," 2017. [Online].

Available: https://worldwide.espacenet.com/publicationDetails/originalDocument?CC=US{&}NR=9596610B1{&}KC=B1{&}FT=D{&}ND=3{&}date=20170314{&}DB=EPODOC{&}locale=en{_}EP (Cited on pages 148, 149, and 170.)

[150] R. Onrubia, D. Pascual, J. Querol, J. Castellvi-Esturi, J. Corbera, H. Park, and A. Camps, "Preliminary altimetry results of the MALYGNSS instrument in the HUMIT project," in *2018 IEEE International Geoscience and Remote Sensing Symposium (IGARSS)*, Valencia, Spain, jul 2018. (Cited on page 159.)

[151] J. Castellvi-Esturi, A. Camps, J. Corbera, R. Onrubia, R. Alamús, D. Pascual, J. Querol, and H. Park, "3CAT-3/MOTS, An Experimental Nanosatellite for Multispectral and GNSS-R Earth Observation: Airborne Optical and GNSS-R Campaign," in *2018 IEEE International Geoscience and Remote Sensing Symposium (IGARSS)*, Valencia, Spain, jul 2018. (Cited on pages 159 and 161.)

[152] A. J. Schoenwald, D. C. Bradley, P. N. Mohammed, J. R. Piepmeier, and M. Wong, "Performance analysis of a hardware implemented complex signal kurtosis radio-frequency interference detector," in *2016 14th Specialist Meeting on Microwave Radiometry and Remote Sensing of the Environment (MicroRad)*. IEEE, apr 2016, pp. 71–75. (Cited on page 163.)

[153] E. M. Julian Ortin, "Real-time radio-frequency interference mitigation system for radio navigation receivers," M.Sc. Thesis, UPC-BarcelonaTech, 2016. (Cited on pages 170 and 181.)

[154] I. Pitas and A. N. Venetsanopoulos, *Nonlinear Digital Filters*, 1990. (Cited on page 173.)

[155] R. Crochiere and L. Rabiner, *Multirate digital signal processing*, prentice-h ed. Englewood Cliffs, New Jersey: Prentice-Hall, 1983. (Cited on page 177.)

[156] J. Querol, R. Onrubia, D. Pascual, H. Park, and A. Camps, "RFI mitigation for GNSS-R intruments: FENIX, the Front-End GNSS Interference eXcisor," in *2017 Specialist Meeting on Reflectometry using GNSS and other Signals of Opportunitty (GNSS+R)*, Ann Arbor, MI, USA, 2017. (Cited on page 196.)

[157] J. Querol and A. Camps, "Real-time Pre-correlation Anti-jamming System for Civilian GNSS Receivers," in *Proceedings of the 30th International Technical Meeting of The Satellite Division of the Institute of Navigation (ION GNSS+ 2017)*, Portland, Oregon, sep 2017, pp. 1267–1288. (Cited on page 196.)

[158] J. Querol, R. Onrubia, D. Pascual, H. Park, and A. Camps, "FENIX, a real-time anti-jamming system for GNSS receivers," in *6th International Colloquium on Scientific and Fundamental Aspects of GNSS/Galileo*, Valencia, Spain, 2017. (Cited on page 196.)

[159] J. Querol, A. Camps, E. Garbin, and R. Píriz, "An Anti-Jamming System for GNSS Timing Applications," in *32nd European Frequency and Time Forum 2018*, Torino, apr 2018. (Cited on page 196.)

[160] E. Garbin, J. Querol, R. Píriz, and A. Camps, "Effects of Interference Mitigation in Timing Solutions of GNSS Receivers," in *Proceedings of the 31th International Tech-*

nical Meeting of The Satellite Division of the Institute of Navigation (ION GNSS+ 2018), Tampa, FL, USA, 2018. (Cited on page 196.)

[161] D. Borio, "Swept GNSS jamming mitigation through pulse blanking," in *2016 European Navigation Conference, ENC 2016*, 2016. (Cited on page 196.)

[162] J. G. Proakis and D. G. Monolakis, *Digital signal processing: principles, algorithms, and applications*, 1996. (Cited on page 201.)

[163] SkyTraq, "Venus638LPx 20Hz -165dBm GPS Receiver Module." [Online]. Available: http://www.skytraq.com.tw/datasheet/Venus838LPx{_}DS{_}v4.pdf (Cited on page 209.)

[164] U-blox, "LEA-6: u-blox 6 GPS Modules Datasheet." [Online]. Available: https://www.u-blox.com/sites/default/files/products/documents/LEA-6{_}DataSheet{_}{%}28UBX-14044797{%}29.pdf (Cited on page 209.)

[165] Trimble, "Trimble BD982, GNSS Receiver Module." [Online]. Available: http://www.trimble.com/oem{_}receiverhelp/v4.91/en/bd982pdf.pdf (Cited on page 209.)

[166] Septentrio, "AsteRx2: GPS/GLONASS Dual-frequency Receiver family." [Online]. Available: http://www.terrisgps.com/product{_}files/AsteRx2{_}251.pdf (Cited on page 209.)

[167] D. Kewalramani, "Robust tracking system in front of Radio-Frequency Interferences. Part I: Communications and hyperbolic navigation," M.Sc. Thesis, UPC-BarcelonaTech, may 2016. (Cited on page 224.)

[168] P. J. Cara Reyes, "Robust tracking system in front of Radio-Frequency Interferences. Part II: Transceivers and error estimation," M.Sc. Thesis, UPC-BarcelonaTech, 2016. (Cited on page 224.)

[169] A. Gil Sorribes, "Robust Tracking System in front of Radio-Frequency Interferences. Part III: Signals, Modulations, and Reliability analysis," M.Sc. Thesis, UPC-BarcelonaTech, 2016. (Cited on pages 224 and 241.)

[170] F. Gustafsson and F. Gunnarsson, "Positioning using time difference of arrival measurements," in *2003 IEEE International Conference on Acoustics, Speech, and Signal Processing, 2003. Proceedings. (ICASSP '03).*, vol. 1, 2003, pp. VI–553–6. (Cited on pages 225 and 226.)

[171] Haixin Sun, Shan Luo, and Yaowu Shi, "Broadband interference suppression in fractional fourier domain communication system," in *2011 8th International Conference on Information, Communications & Signal Processing.* IEEE, dec 2011, pp. 1–5. (Cited on page 254.)

[172] A. Bultan, "A four-parameter atomic decomposition of chirplets," *IEEE Transactions on Signal Processing*, vol. 47, no. 3, pp. 731–745, mar 1999. (Cited on page 254.)

[173] K. Sun, T. Jin, and D. Yang, "An Improved Time-Frequency Analysis Method in Interference Detection for GNSS Receivers," *Sensors*, vol. 15, no. 4, pp. 9404–9426, apr 2015. (Cited on page 254.)

[174] "GNSS Market Report 2015." [Online]. Available: http://www.gsa.europa.eu/2015-gnss-market-report (Cited on pages 255 and 256.)

[175] C. Strässle, D. Megnet, H. Mathis, and C. Bürgi, "The squaring-loss paradox," in *GNSS 20th International Technical Meeting of the Satellite Division*, 2007. (Cited on page 262.)

[176] "Programmable Resolution 1-Wire Digital Thermometer." [Online]. Available: https://datasheets.maximintegrated.com/en/ds/DS18B20.pdf (Cited on pages 306 and 307.)

[177] "0.5 Degree Range Maximum Accuracy Digital Temperature Sensor." [Online]. Available: http://ww1.microchip.com/downloads/en/DeviceDoc/25095A.pdf (Cited on pages 306 and 307.)

[178] K. H. Ang, G. Chong, and Y. Li, "PID control system analysis, design, and technology," *IEEE Transactions on Control Systems Technology*, vol. 13, no. 4, pp. 559–576, 2005. (Cited on pages 307 and 308.)

[179] W. M. Siebert, "Studies of Woodward's uncertainty function," *MIT Quarterly Progress Report*, pp. 90–94, 1958. (Cited on page 312.)

[180] C. Stutt, "A note on invariant relations for ambiguity and distance functions," *IEEE Transactions on Information Theory*, vol. 5, no. 4, pp. 164–167, dec 1959. (Cited on page 312.)

[181] J. A. Avila-Rodríguez, "On Generalized Signal Waveforms for Satellite Navigation," Ph.D. dissertation, University FAF Munich, 2008. (Cited on pages 317 and 318.)

[182] A. Papoulis, "Probability, Random Variables And Stochastic Processes," *Book*, p. 678, 1991. (Cited on page 322.)

[183] J. Eriksson, E. Ollila, and V. Koivunen, "Essential Statistics and Tools for Complex Random Variables," *IEEE Transactions on Signal Processing*, vol. 58, no. 10, pp. 5400–5408, 2010. (Cited on pages 322 and 323.)

[184] E. Ollila, J. Eriksson, and V. Koivunen, "Complex elliptically symmetric random variables - Generation, characterization, and circularity tests," *IEEE Transactions on Signal Processing*, vol. 59, no. 1, pp. 58–69, 2011. (Cited on pages 323, 324, and 325.)

[185] E. Ollila and V. Koivunen, "Generalized complex elliptical distributions," in *Processing Workshop Proceedings, 2004 Sensor Array and Multichannel Signal.* IEEE, 2004, pp. 460–464. (Cited on pages 324 and 325.)

[186] B. Picinbono, "On circularity," *IEEE Transactions on Signal Processing*, vol. 42, no. 12, pp. 3473–3482, 1994. (Cited on page 324.)

[187] D. Bradley, J. M. Morris, T. Adali, J. T. Johnson, and M. Aksoy, "On the detection of RFI using the complex signal kurtosis in microwave radiometry," in *13th Specialist Meeting on Microwave Radiometry and Remote Sensing of the Environment, MicroRad 2014 - Proceedings*, 2014, pp. 33–38. (Cited on pages 325 and 330.)

[188] L. Isserlis, "On Certain Probable Errors and Correlation Coefficients of Multiple Frequency Distributions with Skew Regression," *Biometrika*, vol. 11, no. 3, pp. 185–190, 1916. (Cited on page 326.)

[189] ——, "On a Formula for the Product-Moment Coefficient of any Order of a Normal Frequency Distribution in any Number of Variables," *Biometrika*, vol. 12, no. 1/2, p. 134, nov 1918. (Cited on page 326.)

[190] W. Navidi, *Estadística para ingenieros y científicos*, 2006. (Cited on page 326.)

[191] C. Rose and M. D. Smith, "mathStatica: Mathematical Statistics with Mathematica," in *CompStat 2002*, 2002, pp. 437–442. [Online]. Available: http://link.springer.com/chapter/10.1007{%}2F978-3-642-57489-4{_}66 (Cited on page 329.)

[192] E. Pearson, "A Further Development of Tests for Normality," *Biometrika*, vol. 22, no. 1-2, pp. 239–249, jul 1930. (Cited on page 330.)

[193] H. A. David, H. O. Hartley, and E. S. Pearson, "The Distribution of the Ratio, in a Single Normal Sample, of Range to Standard Deviation," *Biometrika*, vol. 41, no. 3-4, pp. 482–493, 1954. (Cited on page 330.)

List of Publications

Granted Patents

[GP1] J. Querol Borràs and A. J. Camps Carmona, "System and method for detecting and eliminating radio frequency interferences in real time, US Patent US9596610B1, issued March 14 2017. [Online]. Available: https://worldwide.espacenet.com/publicationDetails/originalDocument?CC=US&NR=9596610B1&KC=B1&FT=D&ND=3&date=20170314&DB=EPODOC&locale=en_EP

Journal Articles

[JA1] J. Querol, A. Alonso-Arroyo, R. Onrubia, D. Pascual, H. Park, and A. Camps, "SNR Degradation in GNSS-R Measurements Under the Effects of Radio-Frequency Interference," *IEEE Journal of Selected Topics in Applied Earth Observations and Remote Sensing*, vol. 9, no. 10, pp. 4865–4878, oct 2016.

[JA2] J. Querol, R. Onrubia, A. Alonso-Arroyo, D. Pascual, H. Park, and A. Camps, "Performance Assessment of Time–Frequency RFI Mitigation Techniques in Microwave Radiometry," *IEEE Journal of Selected Topics in Applied Earth Observations and Remote Sensing*, vol. 10, no. 7, pp. 1–11, 2017.

[JA3] J. Querol, J. M. Tarongí, G. Forte, J. J. Gómez, and A. Camps, "MERITXELL: The Multifrequency Experimental Radiometer with Interference Tracking for Experiments over Land and Littoral—Instrument Description, Calibration and Performance," *Sensors*, vol. 17, no. 5, p. 1081, may 2017.

[JA4] G. F. Forte, J. Querol, A. Camps, and M. Vall-llossera, "Real-Time RFI Detection and Mitigation System for Microwave Radiometers," *IEEE Transactions on Geoscience and Remote Sensing*, vol. 51, no. 10, pp. 4928–4935, oct 2013.

[JA5] H. Carreno-Luengo, A. Camps, J. Querol, and G. Forte, "First Results of a GNSS-R Experiment From a Stratospheric Balloon Over Boreal Forests," *IEEE Transactions on Geoscience and Remote Sensing*, vol. 54, no. 5, pp. 2652–2663, may 2016.

[JA6] D. Pascual, H. Park, R. Onrubia, A. A. Arroyo, J. Querol, and A. Camps, "Crosstalk Statistics and Impact in Interferometric GNSS-R," *IEEE Journal of Selected Topics in Applied Earth Observations and Remote Sensing*, pp. 1–10, 2016.

[JA7] R. Onrubia, J. Querol, D. Pascual, A. Alonso-Arroyo, H. Park, and A. Camps, "DME/TACAN Impact Analysis on GNSS Reflectometry," *IEEE Journal of Selected Topics in Applied Earth Observations and Remote Sensing*, pp. 1–10, 2016.

[JA8] A. Alonso-Arroyo, A. Camps, A. Monerris, C. Rudiger, J. P. Walker, R. Onrubia, J. Querol, H. Park, and D. Pascual, "On the Correlation Between GNSS-R Reflectivity and L-Band Microwave Radiometry," *IEEE Journal of Selected Topics in Applied Earth Observations and Remote Sensing*, vol. 9, no. 12, pp. 5862–5879, dec 2016.

[JA9] A. Alonso-Arroyo, J. Querol, C. Lopez-Martinez, V. Zavorotny, H. Park, D. Pascual, R. Onrubia, and A. Camps, "SNR and Standard Deviation of cGNSS-R and iGNSS-R Scatterometric Measurements," *Sensors*, vol. 17, no. 1, p. 183, jan 2017.

[JA10] H. Park, A. Camps, D. Pascual, Y. Kang, R. Onrubia, J. Querol, and A. Alonso-Arroyo, "A Generic Level 1 Simulator for Spaceborne GNSS-R Missions and Application to GEROS-ISS Ocean Reflectometry," *IEEE Journal of Selected Topics in Applied Earth Observations and Remote Sensing*, vol. 10, no. 10, pp. 4645–4659, 2017.

[JA11] D. Guan, H. Park, A. Camps, Y. Wang, R. Onrubia, J. Querol, and D. Pascual, "Wind direction signatures in GNSS-R observables from space," *Remote Sensing*, vol. 10, no. 2, 2018.

Conference Proceedings

[CP1] J. Querol, G. F. Forte, and A. Camps, "Study of RFI signals in protected GNSS bands generated by common electronic devices: Effects on GNSS-R measurements," in *2014 IEEE Geoscience and Remote Sensing Symposium*, Quebec, Canada, 2014, pp. 4050–4053.

[CP2] J. Querol, A. Alonso-Arroyo, R. Onrubia, D. Pascual, and A. Camps, "Assessment of back-end RFI mitigation techniques in passive remote sensing," in *2015 IEEE International Geoscience and Remote Sensing Symposium (IGARSS)*. Milan, Italy: IEEE, jul 2015, pp. 4746–4749.

[CP3] J. Querol, R. Onrubia, D. Pascual, A. Alonso-Arroyo, H. Park, and A. Camps, "Impact of Radio-Frequency Interference on Conventional GNSS-Reflectometry," in *2015 IEEE Young Professionals Conference on Remote Sensing*. Barcelona: IEEE, dec 2015.

[CP4] J. Querol, A. Alonso-Arroyo, R. Onrubia, D. Pascual, and A. Camps, "SNR degradation in conventional GNSS-R measurements under the effects of radio fre-

quency interference," in *8th Workshop on GNSS Reflectrometry*, GFZ, Potsdam, Germany, may 2015, p. 1.

[CP5] J. Querol, E. M. Julian, R. Onrubia, A. Alonso-Arroyo, D. Pascual, and A. Camps, "Preliminary Results of FENIX: Front-End GNSS Interference eXcisor," in *2016 IEEE International Geoscience and Remote Sensing Symposium (IGARSS)*. Beijing, China: IEEE, jul 2016.

[CP6] J. Querol, R. Onrubia, D. Pascual, H. Park, and A. Camps, "A Radio-Frequency Interference detector for GNSS navigation and GNSS-reflectometry applications," in *International Geoscience and Remote Sensing Symposium (IGARSS)*, vol. 2017-July, 2017.

[CP7] J. Querol and A. Camps, "Real-time Pre-correlation Anti-jamming System for Civilian GNSS Receivers," in *Proceedings of the 30th International Technical Meeting of The Satellite Division of the Institute of Navigation (ION GNSS+ 2017)*, Portland, Oregon, sep 2017, pp. 1267–1288.

[CP8] J. Querol, R. Onrubia, D. Pascual, J. Castellvi-Esturi, H. Park, and A. Camps, "RFI Analysis and Mitigation in Airborne GNSS-R Campaign," in *2018 IEEE International Geoscience and Remote Sensing Symposium (IGARSS)*. Valencia, Spain: IEEE, jul 2018.

[CP9] J. Querol, A. Camps, E. Garbin, and R. Píriz, "An Anti-Jamming System for GNSS Timing Applications," in *32nd European Frequency and Time Forum 2018*, Torino, apr 2018.

[CP10] G. Forte, J. Querol, H. Park, and A. Camps, "Digital back-end for RFI detection and mitigation in earth observation," in *2013 IEEE International Geoscience and Remote Sensing Symposium - IGARSS*. Melbourne, VIC, Australia: IEEE, jul 2013, pp. 1908–1911.

[CP11] H. Carreno-Luengo, A. Camps, J. Querol, G. Forte, R. Onrubia, and R. Diez, "A stratospheric balloon GNSS-R experiment: The 3Cat-2 project in DLR/SNSB BEXUS," in *2014 IEEE Geoscience and Remote Sensing Symposium*. IEEE, jul 2014, pp. 3626–3629.

[CP12] A. Camps, J. F. Marchan-Hernandez, X. Bosch-Lluis, N. Rodriguez-Alvarez, I. Ramos-Perez, E. Valencia, J. M. Tarongi, H. Park, H. Carreno-Luengo, A. Alonso-Arroyo, D. Pascual, R. Onrubia, G. Forte, and J. Querol, "Review of GNSS-R instruments and tools developed at the Universitat Politecnica de Catalunya-Barcelona tech," in *2014 IEEE Geoscience and Remote Sensing Symposium*. IEEE, jul 2014, pp. 3826–3829.

[CP13] R. Onrubia, L. Garrucho, D. Pascual, H. Park, J. Querol, A. Alonso-Arroyo, and A. Camps, "Advances in the MIR instrument: Integration, control subsystem and analysis of the flight dynamics for beamsteering purposes," in *2015 IEEE International Geoscience and Remote Sensing Symposium (IGARSS)*. IEEE, jul 2015, pp. 4765–4768.

[CP14] A. Alonso-Arroyo, S. Torrecilla, J. Querol, A. Camps, D. Pascual, H. Park, and R. Onrubia, "Two dedicated soil moisture experiments using the scatterometric

properties of GNSS-reflectometry," in *2015 IEEE International Geoscience and Remote Sensing Symposium (IGARSS)*. IEEE, jul 2015, pp. 3921–3924.

[CP15] R. Onrubia, J. Querol, D. Pascual, A. Alonso-Arroyo, H. Park, and A. Camps, "DME/TACAN Impact Analysis on Spaceborne iGNSS-R," in *2015 IEEE Young Professionals Conference on Remote Sensing*. Barcelona: IEEE, dec 2015.

[CP16] D. Pascual, H. Park, A. Camps, A. Alonso-Arroyo, R. Onrubia, and J. Querol, "Study of the Cross-Talk Effect in GNSS Reflectometry," in *2015 IEEE Young Professionals Conference on Remote Sensing*. Barcelona: IEEE, dec 2015.

[CP17] H. Park, D. Pascual, A. Camps, A. Alonso-Arroyo, R. Onrubia, and J. Querol, "Antenna beam impact on GEROS-ISS instrument observables," in *2015 Workshop on GNSS Reflectrometry*, may 2015, p. 1.

[CP18] D. Pascual, H. Park, A. Camps, A. Alonso-Arroyo, R. Onrubia, and J. Querol, "Cross-talk statistics of interferometric GNSS-R," in *2015 Workshop on GNSS Reflectrometry*, may 2015, p. 1.

[CP19] H. Park, D. Pascual, A. Camps, A. Alonso-Arroyo, R. Onrubia, and J. Querol, "GEROS instrument simulator built by using P2EPS," in *2015 Workshop on GNSS Reflectrometry*, may 2015, p. 1.

[CP20] R. Onrubia, J. Querol, D. Pascual, A. Alonso-Arroyo, H. Park, and A. Camps, "DME/TACAN interference impact in interferometric GNSS-R," in *2015 Workshop on GNSS Reflectrometry*, may 2015, p. 1.

[CP21] A. Alonso-Arroyo, J. Querol, C. Lopez, A. Camps, H. Park, D. Pascual, and R. Onrubia, "GNSS-R correlation Peak statistics, SNR estimation and its relation to geophysical parameters," in *2015 Workshop on GNSS Reflectrometry*, may 2015, p. 1.

[CP22] A. Alonso-Arroyo, A. Camps, A. Monerris, C. Rüdiger, J. P. Walker, Y. Gao, J. Querol, H. Park, D. Pascial, and R. Onrubia, "On the Comparison between Airborne L-Band Brightness Temperature and GNSS-Reflectivity: A case study in Australia," in *2016 14th Specialist Meeting on Microwave Radiometry and Remote Sensing of the Environment (MicroRad)*. Espoo, Helsinki, Finland: IEEE, apr 2016.

[CP23] J. Querol, R. Onrubia, D. Pascual, A. Alonso-Arroyo, H. Park, and A. Camps, "Comparison of real-time time-frequency RFI mitigation techniques in microwave radiometry," in *2016 14th Specialist Meeting on Microwave Radiometry and Remote Sensing of the Environment (MicroRad)*. Espoo, Helsinki, Finland: IEEE, apr 2016, pp. 68–70.

[CP24] A. Alonso-Arroyo, J. Querol, A. Camps, R. Onrubia, H. Park, and D. Pascual, "Can we measure Vegetation Water Content and Vegetation Opacity at L-Band with a single GPS Receiver?" in *2016 IEEE International Geoscience and Remote Sensing Symposium (IGARSS)*. Beijing, China: IEEE, jul 2016.

[CP25] A. Camps, H. Park, R. Onrubia, D. Pascual, J. Querol, A. Alonso-Arroyo, J. Benito, A. Andres-Beivide, S. Moreno, X. Ballesteros, M. Segarra, R. Vilaseca,

A. Rius, and M. Martin-Neira, "Altimetric Performace of the GEROS Experiment at the ISS," in *2016 IEEE International Geoscience and Remote Sensing Symposium (IGARSS)*. Beijing, China: IEE, jul 2016.

[CP26] H. Park, A. Camps, D. Pascual, A. Alonso-Arroyo, J. Querol, and R. Onrubia, "Improvement of PAU/PARIS End-to-End Peformance Simulator (P2EPS): Land Scattering Including Topography," in *2016 IEEE International Geoscience and Remote Sensing Symposium (IGARSS)*. Beijing, China: IEEE, jul 2016.

[CP27] H. Park, A. Camps, I. Sekulic, J. M. Rius, D. Pascual, A. Alonso-Arroyo, J. Querol, and R. Onrubia, "Impact of Multi-Path by ISS Structure on GEROS-ISS Measured Waveforms," in *2016 IEEE International Geoscience and Remote Sensing Symposium (IGARSS)*. Beijing, China: IEEE, jul 2016.

[CP28] R. Onrubia, J. Querol, D. Pascual, H. Park, A. Alonso-Arroyo, and A. Camps, "Assessment of DME/TACAN RFI Mitigation Techniques in GNSS-R," in *2016 IEEE International Geoscience and Remote Sensing Symposium (IGARSS)*. Beijing, China: IEEE, jul 2016.

[CP29] D. Pascual, R. Onrubia, J. Querol, A. Alonso-Arroyo, H. Park, and A. Camps, "First Delay Doppler Maps obtained with the Microwave Interferometric Reflectometer (MIR)," in *2016 IEEE International Geoscience and Remote Sensing Symposium (IGARSS)*. Beijing, China: IEEE, jul 2016.

[CP30] D. Pascual, R. Onrubia, J. Querol, H. Park, and A. Camps, "Calibration of GNSS-R receivers with PRN signal injection: Methodology and validation with the microwave interferometric reflectometer (MIR)," in *International Geoscience and Remote Sensing Symposium (IGARSS)*, vol. 2017-July, 2017.

[CP31] R. Onrubia, D. Pascual, J. Querol, H. Park, and A. Camps, "Beamformer characterization of the MIR instrument: The microwave interferometric reflectometer," in *International Geoscience and Remote Sensing Symposium (IGARSS)*, vol. 2017-July, 2017, pp. 5026–5029.

[CP32] J. Castellvi-Esturi, A. Camps, J. Corbera, R. Onrubia, R. Alamús, D. Pascual, J. Querol, and H. Park, "3CAT-3/MOTS, An Experimental Nanosatellite for Multispectral and GNSS-R Earth Observation: Airborne Optical and GNSS-R Campaign," in *2018 IEEE International Geoscience and Remote Sensing Symposium (IGARSS)*, Valencia, Spain, jul 2018.

[CP33] R. Onrubia, D. Pascual, J. Querol, J. Castellvi-Esturi, J. Corbera, H. Park, and A. Camps, "Preliminary altimetry results of the MALYGNSS instrument in the HUMIT project," in *2018 IEEE International Geoscience and Remote Sensing Symposium (IGARSS)*, Valencia, Spain, jul 2018.

[CP34] E. Garbin, J. Querol, R. Píriz, and A. Camps, "Effects of Interference Mitigation in Timing Solutions of GNSS Receivers," in *Proceedings of the 31th International Technical Meeting of The Satellite Division of the Institute of Navigation (ION GNSS+ 2018)*, Tampla, FL, USA, 2018.

Co-directed Final Degree Projects

[DP1] E. M. Julian Ortin, "Real-time radio-frequency interference mitigation system for radio navigation receivers," B.Sc. Thesis, UPC-BarcelonaTech, 2016.

[DP2] D. Kewalramani, "Robust tracking system in front of Radio-Frequency Interferences. Part I: Communications and hyperbolic navigation," B.Sc. Thesis, Universitat Politècnica de Catalunya, 2016.

[DP3] P. J. Cara Reyes, "Robust tracking system in front of Radio-Frequency Interferences. Part II: Transceivers and error estimation," B.Sc. Thesis, Universitat Politècnica de Catalunya, 2016.

[DP4] A. Gil Sorribes, "Robust Tracking System in front of Radio-Frequency Interferences. Part III: Signals, Modulations, and Reliability analysis," B.Sc. Thesis, Universitat Politècnica de Catalunya, 2016.

[DP5] J. J. Gómez López, "Control of the back-end and positioning systems of the MERITXELL radiometer," B.Sc. Thesis, Universitat Politècnica de Catalunya, 2017.